

REF. FILE CODE

SANDIA REPORT

SAND88-2473C • U-13

Unlimited Release

Printed October 1988

AD-A214 579

59th

Shock and Vibration Symposium

Volume II

DTIC
ELECTE
NOV 07 1989
S B D
Co

Prepared by

Sandia National Laboratories

Albuquerque, New Mexico 87185 and Livermore, California 94550

for the United States Department of Energy

under Contract DE-AC04-76DP00789

Proceedings of a conference sponsored by
The Department of Defense and
The Department of Energy
held in Albuquerque, New Mexico
October 18-20, 1988

DISTRIBUTION STATEMENT A

**Approved for public release;
Distribution Unlimited**

SF2900Q(8-81)

89 11 06 036

SAND88-2473C
Unlimited Release

Distribution
Category UC-13

59th Shock and Vibration Symposium

Volume II

**Proceedings of a conference sponsored by
The Department of Defense and
The Department of Energy
held in Albuquerque, New Mexico
October 18-20, 1988**



Sandia National Laboratories

SYMPOSIUM MANAGEMENT

Host Representatives:

Mr. David O. Smallwood - Sandia National Laboratories
Mr. Rodney G. Galloway - Air Force Weapons Laboratory

Contract Management:

Mr. David O. Smallwood - Sandia National Laboratories

SYMPOSIUM MANAGER

Henry C. Pusey
4193 Sudley Road
Haymarket, VA 22069

REGISTRATION MANAGER

Sallie C. Pusey

59TH SYMPOSIUM PROGRAM COMMITTEE

Lt. C-M Carlin, USN
Defense Nuclear Agency
SPWE
6801 Telegraph Road
Alexandria, VA 22310

Rodney G. Galloway
U.S. Air Force
AFWL/NTES
Kirtland AFB, NM 87117-6008

J. Scott Milne
NASA/GSFC
M/C 302
Greenbelt, MD 20771

Jerome Pearson
U.S. Air Force
AFWAL/FIBG
Wright-Patterson AFB, OH 45433

John A. Robinson
U.S. Army Combat Systems Test Act.
STECS-EN-EV
Aberdeen Proving Ground, MD 21005

Lt. Col. Al Schenker
Defense Nuclear Agency
TTST
Kirtland AFB, NM 87115-5000

David O. Smallwood
Sandia National Laboratories
Division 7544
P.O. Box 5800
Albuquerque, NM 87185

Rudolph H. Volin
Naval Research Laboratory
Code 6337
Washington, DC 20375



COMPILATION OF PROCEEDINGS

Henry C. Pusey
Sallie C. Pusey

PRODUCTION OF PROCEEDINGS

Vibration Institute

Accession For	
NTIS GRA&I	<input checked="checked" type="checkbox"/>
DTIC TAB	<input type="checkbox"/>
Unannounced	<input type="checkbox"/>
Justification	
By	
Distribution/	
Availability Codes	
Dist	Avail and/or Special
A-1	

TABLE OF CONTENTS

Papers Appearing in Volume II

DYNAMIC TESTING	1
STAR 63F Q-3 Qualification Vibration Test	
B. G. Johnson	3
Correlation Between Vibration and Computer Operator Response Onboard a UH-1H Helicopter	
G. O. White	27
Shaker Shock Testing Using Nonstationary Random Transients	
T. L. Paez and T. J. Baca	57
and High Velocity Impact Testing of an Accident Resistant Container Using a Large Centrifuge	
J. R. Garcia and R. L. Weatherbee	73
SHOCK	89
Pyrotechnic Shock Data Reduction Procedures and Problems	
H. D. Riead	91
Time Domain Analysis of Pyrotechnic Shock Utilizing Resonant Beam Test Apparatus	
F. Ehorn	105
Equipment Limitations in Pyrotechnic Shock Testing	
J. W. Rehard and J. Czajkowski	119
Shock Response Spectrum Anomalies Which Occur Due to Imperfections in the Data	
R. G. Bell and N. T. Davie	145
A Fourier Transform for Almost Any Number of Data Points With Reasonable Run-Times	
J. B. Cheek	165
Shock Spectrum for Classes of Excitations	
W. D. Pilkey and M. Rosenstein	171
A Technical Procedure for the Optimum Shock Hardening of Aircraft Support Equipment	
W. R. Lauderdale, D. Croce and B. C. McNaught	185
and Boundary Integral Technique for Explosion Bubble Collapse Analysis	
S. A. Wilkerson	209
DYNAMIC ANALYSIS	239
Modeling of Vibration Transmission in a Damped Beam Structure Using Statistical Energy Analysis	
S. S. Sattinger	241
Solar Array Deployment Nonlinear Dynamics Analysis	
R. A. Mills	255
Experimental Observations of Low and Zero Gravity Nonlinear Fluid-Spacecraft Dynamics	
L. D. Peterson	269
Vibratory System Dynamic Analysis Using a Graphics Based Self-Formulating Program	
J. Alanoly and S. Sankar	293
Design of Upper Atmosphere Research Satellite (UARS) Using Transient Loads Analysis	
S. Mittal, M. Garnek and C. Stahle	303
Analytical Approaches for Determining Effective Weights Used in the Method of Weighted Accelerations for Force Measurements	
T. J. Kreitinger, M. Wang and H. L. Schreyer	315
Shock Response of a Mine Hunter Due to Sea Ground Mine Explosions	
Numerical Simulations	
W. E. Pfrang, H. Lütje and J. Freercks	337

An Analysis of Newmark Beta Integration for Structural Dynamics	
R. L. Bort	353
Response of Nonlinear Continuous Systems Subjected to Transient Loads:	
An Analytical Approach	
S. C. Sinha	361
Influence of Elastic Coating on the Plastic Deformation of a Beam in Water Subjected to a	
Shock Wave	
A. L. Stiehl and R. C. Haberman	377
Approximate Method for Predicting the Permanent Set in a Circular Plate in	
Water Subjected to a Shock Wave	
A. L. Stiehl and R. C. Haberman	387
Computer Code SPIDS; Shock Propagation in Durtig System	
R. H. Fashbaugh and T. C. Knight	397

Papers Appearing in Volume I

FEATURED PAPERS

Development Testing at Sandia

D. M. Olson

The Quest for $\omega = \sqrt{K/M}$: Notes on the Development of Vibration Analysis

N. F. Rieger

Statistical Energy Analysis: An Overview of Its Development and Engineering Applications

J. E. Manning

DATA BASES

DOE/DOD Environmental Data Bank

C. A. Davidson

GREEDI - The Computerization of the DOE/DOD Environmental Data Bank

C. R. Adams and E. M. Kephart

A Shock and Vibration Database for Military Equipment

R. A. McKinnon

Vibration Data Base for Aircraft and Its Application

M. T. Orth

VIBROACOUSTIC PAYLOAD ENVIRONMENT PREDICTION SYSTEM (VAPEPS)

The Importance of Non-Resonant and Inplane Vibration Transmission in
Statistical Energy Analysis

R. E. Powell and J. E. Manning

Vibroacoustic Response Using the Finite Element Method and Statistical Energy Analysis

F. L. Gloyna

Study of Helium Effect on Spacecraft Random Vibration with VAPEPS Program

Y. A. Lee

Validation of LACE Spacecraft Vibroacoustic Prediction Model

A. A. Salzberg

Comparison of VAPEPS Predictions with IUS Vibroacoustic Data

C. J. Beck

DYNAMIC MEASUREMENT

Prediction and Measurement of the Acoustic Environment of the Airborne Seeker Evaluation
Test System

L. L. Shaw and K. R. Wentz

PVDF Applications in Shock and Vibration Measurements and Control

L. M. Lee, J. P. Berhault, J. P. Chambard and F. Bauer

Inertial Reference and Tracking System for the Measurement of Blast Induced Displacements

P. H. Frisch and R. Pearson

Mechanical Shock Sensors (A Feasibility Study)

D. Frommer, M. Gross and D. Heller

Built-In Mechanical Filter in a Shock Accelerometer

A. S. Chu

Mechanical Impedance Measurements Using Oblique Excitation

L. J. Nucci and J. R. Reed

DYNAMIC CRITERIA

Simulating Vehicle Dynamics: The Importance of a Valid Forcing Function

G. L. Ferguson

Underlying Assumptions in the Development of Tracked Vehicle Vibration Schedules

W. H. Connon, III

Structural Response and Cosmetic Cracking in Residences from Surface Mine Blasting

D. E. Sis'ind and M. S. Stagg

MODAL APPLICATIONS

Using Modal Testing to Identify Dynamic Changes in Battle Damaged F-16 Wings

A. B. Pacia

Modal Identification Using Solid Rocket Motor Static Firing Data - A Case Without Knowing the External Excitation

C. F. Chang and D. Mason

Nonlinear Systems in Vibration

E. G. Endebrock and N. F. Hunter, Jr.

Papers Appearing in Volume III

MACHINERY VIBRATION

Some Recent Contributions to Mechanical Signature Analysis

R. L. Eshleman

High Frequency Vibration Analysis for Rotating Equipment and Piping Systems

R. M. Jones

Diagnosing Problems in Modern 2-Pole Induction Motors

R. M. Kolodziej

Absolute Ball Bearing Wear Measurements from SSME Turbopump Dynamic Signals

M. J. Hine

Spectral Normalizing

B. Lundgaard and S. B. Stocking

Kinematics of a Flexible Length Redundant Robotic Arm

A. Choudhury and J. Genin

VIBRATION CONTROL

Optimization of a Five-Parameter Nonlinear Shock Mount

N. A. Roy and V. H. Neubert

Active Damping Design of Flexible Structures Based on Non Collocated Sensor-Actuator Velocity Feedback

Q. Zhang, S. Shelley X. N. Lou and R. J. Allemang

Relating Material Properties and Wave Effects in Vibration Isolators

M. C. Reid, S. O. Oyadiji and G. R. Tomlinson

Compensation for Actuator Dynamic Effects Using Model Following Adaptive Control

Q. Zhang, S. Shelley, D. L. Brown and G. L. Slater

Damping and Vibration Control of Unidirectional Composite Beams Using Add-on Viscoelastic Materials

C. T. Sun, B. V. Sankar and V. S. Rao

Creep and Load-Deflection Characteristics of Rubber Element for Vibration Control Devices

E. I. Rivin and B. S. Lee

AIRBLAST

Envelope Models for Finding the Response of Structures in Blast Waves

S. J. C. Dyne and J. K. Hammon

Dynamic Nonlinear Frame Analysis for Blast and Shock

L. M. Bryant, S. D. Campbell and D. Nebuda

Behavior of a Reinforced Concrete Blast Shelter in an Overload Environment

T. R. Slawson and J. L. Davis

Shelter Response in a Simulated 8-KT Nuclear Blast Environment

R. L. Holmes, S. C. Woodson and T. R. Slawson

Blast Induced Liquefaction Field Explosive Tests

H. A. Hassen and W. A. Charlie

GUNS AND PROJECTILES

Wave Coupling and Resonance in Gun Tubes

T. E. Simkins

The Blast Field Produced by a Cannon Having a Perforated Muzzle Brake

G.C. Carofano

Lagrangian Modelling of Blunt Projectile Impacts Against Thick Plates

J. C. Schulz and O. E. R. Heimdahl

Analytical Estimate of Artillery Projectile Balloting Load Based Upon Correlation with Strain Gage Test Data

A. Meyer

Papers Expected to Appear in Volume IV

FEATURED PAPERS

Keynote Address: Estimating Effectiveness

D. Greenlee

Validation Testing of Nuclear Survivable Systems

E. Sevin

VIBROACOUSTIC PAYLOAD ENVIRONMENT PREDICTION SYSTEM (VAPEPS)

Using the VAPEPS Program to Support the TOPEX Spacecraft Design Effort

T. D. Scharton and D. L. Kern

Statistical Energy Analysis Modeling of Nonstructural Mass on Lightweight Equipment Panels

Using the VAPEPS Program

M. L. Slay

Stress Estimation and Statistical Energy Analysis of the Magellan Spacecraft Solar Array

Using the VAPEPS Program

G. A. Badilla and V. C. Thomas

DYNAMIC MEASUREMENT

An Automated Vibration Transducer Calibration System Using Advanced FFT Techniques

E. Schonthal and T. R. Licht

DYNAMIC CRITERIA

Avionics Environmental Reliability (Vibration)

A. Bhungalia

Seismic and Cultural Vibration Levels in Search of a New Advanced Test Laboratory

M. E. Rhine and C. H. Barker

MODAL APPLICATIONS

Structural Verification Using Modal Frequency Testing: A Nondestructive Evaluation

T. F. Prouillard, D. N. Iklé and D. K. Gustaveson

Modal Analysis and Testing of Layered Shell Structures

D. R. Martinez and A. R. Nord

Model Validation Using Substructure Modal-Testing, Applied to a Large and Very Flexible Wind Turbine

T. G. Carne, J. P. Lauffer, A. J. Gomez and T. D. Ashwill

Analytical Estimation of Earth Penetrator Structural Response and Comparison with Laboratory Shock and Modal Test Data

R. J. Kipp and V. I. Bateman

SHOCK

High Impact Shock to Piping

B. J. Scavuzzo and P. C. Lam

DYNAMIC ANALYSIS

Bubble Jet Calculations Using the DYSMAS/E Finite Difference Code

S. A. Wilkerson and H. Schittke

Convergence of Finite Element Frequency Analysis for a Thin Walled Cylinder

J. M. Santiago and H. L. Wisniewski

Integral Method for Free Edge Plates with Stiffeners

B. P. Wang and S. Nomura

VIBRATION CONTROL

Shock Isolation Using an Active Magnetostrictive Element

R. S. Reed

Prediction of Modal Characteristics and Harmonic Response of Viscoelastically Damped Structures

M. Lallanne, H. T. Zhou, J. Der Hagopian and G. Ferraris

AIRBLAST

The Effects of Heavy Tungsten Casings on the Airblast Characteristics of a Cylindrical Charge

K. A. Marchand and L. M. Vargas

DYNAMIC TESTING

STAR 63F Q-3 QUALIFICATION VIBRATION TEST

B. G. Johnson
Morton Thiokol, Inc.
Strategic Operations
Brigham City, UT

INTRODUCTION

Morton Thiokol, Inc. recently completed qualification of the STAR 63F space motor design. This is a 63-in. diameter, 10,156-lb solid rocket motor for spacecraft insertion into a geostationary transfer orbit. The motor was qualified for use in the Space Transportation System (STS) and the Titan (ELV) launch vehicles. Among other things, qualification of this design required a rigorous sinusoidal and random vibration test which fully exercised the motor's structural capability. This was most evident following the STAR 63F Q-3 motor vibration test where delaminations were found in the motor's composite case and one of the redundant ignition propagation cords (IPC) failed on the first attempt to fire the motor. Case delaminations were determined by analysis to show positive margins and therefore to be noncritical to the motor's operation. The motor was then successfully static test fired using the second IPC.

The significance of the STAR 63F Q-3 vibration test is that it drove the motor design to the threshold of its capability without causing motor failure. Dynamic environments seldom drive the design of solid rocket motors. This is an ideal condition for finding the structural dynamic capabilities of the system and is an informative benchmark in the relatively new field of space motor design.

This paper documents the important structural features of the STAR 63F motor design, the Q-3 vibration test procedure, and details of the motor damage. It contains the simulated load response levels responsible for the case delaminations and the predicted failure mode of the primary IPC. The paper then discusses how the damage affected motor qualification and, most importantly, the value of these test results relative to the future testing of space motors.

SUMMARY AND CONCLUSION

The STAR 63F Q-3 vibration test was very rigorous. The test exercised the case design close to the limit of its capability causing minor delaminations which were not critical to the operation of the motor. The test also contributed to the failure of one of the two redundant ignition propagation cords (IPC), which was corrected by a change in installation procedures. Successful operation of the Q-3 motor was still achieved using the second IPC.

This vibration test was beneficial because it identified an IPC installation problem that was not formerly known. The test also served as an excellent indicator of the case structural dynamic capabilities. Simulated load response levels on the aft polar boss of the motor that are responsible for the case aft dome delaminations are listed in Table I. Knowing the STAR 63F dynamic load capabilities at the aft polar boss and the damage mode will be of great value in designing and testing future rocket motors.

Table I. Simulated STAR 63F Lateral Axis Vibration Testing
Aft Polar Boss Peak Load Response Levels

	<u>Axial (lb)</u>	<u>Lateral (lb)</u>	<u>Moment (in.-lb)</u>
Sinusoidal	3,970	5,270	184,000
Random	3,610	1,860	64,000

Knowing the severity of this test, there is some concern regarding the necessity of the STAR 63F qualification vibration requirements. A slight overtest is generally desirable during qualification testing. However, when the test begins to drive the motor design, an overly conservative test could be costly. The STAR 63F design did successfully endure this vibration test, making it an excellent engineering evaluation test. In future solid rocket space motor designs, it is recommended that the specified vibration test requirements be given careful consideration to avoid a potentially costly redesign to satisfy unnecessarily high requirements. On the other hand, if the STAR 63F vibration test requirement was not excessive, then future space motor designs desiring larger nozzles may face case design problems in the aft dome polar boss region.

STAR 63 MOTOR STRUCTURAL DESIGN FEATURES

The STAR 63F motor is a solid propellant rocket motor for spacecraft insertion into orbit. The motor is 63 in. in diameter and weighs 10,156 pounds. A cross sectional view of the motor is shown in Figure 1 which identifies many of the motor design features. The principle structural design features of the motor are the case, nozzle and propellant. They will be discussed separately in the following sections.

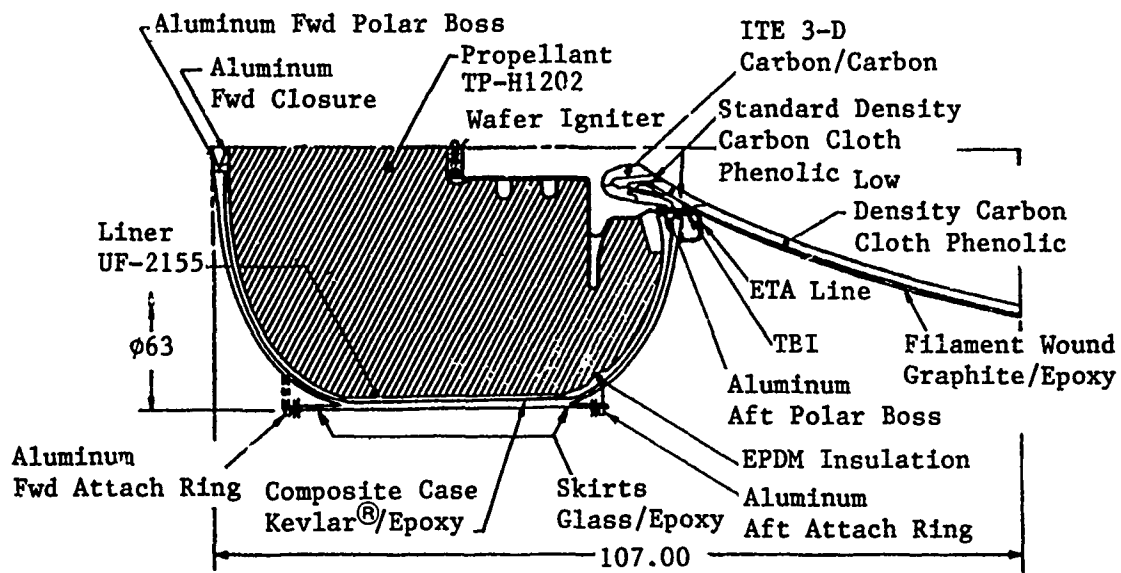


Figure 1. STAR 63F Motor Design Features

Case

The case is a thin-shelled, filament-wound, composite structure (Figure 2). Its primary function is to act as a pressure vessel for containing the high internal pressures while burning. It is composed of Kevlar 49/VF-3299 fiber windings and semi-flex epoxy resin. The case is basically cylindrical in shape with domes on each end. Seven layers of the Kevlar fibers wrap around the motor from the top of the forward dome to top of the aft dome. These are known as the polar layers. They are wrapped in such a way that the winding angle is 90 deg to the motor axis at the top of the domes and 11.5 deg across the cylinder. These 7 polar layers are the only fiber windings in the case domes. The cylindrical portion of the motor also has 23 hoop plies of the Kevlar fiber intermingled with the polar layers. When the case is wound, the fibers are dressed with the epoxy resin which bonds the fibers together resisting interlaminar shear stresses. Skirts have been placed on the forward and aft end of the case for structural interfacing with the motor. They are short extensions of the case cylinder composed of S-2 glass hoop and E-341 glass cloth layers with UF-3298 rigid epoxy. The

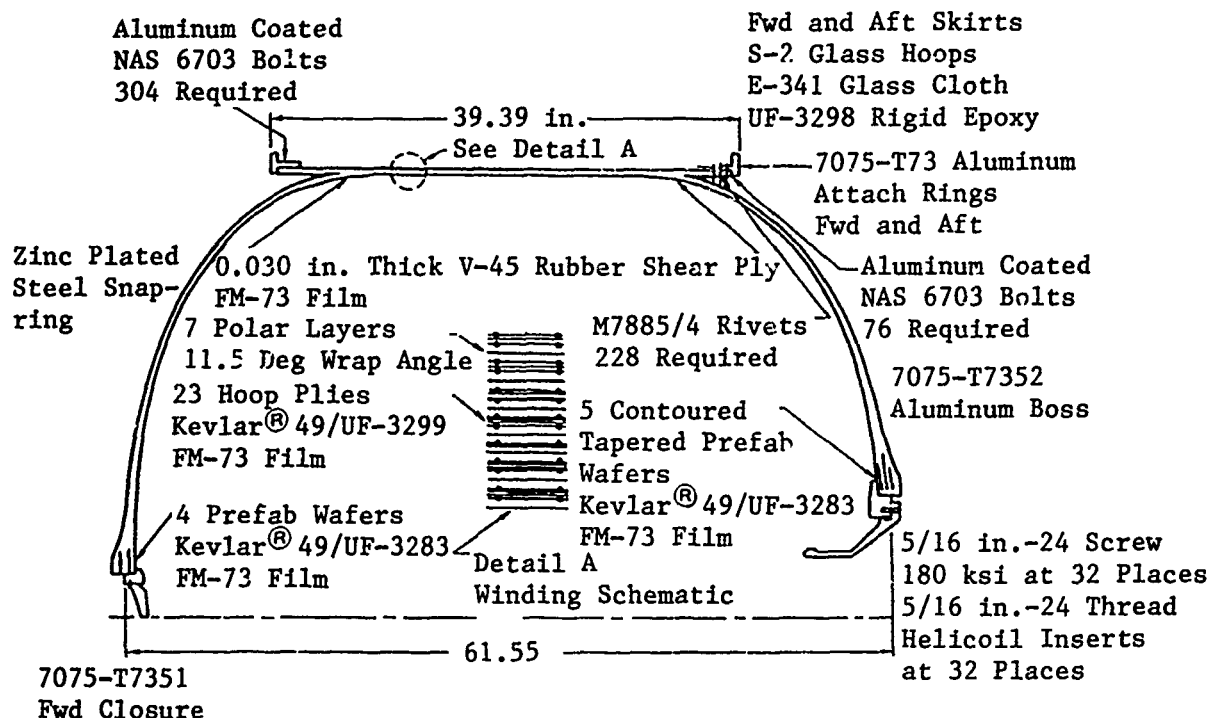


Figure 2. STAR 63F Case Design

skirts are wrapped separate from the pressure vessel and then bonded on with a thin V-45 rubber shear ply. Other parts of the case include the aluminum attach rings bolted and riveted to the ends of each skirt, an aluminum boss and forward closure bonded to the opening at the top of the forward dome and an aluminum boss bonded to the opening in the aft dome for attaching the nozzle.

Nozzle

The STAR 63F motor features a particularly large one-piece nozzle for increased performance (Figure 3). It is a stationary nozzle design (nonvectoring) that attaches to the motor via the case aft boss. The exit cone portion of the nozzle has a thick, carbon cloth, phenolic, inner layer which provides abrasion resistance and thermo protection. This layer also provides some strength and stiffness for the exit cone. Then there is a thin, glass, epoxy, outer layer which provides the majority of the structural capability of the exit cone. The throat region of the nozzle is composed of a variety of materials (aluminum, steel, EPDM-CF, carbon cloth phenolic and 3-D carbon/carbon) which are bonded, bolted, or threaded together.

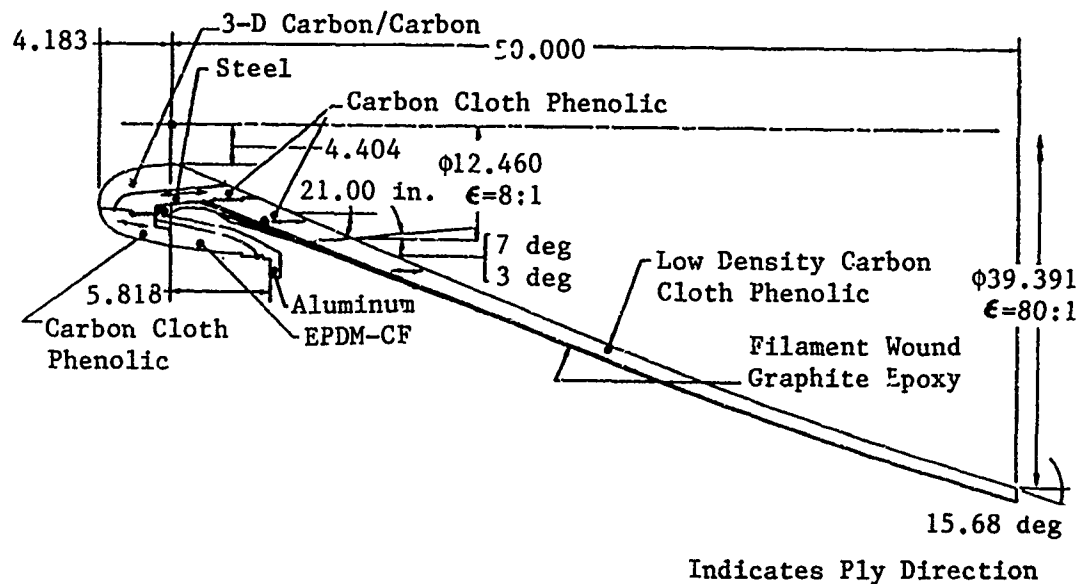


Figure 3. STAR 63F Nozzle Design

Propellant

The STAR 63F motor uses a TP-H1202 propellant which is cast in the case as shown in Figure 1. When cured, the propellant is a flexible rubbery solid. Even though the propellant is soft, it is extremely important structurally because of its large volume. It is also a highly damped material which greatly attenuates the structural dynamic response of the motor.

VIBRATION TEST

The vibration test was conducted to qualify the motor design for launch vibration environments. Sinusoidal and random vibration testing was required in both the thrust and lateral axes of the motor. Test configuration, instrumentation, and criteria are all outlined in the following sections (1).

Test Configuration

The STAR 63F vibration test was designed to exercise the motor in a fixed forward skirt/free aft skirt condition. This was done by installing the motor in a nozzle-up configuration on a vibration fixture with the forward skirt securely bolted to the fixture. The fixture with the motor was then driven by two Ling Electro Dynamic Shakers as shown in Figures 4 and 5 for thrust and lateral axis excitation, respectively. Motor orientation with respect to the axes of excitation shown in Figures 4 and 5 is shown in Figure 6.

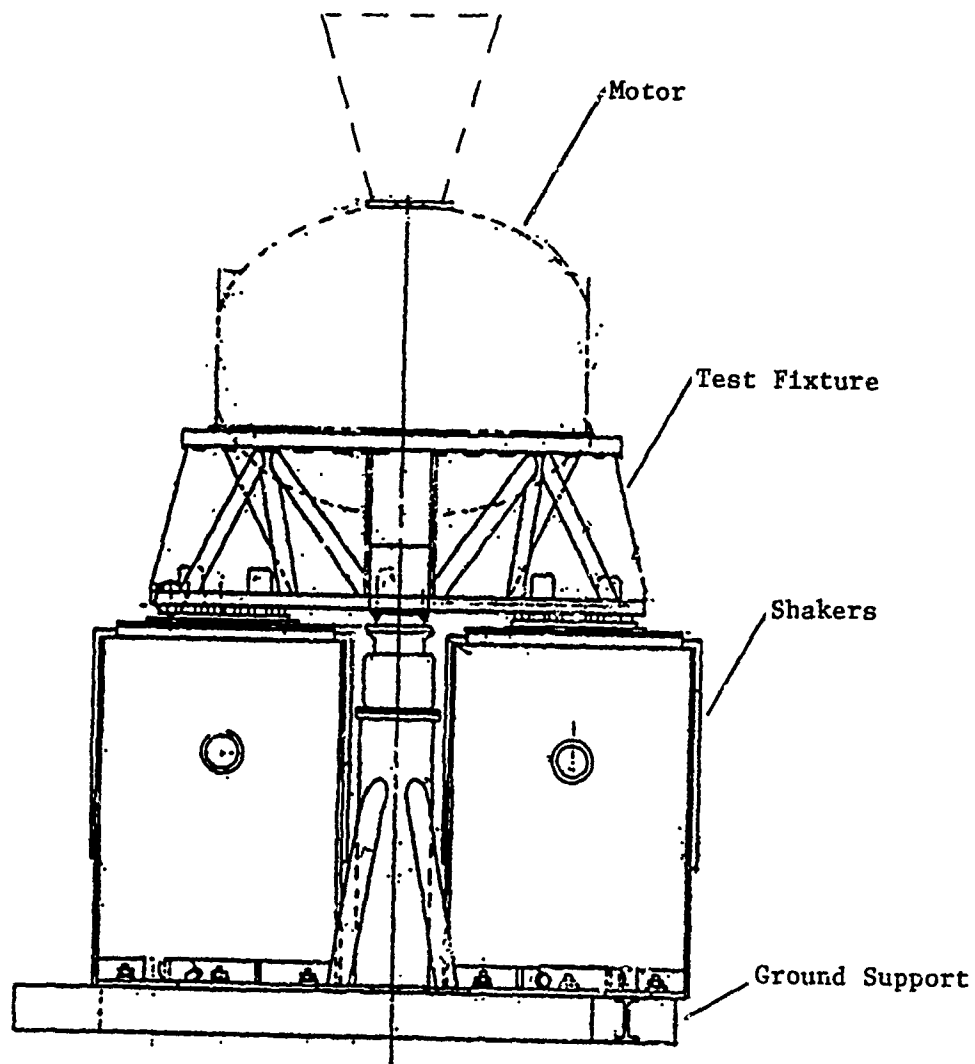


Figure 4. Vibration Test Arrangement
for Thrust (Z-Axis) Excitation

Instrumentation

Instrumentation was installed on the motor and monitored per Table II and located in accordance with Figure 7.

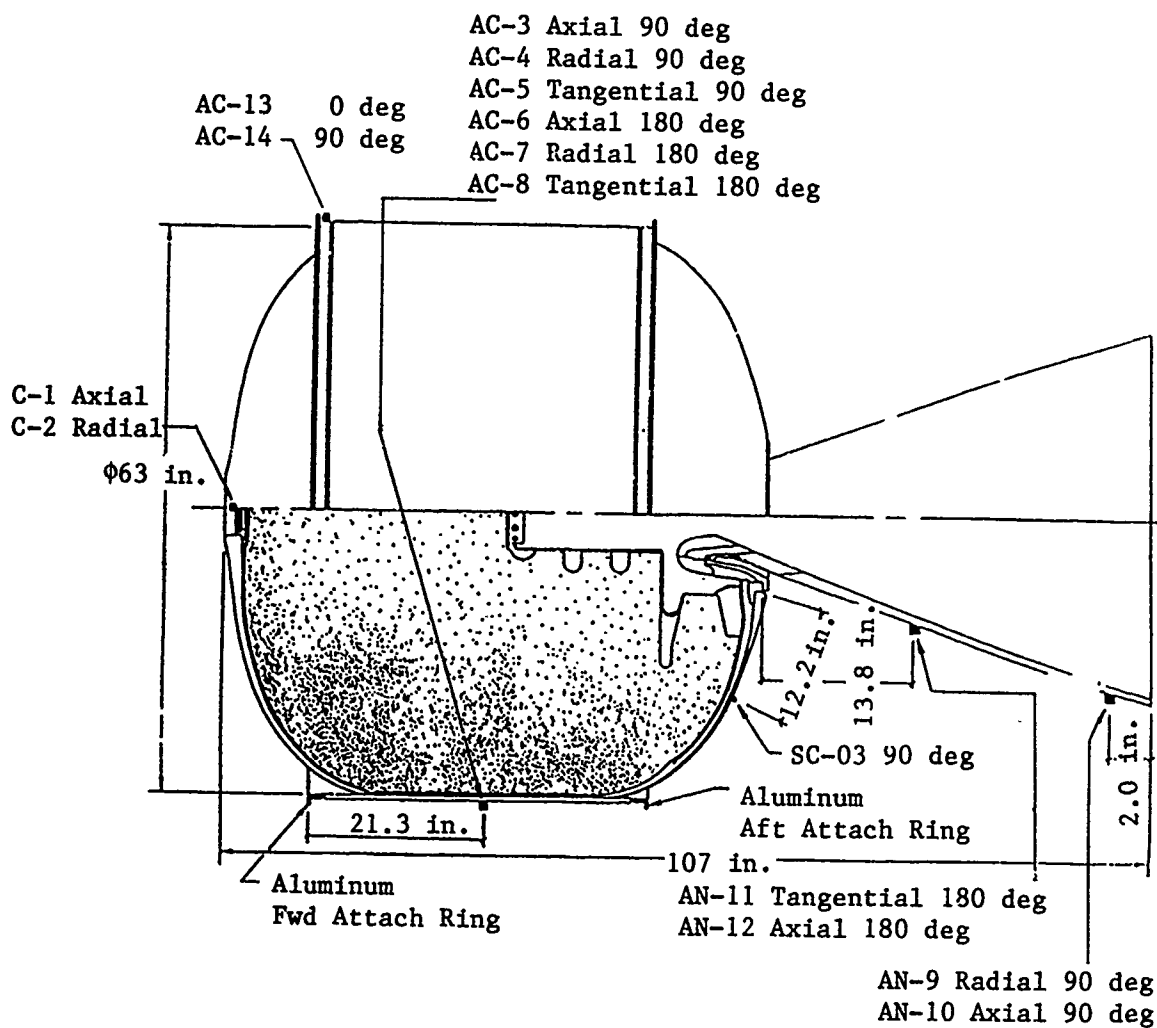


Figure 7. Instrumentation Location

Table II. Instrumentation List

<u>Accelerometers</u>	<u>Expected Range (g)</u>	<u>Required Accuracy (%)</u>	<u>Recording FM - Oscill.</u>	<u>Direction</u>	<u>Description</u>
AC-1	±20	±5	2KHz	A	Accel, Case Fwd Closure
AC-2	±20	±5	2KHz	R	Accel, Case Fwd Closure
AC-3	±20	±5	2KHz	A	Accel, Case Cylinder 90 deg
AC-4	±10	±5	2KHz	R	Accel, Case Cylinder 90 deg
AC-5	±10	±5	2KHz	T	Accel, Case Cylinder 90 deg
AC-6	±20	±5	2KHz	A	Accel, Case Cylinder 180 deg
AC-7	±10	±5	2KHz	R	Accel, Case Cylinder 180 deg
AC-8	±10	±5	2KHz	T	Accel, Case Cylinder 180 deg
AC-9	±100	±5	2KHz	R	Accel, Nozzle Exit Cone 90 deg
AC-10	±50	±5	2KHz	A	Accel, Nozzle Exit Cone 90 deg
AC-11	±50	±5	2KHz	T	Accel, Nozzle Exit Cone 180 deg
AC-12	±50	±5	2KHz	A	Accel, Nozzle Exit Cone 180 deg
AC-13	±10	±5	2KHz	Control	Accel, Input Control Fwd Skirt Ring 0 deg
AC-14	±10	±5	2KHz	Control	Accel, Input Control Fwd Skirt Ring 90 deg
SC-03	±2,000 μ in./in.	±5	2KHz	A	Strain, Aft Dome 90 deg (exterior)

Test Qualification Criteria

The STAR 63F vibration test was conducted according to the following criteria.

Thrust Axis Sine Test. The criteria for thrust axis sine vibration were:

<u>Frequency</u>	<u>Level</u>
5-55 Hz	1.2 G _{o-p}
Sweep Rate = 2 Octaves/Minute	

Lateral Axis Sine Test. The criteria for lateral axis sine vibration were:

<u>Frequency</u>	<u>Level</u>
5-55 Hz	1.2 G _{o-p}
Sweep Rate = 2 Octaves/Minute	

Thrust Axis Random Test. The criteria for thrust axis random vibration were:

<u>Frequency</u>	<u>Level</u>
20-2000 Hz	0.04 G ² /Hz
Grms = 8.9	
Duration = 120 Seconds	

Lateral Axis Random Test. The criteria for lateral axis random vibration were:

<u>Frequency</u>	<u>Level</u>
20-30 Hz	0.013 G ² /Hz
30-50 Hz	+6.14 dB/Oct
50-2000 Hz	0.04 G ² /Hz
Grms = 8.79	
Duration = 120 Seconds	

MOTOR DAMAGE

Pretest analysis provided ample warning that this vibration test would tax the capabilities of the STAR 63F motor, especially in the aft polar boss region. Every effort was made to protect the motor and ensure a successful test. This included careful monitoring of the test with response limiting gages to guard against overloading the motor and pre-approved notching of the random vibration test criteria. In spite of the efforts to protect the motor, there was still minor damage done to the case aft dome and one of the two redundant IPCs.

Case Aft Dome

X-rays of the motor showed case aft dome delaminations near the polar boss from 0 deg to 180 deg. Figure 8 shows the general nature of the delaminations. In the figure, the numbered lines with arrow heads on them represent the seven Kevlar/epoxy polar wraps which entirely make up the case domes. The heavier dark lines represent Kevlar wafers placed in the matrix to provide meridional stiffness near the aft polar boss. As shown, the delaminations occurred in the first filament wound layer. Figure 9 shows the extent of case delamination identified by X-rays at 30-deg increments circumferentially around the motor (2).

Ignition Propagation Cord

The IPC is 1/8 in. in diameter and consists of explosive powder encased in lead with a polyethylene sheath on the outside. The IPC transmits a firing signal to the motor igniter starting motor ignition.

The first attempt to static fire the STAR 63F Q-3 motor failed due to the primary IPC's failure to propagate the ignition signal. Figure 10 shows the IPC configuration within the motor and the point beyond which the ignition signal failed to propagate (3). After propagating the signal the IPC disintegrates, making the point of failure quite obvious. Previous testing of the cord demonstrated that nothing short of a sharp 90-deg bend in the line or a complete break and separation of ends would cause propagation failure. The IPC must have been severely damaged in order to prevent signal propagation.

MOTOR RESPONSE

A summary of STAR 63F Q-3 vibration test response levels is given in Table III. This gives the maximum G_{Q-P} and G_{rms} response levels for the accelerometers listed in Table II. Of primary interest here is understanding the motor response modes and levels which caused the motor damage. The structural dynamics of the STAR 63F motor design in the vibration test configuration was studied thoroughly by finite element analysis and modal survey testing. Based on those studies and the vibration test results, the following conclusions were reached regarding the motor structural dynamic response relative to the motor damage (4).

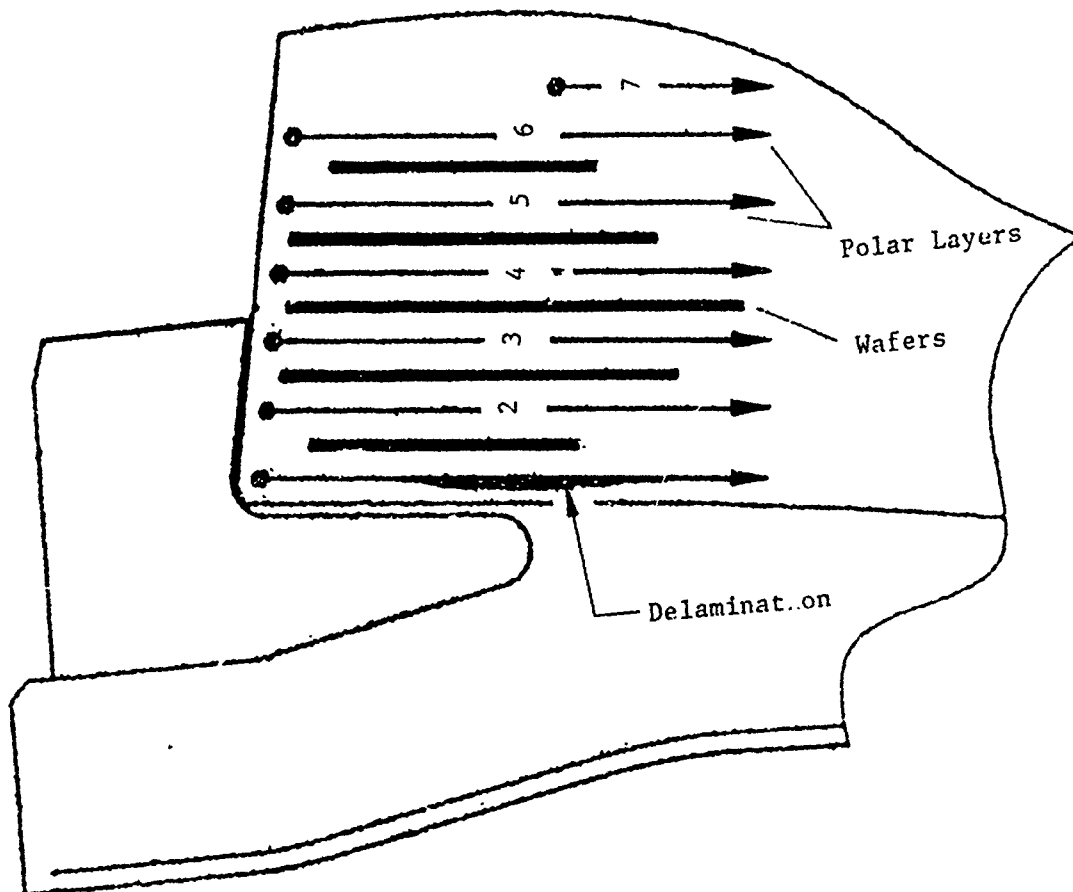
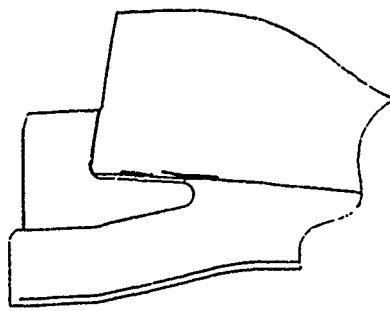
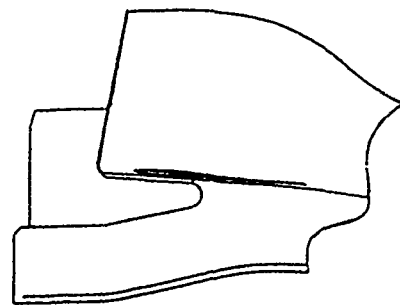


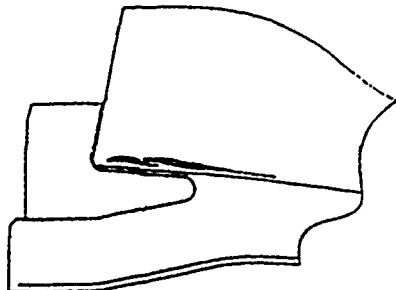
Figure 8. Location of Case Aft Dome Delaminations



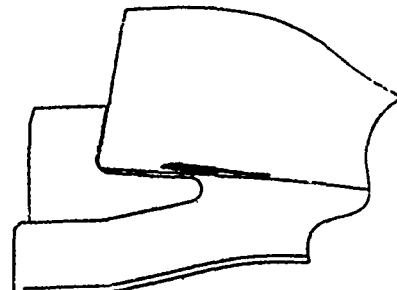
0 Deg



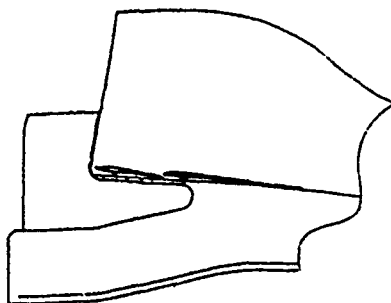
120 Deg



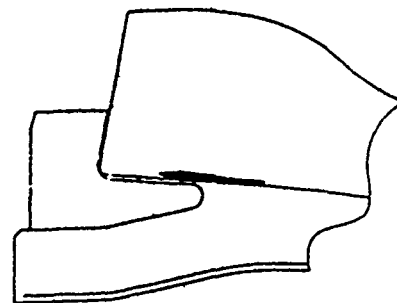
30 Deg



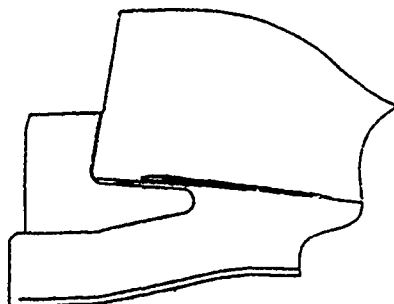
150 Deg



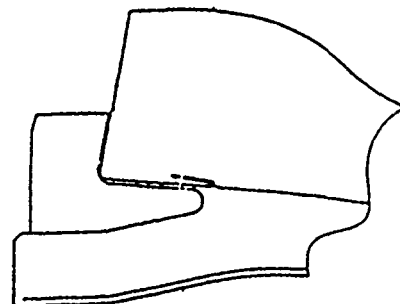
60 Deg



180 Deg



90 Deg



210 Deg

Figure 9. STAR 63F Q-3 X-Ray Sketches of Aft Dome Delaminations

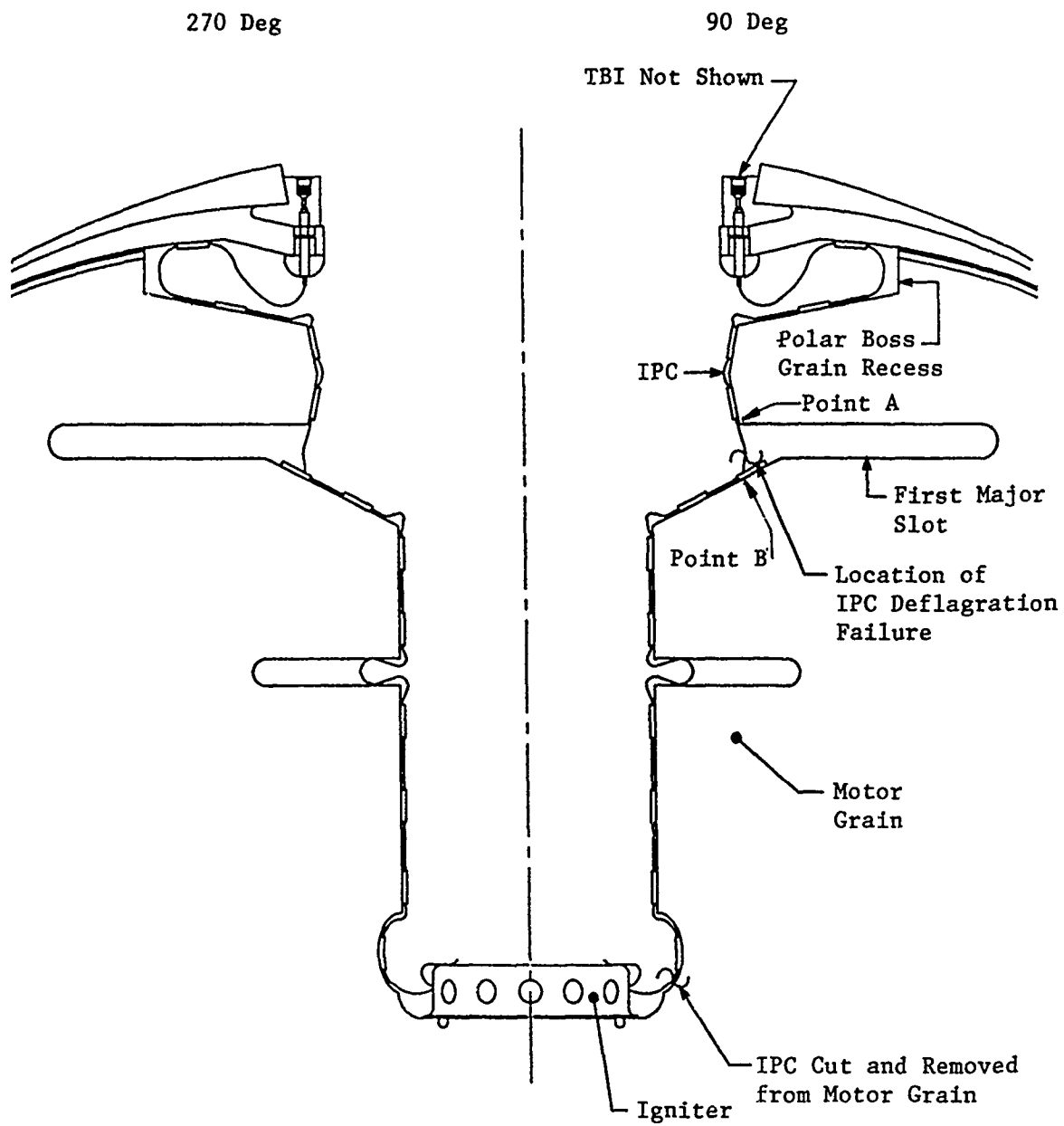


Figure 10. STAR 63F Q-3 IPC Routing Definition

Table III. Summary of STAR 63F Q-3 Vibration Test Response Levels

Accel	Location	Sinusoidal (Max Go-p)				Rando (RMS)			
		Low Level (<100 Hz)		Qual Level (<55 Hz)		Low Level		Qual Level	
		Thrust	Lateral	Thrust	Lateral	Thrust	Lateral	Thrust	Lateral
AC-1	Fwd Closure, Ax	1.27	0.60	3.10	1.45	0.73	0.15	3.51	0.33
AC-2	Fwd Closure, Rad	0.25	2.54	0.46	1.50	0.16	0.67	0.55	3.50
AC-3	Case 90, Ax	0.89	1.96	2.50	3.60	0.72	0.96	3.26	3.08
AC-4	Case 90, Rad	0.60	1.68	0.70	4.76	0.40	0.39	1.50	1.17
AC-5	Case 90, Tan	0.20	0.60	0.50	1.00	0.26	0.28	0.74	0.63
AC-6	Case 180, Ax	0.60	0.60	1.70	0.64	0.90	0.39	3.27	0.89
AC-7	Case 180, Rad	0.40	0.55	0.42	0.80	0.31	0.22	1.11	0.61
AC-8	Case 180, Tan	0.11	1.84	0.25	6.00	0.16	0.33	0.54	0.96
AC-9	Nozzle Exit Plane 180, Rad	1.07	4.40	3.37	51.00	0.39	2.23	1.73	7.18
AC-10	Nozzle Exit Plane 180, Ax	7.53	5.10	24.45	29.00	1.38	1.63	6.49	5.90
AC-11	Nozzle Exit Cone 180, Tan	0.58	11.45	1.90	24.00	0.27	0.63	0.86	2.80
AC-12	Nozzle Exit Cone 180, Ax	6.50	0.98	20.78	8.28	1.18	0.90	5.94	3.55
AC-13	Fwd Skirt Ring 0, Control	0.70	0.62	1.70	1.75	2.08	1.314	7.77	5.20
AC-14	Fwd Skirt Ring 90, Control	0.80	0.70	1.20	1.75	2.51	3.073	9.22	9.44
Average Control		---	0.65	---	1.75	---	2.761	9.29	8.971

Case Aft Dome Delaminations

High response levels in the aft polar boss region were anticipated prior to testing, so when case aft dome delaminations were found, the reasons were well understood. Finite element analysis did a good job of simulating the motors structural response as shown by the simulated nozzle CG response versus measured in Figure 11 (5). Test fixture compliance is primarily responsible for downward frequency shift of the measured resonant peaks. Simulated aft polar boss load response levels for the sine and random vibration testing are listed in Table I. Case stress analysts have a difficult time predicting the stress distribution in the polar boss region, but present information suggests that the simulated 184,000 in.-lb aft polar boss moment from the lateral axis sine vibration testing was enough to cause the delaminations (6). Two low frequency vibration modes were identified as the response drivers. They are the motor fundamental lateral (22.0 Hz) and nozzle/aft dome pitch (27.4 Hz) modes shown in Figure 12. Peak load response occurred at 27.4 Hz in response to the nozzle/dome pitch mode, but the more massive motor fundamental lateral mode, just 5.4 Hz lower in frequency, also provided some load amplification. This can be seen in the simulated lateral sine test response plot for the aft polar boss moment shown in Figure 13. Physically speaking, the geometrically large nozzle and the flexible case aft dome were the reasons for the big load response.

Ignition Propagation Cord Failure

In the case of the IPC failure, cord installation was very important. Figure 10 shows the IPC routing for the STAR 63F Q-3 motor. Every two to four inches, the cord was securely attached to the propellant grain by bonding in 1-in. adhesive clips. Where possible between clips, the cord was bonded to the grain by additional adhesive. The problem with the IPC in the Q-3 motor was that no slack or strain relief was provided in the cord where it crossed over the major slot in the propellant.

Analysis indicates that a great deal of motion takes place in the grain during the vibration test. Table IV lists the predicted grain axial motion of Point A relative to Point B as shown in Figure 10. Peak motion occurred during the axial random vibration test. The simulated relative displacement PSD of this motion is shown in Figure 14. The predominant response mode in Figure 14 is a 44 Hz axial grain response shown in Figure 15. Solid propellant is a rubbery type material and very capable of these kinds of motion. Sinusoidal testing of the failed STAR 63F Q-3 IPC configuration to the 3 axial random vibration level (0.21 in.) at the dominant frequency (44 Hz) produced failure (breaking of the cord) after just a few (2-5) cycles repeatedly (7). Further testing of an IPC configuration with sufficient strain relief showed no sign of fatigue after thousands of cycles at 0.21 in. amplitude and 44 Hz. This information not only provides strong evidence that vibration testing caused the failure of the Q-3 IPC, but also demonstrates the solution to the problem. Q-3 was the only qualification motor with an inadequate strain relief of the IPC over the major slot. The other qual motor (STAR 63F Q-1) with cord installation as shown in Figure 16, had no problems after receiving similar vibration testing.

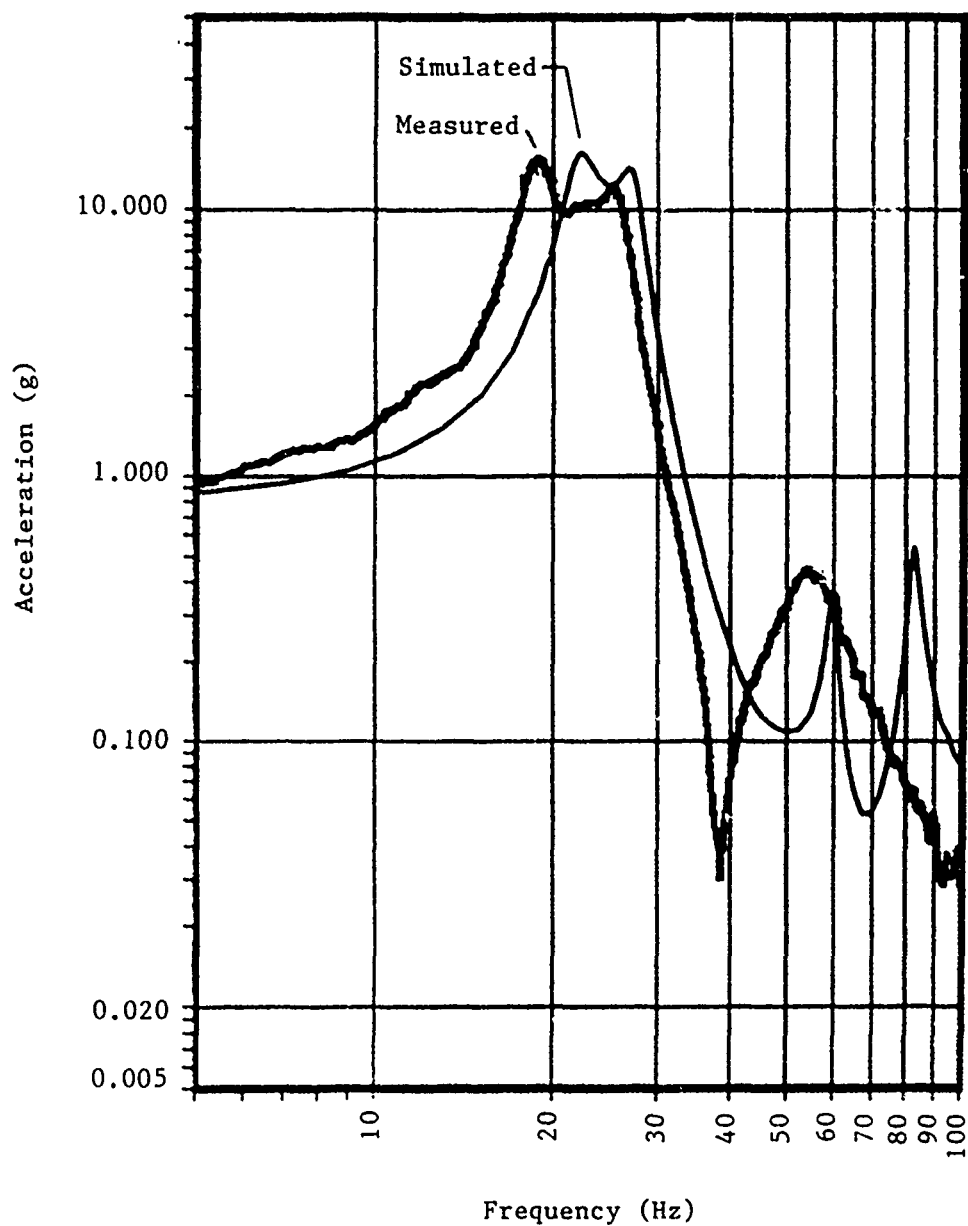
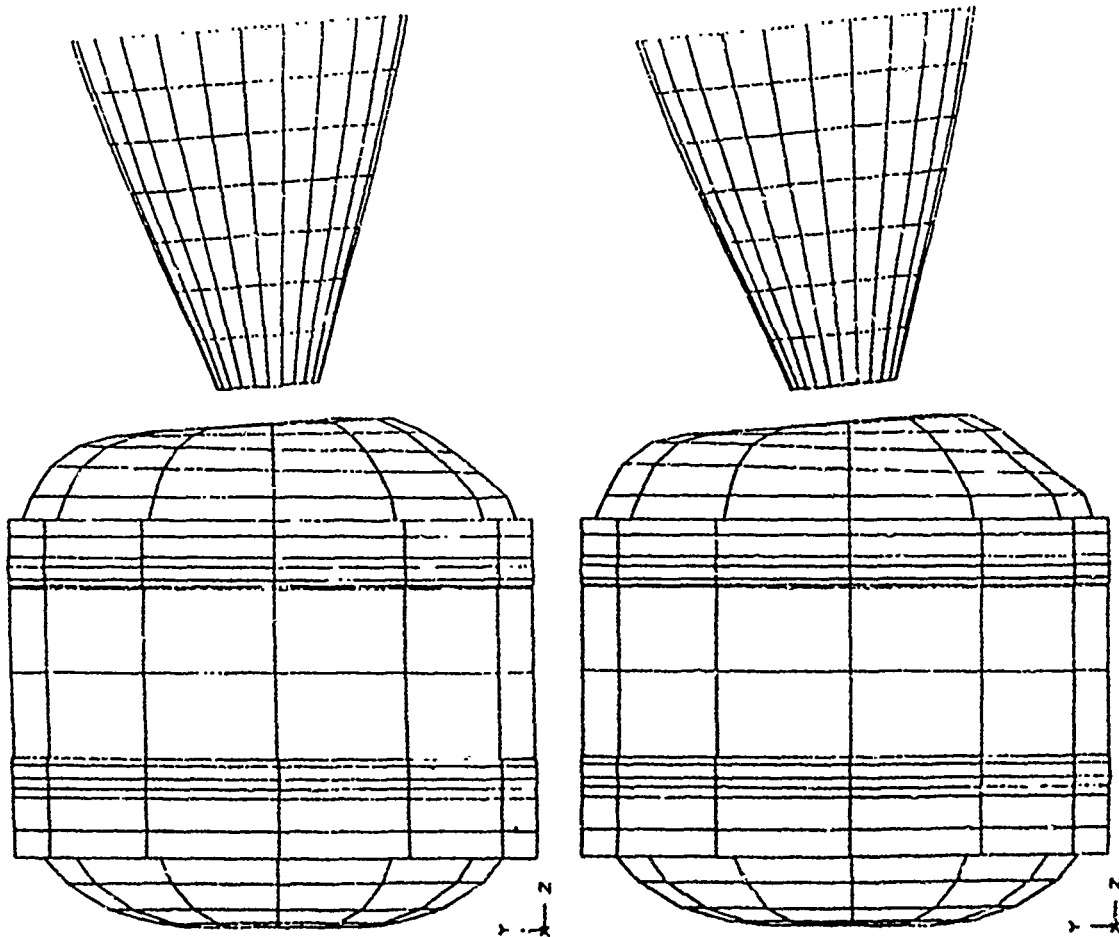


Figure 11. Simulated Versus Measured Lateral Axis Sine Test Nozzle CG Response



Motor Fundamental
Lateral Mode
(22.0 Hz)

Nozzle/Aft Dome Pitch Mode
(27.4 Hz)

Figure 12. Motor Modes of Vibration Responsible for
Case Aft Dome Delaminations

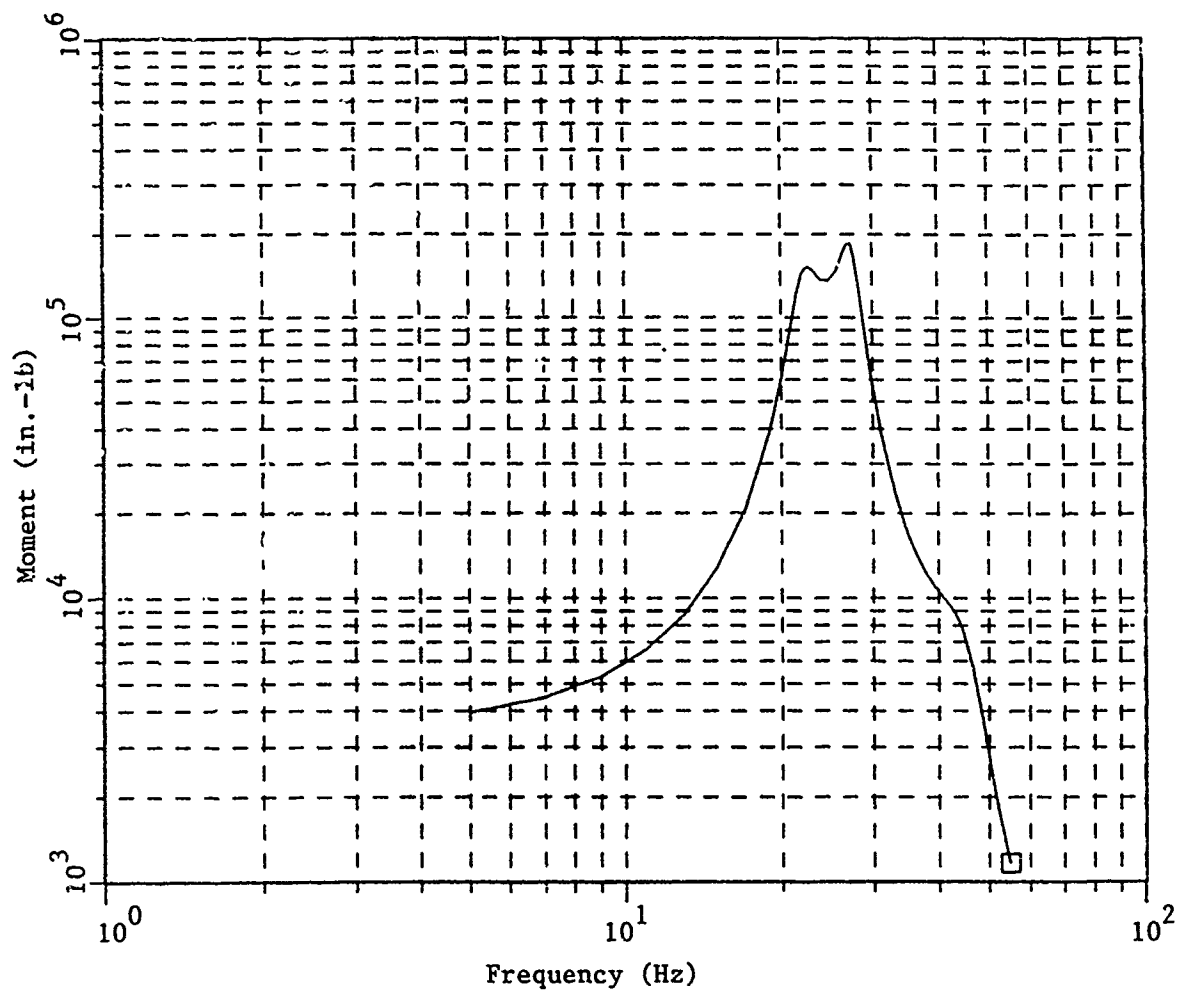


Figure 13. Simulated STAR 63F Q-3 Lateral Sine
Vibration Test Aft Polar Boss Moment Response

Table IV. Simulated STAR 63F Q-3 Grain Relative Axial Displacement Response Levels across the Major Slot

	Vibration Test			
	Random	(3 σ)	Sinusoidal (o-p)	
	<u>Axial</u>	<u>Lateral</u>	<u>Axial</u>	<u>Lateral</u>
Displacement (in.)	0.207	0.057	0.107	0.041
Predominant Frequency (Hz)	44		44	

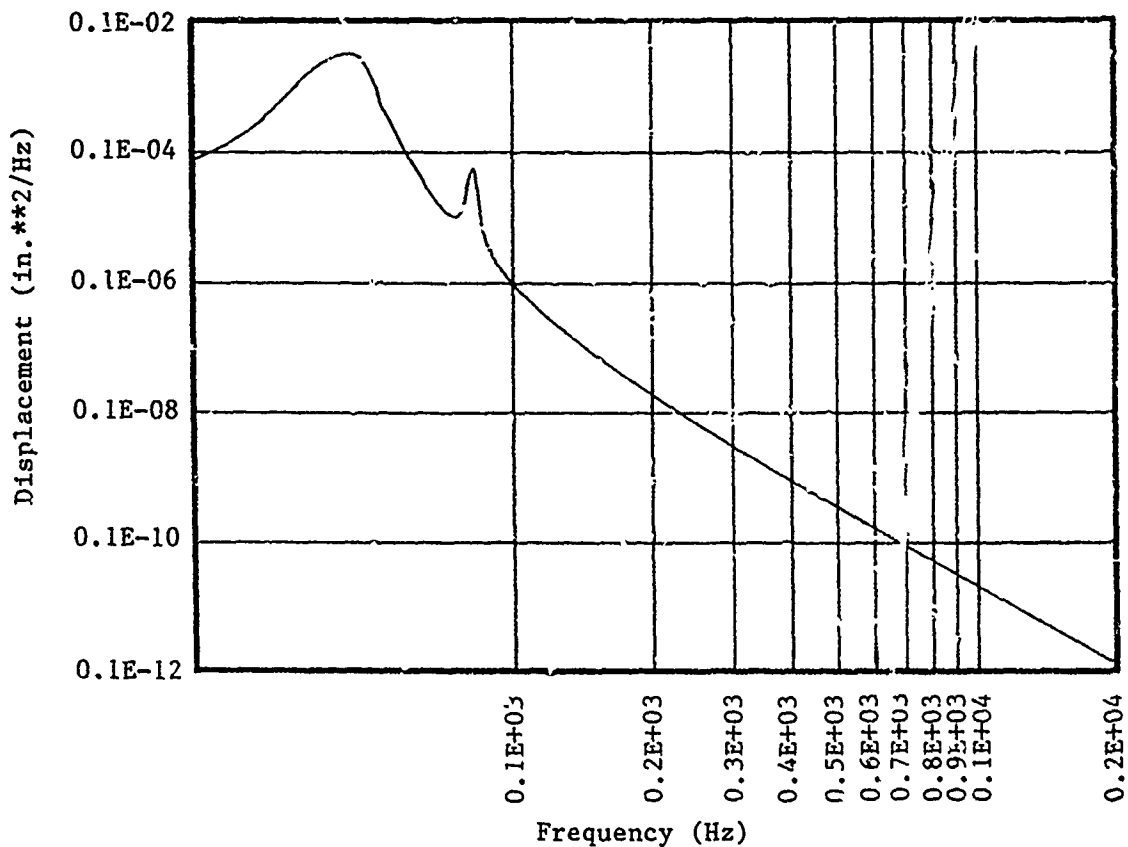


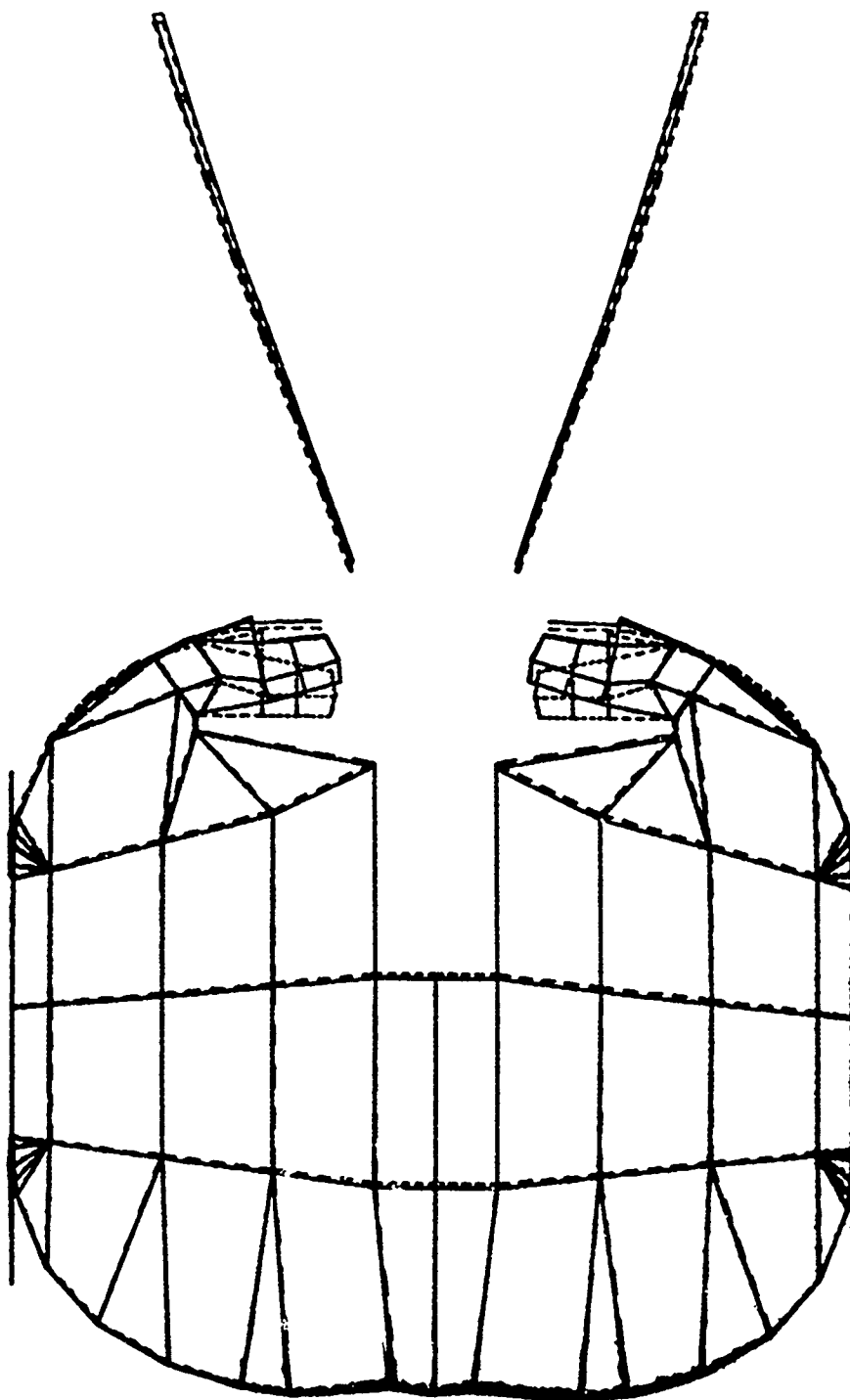
Figure 14. STAR 63F Q-3 Grain Relative Axial Displacement PSD across the Deepest Fin

MOTOR QUALIFICATION

In spite of the damage caused by the vibration testing, the STAR 63F case and IPC design was determined to be successfully qualified.

The case aft dome delaminations were determined to be noncritical to motor operation for the remainder of motor qualification testing (motor static firing). Therefore, qualification testing was completed, which the motor case successfully endured. In addition to successfully completing qualification, it is important to note that the vibration testing may have been excessive. Time and expense dictated that existing fixturing be used to perform this vibration test. Analysis indicates that this fixturing tested the motor in a more severe configuration than the motors operating launch configuration. For this reason, Morton Thiokol, Inc. believes the vibration test exercised the motor beyond those levels required for qualification.

As previously mentioned in the section titled, "Ignition Propagation Cord Failure", the primary IPC failed during vibration because it was installed without adequate strain relief in the line across the major propellant slot (Figure 10). Fortunately, the second IPC functioned properly and the motor was qualified. However, to insure that this problem would not happen again, specific installation procedures have been defined on engineering drawings to install the IPC similar to the STAR 63F Q-1 IPC installation shown in Figure 16.



Grain Axial Mode (44.0 Hz)

Figure 15. Motor Mode of Vibration Primarily Responsible
for IPC Failure

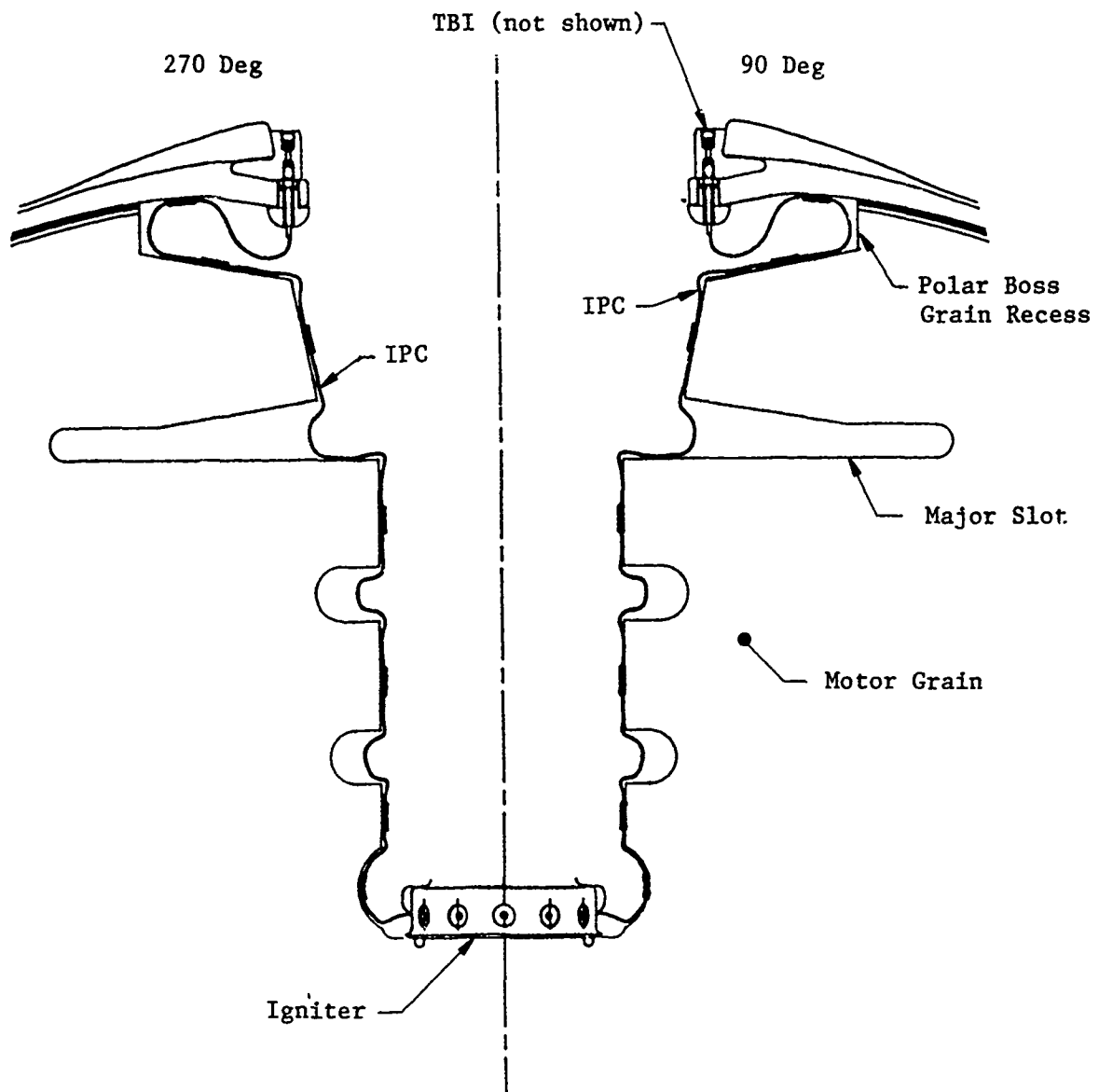


Figure 16. STAR 63F Q-1 IPC Routing Definition

REFERENCES

1. TWR-32839, STAR 63F Qualification Vibration Test Plan, Rev B, 22 February 1988, B. G. Johnson.
2. Presentation, STAR 63F Q-3 Delamination Investigation, 20 April 1988, M. A. Darais.
3. TWR-33033, STAR 63F Rocket Motor Static Test Report Q-03, July 1988, J. T. Wilson.
4. TWR-32740, STAR 63F Structural Dynamics Analysis, 21 July 1987, B. G. Johnson.
5. TWR-33013, STAR 63F Q-3 Vibration Test Report, 12 April 1988, B. G. Johnson.
6. Memo M513:FY89:M013, Delaminations in the Aft Dome Found on X-ray Film Taken After Vibration Testing of STAR 63F Q-3 Motor, 21 July 1988, M. A. Darais.
7. Memo M040:FY88:069, STAR 63F Ignition Propagation Cord Failure Investigation, 27 June 1988, J. T. Wilson.

CORRELATION BETWEEN VIBRATION AND COMPUTER OPERATOR RESPONSE ONBOARD A UH-1H HELICOPTER

**Mr. George O. White
U.S. Army Combat Systems Test Activity
Attn: STECS-EN-EV
Aberdeen Proving Ground, MD 21005-5059**

This paper discusses a test which was conducted to determine if there was any correlation between helicopter vibration and onboard computer operator response. Acceleration data were measured on two computer displays and two seat pads in a UH-1H helicopter. Frequency domain power spectral density (PSD) overlays were created, and two types of ride quality analysis were performed on the data from the seat pad locations. The first ride quality analysis technique involves the integration of PSD data over frequency bands that correspond approximately with those of International Standards Organization (ISO) Standard 2631-1985, and the second technique requires determining the power absorbed (in watts) by the subject seated at the monitored position. These techniques are discussed in some detail. Linear regression and rank correlation analyses were then performed to correlate the operator mean input time with the various types of acceleration data. Examination of the data yields no apparent relationship between onboard computer operator response and acceleration of the computer displays or ride quality measured on the seats on which the computer operators sat in the helicopter. Various plots illustrating this lack of correlation, and tables of the plotted values and their corresponding correlation coefficients, are provided, and the pertinence of the lack of correlation is discussed.

INTRODUCTION

The U.S. Army Combat Systems Test Activity (USACSTA) was tasked by the U.S. Army Human Engineering Laboratory (USAHEL) to provide helicopter in-flight vibration data and to assist in determining whether onboard computer operator response was vibration dependent. This paper is a direct result of that effort.

SYSTEM DESCRIPTION

The UH-1H helicopter (Serial No. 70-16302) used in this testing weighs approximately 2115 kg (4667 lb) empty and 3650 kg (8050 lb) when fully loaded for testing, which includes fuel, equipment, and personnel. The UH-1H has a two-blade semi-rigid main rotor; its fuselage is all metal, semi-monocoque. The Lycoming turboshaft engine, which is mounted in back of the transmission and enclosed in cowlings, is rated at 1044 kW (1400 shp). Both the main and tail rotors are shaft

driven, and the main rotor speed of the UH-1H in flight is between 294 and 324 rpm. The UH-1H has a cruising speed of approximately 204 km/hr (127 mph) and a range of 511 km (318 mi). A photograph of the test helicopter is shown in Figure 1.

TEST PROCEDURE

The UH-1H helicopter was instrumented with six uniaxial piezoresistive accelerometers and two ride quality pads. A ride quality pad is a triaxial piezoresistive accelerometer molded in a semi-rigid rubber disc. A sketch showing specifications for such a disc as recommended by the Society of Automotive Engineers (SAE) Recommended Practice J1013 [1] is provided in Figure 2. The uniaxial accelerometers were mounted on the frames supporting two computer displays which were installed in the helicopter, and the ride quality pads were installed on the seats the computer operators sat upon. The locations of the transducers are described in Table 1, and the locations of the computer display accelerometers are shown in Figures 3 and 4. Notice in Figure 3 that the accelerometers are oriented with respect to the helicopter, not the displays.

TABLE 1. ACCELEROMETER LOCATIONS

<u>Channel</u>	<u>Location, axis</u>
1	Left seat pad, vertical
2	Left seat pad, transverse
3	Left seat pad, longitudinal
4	Right seat pad, vertical
5	Right seat pad, transverse
6	Right seat pad, longitudinal
7	Left display, vertical
8	Left display, transverse
9	Left display, longitudinal
10	Right display, vertical
11	Right display, transverse
12	Right display, longitudinal

An onboard pulse code modulation (PCM) data acquisition system was used to acquire the acceleration data during the test. A block diagram of the acquisition system is shown in Figure 5. The data were digitized onboard the UH-1H and transmitted to a data handling facility on the ground. System checks and calibrations were performed at the beginning of each test day so that problems could be corrected before the helicopter began its flight maneuvers.

The UH-1H was subjected to two sets of flight maneuvers, but the only difference between the sets was the order of the maneuvers. Each set constituted a flight and consisted of 13 maneuvers, two of which were ground maneuvers: ground idle (engine idle) and ground static (engine off). Data were collected on all of the flight maneuvers except ground static. A total of 16 flights were made, but vibration data were collected on only 5 flights due to the time

required to process the data and store it digitally on magnetic tape. The 16 flights were made in order to have several subjects respond to the computer display instructions during both sets of flight maneuvers. This was necessary to complete USAHEL's portion of the testing. The maneuvers corresponding to flight set 2 are shown in Table 2. All the analyses performed correspond to these maneuver numbers.

TABLE 2. FLIGHT MANEUVERS

<u>Maneuver No.</u>	<u>Description</u>
1	Ground idle
2	Hover-in-ground effect
3	500-fpm climb
4	30° banking left turn at 90 knots
5	15° left descending turn at 500 fpm
6	60-knot level flight
7	15° left climbing turn at 500 fpm
8	15° right descending turn at 500 fpm
9	110-knot level flight
10	15° right climbing turn at 500 fpm
11	30° banking right turn at 90 knots
12	152-fpm descent
13	Ground static

DISCUSSION

In addressing whether the response of onboard computer operators in the UH-1H was vibration dependent, decisions had to be made regarding where to measure vibration and how to monitor operator response.

It was speculated by USAHEL that the operator response would most likely be related to either the acceleration of the displays or to the acceleration the computer operators themselves were subjected to. These quantities were measured by USACSTA. In order to monitor operator response, USAHEL measured response time, input time, and frequency of errors as the operators responded to computer commands with keystrokes. Response time was the time required for the operator to touch a key after being signaled to do so, and input time was the time from the first touch of any key to the complete release of the proper key. Errors were recorded whenever an incorrect key was struck. At the recommendation of USAHEL,

the input time was chosen to represent operator response in the comparison. USAHEL provided USACSTA with data they collected, including mean input times for each flight maneuver.

To look at the data in the time domain, acceleration amplitude distribution data were compiled by histogramming the data into a 512-bin field and calculating cumulative distributions. Table 3 shows sample amplitude distribution data. These data were not used in the actual analysis, but were used to monitor channels throughout the testing. The units for the accelerometer amplitude distribution data are g's.

TABLE 3. AMPLITUDE DISTRIBUTION DATA

Maneuver 1, Set 2, Flight 5

<u>Description</u>	<u>rms</u>	<u>+Peak</u>	<u>-Peak</u>	<u>+99%</u>	<u>-99%</u>	<u>+90%</u>	<u>-90%</u>
(V) Left seat pad	.28	1.02	-.71	.68	-.55	.37	-.36
(T) Left seat pad	.31	1.08	-.78	.71	-.62	.39	-.42
(L) Left seat pad	.23	.96	-.65	.66	-.50	.29	-.27
(V) Right seat pad	.22	.94	-.58	.62	-.42	.26	-.26
(T) Right seat pad	.24	.85	-.64	.59	-.49	.33	-.31
(L) Right seat pad	.36	1.19	-.92	.81	-.73	.46	-.46
(V) Left display	.39	1.30	-.97	.86	-.81	.50	-.49
(T) Left Display	.21	.95	-.60	.64	-.44	.24	-.24
(L) Left display	.19	.91	-.54	.64	-.41	.21	-.23
(V) Right display	.39	1.26	-1.03	.90	-.83	.50	-.51
(T) Right display	.21	.97	-.53	.65	-.42	.22	-.26
(L) Right display	.22	.99	-.64	.72	-.46	.26	-.24

The program which performs the amplitude distribution analysis and creates tables such as the one above performs a number of data validity tests for each channel and provides messages such as:

- a. Channel inactive
- b. Data one-sided
- c. Data noisy
- d. Data clipped
- e. Large rms value
- f. Large DC offset
- g. No data spread
- h. Shock present in data

Although the program is not foolproof, and the rules which determine data validity are arbitrary, it provides a very useful tool for "quick look" analysis.

After the "quick look" was completed, the test data were checked for stationarity. The stationarity test is performed to determine whether the data are time invariant and thus validates the assumption that a single time history record adequately defines the distribution of the data.

In order to obtain a more complete picture, the acceleration data were examined in the frequency domain by using a Fast Fourier Transform (FFT) algorithm and creating power spectral density (PSD) files. A PSD file was created for each valid data run, a run consisting of one maneuver in any given flight. These files were then overlayed to yield an "average" PSD for each maneuver. The overlayed PSDs were integrated to provide mean square values for each acceleration channel in the range of 0.5 to 100 Hz. This calculation supplied the rms values that were used to correlate the computer display acceleration with operator response. There were two reasons for using this approach to determine rms values. First, using this frequency range for analysis prohibited higher frequency noise from contributing to the rms values. Second, this approach provided a bit of statistical reliability in the PSD calculation by combining the PSDs from multiple runs of the same maneuver into one PSD representing that maneuver.

Samples of the overlayed PSDs are included in Figures 6 through 8. It was interesting to note that the fundamental frequency corresponded exactly with two times the main shaft frequency (approximately 324 rpm). This comes from the two-bladed rotor blade passing frequency. The fundamental was approximately 11 Hz for all the maneuvers except ground idle, where it was about 7 Hz. Most of the energy was usually at the fundamental frequency, but occasionally there was more energy in one of the harmonics than in the fundamental. In some of the maneuvers, the seat pad locations even showed significant energy at a subharmonic which was half the fundamental. This is probably not actually a subharmonic, but rather is energy associated with the main shaft speed. This subharmonic energy became even more significant because it corresponded to the most sensitive ride quality frequency.

RIDE QUALITY ANALYSIS

There are two types of ride quality analysis that are commonly used by the United States military today. The first technique involves analyzing the data into 1/3 octave component accelerations for the center frequencies given in International Standards Organization (ISO) Standard 2631-1985 [2]. This was simulated by integrating power spectral density (PSD) data over frequency bands that correspond approximately with those of the ISO standard. This PSD integration is performed to simulate what is normally accomplished by 1/3 octave band filters (analog or digital), and is an SAE recommended technique [1]. A table of the ISO bands is shown in Table 4. The second commonly used technique requires determining the power absorbed by the subject seated at the monitored position. The absorbed power method is discussed in detail in the article by Richard A. Lee and Fred Pradko entitled "Analytical Analysis of Human Vibration," an SAE paper presented in 1968 [3].

The ISO standard that describes human response to whole-body vibration was ratified by 19 countries, including the United States. The ISO standard considers the frequency range from 1 to 80 Hz (i.e. center frequencies of 1/3 octave bands), and defines numerical limits for exposure to vibrations in that frequency range in terms of weighted root-mean-square (rms) accelerations. The accelerations are "weighted" to account for resonances in the human body. The ISO defines its limits in terms of three criteria of preserving comfort, working efficiency, and safety or health. The limits set according to these criteria are named respectively: "reduced comfort boundary", "fatigue decreased proficiency boundary", and "exposure limit". For example, where the main concern is maintaining the working efficiency of a vehicle driver, the "fatigue decreased

proficiency boundary" would be used as the guiding limit in determining vibration specifications, while in designing passenger accommodations, the "reduced comfort boundary" should be used. The method used to evaluate the three criteria is to separately compare each rms acceleration level for 1/3 octave bands of specified center frequencies against the recommended level at each frequency. This assumes that there are no interactions between frequencies, at least in regard to human tolerance. Another method of evaluating the criteria involves weighting the values and producing an overall weighted rms value which is also compared to the standard. This method simulates the SAE ride quality meter [4].

TABLE 4. One-Third Octave Filter Bands

<u>Beginning Frequency</u>	<u>Ending Frequency</u>
0.89	1.11
1.11	1.40
1.40	1.77
1.77	2.25
2.25	2.82
2.82	3.56
3.56	4.49
4.49	5.66
5.66	7.13
7.13	8.98
8.98	11.31
11.31	14.25
14.25	17.96
17.96	22.63
22.63	28.51
28.51	35.92
35.92	45.26
45.26	57.02
57.02	71.84
71.84	90.52

The second technique requires measuring the rate at which vibrational energy is absorbed by the human body. Lee and Pradko established absorbed power in watts as a desirable quantity to express human tolerance to vibration. They studied the vibrations in the frequency range of 0.1 to 12.0 Hz and made measurements at the points of contact at the buttocks in the vertical, longitudinal, and transverse directions, along with the vertical input to the feet, of a seated person. An advantage of this approach is that average absorbed power is a scalar quantity, and as such, can be summed in complex multi-degree of freedom systems to yield a single value describing the total average absorbed power. This value can then be used to develop criteria concerning the human acceptability of various ride quality environments. An upper limit of 6 to 10 watts total absorbed power is generally accepted for operation of off-road vehicles, although some would argue that these values are based primarily on subjective data.

Both the ISO and the absorbed power method are frequency weighted to account for resonances in the human body, but the weighting factors are slightly different. Figures 9 through 11 compare the weighting factor curves. The absorbed power curve does not show the actual weighting factors but is normalized

to a maximum value of one for the purpose of comparison. There continues to be much debate as to which method is better, although there are similarities both in the frequency weighting and in the results of the two techniques. European countries in particular express concern over using absorbed power rather than the ISO method to describe effects of vehicle vibrations. Reference 4 discusses and compares the two in more detail and points out that each has its advantages as well as its shortcomings. Using both techniques and comparing the results gives some assurance that a competent ride quality analysis has been performed.

In the comparison of computer operator response and the acceleration the computer operators were subjected to, rms values as determined previously were not used. Instead, the two types of ride quality analysis discussed above were performed on the overlaid PSD files. Integration over the ISO bands (Table 4) produced a weighted acceleration, and this weighted acceleration was correlated to operator mean input time.

In the alternative ride quality technique, the absorbed power is calculated by multiplying the PSD (again, the overlaid PSD) by certain weighting factors. These factors are different for each of the three measured mutually perpendicular axes. Plots of the three weighting factors are included in Figures 9 through 11. See reference 3 for actual values and units of the absorbed power weighting factors.

The reason ride quality analysis was chosen over gross rms acceleration to represent computer operator acceleration was because ride quality analysis takes resonances of the human body into account. These resonances occur below 10 Hz, and ride quality analysis gives more weight to energy in this low frequency range. For this reason, the ground idle maneuver had higher or worse ride quality values than the other maneuvers, as did those maneuvers which showed energy at a subharmonic frequency.

CONCLUSION

There are now three correlations to be made for each computer operator in the helicopter: mean input time vs. ride quality, mean input time vs. absorbed power, and mean input time vs. rms acceleration of the computer displays. There were two computer operators in the UH-1H, so this yields six comparisons, and since this was done for each axis (vertical, transverse, and longitudinal), there are a total of 18 correlations to be made. Although superposition can be applied to the absorbed power quantities for each location (i.e. the value for each axis may be added directly), this was not done in case one particular axis showed a positive correlation. The correlations were made by performing linear regression as well as rank correlation analyses. All these correlations were performed, but in the interest of brevity, only the results from the left computer display and seat pad are presented in this paper. These are shown tabularly in Tables 5 through 7 and graphically in Figures 12 through 20.

Rank correlation analysis involves rather simple calculations and tests whether two compared variables are independent [6]. It makes no assumptions about the distributions of the variables. The rank correlation coefficient is similar to the linear regression correlation coefficient in that its values range from -1 to 1 and a value of 1 indicates perfect agreement. A value of -1 indicates opposite ranking. The rank correlation coefficient is defined by the following equation.

$$r_s = 1 - (6 \sum d_i^2) / [n(n^2 - 1)]$$

where : r_s - the rank correlation coefficient

$\sum d_i^2$ - the sum of the squared differences in rank for each of the paired values

n - the number of ordered pairs

TABLE 5. CORRELATION BETWEEN TRIAXIAL ACCELERATIONS AND INPUT TIME LEFT DISPLAY

Maneuver		Mean	Acceleration (g rms)		
No.	Description	Input Time (sec)	Vert	Tran	Long
1	Ground idle	0.498	0.47	0.22	0.25
2	Hover-In-ground effect	0.403	0.48	0.27	0.25
3	500 fpm climb	0.464	0.74	0.39	0.58
4	30° banking left turn	0.418	0.91	0.34	0.46
5	15° left descending turn	0.387	0.74	0.33	0.43
6	60 knot level flight	0.382	0.72	0.35	0.36
7	15° left climbing turn	0.407	0.84	0.33	0.50
8	15° rt descend turn 500 fpm	0.364	0.70	0.41	0.47
9	110 knot level flight	0.390	1.01	0.46	0.54
10	15° right climbing turn	0.403	0.84	0.33	0.47
11	30° banking rt turn 90 knot	0.465	1.01	0.41	0.48
12	500 fpm descent	0.355	0.74	0.32	0.42
13	Ground static	0.346	*	*	*
** Correlation Coefficient Squared :			0.015	0.068	0.013
*** Rank Correlation Coefficient :			0.189	-0.147	0.161

TABLE 6. CORRELATION BETWEEN ISO RIDE QUALITY AND INPUT TIME
LEFT SEAT PAD

Maneuver		Mean Input Time (sec)	(m/sec ²) Weighted rms Accel		
<u>No.</u>	<u>Description</u>		<u>Vert</u>	<u>Tran</u>	<u>Long</u>
1	Ground idle	0.498	3.16	0.20	0.46
2	Hover-in-ground effect	0.403	0.86	0.22	0.23
3	500 fpm climb	0.464	1.22	0.20	0.36
4	30° banking left turn	0.418	1.49	0.21	0.39
5	15° left descending turn	0.387	1.21	0.17	0.32
6	60 knot level flight	0.382	1.06	0.18	0.32
7	15° left climbing turn	0.407	1.42	0.18	0.39
8	15° rt descend turn 500 fpm	0.364	1.21	0.18	0.29
9	110 knot level flight	0.390	1.84	0.28	0.40
10	15° right climbing turn	0.403	1.43	0.20	0.39
11	30° banking rt turn 90 knot	0.465	1.46	0.23	0.39
12	500 fpm descent	0.355	1.10	0.17	0.29
13	Ground static	0.346	*	*	*
** Correlation Coefficient Squared :			0.414	0.066	0.424
*** Rank Correlation Coefficient :			0.622	0.622	0.601

TABLE 7. CORRELATION BETWEEN ABSORBED POWER AND INPUT TIME
LEFT SEAT PAD

Maneuver No.	Description	Mean Input Time (sec)	Absorbed Power (Watts)		
			Vert	Tran	Long
1	Ground idle	0.498	12.14	0.07	0.42
2	Hover-in-ground effect	0.403	1.15	0.08	0.15
3	500 fpm climb	0.464	2.32	0.04	0.16
4	30° banking left turn	0.418	3.63	0.04	0.16
5	15° left descending turn	0.337	2.35	0.03	0.11
6	60 knot level flight	0.382	1.54	0.03	0.11
7	15° left climbing turn	0.407	3.13	0.03	0.16
8	15° rt descend turn 500 fpm	0.364	2.47	0.03	0.09
9	110 knot level flight	0.390	4.57	0.08	0.19
10	15° right climbing turn	0.403	3.13	0.04	0.16
11	30° banking rt turn 90 knot	0.465	3.28	0.04	0.17
12	500 fpm descent	0.355	1.83	0.03	0.10
13	Ground static	0.346	*	*	*
** Correlation Coefficient Squared :			0.431	0.103	0.600
*** Rank Correlation Coefficient :			0.510	0.580	0.839

* These were not measured; although they may be assumed to be approximately zero, they were not included in the linear correlation calculation.

** These values were obtained by performing a linear regression analysis (** rank correlation analysis) of mean input time vs. absorbed power.

Each linear regression analysis showed that there was no correlation to be found between acceleration of the computer displays and computer operator mean input time or between acceleration the operators were subjected to and operator mean input time. This could be readily deduced by glancing at Figures 12 through 20, and is verified by correlation coefficient (r) squared values as low as 0.015 (Table 5). In fact, the largest value for r^2 was 0.600 (Table 7). A perfectly linear correlation would have r^2 equal to one, and any value less than 0.8 would

indicate that no linear correlation exists. The note at the bottom of Tables 5, 6, and 7 states that the values from the ground static maneuver may be assumed to be zero but were not included in the linear regression calculation. Actually, the correlation was performed both ways, and neither calculation indicated that any correlation existed. It should be mentioned that vibration input to the feet of the operators was ignored, but this is very unlikely to change the results of these comparisons.

Results of the rank correlation analysis also indicated no correlation existed. As with the linear regression calculations, the rank correlation analysis was performed both by excluding the ground static maneuver and by including it with a value of zero. As before, neither method affected the outcome; there simply was no correlation to be found. Rank correlation was performed in the event there was some correlation, but that it was not linear. It was comforting to have the two types of analyses produce agreeable results. These results are probably contradictory to what many would have expected, and that very fact makes the results pertinent. Most experts would likely be of the opinion that any activity taking place in a helicopter would be affected by the environment, and while that may generally be a valid assumption, in this specific vibration situation under these specific conditions, the data do not support it.

A reason for the lack of correlation may be that the levels were below some threshold that affects humans for short periods of time. In fact, a look at the fatigue decreased proficiency boundaries from the ISO ride quality analysis provide some weight to this possibility. Almost without exception, the exposure limits were at least one hour, while each test flight lasted about 40 minutes. If the ISO analysis is correct, the vibration levels measured on the seat pads should not have affected the operators performance. Also, the test was performed in "clean" air. Severe turbulence, which was not experienced during the testing, may have provided different results.

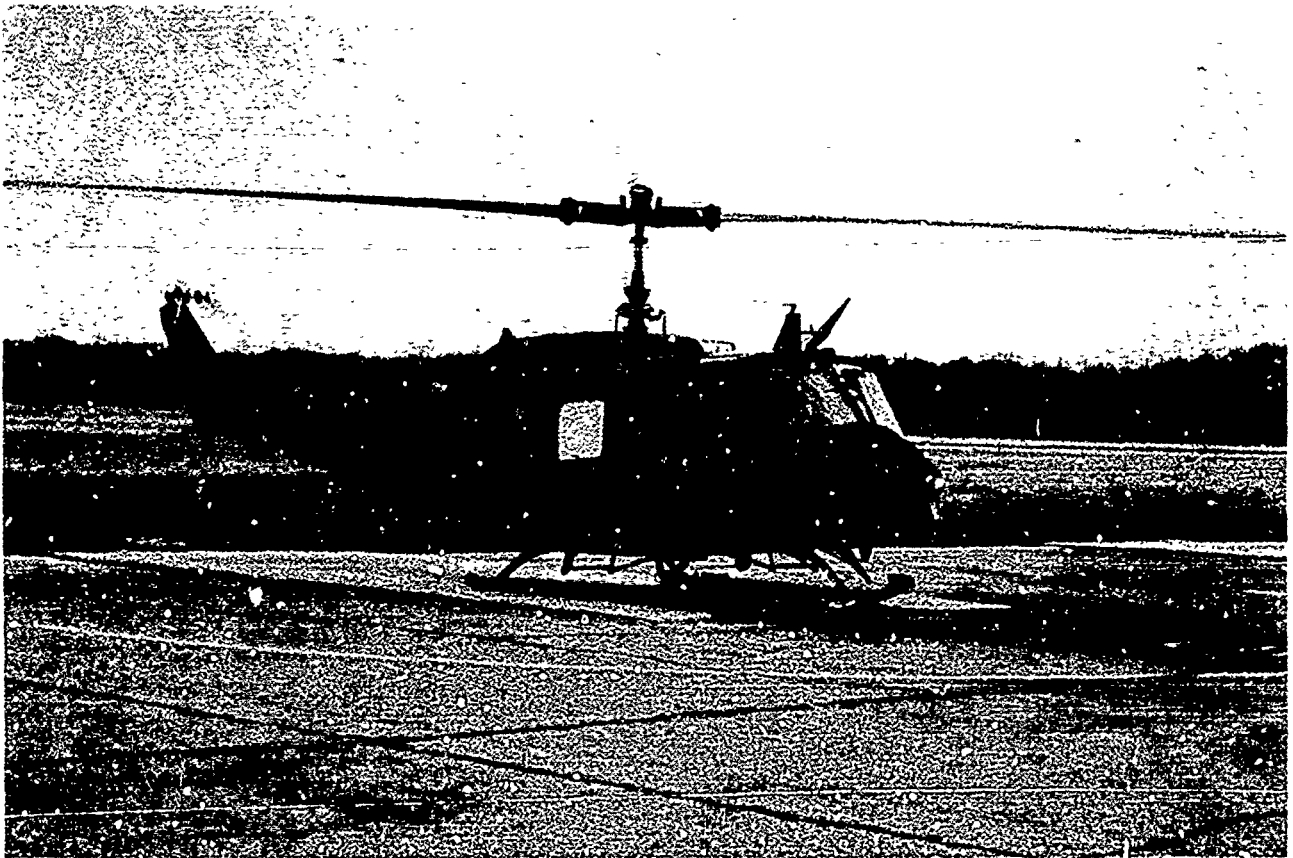


Figure 1. Photo of Test Helicopter.

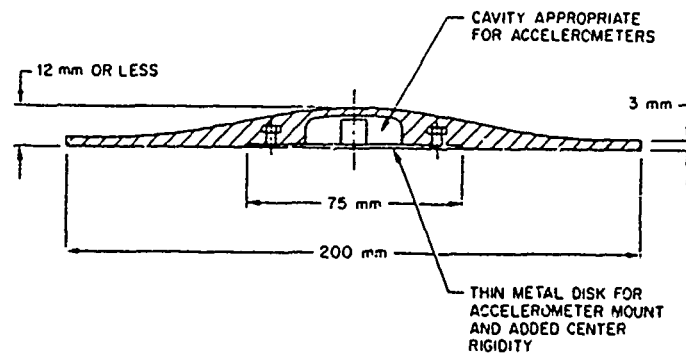


Figure 2. SAE Suggested Design for Semi-Rigid Ride Quality Pad.



Figure 3. Photo of Left Display Triaxial Accelerometer Location.

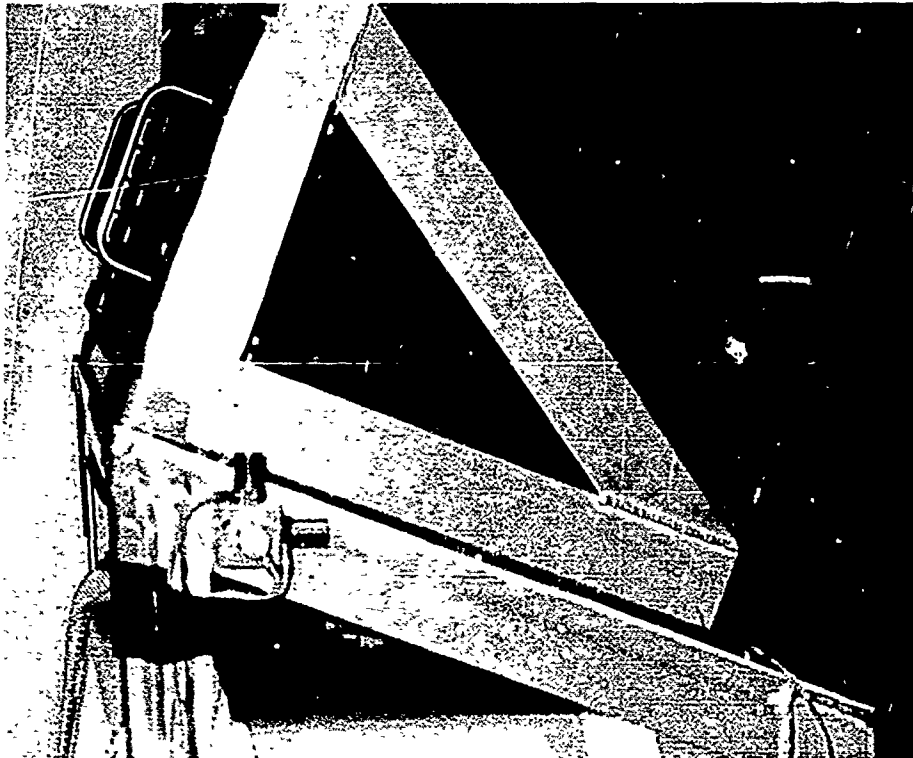


Figure 4. Photo of Right Display Triaxial Accelerometer Location.

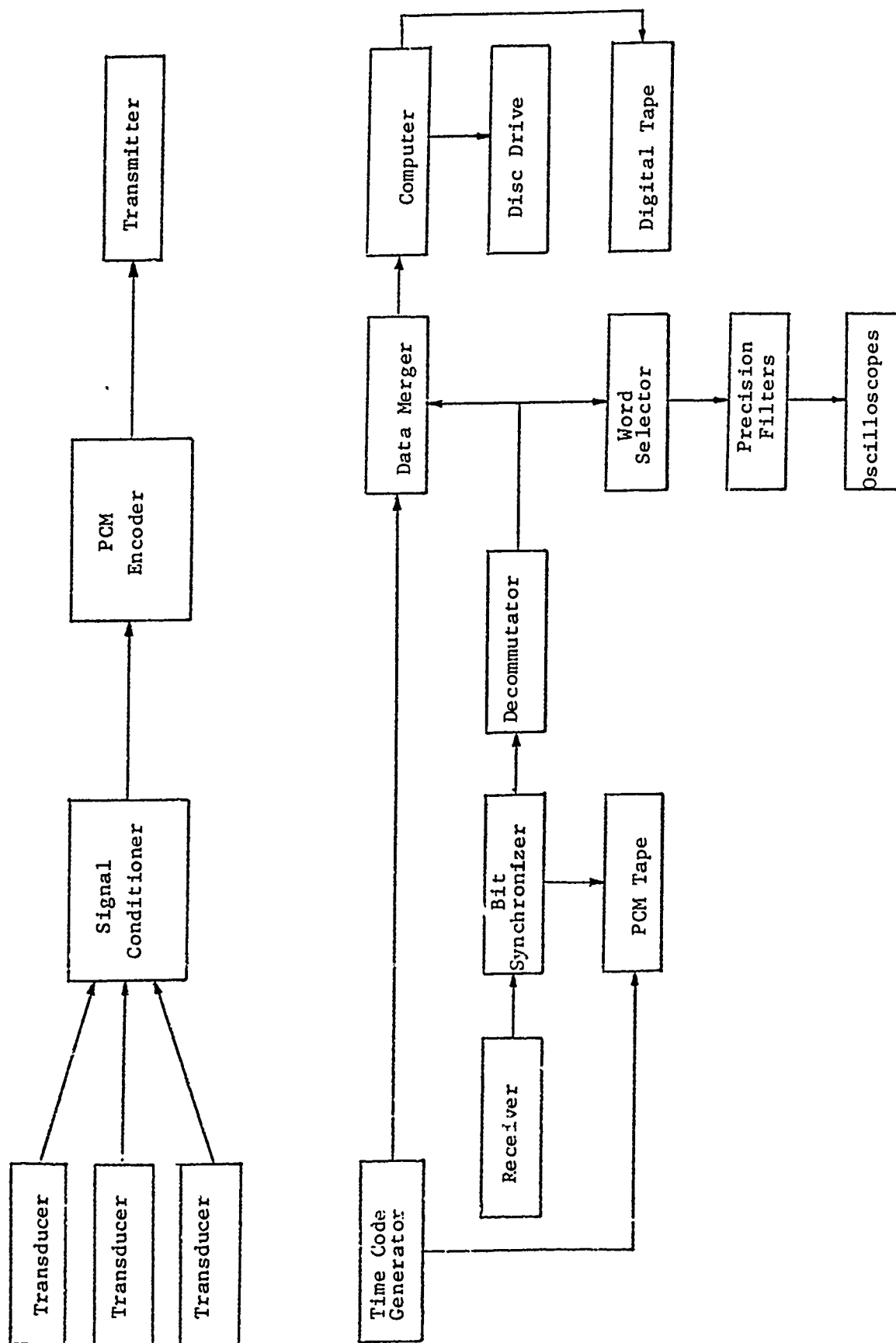


Figure 5. Block Diagram of PCM Data Acquisition System.

MANEUVER 5 DESCENDING LEFT TURN

— LEFT SEAT (V)

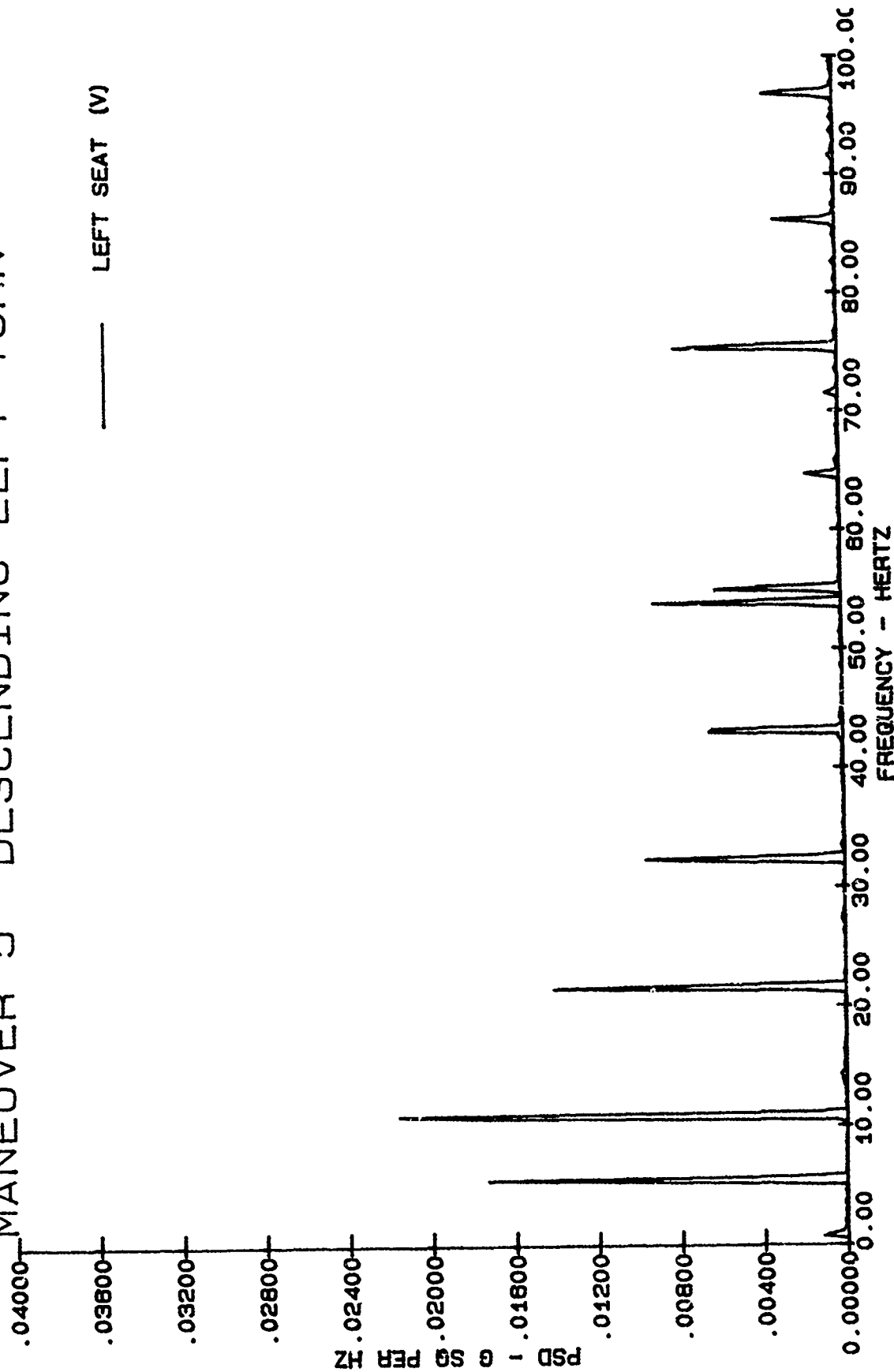


Figure 6. Sample PSD Data

MANEUVER 5 DESCENDING LEFT TURN

— LEFT SEAT (T)

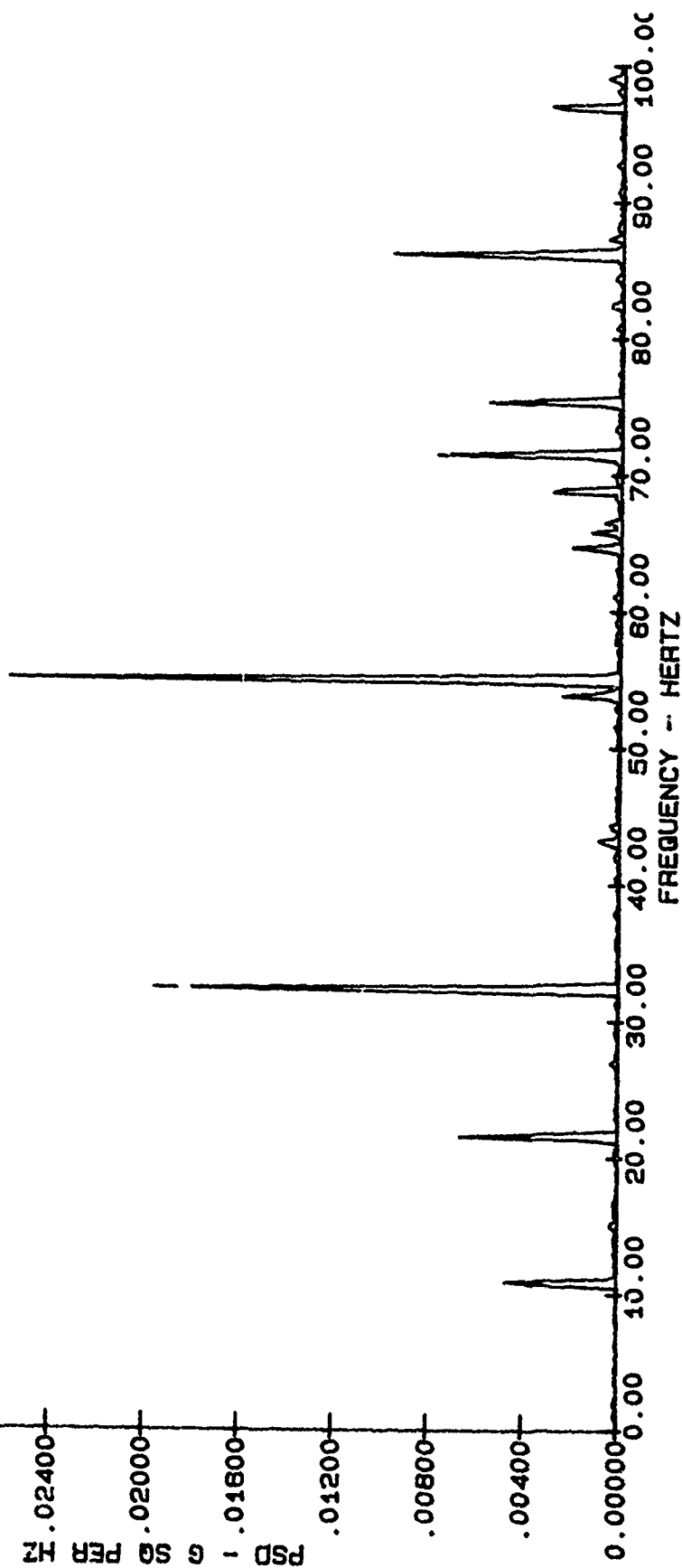


Figure 7. Sample PSD Data

MANEUVER 5 DESCENDING LEFT TURN

LEFT SEAT (L)

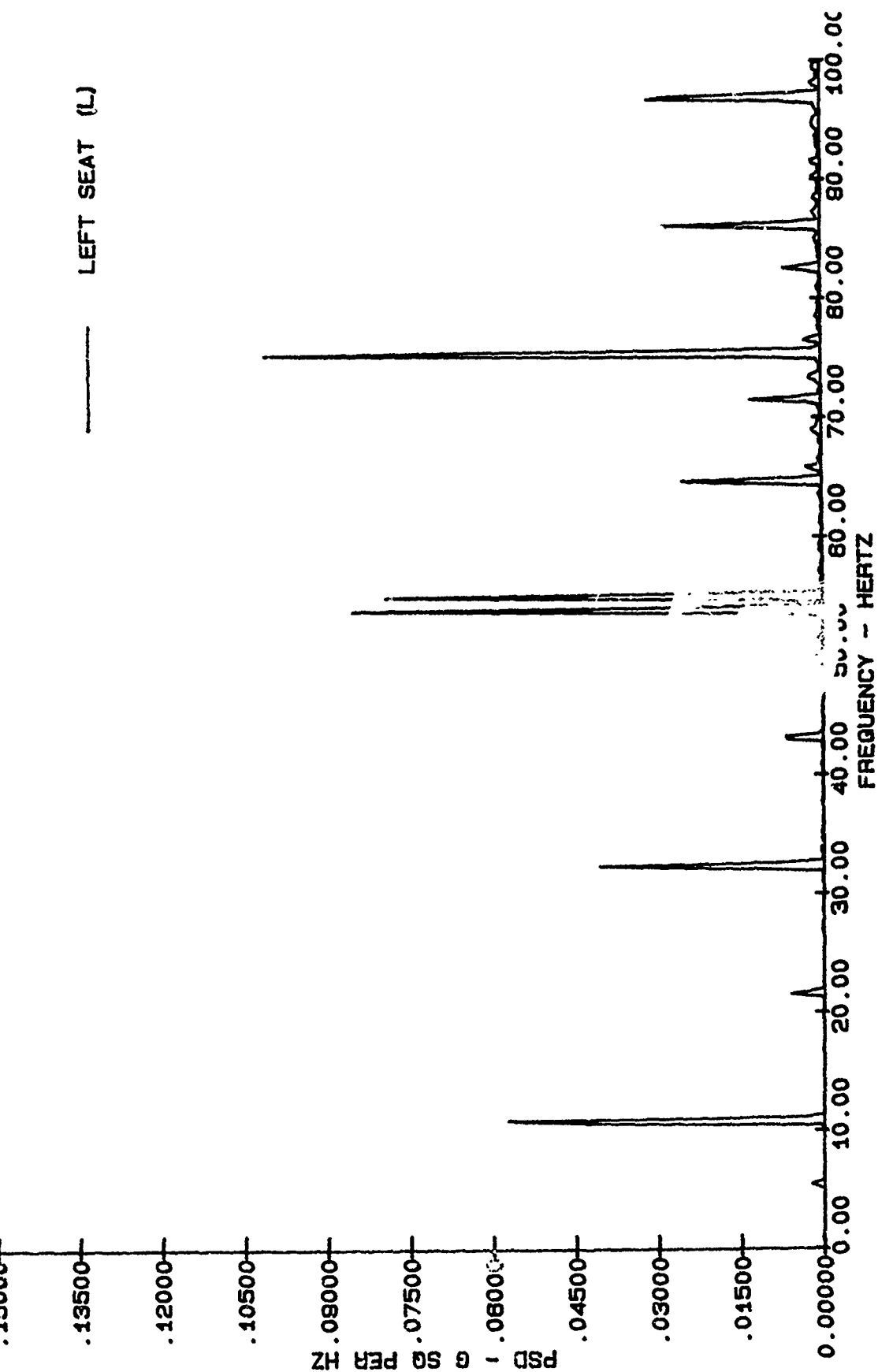


Figure 8. Sample PSD Data

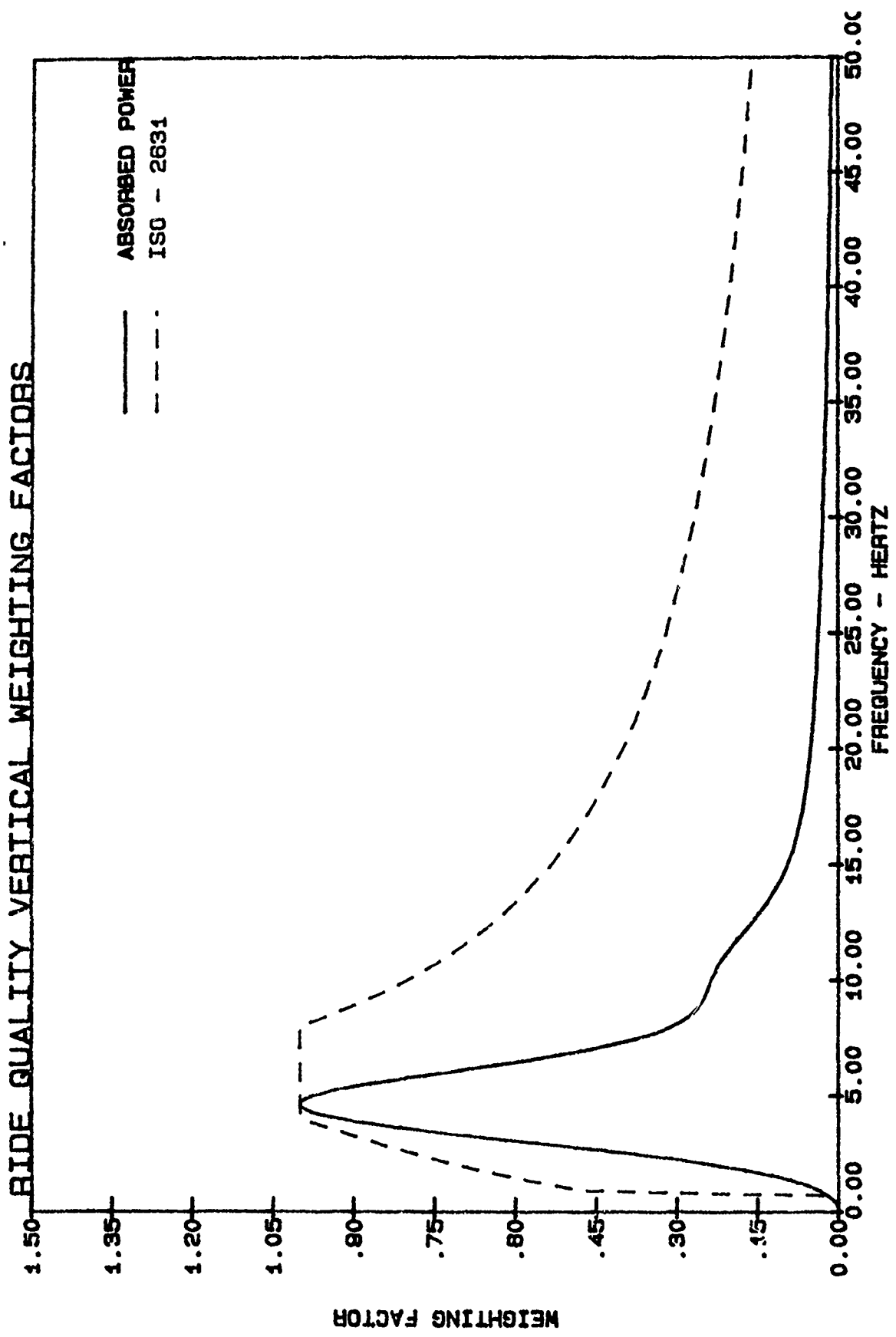


Figure 9. Comparison of Ride Quality Weighting Factors

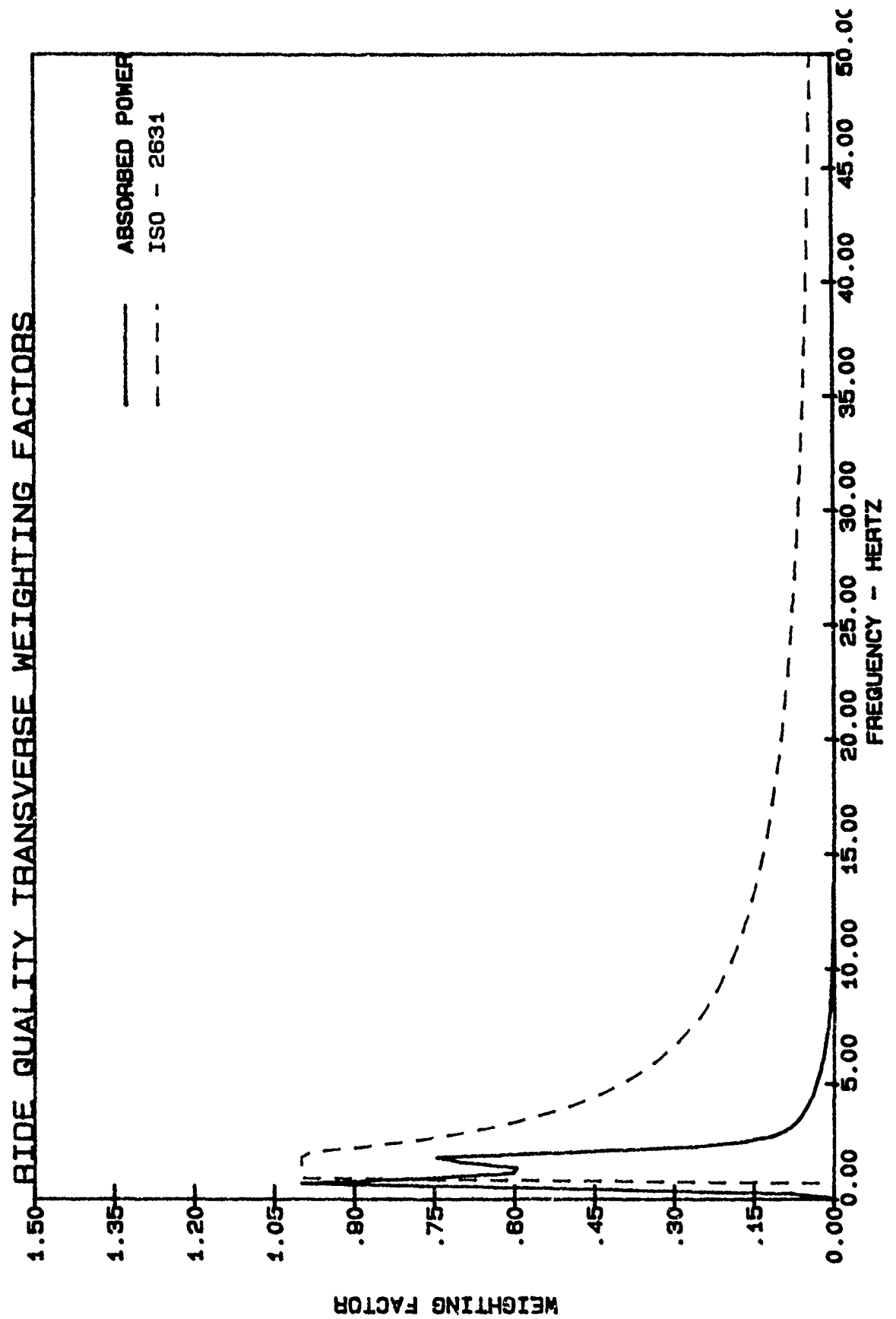


Figure 10. Comparison of Ride Quality Weighting Factors

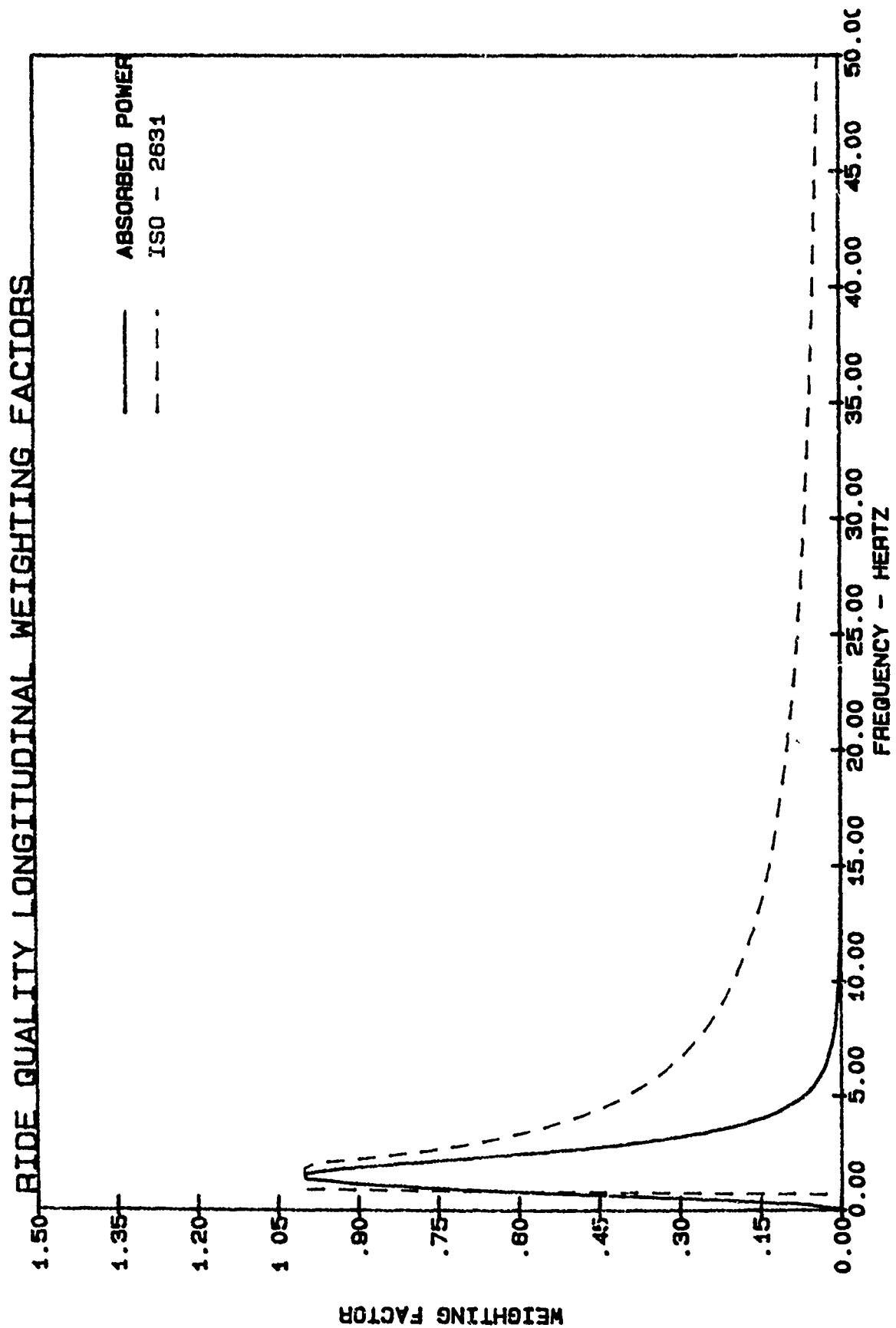


Figure 11. Comparison of Ride Quality Weighting Factors

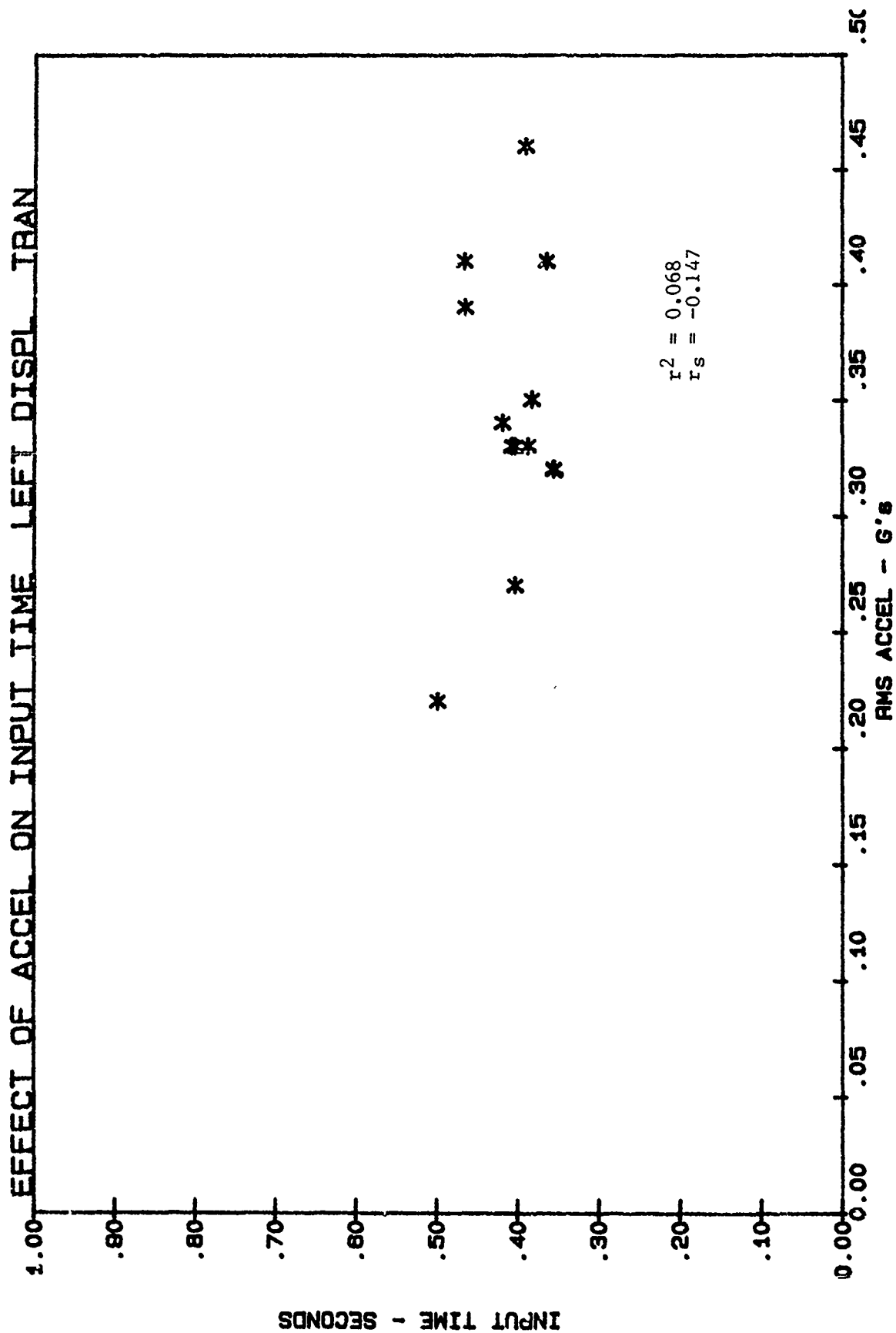


Figure 13. Plot of Correlation Data

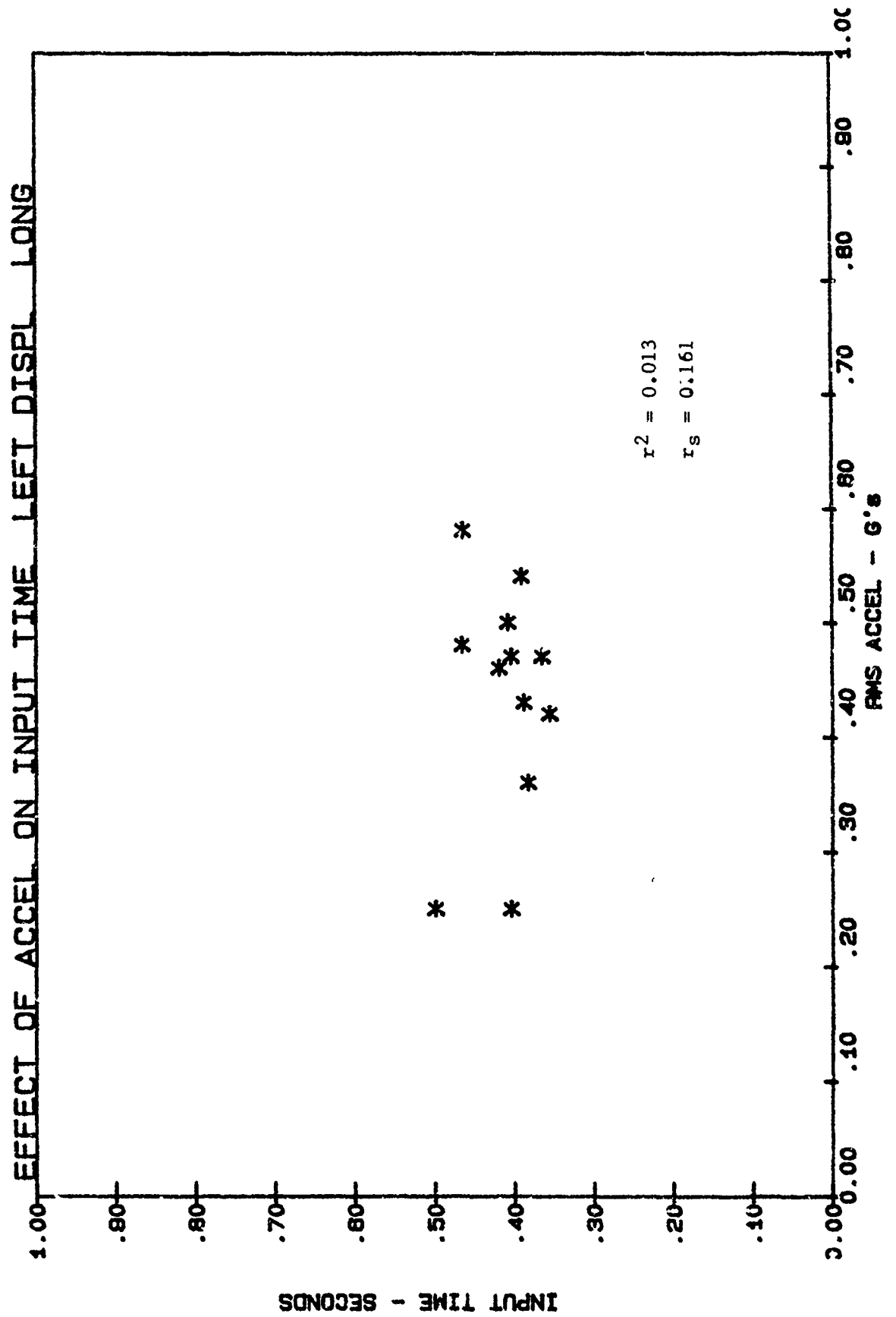


Figure 14. Plot of Correlation Data

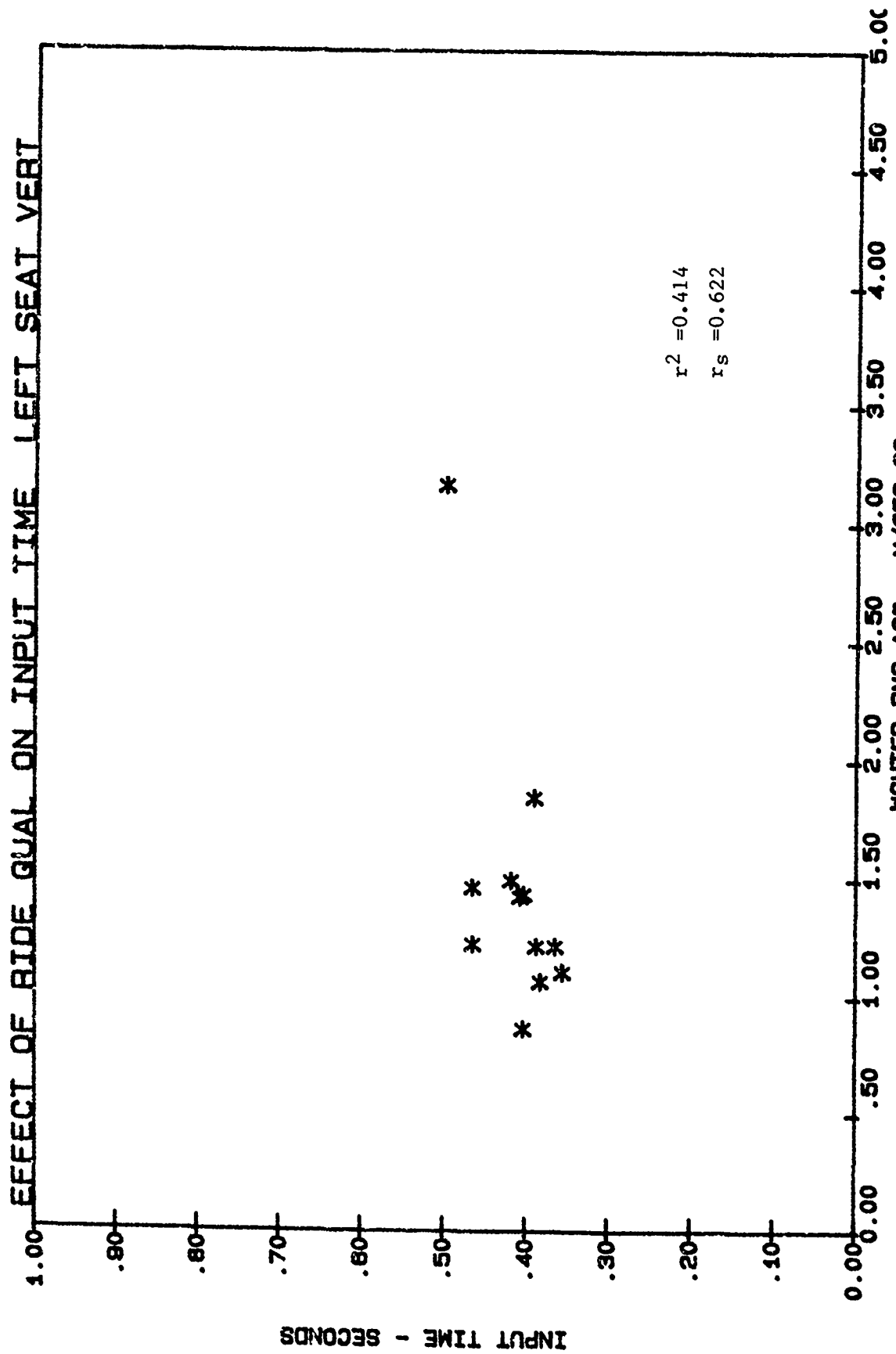


Figure 15. Plot of Correlation Data

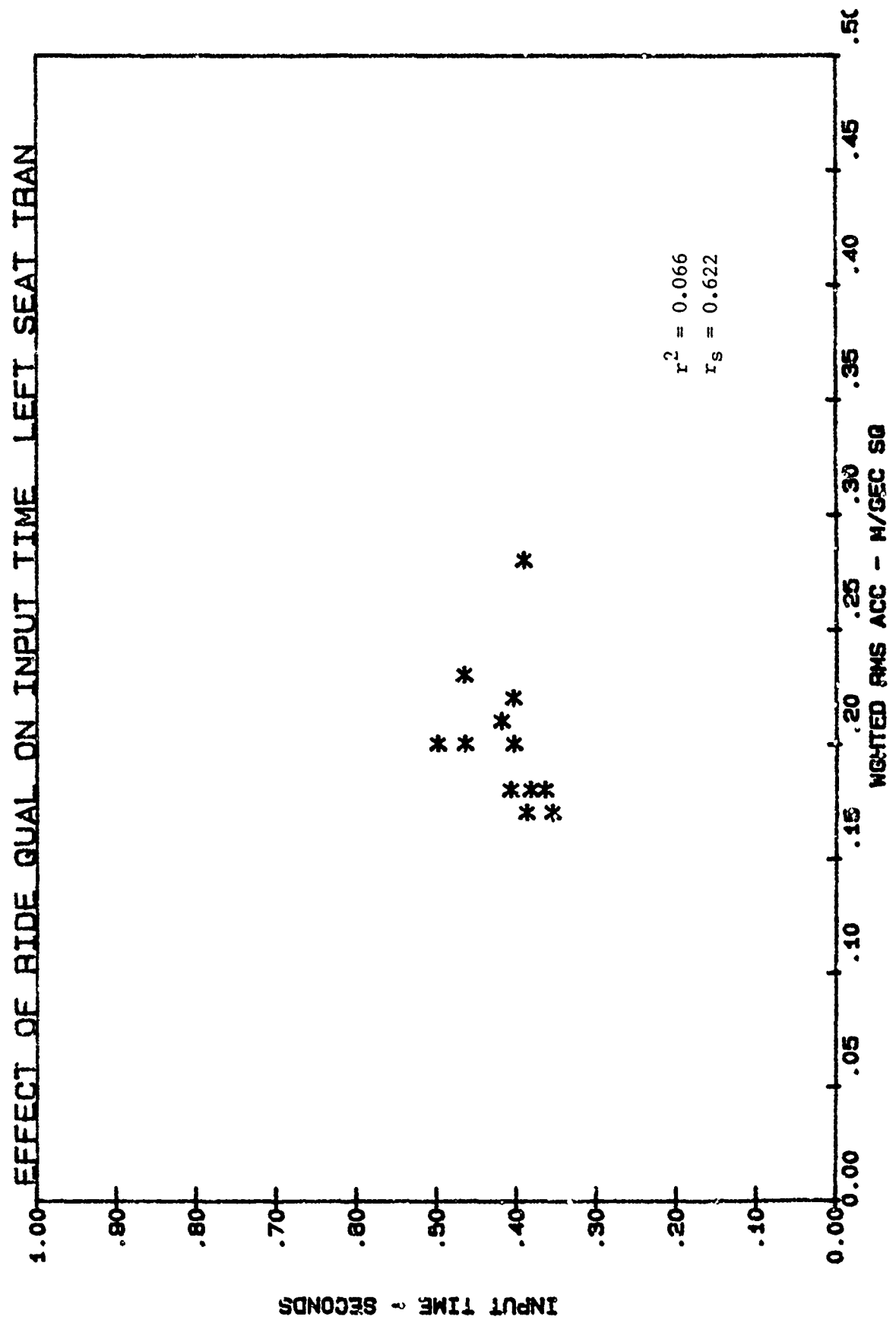


Figure 16. Plot of Correlation Data

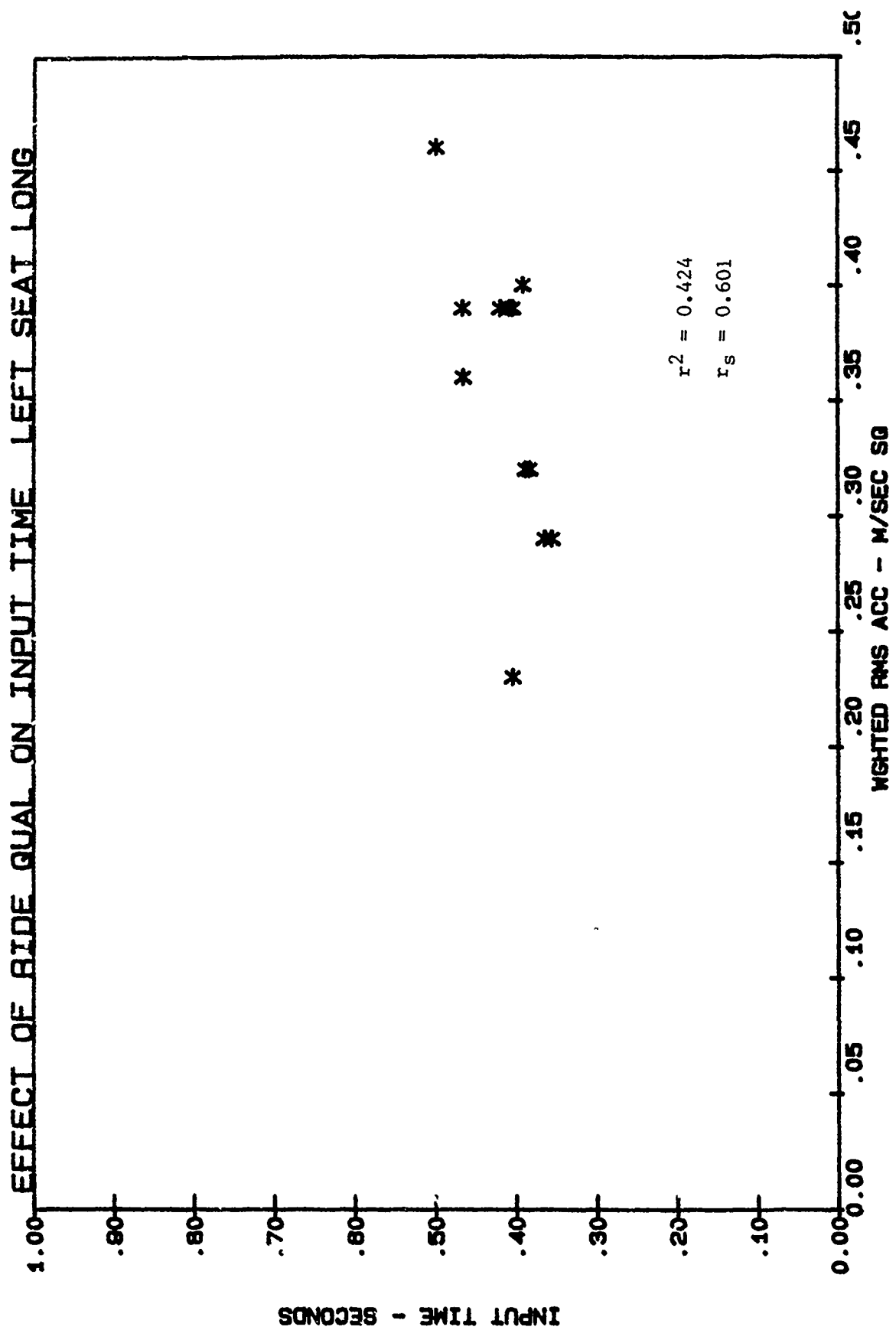


Figure 17. Plot of Correlation Data

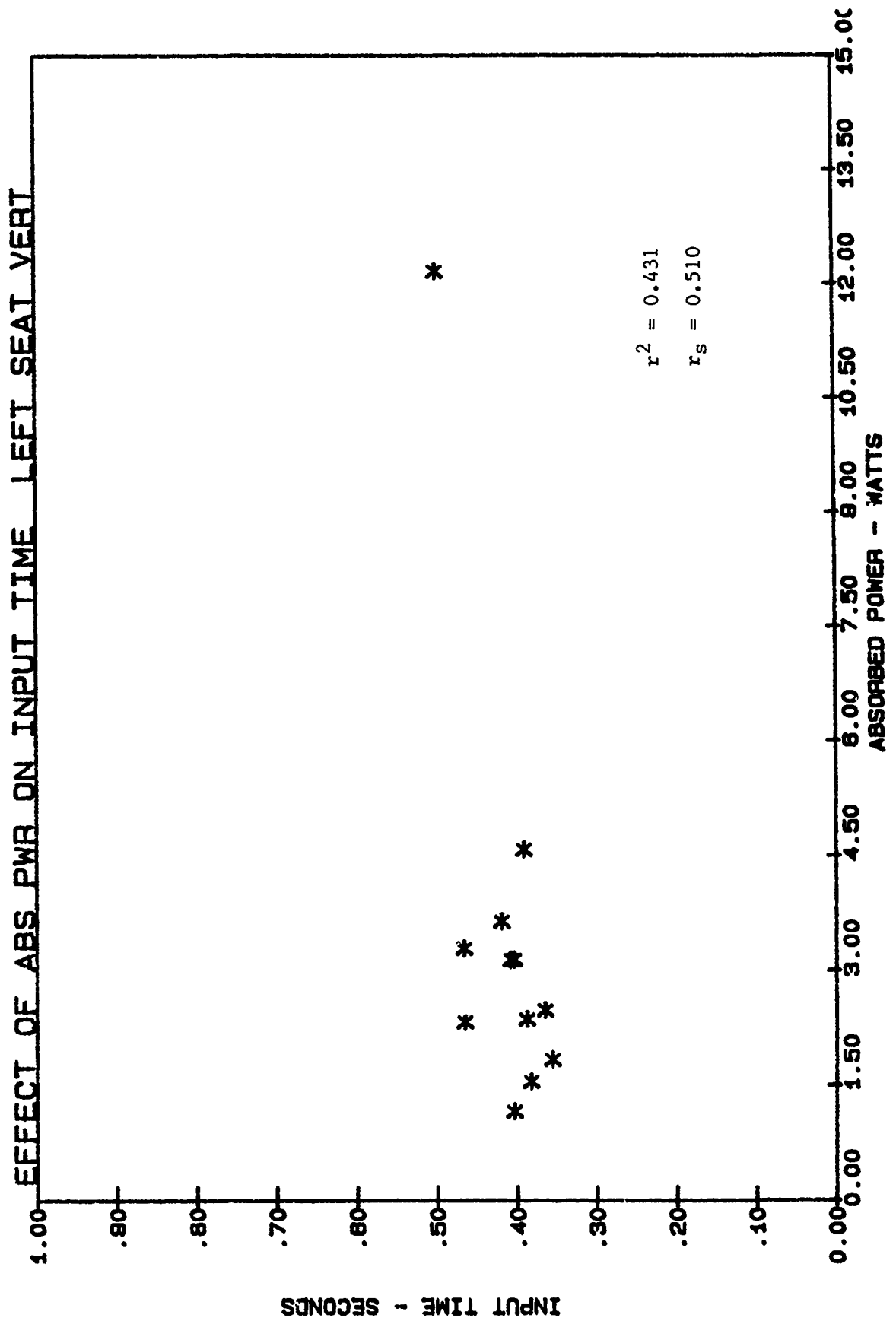


Figure 18. Plot of Correlation Data

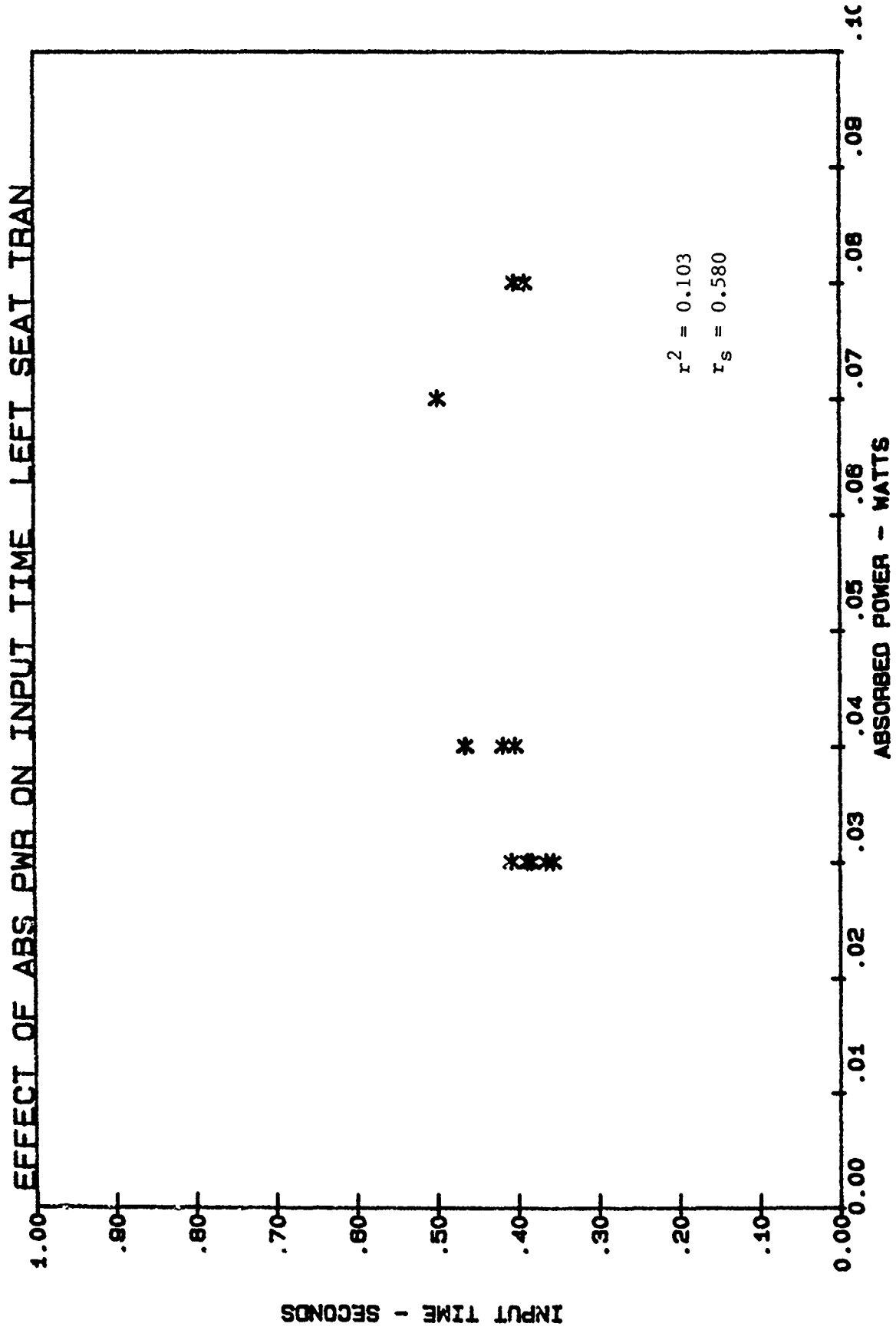


Figure 19. Plot of Correlation Data

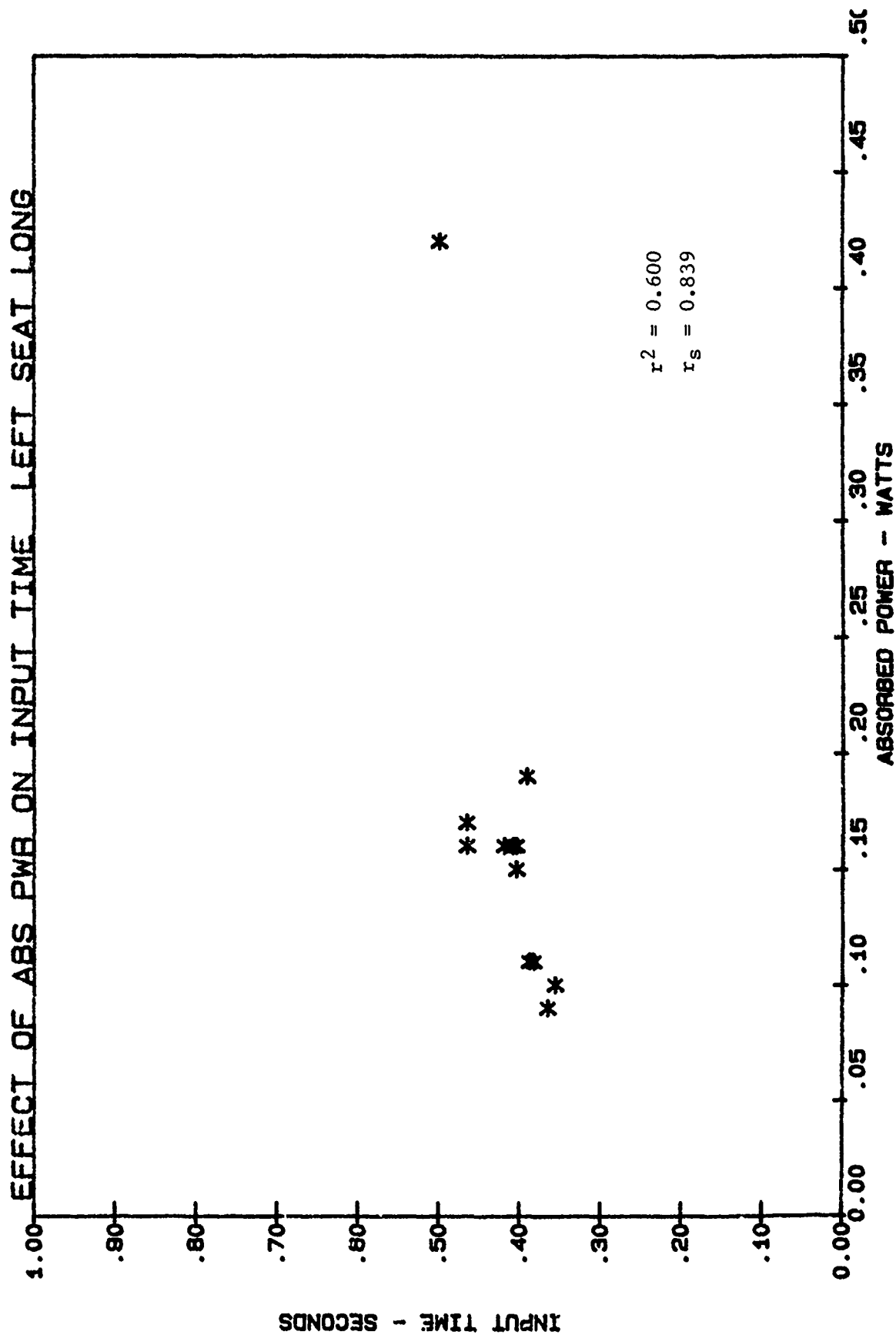


Figure 20. Plot of Correlation Data

REFERENCES

1. Society of Automotive Engineers Recommended Practice J1013, "Measurement of Whole Body Vibration of the Seated Operator of Off-Highway Work Machines," January 1980.
2. International Standards Organization (ISO) 2631-1985. "Guide for the Evaluation of Human Exposure to Whole-Body Vibration."
3. Lee, Richard A. and Fred Pradko, Analytical Analysis of Human Vibration, SAE Paper No. 680091, January 1968.
4. Murphy, Newell R. Jr., Further Developments in Ride Quality Assessment, 1984 Proceedings, 30th Annual Technical Meeting, Institute of Environmental Sciences.
5. Dixon, Wilfrid J. and Frank J. Massey, Jr., Introduction to Statistical Analysis, pp. 349-351, McGraw-Hill, 1969.

SHAKER SHOCK TESTING USING NONSTATIONARY RANDOM TRANSIENTS*

Thomas L. Paez and Thomas J. Baca

Experimental Mechanics Department
Sandia National Laboratories
Albuquerque, NM 87185

Shock testing plays a critical role in the development of a wide range of structures. Conducting controlled laboratory shock tests on these structures provides essential data on their ability to survive their operational shock environments. Laboratory test specifications establish equivalence relationships between the actual shock environments and the laboratory shock test inputs. In recent years the electrodynamic shaker has proven itself to be a very versatile machine for applying transients to aerospace components. Shaker control techniques now exist which allow reproduction of shock transients composed of summed deterministic functions (e.g. decaying sinusoids). This paper reports the results of a study in which nonstationary random transients are used as the basis for defining shaker shocks. After describing the test specification and implementation procedures, the paper compares the results of some tests conducted on a simple cantilever beam structure. One test is a direct simulation of a nonstationary random process environment; two other tests represent the shock source using excitations established via the method of shock response spectra. The advantages and limitations of each approach are summarized.

Introduction

Experience has shown (Reference 1) that in many aerospace applications the most severe environments to which structures are subjected are extreme transient environments. In view of this, it is important to accurately simulate these sources of shock excitation. There are several mechanical systems used to simulate shock environments. Among these are drop table shock machines, air guns, actuators, reverberant plates and electrodynamic and hydraulic shakers. These test machines differ in the types of shocks they can impart to structures being tested, and in the level of effort required to perform a test. Shock machines, air guns and actuators are used to generate classical pulse test excitations, and they are relatively easy

* This work was supported by the U. S. Department of Energy under Contract No. DE-AC04-76-DP00789.

to use. Reverberant plates generate high intensity, decaying oscillatory excitations to test items, however, they are more difficult to use. Electrodynamic shakers are used to synthesize a wide variety of excitations, but are generally more difficult to use than the other types of shock test equipment.

Shock tests have generally been specified by the method of shock response spectra. In applying this technique to test specification, the test engineer first collects samples of the environment to be simulated and characterizes these individually with their shock response spectra. Next, all the shock response spectra are plotted on one graph and enveloped by one shock response spectrum curve that conservatively characterizes the entire collection. This curve is called the test specification shock response spectrum. Then the test engineer establishes a test by choosing an excitation whose shock response spectrum matches or envelops the test specification shock response spectrum. It is assumed in the method of shock response spectra that the test time history chosen in the above manner is a reasonable representation of the underlying environment for purposes of verifying structural integrity through laboratory simulation.

Although transient environments are not generally analyzed using the methods of statistics, it is usually agreed that shock signals are random in nature. Specifically, most transient signal sources are nonstationary random processes. It has been shown in some recent papers (References 2, 3, 4) that nonstationary random processes can be characterized, and that tests can be run on electrodynamic shakers to directly simulate these nonstationary random process sources. Several steps must be taken to run a test that simulates a nonstationary random process. These steps are described in a general framework in the following paragraphs.

First, a model for the random process must be chosen. In nonstationary random process simulation, a parametric model will typically be used. The model must be one that has appropriate form and sufficient parameters to accurately characterize the field source of interest. The model may include elements that describe both the time-domain and the frequency-domain features of the random source.

Second, the parameters of the nonstationary random process model must be identified using measured realizations from the random process source. There are several statistical approaches useful in parameter estimation, and the approach that is best depends on the parametric model and the specific application.

Third, the nonstationary random process model parameters used in generating the test excitation must be chosen. The choice of test parameters must be related to the desired confidence level for the test, and this is related to the confidence intervals that are established in the statistical analysis of the data.

Fourth, one or more realizations of the test random process must be generated. This step can be accomplished using the standard techniques of random signal generation and the parametric model of the random process source. Measures of severity of the individual test signals can be compared to theoretical measures of severity of the random process source. (Severity of transient environments is discussed extensively in References 5 and 6.)

Fifth, one or more tests must be executed using the test nonstationary random process realization generated above. The objective is to reproduce the test signal as accurately as possible on a shaker. An approach for controlling an electrodynamic

shaker to create a desired time history is described in Reference 7. The severity of the actual test can be compared to the desired level of test conservatism.

This paper describes a general model for nonstationary random processes, then shows how it can be specialized for the description of actual transient signal sources. Next, the results of an experimental example are presented, where a simple beam structure is excited by a realization of a nonstationary random process and some shock pulses that are used to represent the random source. The results of the experiment and other factors are used to compare the direct simulation of nonstationary random process sources to test specification via the method of shock response spectra. Finally, conclusions are drawn, and recommendations for testing systems excited by random signals in the field are presented.

A General Parametric Model for Nonstationary Random Processes

In establishing a model for nonstationary random process sources, it is desirable to create a model that is general. Generality, in this sense, implies that most nonstationary random process identifications will be performed using special-purpose digital signal analysis computer programs, and that in writing such a program, it is desirable to create a code that is user friendly, has a stable parameter estimation procedure, and is accurate in its representation of many random process sources. A model that is quite general is presented here.

Let $\{X(t), 0 \leq t < \infty\}$ be the nonstationary random process source that is to be modelled. (Because it is meant to simulate a transient event, the random process is arbitrarily initiated at time zero, but this start time can be varied. Further, it is anticipated that the magnitude of the values in the random process will tend to decay in a consistent manner.) $\{X(t)\}$ is formed as the sum of N component nonstationary random processes, $\{X_j(t), 0 \leq t < \infty\}$, $j=1, \dots, N$, as shown in Equation 1.

$$X(t) = \sum_{j=1}^N X_j(t), \quad t \geq 0 \quad (1)$$

The character of the random process $\{X(t)\}$ clearly depends on the behavior of the components $\{X_j(t)\}$.

Each of the component random processes $\{X_j(t)\}$ is the product of a stationary random process, $\{Y_j(t), -\infty < t < \infty\}$, and a deterministic function of time, $a_j(t)$, $t \geq 0$.

$$X_j(t) = a_j(t) Y_j(t), \quad \begin{matrix} t \geq 0 \\ j=1, \dots, N \end{matrix} \quad (2)$$

The random processes $\{Y_j(t)\}$, $j=1, \dots, N$, are normally distributed, with mean zero, and two-sided spectral densities, $S_j(f)$, $F_{1j} \leq |f| \leq F_{2j}$, $j=1, \dots, N$. The frequencies F_{kj} , $k=1, 2$, $j=1, \dots, N$, are chosen so that $F_{11} \geq 0$, and $F_{2j} = F_{1(j+1)}$. That is, the frequency where the j th component has its power cut-off is the frequency where the $(j+1)$ st component starts; there is no overlap in the frequency bands of the stationary random processes $\{Y_j(t)\}$ and $\{Y_m(t)\}$ for $j \neq m$, therefore, the component random processes are generally uncorrelated.

The deterministic functions $a_j(t)$, $j=1, \dots, N$, are parametric functions of time. It is usually expected that the variations in the functions $a_j(t)$ will be much slower than the oscillations in the random processes $\{Y_j(t)\}$, and this can be enforced by proper choice of the form of the $a_j(t)$.

The model presented here is quite general because it permits the characterization of a nonstationary random process using potentially different features in different frequency bands. The underlying random processes $\{Y_j(t)\}$ are uncorrelated, and this fact makes it easy to generate realizations of $\{X(t)\}$. However, the use of uncorrelated components establishes a limitation in the model, since there may be some sources whose components in different frequency bands are correlated. In general, when an excitation is predominantly the result of the operation of a random process on a linear system, then the excitation will have uncorrelated components. When an excitation is predominantly the result of the operation of a random process on certain types of nonlinear system, then the components of the excitation may be correlated. In the modelling of nonstationary random excitations, the more basic problem, and therefore the first one that needs to be addressed, is the case where the excitation components are uncorrelated.

Identification of the model in Equations 1 and 2 involves estimation of the component spectral densities $S_j(f)$, and estimation of the parameters in the functions $a_j(t)$. In some applications the spectral densities of the random processes $\{Y_j(t)\}$ will be taken as constants; in these applications the magnitudes of the $S_j(f)$ need not be separately identified, but must be tied to the magnitudes of the functions $a_j(t)$. (See References 2 and 3.) When the $S_j(f)$ are not taken as constants they must be identified, and a method for doing this was presented by Piersol in Reference 8. The technique takes advantage of the fact that the spectral density of a severely clipped signal has the same shape as the spectral density of the signal itself.

Identification of the parameters in the functions $a_j(t)$ can be accomplished using a number of approaches. For example, a formal statistical approach to the estimation of model parameters is the method of maximum likelihood, described, for example, in Reference 9. With this approach, the likelihood function involving the parameters in $a_j(t)$ is maximized with respect to the parameters. Another approach to the estimation of parameters in $a_j(t)$ is the least squares technique, also described in Reference 9. Using this technique, the mean square of a component $\{X_j(t)\}$ can be estimated with measured data, and then fit to a measure of the function $a_j(t)$ in a least squares sense. An approach to parameter estimation that is especially well suited to use in an interactive environment with inexperienced users is the orthogonal regression method, described in Reference 10. Parameter estimation by this method is very stable, and would require a minimum of decision making by the user. Finally, in an interactive program, the user may simply be shown a time history of a measure of $\{X_j(t)\}$, like the mean square, and given guidelines for the choice of parameters in the function $a_j(t)$. This is one of the approaches used in Reference 2.

A Specific Nonstationary Random Process Model

This section describes a specific nonstationary random process model using the general framework established in the previous section.

Two elements must be provided to characterize the model. The first is a form for the spectral density functions, $S_j(f)$. The second is an expression for the functions $a_j(t)$. In the present application the spectral density is taken as a constant over the appropriate frequency band, and that constant is chosen to be unity.

$$S_j(f) = 1, \quad F_{1j} \leq f \leq F_{2j} \quad (3)$$

$$j=1, \dots, N$$

In other words, the underlying stationary random processes, $\{Y_j(t)\}$, are band-limited white noise random processes with unit spectral density. The j th random process has the mean square value

$$E[Y_j^2(t)] = 2 (F_{1j} - F_{2j}), \quad j=1, \dots, N \quad (4)$$

This is simply the area under its spectral density curve.

The form chosen for the deterministic functions, $a_j(t)$, yields a slowly varying pulse. (See Reference 3 for some other useful modulating functions.)

$$a_j(t) = \alpha_j t \exp(-\beta_j t), \quad t \geq 0 \quad (5)$$

$$j=1, \dots, N$$

The pulse has an initial value of zero at time zero, increases rapidly, and then decays exponentially. The amplitude of the pulse is determined by the magnitude of the parameter α_j . The rise and decay rates of the pulse are determined by the parameter β_j .

Parameter identification for this model is accomplished using measured realizations of the random process $\{X(t)\}$ in an interactive computer program. The program uses the method of maximum likelihood or observations on the mean square of the realizations to estimate the parameters. The program is described in Reference 2.

Comparison of Tests

This section presents an experimental example where a structure is excited using various inputs. The actual excitation source is assumed to be a nonstationary random process. An objective of the experiment is to compare some excitations used to simulate the shock source. One excitation is a direct simulation of the source nonstationary random process. Two other excitations were chosen using the method of shock response spectra. One of these excitations is a compensated sum of exponentially decaying sinusoids (Reference 7). The other excitation is a classical pulse generated on a drop table shock machine (Reference 11). Another objective of the experiment is to measure the response of a simple structure to the test excitations. The structure is a simple cantilever beam shown schematically in Figure 1.

The excitation source is assumed to be the nonstationary random process described in Equations 1, 2, 3, and 5, with the parameters listed in Table 1.

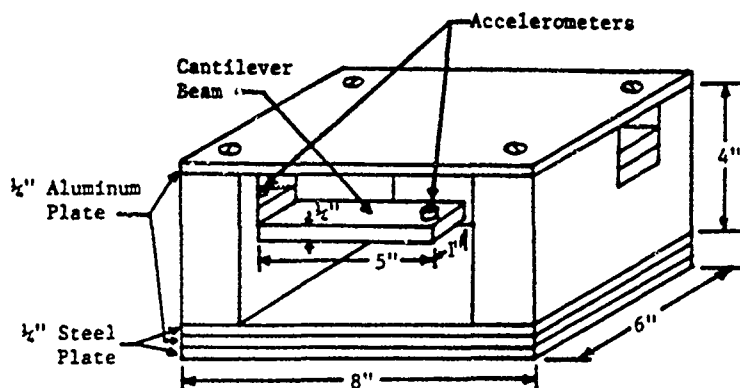


Figure 1 Cantilever Beam Shock Test Fixture.

Table 1. Parameters of the Example Nonstationary Random Process

Component Number, j	Low Frequency Cutoff, F_{1j} (Hz)	High Frequency Cutoff, F_{2j} (Hz)	Amplitude Parameter, α_j (g)	Decay Parameter, β_j (sec^{-1})
1	20	40	500	40
2	40	80	500	40
3	80	125	500	40
4	125	250	500	40
5	250	500	1500	40
6	500	1000	4000	40
7	1000	2000	9000	40

A realization of the nonstationary random process is shown in Figure 2a. Generation of multiple realizations of the random process shows that the time histories generated by the source are random, and the characteristics of the signals generated (such as peak values) vary from one sample to the next.

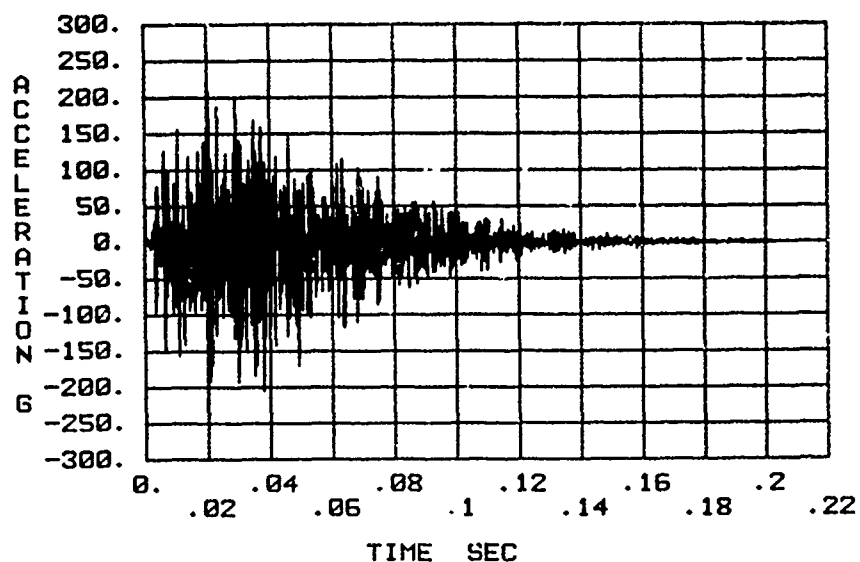


Figure 2a. Theoretical Realization of Nonstationary Random Process Based upon Parameters from Table 1.

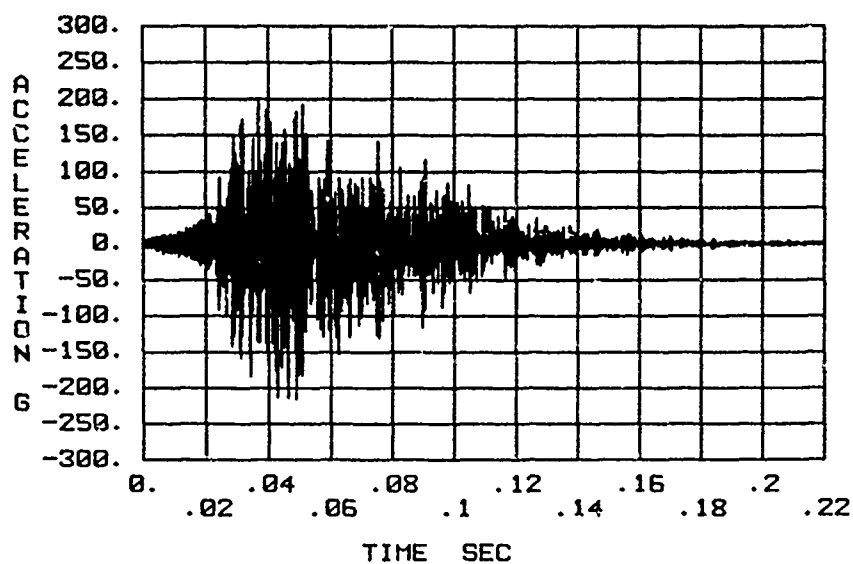


Figure 2b. Experimental Realization of Nonstationary Random Process Based upon Parameters from Table 1.

A shock generation computer program in use at Sandia National Laboratories and an electrodynamic shaker were used to generate a nonstationary random transient based on the parameters in Table 1 in a physical experiment. The experimentally generated input is shown in Figure 2b. Comparison of Figures 2a and 2b shows that the excitations do not match precisely, but their characteristics are quite close. The initial buildup in Figure 2b is characteristic of pulses generated on electrodynamic shakers.

The structural response to the excitation in Figure 2b is shown in Figure 3. This response was measured at the end of the cantilever beam during a physical experiment where the excitation was generated on an electrodynamic shaker. All the characteristics of the response depend on the specific features of the excitation, and to the extent that the excitation is random, the response is also random.

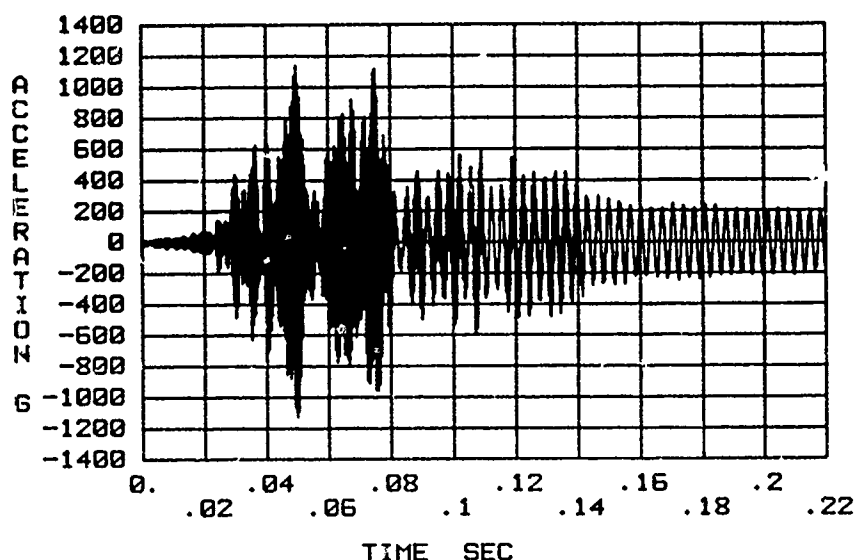


Figure 3. Structural Response at End of Beam Due to Shock Input in Figure 2b Controlled at Base of Beam.

In order to compare excitation and response for the actual environment to the excitation and response obtained when the test input is specified using the method of shock response spectra, the shock response spectrum of the signal shown in Figure 2a was computed. This shock response spectrum is shown in Figure 4a by the dashed line. To establish a test excitation via the method of shock response spectra whose severity is comparable to the nonstationary random process source, a test excitation whose shock response spectrum matches the nonstationary random process shock response spectrum was defined. To simplify the procedure for defining such a test excitation, the straight-line test specification is shown as a solid line in Figure 4a. A computer program was used to iteratively choose the parameters of a test pulse so that its shock response spectrum matches the solid line in Figure 4a. The test is a CEDS pulse (compensated sum of exponentially decaying sinusoids, Reference 7), defined by the parameters in Table 2. The shock response spectrum for the CEDS

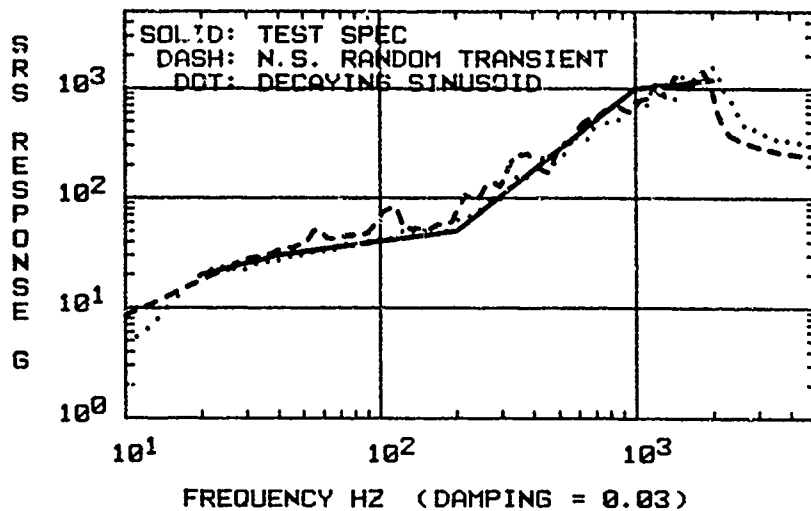


Figure 4a. Comparison of Test Specification with Decaying Sinusoid and Nonstationary Random Transient Shock Spectra Based upon Theoretical Test Inputs (Figures 2a and 5a).

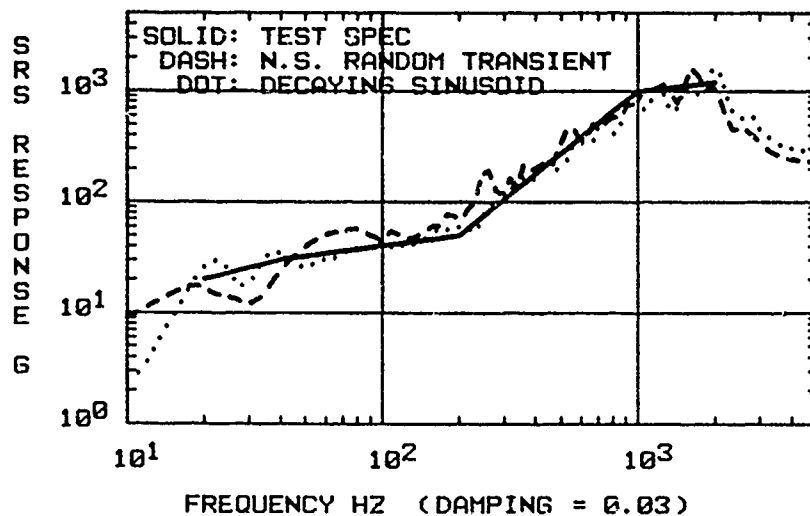


Figure 4b. Comparison of Test Specification with Decaying Sinusoid and Nonstationary Random Transient Shock Spectra Based upon Experimental Test Inputs (Figures 2b and 5b).

pulse is shown by the dotted line in Figure 4a. Figure 4b shows a comparison of the shock response spectra produced during actual shaker tests involving the CEDS pulse and the nonstationary random transient. The time history of the theoretical CEDS pulse is shown in Figure 5a. The CEDS pulse used to excite the cantilever beam structure in the experiment is shown in Figure 5b. The response at the end of the beam is shown in Figure 6.

Table 2. Parameters for CEDS Waveform.

Component Number	Frequency (Hz)	Decay Rate	Amplitude (g)	Delay (sec)
1	10	1.0	-6.65	0.0
2	20	0.12	8.39	0.0014
3	26	0.09	-6.25	0.0014
4	33	0.07	5.25	0.0014
5	43	0.06	-4.08	0.0014
6	56	0.04	4.11	0.0014
7	72	0.03	-3.93	0.0014
8	93	0.02	4.26	0.0014
9	120	0.02	-4.67	0.0014
10	155	0.016	4.94	0.0014
11	200	0.012	-4.96	0.0014
12	258	0.011	7.81	0.0014
13	335	0.008	-12.1	0.0014
14	430	0.006	16.5	0.0014
15	560	0.004	-25.2	0.0014
16	720	0.004	35.8	0.0014
17	930	0.002	-56.1	0.0014
18	1200	0.002	69.4	0.0014
19	1550	0.002	-85.1	0.0014
20	2000	0.002	117.	0.0014

The nonstationary random process was also simulated using a classical haversine pulse. To identify a classical pulse that represents the random process shock environment, we compared the shock response spectrum of a classical pulse to the test specification shock response spectrum. We chose a classical pulse whose shock response spectrum envelops the test specification shock response spectrum shown by the solid line in Figure 4a. The test specification shock response spectrum and the shock response spectrum of an actual haversine test input are compared in Figure 7. The time history of the classical pulse test is shown in Figure 8. The response excited in the cantilever beam structure is shown in Figure 9. The pulse used in the test is approximately a haversine pulse with 700 g amplitude and 0.5 msec duration.

Discussion

The results of the experimental example and other tests performed by the authors provide a basis for the comparison of tests that directly simulate a nonstationary random environment and shock tests specified by the method of shock response

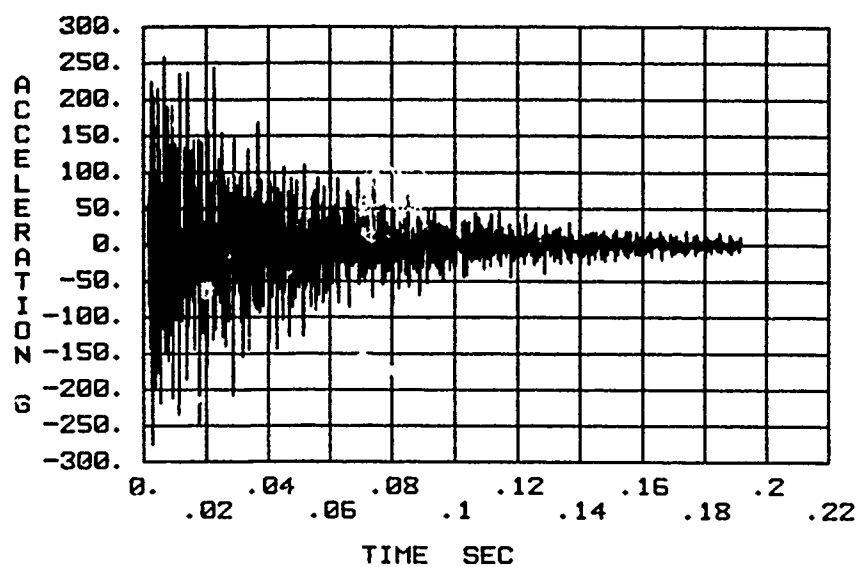


Figure 5a. Theoretical CEDS Waveform Based upon Parameters in Table 2.

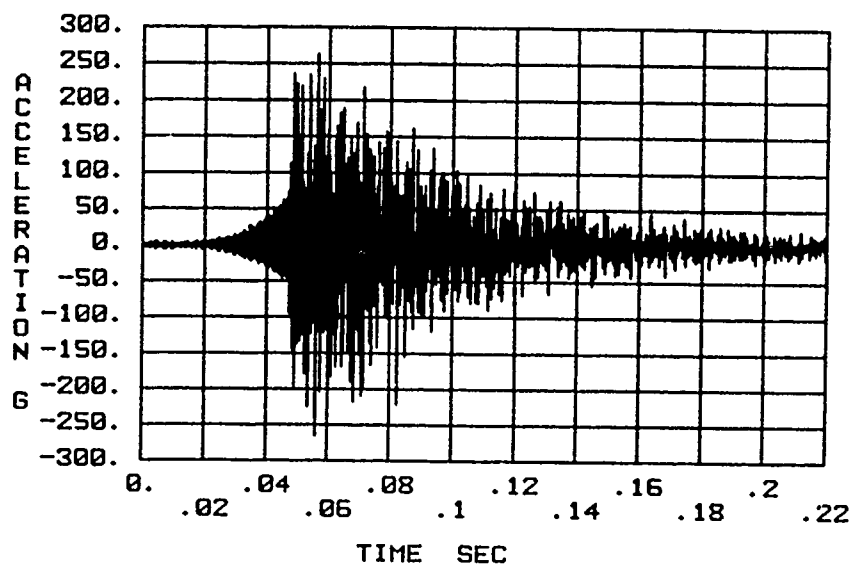


Figure 5b. Experimental CEDS Waveform Based upon Parameters in Table 2.

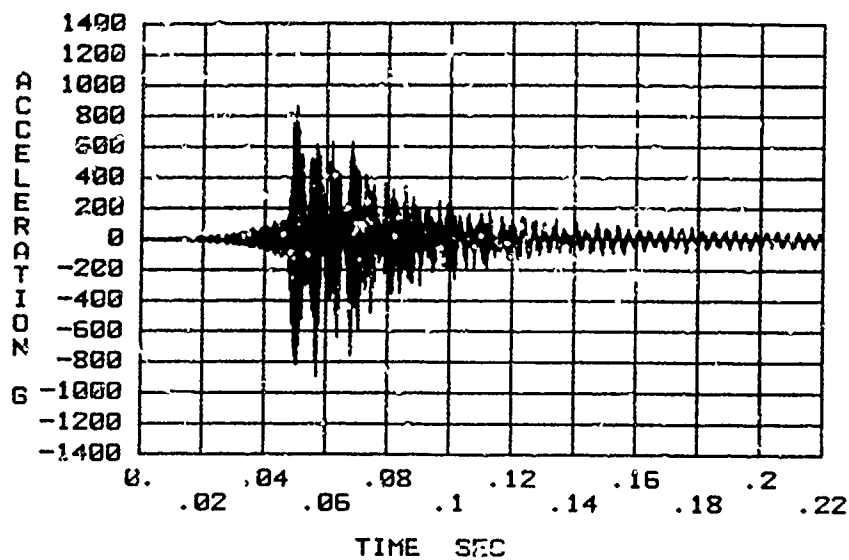


Figure 6. Structural Response at End of Beam Due to Shock Input in Figure 5b Controlled at Base of Beam.

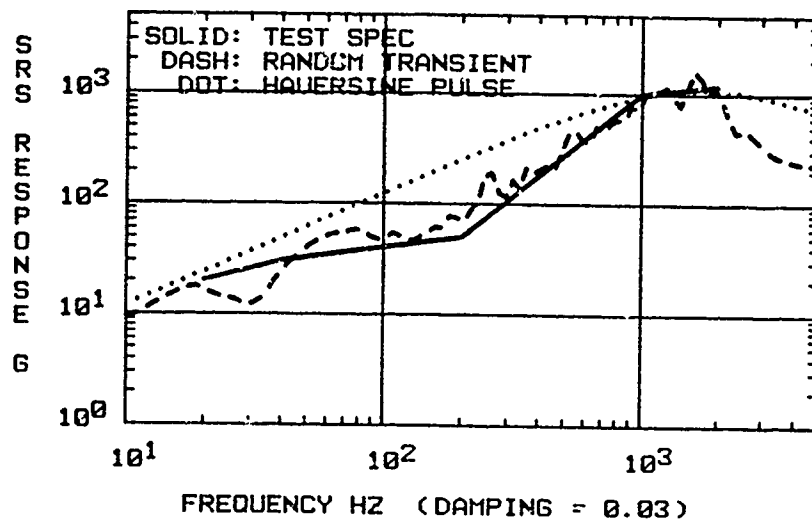


Figure 7. Comparison of Test Specification with Haversine Pulse and Nonstationary Random Transient Shock Spectra Based upon Experimental Test Inputs (Figures 2b and 8).

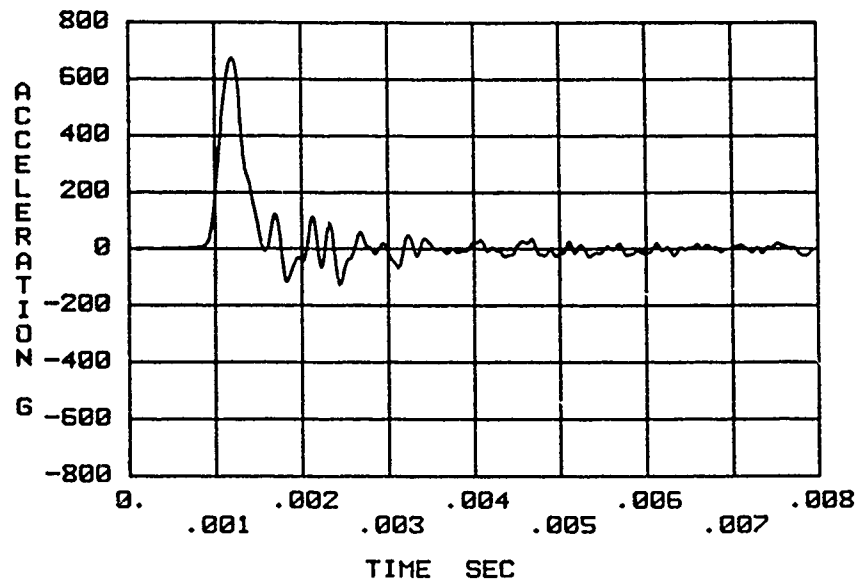


Figure 8. Experimental Haversine Shock Input to Beam.

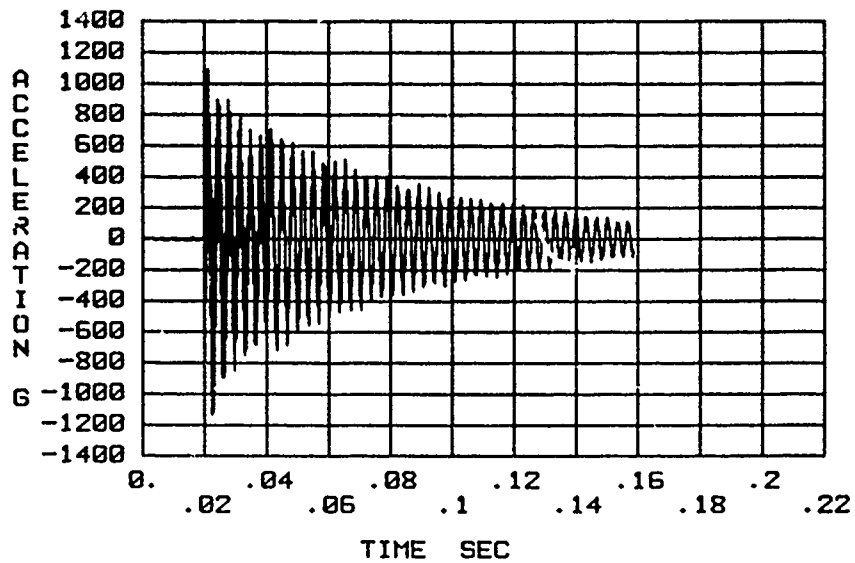


Figure 9. Structural Response at End of Beam Due to Haversine Shock Input in Figure 8 Controlled at Base of Beam.

spectra. The present example uses a nonstationary random source that is rich in frequency content over the interval 20 Hz to 2000 Hz. Several realizations of the random process were generated, and these show that the random process tends to generate signals that have a practical duration of about 150 msec. The realizations tend to increase for about 30 msec, then they decay until their magnitudes are negligible. Peak accelerations of the random process realizations tend to be in the range of about 200 g to 230 g. The physical signal shown in Figure 2b, the result of an attempt to match the random process realization in Figure 2a, provides a reasonable representation of the theoretical source. The peak value of the test excitation is about 220 g. The response in the beam, shown in Figure 3, has a peak value of about 1130 g.

The test excitations generated using the method of shock response spectra differ from the random process excitation in some fundamental ways. The CEDS pulse is oscillatory, but it does not have the same rise and decay characteristics as the random source. The CEDS pulse, shown in Figure 5a, has frequency content in the interval 20 Hz to 2000 Hz, but this frequency content is created by the use of 19 decaying sinusoidal pulses rather than the much larger number of components in the random source. The decaying character of the components in the CEDS pulse tends to spread their frequency content, but it does so in a different manner than the actual shock source. The peak value in the CEDS pulse used to represent the random source is about 290 g. Using this criterion, the CEDS pulse appears to be slightly more severe than the shock source it is meant to represent. The response in the cantilever beam excited by the CEDS pulse, shown in Figure 6, has a character different from the response excited by the random process excitation. This is to be expected, based on the differences in the excitation pulses. Though the CEDS pulse test excitation must be considered acceptable based on the method of shock response spectra, the response it excites in the beam appears less severe than the response excited by the nonstationary random process realization. In fact, the peak value in the response is only about 900 g.

The simulation of the actual environment provided by the CEDS pulse and the response it excited in the beam may be considered quite reasonable in this case. In general, as long as the pulse used to generate a shock test looks like the source it is meant to represent, the method of shock response spectra may provide useful tests. When this is no longer true, overtesting or undertesting may occur.

The simulated haversine excitation, shown in Figure 8, is considerably different from the nonstationary random process realization. The shock response spectrum of the haversine pulse, shown in Figure 7, indicates that the pulse has frequency content from low frequencies through several thousand Hz. This pulse gains its bandwidth because of its short duration; Figure 8 indicates that the main pulse lobe has a duration of about 0.5 msec. The excitation amplitude is about 700 g, and in this respect, the excitation is quite conservative. The response of the cantilever beam structure excited by the haversine pulse, shown in Figure 9, is strongly dominated by a 300 Hz component, the fundamental frequency of the beam. The response is primarily a free decay response, and has a peak value of about 1150 g - similar to the response caused by the nonstationary random process excitation. In this regard, the haversine pulse is a reasonable representation of the actual source.

The experimental example presented here cannot be used to draw wide-ranging conclusions about all shock tests, but it does show that tests specified with the method of shock response spectra may provide reasonable inputs, especially when the

system of interest is simple in nature and the primary criterion for judging test adequacy is peak structural response. The logical standard of comparison has been taken as a direct simulation of the actual environment; this is always to be preferred when it can be used because it simulates the actual source in all respects.

Experience shows that there are situations when test specification by the method of shock response spectra does not work very well. Specifically, when the system to be tested is structurally complicated, the potential for over or under-test exists. Further, if the damage criterion is something other than peak response, or if the damage criteria are unknown, then use of the method of shock response spectra may provide poor results.

Conclusion

This paper shows that the simulation of nonstationary random transients is possible. The simulation procedure involves the choice of a mathematical model, the identification of its parameters, and the use of the model to generate samples from the random source. Under most circumstances, direct simulation of a random source is the preferred method for specifying a shock test, but there are some circumstances when the direct simulation cannot or should not be used, and there are other situations when the use of a direct simulation is especially important.

The direct simulation of a shock source as a nonstationary random process should not be pursued when the shock source is, in fact, a deterministic (or nearly deterministic) signal source. This situation occurs most frequently when the item to be tested is located near the primary source of the shock and the shock generation mechanism is physically simple. Transient excitation sources cannot be directly simulated when the testing cannot be done on an electrodynamic or electrohydraulic shaker. The generation and matching of nonstationary random process realizations is a relatively complicated process, and, at present, it only appears feasible to execute this process on a shaker. This limits the shock amplitudes that can be generated (depending on the available equipment) to a few hundred g's, and the frequency content to about 2000 Hz. Moreover, a shaker cannot provide a realistic test when an important feature of the shock environment is a large change in velocity. In these situations tests should be specified by the method of shock response spectra.

There are times when it is especially important to directly simulate a shock source nonstationary random process. When the damage criteria of the system being tested are unknown or not well known, then the test should simulate the actual environment to maximize the equivalence between the test and the environment. Further, when the actual environment is a nonstationary random process, sufficient measurements are available to characterize the random process, and the transient source characteristics are compatible with shaker capabilities, then it is advisable to simulate the nonstationary random process.

The authors view the direct simulation of nonstationary random transient environments in contrast to other methods for specifying "equivalent" shock tests, as being analogous to the use of stationary random vibration testing in contrast to swept sine testing. When their use is feasible and the application is appropriate, the former methods are to be preferred.

Given the feasibility of direct simulation of nonstationary random transient environments and the widespread use of the method of shock response spectra, both methods should be investigated further.

Acknowledgement

The authors wish to acknowledge the laboratory assistance provided by Ronald Coleman, Luther Otero, and Ervin Smith of the Experimental Mechanics Department at Sandia National Laboratories.

References

1. Moening, C., "Pyrotechnic Shock Flight Failures," IES Pyrotechnic Shock Tutorial Program, Las Vegas, Nevada, May 1985.
2. Baca, T., Paez, T., "Mechanical Test Specification Using Nonstationary Random Excitation Models," Dynamic Failure, Proceedings of the 1987 SEM Fall Conference, Savannah, Georgia, October 1987.
3. Paez, T., Baca, T., "Implementation of a New Shock Testing Procedure Using Nonstationary Random Excitation," Dynamic Failure, Proceedings of the 1987 SEM Fall Conference, Savannah, Georgia, October 1987.
4. Paez, T., "Characterization of Nonstationary Random Processes," Proceedings of the Institute of Environmental Conference, Las Vegas, Nevada, May 1985.
5. Baca, T., "Characterization of Conservatism in Mechanical Shock Testing of Structures," SAND-82-2186, Sandia National Laboratories, 1983.
6. Baca, T., "Alternative Shock Characterizations for Consistent Shock Test Specifications," Shock and Vibration Bulletin, Vol. 54, Part 2, June 1984.
7. Smallwood, D., "Shock Testing Using Digital Control," SAND85-0352J, Sandia National Laboratories, 1985.
8. Piersol, A., "The Analysis of Nonstationary Vibration Data," Proceedings of the 58th Shock and Vibration Symposium, Vol. 1, NASA Conference Publication 2488, October 1987.
9. Brownlee, K., Statistical Theory and Methodology in Science and Engineering, John Wiley and Sons, New York, 1967.
10. Billings, S., Korenberg, M., Chen, S., "Identification of Nonlinear Output-Affine Systems Using an Orthogonal Least Squares Algorithm," Research Report No. 313, Department of Control Engineering, University of Sheffield, Sheffield S1 3JD, March 1987.
11. Clements, E., Sullivan, J., Vigness, I., "Shock Testing Machines," in Shock and Vibration Handbook, 3rd Edition, Harris, C., ed., McGraw-Hill, New York, 1988.

HIGH VELOCITY IMPACT TESTING OF AN ACCIDENT RESISTANT CONTAINER USING A LARGE CENTRIFUGE

**John R. Garcia and Richard L. Weatherbee
Dynamics Loads and Facility Development Division 7531
Sandia National Laboratories
Albuquerque, NM 87185**

An impact test technique using the 35-foot centrifuge located in Area III at Sandia National Laboratories in Albuquerque, New Mexico is described. An Accident Resistant Container was thrown into a hard target at impact velocities of up to 425 ft/s using the tangential velocity of the centrifuge. The dynamics of motion in a curvilinear path, design considerations and limitations, hardware, target setup, release mechanism, and instrumentation are discussed.

INTRODUCTION

The Area III 35-foot centrifuge at Sandia-Albuquerque has the capability to achieve a rotational velocity up to 15.2 rads/s, which corresponds to a maximum tip tangential velocity of 558 ft/s (380 mph). This velocity regime (0 to 380 mph) is a convenient one for releasing test items from the moving arm into a hard target. Test costs are relatively inexpensive when compared to other methods of impact testing, and a multitude of tests can be performed in a short period of time once the experiment is set up.

The impact test idea is not a new one for the 35-foot centrifuge. In the early 1970's the centrifuge was used to release Accident Resistant Containers (ARCs) into various hard targets at velocities of 275 ft/s (180 mph).¹

A renewed interest in ARC designs with more stringent survivability constraints created a need for more ARC impact testing. The Trident II Warhead Division 5153 at Sandia National Laboratories designed a new Accident Resistant Container which required impact testing up to 425 ft/s (290 mph) into a hard target to verify its structural and functional adequacy.²

It is the purpose of this paper to describe the test parameters and techniques of ARC impact centrifuge testing, which are substantially different from previous ARC testing. New fixturing and different release circuitry and mechanisms have improved the test technique. The report will also show once again that impact testing using the 35-foot centrifuge is a feasible alternative to other impact test techniques.

DYNAMICS OF MOTION IN A CURVILINEAR PATH

In analyzing the ARC experimental setup, it is important to understand the governing equations of motion as applied to ARC centrifuge testing.

The general velocity equation in vector notation and polar coordinates (Figure 1) for a moving particle in a curvilinear path is as follows:

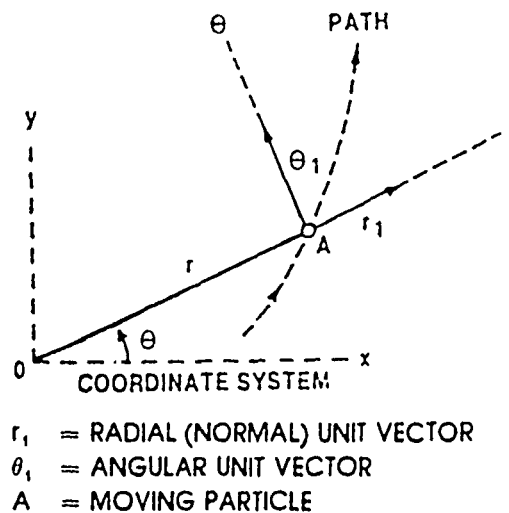


Figure 1. Coordinate System

$$V = \dot{r} r_1 + r \dot{\theta} \theta_1 \quad (1)$$

where

$$V_r = \dot{r}$$

$$V_\theta = r \dot{\theta}$$

$$V_{TOT} = (V_r^2 + V_\theta^2)^{1/2}.$$

Since r is constant before the unit is released, then

$$V_r = 0$$

$$V_\theta = r \dot{\theta}.$$

Hence,

$$V = r \dot{\theta} \theta_1. \quad (2)$$

In the postrelease condition, it is assumed that

$$V_{\text{initial}} = V_{\text{tangential}} = r\dot{\theta} ,$$

and therefore,

$$V_{\text{impact}} \approx r\dot{\theta} . \quad (3)$$

It may be further noted that $\dot{\theta}$ is rotational velocity ω , and therefore impact velocity is given by

$$V = r\omega . \quad (4)$$

Taking the derivative of the general velocity equation (1) gives the acceleration components (Figure 2) in Eq (5):

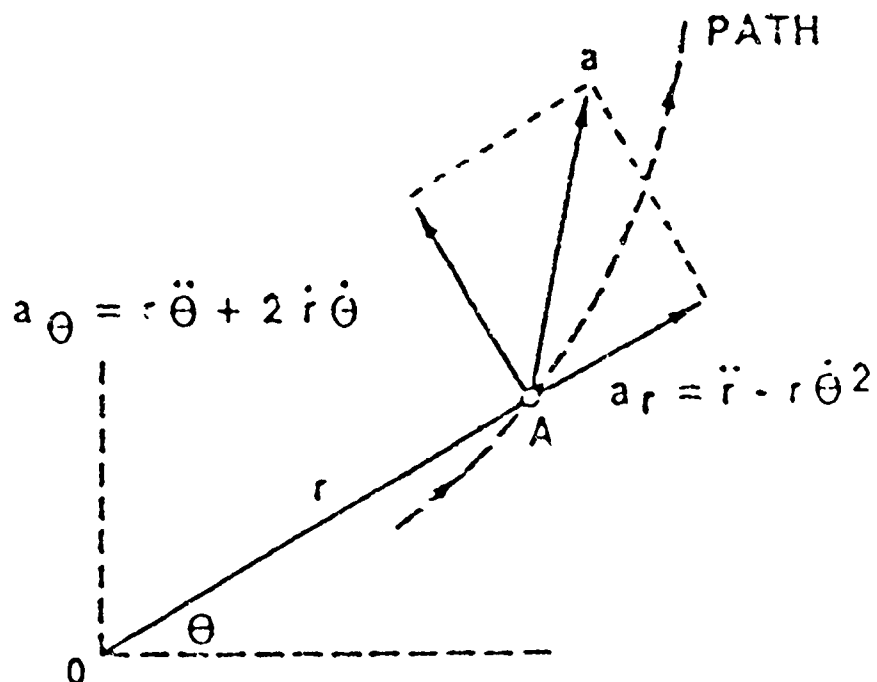


Figure 2. Acceleration Components

$$a = (\ddot{r} - r\dot{\theta}^2)r_1 + (r\ddot{\theta} + 2\dot{r}\dot{\theta})\theta_1 . \quad (5)$$

Note that

$$\begin{aligned} r_1 & \left\{ \begin{array}{l} \ddot{r} = \text{Acceleration along radius in the absence of change of } \theta . \\ -r\dot{\theta}^2 = \text{Normal component of acceleration if } r \text{ were constant as in} \\ \text{circular motion (centrifugal accel) } (\dot{\theta} \text{ is due to fact that} \\ \text{system is rotating).} \end{array} \right. \\ \theta_1 & \left\{ \begin{array}{l} r\ddot{\theta} = \text{Tangential acceleration which particle would have if } r \text{ were} \\ \text{constant, but is only a part of acceleration due to} \\ \text{change in magnitude of } V_\theta \text{ when } r \text{ is variable } (\ddot{\theta} \text{ is zero at} \\ \text{constant rpm)} \\ 2\dot{r}\dot{\theta} = \text{Comes from two effects:} \\ \text{a) change in magnitude of } V_\theta \text{ due to change in } r \\ \text{b) change in direction of } V_r. \end{array} \right. \end{aligned}$$

Since r is constant, both the first and second derivatives of r are zero. Also note that at constant rpm, the second derivative of θ is zero also. Therefore, the general acceleration equation simplifies to:

$$a = r (\dot{\theta}^2). \quad (6)$$

Substituting ω for $\dot{\theta}$ in Eq (6) gives

$$a = r (\omega^2). \quad (7)$$

These two simple velocity and acceleration equations, (4) and (7), are used as the basic design parameters for setting up the ARC experiment on the centrifuge.

DESIGN CONSIDERATIONS

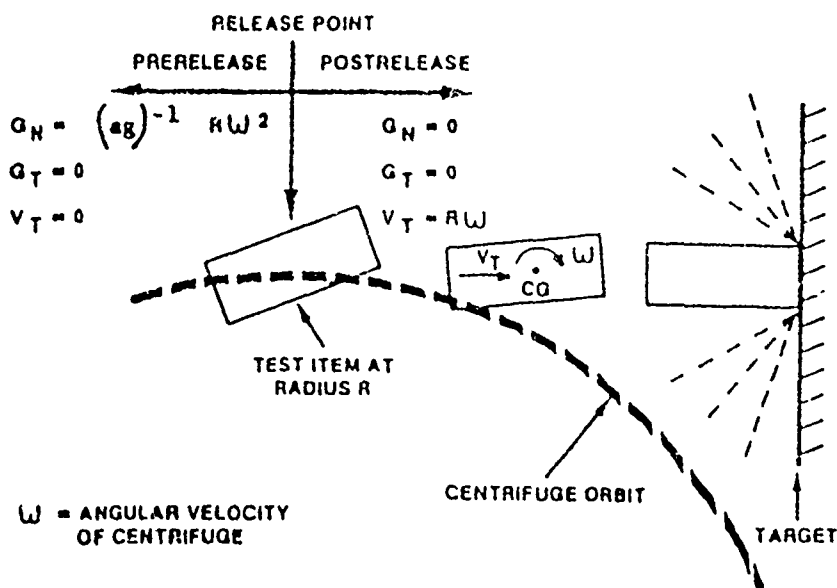
The hydraulically driven 35-foot centrifuge has the following design capabilities and limitations:

• Maximum Speed (fairred)	15.2 rad/s (145 rpm)
• Maximum Speed (unfairred)	8.4 rad/s (80 rpm)
• Payload Limit	10,000 lb
• Dynamic Load Limit	450,000 G-lb
• Maximum Normal Acceleration (1800-lb payload @ 35 ft)	245 G's
• Overall Length of Rotating Arm	56 ft
• Radius (center of rotation to payload bay)	35.5 ft
• Radius (center of rotation to counter weight end)	20.5 ft

The ARC experiment had a design impact velocity of 425 ft/s which corresponded to a centrifuge rotational velocity of 108 rpm. At a 37-ft test radius, the entire payload would see up to 148 G's before release of the test item. At 148 G's, the dynamic load limitation on the machine limited the entire payload weight to 3000 lbs.

With the above design constraints, a fixture was designed such that the container could impact the target axially, longitudinally, and at a 45° angle of attack. The fixture also allowed the unit to rotate about its CG, so that a normal impact would occur on the hard target (Figure 3)¹.

FREE-FLIGHT ENVIRONMENT OF TEST ITEM



Source: J. V. Otts, *Impact Testing With the 35-Foot Centrifuge*, SC-DR-72 0795. Albuquerque, NM: Sandia Laboratories, December 1972.

Figure 3. Free-Flight Environment of the Test Item

HARDWARE

ARC Unit

The 85-lb quarter-scale ARC unit was a 12.770-in.-diameter cylinder that was 26.996-in. long. There were three Endevco accelerometers (model 7270A) mounted within the main warhead cavity of the container, with one instrumentation cable coming out the side of the canister (Figure 4). Ten feet of instrumentation cable were wound in "accordion" style so that the cable would not break until after impact.

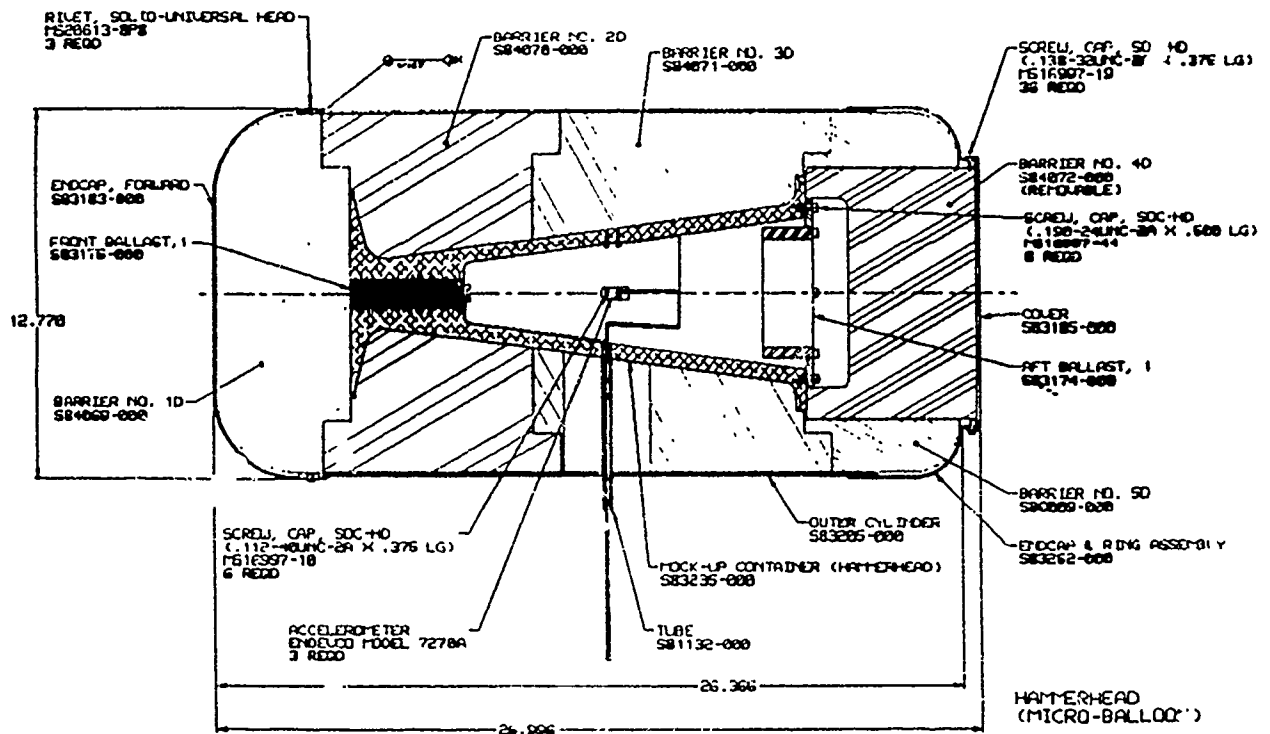


Figure 4. Quarter-Scale ARC

Centrifuge Fixture

The centrifuge variable angle fixture, (Figure 5), designed specifically for the quarter-scale ARC, has the capability to withstand a 220-G load with a 100-lb container mounted to it. (Reference 3, Figure 6). The customer requested that the 60-mil-thick outer canister of the unit not be crushed under the G load, and hence a large circular cradle with sufficient cross-sectional area to distribute the load was designed. Note too, that a specially fabricated 4-in.-wide Kevlar strap was used to mount the canister to the cradle. The cradle was designed such that a 3-in.-axial elongation could be preloaded into the Kevlar strap so that it would not stretch under the G field. Also, a Horex cable was slipped onto a 3-in.-long 0.5-in.-diameter piece of Kevlar rope which was connected to the main Kevlar strap for release purposes. (See details of Horex cable cutter and release mechanism in later paragraphs.)

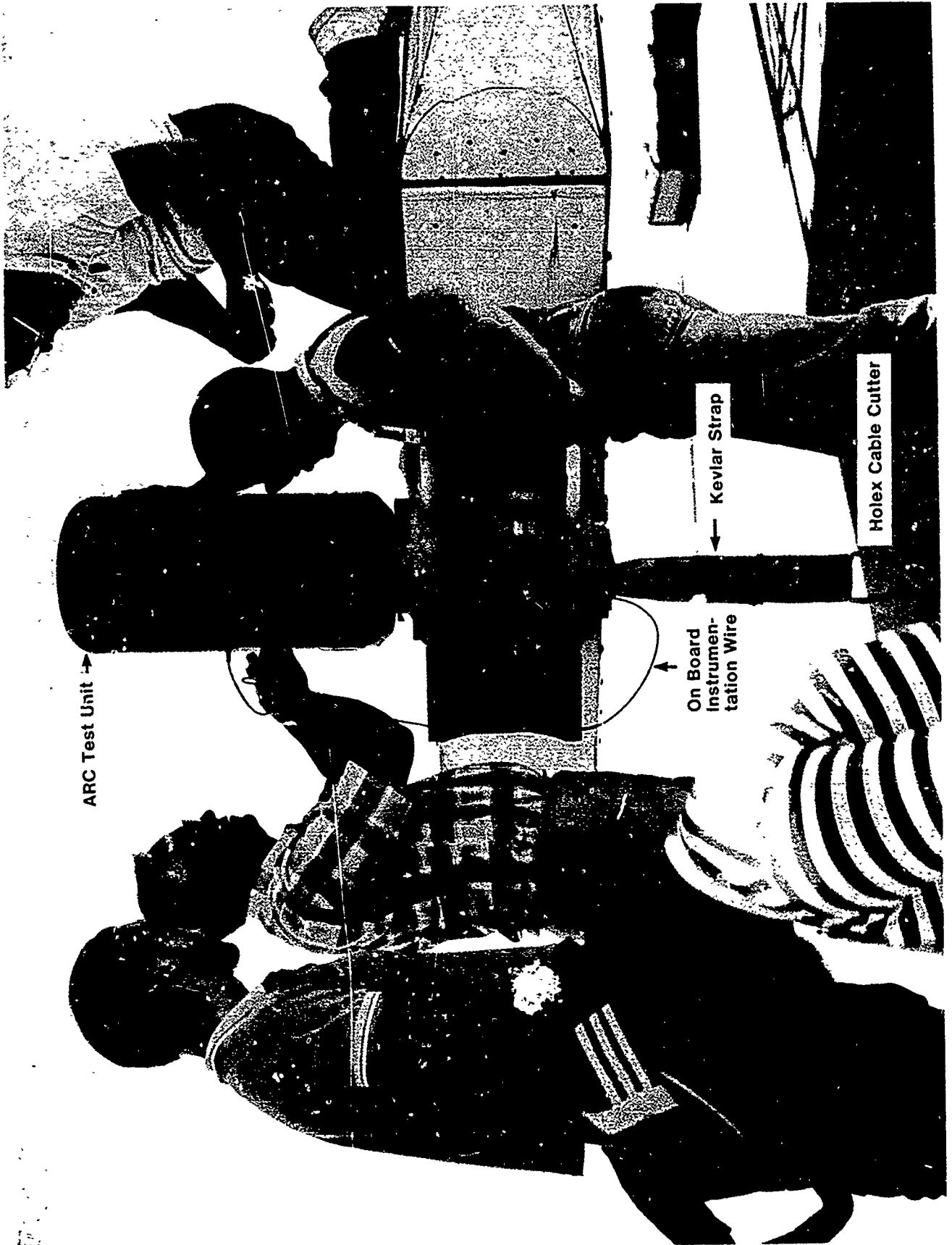


Figure 5 - Centrifuge Fixture

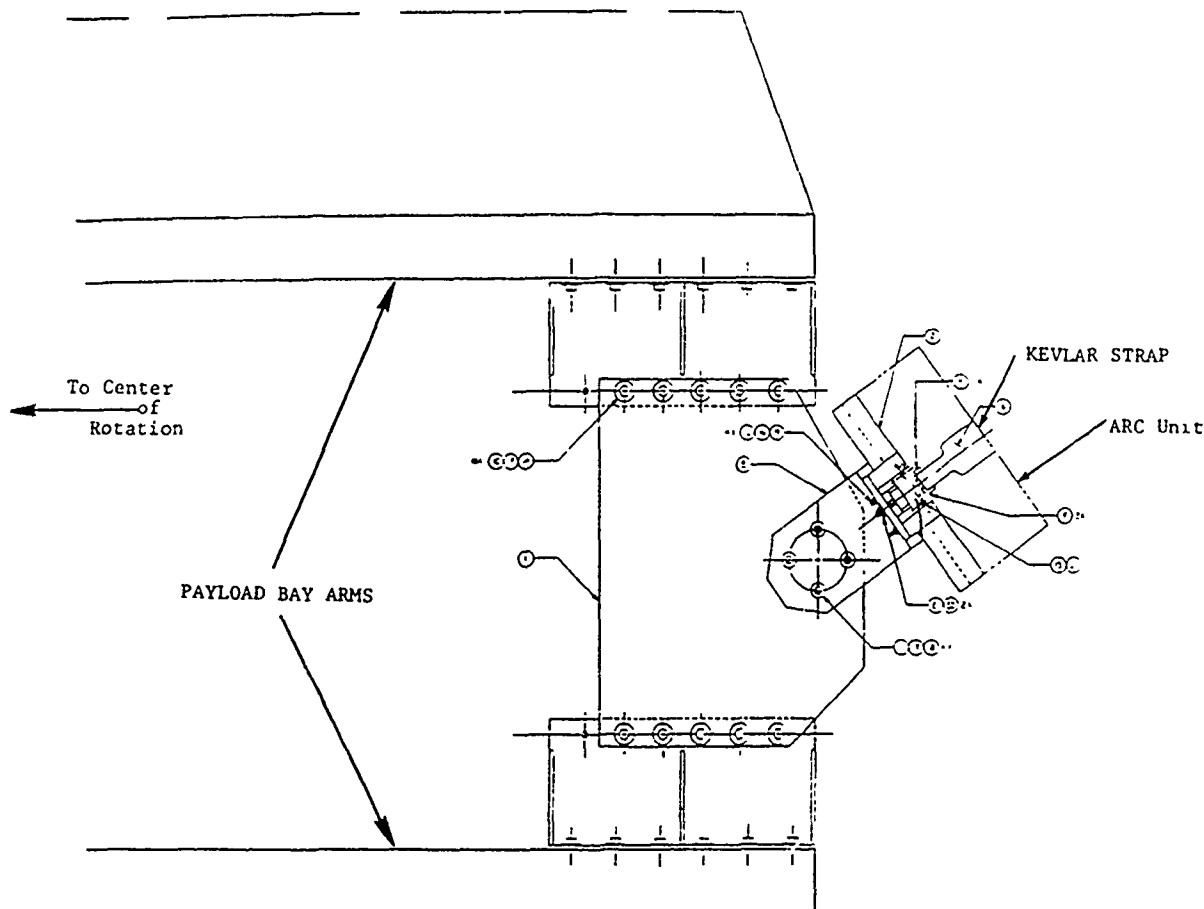


Figure 6. Plan View of Centrifuge Variable Angle Fixture

Target Area

The amount of mass required to prevent the impact target from moving was determined from an impulse-momentum relationship. Hence, an impact target (Figure 7) consisting of a reinforced concrete block 5 X 2 X 12 ft ($\approx 18,000$ lb) faced with a steel plate 4 X 8 X 2-in. (≈ 2600 lb) was designed to absorb the impact loads of the ARC. Of course, the CG of the combined mass was difficult to hit with the container, and bracing of the block was required to keep the block from rotating after every shot.

A major concern in the target area was the rebound of the ARC into the path of the rotating centrifuge arm. It was possible that the ARC could be "batted" out of the 48-foot diameter bullpen which surrounds the centrifuge. Hence, three catcher sandboxes (12 X 12 X 1 ft) were placed on the ground in front of the impact area to absorb some of the rebound energy of the container.

High speed cameras were mounted for orthogonal views of the angle of attack of the unit. A 2000-frames/second (fps) camera was mounted on the overhead bridge crane structure, and a second 2000-fps camera was mounted on top of the bullpen wall. An overall camera set at 400-fps monitored the entire impact area. A real-time videotape tape of the event was recorded for each shot and a videotape of impact testing is available.

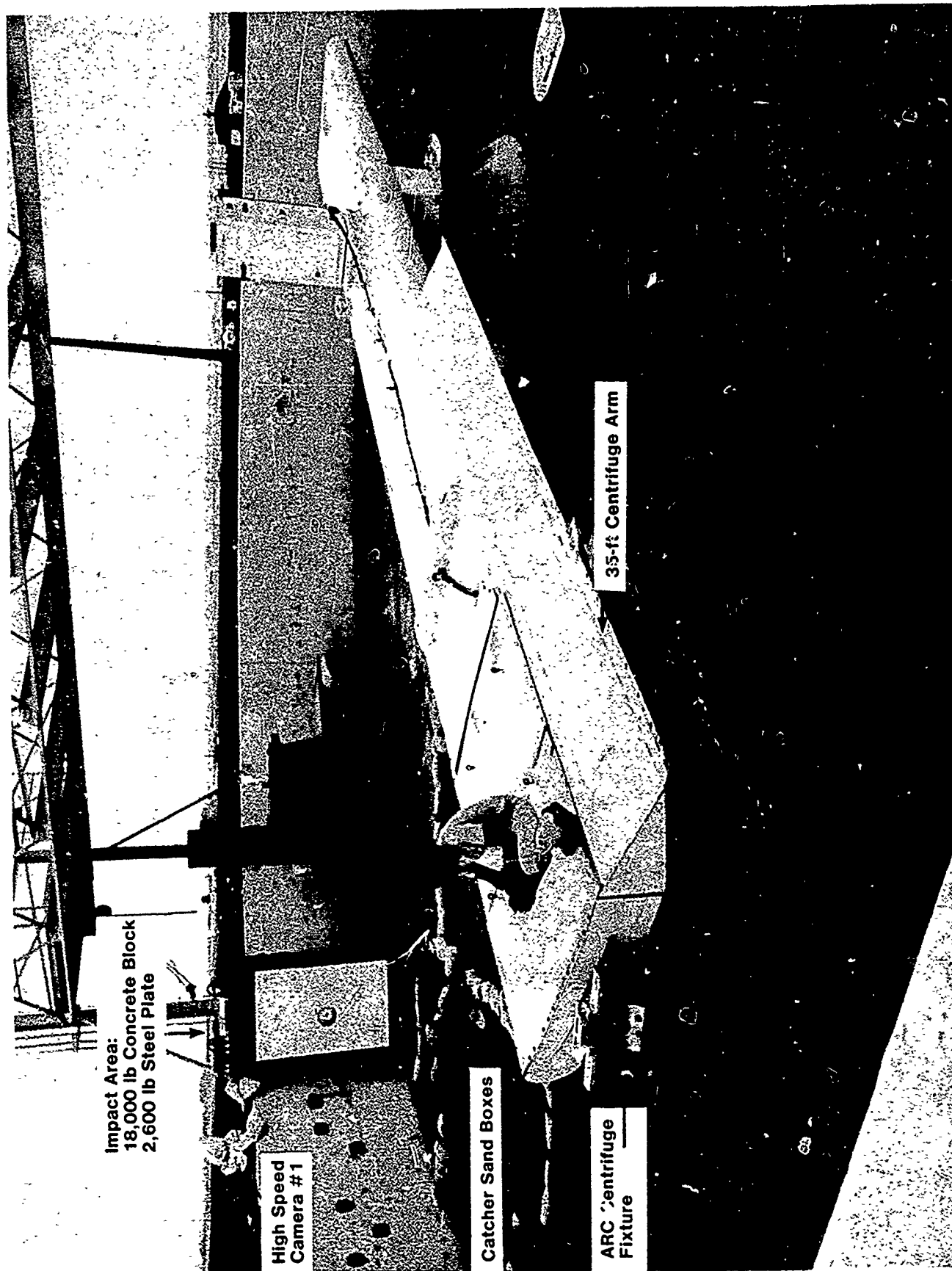


Figure 7 - ARC Target Setup

RELEASE MECHANISM

During previous impact testing programs in the 1970's, a photo diode was mounted to the base of the centrifuge structure to reference the position of the arm to a desired release point of the test object. A signal from the photo diode was fed to the control room in Building 6526 and to the firing circuit mounted in the doghouse on the centrifuge arm. The photo diode signal would energize a light emitting diode at the firing panel, in Building 6526, each time the centrifuge arm passed the release point. Once the centrifuge system was at the correct speed, the firing relays were energized and the photo diode would fire the cable cutter the next time it passed the release point.

A Hoxley cable cutter was used to release the ARC unit in both previous tests in the 1970's and in the current tests (Figure 8). The explosive guillotine cutter used in current tests (model 2803) is designed to operate with a 0.5-A no-fire and a 1.5-A all-fire condition. To fire the Hoxley cable cutter a 28-V, 5-A power supply was used to supply the current to the cutter, and an SCR (2N688) was used to control the switching of the firing current (Figure 9). To maintain a safe operating procedure, the facility has developed a step-by-step checklist called IMPK-CHK (see Appendix) that must be used to fire the release system at the centrifuge.

It should be noted that the previous ARC test parameters (1970's) were slow enough (≈ 1 revolution per second, rps) to allow the operator to energize a toggle switch between revolutions. However, the new ARC system was turning at nearly 2 rps, and the high-speed cameras had to be started 1 revolution before impact to allow the cameras to come up to speed before filming the impact shot. Hence, a different method of release was designed.

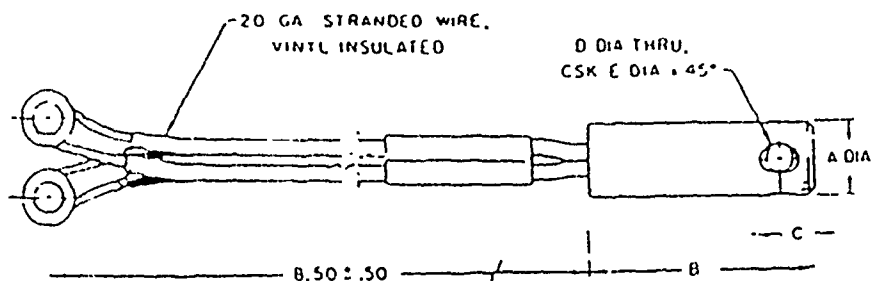
To release the ARC unit at a specific location, a precise way of determining the position of the arm was needed. To do this the incremental shaft encoder on the centrifuge was used. This optical encoder, model number H25E-SS-6000 made by BEI Electronics, puts out 6000 counts per revolution (± 1 count) plus one reference pulse per revolution. Note that the encoder is normally used to determine the rotational velocity of the centrifuge while operating. The encoder is adjustable, however, on the shaft of the centrifuge and therefore the reference pulse can be changed to match the release point of the ARC unit. The exact release point of the ARC unit, plus the delay time of the Hoxley cable cutter, was determined and the reference point of the encoder was adjusted to match this point. The reference pulse was then fed to a timing counter that was used to start the high speed cameras and to activate the firing circuit for the Hoxley cable cutter. The timing counter was activated by the facility operator when the centrifuge was at the speed requested by the test consultants. Once the timing counter was activated, it would cause the high speed cameras to start the first time the centrifuge arm would pass the release point, and would activate the firing circuit for the Hoxley cable cutter the second time the centrifuge arm passed the release point.

To compute the delay time in the timing system, a Nicolet high-speed digital scope, model 2090, was used. The reference pulse, at the encoder, was fed to one channel of the scope, and a break wire that was cut by the Hoxley cable cutter was fed to the second channel. The system was activated by the

HOLEX SERIES 2800 GUILLOTINES

DESCRIPTION

The HOLEX 2800 Series Guillotines are small, propellant actuated cutting devices. The unit is electrically initiated and a propellant charge drives a piston with a wedge-shaped knife through the cable, hose or bolt located in the guillotine opening. The severance of the cable, tube or bolt is clean and practically silent. The unit does not give off shrapnel in operation, and may be fired without a cable or tube in the opening without danger of fragmentation. The HOLEX Model 2800 Guillotines are classified as "Class C" Explosives and may be shipped by either Air Express or Air Freight as well as by surface transportation. The 2800 Series Guillotines are a simple, reliable, efficient and safe unit for accomplishing rapid severance of mechanical units. The significant characteristics of these units are given below.



APPLICATION DATA

The 2800 series guillotines have been extensively tested for operation over a temperature range of -60°F to $+200^\circ\text{F}$ and are designed to meet most current military environmental specifications.

These guillotines will cut the following specific cables:

MODEL 2800— $3/32$ DIA 7×7 CRES CABLE PER MIL-C-5424

MODEL 2801— $3/16$ DIA 7×19 CRES CABLE PER MIL-C-5424

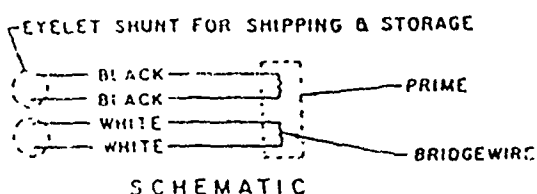
MODEL 2802— $3/8$ DIA 7×19 CRES CABLE PER MIL-C-5424

MODEL 2803— $7/16$ DIA 7×19 CRES CABLE PER MIL-C-5424

$1/2$ DIA 6×19 GALV STL COMMERCIAL CABLE

For applications involving other sizes and materials please contact HOLEX Incorporated.

HOLEX PART NO.	DIA A $\pm .005$	DIM B $\pm .035$	DIM C $\pm .025$	DRILL D DIA	CSK E DIA	UNIT WT (OZ)
2800	.375	1.490	.200	#30 (.1263)	188	718
2801	.500	2.01	.250	1/4 (.2500)	11/32	1
2802	.875	3.120	.870	7/16 (.4375)	5/8	3-1/2
2803	1.125	3.500	1.000	9/16 (.5625)	7/8	6



FIRING CHARACTERISTICS (EACH BRIDGEWIRE)

NO-FIRE CURRENT	0.5 AMP MAX
ALL-FIRE CURRENT	1.5 AMPS MIN
BRIDGEWIRE RESISTANCE (THRU LEADWIRE)	0.66 $\pm .08$ OHM
LEADWIRE-TO-CASE NO-FIRE	1000 V AC RMS MAX
LEADWIRE-TO-CASE RESISTANCE	2 MEGOHMS MIN AT 500 V DC
RECOMMENDED ALL-FIRE CURRENT	5 AMPS PER BRIDGE

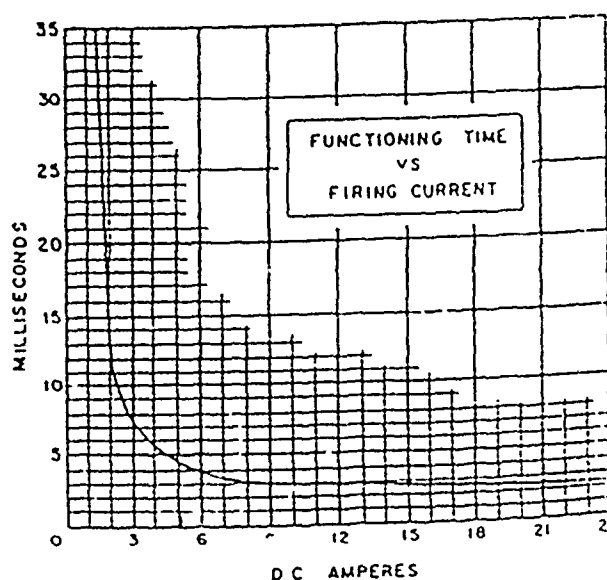


Figure 8. Holey Cable Cutter Data Sheet

1. ALL RESISTANCE VALUES ARE IN OHMS.
2. ALL CAPACITOR VALUES ARE IN MICROFARADS.
3. TELETYPE 640-1 RELAYS RETURN 1, SEC. TO CLOSE.

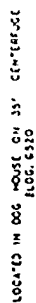


Figure 9 - Impact Release Mechanism Schematic

reference pulse, which was recorded on the first channel and the Horex cable cutter fired which in turn cut the break wire giving a second pulse that was recorded on the second channel. The difference in the two pulses on the scope represented the actual delay time in the complete circuit, including the long lead lines and the propagation time of the explosive charge in the Horex cable cutter. This time delay turned out to be approximately 5.5 ± 0.5 ms. Because of the monetary expense involved in using an actual Horex cable cutter for circuit time delay determination, only 5 trial runs were made. The release time was very repeatable, but inherent noise problems, caused by the long lead lines and the old slip rings, were of a large enough voltage amplitude to cause the SCR to go into conduction accidentally. This in turn would cause a spontaneous firing of the Horex cable cutter. There were three such incidents in the ARC test series. It was felt that this problem could be solved in the future by optically coupling the timing circuit and the firing circuit.

To test the position of the release point, an audible detector was connected to the reference pulse signal and a plumb bob was connected to the CG of the test item. By using this system, the exact release point was located by rotating the centrifuge (by hand) to the release point until the audible detector sounded. After this point was located, a distance equal to the time delay and was added in, and the new release point was shifted by this amount.

CONCLUSION

Impact testing at the centrifuge in Area III provides a convenient method of testing the structural and functional adequacy of a consultants' design of a test item. This process, although not a new one, has been refined to allow higher tangential velocities and more accurate release points. It is a relatively inexpensive impact test method with a quick turnaround time.

A major advantage to impact testing on the centrifuge, as opposed to other impact test environments, is that it allows the test consultants to do an instrumentation pre-check, once at the required velocity, before actually releasing the test unit. This would allow the consultant to abort the test without destroying the test item. The test item must, however, meet the size, weight, and velocity constraints mentioned within this report.

A total of 16 actual test units were impacted into the target. Some of the 16 were instrumented with accelerometers located at the center of the warhead container, and others were thrown without accelerometers to verify the structural design of the unit. All information from these transducers is given in Reference 2.

The high-speed camera coverage that is available through Sandia's photometric division allows a detailed viewing of the events that occurred during impact of the test item into the target area. It was noted in the films, however, that the Horex cable cutter fired randomly in approximately 2 out of every 10 container releases. This is due primarily to the inherent noise problems caused by the long lead lines and old slip rings on the 35-ft centrifuge.

REFERENCES

¹J. V. Otts, Impact Testing with the 35-Foot Centrifuge, SC-DR-72 0795, (Albuquerque, NM: Sandia Laboratories, December 1972).

²R. K. Thomas, N. G. Rackley, and R. E. Howell, Feasibility Study of an Accident Resistant Container for Fleet Ballistic Missile Reentry Bodies, and the Impact of the Risk of Air Transport, SAND87-2845 (Albuquerque, NM: Sandia National Laboratories, to be published).

³J. R. Garcia, Letter to T. B. Lane, "ARC Centrifuge Fixture Design Capabilities and Limitations", (Albuquerque, NM: Sandia National Laboratories, June 1987).

APPENDIX

IMPK-CHK:

CHECK LIST FOR IMPACT FIRING AT THE 35-FOOT CENTRIFUGE

BEFORE WIRING THE HOLEX CABLE CUTTER:

- _____ 1. "IMPACT FIRE TIMING PANEL" - POWER OFF
- _____ 2. "IMPACT REMOTE FIRE PANEL" - KEY SWITCH IS OFF & ARM-SAFE SWITCH IS IN "SAFE" POSITION
- _____ 3. 28-VOLT POWER SUPPLY IN DOGHOUSE IS OFF
- _____ 4. WIRE UP CABLE CUTTER ACCORDING TO SOP #06801 8705

BEFORE TEST

- _____ 5. TURN 28 VOLT POWER SUPPLY ON
(Note: this supplies power to the firing circuit in the doghouse)
- _____ 6. "IMPACT FIRE TIMING PANEL" - POWER ON AND PUSH RED RESET BUTTON
(Note: Energizing the "IMPACT FIRE TIMING PANEL" will energize the 12-Vdc power supply. See schematic impact release mechanism)
- _____ 7. BRING CENTRIFUGE UP TO REQUIRED R.P.M.
- _____ 8. START 10 SECOND COUNT DOWN
- _____ 9. AT COUNT 10 - "IMPACT REMOTE FIRE PANEL" - TURN KEY SWITCH ON
- _____ 10. AT COUNT 1 - "IMPACT REMOTE FIRE PANEL" - ARM-SAFE SWITCH TO "ARM"
(Note: When Key switch and toggle switches are both energized the 12-Vdc is applied to the remote firing circuit.)
- _____ 11. AT COUNT 0 - ENERGIZE TOGGLE SWITCH ON TIMING BOX
(1ST REV. CAMERAS ARE TURNED ON)
(2ND REV. CUTTER IS FIRED)

AFTER RELEASE

- _____ 12. "IMPACT FIRE TIMING PANEL" - POWER OFF
- _____ 13. "IMPACT REMOTE FIRE PANEL" - KEY SWITCH IS OFF & ARM-SAFE SWITCH IS IN "SAFE" POSITION
- _____ 14. 28-V POWER SUPPLY IN DOGHOUSE IS OFF

SHOCK

PYROTECHNIC SHOCK DATA REDUCTION PROCEDURES AND PROBLEMS

**Harry D. Riead
General Dynamics/Convair Division
P.O. Box 85357
San Diego, CA 92138**

The U/RGM-109D is a submunitions version of the Tomahawk cruise missile. The submunitions are protected during underwater launch by large covers which are separated during flight by cutting the perimeter with FLSC (flexible linear shaped charge). A series of tests and investigations was performed following a flight failure associated with cover separation shock. This review presents the data reduction procedures along with some of the data reduction problems encountered during these investigations.

INTRODUCTION

The U/RGM-109D is a submunitions version of the Tomahawk cruise missile. The submunitions area of the missile is protected during submarine launch by two large payload covers. The payload covers are separated from the missile prior to submunition dispense by cutting the 15 foot cover perimeter with 10 grain/foot flexible linear shaped charge (FLSC). A schematic of the missile is shown in Figure 1.

The U/RGM-109D experienced a flight failure resulting from alteration of the guidance set memory coincident with the shock caused by payload cover separation. A series of tests and investigations was initiated to lower the shock levels, to isolate and eliminate the failure mechanism and to explore other methods of preventing future flight failures.

This paper presents the data reduction procedures along with some of the data reduction and interpretation problems encountered during the shock reduction studies.

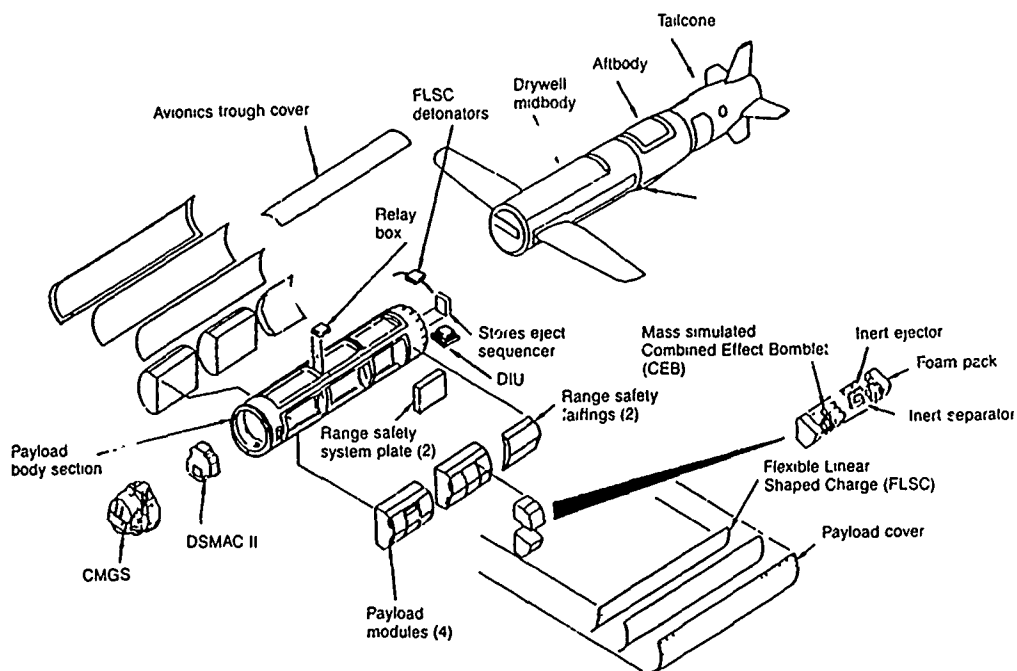


Fig. 1 - U/RGM-109D Tomahawk Cruise Missile

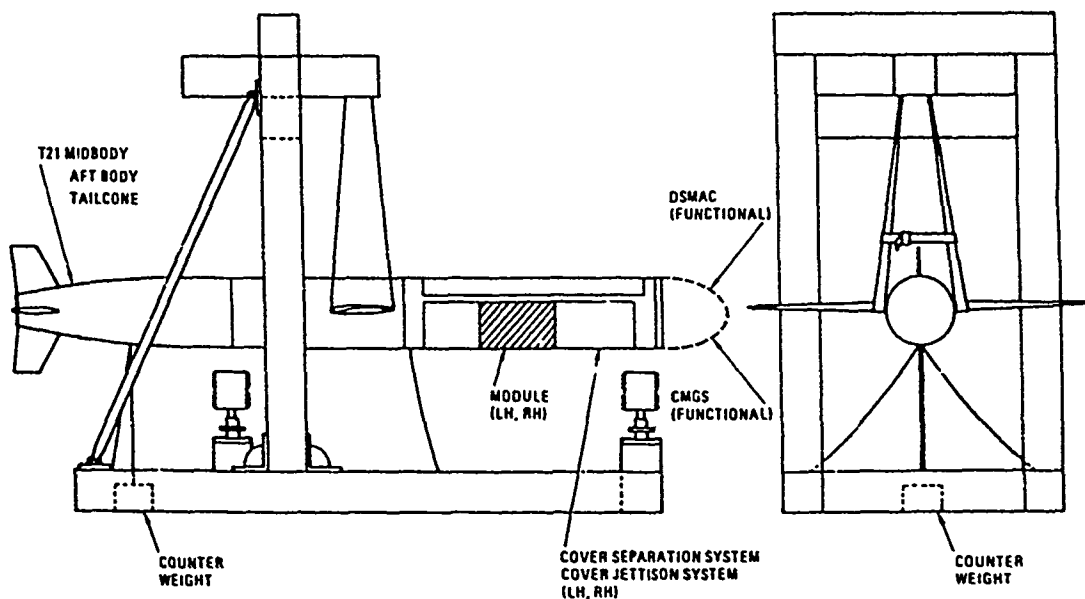


Fig. 2 - Cover Separation Ground Test Fixture

Test Performance

The missile covers were separated with the missile supported by straps from a fixture, as shown in Figure 2.

The data instrumentation and the processing procedure used for a typical test are shown in Figures 3 and 4. Data acquisition and processing involved the following major steps: 1) Pass the analog data through a 7 pole constant delay low pass filter (13,200 or 20,000 Hz). 2) Digitize the data at 40,000 samples per second (maximum rate available at the time). 3) Remove any time history data preceeding the start of the event. 4) Remove any D. C. bias by forcing the average of all remaining data points to zero. 5) Calculate the $Q=10$ spectra. Shock spectra were typically generated using 15 to 20 ms of data following the start of the event.

Data Interpretation

Shock spectra for accelerometers located on hard structure close to the charge typically approached straight lines with a slope of 6 to 10 dB per octave on log-log plots (see Figure 10). A straight line with a slope of 6 dB per octave is the spectrum for a short duration impulse. Spectra for accelerometers well removed from the charge, or on soft mounted structure, deviated substantially from the straight line slope. Most data processing problems occurred for accelerometers mounted on hard structure, close to the charge, for the following reasons: 1) The high acceleration levels at high frequencies excited accelerometer resonances and produced frequency aliasing. 2) The high acceleration levels at high frequencies necessitated high charge amplifier ranges. These high ranges produced a signal to noise ratio problem at lower frequencies (typically below 800 Hz) where the acceleration levels are much lower.

Data interpretation and identification of trends was also complicated by the fact that there was a typical test to test variation of up to 6 dB in the spectra of all measurements.

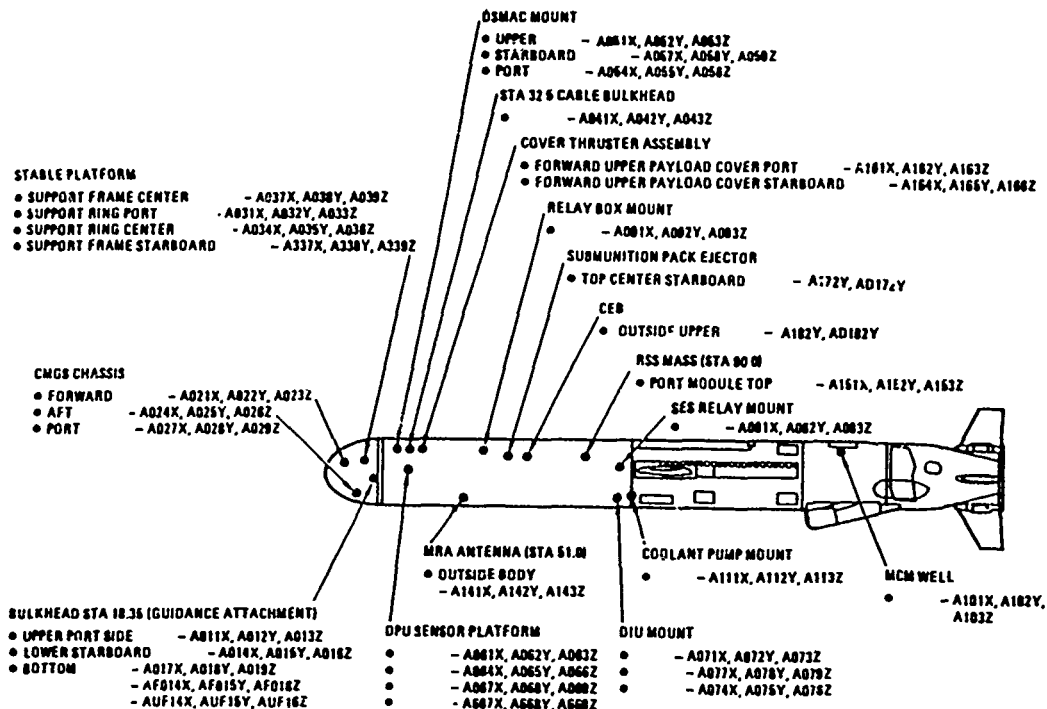


Fig. 3 - Cover Separation Ground Test Typical Accelerometer Locations

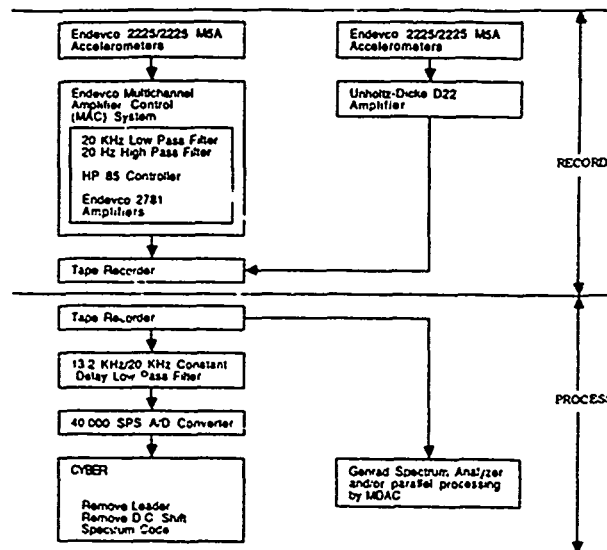


Fig. 4 - Cover Separation Ground Test Shock Data Recording and Processing

Data Reduction Problems

Shock data reduction problems were generally from one of the following sources:

- 1) Accelerometer Resonances
- 2) Frequency Aliasing
- 3) Noise
- 4) Charge Amplifier Saturation
- 5) D. C. Shifts

Accelerometer Resonances

A shock spectrum from a Endevco 2225 M5A accelerometer mounted on a flat plate which is excited with detonating cord is shown in Figure 5.¹ The spectrum shows a clear resonance at about 37,000 Hz. This resonance was identified by Endevco as a resonance of the accelerometer.

Figure 6 shows the overlay of the shock spectrum of a very short duration impulse on the spectrum of the response to the same impulse of a lightly damped single D.O.F. oscillator tuned to 37,000 Hz. The figure shows that there is a strong possibility that the true shock spectrum will be masked by the resonance spectrum. This problem would be solved if the 37,000 Hz. accelerometer response could be filtered out. Figure 7 shows the characteristics of the 7 pole constant delay (CD) low pass filters used by General Dynamics Convair Division during data reduction. This figure indicates that if the filter frequency is set low enough to substantially reduce the 37,000 Hz accelerometer resonant response, the amplitudes in the frequency range of interest (below 10,000 Hz) will also be significantly reduced. Constant amplitude (CA) filters produce a much sharper initial roll-off but could not be used because of a tendency to overshoot and "ring" when subjected to sharp transients. Overshoot and ringing can be seen in the comparison of outputs from CA and CD filters to a sample pulse in Figures 8A and 8B.

1) Courtesy Ed White, McDonnell Douglas Astronautics, St. Louis, Mo.

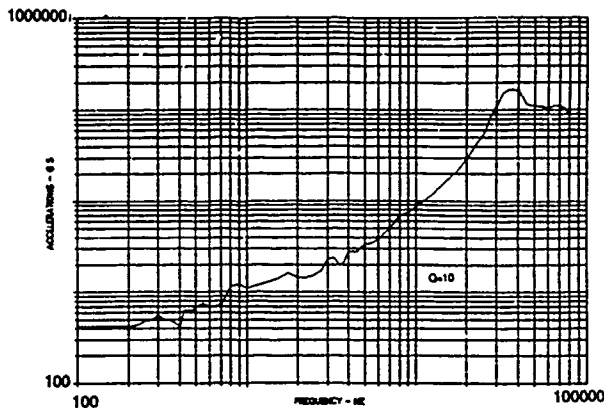


Fig. 5 - Typical Shock Spectrum From M5A Accelerometer on Flat Plate Pyro Test

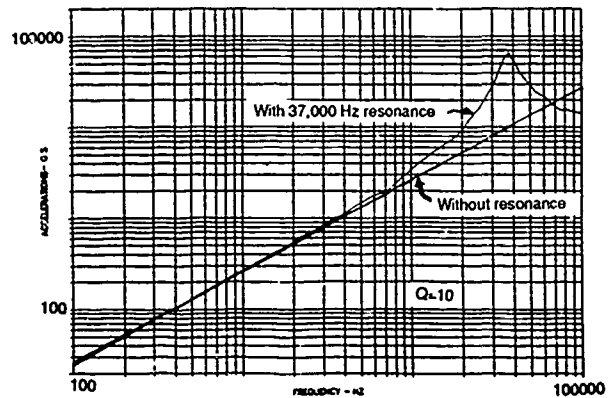


Fig. 6 - Analytical Spectra From Short Impulse

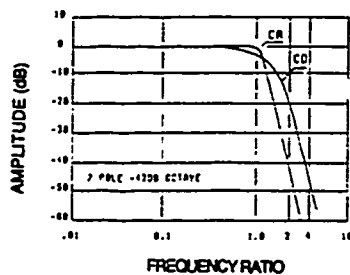


Fig. 7 - Comparison of 7 Pole CD and CA Filters

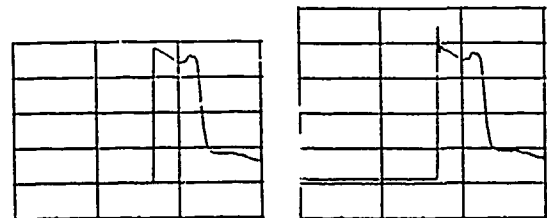


Fig. 8A - CD Filter Fig. 8B - CA Filter

Fig. 8 - Pulse Reproduced with CD and CA Filters

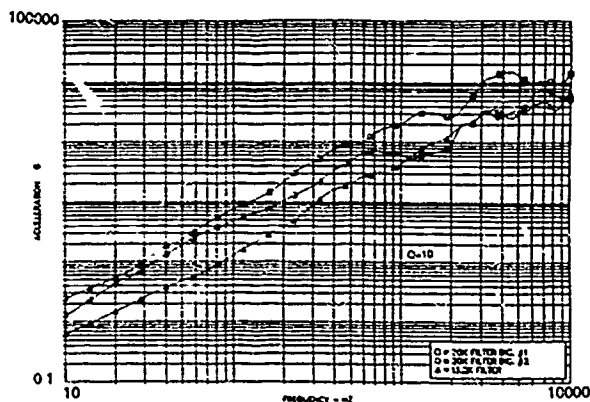


Fig. 9 - Aliasing with 20 KHz Filter and 40,000 SPS Digitization Rate

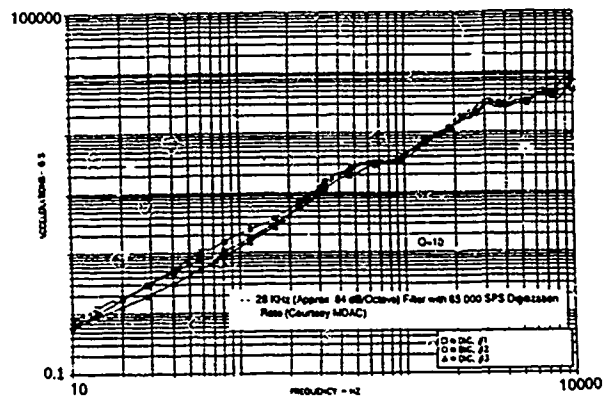


Fig. 10 - Digitization Repeatability with 13.2 KHz Filter and 40,000 SPS Digitization Rate

Frequency Aliasing

The maximum digitization rate available at Convair at the time this data was processed was 40,000 samples per second. Prior to digitization, the analog signal is filtered using constant delay filters with the characteristics shown in Figure 7. Figures 9 and 10 compare shock spectra produced using data filtered at 13,200 and 20,000 Hz with a 40,000 SPS digitization rate. Evidence of aliasing can be clearly seen in the spectra produced using the 20,000 Hz filter. The data is aliased because the levels induced by the accelerometer resonance (at about 37,000 Hz) contaminate the lower frequency response, in spite of being passed through the filter. Figure 11 shows the aliasing that would result if a 37,000 Hz constant amplitude sine wave were sampled at 40,000 samples per second. In this example the 37,000 Hz data is "aliased" to a frequency of about 3000 Hz. The 13,200 Hz filter reduces this problem at the expense of lowering the shock spectrum levels above about 6000 Hz.

Noise

Figure 12 compares typical shock spectra for left and right cover separation events with spectra of noise. The noise spectra are for data recorded on the FM tape immediately before the event and about 2 seconds after the event. The same length of time was analyzed for the noise and event spectra. Since the noise is not constant spectra were generally only considered to be valid when the signal to noise ratio was 6 dB or greater. This approach was used to establish a lower frequency limit for using the shock spectra.

Charge Amplifier Saturation

A time history and shock spectrum from a saturated charge amplifier are shown on Figures 13 and 14. For this measurement the charge amplifier range was ± 4200 G and clipping of the data is clearly evident. In many cases, however, the charge amplifier may be saturated even though the peaks in the final time history are well below the range of the amplifier. This is because the low pass filter reduces the high frequency peaks and the sampling process can miss peaks in the high frequency response. Charge amplifier saturation was typically characterized by a step shift in mean acceleration levels followed by a return toward zero over a period of several milliseconds.

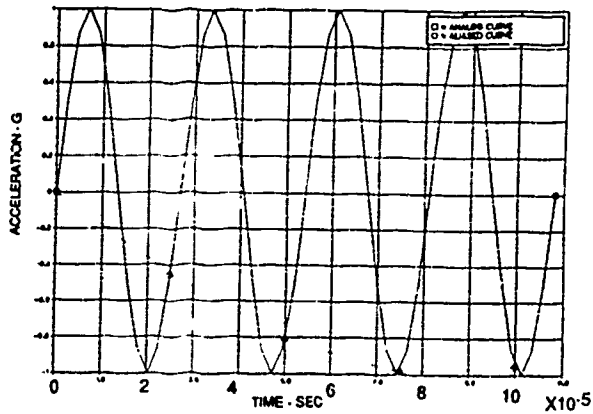


Fig. 11 - Data Aliasing Example
37000 Hz Sinusoid
Sampled at 40000 SPS

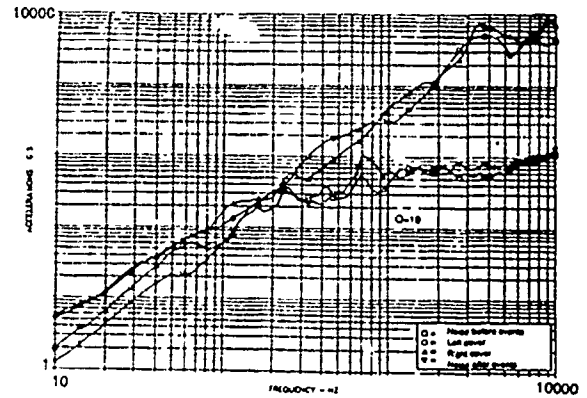


Fig. 12 - Signal and Noise Spectra
Comparison

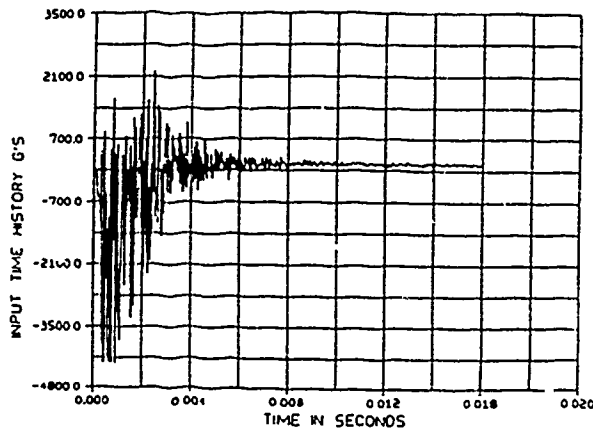


Fig. 13 - Time History From Saturated
Amplifier

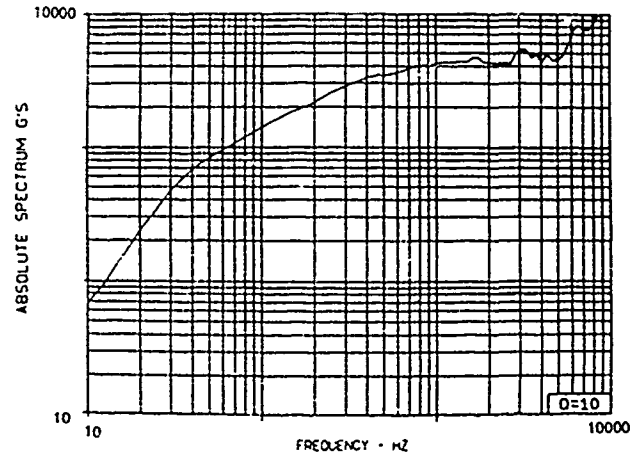


Fig. 14 - Shock Spectrum From Saturated
Amplifier

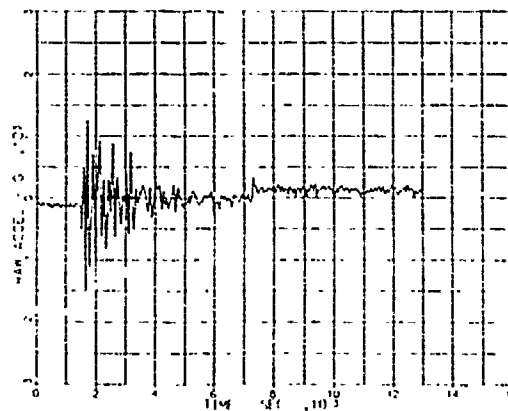


Fig. 15 - Acceleration Time History With
DC Shifts (Courtesy MDAC)

D. C. Shift

An example of an unexplained D. C. shift is shown in Figure 15. The Figure shows a shift at the beginning of the event and a second shift about 6 ms after the start of the event. Shifts associated with charge amplifier saturation typically show a return toward zero as shown in Figure 13. The shifts of Figure 15, however, show no tendency to return to zero and are of unknown origin.

Special Analysis Techniques

In addition to acceleration time histories and shock spectra the following analysis procedures were found to be very useful in evaluating shock data credibility.

Velocity Time Histories

Figures 16 and 17 show a shock spectrum and acceleration time history from an accelerometer located on hard structure close to the charge. The shock spectrum was suspect because it was substantially higher than spectra obtained from the same accelerometer during previous tests. There is, however, no readily obvious problem with the acceleration time history. Figure 18 shows the velocity time history of the same measurement. The velocity time history was produced by trapezoidal integration of the acceleration time history. The velocity time history clearly shows a large velocity step at a time corresponding to a broad acceleration spike in figure 17. Since a 200 ips velocity change of the structure was not physically possible the measurement was discarded. Acceleration and velocity time histories of a good measurement are shown on Figures 19A and 19B. Velocity time histories are useful since they exaggerate D. C. and low frequency phenomena which are not readily visible in acceleration time histories.

Energy Spectra

The energy spectrum $G_X(f)$ can be approximated by

$$G_X(\omega) = 2|X(\omega)|^2 \quad [1]$$

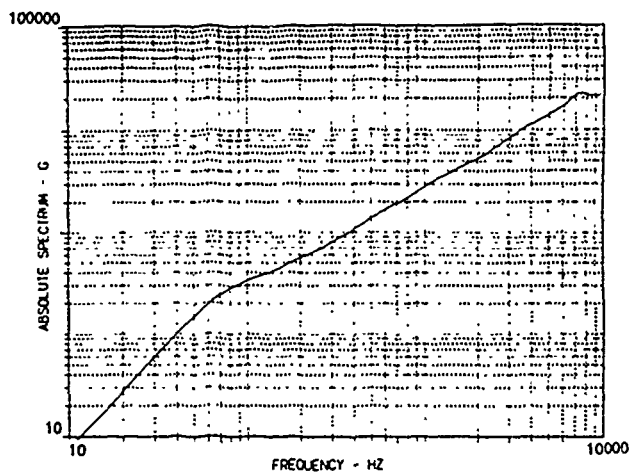


Fig. 16 - Spectrum of Acceleration Time History With Data Spike

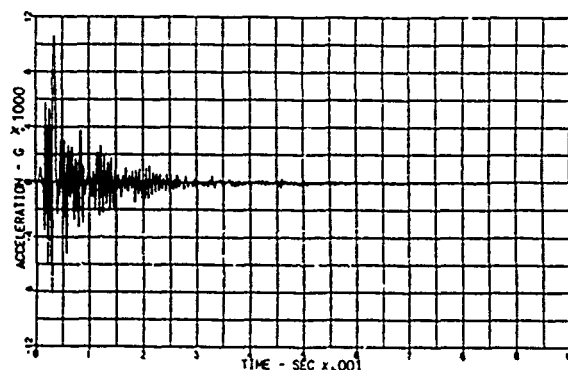


Fig. 17 - Acceleration Time History With Data Spike (Courtesy MDAC)

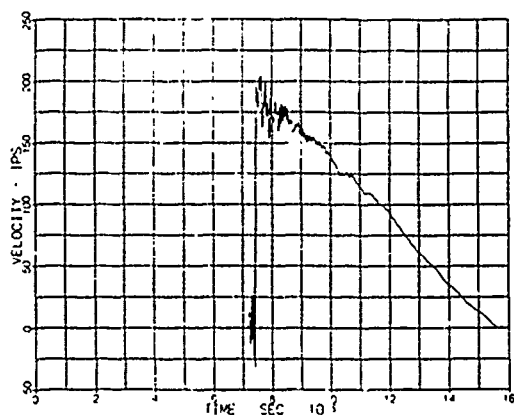


Fig. 18 - Velocity Time History With Data Spike (Courtesy MDAC)

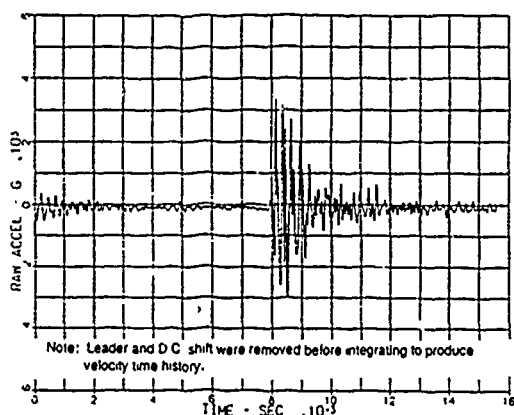


Fig. 19A - Acceleration Time History of "Good" Measurement

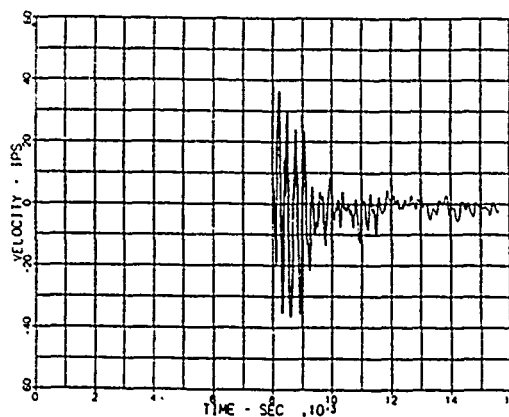


Fig. 19B - Velocity Time History of "Good" Measurement

$|X(\omega)|$ is the Fourier amplitude spectrum of the measured acceleration and can be calculated by

$$|X(\omega)| = \text{Res}_0(\omega)/\omega$$

$\text{Res}_0(\omega)$ is the residual shock spectrum (absolute magnitude of the peak oscillator response after the transient is complete) for zero damping. Note that an energy spectrum is identical to a power spectral density except that the energy spectrum is not divided by sample time.

The above formulation of the energy spectrum was convenient because the spectrum could be calculated with minor modifications to the Fortran code used to calculate shock spectra. The code used to calculate shock spectra was based on [2]. This code calculated the residual shock spectrum separately from the forced response spectrum. The only modifications to the code to obtain the Fourier amplitude spectrum were to save the residual shock spectrum terms and to divide by ω .

An additional modification was made to the shock spectrum code to produce the sums of $a(t)^2 dt$ and $|X(\omega)|^2 d\omega$. A check on the correctness of the energy spectrum calculations could then be made using Parseval's formula for integrals

$$\int_{-\infty}^{\infty} a(t)^2 dt = \int_0^t a(t)^2 dt = 1/2\pi \int_0^{\infty} |X(\omega)|^2 d\omega.$$

Since the energy spectra were calculated over a limited frequency range (typically 10 to 10,000 Hz) this equation was re-written as an inequality

$$\int_0^t a(t)^2 dt \geq 1/2\pi \int_{2\pi \times 10}^{2\pi \times 10,000} |X(\omega)|^2 d\omega.$$

For measurements well removed from the pyrotechnic charge the frequency integral was only slightly smaller than the time integral since the response at frequencies above 10,000 Hz was small. For some measurements close to the pyrotechnic charge the time integral was several times larger than the frequency integral. A large difference between the time and frequency integrals was taken as an indication that the measurement may be susceptible to the aliasing problems previously discussed.

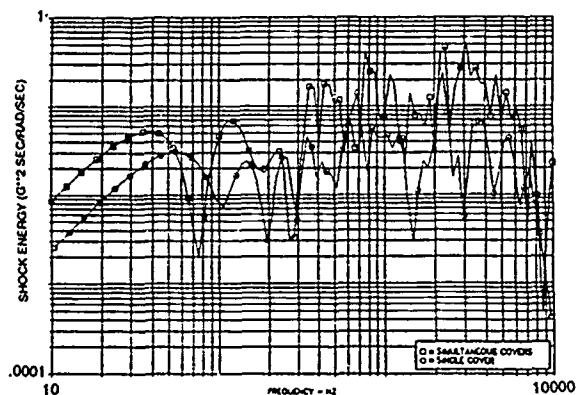


Fig. 20 - Energy Spectra of Guidance Bulkhead Accelerometer A013Z

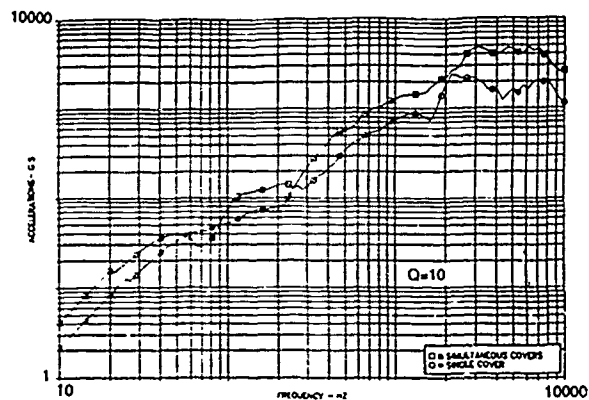


Fig. 21 - Shock Spectra of Guidance Bulkhead Accelerometer A013Z

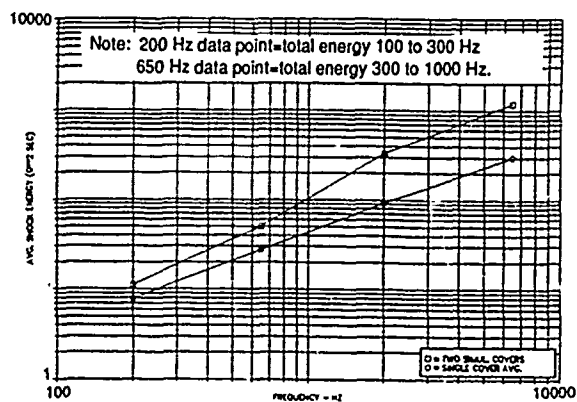


Fig. 22 - Average Energy of Guidance Bulkhead Accels. A011X, A012Y and A013Z

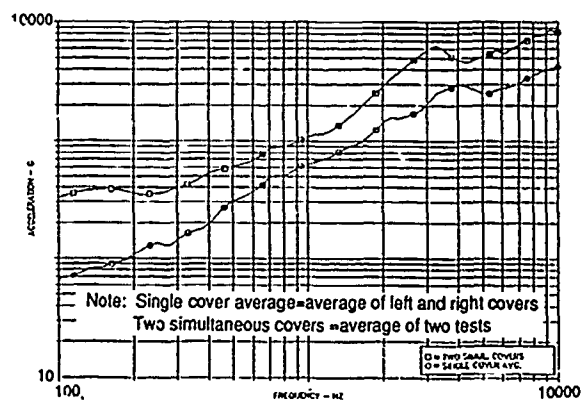


Fig. 23 - Average Shock Spectra for Guidance Bulkhead Accels A011x, A012Y and A013Z

Shock spectra and energy spectra for separation of a single cover and simultaneous separation of two covers are compared in Figures 20 and 21. While both the shock spectra and energy spectra indicate that the single cover levels are lower overall it is difficult to quantify the difference because of the fluctuations in the spectra.

Figure 22 shows a simplified way to present the levels and to quantify the difference in energy between the single cover and simultaneous cover separation events. The results in Figure 22 were produced using frequency ranges of 100 to 300 Hz, 300 to 1000 Hz, 1000 to 3000 Hz, and 3000 to 10,000 Hz. The average energy for all three axes was then obtained for guidance bulkhead accelerometers A011X, A012Y, and A013Z. The single cover curve is the average of a left and right hand cover separation event. The simultaneous covers curve is the average of two simultaneous cover separation events.

Figure 23 shows the result that was obtained when a similar approach was used with shock spectra. The spectra were created by averaging the spectra from three different accelerometers for two tests. Both Figures 23 and 24 indicate that an averaging over several tests and multiple measurements is useful in quantifying and presenting the overall effects of system changes.

References:

1. Bendat and Piersol, "Random Data: Analysis and Measurement Procedures", Wiley, 1971
2. Cox, "Effective Algorithms for Calculating Shock Spectra on General Purpose Computers", Proceedings of the Symposium on Shock and Vibration, 1982

TIME DOMAIN ANALYSIS OF PYROTECHNIC SHOCK UTILIZING RESONANT BEAM TEST APPARATUS

**Mr. Fritz Ehorn
Motorola, Inc.
Government Electronics Group
8220 E. Roosevelt St. (MD-R4246)
Scottsdale, AZ 85252**

To generate pyrotechnic shock spectrums utilizing resonant beam test apparatus, it is necessary to first impose high impulsive forces on the test equipment and then recover the transient acceleration time-histories at the control (test article) end of the testing device. The calculation of the resulting shock spectrum then follows. In a typical test laboratory this process is highly iterative in nature before eventually "homing in" on the desired spectrum. Analytical procedures have been successfully employed which not only aid in tuning the resonant beam test configuration for an acceptable output spectrum, but more importantly, also create acceleration time-histories which compare favorably with those developed in test. These time-histories are ultimately applied (as base accelerations) to output from finite-element modal models of the electronic items under test to provide realistic predictions of phased response during initial stages of the electronic packaging design.

Introduction

An important environmental consideration when designing certain types of electronic equipment is the pyrotechnic shock specification normally imposed by an agency of the Department of Defense. In general, these specifications are intended to simulate inputs into the electronics such as could be created by the action of separation nuts, bolt cutters, shaped linear charges, etc. These conditions often occur in the staging of rockets and satellites. However, unlike other common dynamic environments, such as sine sweeps, random vibration or drop shocks, there are no well established methods or implements for pyrotesting of equipment. Normally the stipulating agency provides shock spectrum envelopes with tolerance bands as the only data on which to base testing and pass/fail criteria. Due to the extremely damaging nature of certain elevated shock spectrums (for example, MIL-STD-

1540A & MIL-STD-1540B) to electronic components, the advantages of circumventing the "trial and fix" manner of design are readily understood. The method to be outlined herein has been found to be an effective addition to the design of electronics packages.

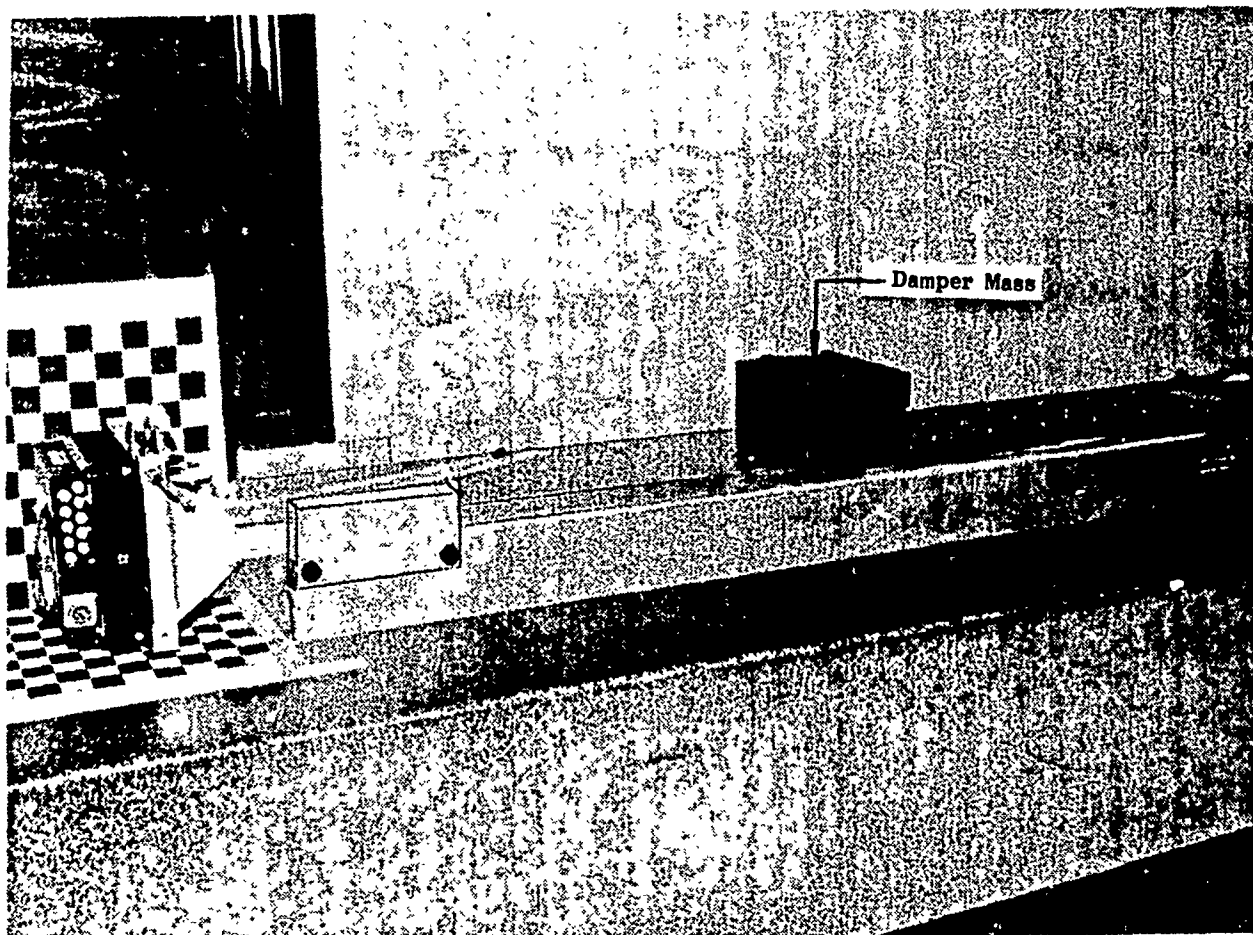


Figure 1 - 50" Resonant Beam with Test Article and Damper Mass

Resonant Beam Test Apparatus

The analytical techniques noted above have been applied to a particular type of pyrotechnic shock test instrument, namely, resonant beams. Figures 1 through 3 show detailed photographs of one these typical setups. Figure 1 depicts the 1" x 7.25" x 50" aluminum beam, the mounting plate, test object and "damper" mass. The beam is constrained from lateral motion via two guide plates and rests on a layer of grease over an aluminum support block. The impact end of the beam is shown in Figure 2. The pneumatically driven 9 lb. steel projectile and trapezoidal pulse shaper are evident as are the two constraining shock absorbers. Figure 3 details the test item end of the beam and indicates the tri-axial arrangement of accelerometers near the mounting points of the test article. These accelerometers act as controls for the measurement and verification of compliance within the

desired spectral response tolerances.

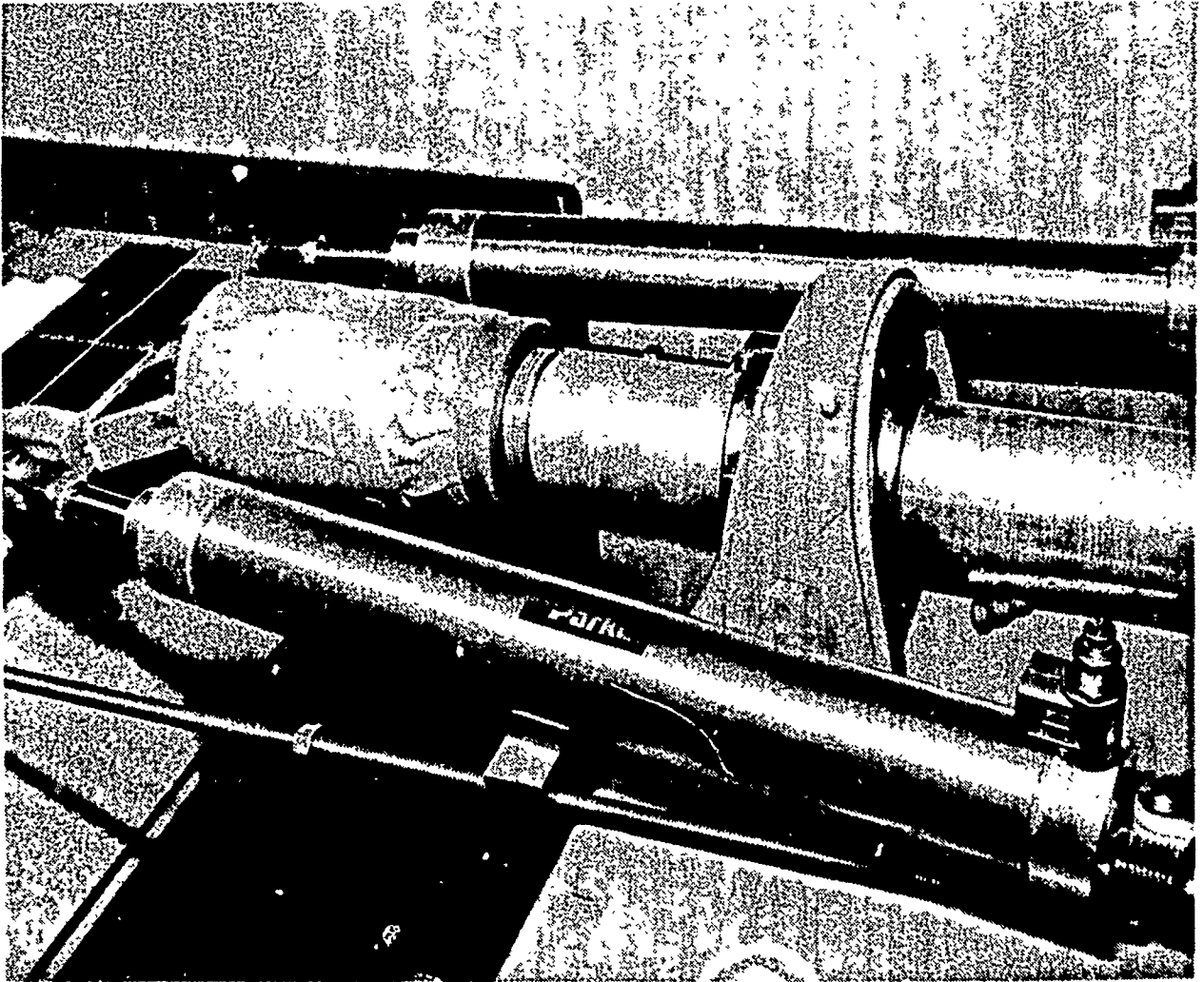


Figure 2 - Impact End Showing 9 lb. Projectile and Trapezoidal Pulse Shaper

The effect of the projectile impacting the shaper longitudinally takes the rough form of a half-sine pressure pulse of variable duration and amplitude ($\approx .3$ msec and 10,000 psi) at the beam end. The reaction of the beam structure to the many harmonics and associated waves generated is recorded as an acceleration time-history at the control point. This record is then employed to compute the associated shock spectrum for comparison with that specified. Figure 4 shows a typical acceleration time-history from an actual pyroshock test and Figure 5 depicts the resultant shock spectrum calculated at $1/6$ octave intervals. Although the structural response of the beam is considerably more complicated than that of a simple free-free bar in longitudinal vibration, the predominate harmonics are still normally found and are predicted by the relation,

$$f_n = \frac{n}{2L} \sqrt{E/\rho} \quad (1)$$

where n is the number of the mode or harmonic and L is

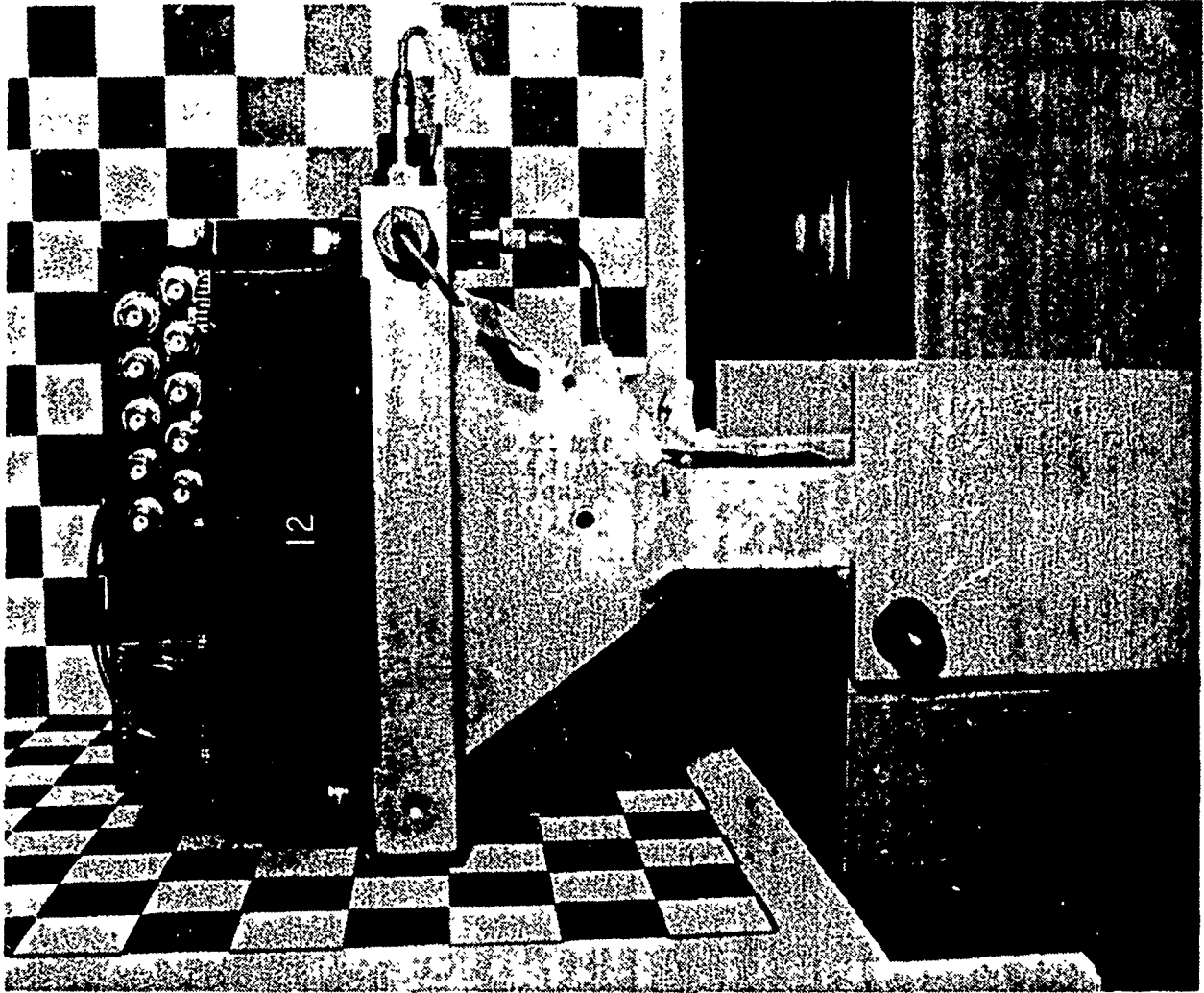


Figure 3 - Test Article Mounted on Symmetric End Plate

the length of the beam. Another relationship which will be shown to be significant involves the displacement mode shapes associated with this same free-free beam. They are known to be cosine waves of the form,

$$\Phi(x) = \phi_0 \cos n\pi \frac{x}{L} \quad (2)$$

where x is the position along the length of the beam.

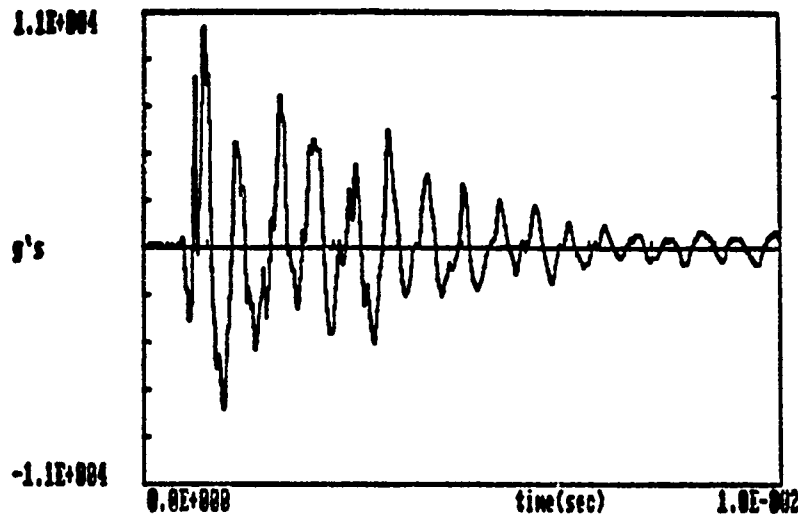


Figure 4 - Acceleration Time-History at Control Location; 50" Resonant Beam with 25 lb. Damper Mass at Impact End

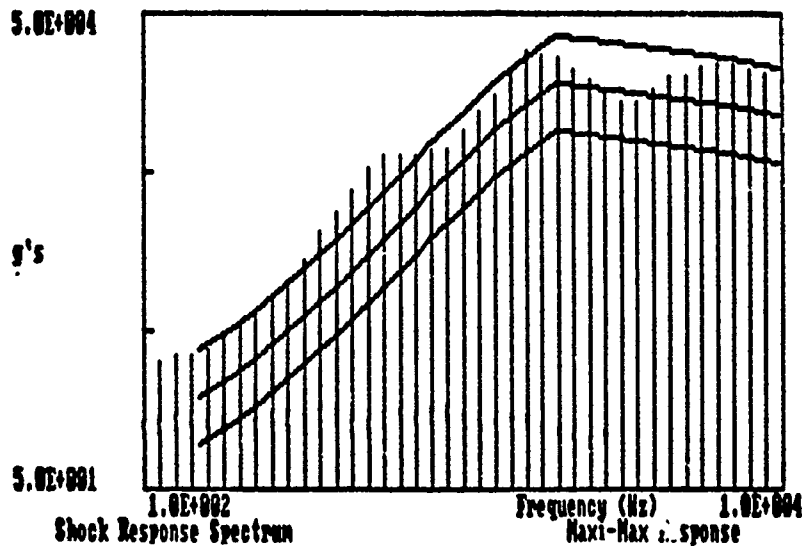


Figure 5 - Shock Spectrum Generated at 1/6 Octave Intervals from Time-History of Figure 4 ($Q=10$)

Tuning Beam Response Via Damper Masses

The judicious placement of damper masses (10 to 25 lbs) has been observed in testing to aid in the absorption of both kinetic and strain energy at desired frequencies and, in so doing, allow the test operators to correctly "shape" the spectrum responses at the control point to

within tolerance. A qualitative understanding of their effects can be gained by simply observing plots of Equation (2) for a free-free beam as seen in Figures 6 through 9.

Although these plots are made for a theoretical free-free bar without lumped masses, the implications are certainly valid for the somewhat more complicated apparatus described above. The vertical axes of these four figures show a normalized displacement eigenvector vs. position along the beam length for each of the first four beam harmonics. The first mode shape, for example, indicates a stationary node in the middle of the beam about which the ends vibrate in opposing directions. The effect of placing a damper weight in the center of the beam should be negligible for that contribution of the first harmonic to the total system response. Conversely, the second and fourth mode shapes indicate that the centrally placed mass would be active at these frequencies. Note that in all instances, the ends of the beam are positions of maximums for the displacement eigenvectors. Thus, damper weights situated on the free end of a beam should have the most effect in altering the response of the test article. This has been confirmed through experimentation and analysis.

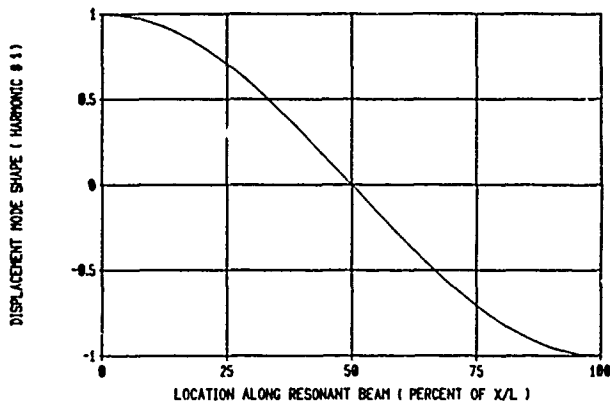


Figure 6 - Harmonic #1 Mode Shape

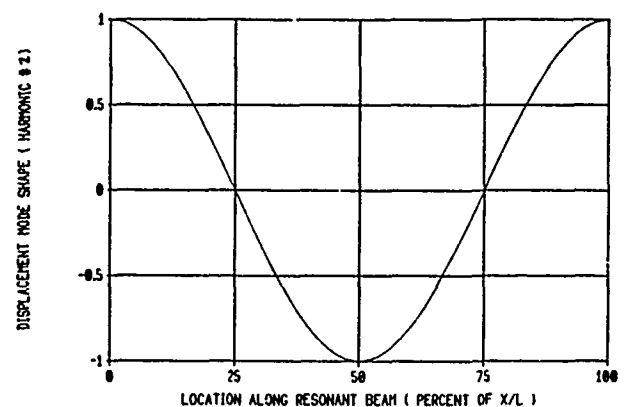


Figure 7 - Harmonic #2 Mode Shape

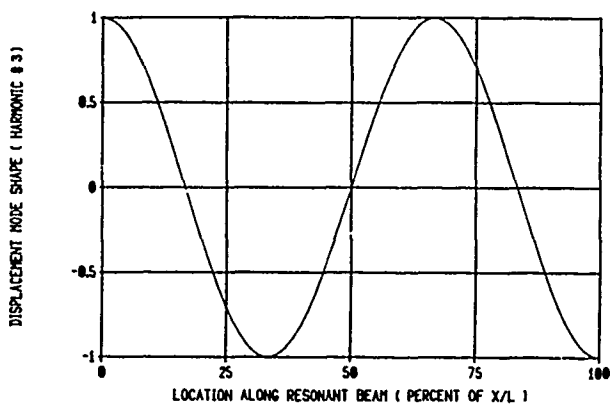


Figure 8 - Harmonic #3 Mode Shape

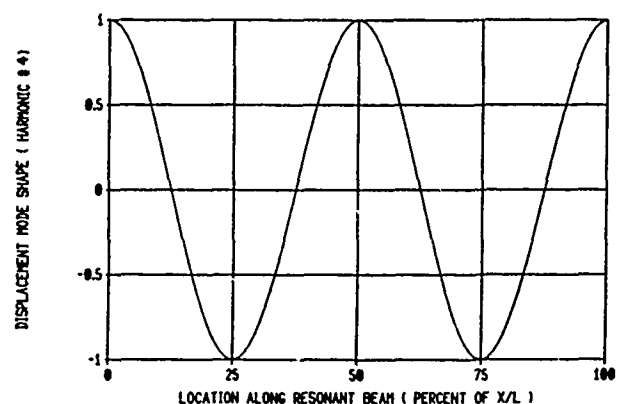


Figure 9 - Harmonic #4 Mode Shape

It has been possible (and cost effective) to predict, theoretically, the effect of changing the configuration of the test setup with regard to the placement of "damper" masses bolted to

the resonant beams. For example, Figure 10 shows three shock spectrums analytically generated at the test article (control accelerometer) end with the only variation being the position of 10 lb. masses on a 75" long beam configuration. In general, the centrally placed mass provided the least attenuation of response and the mass set at the impact end supplied the most. Utilizing this theoretical information, it is possible to roughly tune a given beam test geometry before actual testing begins. The analytical technique for creating these theoretical results, which are plotted in Figure 10, will be described in the following sections.

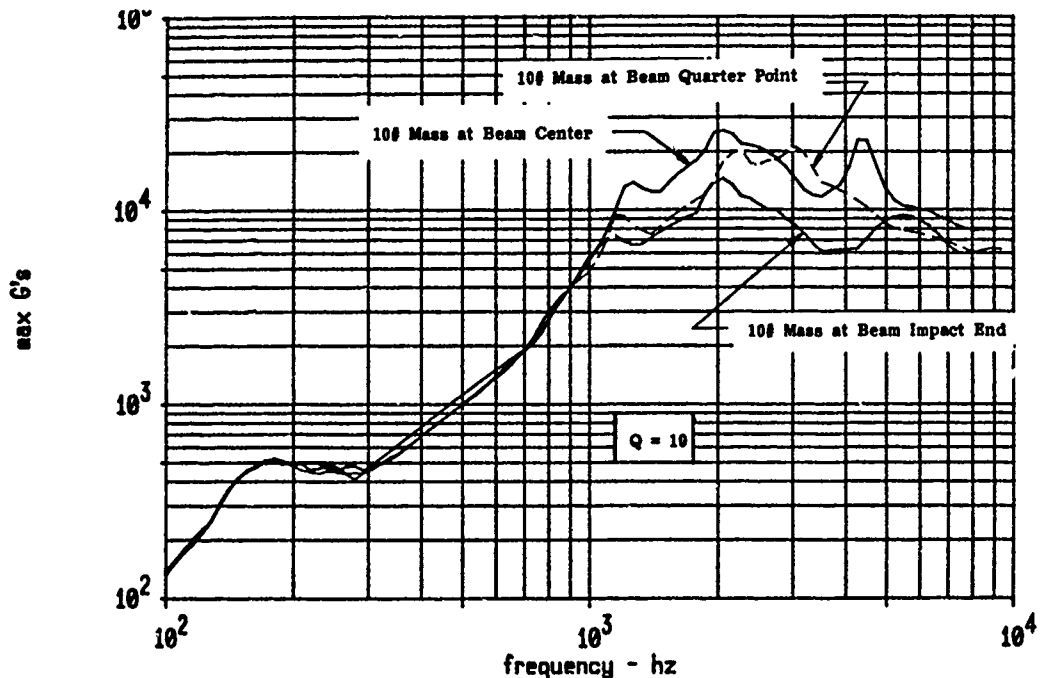


Figure 10 - Theoretical Shock Spectrum Variation with Position of 10 lb. Damper Mass (75" Resonant Beam Model)

Modeling and Data Extraction

Clearly, it is advantageous to be able to predict equipment reactions to these dynamic events before the design effort is completed. Techniques employing ANSYS finite-element modal models of actual resonant beams/test items have been developed which provide data for running time domain simulations (in separate computer programs) of the actual pyrotechnic event and generating the resulting responses at any point on the structures. Figures 11 and 12 show the 640 element finite-element model of a typical resonant beam structure including a coarse simulation of the test object mass. Also, the so-called "damper" mass is indicated. The majority of the model is constructed of 3-dimensional solid elements (3 DOF per node) for the beam. Plate/shell elements (6 DOF per node) are used for the test article simulation and the damper mass is attached via beam elements (6 DOF per node).

The process first requires a modal analysis utilizing a "dummy", or artificial, displacement spectrum of unit value for all frequencies. This spectrum is generated for

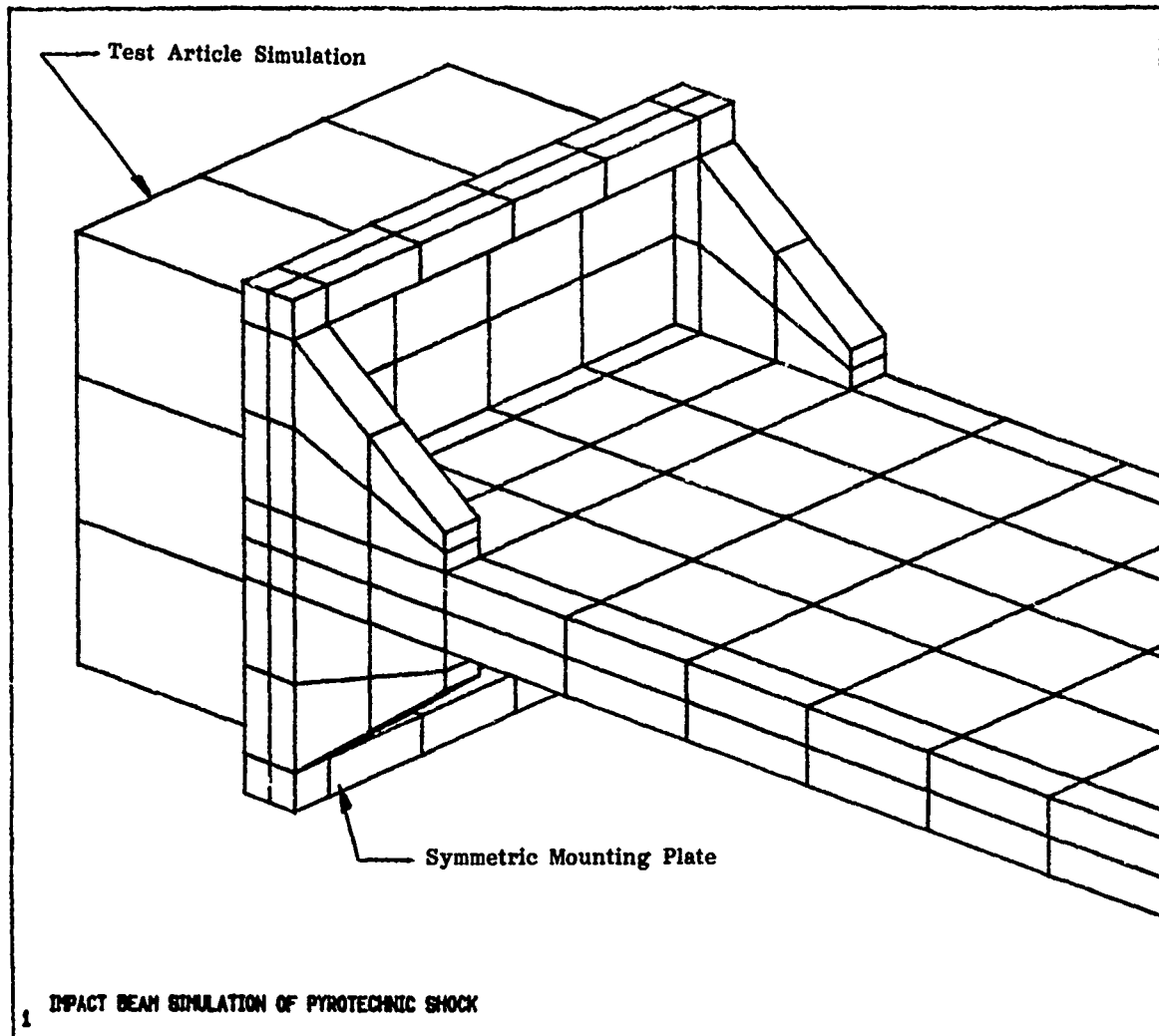


Figure 11 - Finite-Element Model of 50" Beam Shown in Figure 1 (Test Article End Shown)

frequencies up to 10,000 hz, the typical upper limit for pyrotechnic shock spectrums. All resultant mode shapes are expanded at each node for data recovery from an output file.

Upon completion of this computer run, interactive software developed by the author is used to search for and extract the modal participation factors (Γ_i), and the fundamental frequencies (ω_i) from the binary output file, FILE09, for each mode i . This particular file is, of course, unique to the ANSYS finite-element code. Also, contained within another binary output file, FILE12, are displacement (and stress, force, etc.) mode shapes $\Phi_i(x)$, in the format,

$$S_i(x) = \Gamma_i \Phi_i(x) \quad (3)$$

Thus, by dividing this artificial spectral value S_i recovered from FILE12 by

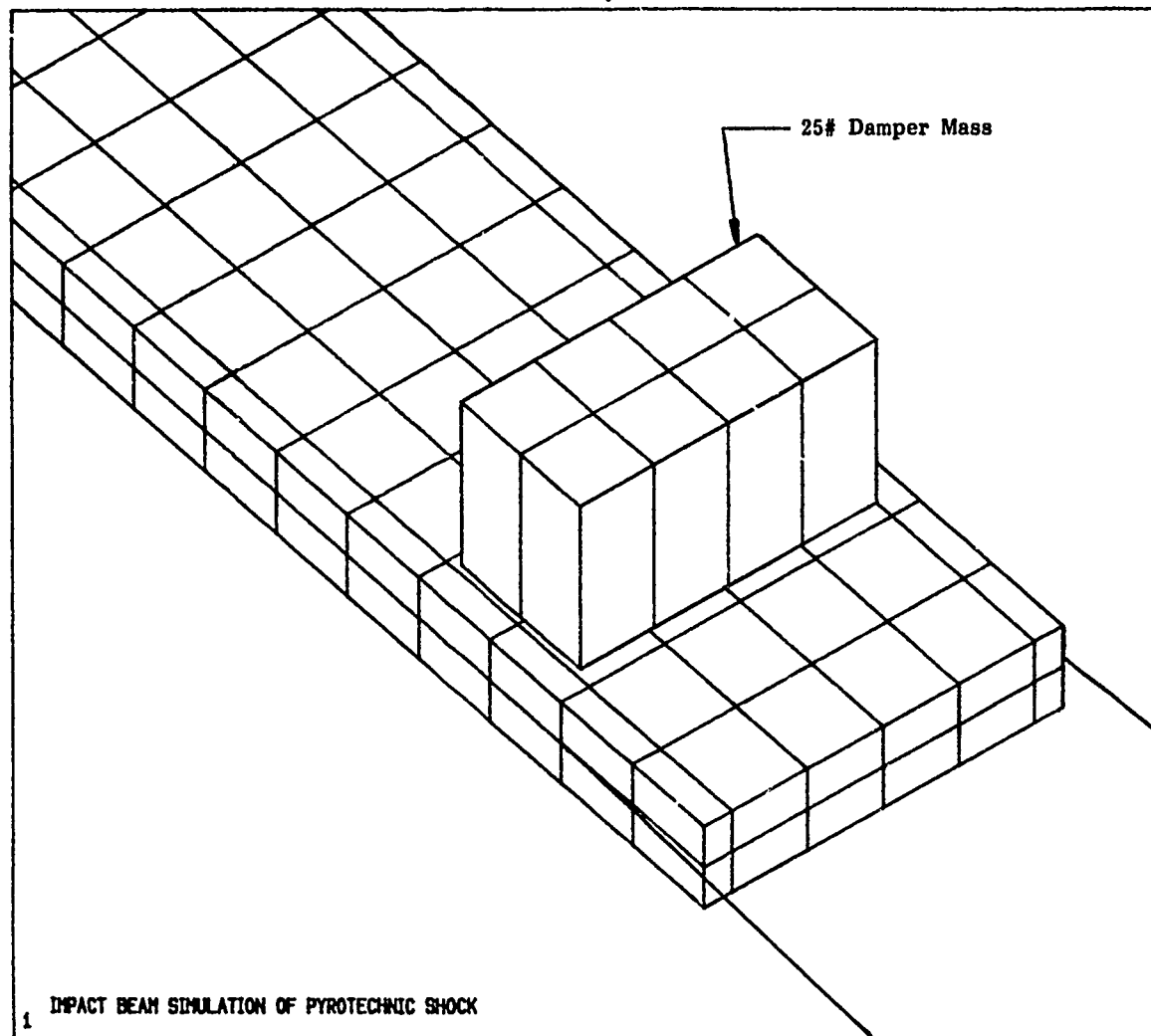


Figure 12 - Finite-Element Model of 50" Beam Shown in Figure 1 (Impact End Shown)

the participation factor for that mode it is possible to obtain the true mode shape necessary for use in the next step. Note that these recovered mode shapes are normalized to a generalized mass matrix set to unity within the ANSYS code. The consequence of this extraction process is the creation of a database which is downloaded to PC's for use outside of ANSYS. In this application, it is tailored to allow the user to quickly run transient (or steady-state) analyses outside of the mainframe environment of the finite-element code. Not only are cost savings realized, but it has also been found that a much wider variety of transient inputs can be investigated. Before further discussion of the results, a brief

description of the applicable theoretical basis will be presented.

Transient Analysis Employing Modal Superposition Methods

As stated before, the major reason for the recovery of modal data from the ANSYS files is to utilize this data for the application of transients (in this case, a pressure pulse at the end of the beam model) to obtain phased, time domain reactions of the beam/test object structure. Without going into extensive derivations of the theory (sometimes referred to as generalized coordinate response theory) at this point, note that the basic premise involves the separation of physical coordinates into uncoupled functions of time and position. This can be written as,

$$\left\{ X_i \right\} = \left\{ X_i(x_i, t) \right\} = \sum_{j=1}^{n \text{ modes}} \Phi_j(x_i) q_j(t) \quad \text{or} \quad (4)$$

$$\left\{ X_i \right\} = \left[\Phi_{ij} \right] \left\{ q_j \right\}, \quad i = \text{position}; \quad j = \text{mode}$$

the term q being the generalized coordinate which is a function of time. When Equation (4) is substituted into the basic equation of motion, and the diagonalized matrices are calculated, the following uncoupled differential equations of motion are produced for each of n modes,

$$M_n \ddot{q}_n + 2\zeta_n M_n \omega_n \dot{q}_n + M_n \omega_n^2 q_n = Q_n \quad (5)$$

where for any mode n ,

M_n = generalized mass (normalized to 1.0 in the ANSYS program)

ω_n = natural frequency

ζ_n = critical damping ratio (viscous)

Q_n = generalized forces in the following variations:

= $-\Gamma_n \ddot{u}(t)$ (base acceleration; Γ_n is the modal participation factor)

= $\Phi_n(x_i) f(t)$ (force function at a point)

= $p(t) \sum_{i=1}^{k \text{ points}} \Phi_n(x_i) \Delta A_i$ (pressure function on a surface of k points)

This method allows one to predict the response of any structure which has calculated mode shapes available. By performing numerical integration of Equation (5) at each time t , the values of q_n , \dot{q}_n and finally, \ddot{q}_n can be obtained. Then by substituting into Equation (4), values of the true physical entities, $\{X_i\}$ are determined for each time step. Since these values can be stored at every time step, it is possible to create acceleration time-histories (or displacements, stresses, forces, etc.) at any location on the theoretical model.

Sample of Output

Figure 13 shows a plot of just such a file taken from a point on the model comparable to the position of a control accelerometer on actual test equipment. Comparison with Figure 4 shown before indicates considerable

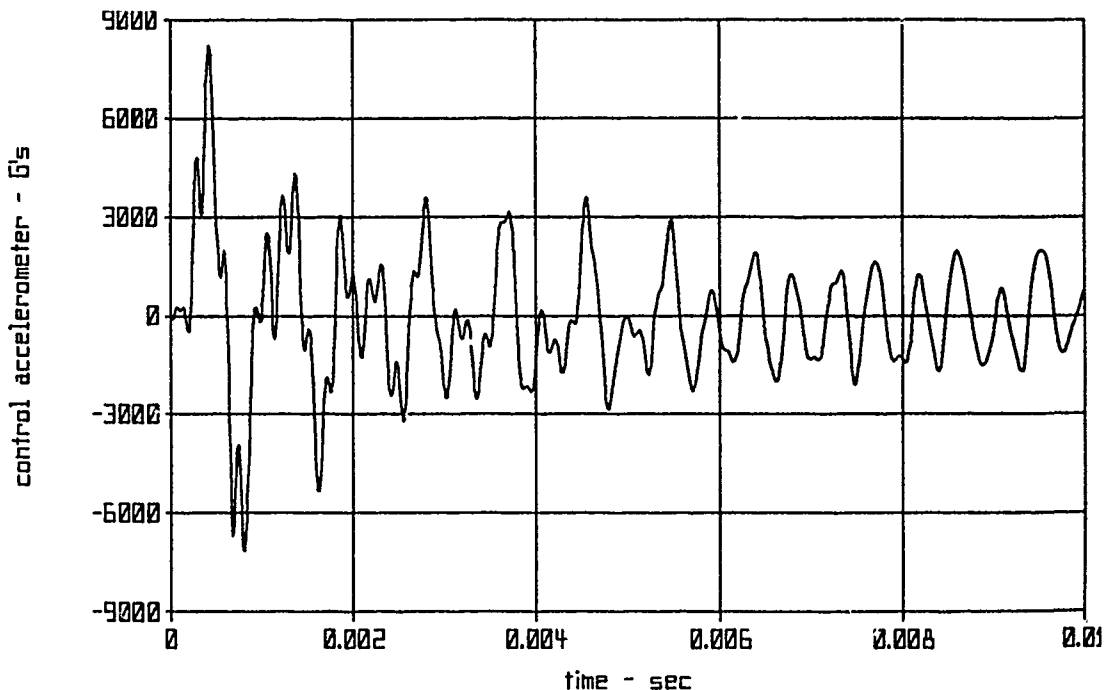


Figure 13 - Acceleration Time-History (Analytical Model); 50" Resonant Beam with 25 lb. Damper Mass at Impact End

similarities in both amplitude and "content". From this file, shock spectrums are easily calculated using a separate PC program. Figure 14 displays this final plot produced for comparison with Figure 5. In reality, to achieve spectrums similar to those specified requires several analytical iterations, mainly through small variations of pressure pulse amplitude and duration. The duration of the pulse was noted to have the most effect on the frequency content observed in the resulting spectral plots. Also, some variation in modal damping was

assumed in the mathematical formulation, although it was found to have less effect than might be supposed. Generally, a value of .01 for ζ was found reasonable for all modes. Mathematically, the viscous damping formulation was assumed as can be seen from Equation (5).

Since only the shock spectrum tolerance limits are stipulated for compliance in final testing, and not the acceleration time-histories, it should be realized that there are obviously an infinitely large number of acceptable spectrums and their associated time-histories. If the actual time-histories were provided as part of the requirements, the analytical inputs into the electronics package model would not need the creation of the beam model. Naturally, the testing

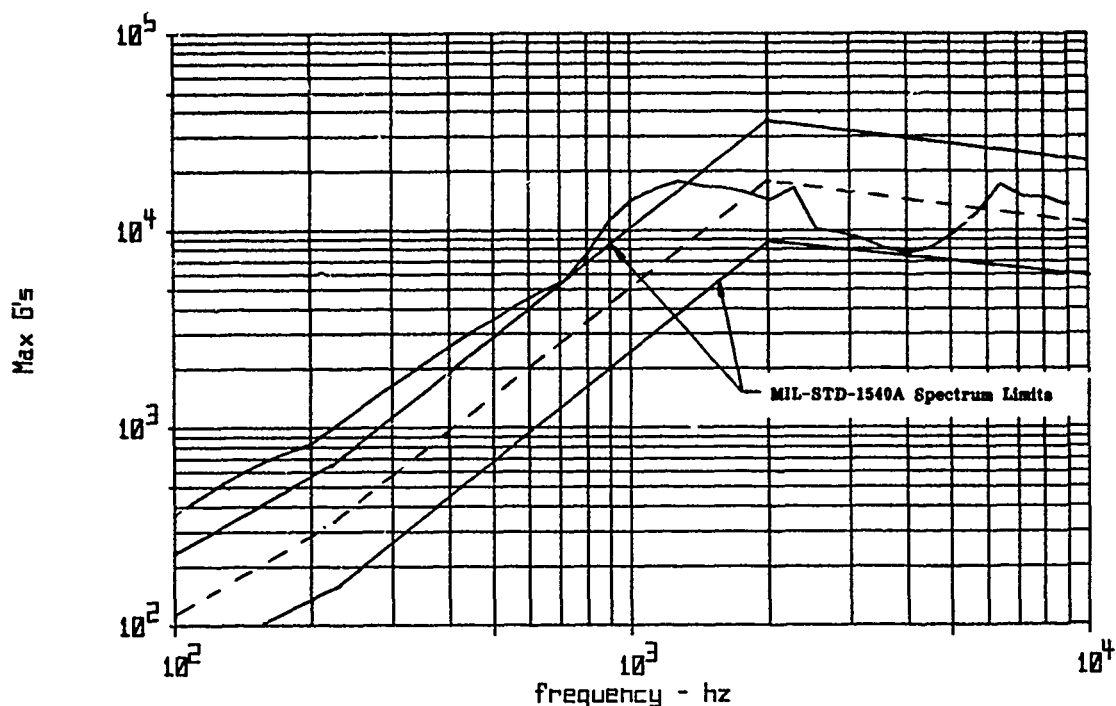


Figure 14 - Shock Spectrum Generated at 1/6 Octave Intervals from Analytical Time-History of Figure 13 ($Q=10$)

process would also have a very difficult time in actually matching an "exact" time-history at the control point, which represents the input to the test article.

The ultimate use of this entire analytical process is the input of the time-history produced, $\ddot{u}(t)$, as base accelerations into detailed finite-element modal models (not shown) of electronics packages, ideally, before any testing takes place. This method has proven to be quite successful in determining potential trouble areas in equipment being designed. Some of the shock spectrum levels specified are very damaging to many of the devices mounted on PWB's, and contrary to commonly held beliefs, amplifications do occur within many areas of

typical housings. Accelerometers placed on active areas of PWB's have confirmed the 2 to 3 amplification levels predicted by transient analyses carried out, as described herein, on certain electronic packages.

Before detailed analysis techniques were initiated, leaded chip carriers, lids on hermetically sealed devices, inadequately staked capacitors, wire bonds, solder joints, and even the mounting feet of the entire test article have been destroyed on various projects during the high G, high frequency pulses initiated on the far end of the resonant beams. For example, it has been found that just staking a component does not necessarily assure its survival. This is because many staking compounds in common usage have very low moduli of elasticity. Analysis has shown that epoxies with higher values of E (100,000+ psi) are often required, in order to limit deflections and solder joint stresses to acceptable levels under these large pyrotechnic shock loadings.

Conclusions

This evaluation process has been both interesting and useful. The analytical tools detailed herein have been proven to provide cost effective simulations of actual test environments. Improvements in equipment design, both on an individual basis and a generic basis have been identified. Furthermore, after-the-fact analyses of previously failed devices have confirmed their vulnerability to these damaging shocks.

This method allows practically any structure to be modeled and its transient response efficiently calculated. It would serve well in optimizing the location of sensitive equipment in actual space bound structures given that the time-dependent nature of the inputs entered into the overall assembly is known. Further work could be directed towards more fully understanding and improving the accuracy of predicting the highly complicated structural behavior of the beam/test assembly setups. Variations in mounting plate design, beam length, optimal damper mass/placement and pulse definition are areas which need additional analysis. Another area of interest might involve the determination of ways to attenuate the high loads entered into test items. Constrained layer damping techniques have been successfully incorporated into various high G environments to reduce the response of printed wiring boards, thin panels and lightweight frame structures. In the case of typical electronic housings, it may be possible to use some form of constrained layer damping which is an integral part of the housing mounting arrangement. Thus, the shock loads, theoretically, could be reduced before arriving at any electronic circuitry.

EQUIPMENT LIMITATIONS IN PYROTECHNIC SHOCK TESTING

John W. Rehard and John Czajkowski
National Technical Systems
20988 W. Golden Triangle Road
Saugus, CA 91350

As the title of our presentation indicates, we're here to talk about one of the major issues in pyrotechnic shock testing: limitations in the equipment used to measure, analyze, and record ordnance-induced pyrotechnic shocks. And our intent is to point out our limitations rather than deficiencies, because we feel that there is a problem in pyrotechnic shock testing as performed today, and the problem is not so much the equipment as the way it is used. If our research is correct--and everything that we've done so far indicates that it is--then an overwhelming percentage of pyrotechnic shock test data that is being generated today is not accurate, and the error is that the data indicates higher levels than the hardware is actually experiencing. This means that parts are being undertested, and with pyrotechnics figuring so largely in today's technology, undertesting is not something that we can afford to do.

What we'd like to do, however, is to remedy the situation, not point fingers. We are advocating that a standard be established for pyrotechnic shock testing, and the only way that such a standard can be set up is if we know what we are doing right and what we are doing wrong. That, in part, is the intent of our presentation.

We're going to concentrate on the data acquisition and analysis systems, because it is in this area that we feel most of the problems exist. Our focus will be on the four primary components of the data acquisition and analysis systems--accelerometers, tape recorders, filters, and analyzers--with specific emphasis on the limitations of these items in a high-level shock environment.

BACKGROUND

Pyrotechnic shocks are high-level, short duration transients typically generated by an explosion of some sort. Separation of individual stages in a rocket or missile, for example, is accomplished by setting off a linear shaped charge (LSC) located at the joint between the two stages. Explosive bolts also generate pyrotechnic shocks, as do detonators, and any other ordnance devices. The shocks generated by such devices are oscillatory transients, with significant frequency content from 100 to 10,000 Hz--and higher, as we shall see--and which decay to a few percent of their maximum level in about 5 to 15 milliseconds. Peak accelerations can range into the tens of thousands of g's, with the highest levels, as indicated on response spectra, resulting in knee frequencies from 1000 to 5000 Hz.

To test the effects such shocks have on equipment, a test setup is constructed which consists of a rectangular plate, usually steel, that is suspended either vertically or horizontally by bungee cords (see Photos 1 and 2). A length of prima cord, det cord, or LSC is cut and taped to the plate in at least one location. The explosive is initiated by an electric detonator. The test item is usually bolted to the center of the plate, with a triaxial accelerometer, also bolted or welded to the plate, located as near as possible to one of the test item mounting points. When everything is ready, the explosive charge is initiated, causing a shock wave to propagate through the plate to the test item. Different shock levels can be obtained by increasing the explosive charge, changing the location of the test item on the plate, changing the size of the steel plate--or, as we shall see, by manipulating certain components of the data acquisition system.

ACCELEROMETERS

Perhaps the best place to start the discussion is with accelerometers, because it is the accelerometers which measure the levels of the applied shocks. The basic function of the accelerometer is to convert the shock-induced motion of the plate into an electrical signal, which is then conditioned, amplified, recorded and analyzed. In some cases the initial analog signal is digitized, in some cases not, depending upon the type of data acquisition system being used.

The primary limitations found in accelerometers relate to the dynamic range of the accelerometers and zero-shift of the accelerometer output. (Figure 1 Real time XY plot)

The dynamic range of the accelerometer is just that: the range which the instrument has been designed to measure. Most accelerometers used in pyrotechnic shock testing have a measurable acceleration range up to around 100,000 g, with frequency responses typically peaking at around 10,000 to 20,000 Hz, depending upon the type of accelerometer and its manufacturer.

The limitation as far as accelerometer dynamic range is concerned is that most shock response spectra requirements end at 10,000 Hz, but tests indicate that the energy generated by the shock does not. Our research at NTS indicates

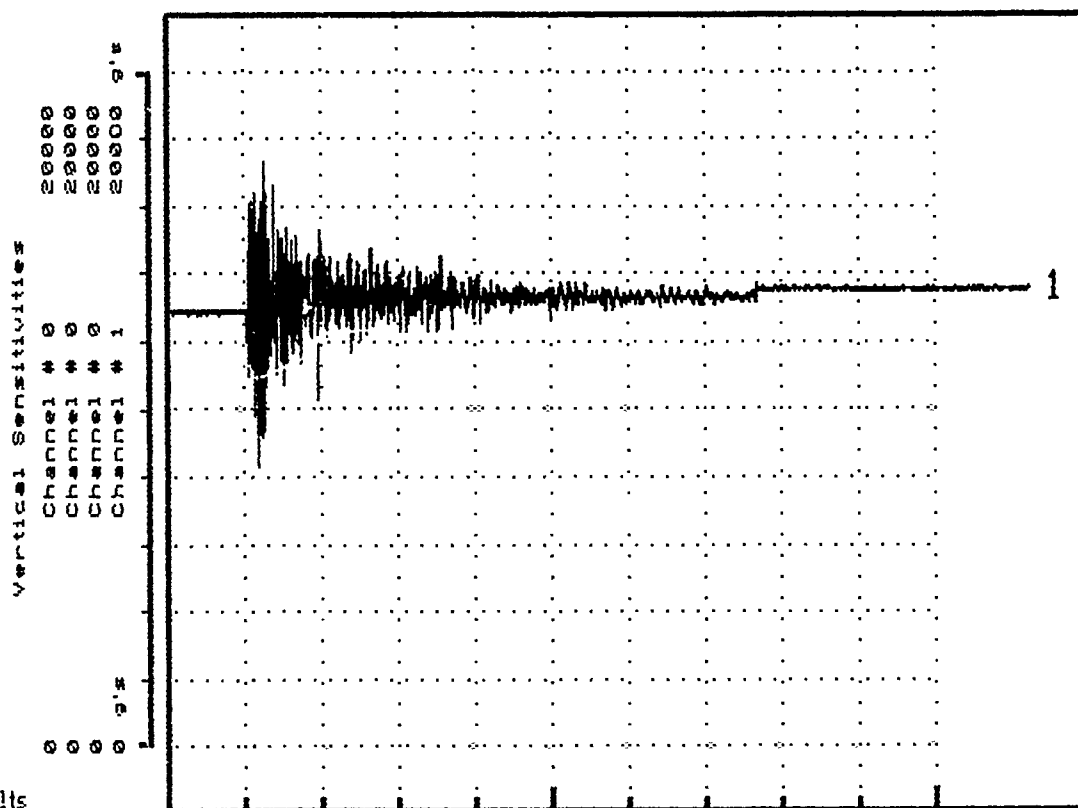
Waveform Test Report

GHI SYSTEMS, INC. TRIAD II-E

Test Ident:
Test Item :
Test Eng. :

Date of Test: 04-07-1988
Test Spec : PYROTECHNIC TEST

Transducer Output	Ch # 1 5000g's/Volt	Ch # 0 /Volt	Ch # 0 /Volt	Ch # 0 /Volt
-------------------	------------------------	-----------------	-----------------	-----------------



Results

CH	TIME	CUR AMP	PEAK AMP	1ST INT	2ND INT	TIME BASE	EXP
1	14.02ms	-312.5 g's	-4531. g's	358.5 In/s		51.2ms	2

Remarks

BARE FIXTURE EQUALIZATION

CONTROL ACCEL. AXIS

FIGURE 1

that there is significant energy well beyond 10,000 Hz, and if there is energy there is a corresponding change in the response spectrum, either in terms of actual data or in terms of the shock's exciting the resonance frequency of the accelerometer. If the accelerometer resonates, its signal is modified, resulting in inaccurate data.

The second limitation applicable to accelerometers is zero-shift, which is a shift in the accelerometer output from the zero reference point. A lot of speculation surrounds the zero-shift phenomenon, with proposed causes ranging from a short-duration "pre-pulse" transient to electronic problems such as amplifier overload. The important point, however, is that it does exist, and it affects the response spectrum which is generated from the accelerometer output. High-pass filters are often used in the data acquisition system to avoid zero-shift, but this treats the symptom, not the cause. Filters, as a matter of fact, can be yet another cause of bad data, and will be discussed a little later in this presentation.

Another limitation which is related to the accelerometer but which is usually attributed to charge amplifiers is saturation of the charge amplifier, which is caused by an excessively high input signal from the accelerometers. The high input signal usually results from the accelerometer's resonant frequency being excited by the applied shock. The effect on the data can be tremendous, with differences up to 20 dB being noted when different charge amplifiers were compared.

TAPE RECORDERS

We all know that FM tape recorders are essential to data acquisition, both in terms of capturing data so that it can be reduced at a later date and in terms of maintaining a record of the data. Like all instruments, however, tape recorders have limitations, and as with all data acquisition system components being discussed in this presentation, the recorder limitations can significantly affect the data generated for a typical pyrotechnic shock test.

The two tape recorder features that are important to our discussion are the input parameters accepted by the tape recorders and the speed at which the data are recorded.

As we've implied several times in our discussion, there is much about pyrotechnic shock testing that we just don't know: What is the optimum frequency range to use for data acquisition, for example, or how dependable is the accelerometer's frequency response at very high frequencies? For tape recorders, what the recorder does with high-level, short-duration transients is the concern. Some of the data obtained, for example, indicate that the recorders get saturated due to extremely high input voltages, some of which are on the order of 7.0 volts peak (normal is 1-to-2 volts rms). When voltage such as this reach the recorder, the recorder will clip the signal amplitude, resulting in a distorted signal and thus erroneous data. Measures to minimize the distortion, such as automatic gain control (AGC) circuitry, can generate additional problems, since their settings also influence the signal from the accelerometer. What's worse, the data clipping may be hidden by the limited frequency response of the amplifier, which may spread the resulting wave over time while reducing the apparent magnitude of the signal.

A related concern for tape recorders is the signal-to-noise ratio of the input signal. When the accelerometers used for data acquisition are set for a particular dynamic range--say, 500,000 g's--this influences the effective noise floor of the data, since the tape recorder acquires the noise floor of the accelerometer system. Using the 50,000 g range for the accelerometer as an example, the recorder noise floor becomes 500 g's, assuming a dynamic range of around 40 dB for the recorder. When the data are reduced to shock response spectra, what will actually be represented are data below about 1000 Hz that are contaminated by noise. Once again, the result is erroneous data that will appear to be good data.

As to tape speed, this is important because of the frequency response of the recorder versus the frequency response of the recorded data: The tape needs to run at very high speeds in order to record the data with even a reasonable degree of accuracy. What we've found at NTS is that data taken off tape can be drastically different from the realtime data, with inter-modulation within the frequency range in some cases even altering the original waveshape of the accelerometer signal. This is in addition to the amplitude clipping which takes place if the input voltage is too high.

FILTERS

Filtering is one of the major issues in pyrotechnic shock testing--next to analyzers, in fact, filters appear to be one of the causes of erroneous data generated by today's pyroshock analysis systems.

For the most part, filtering is a necessary evil: Tape recorders effectively function as low-pass filters, some accelerometers contain integral charge amplifiers that contain a high-pass filtering element, and so on. No instrument can accommodate an infinite bandwidth, so filtering is something that we had all better be prepared to live with.

Our concern, however, is not the filtering effects which are legitimate limitations of the instruments we have to use to perform our tests; what does concern us is the deliberate use--or misuse--of filters to manipulate data, whether to make the data fit a customer requirement or to conceal distortions such as zero-shift.

In a paper entitled "Questionable Effects of Shock Data Filtering," Paul Strauss of Rocketdyne gives an excellent example of the misuse of filters, in his case high-pass filters. He describes the effects of two high-pass filters, one a 20 Hz filter and the other a 200 Hz filter, on a typical shock time history which he simulated electronically. He points out, for example, that the 20 Hz filter noticeably "improved" the response spectrum for the simulated shock, bring it closer to the required spectrum; the 200 Hz filter brought the response spectrum within spec--very close, in fact, to the requirement. He felt that since "in spec" is all most customers need to be satisfied with the test, most people would choose the 200 Hz filter to use in the data acquisition system.

Not satisfied with this, however, Strauss and his colleagues decided to find out why the presence of a particular filter had such a profound effect on the data. What he found was that simply adding a 200 Hz high-pass filter in the system added a sinusoid to the data signal, causing a shift in the time

history and a corresponding shift in the response spectrum. He also found that he could not reverse the process--that is, he could not get back to the original signal, no matter what he did. His overall conclusion was that "filtering by itself, the way we are using it today in most of our test labs, is not giving us a clear signal and a clean idea of what is really happening mechanically."

And we could not agree more. We at NTS have done our own testing to determine the effects of filtering, primarily the effects of the anti-aliasing used in many digital data acquisition systems. What we found supports what others have said before us: filtering tends to distort data. In one of our tests, for example, we paralleled a signal so that the signal was recorded in both the filtered and the unfiltered mode. What we found when we compared the two outputs was that the filtered signal tended to exhibit a resonance at some point whereas the unfiltered signal did not. If there hadn't been an unfiltered version of the signal available for comparison, you understand, we probably would have assumed that there was a resonance in the system, rather than the response of the filter, which is what it was. We then would have let the filter response be analyzed as part of the original data signal, ending up with a response spectrum which looked good but meant little in terms of representing a true test condition. Many of the filters we tested exhibited the same phenomenon--"ringing" at a certain frequency--causing us to seriously question the use of separate filters at all in a pyroshock system. See Figures 2, 3, 4, 5, 6, 7, 8, and 9. Unfiltered, 10K Hz filters - Khron-Hite, Kemo, and TTE (4 each Real Time and SRS plots).

A few more words about filters and then we'll move on to analyzers, which is the last item we'd like to talk about before we open things up for discussion.

A problem which keeps coming up in a digital data acquisition system--and one which we'll discuss in more detail in a few moments--is aliasing. As most of you know, aliasing is a phenomenon which occurs when there are higher frequency components in the signal spectrum which cause a false signal, or "alias," to become a part of the analyzed data. Aliasing is a function of the data sampling rate in a digital system, which is why we'll explore it in more detail in the analyzer section of this presentation.

The reason we're mentioning it now is that the usual way of minimizing--if not eliminating--aliasing errors is with special low-pass filters, appropriately called "anti-aliasing filters." Digital systems typically filter the data before it is digitized (to filter the unwanted data from the original analog signal) and then after the data has been re-converted back to an analog signal (to "smooth out" the digitized data, so that the signal looks more like the original waveform, rather than a step function). We've already discussed some of the potentially harmful aspects of filtering--it tends to distort data by altering the signal essentially any way you want it to--but the reason we're reiterating the idea is because anti-aliasing filters are an integral part of most digital systems, and we believe that a lot of pyroshock data being generated today is in fact distorted. And the distortion shows up as a higher level than is actually obtained.

Anti-aliasing filters treat one problem and cause another: They may minimize aliasing errors, but they also serve to change the data signal by 1)

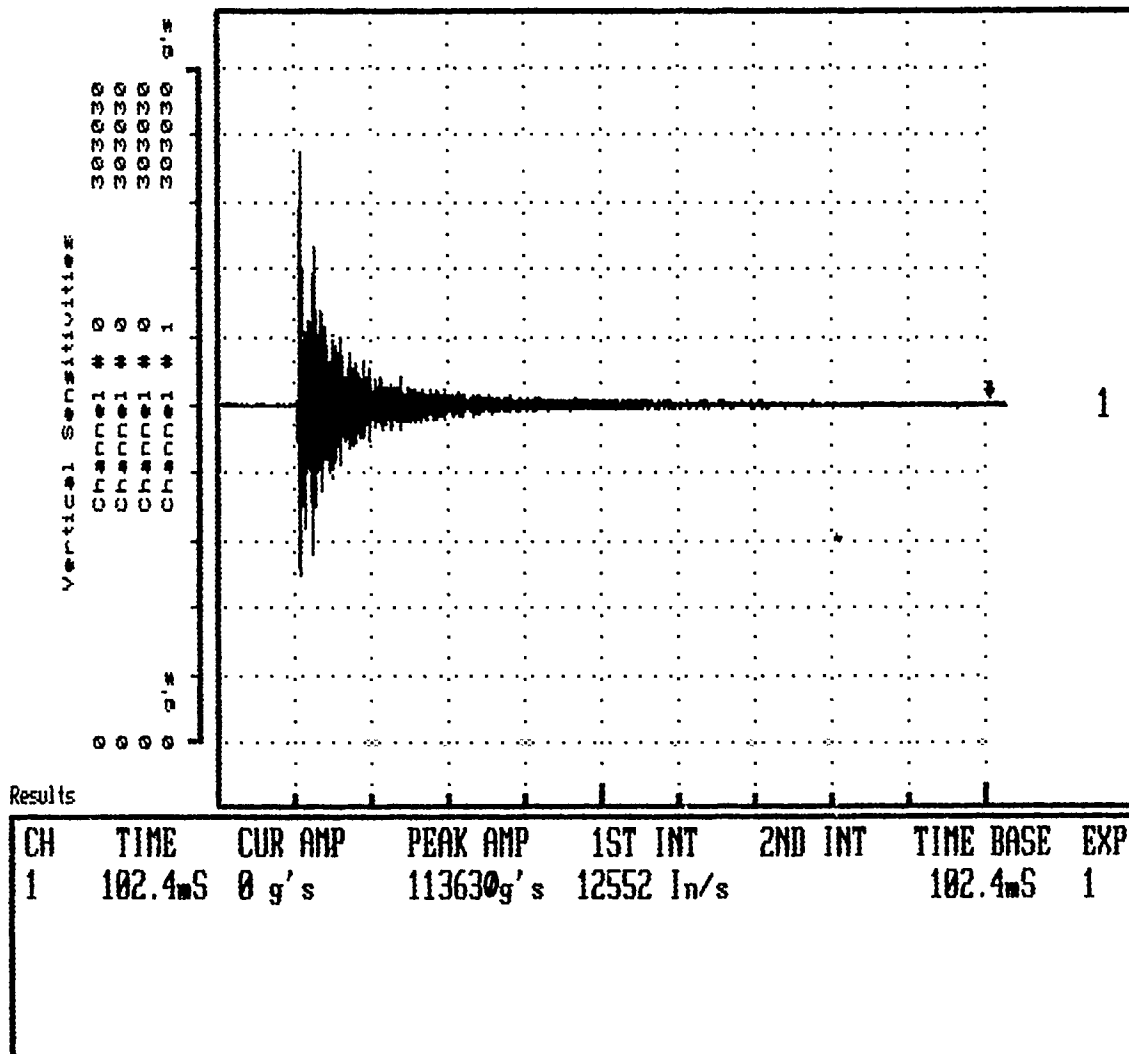
Waveform Test Report

GHI SYSTEMS, INC. TRIAD II-E

Test Ident: -
Test Item : -
Test Eng. : -

Date of Test: 08-23-1988
Test Spec : -

	Ch # 1	Ch # 0	Ch # 0	Ch # 0
Transducer Output	30303g's/Volt	/Volt	/Volt	/Volt



Remarks

channel 1 straight-in,unfiltered

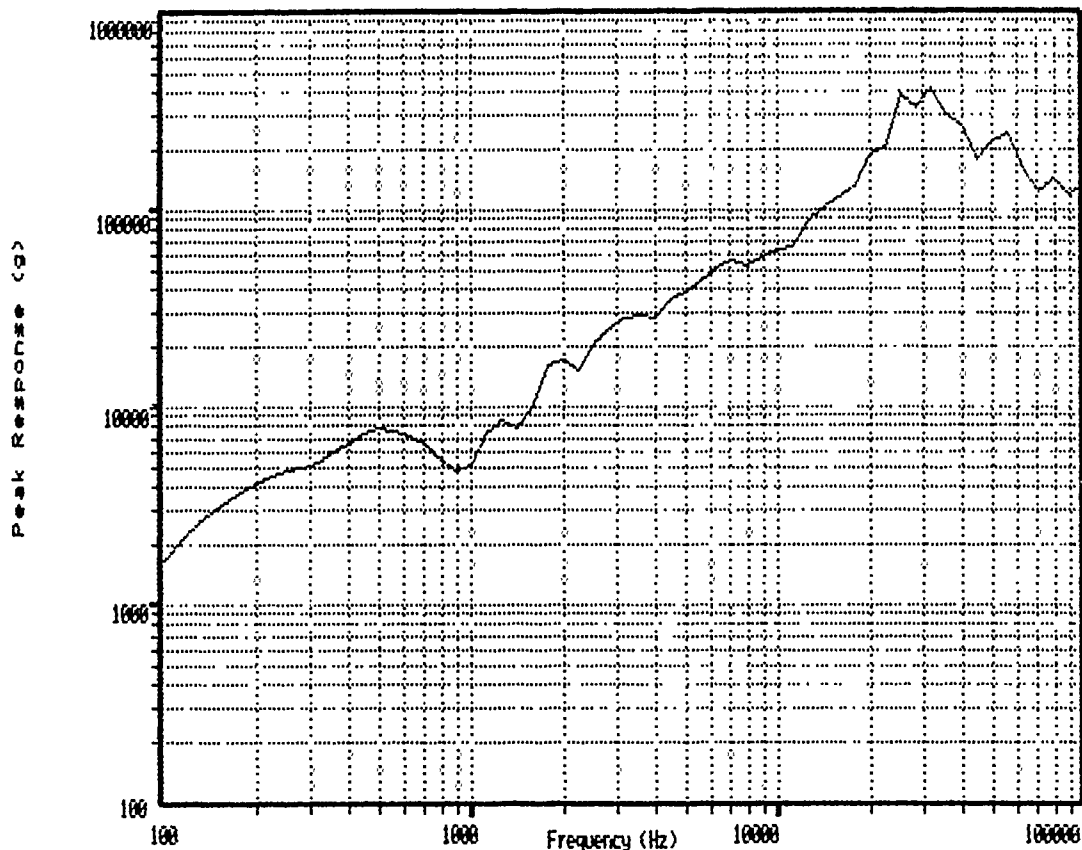
FIGURE 2

Shock Response Spectrum

GHI SYSTEMS, INC. TRIAD II-E

Test Ident: -
 Test Item: -
 Test Eng.: -

Date of Test: 08-23-1988
 Test Spec.: -



Damping= .85 Model: Accel Max Type: Maximax Plot: 6th Oct Samples From Memory Channel # 1

Equiv. Plot Sampling Rate= 156250 P/s Signal Time Duration= 25.6 ms

Peak Signal Amplitude= 113630g's

Remarks

channel 1 straight-in, unfiltered

FIGURE 3

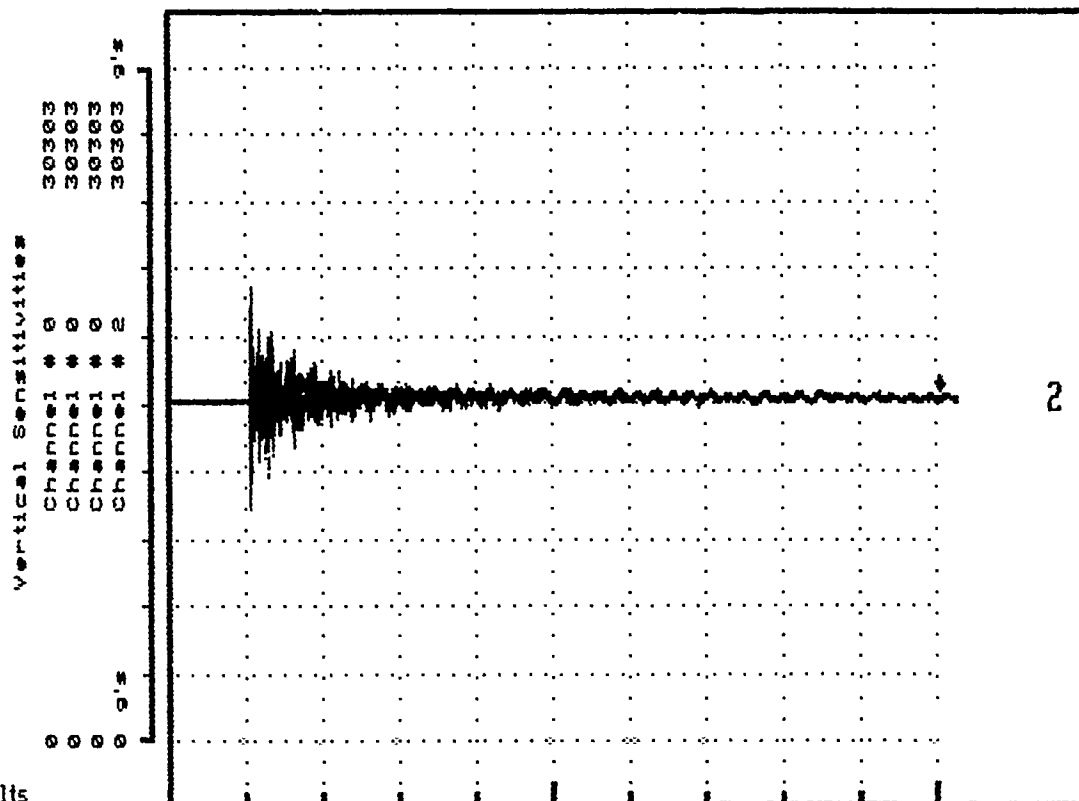
Waveform Test Report

GHI SYSTEMS, INC. TRIAD II-E

Test Ident: -
Test Item: -
Test Eng.: -

Date of Test: 08-23-1988
Test Spec: -

Transducer Output Ch # 2 Ch # 0 Ch # 0 Ch # 0
 30303g's/Volt /Volt /Volt /Volt



Results

CH	TIME	CUR AMP	PEAK AMP	1ST INT	2ND INT	TIME BASE	EXP
2	102.4ms	118.3 g's	5208. g's	7512. In/s		102.4ms	1

Remarks

channel 2 through KROHN-HITE filtered at 10KHz

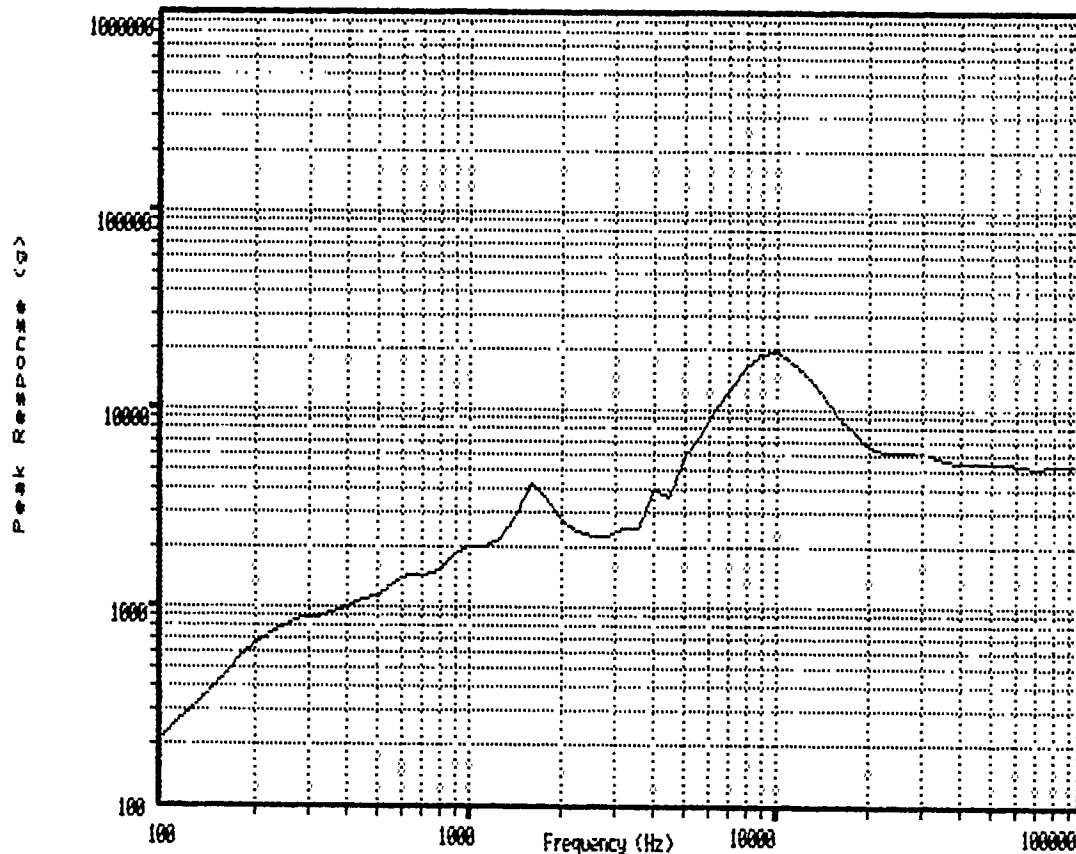
FIGURE 4

Shock Response Spectrum

GHI SYSTEMS, INC. TRIAD II-E

Test Ident: -
 Test Item : -
 Test Eng. : -

Date of Test: 08-23-1988
 Test Spec. : -



Damping= .05 Model: Accel Max Type: Maximax Plot: 6th Oct Samples From Memory Channel # 2

Equiv. Plot Sampling Rate= 156250 P/s Signal Time Duration= 25.6 ms

Peak Signal Amplitude= 5200. g's

Remarks

channel 2 through KROHN-HITE filtered at 10KHz

FIGURE 5

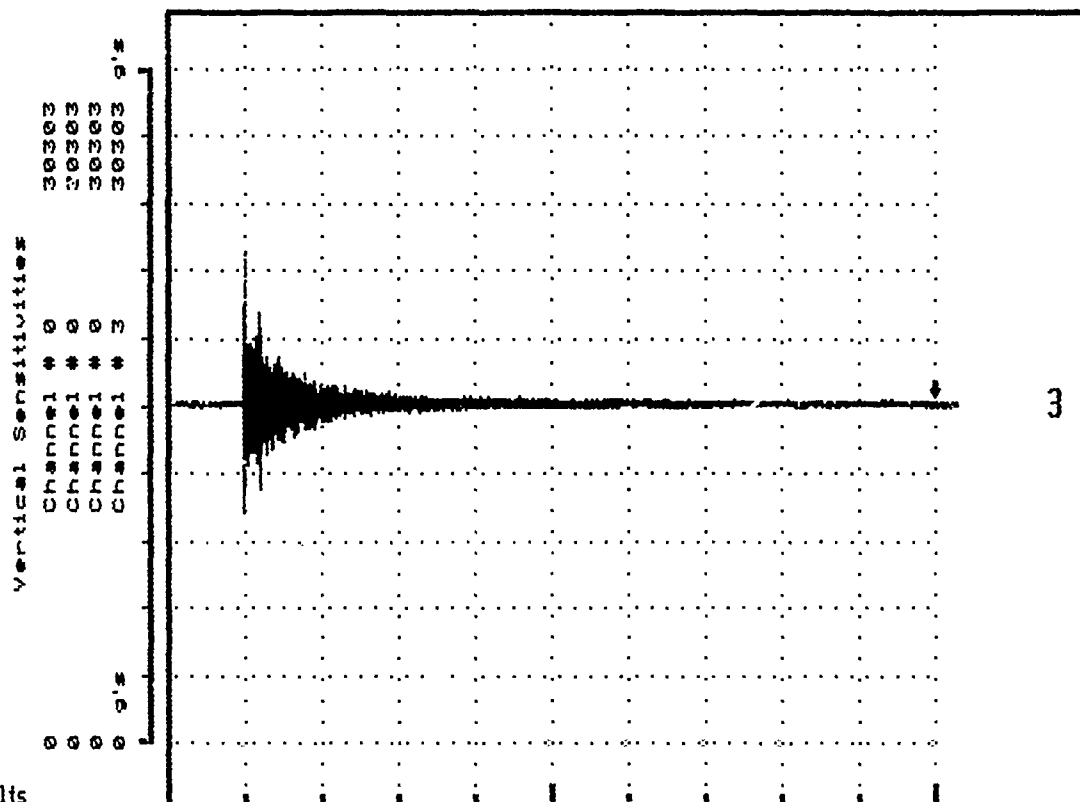
Waveform Test Report

GHI SYSTEMS, INC. TRIAD II-E

Test Ident: -
Test Item: -
Test Eng.: -

Date of Test: 08-23-1988
Test Spec: -

Transducer Output	Ch # 3 30303g's/Volt	Ch # 0 /Volt	Ch # 0 /Volt	Ch # 0 /Volt
-------------------	-------------------------	-----------------	-----------------	-----------------



Results

CH	TIME	CUR AMP	PEAK AMP	1ST INT	2ND INT	TIME BASE	EXP
3	102.5mS	0 g's	6865. g's	1330. In/s		102.4mS	1

Remarks

channel 3 through KEMO filtered at 10KHz

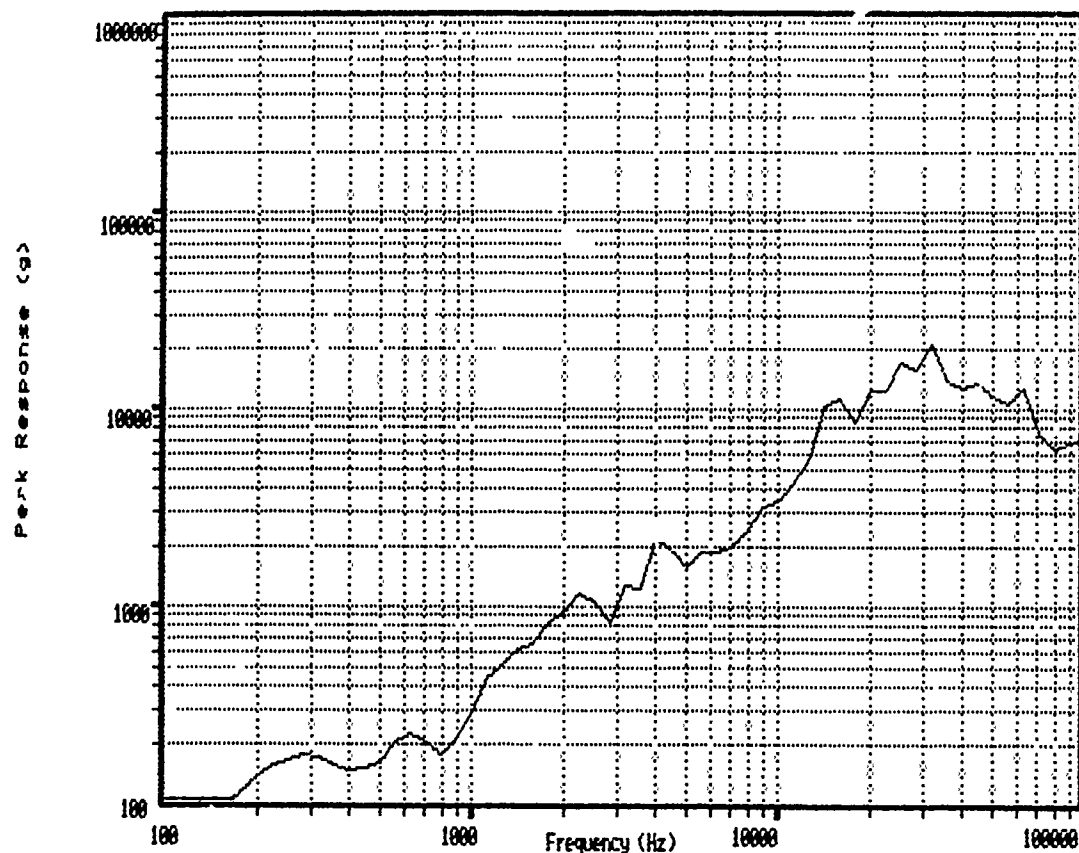
FIGURE 6

Shock Response Spectrum

GHI SYSTEMS, INC. TRIAD II-E

Test Ident: -
 Test Item : -
 Test Eng. : -

Date of Test: 08-23-1988
 Test Spec. : -



Damping= .85 Model: Accel Max Type: Maximax Plot: 6th Oct Samples From Memory Channel # 3

Equiv. Plot Sampling Rate= 156250 P/s Signal Time Duration= 25.6 mS

Peak Signal Amplitude= 6865. g's

Remarks

channel 3 through KEMD filtered at 10KHz

FIGURE 7

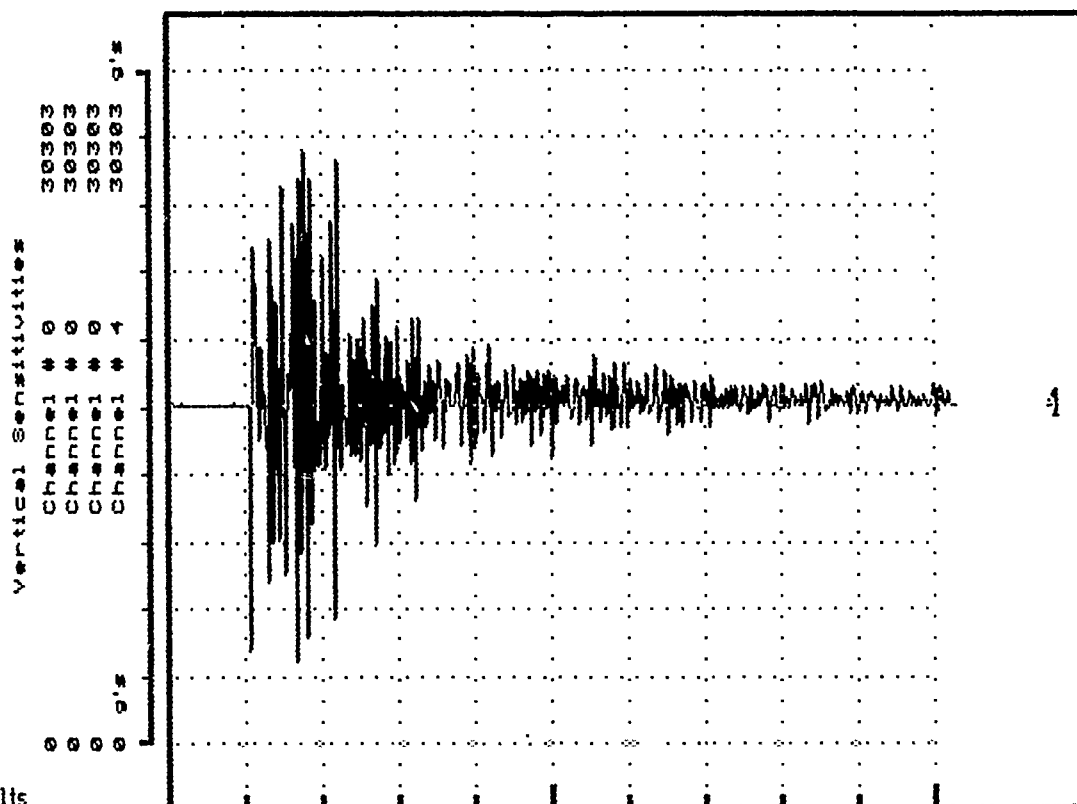
Waveform Test Report

GHI SYSTEMS, INC. TRIAD II-E

Test Ident: -
Test Item: -
Test Eng.: -

Date of Test: 08-23-1988
Test Spec: -

Transducer Output	Ch # 4 30303g's/Volt	Ch # 0 /Volt	Ch # 0 /Volt	Ch # 0 /Volt
-------------------	-------------------------	-----------------	-----------------	-----------------



Results

CH	TIME	CUR AMP	PEAK AMP	1ST INT	2ND INT	TIME BASE	EXP
4	102.4mS	-355.1 g's	15151 g's	10679 In/s		102.4mS	1

Remarks

channel 4 through TTE low pass filtered at 10KHz

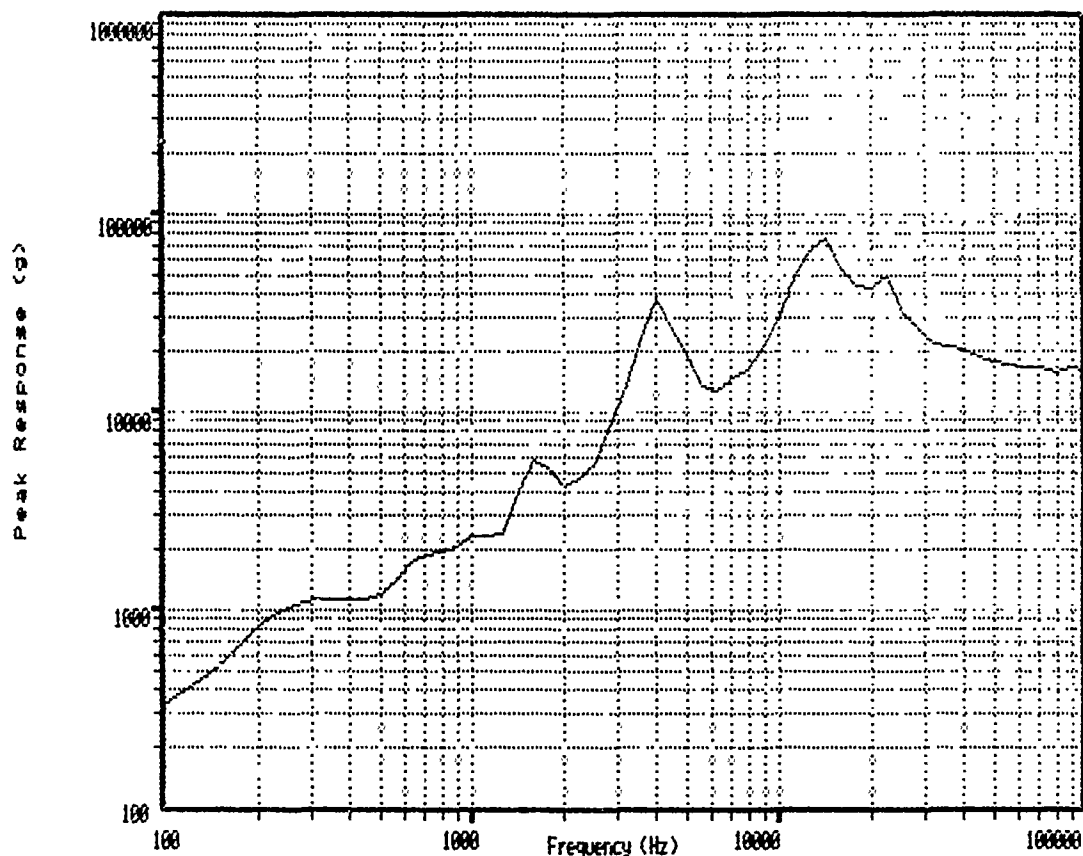
FIGURE 8

Shock Response Spectrum

GHI SYSTEMS, INC. TRIAD II-E

Test Ident: -
Test Item: -
Test Eng: -

Date of Test: 08-23-1988
Test Spec: -



Damping= .05 Model: Accel Max Type: Maximax Plot: 6th Oct Samples From Memory Channel # 4

Equiv. Plot Sampling Rate= 156250 P/s Signal Time Duration= 25.6 ms

Peak Signal Amplitude= 15151 g's

Remarks

channel 4 through TTE low pass filtered at 10KHz

FIGURE 9

attenuating the higher frequencies which, although they contribute to aliasing, contain significant spectral information and 2) by potentially introducing additional errors to the data (the "ringing" effect described earlier). As we shall see in a moment, another way to minimize aliasing errors is to increase the sampling rate of the data acquisition system, and though this introduces yet another set of potential errors, it seems to us the better of the two alternatives.

ANALYZERS

The analyzer is perhaps the most important piece of equipment in the data acquisition system, and we've saved it for last because we feel that it is the analyzer—or, rather, the way the analyzer is used—that is responsible for a lot of bad data. Accelerometers can be improperly ranged or give questionable outputs; tape recorders can be saturated so that the recorded data at best only faintly resembles the actual signal; and filters can be improperly used so that they can distort the data almost beyond recognition.

Analyzers, however, can alter data literally by the pressing of a button or the turn of a knob, and we feel that this is what is happening in our industry today—unintentionally, perhaps, but still happening.

There are primarily two types of analyzers: analog and digital. We could spend hours describing the differences, but the basic difference—and the one that is most important to use here—is that analog analyzers retain the original analog signal as it was output from the transducer, performing whatever analysis they perform on this analog signal; if the signal is output realtime, it is analyzed realtime. Digital analyzers, on the other hand, digitize the data, which means that they sample it at discrete intervals and convert the information to digits (numbers). They analyze it in digital form, then convert it back to its original analog form.

In terms of errors and limitations, both types of analyzers are limited by the data acquisition system components which precede them in the system: the accelerometers, filters, etc. In terms of specific limitations, however, we can sum these up as follows:

ANALOG ANALYZERS

1. Very susceptible to environmental influences such as noise, so that immunity to noise is a function of system resolution and signal level
2. Susceptible to drift (temperature).
3. Limited Dynamic Range (50-55 db).

DIGITAL ANALYZERS

1. Effectiveness is a function of sampling rate (digitizing speed)
2. Potential errors in the software algorithms.

3. Lack of understanding by user.

In short, analog analyzers are extremely dependent upon signal level, which can introduce significant error even if there is only minimal signal distortion, and digital analyzers are extremely dependent upon the specified data sampling rate.

Our main concern is with the digital systems, because we feel that they reflect the state-of-the-art and because many of the large testing laboratories--NBS included--use digital systems for data acquisition in pyroshock. The area of interest is the digitizing rate, because this one function can mean a difference of several thousand g's on a response spectrum, usually because of aliasing.

We brought up aliasing a little while ago, so we'll just expand on it a little more to clarify our point. Digitizing is basically a two-step process, the first step being quantization and the second being sampling. Quantization is the assignment of a particular numerical value to a particular parameter of the signal being digitized: the peak of a sine wave may be assigned a value of "2," while two equidistant points that are on the slopes of the sine wave may be assigned a value of "1."

Sampling is the rate at which discrete data samples are taken from the continuous analog signal supplied by the transducer. Various rules of thumb exist to determine the sampling rate: "The sampling rate should be at least twice the frequency of the highest spectral component" is one rule, though many equipment manufacturers recommend five-to-ten times now. If the sampling rate is insufficient, however, frequency components greater than half the sampling rate will be folded back or aliased into the frequency range being examined. If you're analyzing a 160 Hz sine wave, for example, using a sampling rate of 200 samples per second, you will get an aliasing error: the 160 Hz sine wave will fold back around what is called the Nyquist frequency, which is equal to one-half the sampling rate. The spectrum for the 160 Hz sine wave will fold around the 100 Hz frequency mark, back to a value of 60 Hz. The 160 Hz sine wave will thus appear at 40 Hz ($100 \text{ Hz} - 60 \text{ Hz}$).

What this all means is that the sampling process can actually create a false signal. Because the false signal contributes energy to the initial measurement, and because the energy from the false signal is indistinguishable from the energy contributed by the true signal, the data is amplified, and the analyzer sees a higher input signal. The amplitude of the response spectrum is increased accordingly, resulting in a higher apparent test level.

We have actually proven this in the laboratory by adjusting the sampling rate for a actual shock input signal and then plotting the results as time histories and response spectra. The results were at the very least interesting: we could get acceleration levels that varied by as much as 20 dB from the same input transient. See Figures 10 through 15 for 3 time histories of sample rates; 1.2 m Hz, 600K Hz, 300 K Hz and Shock Response Spectrums.

Part of the problem, we feel, is that people don't always know all the in's and out's of digital systems--and as Paul Strauss stated in his paper, everyone is happy if the results are in spec.

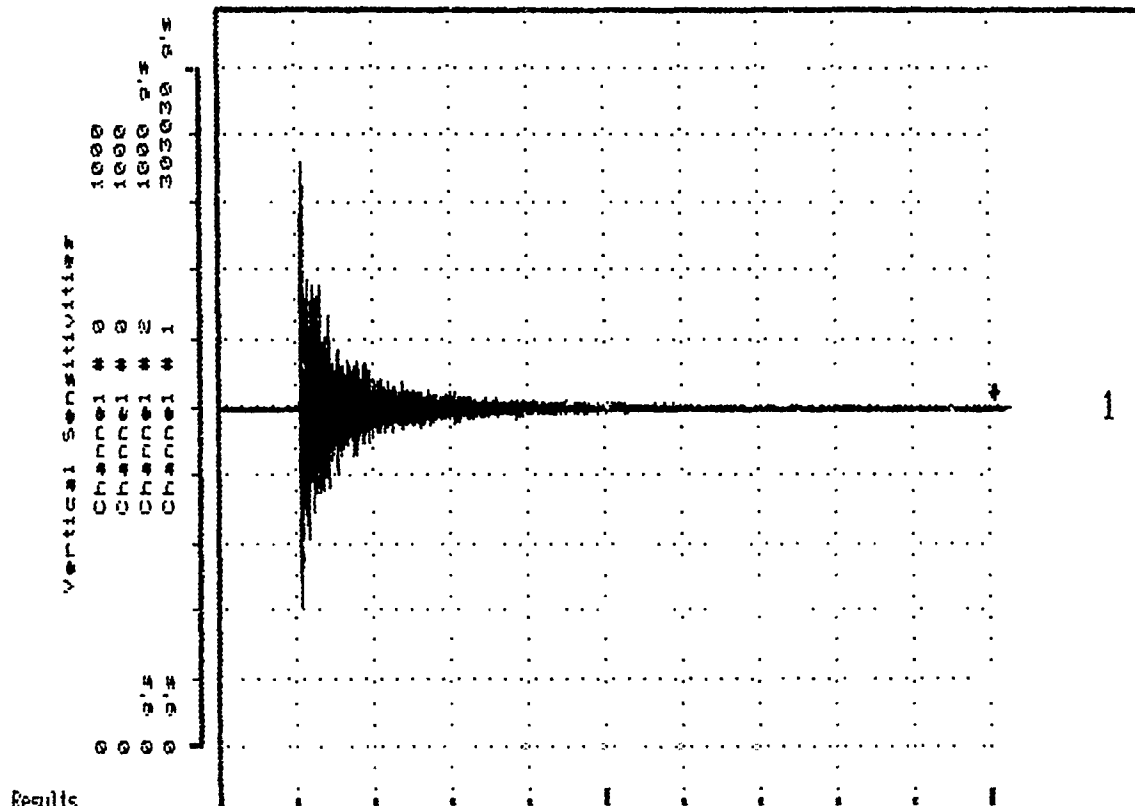
Waveform Test Report

GHI SYSTEMS, INC. TRIAD II-E

Test Ident: -
Test Item: -
Test Eng.: -

Date of Test: 08-22-1988
Test Spec: -

Transducer Output Ch # 1 Ch # 2 Ch # 0 Ch # 0
30303g's/Volt /Volt /Volt



CH	TIME	CUR AMP	PEAK AMP	1ST INT	2ND INT	TIME BASE	EXP
1	102.4ms	0 g's	108900g's	-1498. In/s		102.4ms	1

Remarks

1 channel on GHI with 1.2 MHz sample rate

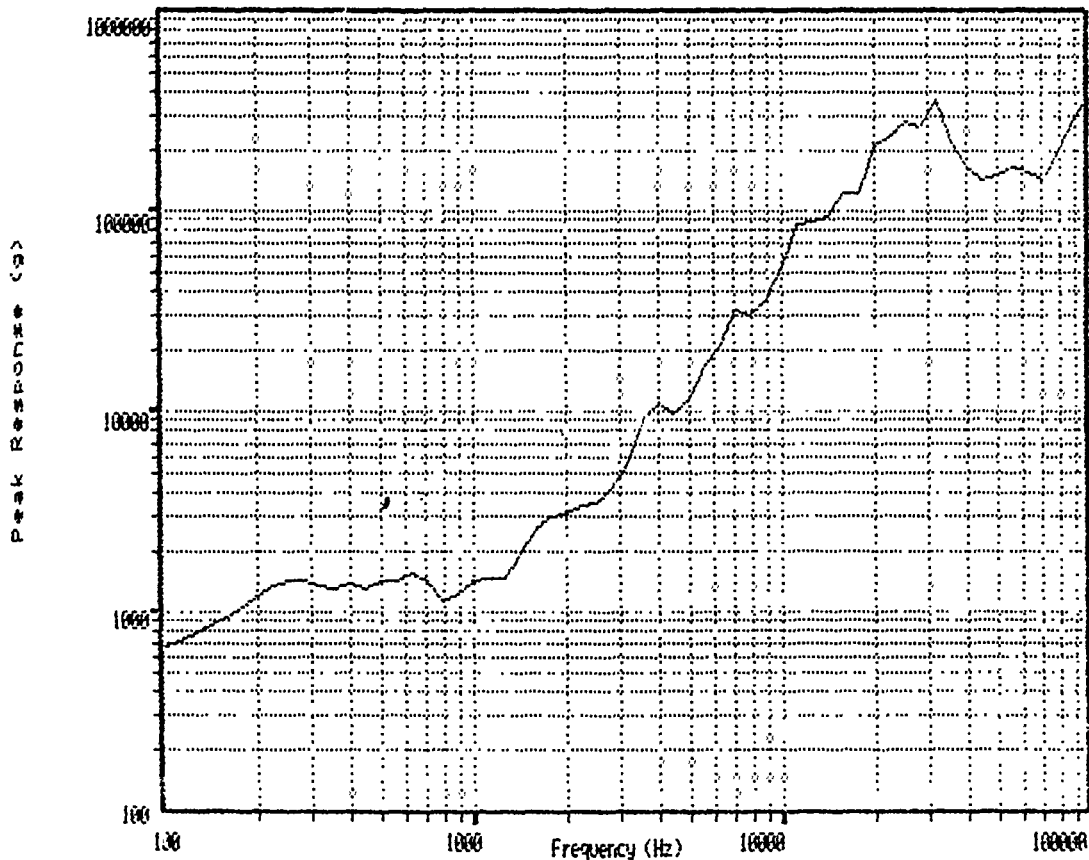
FIGURE 10

Shock Response Spectrum

GHI SYSTEMS, INC. TRIAD II-E

Test Ident: -
Test Item: -
Test Eng.: -

Date of Test: 08-22-1988
Test Spec.: -



Damping= .85 Model: Accel Max Type: Maximax Plot: 6th Oct Samples From Memory Channel # 1

Equiv. Plot Sampling Rate= 625000 P/s Signal Time Duration= 25.6 mS

Peak Signal Amplitude= 100000g's

Remarks

1 channel on GHI with 1.2 MHz sample rate

FIGURE 11

GHI SYSTEMS, INC. TRIAD II-E

Date of Test: 08-23-1988

Test Spec : -

Test Eng. : -

Results

CH	TIME	CUR AMP	PEAK AMP	1ST INT	2ND INT	TIME BASE	EXP
1	102.5mS	0 g's	97064 g's	936.7 In/s		102.4mS	1

2 channels on GHI with 600 KHz sample rate

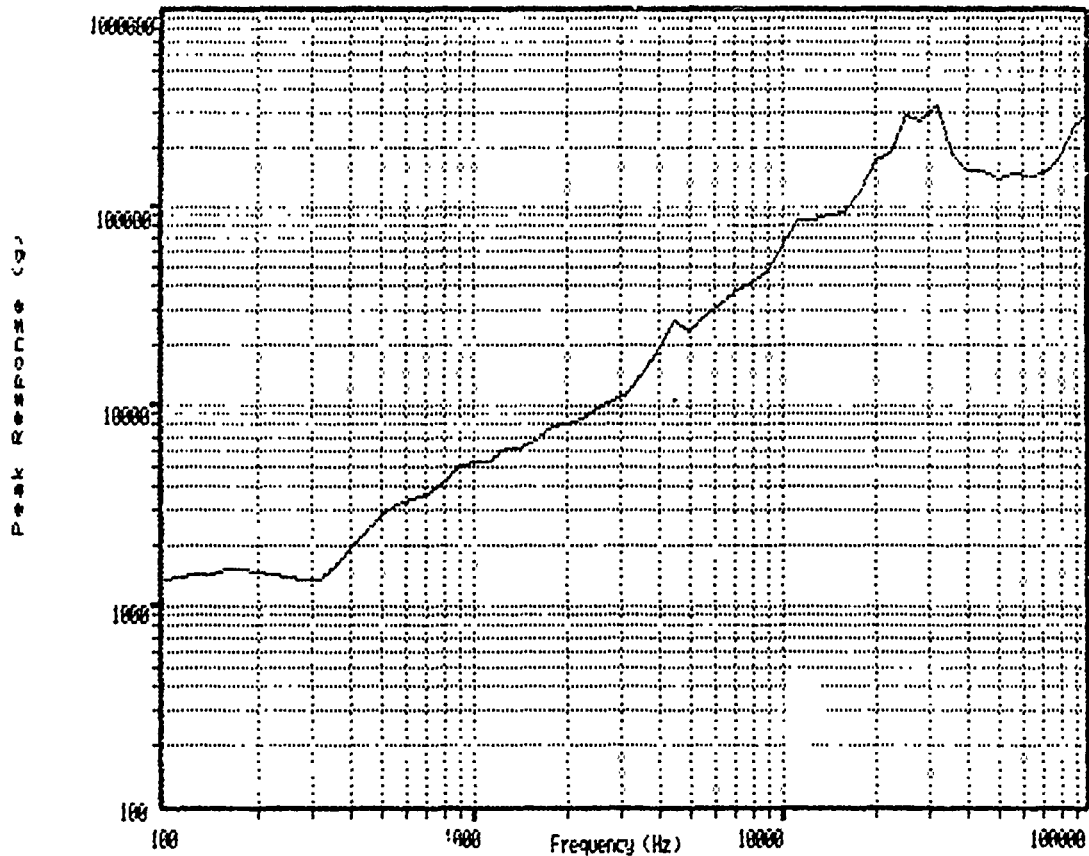
139

Shock Response Spectrum

GHI SYSTEMS, INC. TRIAD II-E

Test Ident: -
Test Item: -
Test Eng: -

Date of Test: 08-23-1988
Test Spec: -



Damping= .65 Model: Accel Max Type: Maximax Plot: 6th Oct Samples From Memory Channel # 1

Equiv. Plot Sampling Rate= 312500 P/s Signal Time Duration= 25.6 ms

Peak Signal Amplitude= 97064 g's

Remarks

2 channels on GHI with 600 KHz sample rate

FIGURE 13

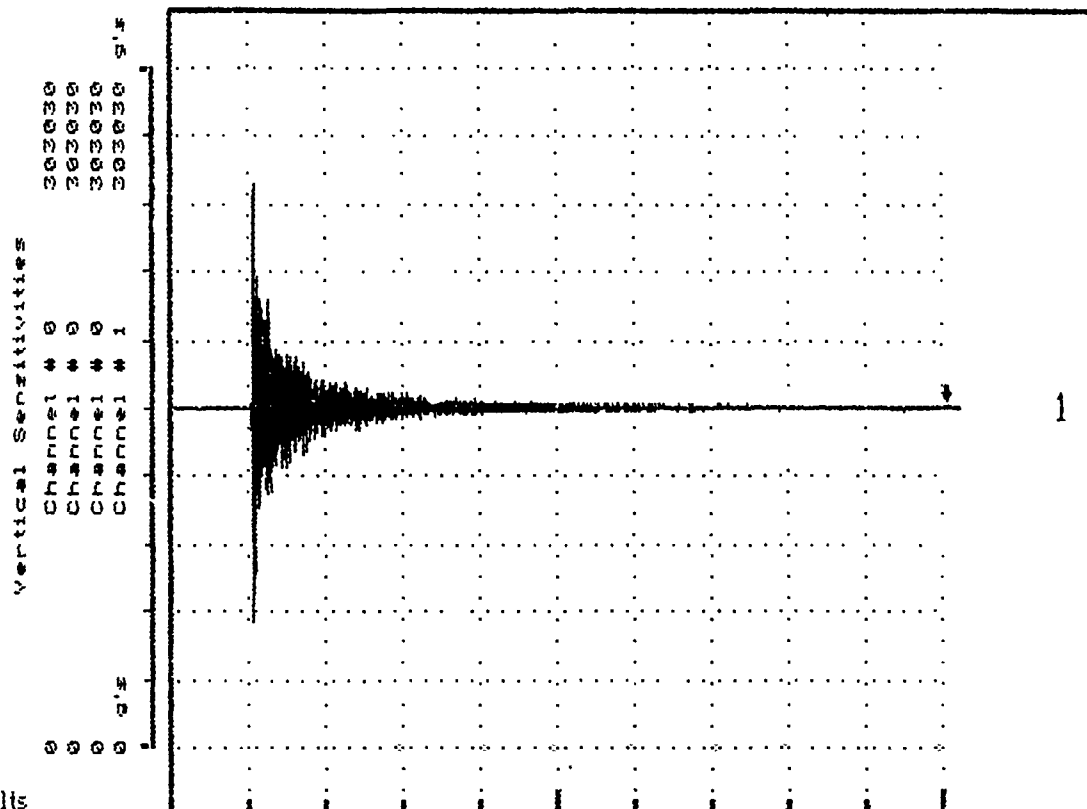
Waveform Test Report

GHI SYSTEMS, INC. TRIAD II-E

Test Ident: -
 Test Item: -
 Test Eng.: -

Date of Test: 08-23-1988
 Test Spec: -

Transducer Output Ch # 1 Ch # 0 Ch # 0 Ch # 0
 30303g's/Volt /Volt /Volt /Volt



CH	TIME	CUR AMP	PEAK AMP	1ST INT	2ND INT	TIME BASE	EXP
1	102.4mS	0 g's	100610g's	18922 In/s		102.4mS	1

Remarks

4 channels on GHI with 300 KHz sample rate

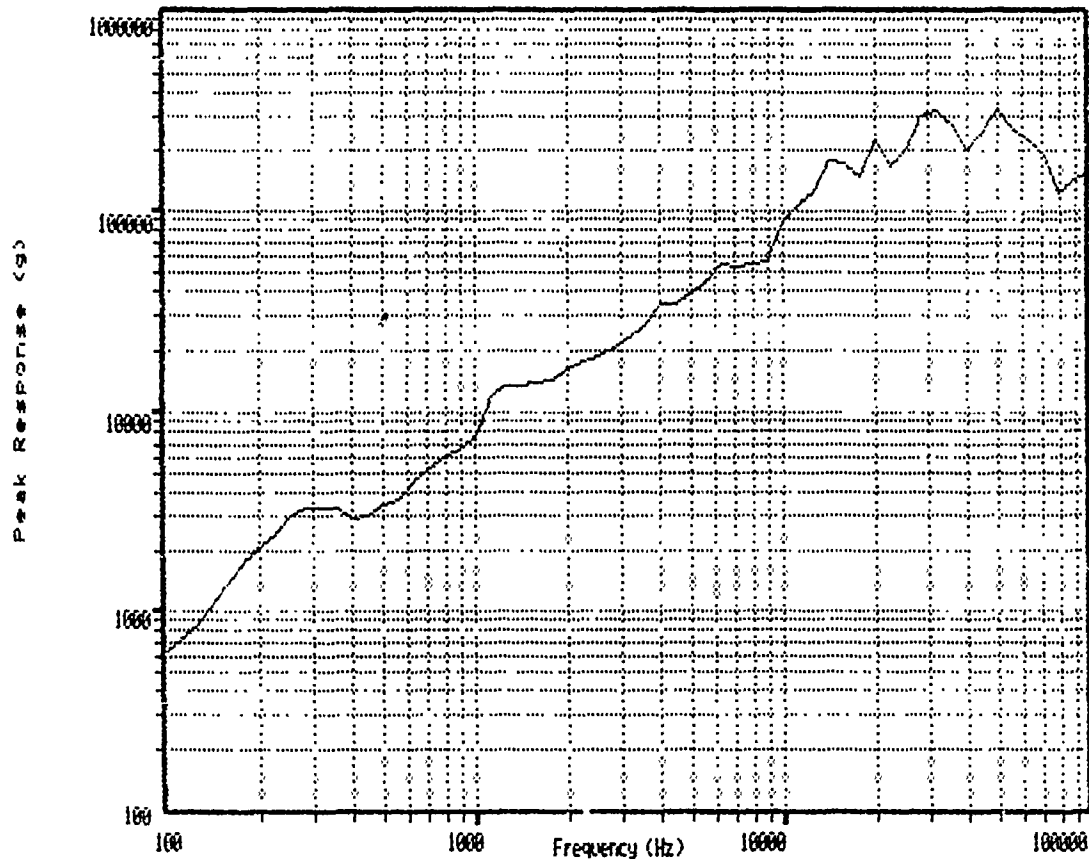
FIGURE 14

Shock Response Spectrum

GHI SYSTEMS, INC. TRIAD II-E

Test Ident: -
Test Item: -
Test Eng. : -

Date of Test: 08-23-1988
Test Spec. : -



Damping= .85 Model: Accel Max Type: Maximax Plot: 6th Oct Samples From Memory Channel # 1

Equiv. Plot Sampling Rate= 156250 P/s Signal Time Duration= 25.6 ms

Peak Signal Amplitude= 100610g's

Remarks

4 channels on GHI with 300 KHz sample rate

FIGURE 15

At this point in the technology, all we can do is pose questions, and hope that the answers are forthcoming. There are, of course, ways to avoid aliasing errors--filtering, as described earlier, or increasing the digitizing rate--but each brings about additional limitations, and each can introduce another type of error (we've already discussed filtering errors, and increasing the sampling rate significantly brings about a greater possibility of error due to data slew-rate or settling-time restrictions).

CONCLUSION

Which brings us back to where we started: we need a set of standards covering such things as filtering, sampling rates, instrument ranges and accuracies, etc.--much like what has been done with vibration and classical shock testing over the years. What we want to avoid is having two laboratories, for example, performing exactly the same test and one lab generating a response spectrum with an amplitude of 20,000 g's and the other lab generating only a 12,000 g spectrum. NIS is a service organization, and the last thing we want to do is tell a customer that we can't meet his specification--particularly if WXYZ Laboratories can meet it with little or no problem. Granted, pyroshock testing is not known for its repeatability, and there will always be some difference in the data. But the fact still remains that the customer sees the end, not the means, and if he or she sees a response spectrum that meets the specification, he or she will probably not question the data. Until the part fails in flight, because it was not tested on the ground.

We solicit your comments.

TEST EQUIPMENT USED

TYPE	MFG.	MODEL
Accelerometer	Endevco	2225M5A
Accelerometer	PCB	305A
Data Acquisition/Analyzer	GHI	TRIAD II E
Amplifier	Endevco	2740B
Power Supply	PCB	483A07
Shock Spectrum Analyzer	Spectral Dynamics	SD320
Oscilloscope	Nicolet	3091
Tape Recorder	Honeywell	101
Filter	Kemo	1100/IU/32
Filter	Khron-Hite	3342
Filter	TTE	LT9-10K

SHOCK RESPONSE SPECTRUM ANOMALIES WHICH OCCUR DUE TO IMPERFECTIONS IN THE DATA

R. Glenn Bell and Neil T. Davie

Experimental Mechanics Department
Sandia National Laboratories
P.O. Box 5800
Albuquerque, NM 87185

Shock response spectra are widely used in analysis, design and qualification of components and systems that are subjected to shock environments. The integrity of the data being used to generate the shock response spectrum is very important. Any inaccuracy such as a spurious spike or a zero shift in the data can have a significant impact on the spectrum. Manipulations of the data, decimation of data, or digital filtering, can also have a definite impact on the shock response spectrum. The degree of influence of the error is not always apparent. The effects of these errors on the generation of shock response spectra is shown for an absolute acceleration spectrum. The awareness of these possible errors is shown to require an understanding of the shock spectrum algorithm and knowledge of the effects of signal processing.

INTRODUCTION

An essential problem in the design or analysis of structures and equipment subjected to hostile environments such as shock or vibration, is its response to base motion. Since its introduction in the 1940's [1,2,3], the shock response spectrum (SRS) has provided a method of quantifying the effect that a specified input has on a structure. A SRS is a plot of the peak response of a series of single-degree-of-freedom (SDOF) systems to a given excitation with respect to the natural frequency of the SDOF system. The single-degree-of-freedom system consists of a rigid mass attached to a base by a massless linear spring and a viscous damper as shown in Figure 1.

This work was sponsored by the U. S. Department of Energy under Contract No. DE-AC04-76-DP00789.

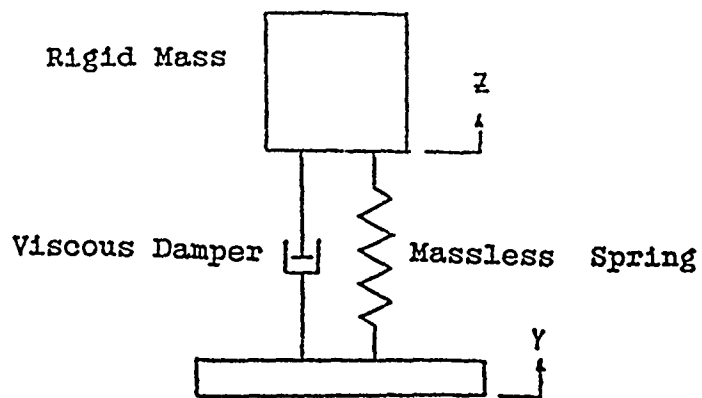


Figure 1. Single Degree of Freedom System

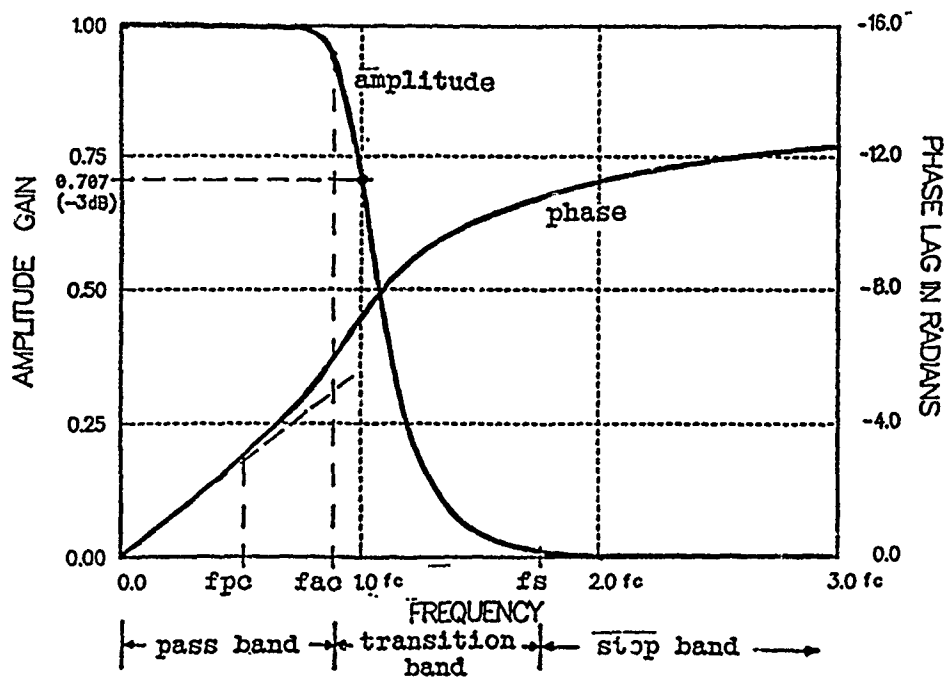


Figure 2. Eight Pole Butterworth Filter

The peak response of the SDOF system is usually described in three ways. The peak response can be the maximum positive, the maximum negative, or the maximum absolute value of the response. The time at which the peak response occurs can also be defined in several ways. Typically, the peak response is evaluated during either the primary response (during the input excitation), the residual response (during the free vibration), or the overall response (both primary and residual). The SRS used in the paper is the maximum absolute, overall response which is commonly called the maximax SRS.

Many different solution techniques are available to solve the differential equations describing the SDOF system for the peak response needed to produce the SRS. Two popular solution techniques are used in this paper: a recursive digital filter method (RDF) [4,5] and the Fox-Goodwin method (FGM) [6,7]. The RDF method uses a digital recursive filter to simulate the SDOF system. The FGM method is a variation of a Newmark numerical integration routine which solves the classical equation of motion for a SDOF system. The differences in the SRS for the two solution methods (FGM and RDF) are usually negligible, therefore no distinction between the methods will be made except when the differences are significant.

Modern data acquisition systems have advanced to the point where even a novice user can easily acquire, digitize, and analyze data without any basic understanding of the analog, digital, or software limitations of the system. Likewise, the calculation of the SRS has become so commonplace that a user does not need to have any knowledge of the limitations of the algorithm. These limitations can have a profound impact on the SRS if they are exceeded. It is appropriate to first briefly review some common limitations of a data acquisition system. Analytically generated data will then be used to evaluate different anomalies that may occur in a SRS due to either the limitations in the data acquisition system or the SRS algorithm. The effects on the SRS will be illustrated by examples in the following sections: 1) the problem associated with an insufficient sample rate; 2) the effects of different filters; 3) the unexpected effects filters can have on the SRS; and 4) problems due to errors in the data.

ANALOG SYSTEM RESPONSE AND ITS LIMITATIONS

The front end of a typical data acquisition system consists of various pieces of analog signal conditioning equipment such as amplifiers, anti-aliasing filters, and data recorders. For the data to be properly interpreted, it is essential to know the amplitude and phase response of this analog system as it is connected for a particular application. This response is usually dominated by a single piece of equipment. As an example, consider the frequency response function of an analog system containing an eight pole Butterworth lowpass filter as shown in Figure 2. Assume that the response of the entire analog system is that of the filter. This would be the case if the rest of the system had a flat amplitude and a linear phase response to frequencies from 0 to well beyond the cutoff frequency of the filter. The amplitude response of the filter consists of three regions; a passband ($0 < f < f_c$) in which the signal amplitude remains essentially unchanged, a transition band ($f_c < f < f_s$) in which the signal is only partially attenuated, and a stopband ($f > f_s$) in which the signal is completely attenuated. Note that the passband does not extend out to the -3dB filter cutoff frequency (f_c), which is the frequency normally referenced when specifying a filter. The phase response of the filter consists of two

frequency regions; a linear band ($f < f_{pc}$), and a non-linear band ($f > f_{pc}$). In this example the passband will be defined as having a unity amplitude within 5%; the stopband will be defined as being less than 1% amplitude gain, while the linear phase band will be defined as less than a 5 degree deviation from the initial slope of the phase response. It is well known that a linear phase filter causes a time delay in the signal without distortion. A non-linear phase filter produces a time delay which is a function of frequency, causing signal distortion [8]. For a signal to pass through the analog system without distortion, it must have frequency content only in the passband and only in the linear phase band. Note that in this example, the filter response is limited by its phase response and not its amplitude response, (i.e., $f_{pc} < f_{ac}$). If the signal has significant frequency content in the transition band or non-linear phase band the desired filter effects will not be achieved. Such distortions may cause significant errors in subsequent shock spectrum calculations. These distortions could be removed with digital processing techniques if the amplitude and phase responses were available. Unfortunately, these characteristics are rarely known. Both the lack of a basic understanding of the analog system being used to collect the data, and the inadequate characterization of the frequency content of the signal may cause undetectable distortions that result in bad data being reported as good.

INSUFFICIENT SAMPLE RATE

The calculation of shock spectrum is a very computational intensive process. One way to minimize calculation time is to decrease the number of points in a data set. In order to minimize the number of points, the signal can be either initially sampled at a minimum rate, or decimated at some later time. Performing either operation without the proper precautions, can result in a sample rate (SR) which is insufficient to produce an accurate SRS. This problem will be shown in the following examples. Analog signals are usually digitized to facilitate their analysis in the computer. The basic limitation of the digital signal is the Sampling Theorem which states that the signal must be sampled at a rate greater than twice the highest frequency contained in the signal [9]. If this theorem is violated, aliasing occurs, i.e., frequencies greater than $SR/2$ (Nyquist frequency) will be manifested as frequencies less than $SR/2$. The usual way to prevent aliasing is to apply an analog lowpass filter such that $SR/2$ is in the stopband of the filter. A common mistake is to assume that the -3dB filter cutoff frequency (f_c) is the start of the stopband, and that equating f_c to $SR/2$ will provide protection from aliasing. Examination of Figure 2 shows why this is not true.

Once the signal has been digitized without aliasing, the data may be accurately processed to provide information such as a SRS. However, the authors have observed that some computer algorithms being used for these calculations implement decimation subroutines to reduce the time required to process the data. This has the same effect as digitizing the data at a lower SR. Therefore, the data must be digitally filtered prior to decimation with the appropriate lowpass filter to prevent aliasing due to the decimation.

Aliasing also causes gross errors in shock spectrum calculations. Figure 3 shows an acceleration versus time plot of a 20 millisecond white noise pulse that has been filtered with a 0.1 to 2 KHz bandpass filter. The sampling theorem requires that this signal be sampled at a rate greater than

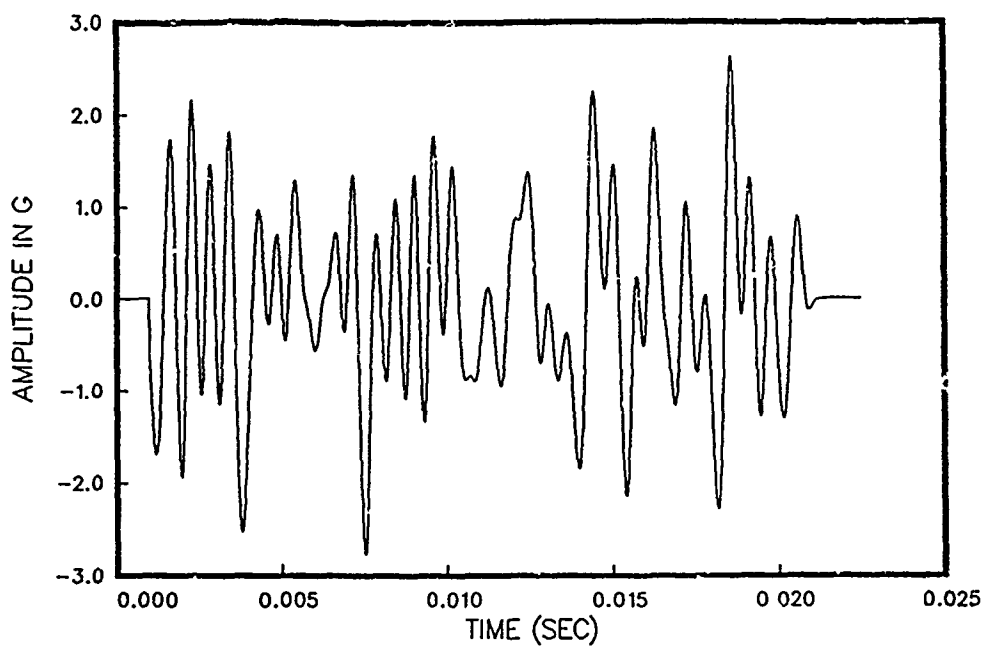


Figure 3. Time History of .1 to 2 KHz White Noise

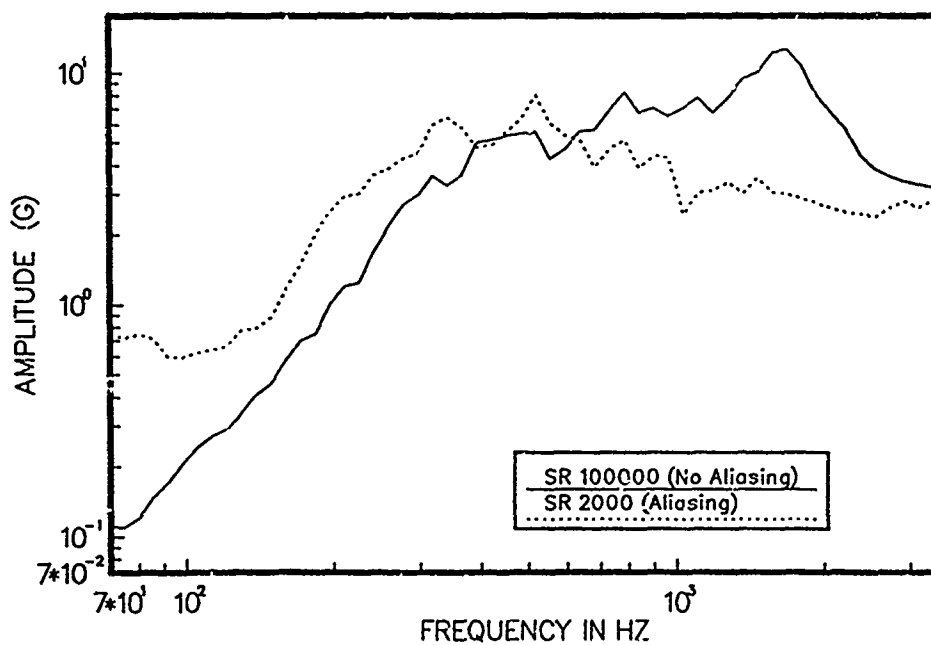


Figure 4. Aliasing Effect Due To Insufficient Sample Rate (Damping: .05)

4 KHz. Figure 4 shows two shock spectra which have been calculated for this signal; one was calculated from data sampled at 100 KHz (no aliasing); the other was calculated from data sampled at 2 KHz (aliasing). Note that aliasing has caused severe errors over the entire frequency range of the shock spectrum. Fortunately aliasing is easily prevented with the proper use of anti-aliasing filters or by not decimating data without first using appropriate digital filters.

In addition to the problem of aliasing, the accuracy of both algorithms can be affected by the sample rate. A good "rule-of-thumb" that is typically followed is for the SR to be greater than $10*f$ where f is the larger of 1) the highest frequency in the input data or 2) the highest frequency to be calculated in the SRS. As previously noted, the SR must be adequate to define the frequency content of the data. The accuracy of both the RDF and FGM algorithm diminishes as the SR is decreased. The FGM algorithm can even go unstable. The Fox-Goodwin algorithm method is conditionally stable for $SR > 2.57*f$ [6]. The RDF method is unconditionally stable, however the accuracy can be greatly affected by numerical errors caused by an insufficient sample rate.

In order to perform a direct comparison of the effects of the sample rate on the accuracy of the SRS, the 0.1 to 2 KHz noise signal was used ($SR=100000$). The signal was decimated at various rates to lower the SR. The accuracy of both algorithms was acceptable for sample rates above 20K which corresponds to a SR that is 10 times the highest frequency (i.e., 2 KHz) in the data. For the RDF method shown in Figure 5, the accuracy decreased for SR less than 20K, while the FGM method shown in Figure 6 proved to have acceptable accuracy for SR as low as 10K. The SR of 10K corresponded to only 5 times the highest frequency in the data, thus the FGM method can be used to generate a reasonably accurate SRS using a much smaller sample rate.

Figure 7 shows the SRS for both solution methods sampled at 4K, which sets the Nyquist frequency equal to the highest frequency in the data. This is the minimum SR allowed without causing significant errors due to aliasing. The stability condition for the FGM method is violated, and the SRS values calculated approach infinity at the higher frequencies. Unfortunately, there is no definite warning for the RDF method that the SR was too small since it remained stable. The resulting SRS in Figure 7 for the RDF method looks reasonable, but its accuracy at the higher frequencies is poor.

A comparison of SRS computation speed of the two algorithms was performed. The FGM method proved to be 2% faster than the RDF method in generating an accurate SRS since it can be run with half the sample rate. Comparisons of the two methods using equal sample rates showed that the RDF method is 22% faster than the FGM method.

EFFECTS OF DIFFERENT TYPES OF FILTERS

Data are routinely passed either through a lowpass analog or a lowpass digital filter. Two commonly used filters are the Butterworth filter and the Chebyshev filter. The Butterworth filters, like the one shown in Figure 2, are characterized by a smooth power gain function having maximum flatness in both the passband and the stopband region and a reasonably sharp cutoff. By allowing a ripple in either the passband or the stopband a sharper rolloff can be achieved in the Chebyshev filter. Some of the flatness of the Butterworth filter has been sacrificed in the Chebyshev filter for a

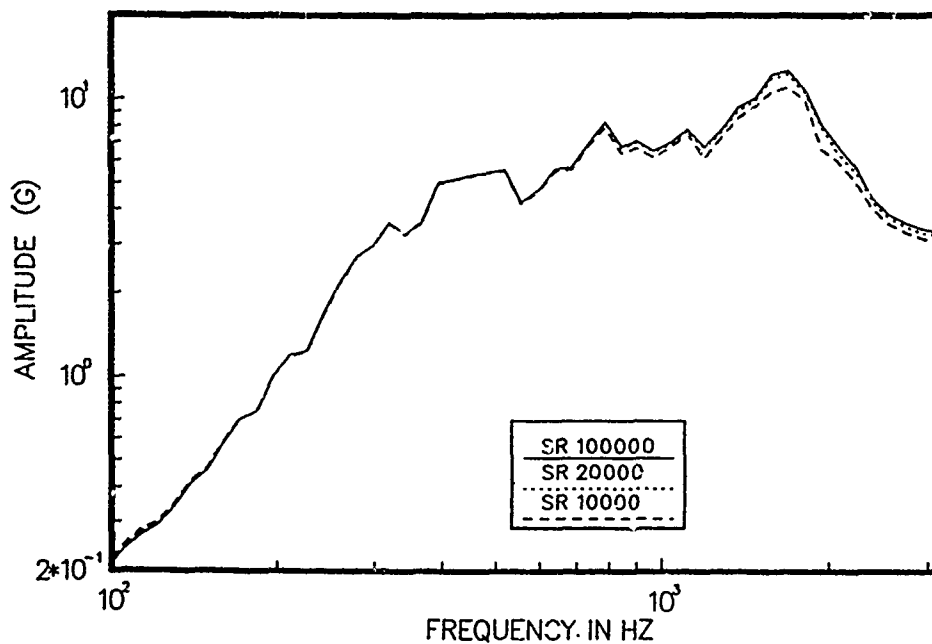


Figure 5. Comparison of the SRS of .1 to 2. KHz Signal Using RDF
Sampled at Different Rates (Damping: .05)

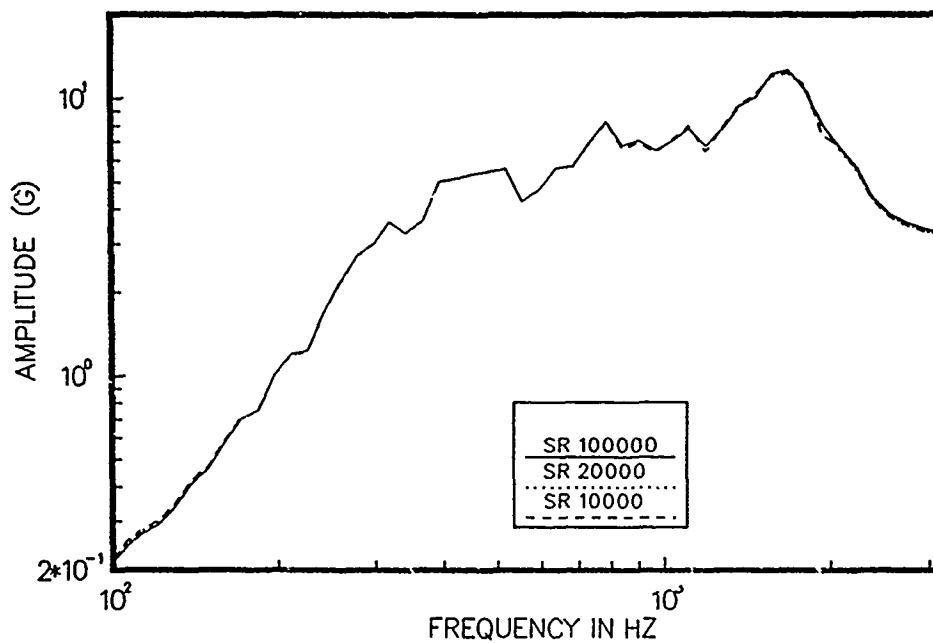


Figure 6. Comparison of the SRS of .1 to 2. KHz Signal Using FGM
Sampled at Different Rates (Damping: .05)

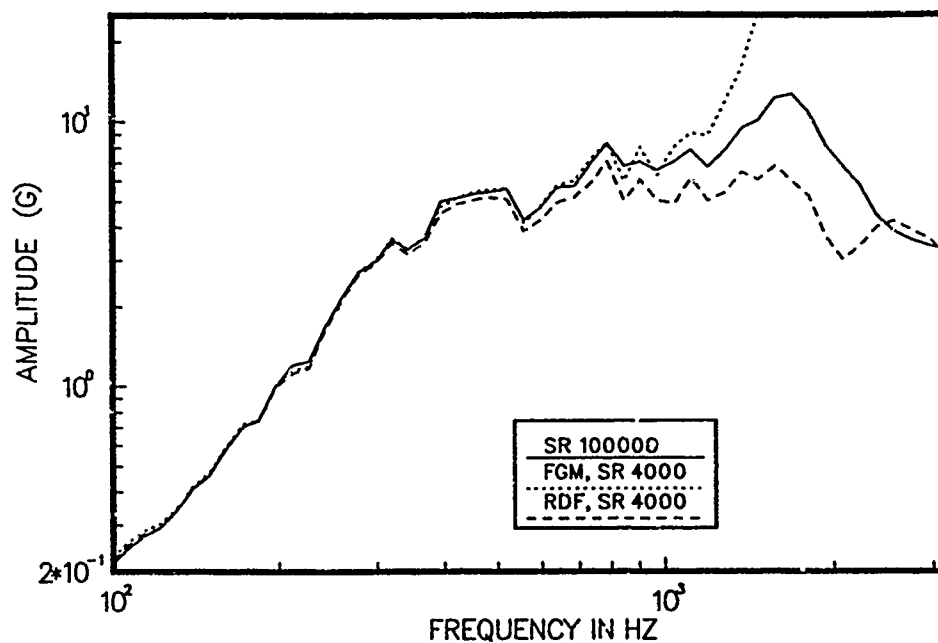


Figure 7. SRS of .1 to 2. KHz Signal Using RDF and FGM Methods
Sampled at 4K (Damping: .05)

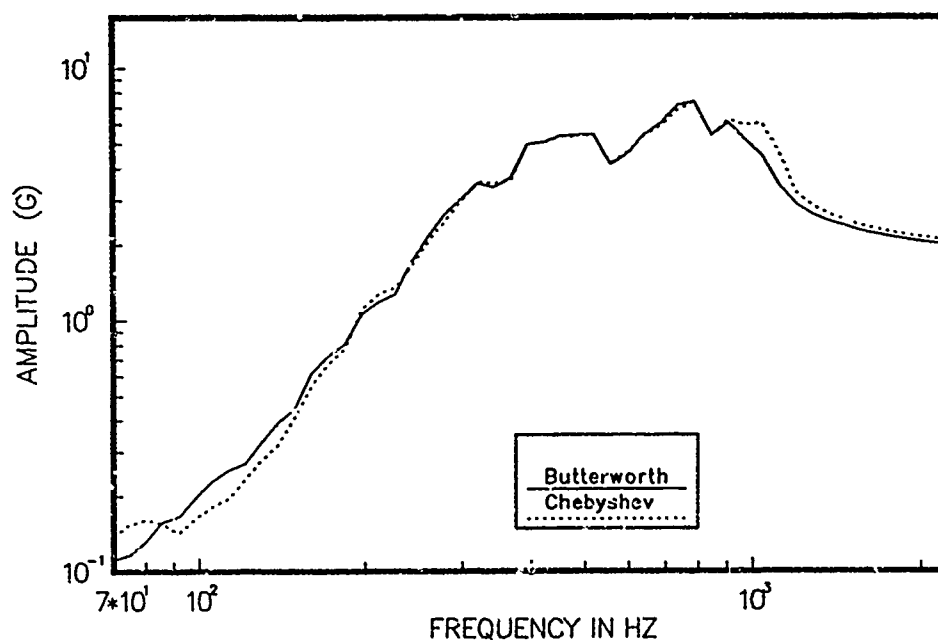


Figure 8. SRS of .1 to 2. KHz Signal Filtered at 1 KHz Using a
Butterworth and a Chebyshev Filter (Damping: .05)

sharper rolloff of the filter. Both the Butterworth and the Chebychev filters exhibit non-linear phase response in their passbands. When post processing data with digital filters, the non-linearity can be eliminated by forward and reserve filtering data which results in a zero phase shift for all frequencies [10].

Figure 8 shows the SRS of the 0.1 to 2 KHz white noise digitally filtered with a Butterworth and a Chebychev filter with cutoff frequencies of 1 KHz. The differences in the amplitude and phase response of the filters produce noticeable differences in the SRS. Variations in the SRS occur for all frequencies. The sharper rolloff of the Chebychev filter is also evident in the SRS at the cutoff frequency. The slower rolloff of the Butterworth filter partially filters some of the data below the 1 KHz cutoff frequency, thus lowering the response of the SRS near the cutoff frequency.

These non-linear phase filters can cause distortions in the data which result in errors in the SRS. Figure 9 shows the SRS of the white noise filtered by a non-linear phase and by a zero phase Butterworth filter. Slight differences in the SRS occur at all of the frequencies, however, the most noticeable difference occurs near the cutoff frequency. The non-linear effect increases if the data are lowpass filtered at a lower cutoff frequency as shown in Figure 10. In this case, the variations in the SRS are more pronounced for all of the frequencies, and are especially pronounced near the cutoff frequency.

The time delay that a non-linear phase filter (such as the Butterworth filter) exhibits can present some additional problems for a digital filter that are not present in an analog filter [10]. If the data set to be filtered does not have sufficient zeros following the signal, the trailing end of the signal will be moved out of the time window, thus truncating some of the data. If the data are then reverse filtered to produce a zero phase filter, the resulting data are inaccurate because of the previous truncation. The resulting SRS generated from data that are truncated for either a non-linear or a zero phase filter is shown in Figure 11 to be appreciably different from SRS generated from the non-truncated data (i.e., the record having enough trailing zeros). Truncation will also occur when a negative time shift is produced by the reverse filter if not enough zeros are on the leading edge of the data. It is important to note that the amount of the time delay increases with an increase in the number of filter sections and a decrease in the cutoff frequency.

COMMON FILTERING MISCONCEPTIONS

Filters can also adversely affect the shock spectrum if we fail to completely understand the total effect of the filter on the data. Data that are experimentally collected may contain high frequency elements that are not desired. A digital filter is then applied to remove the higher frequencies. The resulting signal is assumed to be void of any of the effects of the high frequency signal and the SRS of this signal is assumed to be the same as for a signal that never contained any of the higher frequencies. Unfortunately, this is not true, since the high frequency portion of the signal may contain low frequency components. This is due to the fact that a particular frequency in a finite duration signal is not completely contained at that exact frequency, but parts of the frequency are spread over the entire frequency range. This phenomenon is commonly referred to as leakage [9]. Thus, the low frequency portion of a signal contains not only the low frequencies but portions of the higher frequencies

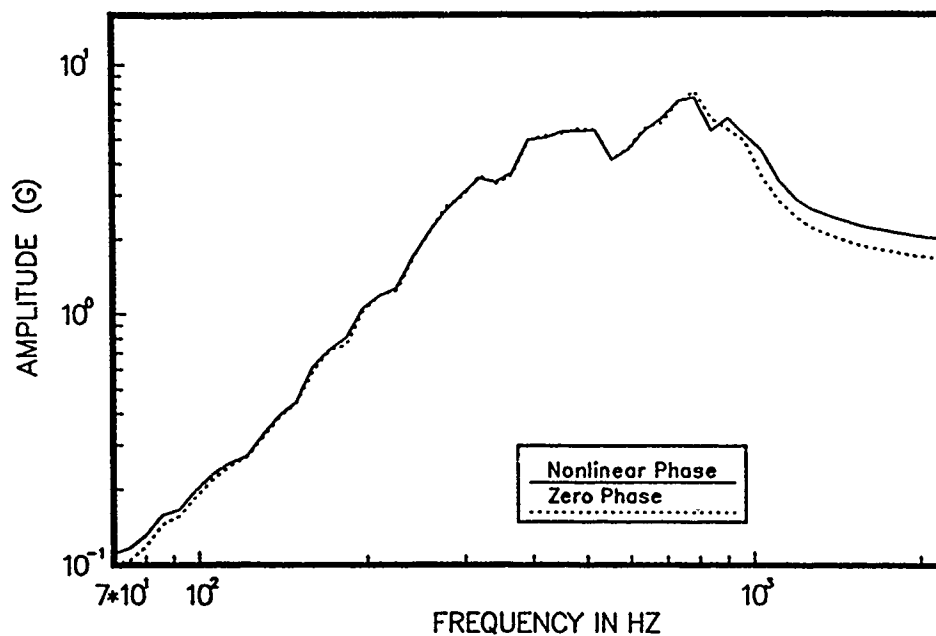


Figure 9. SRS of .1 to 2. KHz Signal Filtered at 1 KHz Using a Zero Phase and a Non-linear Phase Butterworth Filter (Damping: .05)

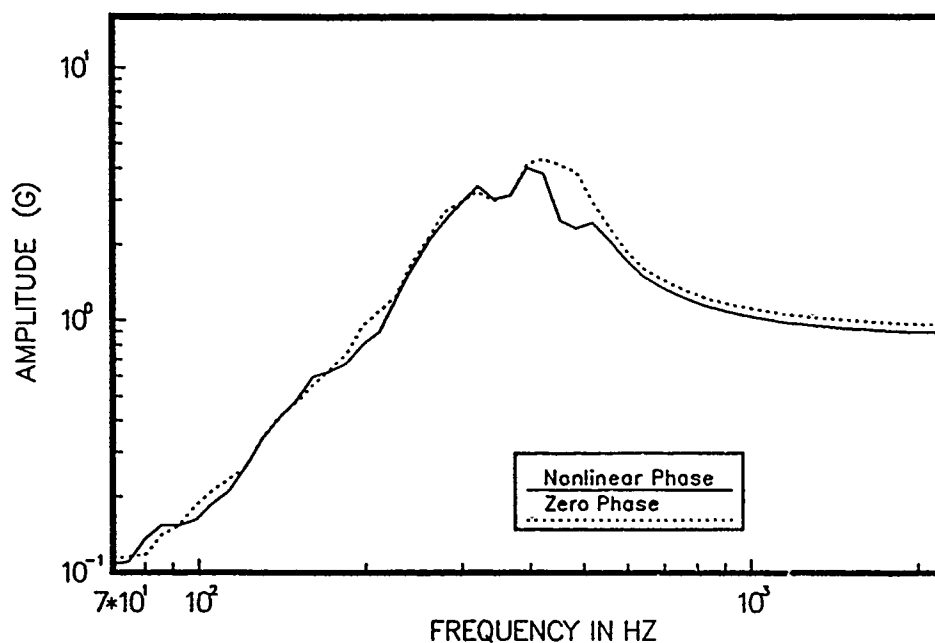


Figure 10. SRS of .1 to 2. KHz Signal Filtered at .5 KHz Using a Zero Phase and a Non-linear Phase Butterworth Filter (Damping: .05)

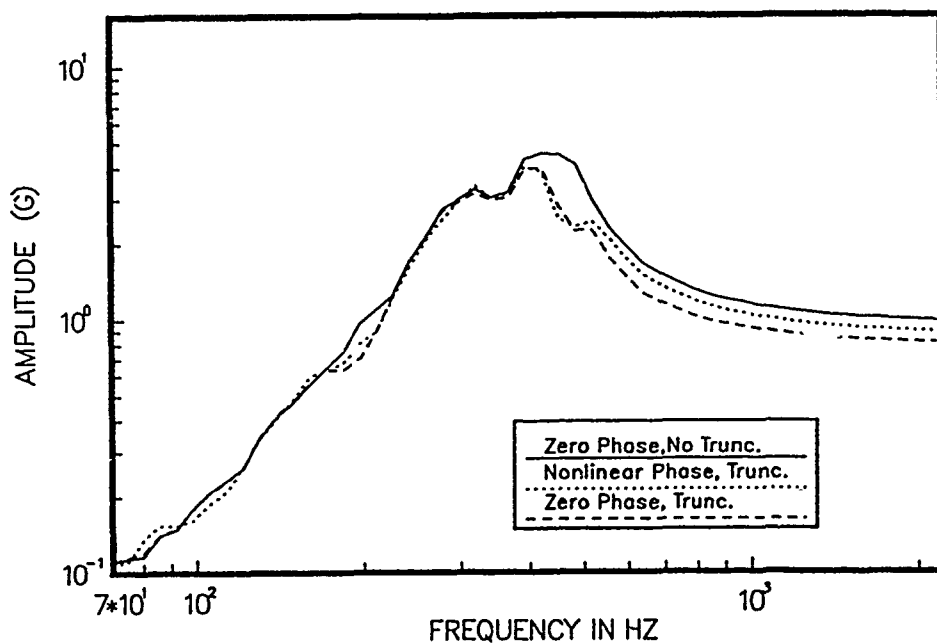


Figure 11. Comparison of the SRS of .1 to 2. KHz Signal Filtered at .5 KHz With Data Truncation (Damping: .05)

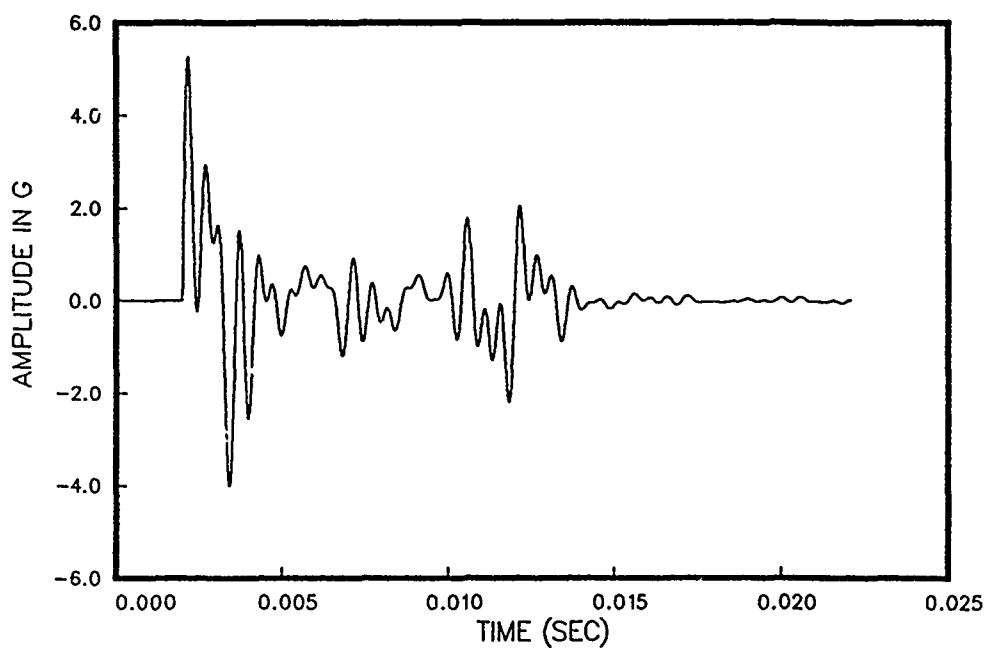


Figure 12. Time History of Signal 1 0.3 to 2 KHz Decaying Sinusoids

as well. This high frequency influence is very important in the development of analytical simulations. Comparison of data from analysis and experiments are made in order to refine an analytical model. The analytically generated data usually model only the lower frequency modes of the structure and are therefore void of any of the high frequency modes. On the other hand, the experimentally collected data are filtered to remove the unwanted high frequencies to facilitate a comparison with the model. Therefore, the analytical model that results from this comparison may be inaccurate.

In order to demonstrate this effect, a signal shown in Figure 12 was analytically generated containing various sequences of equal amplitude decaying sinusoids that were superimposed on each other. Three distinct frequency ranges were used in the signal: 0.3 to 0.6 KHz, 1.2 to 1.5 KHz, and 1.8 to 2.0 KHz. A second signal (shown in Figure 13) was also generated that contained the exact same sinusoids as the 0.3 to 0.6 KHz range in the first signal. The SRS of the second signal represents the results of the first signal without the influence of the higher frequencies. For this example, imagine that the first signal is the experimentally measured data, and that the second signal is the result of an analytical model which makes no attempt to model frequencies above 1 KHz.

The first signal was filtered at two different cutoff frequencies using a zero phase Butterworth filter. Figure 14 shows that the SRS of the filtered signals are not exactly the same as the SRS generated from signal 2 (i.e. the desired results). It is interesting to note that the amplitudes of the low frequency portion of the SRS are exactly the same for both of the filters. In Figure 15 it can be seen that the SRS for unfiltered signal 1 and the filtered signal 1 are exactly the same in the low frequency range. Even though the higher frequencies have been filtered, the influence of the higher frequencies on the lower frequencies remains unchanged. This is due to the fact that a Butterworth filter is designed to be flat in the passband region (i.e., power gain of unity), such that all the frequencies below the cutoff frequency will remain unchanged. This effect is evident in Figure 16 where the Fourier transforms of the filtered signal 1 are exactly the same for the passband region for the unfiltered signal 1. The high frequency influence (i.e., spreading of the frequencies) is also evident in Figure 16 where the magnitude of the Fourier transform for signal 1 is slightly higher than signal 2 in the low frequency region.

The cutoff frequency selection can also make a difference in the SRS. The cutoff frequency should be selected such that the frequency content of the signal to be filtered is in the stopband region of the filter. The frequencies that are in the transitional region will not be completely attenuated, and they can still have some influence on the SRS as shown in Figure 14. This is evident by the second hump that exists in the SRS generated with data filtered at 1.1 KHz that does not exist in the SRS of the data filtered at .9 KHz. The location of the transitional band is defined by the cutoff frequency that is specified. The size of the transitional region is dependent on the rolloff rate of the filter at the cutoff frequency. A sharper rolloff will have a smaller frequency range defining the transition region than a filter that has a slower rolloff like the Butterworth filter shown in Figure 17. The power content of the frequencies in the transitional region will be attenuated more in a filter with a sharp rolloff as opposed to a filter with the same cutoff frequency but a slower rolloff.

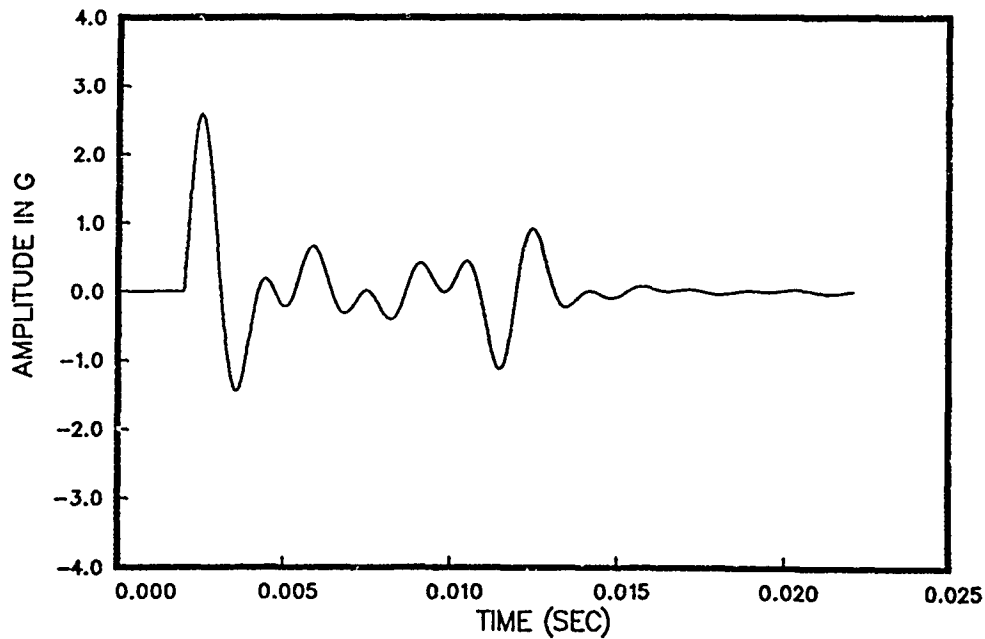


Figure 13. Time History of Signal 2 0.3 to 0.6 KHz Decaying Sinusoids

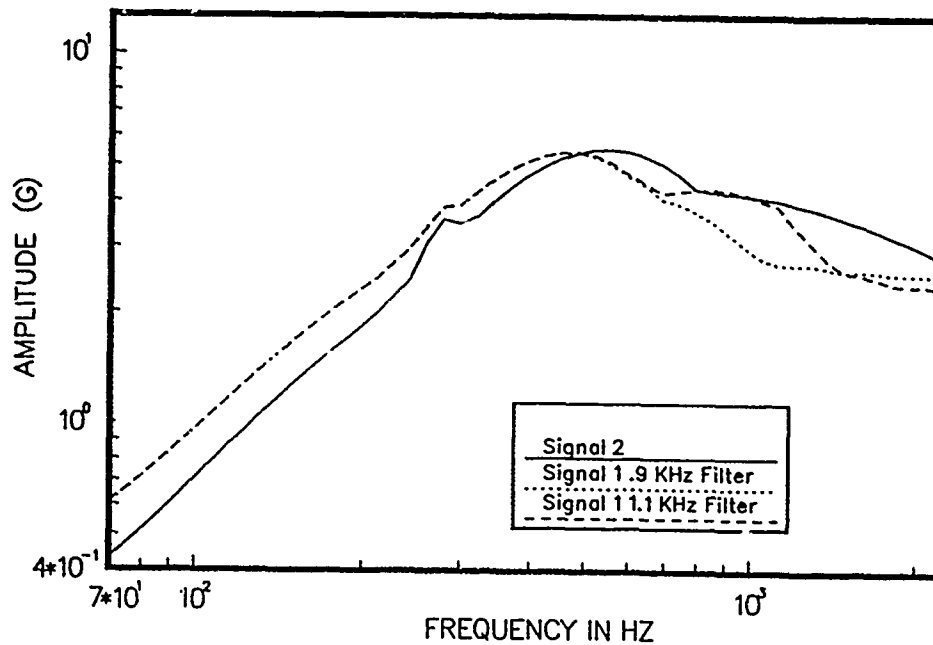


Figure 14. Comparison of the SRS for the .3 to 2. KHz Decaying Sinusoids at Different Cutoff Frequencies (damping: .05)

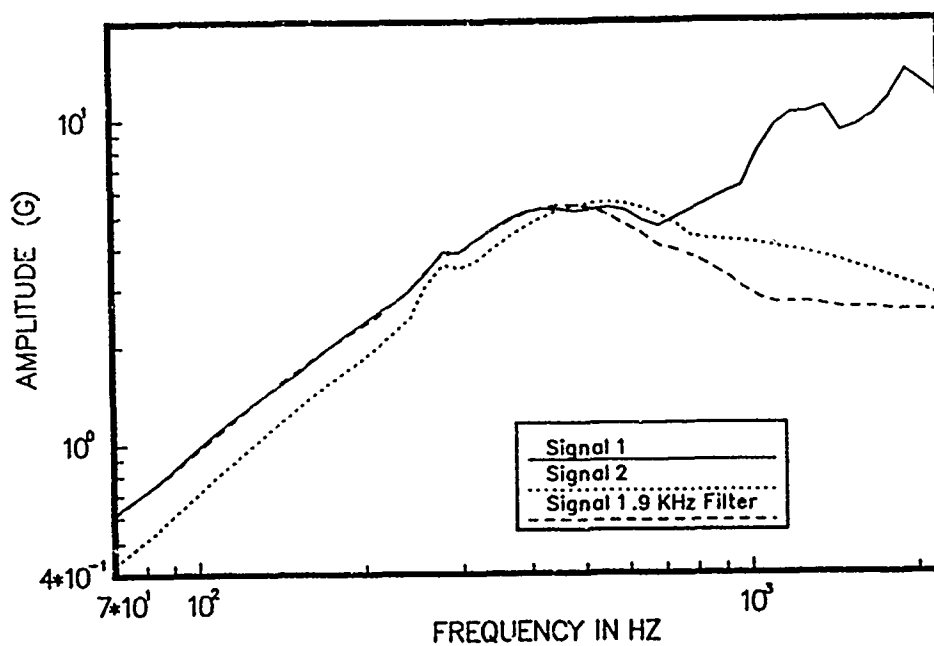


Figure 15. SRS Comparison of Signal 1 and Signal 2

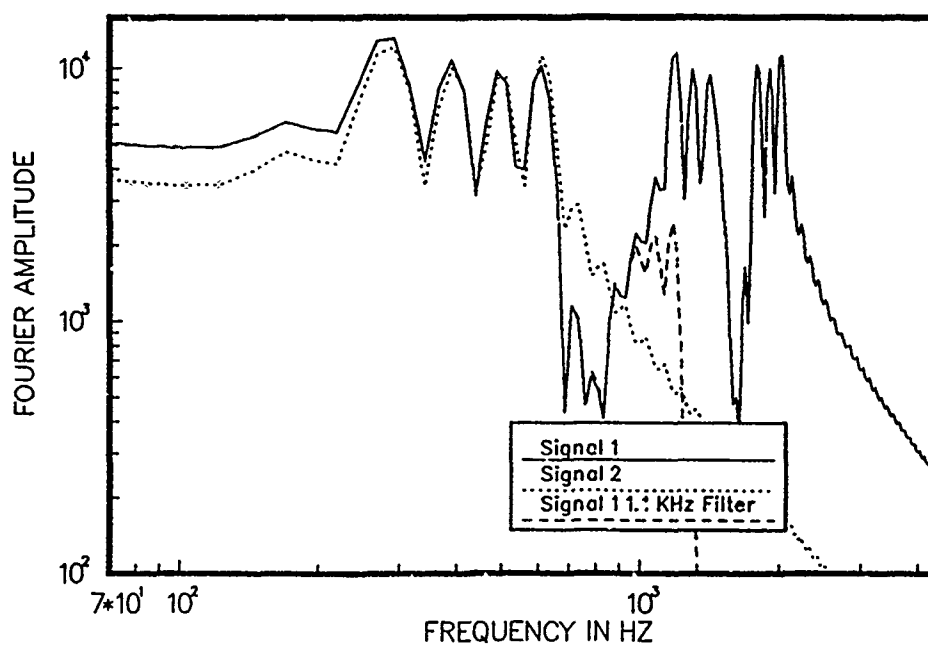


Figure 16. Comparison of the Discrete Fourier Transforms

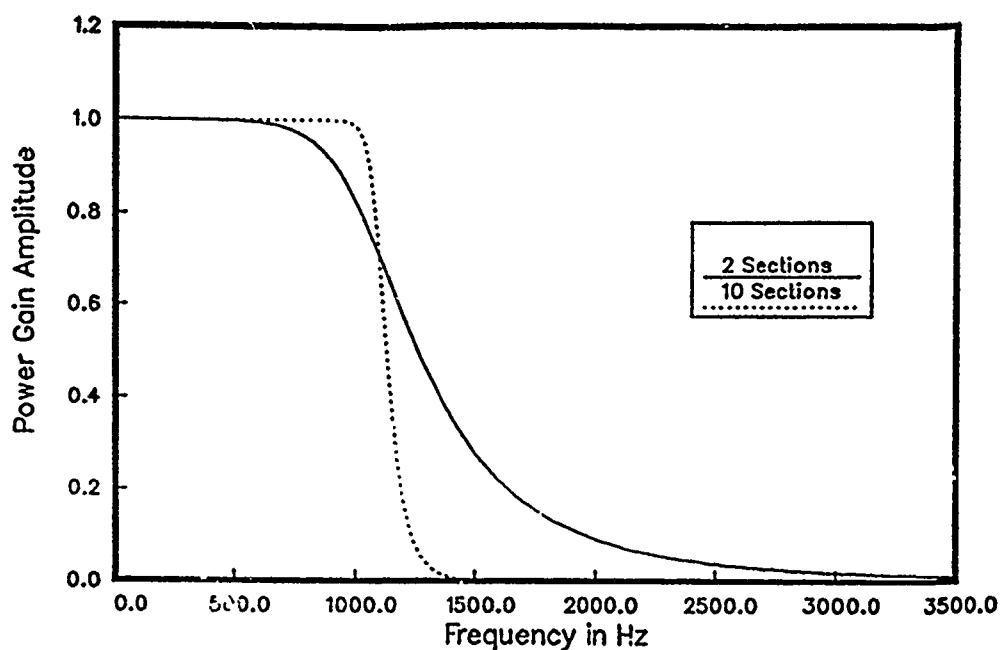


Figure 17. Comparison of a Butterworth Filter Using Different Number of Filter Sections

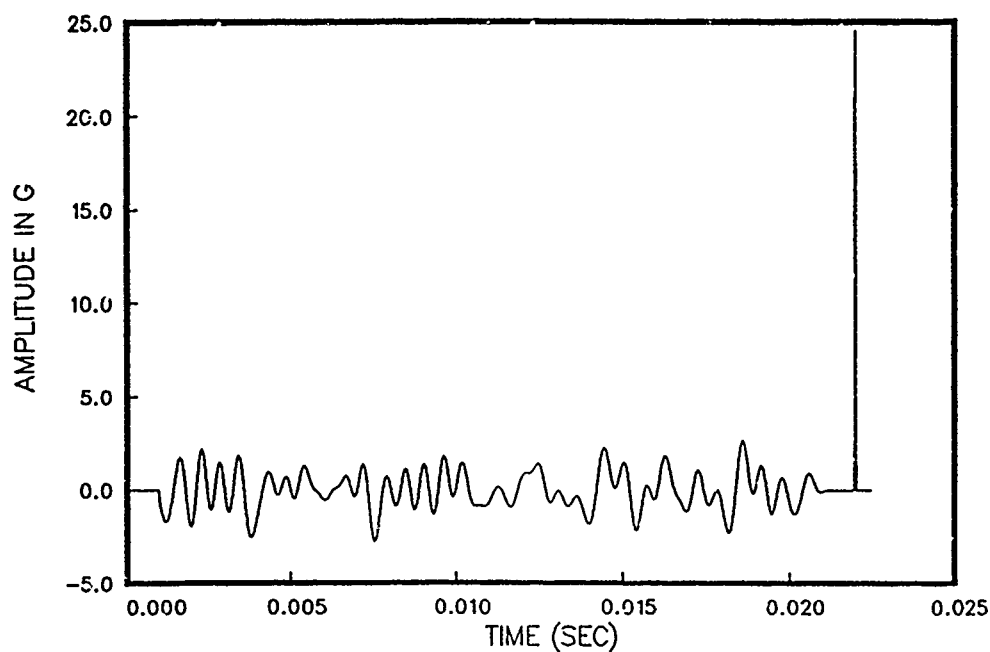


Figure 18. Time History of the .1 to 2 KHz White Noise With a 25 G Spike

EFFECTS DUE TO ERRONEOUS DATA

Occasionally signals are contaminated with high amplitude very short duration spikes. These spikes can be caused by numerous sources such as cable slap, the actuation of solenoids in the vicinity of the data acquisition system, power line noise, etc. When recorded on a wide band data system, these spikes are usually quite apparent, as seen in Figure 18 which shows a 25 G, 60 microsec. spike superimposed on the white noise data used in previous examples. If however the data has been filtered with a 3 KHz lowpass filter for example, the spike is almost indistinguishable from the real data as shown in Figure 19. Figure 20 shows the shock spectra calculated from the uncontaminated data, the unfiltered spike contaminated data, and the filtered contaminated data. Both the unfiltered, and filtered spike data have severe errors in their shock spectra. Particularly note that errors in the low frequency region are not improved with the use of the 3 KHz filter even though the spike has significant frequency content well above 3 KHz.

DC shifts can occur in measured data for a variety of reasons which will not be discussed in this paper [11]. The effect of small DC shifts on shock spectrum calculations can be seen by adding a 0.35 G shift to the white noise signal used in previous examples. The resulting signal is shown in Figure 21 where the shift occurs at 0.0025 sec. and continues for the remainder of the signal duration. The shock spectra for the shifted and unshifted data are compared in Figure 22. Note that most of the error created by the shift occurs at low frequencies, and the error at higher frequencies is negligible. Fortunately, this type of error is easily detected by observing that the signal does not return to zero, and by noting the nearly "flat" shock spectrum response at low frequencies.

Occasionally transient DC shifts occur during the measured transient with no noticeable shift remaining at the end of the signal. To examine the effect of this type of shift, a series of 0.35 G DC shifts (3 positive alternated with 3 negative) were superimposed on the white noise signal as shown in Figure 23. The shock spectra for the shifted and unshifted data are compared in Figure 24. Unlike the constant offset in the preceding example, this transient offset cannot be detected in the data record or in the shock spectrum without some information about the unshifted data. Such information is usually not available unless previous unshifted measurements had been made of the same or similar signal.

CONCLUSION

It has been shown that if data are acquired at too low a sample rate, inaccuracies in the shock spectrum will occur due to either the numerical limitation of the solution routines or to aliasing errors. Different types of filters have also been shown to produce slightly different results in the shock spectrum. An understanding of digital filtering is crucial to the proper interpretation of the shock spectrum. Digital filter algorithms that allow truncation of the data produce substantial errors in the shock spectrum. In addition, the rolloff rate and width of the transitional region of a digital filter can have a definite influence on the shape of the shock spectrum. Components of frequencies in the transitional band may affect the shock spectrum if they have not been attenuated sufficiently. It has also been shown that even though the high frequency component of a signal has been filtered, it still has some influence on the remaining

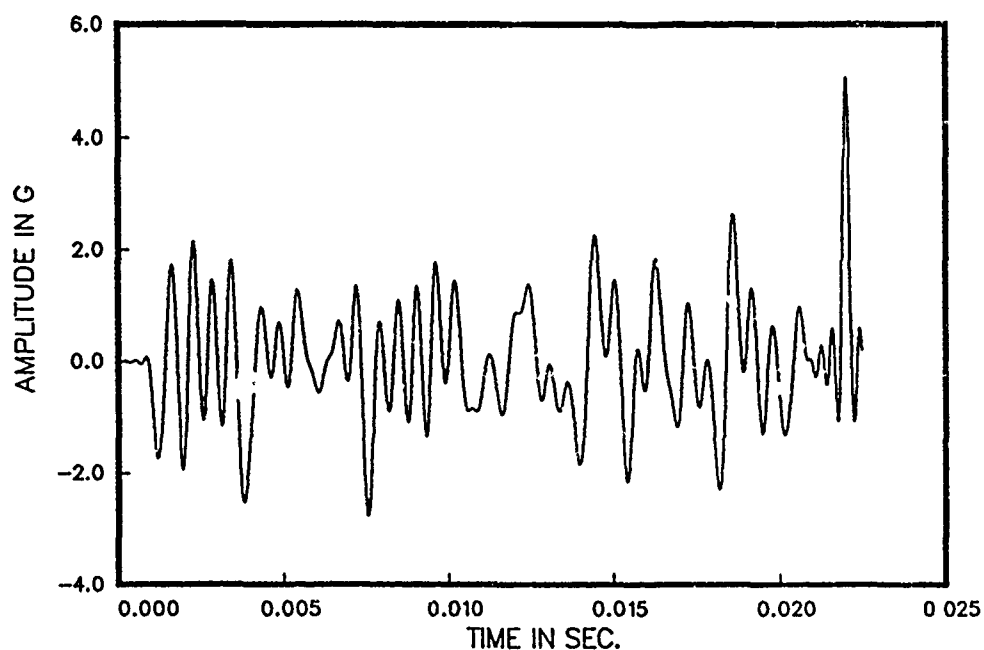


Figure 19. Filtered Time History of the White Noise Containing a 25 G Spike

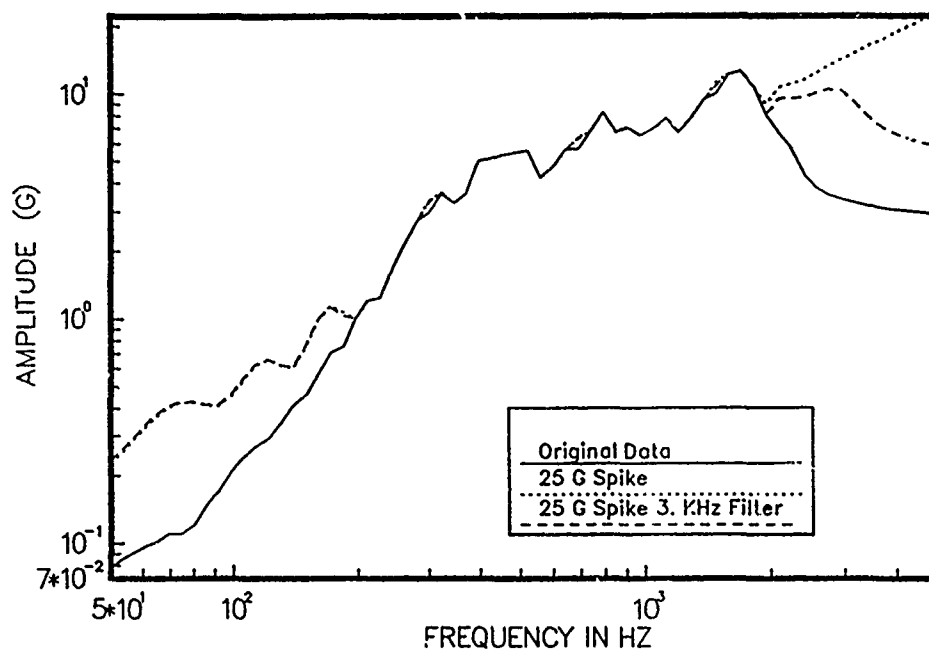


Figure 20. SRS of Data Contaminated By a Spike

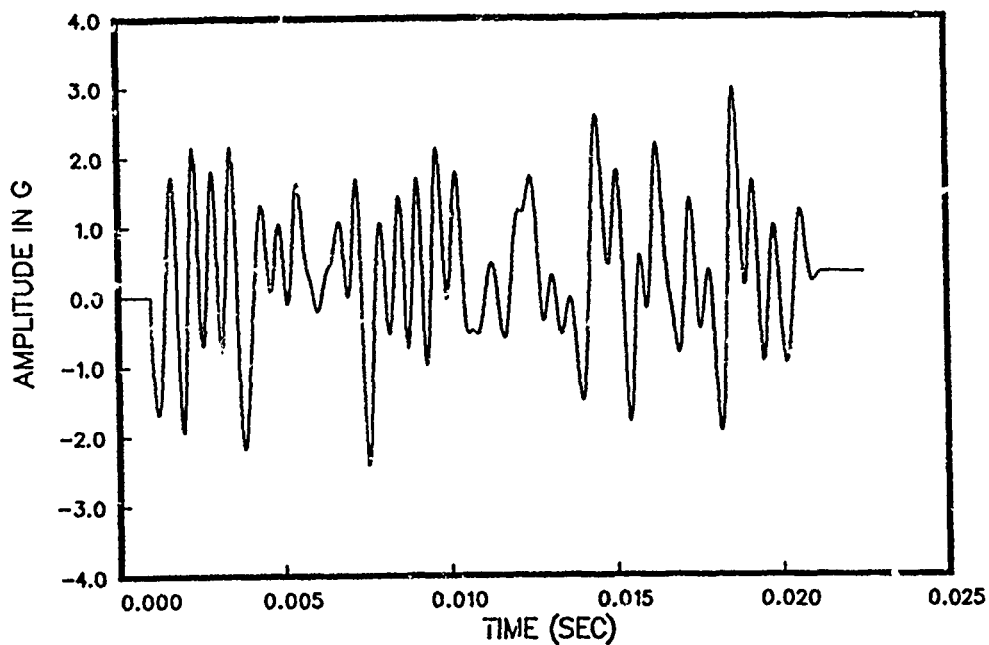


Figure 21. Time History of the .1 to 2 KHz White Noise With a .35 G Linear Shift

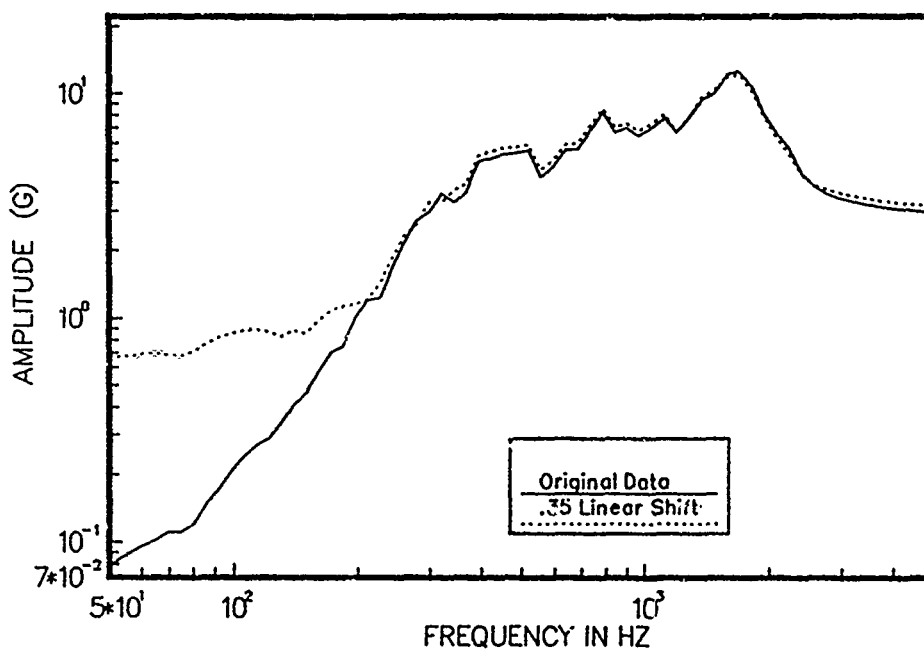


Figure 22. SRS of Data Contaimenated by a Linear Shift

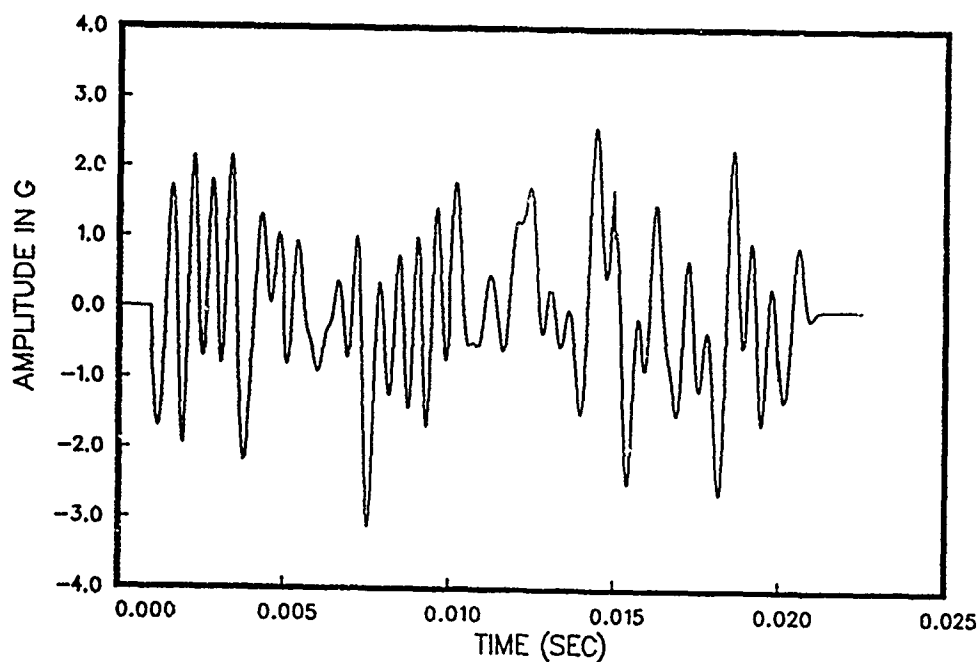


Figure 23. Time History of the .1 to 2 KHz White Noise With a .35 G Non-Linear Shift

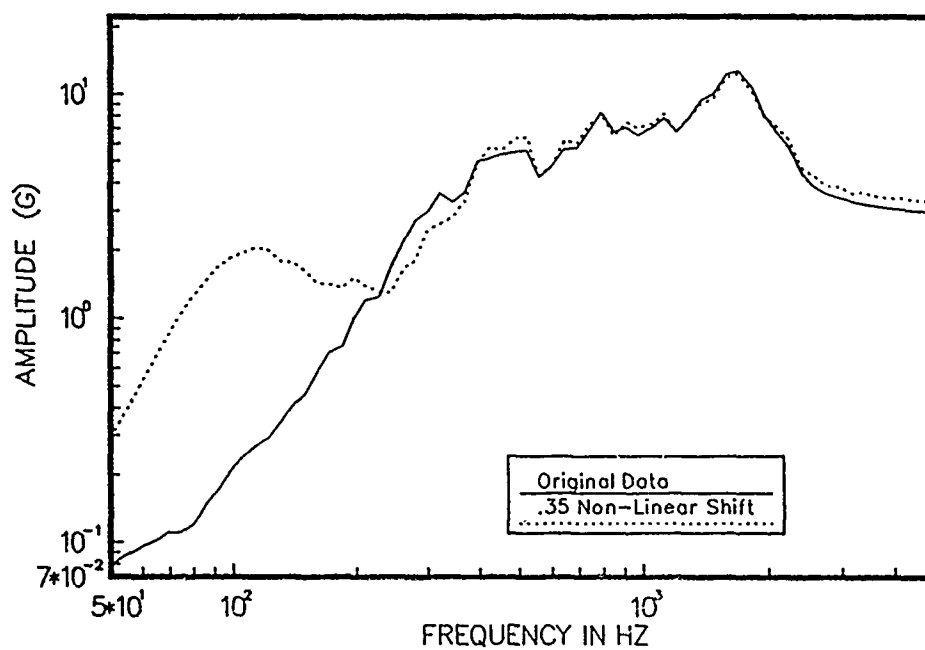


Figure 24. SRS of Data Contaimenated by a Non-Linear Shift

frequency content of the signal. This fact can have a great impact on the use of shock spectrum in design, where analytical data are compared to experimental data that have been filtered. Experimentally collected data are not always perfect and a zero shift or spurious spike may exist in the data in addition to background noise. The presence of these anomalies is not always apparent, and the effect on the shock spectrum can be major. Filtering of the data is not going to remove the bad portion of the data but may act to cover up its existence. Other steps must be taken to identify and remove the errors in the data.

The calculation of SRS cannot be done with a black box into which data are placed and a SRS comes out. A knowledge of the data acquisition technique must be implemented in order to assure the best possible data. Likewise, an understanding of the shock spectrum calculation algorithm is needed to prevent any gross errors in the SRS. Not all the problems with data acquisition and SRS generation can be avoided, but with some engineering judgement, the number of problems can be minimized such that the SRS can be an effective engineering tool.

REFERENCES

1. Biot, M. A., "A Mechanical Analyzer for the Prediction of Earthquake Stresses," Bulletin of the Seismological Society of America, vol. 31, 1941 pp. 151-171.
2. Benioff, H., "The Physical Evaluation of Seismic Destructiveness," Bulletin of the Seismological Society of America, vol 24, Oct. 1943, pp. 398-403.
3. Housner, G. W., "Calculation of the Response of an Oscillator to Arbitrary Ground Motion," Bulletin of the Seismological Society of America, vol. 31, April 1941, pp. 143-149.
4. Smallwood, D. O., "An Improved Recursive Formula for Calculating Shock Response Spectra," Shock and Vibration Bulletin, No. 51, pp. 211-2', May 1981.
5. Smallwood, D. O., "The Shock Response Spectrum at Low Frequencies," Shock and Vibration Bulletin, No. 56, pp. 279-287, Aug. 1986.
6. Belytschko, T., and Hughes, T. J. R., Computational Methods For Transient Analysis, vol. 1, Elsevier Science Publishing Company, New York, 1983.
7. Brown, J. B. M., "The Discretization Error of Newmark's Method for Numerical Intergration in Structural Dynamics," Earthquake Engineering and Structural Dynamics, vol 13, pp. 43-51, 1985.
8. Walter, P. L., "Effect of Measurement System Phase Response Shock Spectrum Computation," Shock and Vibration Bulletin, No. 53, pp 133-142, May 1983.
9. Stearns S. D., Digital Signal Analysis, Hayden Book Company, New Jersey, 1975.
10. Walter, P. L., and Rodeman, R., "Characterization of Digital Filters Used in Sandia Laboratories Test Data Analysis Division," SAND79-1230, Dec. 1979.
11. Chu, A., "Zeroshift of Piezoelectric Accelerometers in Pryoshock Measurements," Shock and Vibration Bulletin, No. 57, pp. 71-80, Jan. 1987.

A FOURIER TRANSFORM FOR ALMOST ANY NUMBER OF DATA POINTS WITH REASONABLE RUN-TIMES

Mr. James (Jay) B. Cheek
DEPARTMENT OF THE ARMY
Waterways Experiment Station, Corps of Engineers
P.O. Box 631
Vicksburg, MS 39180-0631

This paper presents an "almost" solution to a problem in transformations from the time domain to the frequency domain. It describes a previously published transformation procedure that has no constraint on the sample size (the number of data points). The procedure is quite useful when working with previously sampled discrete data (from shock, earthquake, blast, etc.), because the time span can be set to the value best suited to the analysis without concern for the sample size. The cost for this flexibility is a very long run-time for some sample sizes. This paper presents criteria for making minor adjustments to the sample size (hence, an "almost" solution) in order to get a reasonable run-time.

BACKGROUND

Suffice it to say that progress in dynamic analysis is, in many respects, tied to the ability to quickly transform data from the time domain to the frequency domain. Today, most of the computer-based work of this nature is performed with the Fast Fourier Transform (FFT) developed by Cooley and Tukey (CT-FFT). Although it is fast, it is restricted in that the sample size (number of points) must be an integral power of two.

One can hardly call this a restriction when we consider the FFT's long history of extensive use. Many analysts find it imposes no difficulty; they simply adjust their sampling criteria. However, those who work with data streams taken at previously established time intervals (from shock, earthquake, blast, etc) are not so fortunate. Often, the time span (window) they wish to examine does not contain the required number of points. To overcome this difficulty, analysts adjust the data by various means in order to meet the number-of-points requirement while preserving the desired time window. Does this adjustment process degrade the analysis? Perhaps, but the question is unimportant if an adjustment is not necessary.

AN FFT FOR ANY NUMBER OF DATA POINTS

We now see a need in some quarters for an FFT that can transform any sample size. Such an FFT was developed by Glassman (G-FFT) and reported by Warren E. Ferguson, Jr., of the U.S. Army Mathematics Research Center in Technical Summary Report 2029 dated 1979. Having been available for quite some time, it is

interesting to note the sparse reference to G-FFT. Perhaps the limited use is related to the seemingly unpredictable run-times of the G-FFT on various sample sizes.

Our initial experience with the G-FFT brought out the fact that a minor change in the sample size caused a major change in run-time. For example, changing from 4,080 points to 4,078 points causes the run-time to increase from 2.2 seconds to 169 seconds. This is most undesirable. It is particularly vexing for the personal computer user who is waiting (not so patiently) for instant results.

Subsequent investigation proved that predicting run-time is a simple task. Run-time is a function of the sum (S) of the prime factors of the sample size (N) and the number (M) of prime factors of N. A program for calculating S and M aids the analyst in making minor adjustments to the sample size (hence, the time window) in order to process the data in a reasonable amount of time.

This paper discusses the basis for the run-time estimator and the improvement obtained by adjusting N. It shows that the G-FFT can be effectively used for almost any sample size and that the run-time factor (the ratio of the G-FFT run time to that of the CT-FFT) will be less than 3. We believe this greater run-time is an affordable overhead charge for the increased capability offered by the G-FFT to applications in dynamic analysis.

ESTIMATING RUN-TIME IN G-FFT

This discussion shows why N, M, and S establish the run-time of the G-FFT. What follows are the nested "DO" loops that control the processing in subroutine "GLASMN".

```
      DO 130 IC = 1, C
        DO 120 IA = 1, A
          DO 110 IB = 1, B
            DO 100 JCR = 2, C
              C      ***** Inner loop calculations *****
              100      CONTINUE
              110      CONTINUE
              120      CONTINUE
              130 CONTINUE
```

In order to determine the run-time of nested "DO" loops like those shown above, we must know the time required to do the calculations in the innermost loop (TI) and the time to do the bookkeeping (TB) and minor calculations each time a loop is exercised. When TI is large compared to TB (which it is in this program), the parameters that control run-time are those that determine the number of times (K) the inner loop is cycled.

The three outer loops cycle C, A, and B times each, respectively. Unlike the outer loops (which begin with one), the inner loop begins with two. Therefore, each time it is invoked it will cycle C minus one times. The following expression gives the total number of inner loop calculations.

$$K = C * A * B * (C - 1) \quad (1)$$

What remains is to determine how A, B, and C relate to N. This is accomplished by examining the following lines from subroutine "FFT".

```

120 A = C * A
    DO 130 C = 2, B
        IF (MOD(B,C) .EQ. 0) GO TO 140
130 CONTINUE
140 B = B / C
    CALL GLASMN(A, B, C, U, WORK, INVR)
    GO TO 120

```

The process begins with A and C set to one and B set to N. The "DO" loop finds the smallest prime factor of B and places it in C. At statement 140, the newly found prime factor is removed from B. Those values (A, B, and C) are sent to the "GLASMN" subroutine where they control the number of times the inner loop is cycled. Upon returning from "GLASMN", the program does some end-of-task calculations and loops back to statement 120. This time it calculates A as the product of the prime factors of N that have thus far been processed by subroutine "GLASMN". The "DO" loop once again finds the smallest prime factor of B. The new prime is removed from B and the values are sent to subroutine "GLASMN".

With this process in mind, look now at what is actually being provided in A, B, and C at any step in the solution process. Variable C contains the newly found prime factor of B (note that a list of the C values found thus far is an ascending order list of the prime factors of N). Variable A contains the product of the previously found prime factors of N. Variable B contains the product of all of the prime factors of N that remain to be found.

$$B = N / (A * C) \quad (2)$$

Substituting eq. 2 in eq. 1 gives the expression below.

$$K = N * (C - 1) \quad (3)$$

Here we see N is one of the run-time parameters that does not change during successive calls to "GLASMN". On the other hand, C will not be the same for successive calls (unless there are repeated prime factors in N). Therefore, M values of C will be used, each of which causes the inner loop to cycle C minus one times. Consequently, the inner loop will cycle the previously mentioned sum (S) of the prime factors of N (ie, the sum of the C values) less M (since one is subtracted from C at each of the M cycles). The following equation gives an estimate of the run time (T), where Z is the computer dependent scale factor.

$$T = N * (S - M) * Z \quad (4)$$

ADJUSTING SAMPLE SIZE TO REDUCE RUN-TIME

If a minor adjustment to the sample size is allowable, then the criteria for adjusting N is to choose a value such that the sum of its prime factors is small. Conversely, the worst choice for N is a prime. It is interesting to observe that the Cooley Tukey FFT requires that N be an integral power of two. For that case the sum of the prime factors is lower and the number of factors is larger than those of any number between the next lower or higher integral power of two.

Having presented an equation for estimating run-time, we turn now to consider just how much latitude, with respect to sample size, that equation offers. In other words, just how far apart are the sample sizes that offer reasonable run-time? The answer is, quite close. To illustrate this fact, we offer the results presented in Table 1 and Table 2. Each table presents two sequences of twenty sample sizes in ascending numerical order. Each sequence starts at a different initial value (total of four, twenty point sequence). For each sample value, the table shows the number of prime factors of the sample value, the sum of those factors, and the relative speed. The relative speed is the run-time calculated for the sample size value divided by the run-time calculated for the sample size of 4096 (the twelfth power of two). By this means we illustrate the price paid in increased run-time as the chosen sample departs from the optimum value.

The starting points were selected to illustrate the reference sample (4096) in the series starting at 4090; show that series starting at 6000 and 7321 also have good sample size choices; and show the speed at the next integral power of two (8192) in the series starting at 8185.

Table 1 Relative Speed at 4090-4109 and 6000-6019 Points

<u>SAMPLE SIZE</u>	<u>PRIME NUMBER</u>	<u>FACTORS SUM</u>	<u>RELATIVE SPEED</u>	<u>SAMPLE SIZE</u>	<u>PRIME NUMBER</u>	<u>FACTORS SUM</u>	<u>RELATIVE SPEED</u>
4090	3	416	34.366	6000	8	26	2.197
4091	1	4091	340.417	6001	2	370	44.929
4092	5	49	3.663	6002	2	3003	366.455
4093	1	4093	340.750	6003	4	58	6.595
4094	3	114	9.245	6004	4	102	11.971
4095	5	31	2.166	6005	2	1206	147.095
4096	12	24	1.000	6006	5	36	3.788
4097	2	258	21.339	6007	1	6007	734.010
4098	3	688	57.111	6008	4	757	92.042
4099	1	4099	341.750	6009	2	2006	244.996
4100	5	55	4.171	6010	3	608	73.976
4101	2	1370	114.139	6011	1	6011	734.988
4102	3	302	24.953	6012	5	177	21.038
4103	2	384	31.888	6013	2	866	105.697
4104	7	34	2.254	6014	3	130	15.539
4105	2	826	68.818	6015	3	409	49.684
4106	2	2055	171.501	6016	8	61	6.487
4107	3	77	6.183	6017	2	558	68.063
4108	4	96	7.689	6018	4	81	9.428
4109	2	594	49.490	6019	2	476	58.045

Note the occurrence of one or more prime numbers (number of factors is one) in each of the twenty point sequences. Some may be surprised at how frequently primes occur. This illustrates the high likelihood of making a bad choice for the sample size and the rather minor adjustment needed to make a good choice. Just what constitutes a good choice depends on the application. If fast run-time is vital, then the choices are restricted to sample sizes giving relative speeds less than ten. If the time window is critical, then a shift of three or four points causes only a very small change in the window and avoids a ten to one-hundred fold increase in run time.

Table 2 Relative Speed at 7321-7340 and 8185-8204 Points

SAMPLE SIZE	PRIME FACTORS NUMBER	RELATIVE SPEED	SAMPLE SIZE	PRIME FACTORS NUMBER	RELATIVE SPEED
7321	1	1090.286	8185	2	273.100
7322	3	78.803	8186	2	681.667
7323	2	363.826	8187	2	454.722
7324	3	272.981	8188	4	18.658
7325	3	44.708	8189	2	74.639
7326	5	7.601	8190	6	4.499
7327	2	66.484	8191	1	1364.833
7328	6	34.738	8192	13	2.167
7329	3	53.083	8193	2	455.389
7330	3	109.908	8194	3	42.844
7331	1	1093.266	8195	3	27.010
7332	5	9.249	8196	4	114.389
7333	1	1093.863	8197	2	196.120
7334	3	31.483	8198	2	683.667
7335	4	25.369	8199	3	152.464
7336	5	20.746	8200	6	8.508
7337	3	8.956	8201	2	32.703
7338	3	182.883	8202	3	228.445
7339	2	32.550	8203	2	107.144
7340	4	55.552	8204	4	50.073

CALCULATING THE RUN-TIME ESTIMATE

A subroutine to calculate the number and sum of the prime factors along with the run-time estimate is presented in Table 3. A lot of advanced work is being done on procedures for calculating prime factors of large numbers. For this application, a simple procedure is presented in Table 4 for finding the prime factors of values less than 44,521.

Table 3 Calculating the Run-Time Estimate

```

SUBROUTINE SUMPF(N, ISUM, NF, RTE)
C SUM (ISUM) THE PRIME FACTORS OF THE NUMBER (N), COUNT
C THE NUMBER OF SUCH FACTORS (NF) AND CALC THE RUN-TIME
C ESTIMATE (RTE). JAY CHEEK, SAG, SMD, SL, WES, 7 APR. 1988
C
  LOGICAL ENDFTR
C
  ISUM = 0
  NF = 0
  CALL SETNUM(N)
100 CALL PRIMEF(IPF, ENDFTR)
  ISUM = IPF + ISUM
  NF = NF + 1
C QUIT IF ALL PRIME FACTORS HAVE BEEN FOUND)
  IF (.NOT. ENDFTR) GO TO 100
  RTE = N * (ISUM - NF)
  RETURN
END

```


Table 4 Calculating Prime Factors of a Small Number

```

SUBROUTINE PRIMEF(IPF, ENDF)
C FIND THE NEXT PRIME FACTOR OF NN.
C JAY CHEEK, SMD, SL, WES, FEB 1981, JAN 1983, JULY 1988
C
      DIMENSION IPRIME(46)
      LOGICAL ENDF, NP
      DATA IPRIME/2, 3, 5, 7, 11, 13, 17, 19, 23, 29, 31, 37,
&      41, 43, 47, 53, 59, 61, 67, 71, 73, 79, 83, 89, 97,
&      101, 103, 107, 109, 113, 127, 131, 137, 139, 149, 151,
&      157, 163, 167, 173, 179, 181, 191, 193, 197, 199/,
&      MAXN/44520/, NP/.TRUE./
C
C ERROR IF NUMBER TO FACTOR HAS NOT BEEN SET
      IF (NP) STOP 'PRIMEF: NO NUMBER TO FACTOR'
C LOOK FOR THE NEXT PRIME FACTOR.
100 IPF = IPRIME(I)
      LQ = NN / IPF
      LR = NN - LQ * IPF
C IPF IS A FACTOR IF THE REMAINDER (LR) IS ZERO
      IF (LR .EQ. 0) GO TO 110
      I = I + 1
      IF (LQ .GT. IPF) GO TO 100
C THE INITIAL NUMBER IS A PRIME
      IPF = NN
110 NN = NN / IPF
      IF (NN .EQ. 1) NP = .TRUE.
      ENDF = NP
      RETURN
C
C SET THE NUMBER TO FACTOR
      ENTRY SETNUM(IPF)
      NN = IPF
C TEST FOR IPF WITHIN RANGE OF THIS ROUTINE.
      IF (NN .GT. MAXN .OR. NN .LE. 1)
&      STOP 'SETNUM: NUMBER OUT OF RANGE'
      NP = .FALSE.
      I = 1
      RETURN
      END

```

ACKNOWLEDGMENTS

This work was done in support of the data processing and analysis work of the Structural Mechanics Division (SMD), Structures Laboratory, Waterways Experiment Station. Permission was granted by the Chief of Engineers to publish this information. The author wishes to express his appreciation for the support provided by the staff of the Structural Analysis Group of the SMD. This work was completed largely because of their encouragement and able assistance. It is my high pleasure to work with this fine group of engineers

SHOCK SPECTRUM FOR CLASSES OF EXCITATIONS

Walter D. Pilkey
Department of Mechanical & Aerospace Engineering
University of Virginia
Charlottesville, VA 22901

Moshe Rosenstein
Engineering Mechanics Staff
Rafael, P.O. Box 2250
Haifa, Israel

A method is presented by which the least and most favorable shock spectra can be estimated for incompletely prescribed input. Such bounds on spectra are useful in assessing shock severity. The method is based on a game theory formulation and utilizes linear programming for numerical results. A comparison with theory is provided.

INTRODUCTION

The problem of determining the peak response of linear structures subject to deterministically characterized, incompletely defined input has been considered only rarely in the past e., [1-5]. The present work addresses the problem of computing the shock response spectra when the input is not fully prescribed.

The goal of this effort is to provide a procedure for estimating the maximum and the least favorable possible shock spectra for an excitation function which is deterministic, but not completely defined. These spectra are useful in assessing shock severity and potential damage.

Several methods are available for calculating the shock response spectrum for prescribed excitations [6,7]. Numerical calculations are normally employed for general input functions. To deal with input functions that are not fully prescribed, a linear programming technique is utilized here.

The upper and lower bounds on the shock spectra for classes of excitations are a useful tool for two reasons:

1. For the test engineer to use when judging the potential severity of the uncertainty of the environment that hardware may encounter during a mission profile.
2. For designers in estimating the most severe cases for stress-strength considerations.

LINEAR PROGRAMMING FORMULATION

Suppose the class of inputs, shown in Fig. 1, with nothing being said about the probability of occurrence, can be represented by

$$f_j^L < f_j < f_j^U \quad j = 1, 2, 3, \dots, J \quad (1)$$

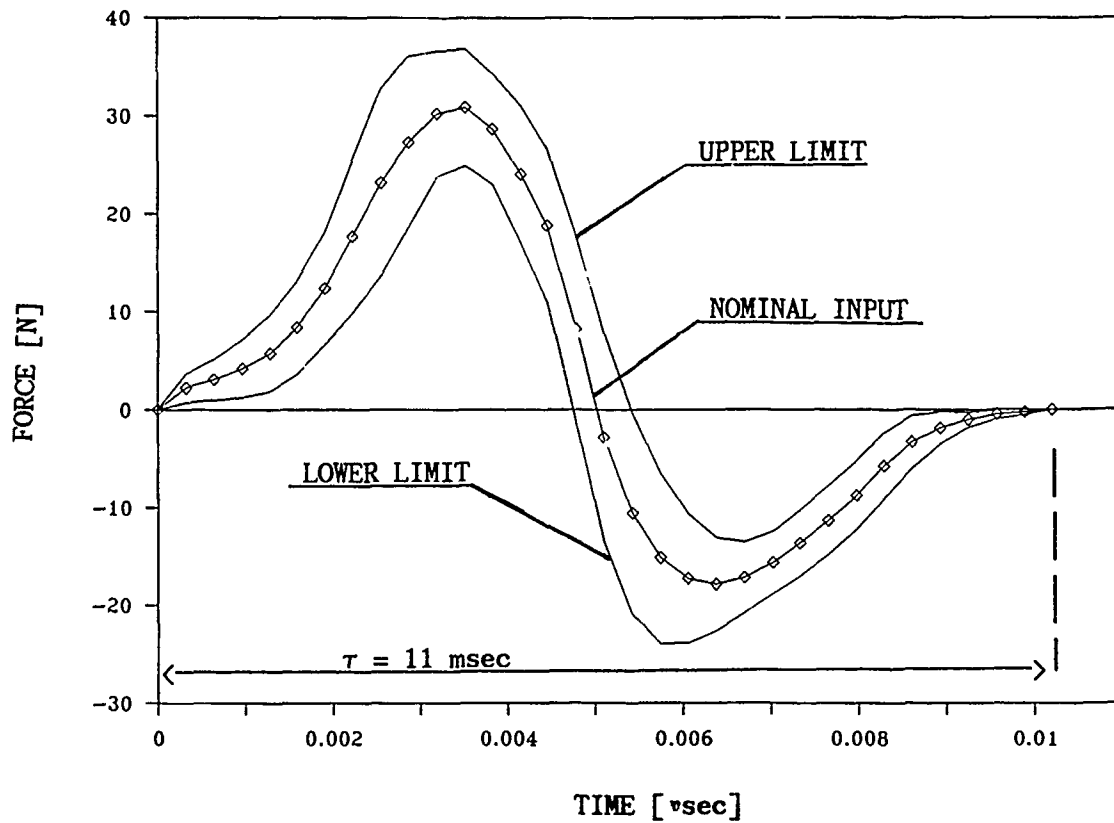


Figure 1: Incompletely prescribed input

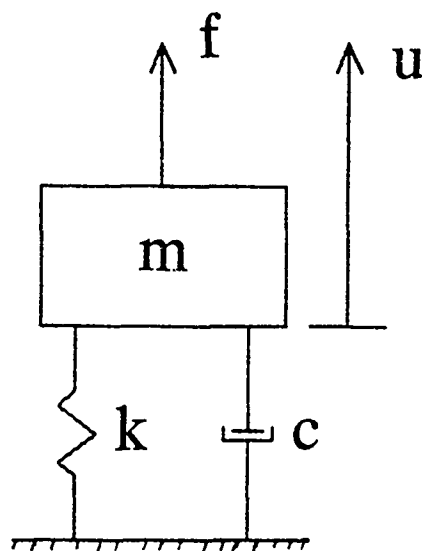


Figure 2: Simple mechanical oscillator

where j is the time value, f is the applied force (excitation), f^L is the lower bound (lower envelope) of the excitation, and f^U is the upper bound of the excitation.

The task is to find a single-valued excitation function f_j , $j = 1, 2, 3, \dots, J$ within these limits that maximizes (worst disturbance), or minimizes (best disturbance), a peak response such as acceleration, velocity, or displacement of a single-degree-of-freedom (SDOF) system (Fig. 2). The governing equation of the SDOF system is

$$\ddot{u} + 2\zeta\omega_n \dot{u} + \omega_n^2 u = f/m \quad (2)$$

where $\omega_n = \sqrt{k/m}$ is the natural frequency, $\zeta = c/2\omega_n$ is the damping ratio, u is the displacement, and m is the oscillator mass

Rewrite Equation (2) in matrix notation as a set of two equations of first order

$$\dot{\underline{u}} = [A] \underline{u} + [B] \underline{f} \quad (3)$$

where $\underline{u}(t)$ is a two-dimensional state vector, and $[A]$ and $[B]$ are constant coefficient matrices represented by

$$[A] = \begin{bmatrix} 0 & 1 \\ -k/m & -c/m \end{bmatrix}$$

$$[B] = \begin{bmatrix} 0 \\ 1/m \end{bmatrix}$$

The solution of Equation (3) in a piecewise constant interval is

$$\underline{u}(t_{j+1}) = [G] \underline{u}(t_j) + [H] [B] \underline{f}(t_j) \quad j = 1, 2, \dots, J \quad (4)$$

where $[G] = e^{[A]\Delta t}$, $[H] = \int_0^{\Delta t} e^{[A](\Delta t - \tau)} d\tau$, and Δt is the time step.

Equation (4) provides the response of the oscillator as a linear function of the excitation.

Worst Case

The worst disturbance analysis is to find

$$\phi_m = \max_{f_j} \max_{t_j} u(t_j) \quad j = 1, 2, \dots, J \quad (5)$$

and the corresponding f_j that satisfies constraints of the type given in Equation (1). The function f_j that generates ϕ_m can be found by maximizing $u(t_j)$ at several

time points (t_i) in the interval $0 < t_i < T$, where T may be greater than t_j . The maximum of these peaks $u(t_i)$ is then the maximum possible $u(t_m)$, where t_m is that t_i when the peak response occurs. In the case of a linear SDOF this is a simple linear programming problem, since the objective function (displacement, velocity or acceleration) is linear in the loading.

Linear programming codes are standard items in many scientific software libraries.

Best Case

The best disturbance is a game theory problem of finding

$$\min_{f_j} \max_{t_j} u(t_j) \quad j = 1, 2, \dots, J \quad (6)$$

and the corresponding excitation function f_j that satisfies Equation (1).

The min-max formulation is somewhat complicated. References [1-3] provide a review of the problem. Define ϕ such that

$$\phi = \max u(t_j) \quad j = 1, 2, \dots, J \quad (7)$$

or equivalently

$$|u(t_j)| < \phi \quad j = 1, 2, \dots, J \quad (8)$$

Then the mathematical programming statement of the problem becomes:

Find f_j , subject to prescribed constraints (1), such that ϕ is minimized and $|u(t_j)| < \phi$ for $j = 1, 2, \dots, J$

As in the max-max case, the problem is linear because the response $u(t_j)$ can be computed as a linear function of the loading f_j (Equation 4). The objective function ϕ of Equation (7) is entered into the constraint set as

$$\begin{aligned} -\phi + u(t_j) &< 0 \\ -\phi - u(t_j) &< 0 \end{aligned} \quad (9)$$

and ϕ becomes the $(J+1)^{\text{th}}$ unknown, with J unknowns f_j .

SHOCK RESPONSE SPECTRUM

The traditional shock spectrum is defined as the maximum response of a linear second order system to a shock excitation, recorded as a function of the natural frequency of the system. The shock response spectrum for incompletely prescribed input is defined in the same way, i.e., the spectrum consists of all maximum responses for a linear SDOF. However, for each frequency, responses corresponding to the min-max and max-max excitations are obtained.

Figure 1 shows the upper and lower bounds for a particular permissible force. Figures 3 and 4 compare the force trajectories (worst disturbance) associated with two diverse frequencies for the max-max problem. Figure 3 presents results for a relatively high frequency, for which $\tau/T = 3.5$, where T is the period of the responding system and τ is the input duration (Fig. 1). Figure 4 shows a typical response for a lower frequency ($\tau/T = 0.3$). The force trajectory results for low and high frequency are quite different. For the low frequency case the trajectory follows reasonably close to the bounds; for the high frequency case the trajectory moves often between the upper and the lower bounds with a frequency that is related to the natural frequency of the resonator.

The response in the low frequency case does not vary significantly from the nominal (Fig. 5). However the response in the high frequency range does vary from the nominal. This behavior is to be expected as the system becomes stiffer.

Figures 6 and 7 show similar results for the high and low frequencies for the min-max problem. It is interesting to note that in the max-max problem for the low frequency case the force trajectory moves first on the lower bound and then switches to follow the upper bound, while in the min-max case it starts with the upper bound and later changes to the lower bound.

The shock response spectrum (acceleration) for the input of Fig. 1 is given in Fig. 7. The central curve is the traditional shock spectrum belonging to the nominal force function $\{(f^U + f^L)/2\}$. A plot of the percentage divergence from the nominal spectrum (Equation 10) is given in Fig. 8.

$$S / S_{\text{nominal}} - 1 \quad (10)$$

where S is the shock spectra of the max-max or min-max problem, and S_{nominal} is the nominal shock spectra.

Figure 9 shows the peak excitation ratios, i.e., the value of the input peak in the max-max to the peak input of the nominal function.

It is of interest to multiply the max-max (min-max) spectrum for each frequency with the force ratio associated with that frequency

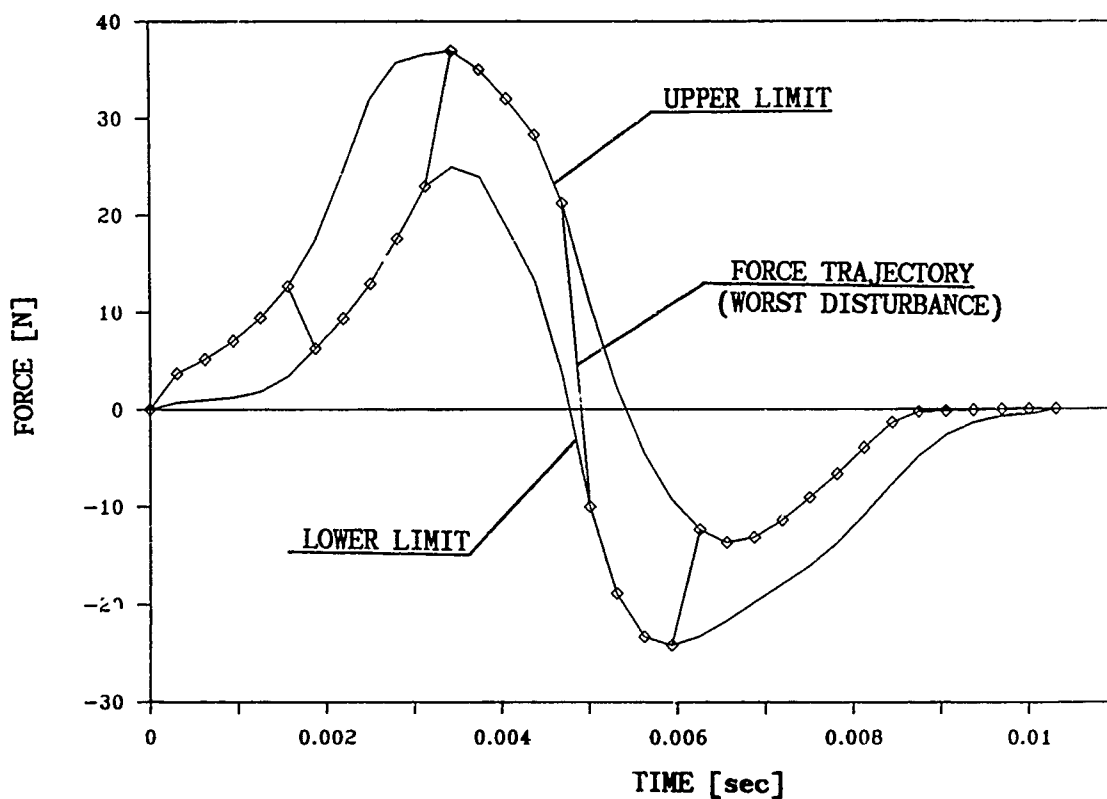
$$[S/S_{\text{nominal}}][f_{\text{peak}}^n / f_{\text{peak}}] - 1 \quad (11)$$

where f_{peak}^n is the peak input associated with the nominal force and f_{peak} is the peak input in the max-max or min-max case.

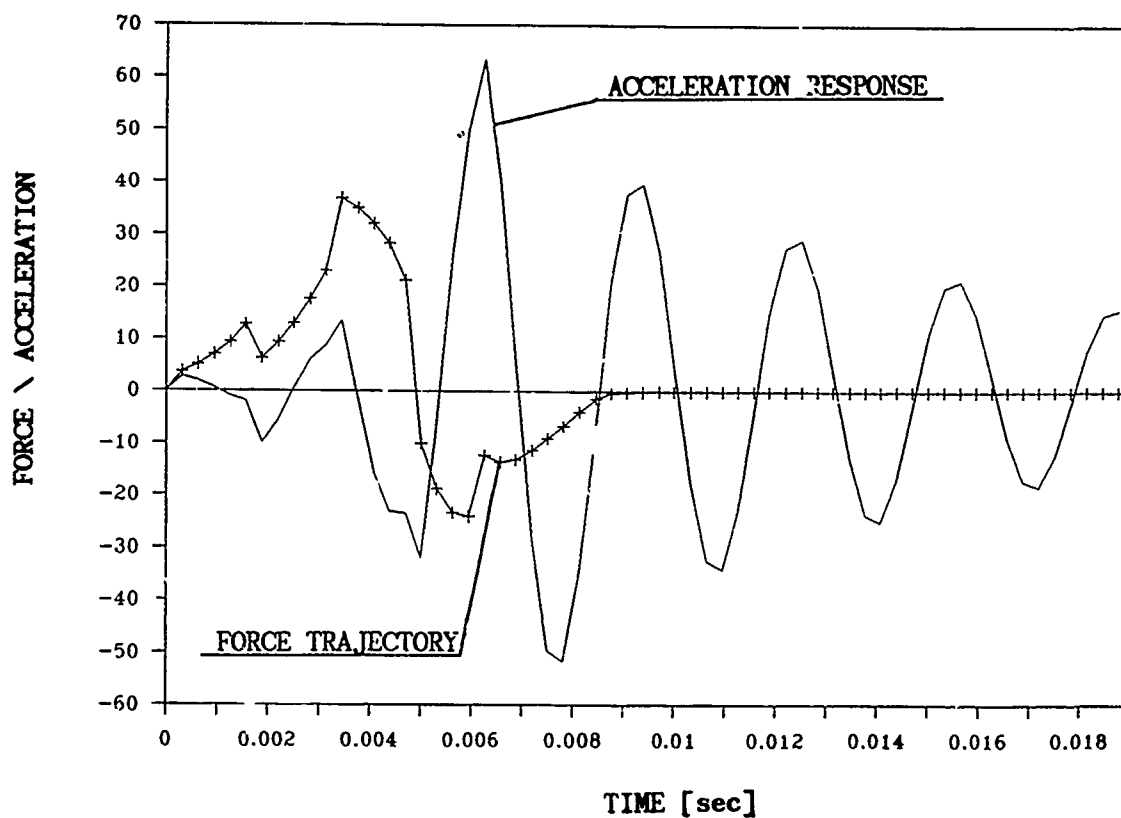
Figure 10 shows the normalized amplification spectra (Equation 11) which is due to the incompletely prescribed input. Note that in the region $\tau/T > 3$ the amplification reaches 100-500 %.

THEORETICAL VERIFICATION FOR THE MAX-MAX PROBLEM

Reference [4] developed a theoretical approach to estimate the peak resonator response, equivalent to a simple version of the max-max problem presented here, for a class of excitations defined by a "mirror image" about the time axis definition of a particular excitation force. The approach is based on an impulse response of an oscillator, convoluted with the input function while using Schwarz's inequality. The results of this reference verify a special case of the max-max problem of this paper. Figure 11 shows results in the time domain for fixed frequency $\tau/T = 3.5$, while Figure 12 compares the shock spectra resulting from the theoretical and the linear programming approaches.

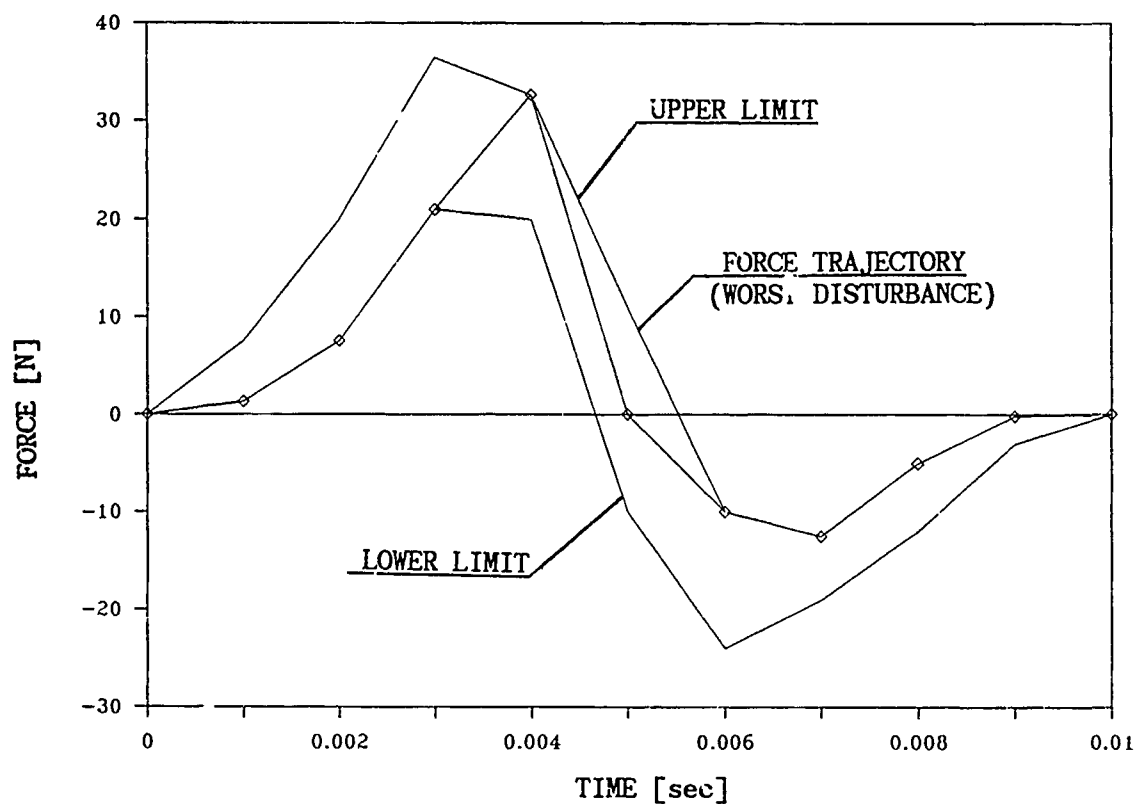


a: Force trajectory and the permissible limits

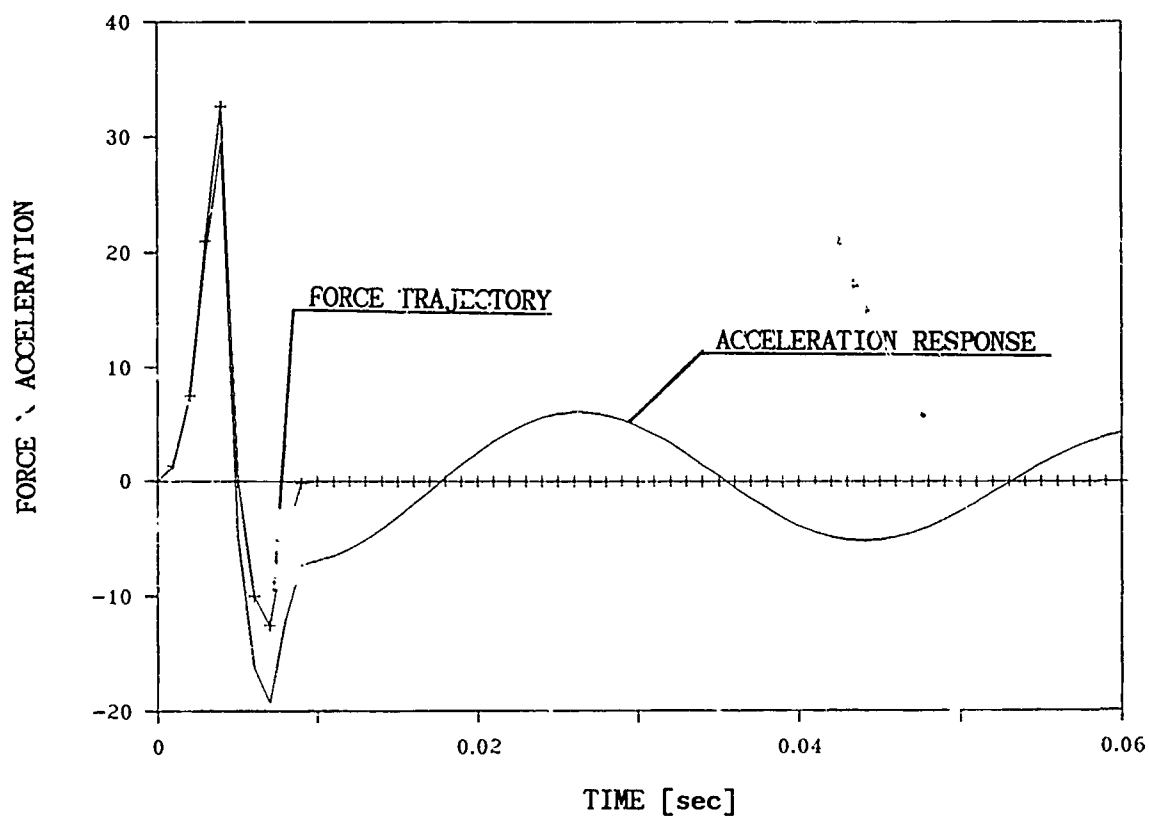


b: Force and acceleration response (max-max problem)

Figure 3: Worst disturbance (high frequency 320 Hz $\tau/T = 3.53$)

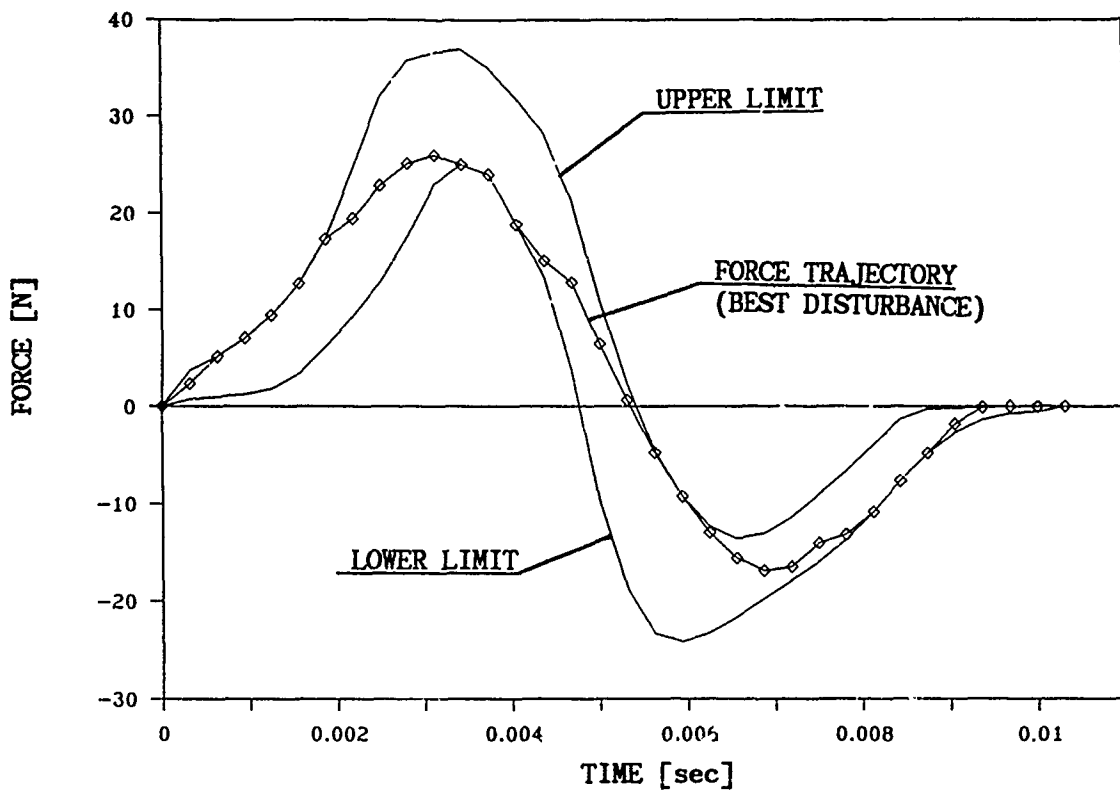


a: Force trajectory and the permissible limits

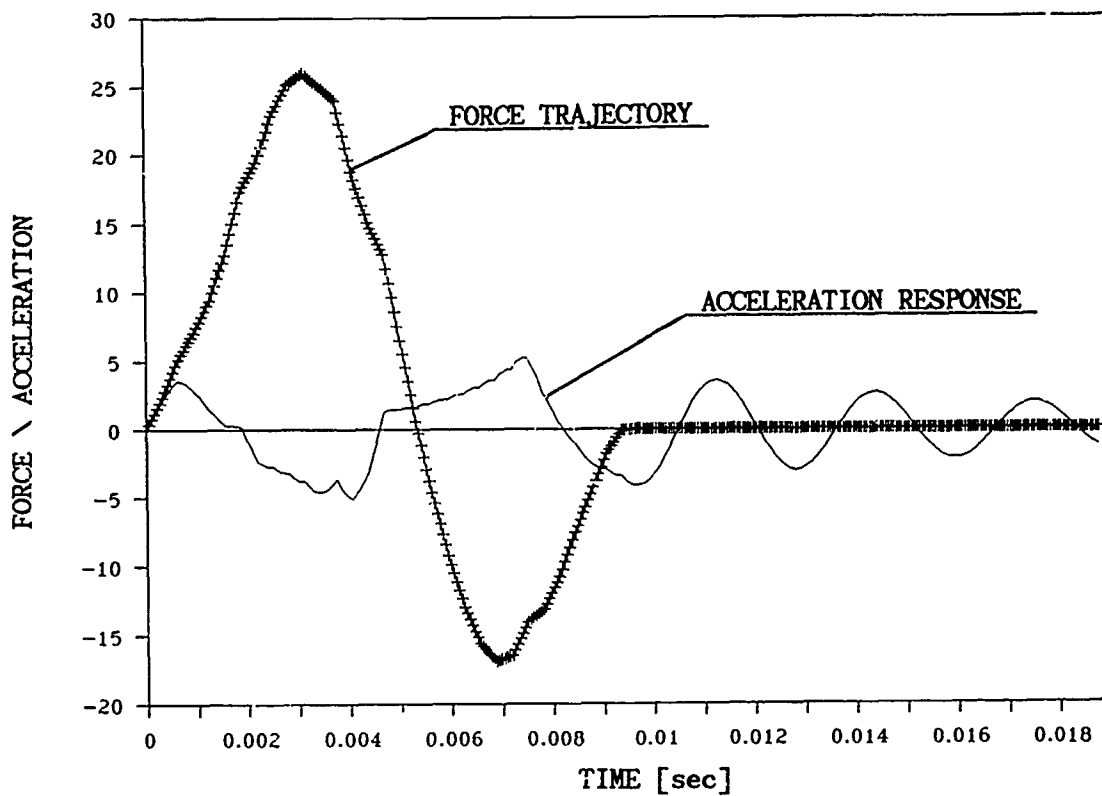


b: Force and Acceleration response (max-max problem)

Figure 4: Worst disturbance (low frequency 28 Hz $\tau/T = 0.31$)

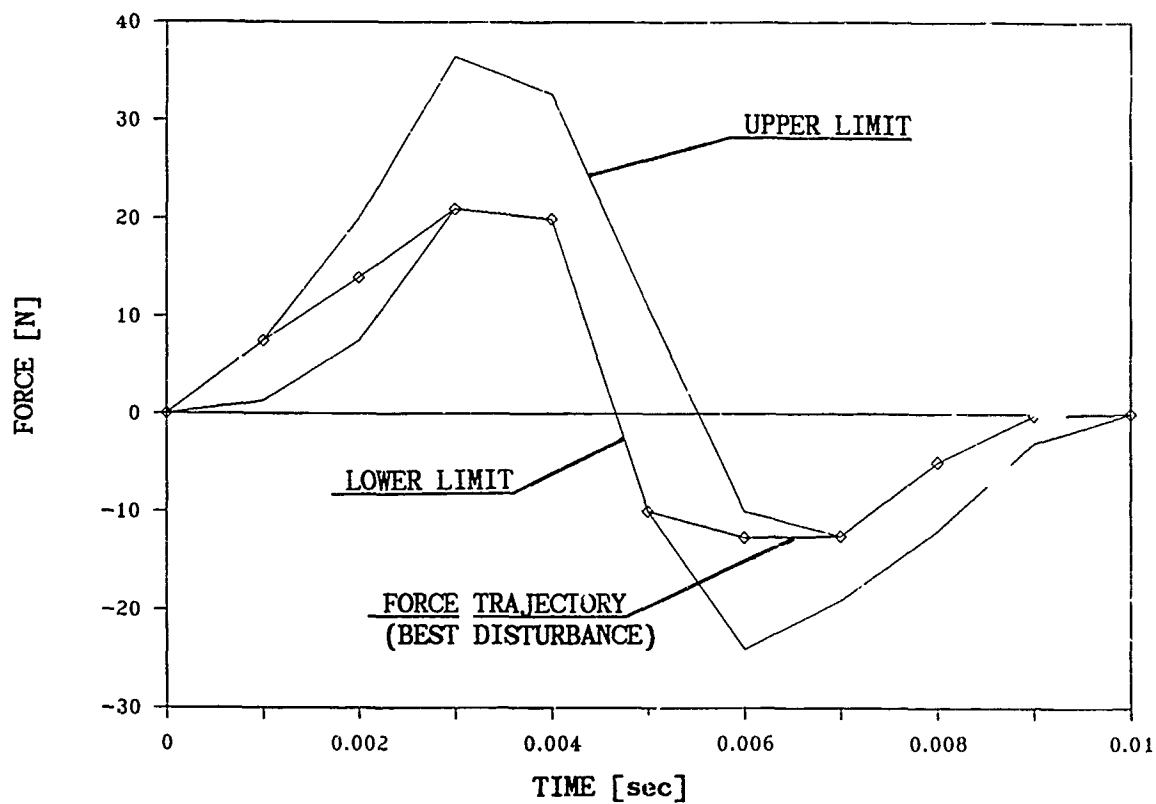


a: Force trajectory and the permissible limits

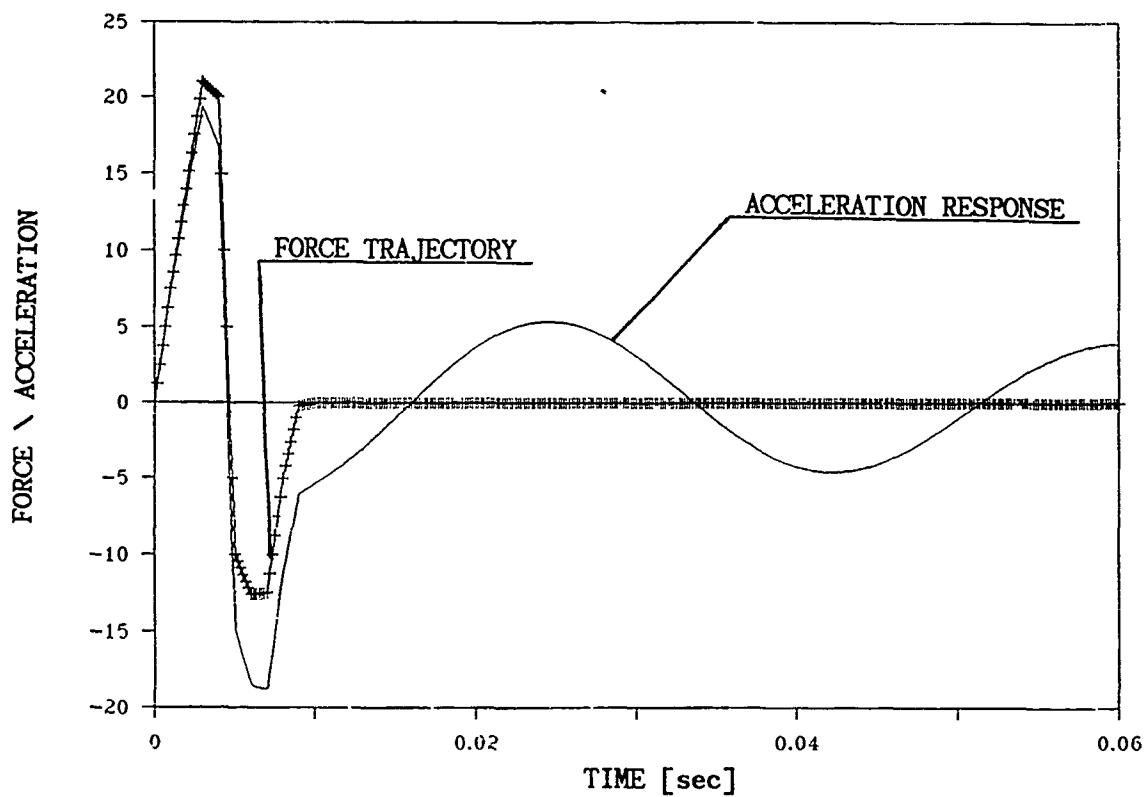


b: Force and acceleration response (min-max problem)

Figure 5: Best disturbance (high frequency 320 Hz $\tau/T = .53$)



a: Force trajectory (min-max problem)



b: Force and acceleration response (min-max problem)

Figure 6: Best disturbance (low frequency 28 Hz $\tau/T = 0.31$)

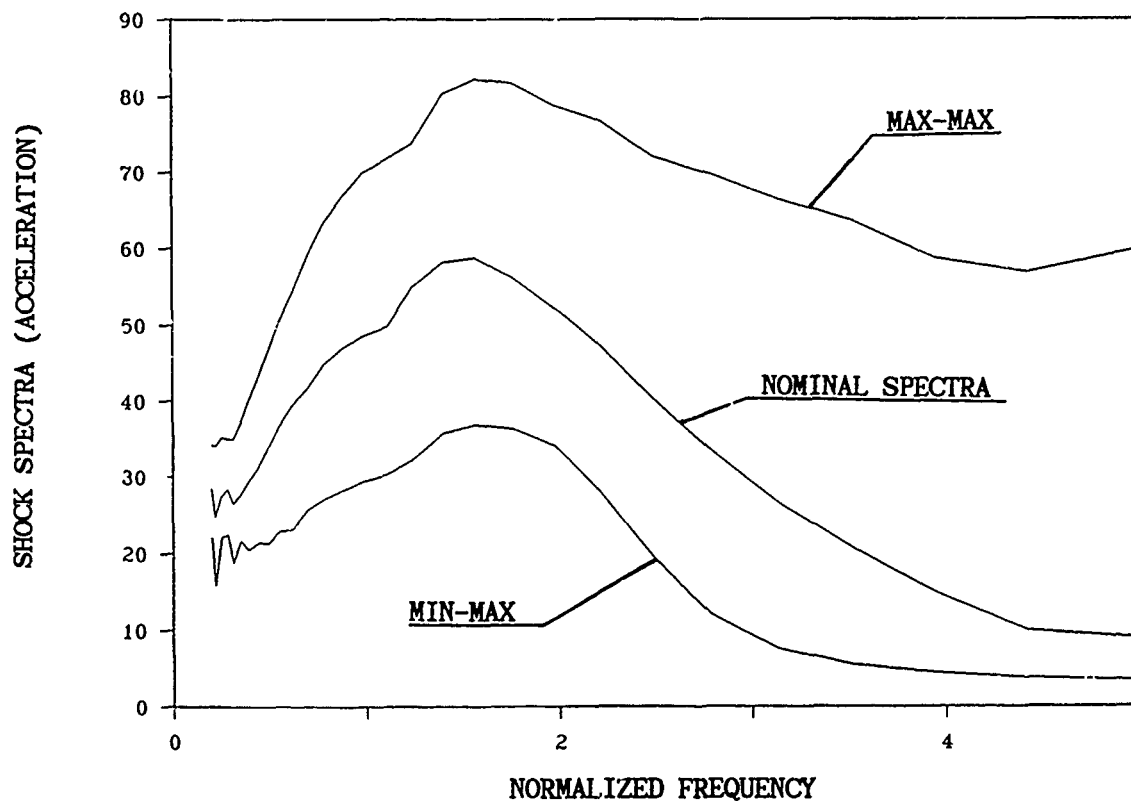


Figure 7: Shock response spectrum for the input in Fig 1

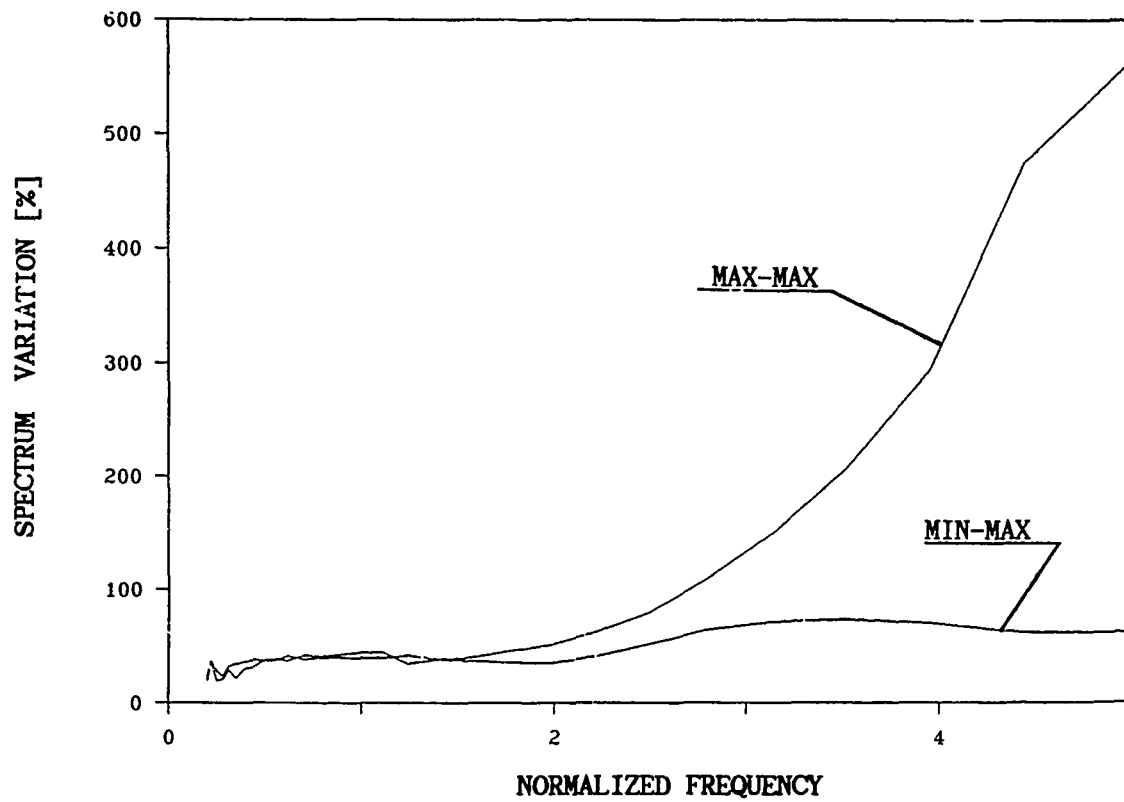


Figure 8: Variation from the nominal shock response spectrum

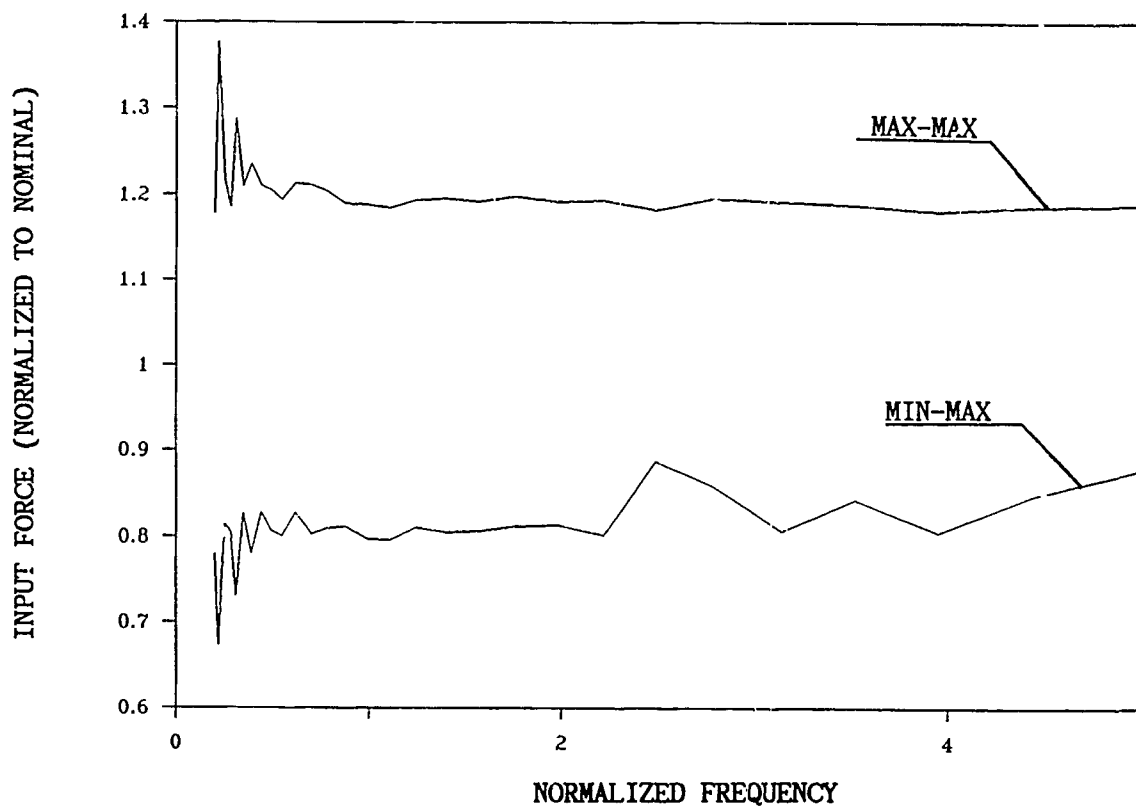


Figure 9: Normalized input amplification spectra

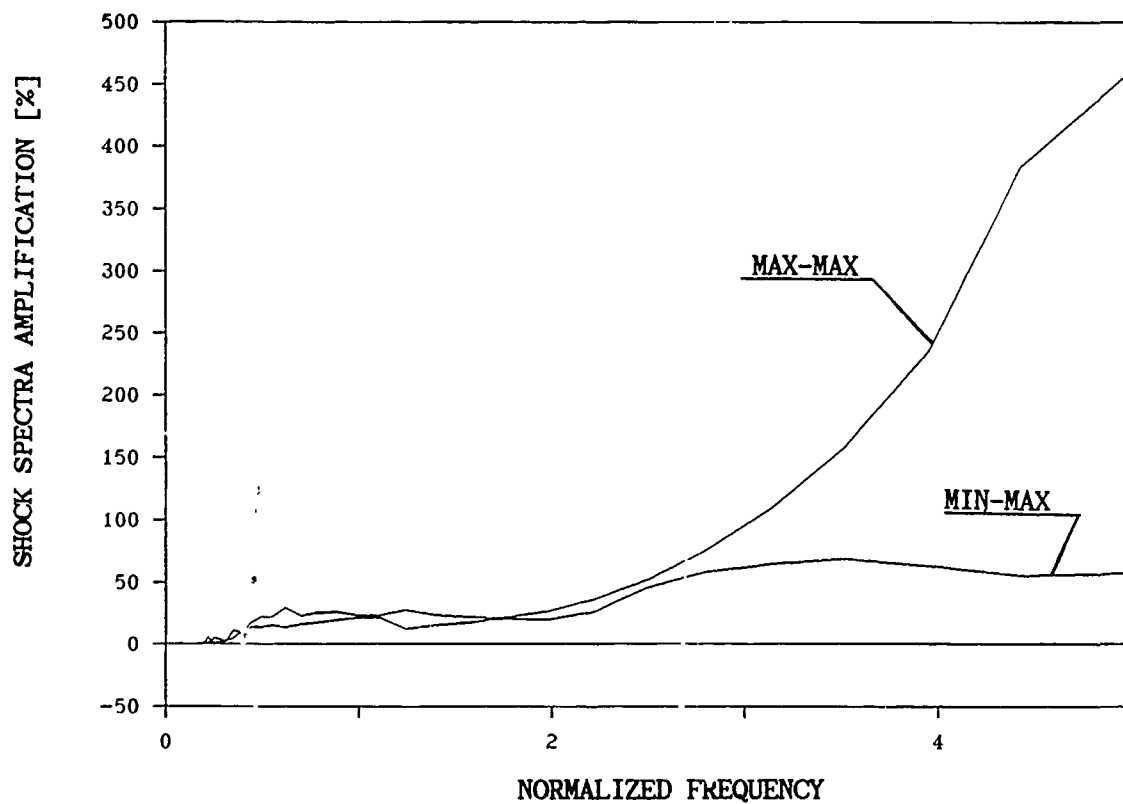
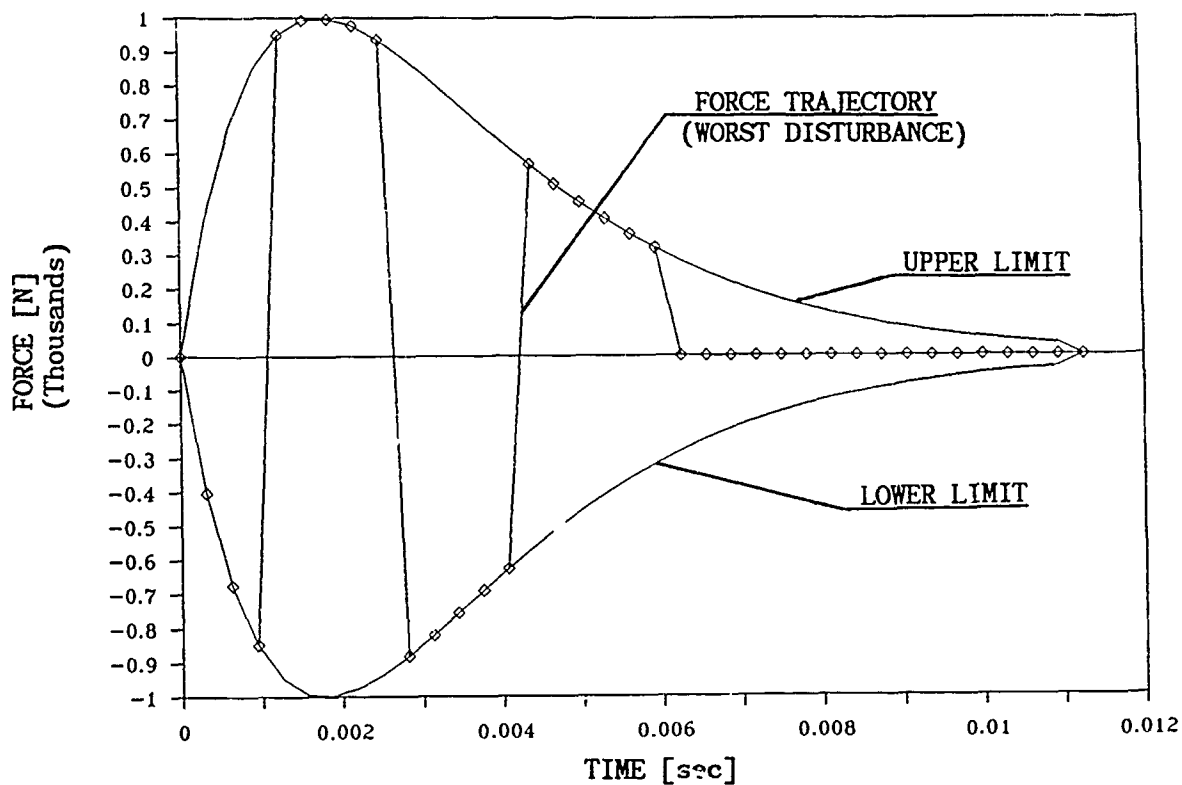
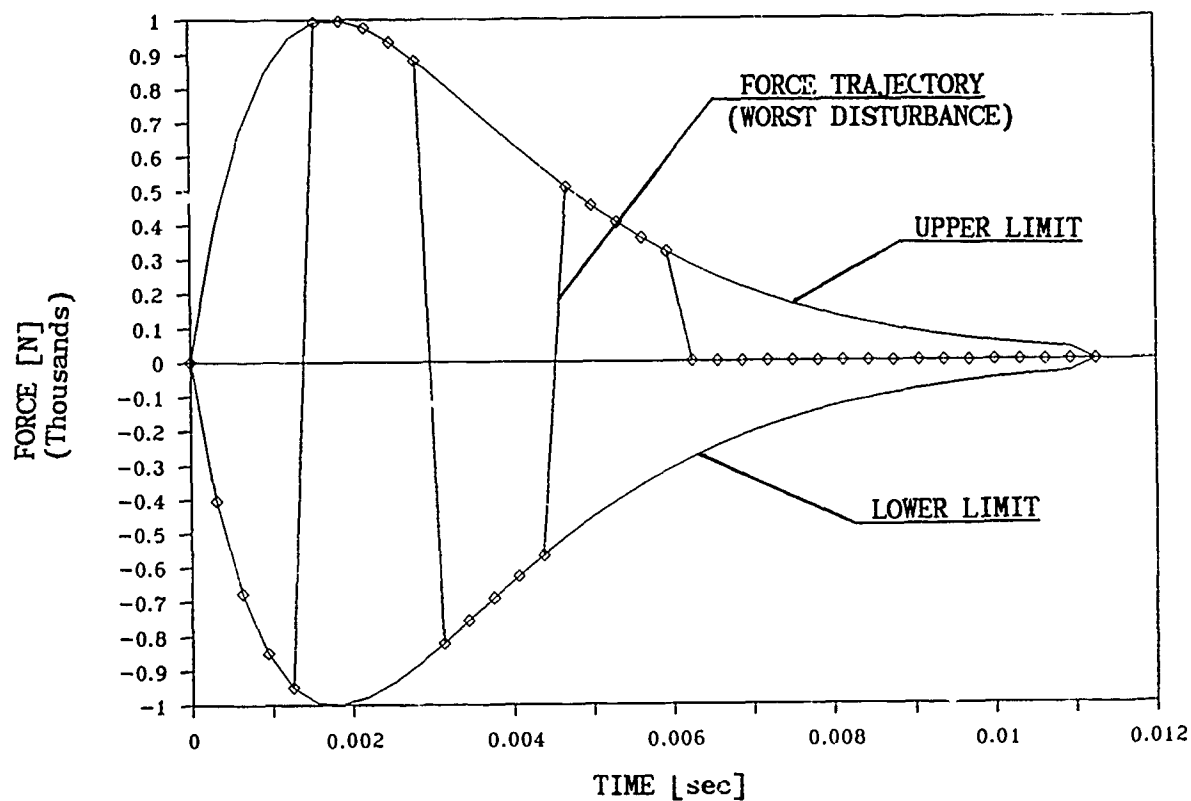


Figure 10: Normalized response amplification shock spectra



a: Theoretical worst disturbance



b: Linear Programming generated worst disturbance

Figure 11: Worst disturbance trajectory comparison

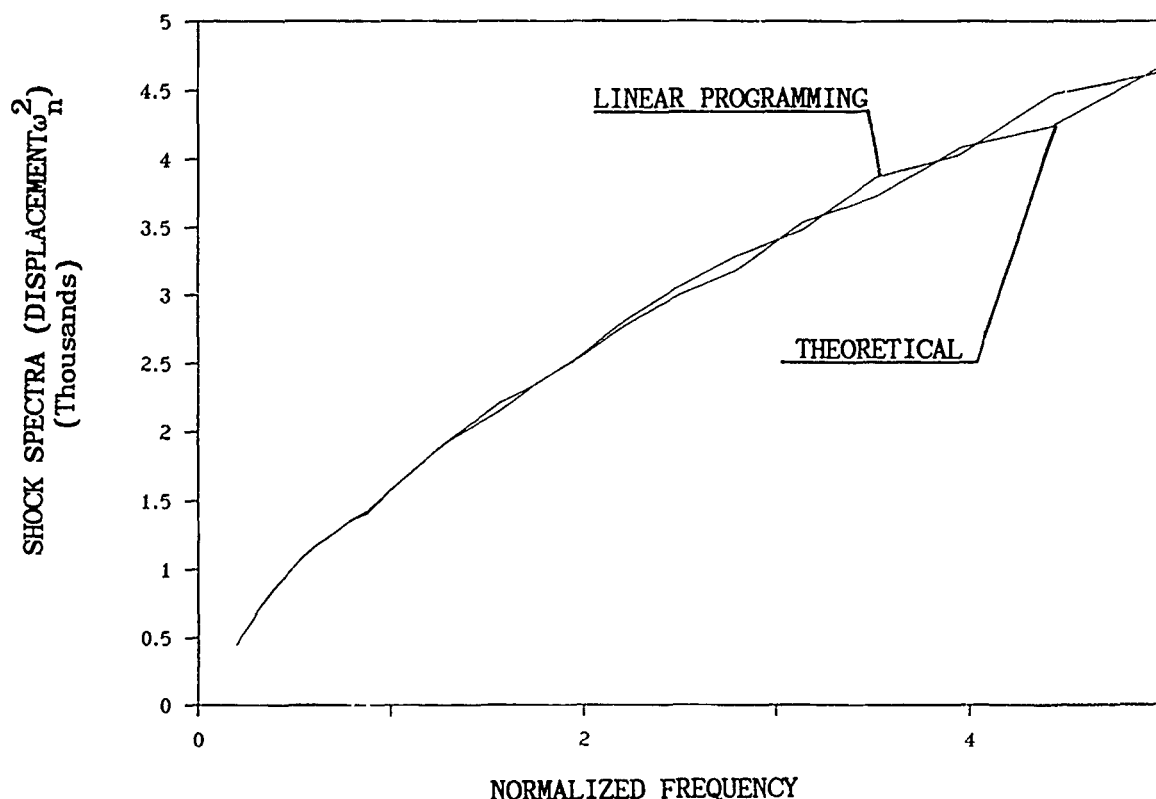


Figure 12: Shock response spectra for the input in Fig. 11

CONCLUSION

A method is presented by which the least and most favorable shock spectra can be estimated for incompletely prescribed input. This method should be of interest to engineers confronted with shock spectra problems for classes of input, as the technique developed here is quite general in terms of the permissible classes of excitation, yet is rather simple to implement.

REFERENCES

1. W. D. Pilkey and A. J. Kalinowski, "Response Bounds for Structures with Incompletely Prescribed Loading," The Shock and Vibration Bull., 1972, Vol. 43, pp. 31-42.
2. A. J. Kalinowski and W. D. Pilkey, "Design for Incompletely Prescribed Loading," ASCE J. of Engineering Mechanics, 1975, Vol. 101, pp.505-510.
3. E. Sevin and W. Pilkey, "Optimum Shock and Vibration Isolation.," 1971, The Shock and Vibration Information, Washington, D.C.
4. Jann-Nan Yang and E. Heer, "Maximum Dynamic Response and Testing.," ASCE J. of Engineering Mechanics, 1971, Vol. 97, pp.1307-1313.
5. G.J. O'Hara, "Maximization and Minimization of Dynamic Load Factors.," The Shock and Vibration Bull., 1973, Vol. 43, pp. 119-127.
6. C.M. Harris and C E. Crede, Shock and Vibration Handbook, 1973, McGraw Hill, New York.
7. R. D. Kelly and G. Richman, Principles Techniques of Shock Data Analysis, 1970. The Shock and Vibration Information Center, Washington, D.C.

A TECHNICAL PROCEDURE FOR THE OPTIMUM SHOCK HARDENING OF AIRCRAFT SUPPORT EQUIPMENT

**LCDR W. R. Lauderdale, Naval Air Systems Command
D. Croce, Naval Air Engineering Center
B. C. McNight, NKF Engineering, Inc.**

This paper details the formulation and implementation of a support equipment (SE) shock hardening project directed by NAVAIR and COMNAVAIRLANT. The project utilized the shock trials of the USS THEODORE ROOSEVELT (CVN-71) for validation of the SE shock protection systems designed. The shock trials also offered the opportunity to acquire an extensive data base of SE mechanical shock response, electrical power monitoring, and equipment performance data. These data bases were collected to formulate specific survivability specifications for the procurement of future fleet SE.

BACKGROUND

The support equipment list of a CV Aircraft Intermediate Maintenance Department (AIMD) contains a large number of Grade A (combat essential) equipments. The preponderance of these Grade A equipments is in the area of automatic test equipment (ATE). These equipments provide testing, and repair monitoring of a myriad of aircraft avionics systems such as navigation, electronic warfare (EW), weapons delivery, anti-submarine weapons (ASW), communication, IFF, radar, and the Automatic Carrier Landing System (ACLS). An example (in this case an S3 ASW aircraft) is provided in Figure 1. Typical ATE is expensive, semi-fragile, state-of-the-art commercial grade equipment. As an example, the cost of outfitting a typical CVN-68 class AIMD is in the neighborhood of 771 million dollars.

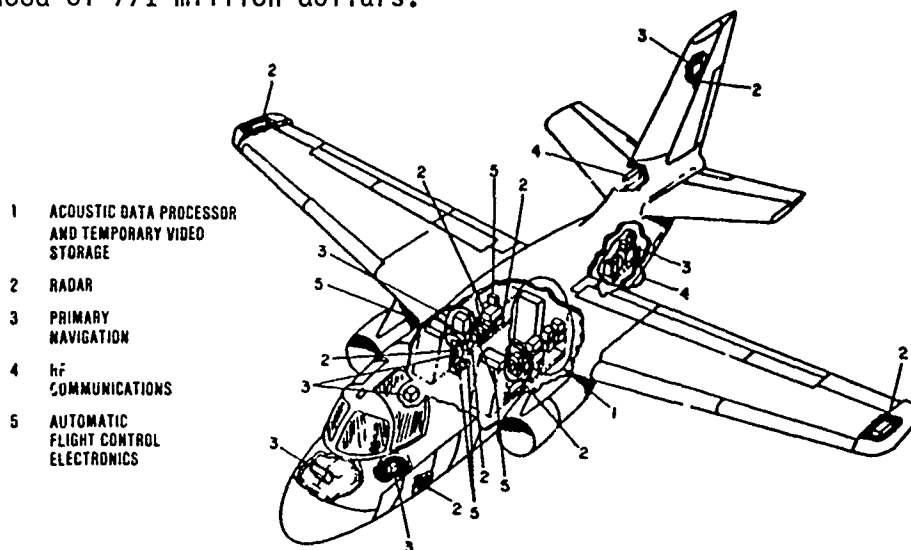


Figure 1. Typical Carrier Aircraft Avionics Supported by ATE

Since the Navy acquisition policy of the AIMD ATE preceeded the designation of it as Grade A, historically no shock specifications were included in the procurement process.

Shock tests against two aircraft carriers [USS FORRESTAL (CV-59) and USS JOHN F. KENNEDY (CV-67)] were conducted without particular attention to AIMD aviation support equipment survivability due to the austerity of these "learning," less than full intensity tests. Most AIMD equipments for those tests, especially avionics ATE benches and EA6B VANS, were off-loaded and/or cross-decked to other vessels in order to meet operational commitments. Consequently, there was a limited amount of existing data regarding functional/operational reaction of AIMD equipment to shipboard high shock levels. But with the planning of the shock trials of the USS THEODORE ROOSEVELT (CVN-71) and the institution of a specific SE shock policy the "AIMD Shock Hardening Project" was commissioned.

THE NAVY SE SHOCK HARDENING GOALS

The new Navy SE shock hardening direction was simple and direct.

- o Insure the shock survivability of all CVN-71 Grade A and selected Grade B SE in the most timely and cost-efficient manner.
- o Provide realistic shock specifications for the acquisition of future SE.

THE TECHNICAL PROCEDURE

The technical procedure evolved to accomplish the two basic Navy SE shock hardening goals forms the first part of this paper. Essentially the procedure was divided into three major elements.

- o Projection of the CV shock environment.
- o Evaluation of the selected AIMD SE.
- o Implementation of shock mounting designs for fragile equipments.

The "test-bed" for implementation of the SE shock hardening procedure was the shock trials of the USS THEODORE ROOSEVELT (CVN-71) in September of 1987.

Projection

The Projection of the CVN-71 environment was from analysis of the USS KENNEDY (CV-67) shock trials data (reference 1). Figure 2 shows the AIMD work centers of the CVN-71.

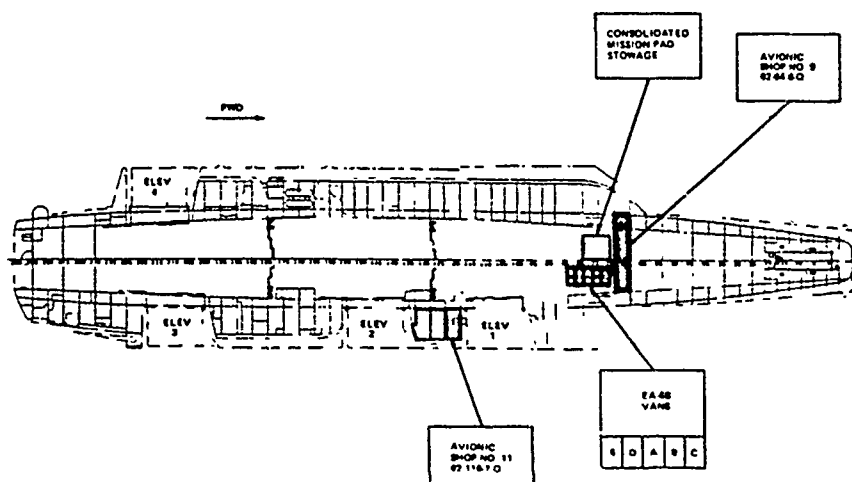
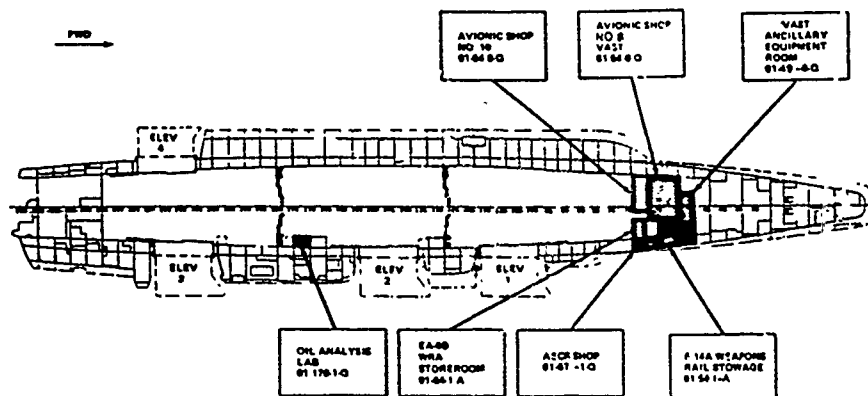
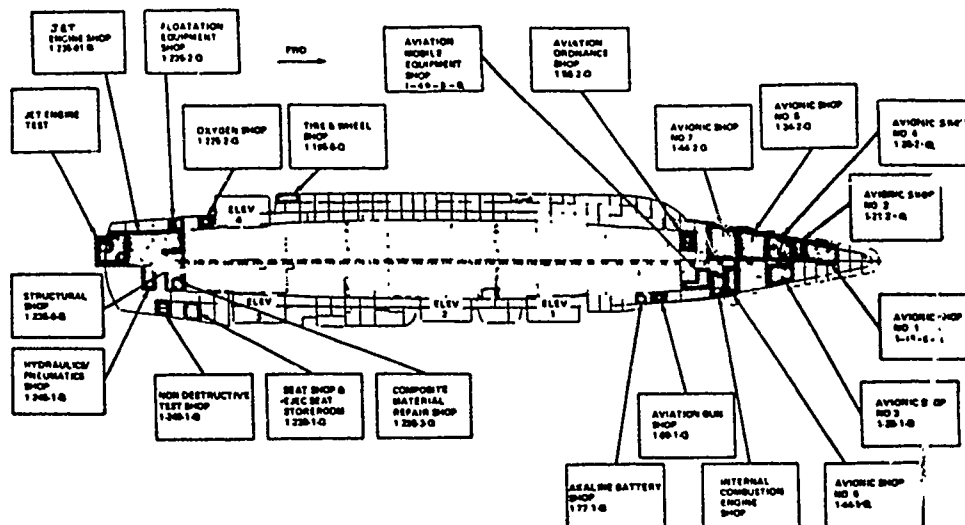


Figure 2. AIMD Work Centers

The objectives of this phase were 1) to review and expand upon the CV-67 shock test data base, and 2) to present the shock environment data predicted for the CVN-71 grade A AIMD equipment items at CVN-71 shock test and design levels. The following tasks were accomplished to achieve these objectives.

- 1) Survey the CV-67 to obtain the status, description and location of test gages and the grade A AIMD equipment items aboard the CV-67 during the shock test which were pertinent to the study.
- 2) Survey the CVN-71 to obtain the status, description, and location of the grade A AIMD equipment scheduled to be aboard the CVN-71 during the shock test.
- 3) Obtain and process the raw data recorded during the CV-67 shock test to obtain a digitized data file of unfiltered acceleration time history data for each CV-67 shock test gage of interest.
- 4) From the CV-67 unfiltered acceleration time histories generate filtered acceleration time histories, velocity time histories, and shock spectra for each selected CV-67 test gage.
- 5) Predict CVN-71 shock environment data at shock test and design levels based on CV-67 data.
- 6) Finally, calculate a specific shock environment for each Grade A AIMD equipment item based on the CVN-71 shock environment predictions.

A complete shock grade review of the AIMD equipment assigned to the CVN-71 was conducted by Naval Air Systems Command wherein over 7500 line items of support equipment were identified and evaluated. The results of this shock grade review determined that 75 of the AIMD equipment systems were to be classified grade A. The status scheduled for each other item during the shock test, i.e., cross decking, shock mounting, or protection stowage, was also determined.

Of the 243 shock measurement transducers aboard the CV-67, 64 accelerometers were selected as shock environment reference points used in predicting the CVN-71 AIMD equipment shock environments. The CV-67 and CVN-71 AIMD equipment items were located on or between the hangar and flight decks; hence the 64 selected accelerometers, which were also located on or between the hangar and flight decks.

The shock environments predicted at selected CVN-71 locations served as the best definition of the shock environments in the vicinity of the grade A AIMD equipment. By cross referencing between the schematics locating the grade A AIMD equipment items on the CVN-71, and the schematics defining the 64 CVN-71 shock environment reference points, a set of primary reference points

were determined for each grade A AIMD equipment item. These primary reference point sets were comprised of the reference points which were located closest to a particular equipment item and would thus most accurately represent the expected shock environment at the mounting location of that particular equipment item.

Evaluation

The Evaluation of the selected AIMD SE was by derivation of a simple logic which included review of manufacturer's published fragilities, ground transportation specifications, acceptance tests if any, and a projected fragility from the SE composition, i.e., CRT's, disk drives, memory types, etc., all compared to the projected SE environment. Figure 3 depicts this basic starting point.

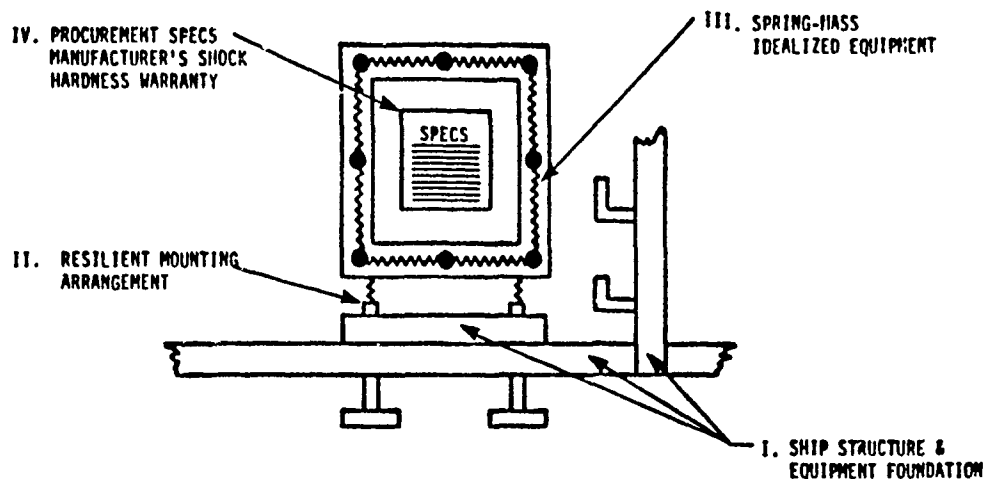


Figure 3. Analytic Components of the AIMD Test Equipment Shock Hardening Program

Shock mounting for the selected CVN-71 AIMD SE items was employed to reduce the severe SE shock response induced by full scale design level ship shock loads. During shock loading, an energy impulse of relatively short duration and large acceleration is transmitted through the hull and ship structure directly into the deck mounted SE item; the SE item responds with a sudden change in velocity and a large peak acceleration. Through the use of properly selected shock mounts, the shock impulse transmitted to the AIMD SE items can be significantly mitigated. The shock energy is absorbed by the deflection of the shock mounts.

The equation of motion defining the shock response of the mounted SE item is (references 2 and 3):

$$M\ddot{X} + C\dot{X} + KX = F(t) \quad (1)$$

or $\ddot{X} + 2\beta\dot{X} + \omega^2 X = f(t)$

where M = mass of mounted SE item
 X = relative displacement of M to deck
 K = mount stiffness
 β = mount damping coefficient
 $= C/M2$
 $f(t)$ = input shock impulse
 where V_{mas} + maximum deck input velocity
 ω = shock mount/SE system natural frequency
 $= \sqrt{K/M}$

The exact solution of Equation (1) defines $X(t)$, the transient response of the shock mounted SE item, as

$$X(t) = e^{-\beta t} \left(\frac{\dot{X}_0 + \beta X_0}{\omega_d} \sin \omega_d t + X_0 \cos \omega_d t \right) \quad (2)$$

where ω_d = damped system natural frequency
 $= \omega \sqrt{1 - \beta^2}$

Note that for $\beta \leq .20$, $\omega_d \geq .98 \omega$. Thus, for practical purposes, the decrease in natural frequency due to damping can be ignored, and Equation (2) can be rewritten as

$$X(t) = e^{-\beta t} \left(\frac{\dot{X}_0 + \beta X_0}{\omega} \sin \omega t + X_0 \cos \omega t \right) \quad (3)$$

inserting the initial conditions

$$\begin{aligned} X_0 &= 0 \\ \dot{X}_0 &= V_{\text{max}} \\ \ddot{X}_0 &= 0 \end{aligned}$$

yields

$$X(t) = e^{-\beta t} \frac{V_{\text{max}}}{\omega} \sin \omega t \quad (4)$$

For purposes of shock mount system design calculations, the maximum response of a mounted SE item excited by a shock impulse can be derived from Equation (4). The maximum shock response of a mounted SE item occurs as the initial peak response; as time increase, damping forces cause the peak responses of the SE item to decay at a rate defined by logarithmic decrement ($= 2\pi\beta/\omega$, the logarithm of the ratio of the two consecutive peaks). The primary effects of damping are to reduce the transient vibration responses of the mounted SE item rather than the initial peak shock responses; as the SE item achieves a peak response almost immediately after excitation by the shock impulse, the damping forces have very little time to affect or dampen the initial peak response. Therefore, more conservative definitions of the initial peak shock responses of the mounted SE item are:

$$X(t) = \frac{V_{\max}}{\omega} \sin \omega t \quad (5)$$

and

$$\ddot{X}(t) = \omega V_{\max} \sin \omega t \quad (6)$$

And solving Equation (5) and (6) for the maximum shock responses of a mounted SE item to be used for design calculation yields:

$$X_{\max} = \frac{V_{\max}}{\omega} \quad (7)$$

$$\ddot{X}_{\max} = \omega V_{\max} \quad (8)$$

$$\ddot{X}_{\max} = \omega^2 X_{\max} \quad (9)$$

Low frequency shock mount systems are generally desirable when designing for optimum shock mitigation; however, these softer systems can create design problems with relatively large peak deflection responses. Such large initial peak deflection are what allow the shock mounts to absorb the spiked, high frequency shock energy inputs and limit the mounted SE item to a smoother, low frequency response. Inspection of equations (7), (8) and (9) reflect this shock response/frequency relationship: the acceleration response of the mounted SE item is directly related to mounted system's natural frequency while the deflection response is indirectly related to the mounted systems natural frequency.

While the initial peak shock response of a shock mounted system is generally the critical factor driving the design of a shipboard shock mount system, the vibration or transient responses are also an important design consideration. If the natural frequency of the shock mounted system coincides with some shipboard forcing frequency, i.e., shipboard structure, blade rate, or residual shock input, a resonant condition can be excited in which the system's transient response is actually amplified instead of mitigated as intended.

As long as shock mounts are selected to avoid any potential resonance conditions, the maximum transient response of the mounted system will be limited to that of the excitation force and will decay at a rate governed by the shock mount's damping coefficient.

Implementation

The Implementation was accomplished in the form of specific resilient mount and sway bracing designs respectively and the generation of ECP and ECP input data. Figure 4 shows the general logic for accomplishment of the required ship alterations.

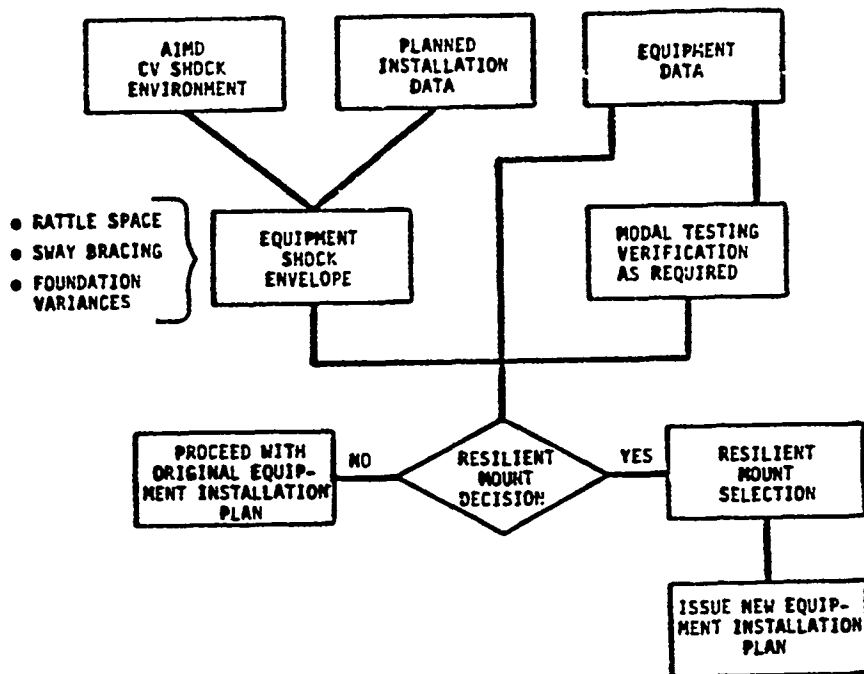


Figure 4. AIMD Test Equipment Shock Hardening Program Logic

Aeroflex isolators were selected for installation with all of the Category 1 and 2 Grade A SE items which were determined to require shock mounting aboard the CVN-71. The allowable dynamic displacements of the Aeroflex isolators provide for a high level of shock attenuation, and their damping characteristics provide for the mitigation of low and high frequency vibration loads (reference 4).

The Aeroflex shock mounts are constructed of stranded stainless steel wire rope wound in the form of a helix and held between two retainer plates made of a corrosion-resistant aluminum alloy. They require little or no maintenance as they resist most destructive environments, i.e., sand, salt spray, oil, grease, organic solvents, and extreme temperatures (-400°F to 700°F). The isolators can isolate compression, tension, shear and roll loads (or any combination thereof), which allows for numerous possible installation configurations.

In addition to the softening spring characteristics of the Aeroflex isolators, the force deflection properties of a new, never-been-used Aeroflex isolator are much stiffer than those "standard values" reported in the Aeroflex catalog. In order for the Aeroflex isolator to perform to design specifications, each isolator must be shock cycled - undergo a series of shocks which force the isolator to deflect to its maximum dynamic travel rating - prior to installation. Figure 5 depicts a local deflection curve of a typical Aeroflex mount.

TYPE CB 1500-20

Methods & Techniques



A shock mount system was designed and verified for each AIMD SE item by using the shock mount design theory described and NASTRAN, a finite element analysis program. Design data input to the maximum shock response equations and the NASTRAN SE/shock mount system model included the predicted maximum input velocities, the SE items' weight, dimensions, and CG locations, and the Aeroflex isolators' dimensions and force-deflection curves (Aeroflex Isolators Catalog).

For each SE item:

- 1) Equation (8) was solved using the appropriate maximum input velocity (V_{max}) and the maximum allowable acceleration (X_{max}) to approximate the equivalent mount stiffness (K_{eq}) required to achieve sufficient mitigation.
- 2) Based on K_{eq} and the SE item's geometry, etc., a candidate set of shock mounts was selected. The candidate shock mounts' dynamic characteristics were included as spring elements in a three-dimensional NASTRAN SE model.
- 3) Using the actual force-deflection properties of the candidate shock mounts, equation (8) was solved again to calculate the maximum acceleration responses at the SE item's CG (a new X_{max}).
- 4) The NASTRAN finite element analysis was executed using the CG acceleration calculated in Step 3 (the shock response loads) to compute the corresponding resulting maximum deflection for each mount.
- 5) A new mount spring stiffness value corresponding to the maximum mount deflection computed in Step 4 was obtained by referring to the appropriate mount force-deflection curve and compared to the initial mount stiffness value. If the new stiffness value was sufficiently different from the original stiffness value, the design procedure was repeated from Step 2.

This iterative shock mount selection procedure was repeated until the new and the old stiffness values were sufficiently close to assume that the correct stiffness-deflection-response had been converged upon. The natural frequency was computed for the SE item/shock mount system using the new, correct stiffness value.

The response characteristics of each AIMD SE/shock mount system were compared against the SE item's maximum allowable acceleration (reference 5), the pertinent critical frequencies, and the shock mounts' maximum allowable deflection to verify that no potential problems would arise with the installation of the shock mount system. If the natural frequency of the shock mount system was close to any critical frequencies or if the maximum response accelerations or deflections were greater than the allowed accelerations or

deflections, new candidate mounts were selected, and the design procedure repeated. Prior to the CVN-71 equipment shock mounting, Medium Weight Shock Machine (MWSM) tests of a CAT IIID SE were performed at NOSC and NRL as a proof of concept. Figure 6 shows the CAT on the MWSM. In all fifteen (15) Category 1 and 2 equipments/systems were shock mounted, eleven (11) Category 3 equipments, and four (4) "last minute" additional systems (references 6, 7 and 8).

THE CVN-71 SHOCK TRIALS VALIDATION

The technical procedure was validated during the CVN-71 shock trials. This experience forms the second part of the paper. The combination of sophisticated motion-time histories coupled with general equipment response data, the Maintenance Action Form (MAF) data taken before and after each UNDEX attack for each Grade A SE, and the electrical power monitoring data forms the data bases to provide realistic design and procurement specifications for future equipment. To coordinate these efforts a Data Acquisition Plan (reference 9) was prepared and issued to all AIMD work centers.

Shock Environment Measurements

Extensive measurements of shock environment were planned to cover the entire AIMD area. Several types of shock gages and instruments were installed on mobile and stationary support equipment, as well as on structural components and decks within AIMD spaces.

The data measurements were essentially in consonance with the overall CVN-71 test plan by providing an analytical basis for study of any equipment failures, validation of engineering technique for selecting/prescribing shock isolators, definition of equipment shock response and regional shock environment in the equipment vicinity.

Velocity meters, accelerometers, and strain gages were attached to ships structure and to various pieces of AIMD equipment in the following locations.

Transducer Locations

Accelerometers, Velocity Gages and Strain Gages

(A) Console Type Equipment - (28) Vertical Gages

- | | |
|-----------------------|-----------------------|
| (1) Avionics Shop #1 | (2) Avionics Shop #8 |
| (1) Avionics Shop #2 | (3) Avionics Shop #10 |
| (4) Avionics Shop #3 | (3) Oxygen Shop |
| (10) Avionics Shop #5 | (2) Hydraulics Shop |
| (1) Avionics Shop #7 | (1) Jet Engine Test |

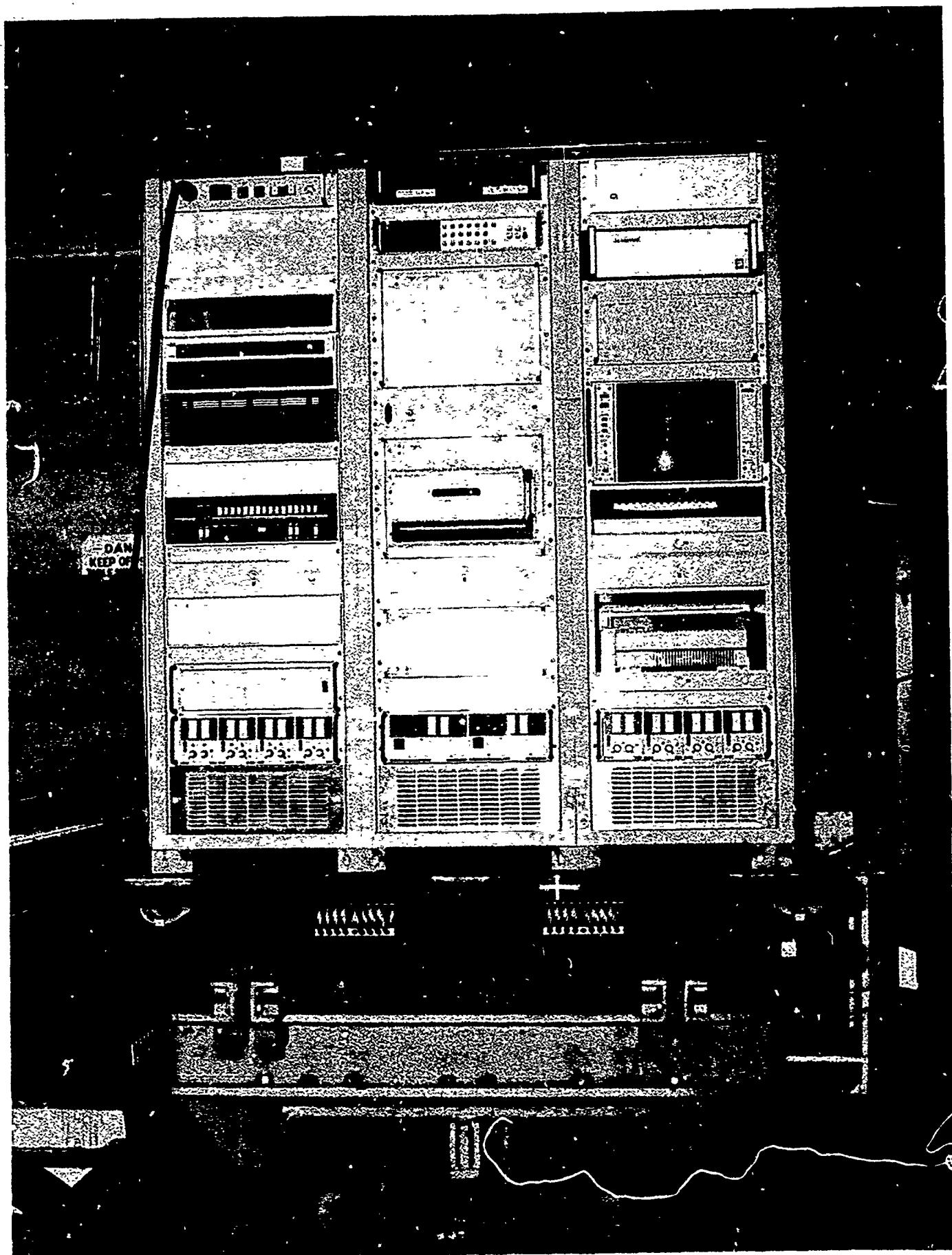


Figure 6. NRL MWSM Test of CAT IIID

- (B) Bench Top Equipment - (7) Vertical Gages
(2) Avionics Shop #6 (3) Avionics Shop #9
(2) Avionics Shop #11
- (C) EA6B Vans Support Structures - (9) Gages
- (D) Interface Device Stowage Racks - (3) Gages
- (E) Structural - (9) Gages

In addition approximately four thousand (4000) limiting accelerometers were installed by test personnel on various Grade "A" and "B" equipments in AIMD. A typical view of a group of these gages mounted on a support equipment is shown in Figure 7. AIMD personnel recorded the data from this type of gage. A procedure for recording and re-setting those gages along with a diagram of locations in each shop was enclosed in each AIMD shop booklet of the Data Acquisition Plan. The following table is an overview of the gage installation:

Total Number of Gages Installed	3204
Number to Record Vertical "g"	1068
Number to Record Athwartship "g"	1068
Number to Record Fore and Aft "g"	1068

Number of Equipments on Which Gages Were Installed 267

Weight Range 23 to 4000 lbs

Angle of Attack System Test Set	23 lbs
HATS USM-403	4000 lbs

Electrical Power Monitoring

During each shock test "shot," electrical power distribution was monitored concurrently with other measurements. The importance of this effort cannot be minimized. Based upon observations made during CV-67 shock tests, a significant number of post-test discrepancies/failures were attributed to electrical abnormalities. The major fault was due to transients or "spikes" in the shipboard power supply which are induced by high shock levels experienced by power generation/transformation machinery.

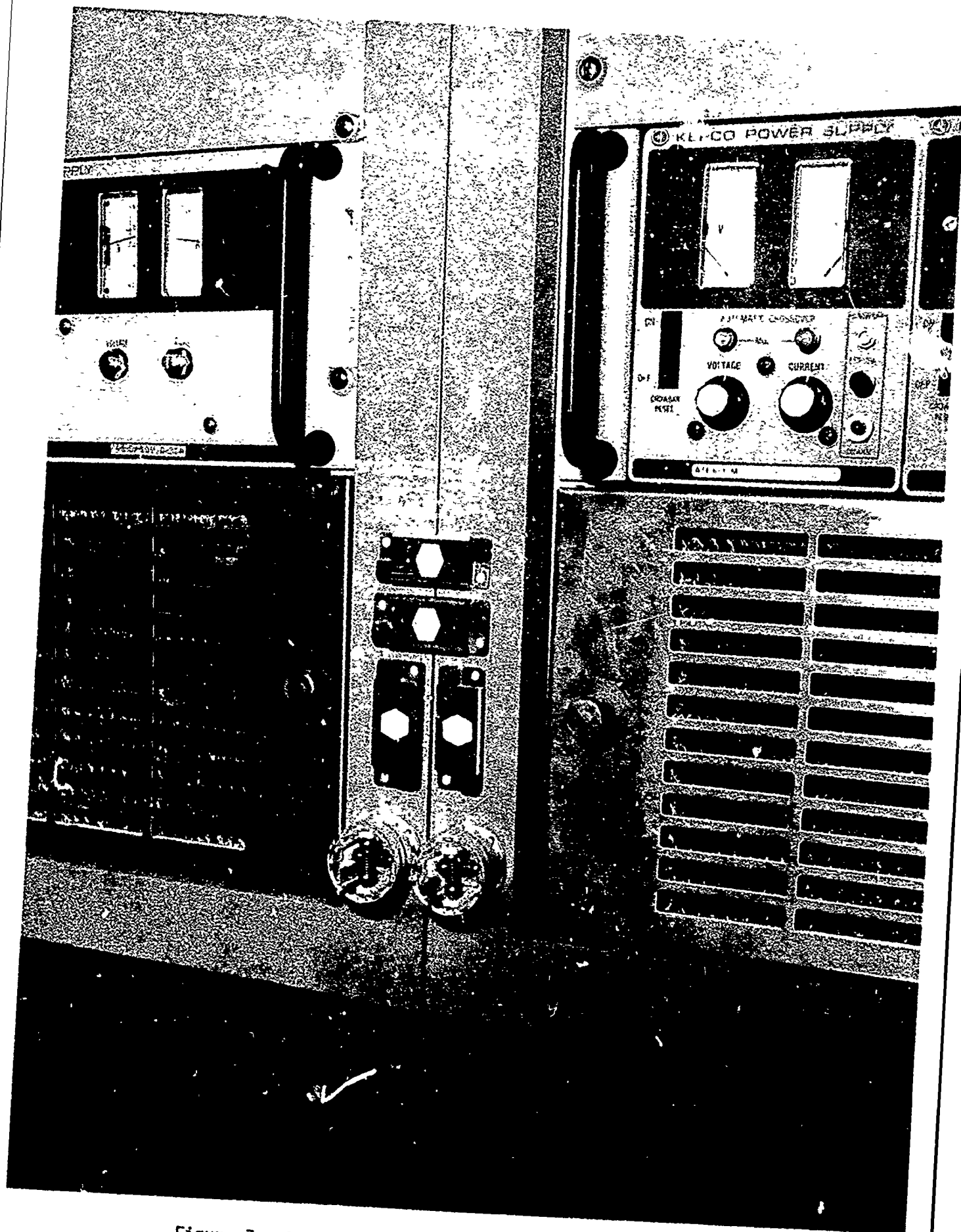


Figure 7. Typical Limiting Accelerometer Arrangement

The objective was to record electrical power parameters; such as voltage, amperage, phase and frequency; at designated locations throughout the ship. The overall electrical power monitoring plan matches the shock measurement instrumentation plan in comprehensive coverage of all departments.

Taps (pick off points) were installed in the ship's power distribution system for power line monitoring. Monitoring points were established for both 60 hz and 400 hz systems in such a manner as to aid in detecting sources of disturbances, the cause of circuit breaker tripping and to relate power transients with equipment failures.

The objective of the AIMD portion was to monitor electrical power inputs into all avionics shops and selected items of ATE.

AIMD Equipment Condition Evaluation

These events consisted of operational and functional tests of each item of AIMD Grade A and B equipment, as listed in the Data Acquisition Plan after each test shot. All equipment was turned on and IN OPERATION during each shot.

The Data Acquisition Plan test booklets for each AIMD space were grouped together by IM-2, 3 or 4 divisions. The booklets typically contained a shipboard shop location map, an individual shop plan view with equipment locations, photos of all grade A and B equipment, within that shop, which would be tested and evaluated, a static gage monitoring procedure and an equipment condition evaluation count-down procedure. The photos also indicated locations where passive shock gages were to be installed in cluster groups.

Operational tests for sixty-five (65) items of AIMD Grade A equipment were performed. Tests for Jet Engine Test, Structural Shop and Mobile Grade A equipment consisted of operational tests conducted by respective AIMD personnel with no requirement for WRA's or SRA's. A jet engine run-up test was coordinated for accomplishment if time and conditions permitted.

The listing of AIMD Grade B equipment included specific support equipment consoles, such as a spectrometer, and a diverse grouping of associated "test equipment," such as portable oscilloscopes, cathode-ray tube testers, frequency counters and assorted, small electrical test boxes. There were approximately one-hundred and twenty (120) Grade B equipments and one-hundred (100) Grade B small testers.

The purpose of the MAF was to assess the condition of AIMD Grade A and B equipment before and after each test shot.

The specific objectives to be accomplished were:

1. Define maintenance procedures necessary to correct minor discrepancies between test shots.
2. Define maintenance procedures necessary to repair damaged equipment.
3. Prepare documentation, MAF's and casualty reports for each incident.

Count-Down Procedure
for
Equipment Condition Evaluation

T = scheduled time for test shot.

<u>Time</u>	<u>Action</u>
T-2:00	Install associated WRA, SRA, I.D. or test object to item of Grade A or B AIMD Support Equipment.
T-1:30	Assure that AIMD equipment and installed test objectives are in proper working condition; conduct preliminary diagnostic tests where necessary. Record results on MAF.
T-1:00	Check all passive gages - ready for test - red arrows showing.
T-0:30	Energize all Grade A and B equipments (if selected equipments require longer warm-up time, or longer time before test to conduct preliminary diagnostic tests, this action should be initiated to satisfy those requirements).
T-0:15	Prepare self-test tapes. ASSURE THAT ALL EQUIPMENT IS IN OPERATION.
T-0:00	Test Shot.
T+0:05	Inspect equipment for obvious physical damage, loose gear or surrounding structure failures. Notify Production Control of major discrepancies.
T+0:15	Monitor passive gages, record data and re-set gages as required in Data Acquisition Plan.

T+0:30	Identify obvious casualties to Production Control and shock test personnel.
--------	---

T+0:45	Conduct self-test or diagnostic test with or without test objects deployed. Record results on MAF.
--------	--

T+1:30	Determine equipment operational capability and condition. Record discrepancies on MAF's.
--------	--

T+2:00	Determine necessary repairs or maintenance actions as required; trouble-shoot for discrepancies, damage or failures; estimate level of repairs necessary.
--------	---

T+2:30	Conduct all repairs - minor, or major. Record corrective action taken on MAF's.
--------	---

T+4:00	Submit all completed MAF's to Production Control. Notify Production Control of equipment still in work.
--------	---

T+4:30	For equipment casualties, or expected casualties on next test shot, initiate protective measures to protect from further damage, with approval of Production Control.
--------	---

T+5:00	Remove test objects and stow all equipments until next count-down sequence before next scheduled test shot.
--------	---

NOTE: WRA's/SRA's were run as directed by Production Control between shots.

RESULTS

The detailed results of the AIMD SE shock trials survivability are described in reference 10. The following summary provides an overview of the results.

Casualty Report Summary

SHOT #1

- (9) Grade "A" and (1) Grade "B"
- No Shock Damage
- All Repaired/Resolved

SHOT #2

- (9) Grade "A"
- (8) Electrical and (1) Minor Problem
- All Repaired/Resolved

SHOT #3

- (11) Grade "A" and (4) Grade "B"
- (9) Electrical and (5) Mechanical Problems
(1) Non-problem
- All Repaired/Resolved - Except Torque Wrench Cal.

SHOT #4

- (14) Grade "A" and (6) Grade "B"
- (9) Electrical and (11) Mechanical Problems
- All Repaired/Resolved - Except ATS and X-RAY Vault

It is interesting to note that ATS was scheduled for shock mounting but it could not be accomplished prior to the shock trials.

Figure 8 shows the response trends of the equipment as measured by the limiting accelerometers. The data is well behaved and consistent with normal equipment shock response levels.

SUMMARY

It is difficult to summarize a project which really started in November of 1983 with the decision to shock test the USS KENNEDY (CV-67) prior to the scheduled shock trials of the USS ROOSEVELT (CVN-71) (still building at that time), and concluded in October of 1988 with the completion of the ROOSEVELT shock trials. A project which eventually involved all 430 of the ROOSEVELT AIMD personnel.

Accordingly, the following chronological summary is offered. In addition it may serve to clean-up some of the usual confusion that is a result of the authors being "too close" to the subject.

o July 1984

NAVSEA requests NAVAIR to re-examine AIMD SE shock grades and develop a POA&M for shock hardening/mounting of Grade "A" SE prior to CVN-71 shock test.

o August 1984

CV-67 shock test raises questions as to SE ability to withstand shock loads.

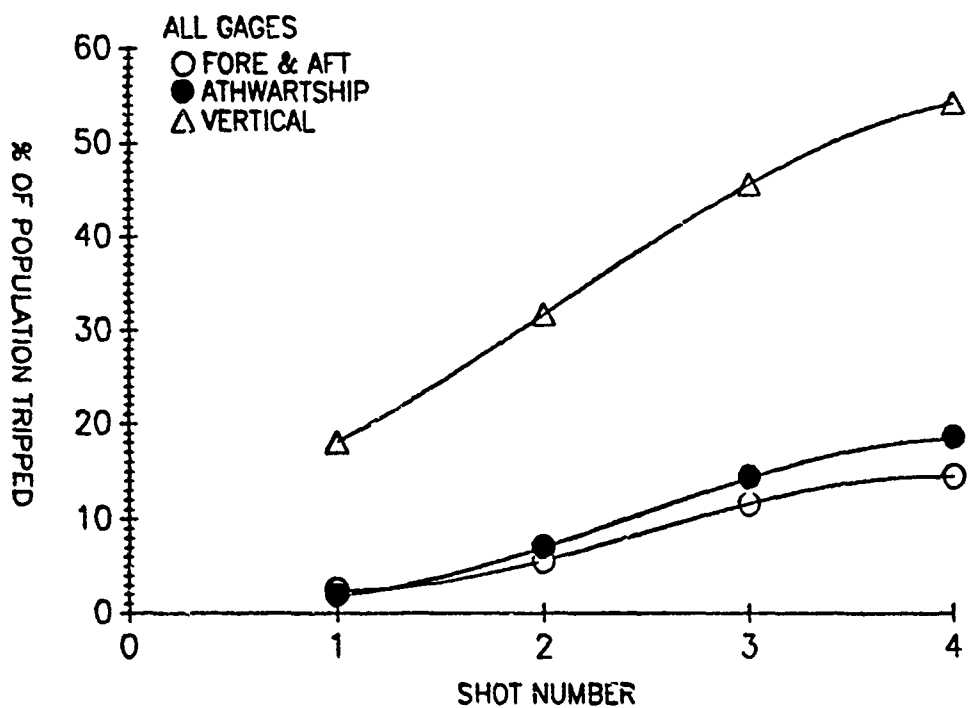
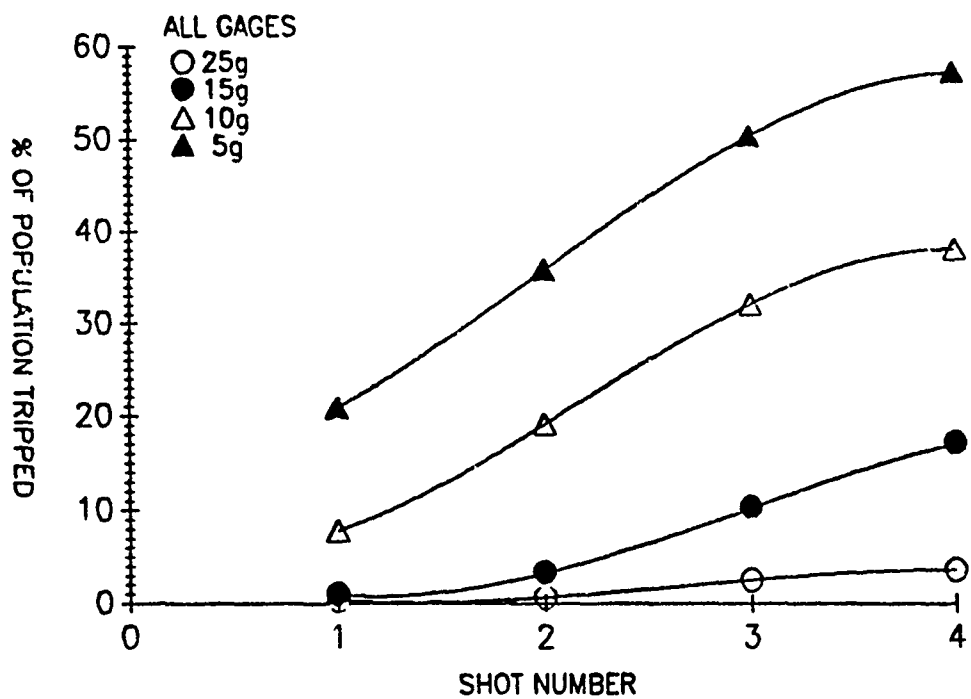


Figure 8. Shock Response Trends of AIMD Equipment

o December 1984

Shock grade review of approximately 7500 items of AIMD SE completed. 75 items/systems considered Grade "A".

o June 1985

Medium Weight Shock machine test of CAT IIID to qualify model. Results inconclusive due to poor condition of CAT (hangar queen).

o September 1985

Review of Grade "A" Categories 1 And 2 AIMD SE items completed. 15 of 43 items/systems require shock mounting.

o December 1985

First ship's facility inspection of Category 1 and 2 installations.

o February 1986

Review of Grade "A" Category 3 AIMD SE items completed. 11 OF 32 items require shock mounting/hardening.

o March 1986

EA6B Van shock environment analysis complete. ECP pending at NAVSEA CCB.

Shock mount selection for 14 grade "A" items requiring shock mounting is complete. Newport News Shipyard and Drydock tasked to perform installation.

o May 1986

AIRLANT determines "O" level items of SE considered Grade "A". Items under review at NAEC.

Stowage facilities (rotatable pool, ID racks, VIDMARS) reviewed. ID rack shock mounts selected - VRT to install.

o August 1986

CVN-71 tasked via AIRLANT to determine Grade "B" items to be protected. Additional requirement.

Second shock test of CAT IIID scheduled for October 1986 - qualify model and shock mount selections.

o **October 1986**

"Brand new" CAT IIID shock tested at NRL on Medium Weight Shock Machine. Three shock hits 1" to 3". All successful.

o **October 31, 1986**

"Emphatic" AIRLANT request for comprehensive AIMD CVN-71 Data Acquisition Plan

o **November 1986 to May 1987**

Weekly visits to CVN-71 for ship checks, photographic file development, resilient mount installation(s) monitoring, development, installation and supervision of Category 3 and Grade B shock mounting.

o **May 1987**

Delivery of formal AIMD Data Acquisition Plan to AIRLANT.

o **July - August 1987**

Installation of resilient mount package for ECAMS, additional mounts for IMUTS and mount packages for selected Category 3 equipment.

o **August 1987**

Training of AIMD personnel for Shock Trials Data Acquisition during AIR OPS at Sea period.

o **September 1987**

Shock Trials of CVN-71 completed, total of four (4) shots as planned.

CONCLUSIONS

The AIMD shock hardening project was a success as proven by the ROOSEVELT shock trials. This success also demonstrated that commercial grade equipment can easily and cost-effectively be protected against the shock environment when required, thus allowing the procurement flexibility and timeliness of acquisition desired by the Navy.

Fleetwide SE Shock Hardening

The majority of the shock installations performed by Newport News Shipbuilding Co. for the large Category 1 and 2 ATE and the EA6B Vans has already been extended to the new CVN construction, i.e., the USS ABRAHAM LINCOLN (CVN-72), the USS GEORGE WASHINGTON (CVN-73) and will be to the as yet

unnamed CVN-74 and CVN-75. These extended installations will require some additional engineering to account for the slightly different "per compartment" response characteristics between the KENNEDY and the ROOSEVELT. But it is the Category 3 (bench-top) equipments which vary the most from CV to CV, and stowage devices which require more detailed planning.

The fleetwide shock hardening of SE is a natural consequence of the AIMD project and requires an application of the technical procedure described above in concert with the existing CV construction and overhaul schedule. Figure 9 depicts a general overview of the process with an upward bound line for the approximate total number of fleet Grade A SE's. The cost savings to the Navy by the institution of the program and the generation of specific CV SE shock procurement and testing specifications is enormous.

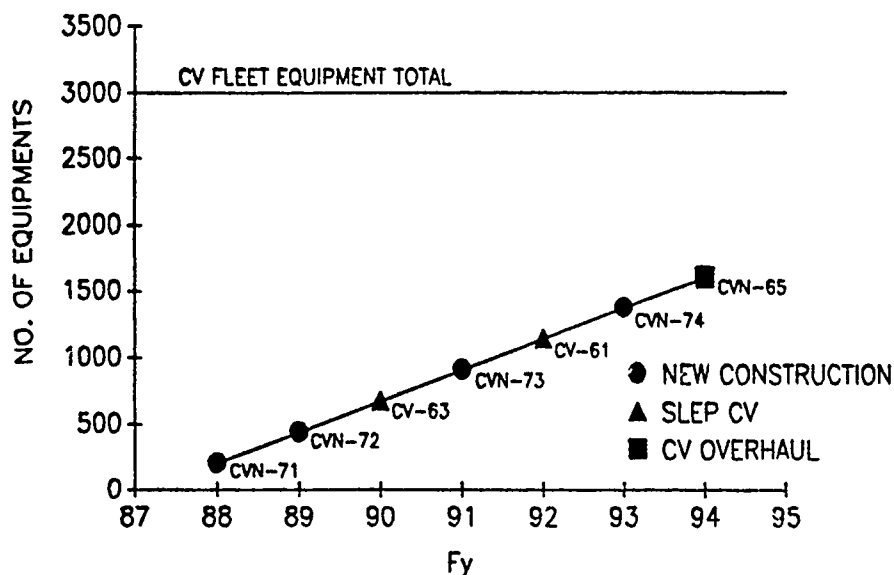


Figure 9. Minimum Cost/Impact Schedule for the Shock Hardening of AIMD CV Equipments

ACKNOWLEDGEMENTS

The outstanding success of the AIMD project was due to the contributions of many; notably Captain Tom Hancock (AIRLANT), CDR Bill Adams (NAVAIR), CDR Bob Lindquist (AIRLANT), Pat Baker, Ben Lennon, Bob Hepp (NKF), and the notorious junior engineers of NAEC (HB's), but particularly the officers and men of the USS THEODORE ROOSEVELT (CVN-71) AIMD.

Captain Hancock to Dom Croce and Brian McNaught (about the AIMD enlisted personnel), "These kids will do anything you ask of them, they are the best there is, all you have to do is tell them what you want!" AND THEY DID.

REFERENCES

1. "Shock Environment Predictions for USS THEODORE ROOSEVELT Grade A AIMD Equipment," in two (2) volumes, NKF Report No. 8500-025A/1, February 1985
2. Biggs, J..M., "Introduction to Structural Dynamics," McGraw Hill, Inc., 1964
3. Harris, C.M. and Crede, C.E., "Shock and Vibration Handbook," McGraw Hill, Inc., 1976
4. Aeroflex Isolators Catalog and Selection Guide, Bulletin 782, Aeroflex International, Inc., Plainview, Long Island, New York
5. "Fragility Factor Study for Avionics Support Equipment," NKF Report No. 8500-114B/2, March 1986
6. "Shock Mount Selections for CVN 71 Category 1 and 2 Grade A AIMD SE," NKF Report No. 8500-116B/2, February 1986
7. "Shock Analysis of EA6B Van Support Structure and Internal Equipment," NKF Report No. 8500-175, August 1986
8. "Shock Mounting Arrangements and Instrumentation Guidelines for CVN-71 AIMD Category 3 and Van Mounted Equipment," NKF Report No. 8500-143, October 1987
9. "AIMD Data Acquisition Plan - CVN-71 Shock Trials," May 1987
10. "Acquisition of Shock Data for Aircraft Intermediate Maintenance Department (AIMD) Equipment Aboard the CVN-71," in two (2) volumes, NKF Report No. 8876-016/4, April 1988

BOUNDARY INTEGRAL TECHNIQUE FOR EXPLOSION BUBBLE COLLAPSE ANALYSIS

Stephen A. Wilkerson
Naval Surface Warfare Center
10901 New Hampshire Ave.
Silver Spring, MD 20903-5000

The Dynamics of an underwater explosion bubble, including its collapse and interaction with a free or hard surface, is analyzed using incompressible flow theory and a boundary integral formulation. The formulation of the solution method and the crux of the numerical treatment are presented in detail. A computer program for axisymmetrical problems has been successfully developed. Numerical results including bubble periods, maximum radii, and velocities of the re-entrant jet-tip are also compared to available experimental data and also to computational results obtained using the PISCES finite difference code.

INTRODUCTION

An underwater bubble can exhibit dynamic behavior similar to a mass spring system. For an explosion bubble, the initially high internal pressure will drive the surrounding fluid outward at a decreasing rate. Due to the fluid inertia, the bubble will over expand, dropping its internal pressure to only a small fraction of the surrounding fluid's hydrostatic pressure. Then the bubble will begin to contract at an increasing rate. The contraction is propelled by the fluid's surrounding hydrostatic pressure. This process will continue until the increasing bubble pressure reverses the process abruptly. Therefore, the elastic properties of the gas and water provide the conditions for an oscillating system. This process is termed bubble pulsation.

During the contraction phase of the bubble pulsation, variations in the surrounding fluid pressure can cause the bubble surface to contract at different rates. These pressure variations can occur due to bubble migration, a nearby object, the natural gradient of pressure with depth in a fluid, and other disturbances. These external pressure variations will cause a higher rate of inward fluid acceleration near a portion of the bubble surface. The portions of the bubble surface near the higher fluid acceleration will form a jet

near the end of the contraction phase of the bubble pulsation. These jets can vary greatly in size and momentum depending on the factors leading to their formation. This phenomenon is termed bubble jetting. The primary purpose of this study was the development of analytical techniques that could be used to study bubble pulsation and bubble jetting.

Much of the interest in underwater bubble dynamics has focused on the behavior of cavitation bubbles. Cavitation bubbles have applications affecting propeller and turbine blade damage and underwater acoustics. Collapsing cavitation bubbles can generate tiny regions with high temperatures, pressures and fluid velocities. A number of authors, Gerri, Lucca, and Prosperetti,¹ Prosperetti, et al.,²⁻¹⁰ Chahine, et al.,¹¹⁻¹⁸ Taib,¹⁹ Blake et al.,²⁰⁻²¹ Chapman and Plesset,²²⁻²³ have demonstrated that in some instances, bubble behavior can be accurately predicted utilizing analytical methods with good accuracy.

The focus of this analytic study is the dynamic expansion and collapse of large bubbles, such as those created by an underwater explosion in the free field, in the vicinity of a free surface, and near a solid body. Bubble collapse is influenced by a number of physical factors. These factors include the gradient of hydrostatic pressure as a function of depth, bubble migration, and a bubble's proximity to nearby solid bodies.

The effect of the pressure gradient on jetting is far more influential for a large bubble than a cavitation bubble. In the former case, the hydrostatic pressure at the bottom of the bubble surface can be as high as twice the hydrostatic pressure at the top of the bubble. On the contrary, bubble migration leads to bubble jetting in both large and small bubbles. In general, bubbles are driven upward by their own buoyancy force. Consequently, the higher velocity of the flow at the head of the bubble leads to a reduction in pressure, while the stagnant flow along the lower surface of the bubble leads to an increase in the fluid pressure. This phenomenon accompanied by the dynamic collapse of the bubble will typically yield a bubble jet near the end of the bubble collapse phase. Further, the proximity of the bubble to a solid boundary can also greatly influence the bubble jetting behavior, (see Figure 1). When a bubble pulsates near a body, the fluid near the object must move faster than the fluid around other portions of the bubble. The result is a decrease in the fluid's pressure near the boundary. This pressure drop in the fluid near the body will generate bubble migration toward the body. Further, when the bubble comes in contact with the body during the expansion phase of its period, the bubble can have a very high water velocity jet. This is in part due to the dynamic nature of the bubble growth. As the bubble expands the internal pressure can drop to only a small fraction of the normal hydrostatic pressure in the surrounding fluid field. The result is the jetting of the bubble's lower surface into the body. Finally, the combination of the various effects influencing bubble collapse and jetting can act in conjunction with one another to increase jetting or oppose one another to reduce jetting. The present method described in this paper allows the opportunity for these behaviors to be studied separately or in combination with one another.

The present study utilizes an axisymmetric boundary integral formulation which has application for a variety of geometric

configurations. The method is computationally efficient due to its dependence on only the boundary's value for the velocity, the potential, and the potential's first derivative. This approach avoids the necessity of solving Laplace's equation in the entire domain occupied by the liquid which would be computationally intensive. The resulting range in computation

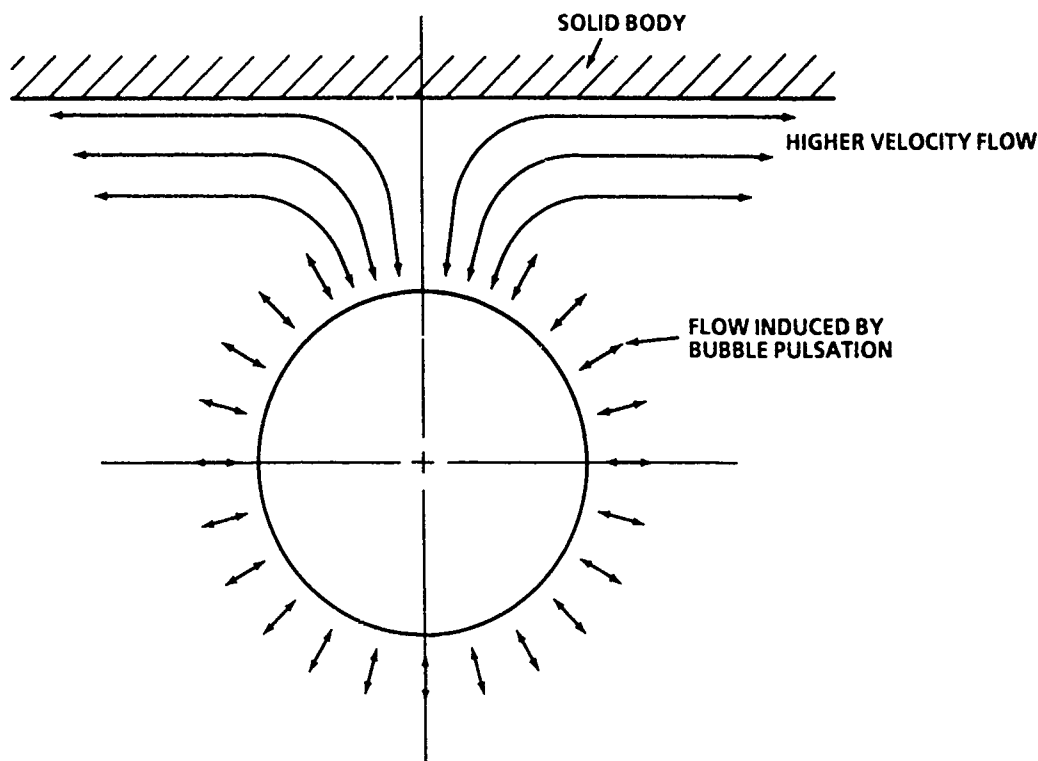


FIGURE 1. FLOW INDUCED MIGRATION NEAR A BOUNDARY

time can vary from minutes for free field calculations, to less than one-half hour for computations involving free surfaces or a boundary. The computational device serving as a basis for these comparisons, is the VAX 8800. To illustrate the performance and accuracy of the method a number of comparisons were made. These comparisons include, exact versus predicted solutions for spherical bubbles, experimental bubble radii and period comparisons, and bubble jet tip velocities versus compressible flow theory calculations using the hydrocode PICSES. In these cases the method is shown in good agreement with available data. Further, a number of calculations very near the free surface are performed showing the idealized formation of the water spray dome. Using this free surface calculation the limitations of the methodology are discussed.

The growth and collapse of large bubbles, such as those created by underwater explosions near non-axisymmetric underwater structures, are also of interest. In this scenario the combination of gravity-induced collapse and collapse caused by migration and proximity to nearby structures can result in extremely high velocities of the bubbles re-entry jet tip. Analysis of bubble-structure interaction is generally three-dimensional in nature due to the effects of gravity and the orientation of the structure. Solution of this problem is briefly discussed in the mathematical formulation.

MATHEMATICAL FORMULATION

In this model the flow induced by one or more bubbles is considered. The fluid occupies a domain Ω bounded by the bubble surfaces, S_b , solid boundaries, S_r , and a surface at infinity, S_∞ , (see Figure 2). The fluid, contained in domain Ω , is considered incompressible and inviscid.

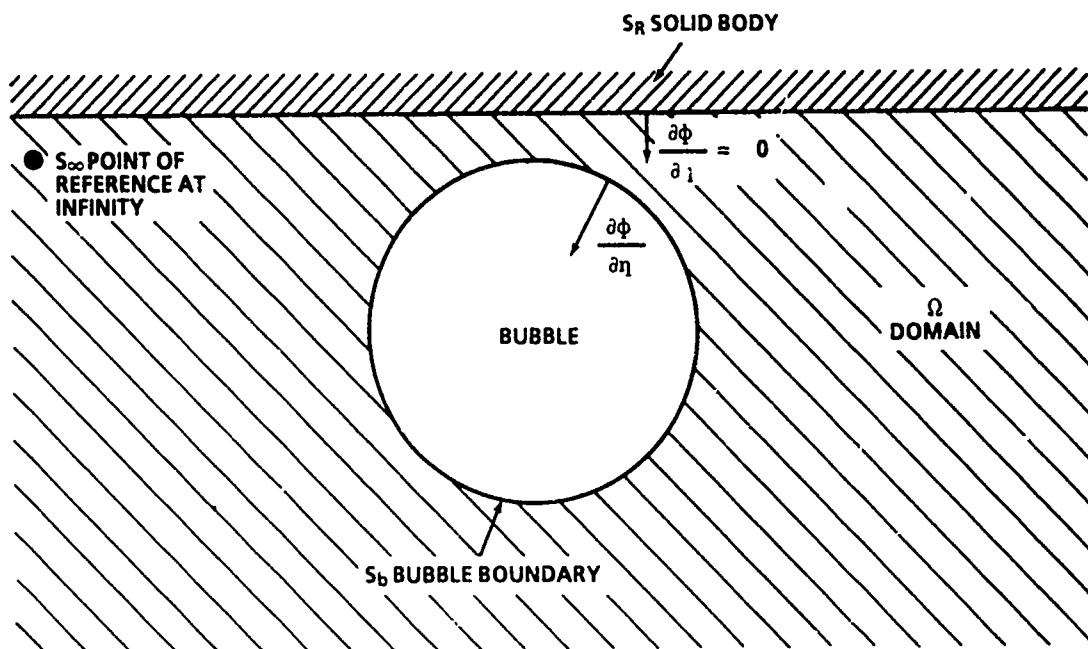


FIGURE 2. BOUNDARY CONDITIONS

In the case of underwater explosive detonations, a chemical reaction converts the original material into a gas at very high temperatures and pressures. The temperatures can be on the order of 3000 C with pressures on the order of 50,000 atmospheres.²⁴ The result of the initial detonation is a compression or shock wave being emitted into the fluid field, followed by the dynamic expansion and contraction of the gas bubble. After the release of the shock wave, which is an early time phenomena, the speed of the bubble surface remains a magnitude smaller than the speed of sound in water. Therefore, imposing an incompressibility condition on the fluid is deemed valid for this flow condition.

Using the bubble radius, in the expansion or contraction phase of the bubble pulse, as a characteristic length, a Reynolds number can be

calculated. The Reynolds number for an underwater explosion is found to be high through most of the bubble growth and collapse. Recalling that the Reynolds number is a ratio of inertial to viscous forces, it is clear that neglecting viscid terms in the conservation of momentum equation detracts very little from the problem solution. Furthermore, under the assumption that the fluid flow is inviscid and irrotational, the velocity field can be found from the gradient of a potential. In the case of a cavitation bubble similar assumptions were shown to be valid by Guerri, Lucca and Prosperetti.¹ and others.

The mathematical problem described above can be stated in the following form. The divergence of the velocity vector is zero for an incompressible fluid. This expression is found from the conservation of mass equation and can be written as:.

$$\nabla \cdot \underline{u} = 0 \quad (1)$$

For irrotational flow the curl of the velocity vector is zero and can be written as:

$$\nabla \times \underline{u} = 0 \quad (2)$$

The above expression is also satisfied when the velocity \underline{u} equals the gradient of a potential which is:

$$\underline{u} = \nabla \phi \quad (3)$$

Combining Equation (1) and (3) yields Laplace's equation. Laplace's equation is satisfied in the domain Ω occupied by the fluid and can be written in terms of the potential as:

$$\nabla^2 \phi = 0 \quad (4)$$

The boundary conditions necessary for the solution of Laplace's equation in the domain Ω can be stated as:

$$\frac{dx}{dt} = \nabla \phi \quad \text{on } S_b \quad (5)$$

$$\phi \rightarrow 0 \quad P \rightarrow P_\infty \quad \text{at } S_\infty \quad (6)$$

with

$$\frac{\partial \phi}{\partial n} = \nabla \phi \cdot \hat{n} = 0 \quad \text{on } S_b \quad (7)$$

where x is the distance to the boundary from a consistent point of reference.

The conservation of momentum, or Navier Stokes equation under the assumption of incompressible fluid and irrotational flow, can be written in the form:

$$\frac{D\underline{u}}{Dt} = -\frac{\nabla P}{\rho} + g \quad (8)$$

where $D\underline{u}$ represents the total derivative, P the pressure, ρ the density and g the gravity. Using the identity:

$$\underline{u} \cdot \nabla \underline{u} = \frac{\nabla u^2}{2} - \underline{u} \times \nabla \times \underline{u} \quad (9)$$

and the relations in Equations (2) and (3), the equation for conservation of momentum reduces to the form given by Euler²⁵ as:

$$\frac{\partial \phi}{\partial t} = \frac{u^2}{2} + \left(\frac{P_\infty - P_R}{\rho} \right) + gz \quad (10)$$

with P_R representing the pressure on the surface of the bubble and P_∞ the pressure at infinity. The pressure P_∞ , can be determined by the choice of a reference point. For example, if the point of reference at infinity is the free surface of the water, P_∞ = one atmosphere and z is the depth of the bubble segment. P_R can be found from the adiabatic pressure balance equation given by Cole²⁴ as:

$$P_R = 7.8 \left(\frac{W}{V} \right)^\gamma + \sigma \quad (11)$$

where W is the weight of the explosive in grams of TNT equivalent, V is the volume in centimeters cubed, and the pressure P_R is given in Kilobars. The σ term is added, to account for the effects of surface tension. For a cavitation bubble a similar adiabatic expression can be used.

The formulation strategy for the time integration of the equation of motion is straightforward. If the bubble surface S_b , internal pressure, and the value of the potential and its first derivative on the bubble surface are known, Equations (7) and (10) can be solved while marching through time. In order to solve for the potential's first derivative on the bubble surface, Laplace's equation, Equation (4), must be solved. This can be accomplished using the boundary conditions given in Equations (5), (6), and (7) and using a boundary integral method. The starting point of this solution to Laplace's equation makes use of Green's second identity which is:

$$\int_V \left(\phi \nabla^2 \psi - \psi \nabla^2 \phi \right) dV = \int_S \left(\phi \nabla \psi \cdot \hat{n} - \psi \nabla \phi \cdot \hat{n} \right) dS \quad (12)$$

with ψ being a function of choice. The dV represents an integral over the volume and the dS an integral over the surface. The most obvious choice for ψ is:

$$\psi = \frac{1}{|\underline{x} - \underline{x}|} \quad (13)$$

which is the solution of the Poisson's equation having the form:

$$\nabla^2 \psi = -4\pi \delta(\underline{x} - \underline{x}) \quad (14)$$

where \underline{x} and \underline{x} are the reference and current coordinates of the bubble surface (see Figure 3). The choice of Poisson's equation and the Dirac function are ideal because the remaining volume integral given on the left-hand side of Equation (12) reduces to a constant along each bubble segment.

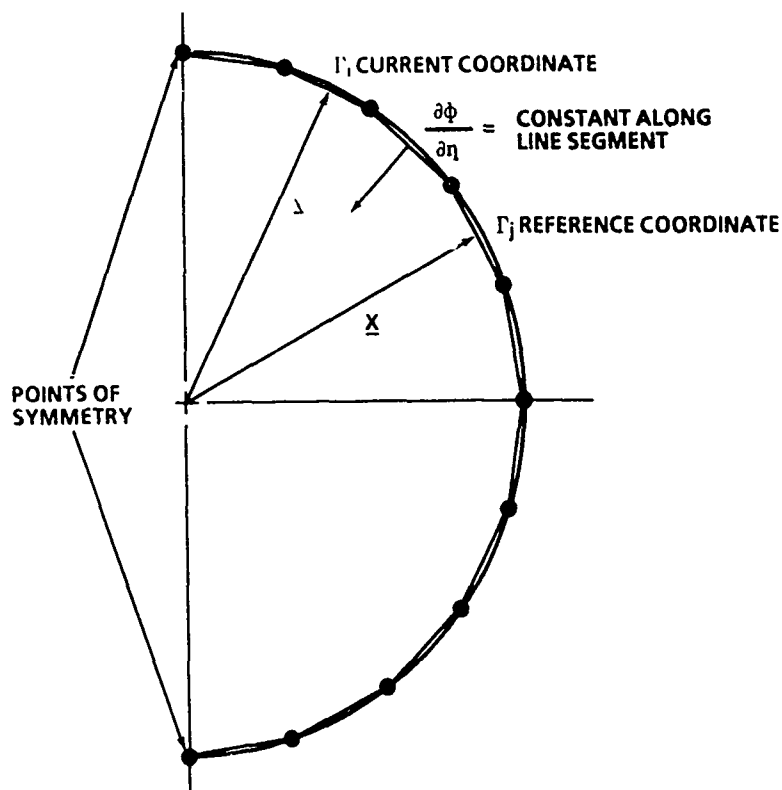


FIGURE 3. BUBBLE PARTITIONING

With the substitution of Equations (4), (13), and (14) into Equation (12), the formulation reduces to a surface integral with the following form:

$$2\pi\phi(\underline{X}) = \int_S \left[\phi \nabla \psi \cdot \hat{n} - \psi \nabla \phi \cdot \hat{n} \right] dS \quad (15)$$

The factor of 1/2 in the left hand-side of the integration in Equation (15) arises from the fact that the integration on the bubble boundary can only be carried out around half the point of reference which is the portion in the domain Ω .

Equation (15) applies to both three-dimensional developments and the present axisymmetric formulation. The three dimensional approach can be accomplished using first order and second order quadrilateral or triangular finite element techniques. The resulting integration would proceed in much the same way as in the axisymmetric case. However, the biggest difference in the three dimensional solution is

in the computation times required to solve problems. The computation time for the three-dimensional case would undoubtedly be an order of magnitude higher than the axisymmetric formulation. Therefore, the present axisymmetric formulation affords some basic advantages in the study of bubble jetting phenomenon. The real drawback is the inability of the present method to tackle more complex interactions of bubbles and various underwater objects such as cylindrical and spherical bodies in non-axisymmetric orientations.

The axisymmetric formulation begins by a suitable choice of coordinate systems. The choice of the cylindrical coordinate system for this case will reduce the integration around the bubble surface to an elliptic integral. Using cylindrical coordinates we can write the following:

$$\underline{x} = (r \cos \theta, r \sin \theta, \zeta) \quad (16)$$

for the reference coordinate system and,

$$\underline{x} = (R, 0, Z) \quad (17)$$

for our current coordinate system. Substitution of these cylindrical coordinates into Equation (15) and the rearrangement of terms reduced the integration to the following form:

$$\frac{1}{2\pi} \int_{\Gamma} r \frac{\partial \phi}{\partial n} \int_0^{2\pi} \frac{d\theta}{|\underline{x}-\underline{x}|} d\Gamma = \phi(\underline{x}) + \frac{1}{2\pi} \int_{\Gamma} r \frac{\partial}{\partial n} \int_0^{2\pi} \frac{d\theta}{|\underline{x}-\underline{x}|} d\Gamma \quad (18)$$

where $d\Gamma$ represents the integral on a surface element (see Figure 3) and θ the angle around the bubble circumference. The integral about $d\theta$ can be reduced to an elliptic integral of the first kind with a fair number of algebraic manipulations. The elliptical integral introduces a logarithmic term which is singular for the cases when the current coordinate and the reference coordinate coincide. The resulting singularity in the integration is bounded and occurs due to the use of the Dirac Delta function. An accurate calculation of this singularity will result in a more stable and accurate bubble model. After some experimentation with various expansions, a Gaussian quadrature with weight $\log(\xi)$ was found to give the best results.²⁶ The quadrature allowed the estimation of error within acceptable limits. The final form of the integration can be written as:

$$\frac{1}{2\pi} \frac{\partial \phi}{\partial n} \int_{\Gamma} G(\underline{x}, \underline{x}) d\Gamma = \phi(\underline{x}) + \frac{1}{2\pi} \phi(\underline{x}) \int_{\Gamma} H(\underline{x}, \underline{x}) d\Gamma \quad (19)$$

where $G(\underline{x}, \underline{x})$ and $H(\underline{x}, \underline{x})$ are functions of the reference and current coordinates and an elliptic integral. Using a straight line approximation for the axisymmetric bubble boundary (see Figure 3), the gradient of the potential can be found using the following matrix expression by a Gaussian elimination routine. The basic expression is:

$$\sum_{j=1}^n a_{ij} \omega_j = b_i \quad i = 1, 2, 3 \dots n \quad (20)$$

where

$$a_{ij} = \frac{1}{2\pi} \int_{\Gamma_j} G(\underline{x}_j, \underline{x}_i) d\Gamma_j \quad (21)$$

$$b_i = \phi(\underline{x}_i) + \sum_{j=1}^n \phi(\underline{x}_j) \frac{1}{2\pi} \int_{\Gamma_j} H(\underline{x}_j, \underline{x}_i) d\Gamma_j \quad (22)$$

and

$$\omega_j = \frac{\partial \phi}{\partial n} = \text{const.} \quad (23)$$

The solution for $\partial \phi / \partial n$ can now be applied to the conservation of momentum equation and marched through time. The updating of line segments and the momentum equation given in Equation (7) is accomplished with a finite difference time integration scheme and linear interpolation between the nodes. The first-order form of the finite difference formula is:

$$\phi_{i+1} = \phi_i + \left[\frac{u^2}{2} + \left(\frac{P_\infty - P_R}{\rho} \right) + gz \right] \Delta t \quad (24)$$

However, higher order formulations, depending on multiple values of the potential, are used after the initial time step. A similar expression is used to update the geometry. These higher order formulations do not increase computation time significantly. The majority of the computation time needed in the calculation is spent doing the integrations in Equation (19) and assembling and solving the matrix formulation given in Equation (20). Therefore, the contributing factors influencing computation time are the number of segments and the number of time steps. The number of line segments determines the total number of integrations in a time step and also the size of the matrix (Equation (20)) that must be solved. For the free field cases, 32 line segments were found to be sufficient. However, in the cases involving the free surface or a solid surface, 84 line segments were used. No attempt to optimize the method was made in the present study. Contrarily, the affects of time step size was investigated. In the free field cases any time step less than $1/450^{\text{th}}$ of the total bubble period was found to cause problems at the beginning and at the end of the bubble period. This is probably due to the relative speed of the individual line segments during these phases of the bubble oscillation period. A formulation involving a variable sized time step dependent on the highest speed of a segment would probably result in greatly reduced computation times. For the present, the author's primary concern was with the validation and accuracy of the methodology and exploring the limitations of this formulation. Consequently, a $1/1000^{\text{th}}$ of the bubble total period was used in all cases examined. The bubble period was estimated using standard empirical rules²⁷ for underwater explosive detonations.

RESULTS

The validation of this methodology was initiated by attempting to solve simplistic problems. The problems were gradually changed to include more complex phenomenon such as bubble interactions with the free surface and solid bodies. The problems and limitations are discussed with some possible solutions extending the method. What follows is a discussion of various problem types, the limitations of the current approach, and possible advantages in the present methodology.

The starting point of the validation was a comparison of the boundary integral method to the exact solution for a spherically symmetric bubble model. The conservation of momentum equation given in Equation (10) was modified to exclude gravity. With gravity removed and in the absence of other bodies, the solution technique should duplicate the exact formulation for a spherically symmetric model. The conservation of momentum equation under spherical symmetry and the conservation of mass equation can be integrated to yield:

$$\dot{R}^2 = \left(\frac{R_o}{R}\right)^3 \dot{R}_o^2 + \left(\frac{2}{3}\right) \left(\frac{P_R - P_\infty}{\rho}\right) \left[1 - \left(\frac{R_o}{R}\right)^3\right] \quad (25)$$

where, \dot{R} represents the current velocity of the bubble surface, R the current radius, and P_R , P_∞ , and ρ (as given in Section 2), are the internal bubble pressure, reference pressure and fluid density. The subscript o represents the referenced values. Using the boundary integral method for R , R_o , and \dot{R}_o , the estimated value for \dot{R} was compared to the exact solution given by Equation (25). In both bubble expansion and bubble contraction, the boundary integral method approached the exact solution, or the limit of the methods accuracy. The accuracy of the method appeared to improve with time. This is caused by the potential's initial condition being assumed zero. Therefore, the method requires a number of steps to calculate a reasonable value for the potential. Furthermore, this assumption is particularly good in the case of an underwater explosion where the internal pressure is large by comparison to the external pressure. The result is that the early bubble motion is dominated by the large pressure differential thus allowing the method to retain good overall accuracy under the zero initial potential assumption. This accuracy is shown for both a first order finite difference integrator and a second-order time integrator in Tables 1 and 2, respectively.

The convergence seen in Tables 1 and 2 occur for two reasons. First, the assumption allowing the potential to be zero initially will require a few time steps to achieve a reasonable level of equilibrium. This error will decrease rapidly at first then only gradually thereafter. The second reason for continued convergence is, the constant reduction in pressure difference as the bubble volume grows. This reduction in pressure difference results in a decrease in the radial velocity of the bubble. Slower velocities under a constant time step attribute to increased convergence. In order to estimate the effects of bubble radial velocity on convergence the method was used with a constant time step under constant pressure. The constant

TABLE 1. BUBBLE EXACT VS CALCULATED VARIABLE PRESSURE (FIRST-ORDER TIME INTEGRATION)			
TIME STEP	RADIAL VELOCITY		ERROR
	EXACT	CALCULATED	
10	51.24	53.10	3.6%
20	33.68	33.77	.25%
30	25.42	25.37	.19%
40	8.19	8.18	-

TABLE 2. BUBBLE EXACT VS CALCULATED VARIABLE PRESSURE (SECOND-ORDER TIME INTEGRATION)			
TIME STEP	RADIAL VELOCITY		ERROR
	EXACT	CALCULATED	
10	58.04	56.67	2.4%
20	34.93	34.94	.02%
30	25.97	25.97	-

pressure will result in a constantly increasing radial velocity. This should allow an estimation of the error attributed to time step size versus bubble radial velocity. The results are summarized in Tables 3 and 4.

The results showed that for a constant time step of .01 and velocities sufficiently low, the convergence and accuracy were quite reasonable. However, if the bubble was allowed to iterate long enough or the pressure differential was increased, the convergence reached a minimum and then began to grow in accordance with bubble radial velocity. By comparing Tables 1 and 2 to Tables 3 and 4, the velocity versus time step effect on error can be seen. In Tables 1 and 2 the time step used was .001 for velocities of order 10^2 , while Tables 3 and 4 have a time step of .01 for speeds of order 10^0 . As expected Tables 3 and 4, which have a smaller velocity versus time step ratio, converge faster to a reasonable error. In as much as the solutions converged to reasonable values in both cases, it indicated that the initial conditions resulted in a reasonable cumulative error. The issue of time step size seems to be the most crucial aspect in keeping the cumulative error to a minimum. This became particularly important for bubble jetting where the velocities can be as high as a thousand feet per second for the bubble segments near the nose of the re-entrant jet tip. These high velocities lead to numerical instabilities which would stop the analysis. Therefore, the bubble maximum velocities were compared to the bubble period so that a rule of thumb could be developed for the time step. It was found that a time step of $1/1000^{\text{th}}$ of the bubble period would give reasonable results in all cases investigated. A further analysis of the time step could lead to a variable step size dependent on only the maximum speed of the fastest bubble segment. However no attempt to find a suitable ratio of time step to segment velocity has been made.

The second phase of the validation was to compare bubble periods and maximum bubble radius to experimental results. A report from the Gas Globe²⁷ by Swift and Decius offered data for an abundant variety of explosive sizes and depths to be evaluated. A number of the shots presented in the Swift report were selected at random and compared to the solution technique presented in this paper. The results are presented in Tables 5 and 6. The results generated in Table 5 are of greater importance because the methods used to record bubble period are more accurate than maximum bubble radius data. The accuracy stems from the use of piezo-electric gauges which can record the pressure waves emitted initially and with each successive bubble pulse. The initial shock wave indicated the beginning of the period and the first bubble pulse, which occurs just after bubble minimum, indicates the end of the period. Due to the high speed of sound in water the method gives very accurate results. For the data compared in Table 5, the analytical method gives reasonable results.

On the contrary, the maximum bubble radii data for the Swift report was not as accurate. These data were obtained from measurements taken from simultaneous photographic records. As the authors of the Gas Globe report pointed out, the relative narrow angle of view from the high-speed cameras and the problems with distortion and lighting made it difficult to make bubble radii measurements better than 2-4 percent. Further, depth measurements were obtained from a weighted line which could vary slightly due to ocean currents. These factors are believed to have contributed to the diminished

TABLE 3. BUBBLE EXACT VS CALCULATED CONSTANT PRESSURE (FIRST-ORDER TIME INTEGRATION)			
TIME STEP	RADIAL VELOCITY		ERROR
	EXACT	CALCULATED	
10	.09091	.09036	.60%
20	.1944	.1943	.046%
30	.3067	.3066	.012%

TABLE4. EXACT VS CALCULATED CONSTANT PRESSURE (SECOND-ORDER TIME INTEGRATION)			
TIME STEP	RADIAL VELOCITY		ERROR
	EXACT	CALCULATED	
10	.0999	.1004	.48%
20	.2048	.2047	.06%
30	.3177	.3177	-

TABLE 5. BUBBLE PERIOD
(CALCULATED VS EXPERIMENT)

SHOT NUMBER	CHARGE WEIGHT POUNDS	CHARGE DEPTH FEET	PERIOD MILLI- SECONDS	CALCULATED MILLI- SECONDS	ERROR PERCENT
G1F	.651	343.	27.40	26.40	1.9%
G2F	.660	304.	29.80	29.76	.13%
G5F	.662	305.	29.89	29.70	.64%
G6F	.658	304.	29.92	29.73	.64%
G7F	.669	298.	30.23	30.39	.50%
G8F	.663	304.	29.82	29.80	0.0%
G9F	.651	304.	29.64	29.62	0.0%
G17F	.660	305.	29.62	29.68	.20%
G18F	.660	302.	29.61	29.92	1.0%
G20F	.660	538.	19.64	18.90	3.7%
G21F	.651	539.	19.10	17.50	9.0%
G23F	.658	567.	18.14	18.30	.88%
G70F	.660	503.	19.90	20.00	.50%
G71F	.658	463.	21.00	21.40	1.90%
G72F	.660	586.	17.85	17.80	.30%
G73F	.655	576.	18.16	18.00	.90%
G74F	.660	556.	18.10	18.60	2.80%
G76F	.660	587.	17.10	17.38	.30%
AVERAGE					1.0%

TABLE 6. BUBBLE MAXIMUM RADIUS

(CALCULATED VS EXPERIMENT)

SHOT NUMBER	CHARGE WEIGHT POUNDS	CHARGE DEPTH FEET	MAXIMUM RADIUS INCHES	CALCULATED RADIUS INCHES	ERROR PERCENT
G1F	.651	343.	-	17.0	-
G2F	.660	304.	18.80	18.49	1.68%
G5F	.662	305.	18.80	18.48	1.70%
G6F	.658	304.	18.80	18.47	1.80%
G7F	.669	298.	18.90	18.70	1.0%
G8F	.663	304.	18.90	18.52	2.1%
G9F	.651	304.	18.70	18.40	1.6%
G17F	.660	305.	19.40	18.46	5.1%
G18F	.660	302.	19.40	18.53	4.7%
G20F	.660	538.	15.90	15.00	6.0%
G21F	.651	539.	15.70	14.40	9.0%
G23F	.658	567.	15.61	14.70	6.3%
G70F	.660	503.	-	15.35	-
G71F	.658	463.	16.60	15.80	4.9%
G72F	.660	586.	15.40	14.50	6.0%
G73F	.655	576.	15.60	14.60	7.0%
G74F	.660	556.	15.70	14.80	6.0%
G76F	.660	587.	15.10	14.50	3.9%

AVERAGE 4.0%

accuracy in the bubble radii comparisons shown in Table 6. Shot number G21F is considered to be a bad data point which was included in the interest of consistency.

The accuracy of the method was summarized by making a number of radius versus time plots in comparing computational values to those found in the Swift report.²⁵ These plots are given in figures 4 through 9. The plots follow the growth and decay profiles of the bubble first period quite well. These plots represent results generated by tests involving a number of charge weights at varying depths.

The deviations of values obtained from theory found in these figures is approximately of the same magnitude as the errors given in Tables 5 and 6. For deeper shots, a larger error occurs with the radius calculations. This is believed to be caused by a number of factors. As pointed out earlier, the experimental data is not as accurate for radius calculations as it is for the bubble period. Further, the initial conditions seem to play an important role in maximum bubble radius calculations. When the initial radius was decreased, the radius estimates improved. This is due to the increase in hydrostatic pressure at increased depths and the effect it plays on the overall pressure difference. Additionally, the effects of bubble radius calculations are less forgiving for smaller charges than larger ones. However, in the interest of consistency, all results calculated in this paper represent the same initial conditions for internal bubble pressure and the potential on the surface.

All of the data compared thus far represents relatively small charges. Therefore, bubble periods for 300-pound charge detonated at shallow depths are compared to results presented in Cole.²⁴ Figure 10 compares the observed periods in Cole versus those predicted by theory. These calculations include the effects of a free surface in the flow field. For the shallower depths, Figures 11 through 14 show the growth and collapse of the bubble surface and the effects of the free surface.

When the bubble is closer to the free surface, the effects of the free surface become more evident. This can be seen in Figures 11 through 13 in terms of bubble migration. The migration is retarded due to its close proximity to the free surface. Figure 14 represents a fictitious scenario. The bubble, in this case would have undoubtedly broken through the free surface, venting its high pressure gases. It was not surprising that the calculation for this case became unstable and terminated the calculation. Therefore, understanding the limitations of the method are important in interpreting the validity of the results. For a bubble at deeper depths, the bubble behavior becomes less influenced by the free surface. At depths greater than 100 feet, for the 300-pound explosive, the bubble profile becomes indistinguishable from the free field profile for a similar calculation.

In order to estimate the accuracy of the method for predicting reentrant water jet tip velocities, a calculation was compared with a PISCES code calculation. The PISCES code has been used for a number of calculations with regard to underwater explosion bubble and is considered reasonably accurate. The comparison for peak re-entrant jet velocities was made between the present method and PISCES. If the boundary integral method presented was valid, it was felt that the two methods should present similar results. As it turned out the exact

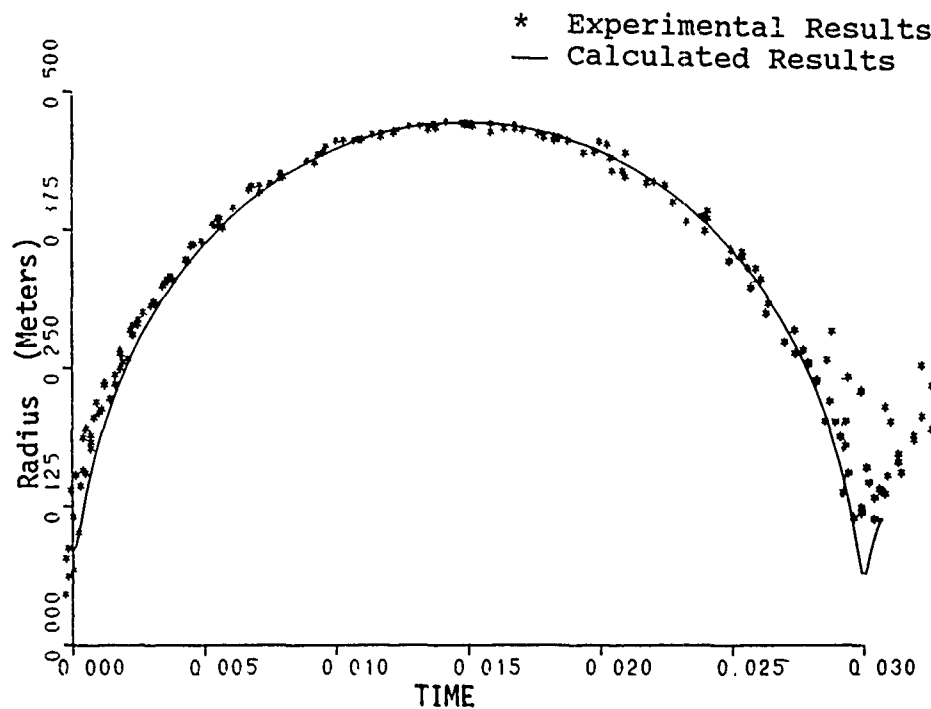


FIGURE 4. BUBBLE RADIUS VS TIME PLOT
(.66 lb TNT 300 ft)

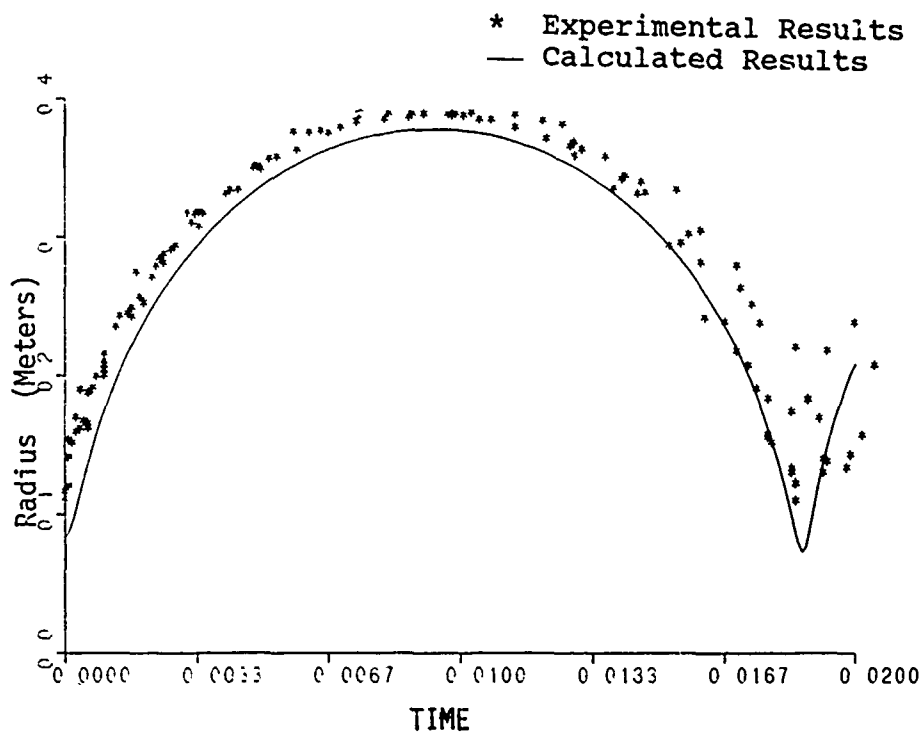


FIGURE 5. BUBBLE RADIUS VS TIME PLOT
(.66 lb TNT 550 ft)

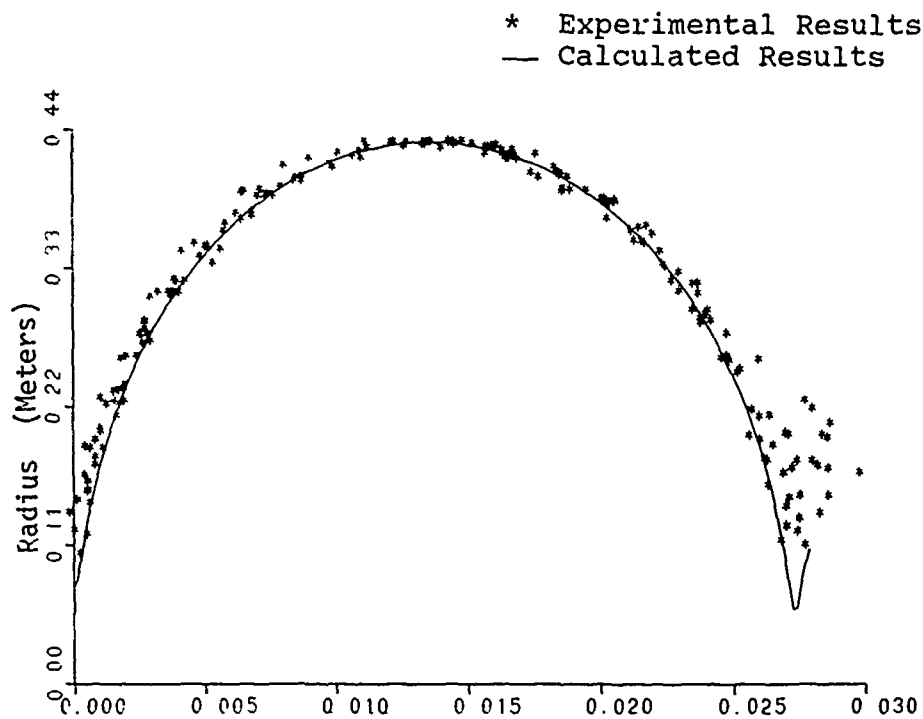


FIGURE 6. BUBBLE RADIUS VS TIME PLOT
(.5 lb TNT 300 ft)

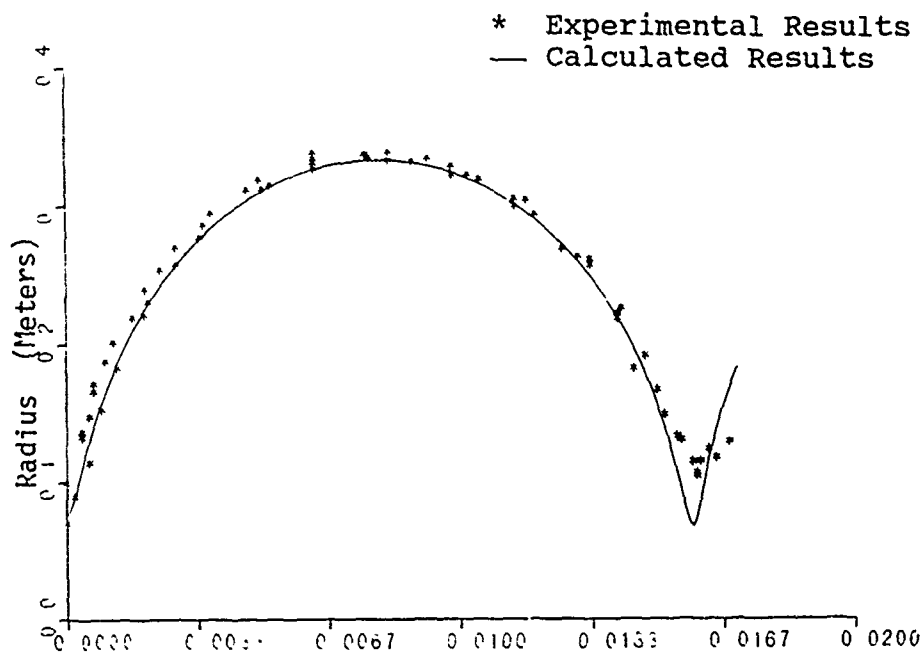


FIGURE 7. BUBBLE RADIUS VS TIME PLOT
(.5 lb TNT 600 ft)

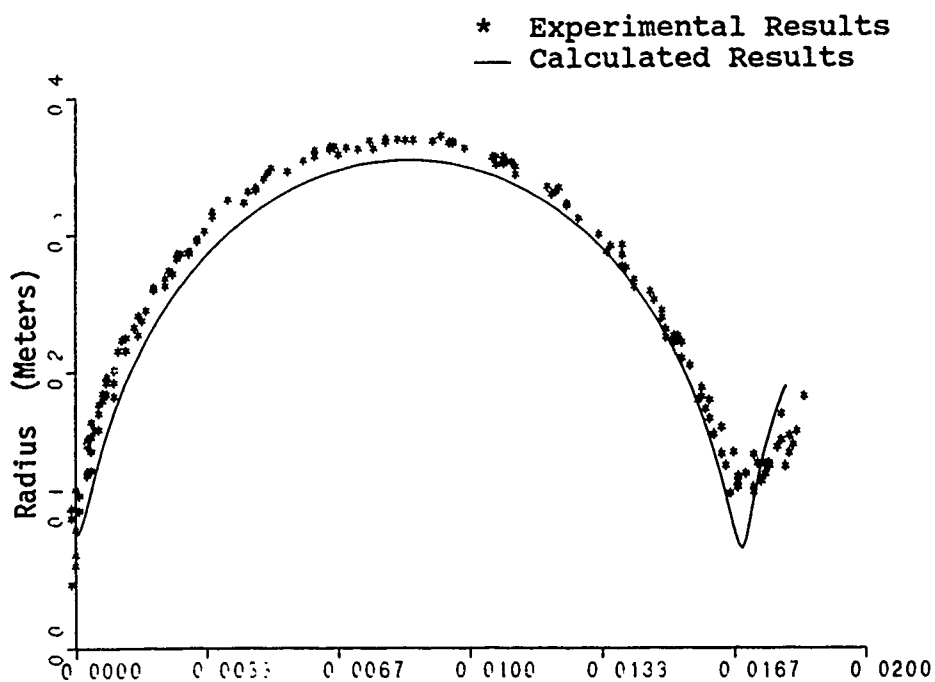


FIGURE 8. BUBBLE RADIUS VS TIME PLOT
(.6 lb TNT 600 ft)

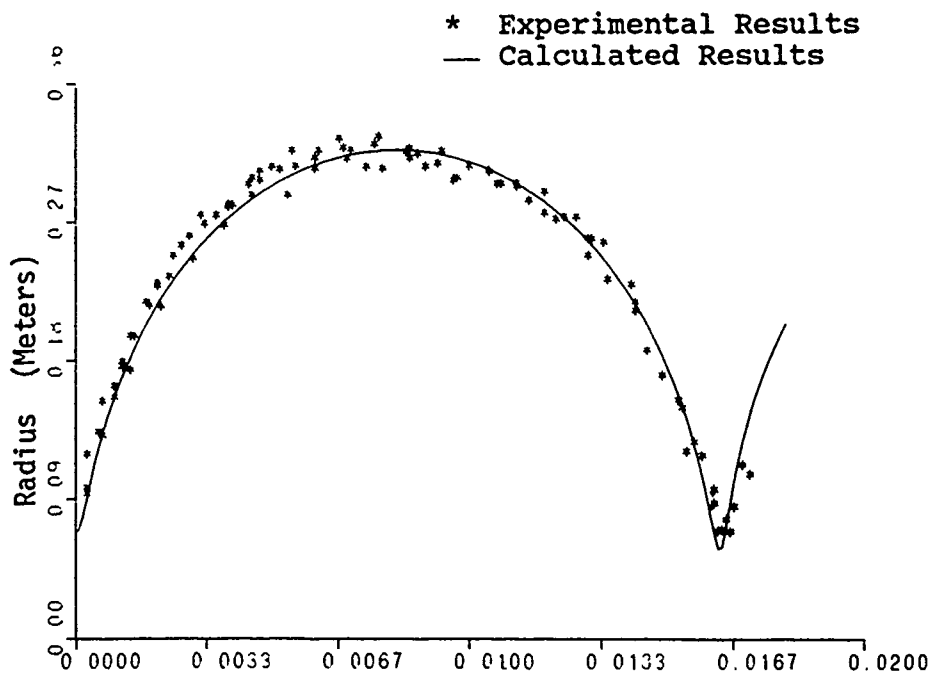


FIGURE 9. BUBBLE RADIUS VS TIME PLOT
(.353 lb TNT 500 ft)

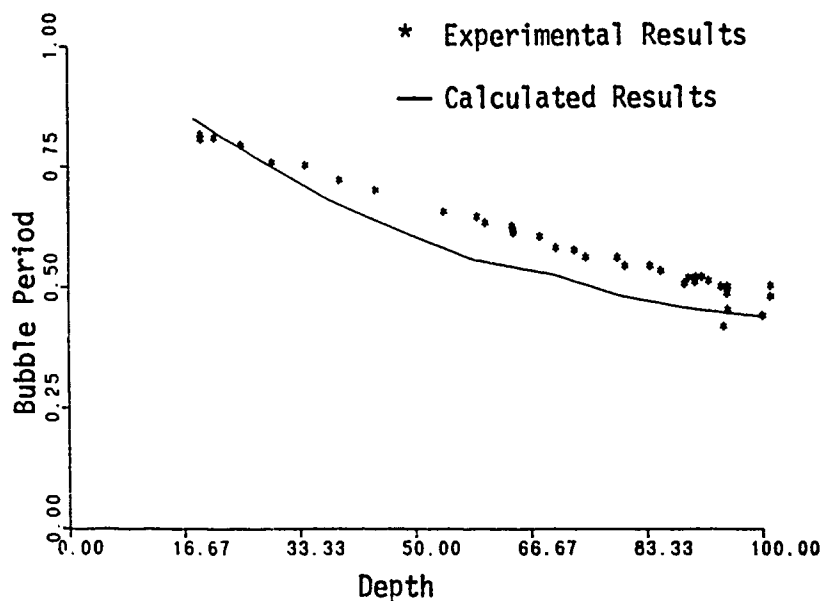


Figure 10. DEPTH VS PERIOD DATA (300 lb)

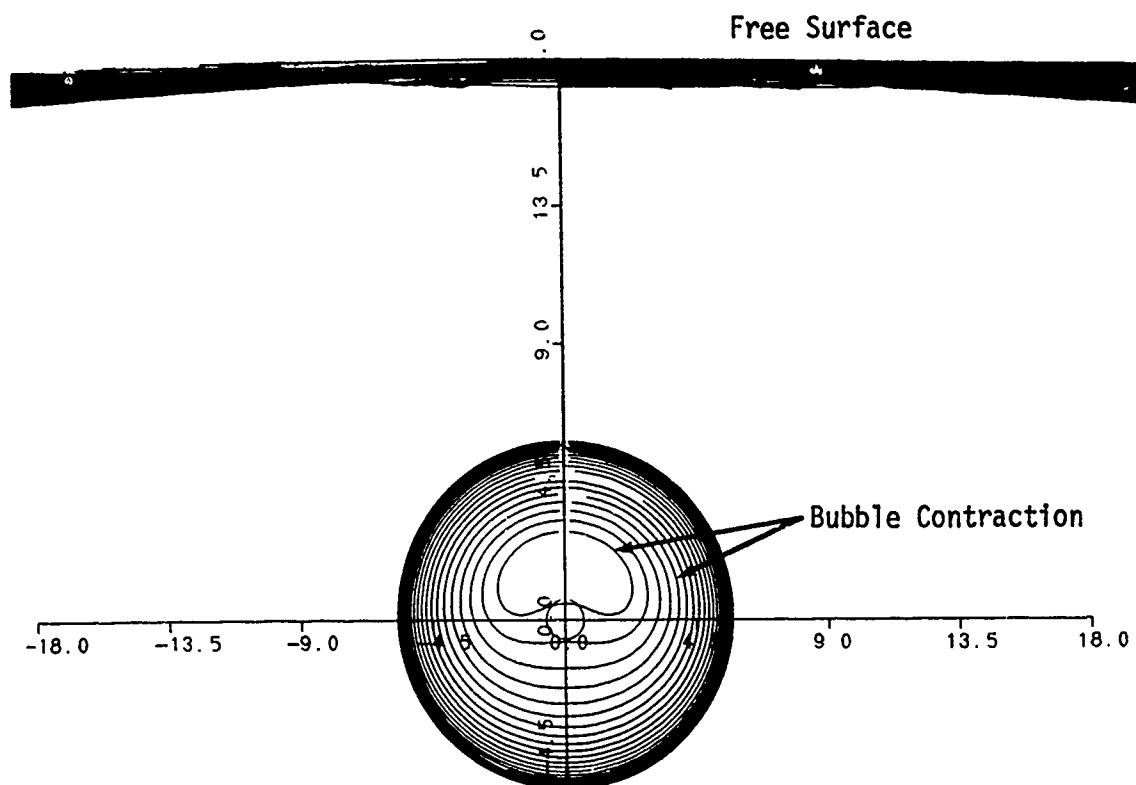


FIGURE 11. BUBBLE PROFILES (300 lb TNT at 18 m)

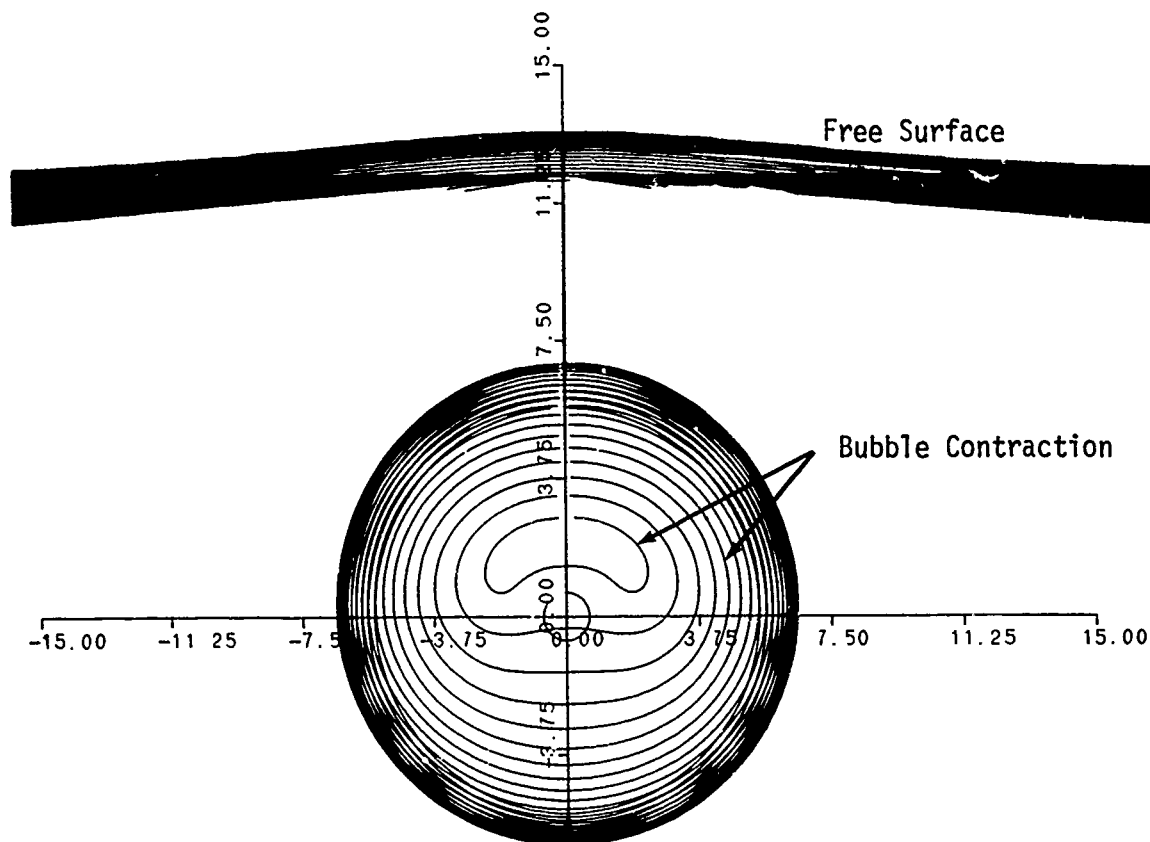


FIGURE 12. BUBBLE PROFILES (300 lb TNT at 12 m)

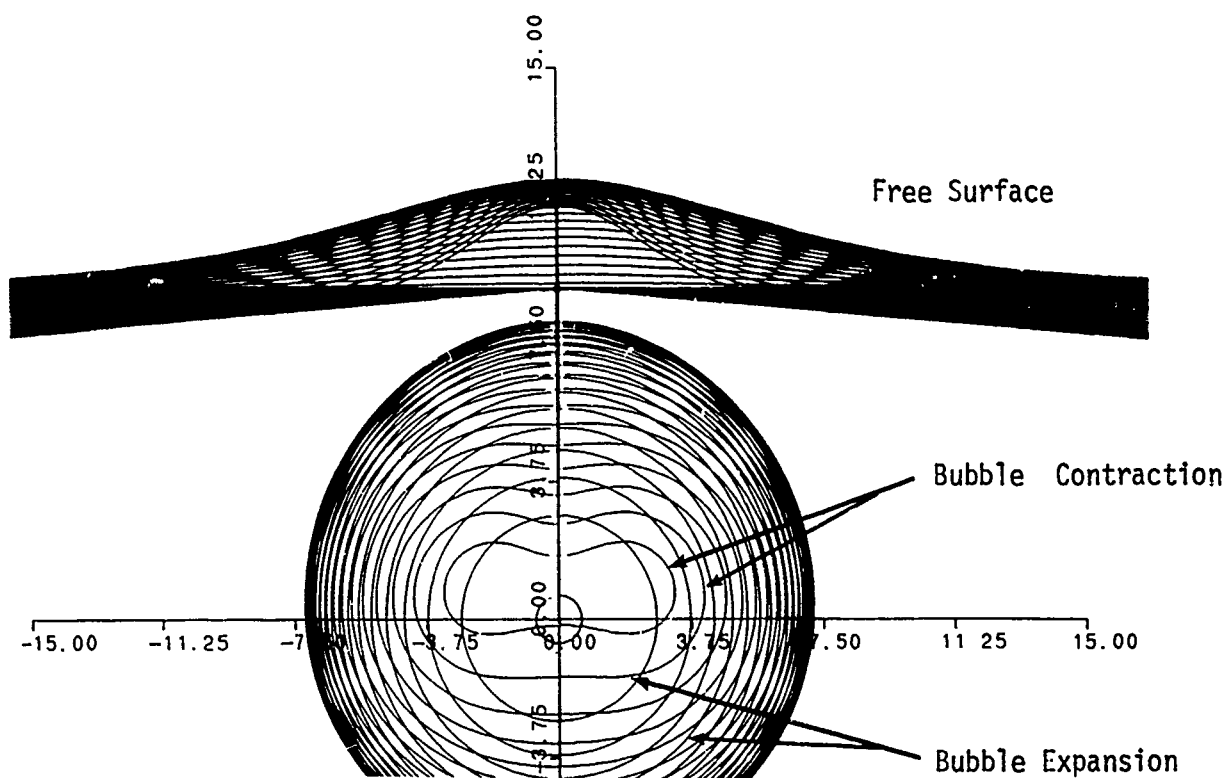


FIGURE 13. BUBBLE PROFILES (300 lb TNT at 9 m)

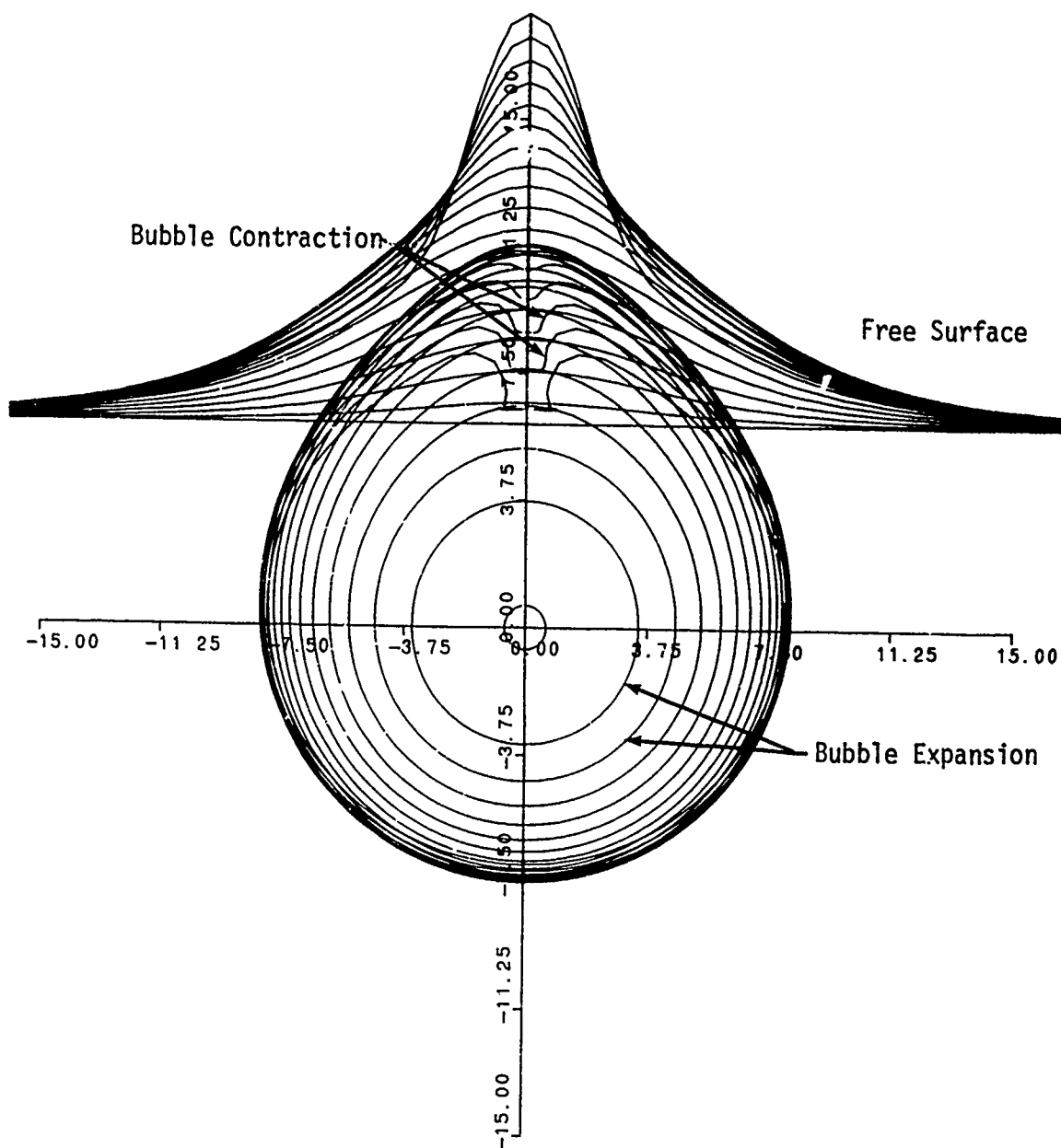


FIGURE 14. BUBBLE PROFILES (300 lb TNT at 6 m)

time and location of the peak jet velocities varied slightly between the two methods. For the PISCES calculation the peak velocity occurred just behind the bubble surface and was found to be 1148 feet per second. A line estimating the location of the bubble surface, with regard to peak velocity, is shown in Figure 15. Since an Euler method has been used in the PISCES calculation, the interface between different materials is not exactly defined. However, an estimated profile is shown in figure 16. For the incompressible flow calculation, the maximums and minimums for the potential must occur on the boundary in order to satisfy the uniqueness of Laplace's equation. The highest velocity recorded in the calculation occurred just as the bubble lower surface broke through the bubble upper surface. This is shown in Figure 17. A dotted line estimating the intersection of the two results is shown in Figure 15. The results indicate a reasonable correlation between the two methods. However, a more accurate estimation of the error can only be made through direct comparison with experimental results which are presently unavailable.

A final calculation was performed for an explosion bubble near a solid boundary. The results showing the collapse and upward migration toward the solid boundary are summarized in figure 18. For this calculation a 300-pound charge of TNT was detonated 12 meters below the solid surface at a water depth of 12 meters. It is interesting to note the similarities and differences between the free surface calculation of the same weight and depth in Figure 12 and this case. The expansion and overall period of the bubble growth are not disproportionately in disagreement. However, as expected, the solid boundary increases migration toward the boundary while having little effect on the formation of a bubble jet. On the other hand, the free surface condition led to decreased migration and a retardation of bubble jet formation. In general, the free surface condition can lead to bubble blow out where the bubble vents through the free surface, bubble downward migration at certain distances from the free surface, and the denial of bubble jetting. Therefore, it is clear that a nearby structure or solid boundary can lead to bubble jetting into the structure even when near the free surface.

SUMMARY

The boundary integral method can be used for the prediction of bubble behavior in a variety of scenarios. While the present study offers only limited results, the method shows promise for future, more in-depth studies. The method shows good agreement with other analytical prediction techniques as well as a variety of experimental data. This report offers the only example of such comparisons that I could find in the literature. The program developed also offers a number of improvements which include efficient programming (under 350 lines of code), and an accurate method for the calculation of the singularity in the problem. This approach allows the analytical study of bubble pulsation and jetting behavior in coordination with experimentation. Future studies of this nature should include the three dimensional aspects of bubble collapse, thus bringing the method to its full potential.

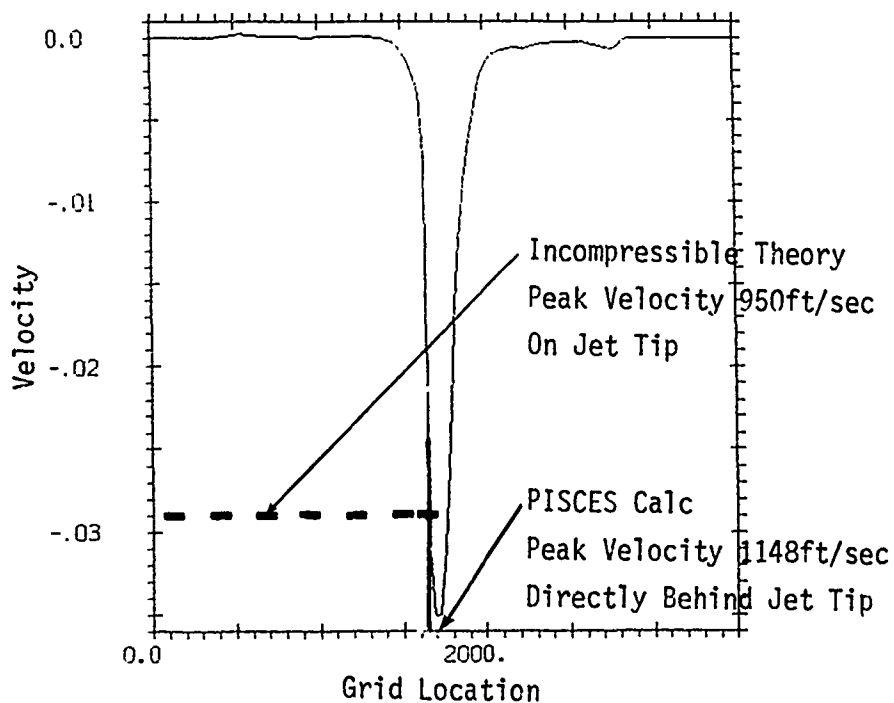


FIGURE 15. PISCES CALCULATION FOR PEAK FLUID VELOCITY
(1200 lb TNT 400ft Depth)

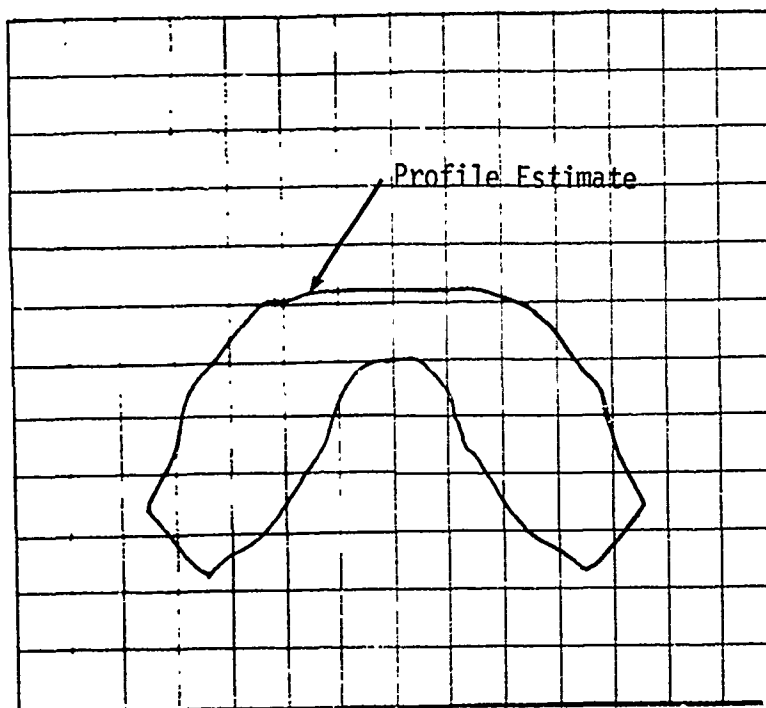


FIGURE 16. PISCES CALCULATION FOR BUBBLE PROFILE
(1200 lb TNT 400ft Depth)

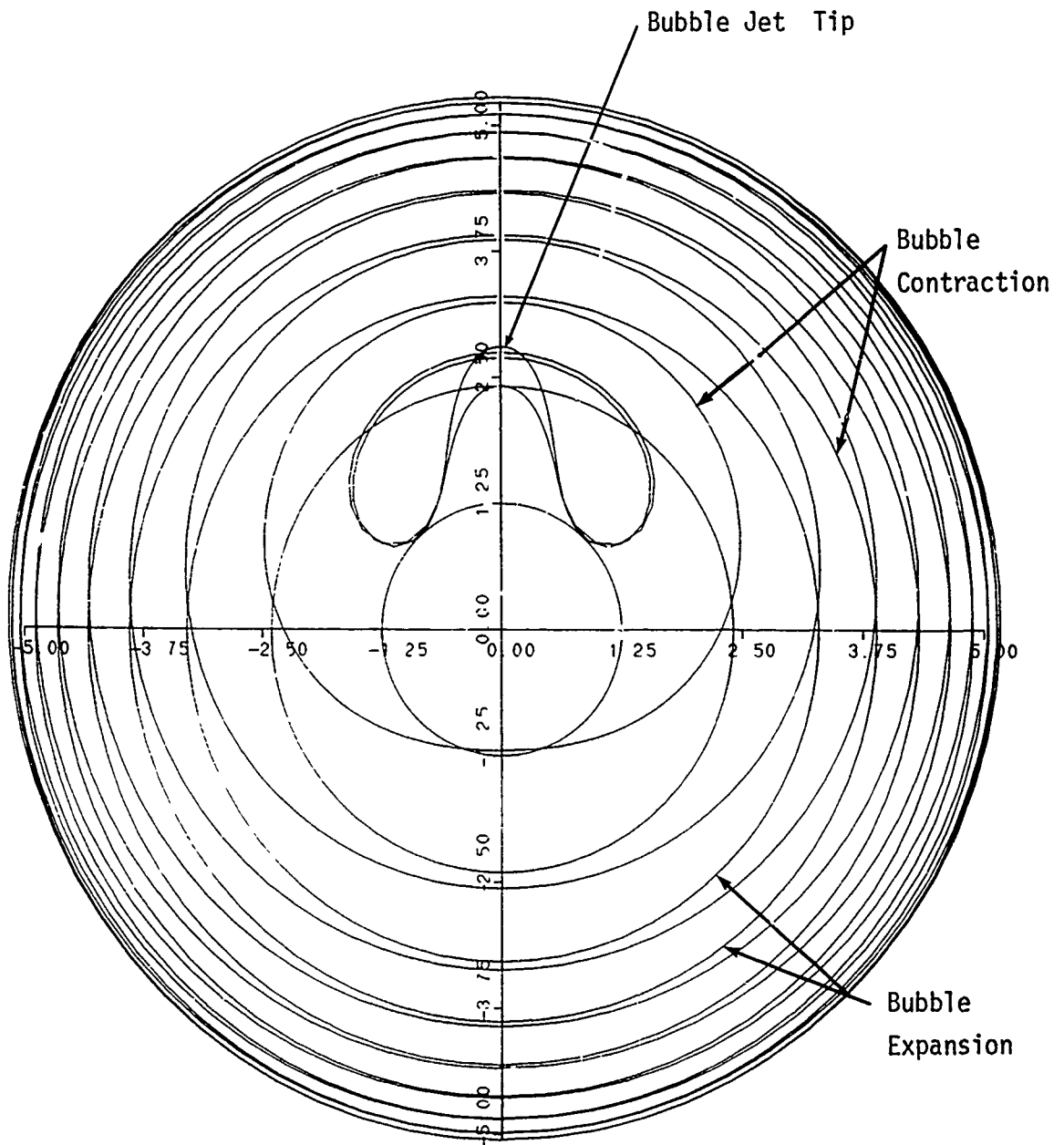


FIGURE 17. INCOMPRESSIBLE FLOW THEORY FOR BUBBLE PROFILE
(1200 lb TNT 400ft Depth)

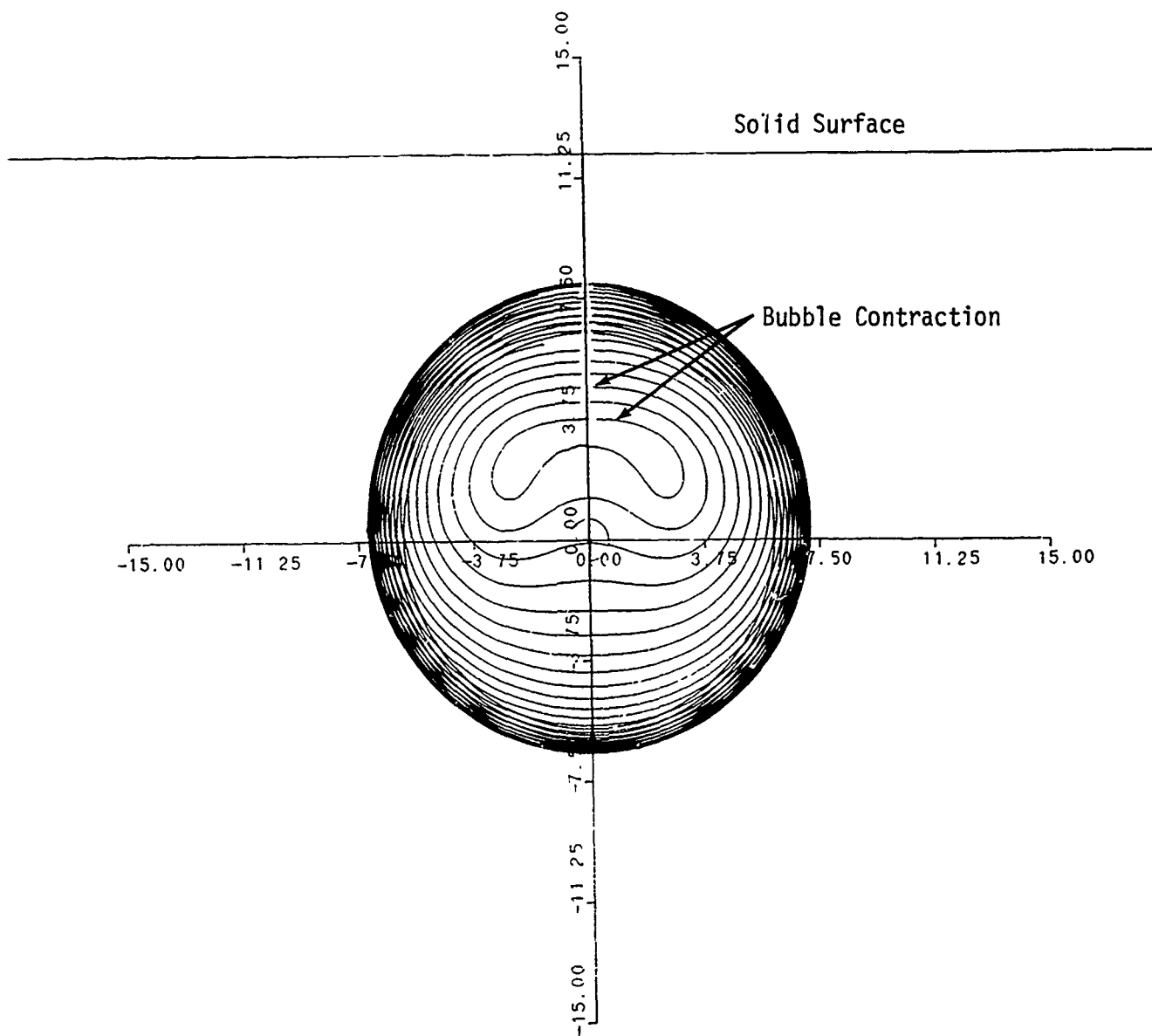


FIGURE 18. SOLID BOUNDARY CALCULATION (300 lb TNT 12 m)

In summary, the methodology presented was simple to use, computationally efficient and reasonably accurate. The overall cost and reliability of the method may prove a valuable aid in guiding and analyzing experimentation.

ACKNOWLEDGMENT

This work was sponsored under the auspices of the Naval Surface Warfare Center's long term study program. This program allows employees the opportunity of continued academic study for the period of 1 year. The study was conducted during the summer and fall of 1987 under the aforementioned program. The purpose of this study was to develop an analytical approach for the prediction of underwater bubble collapse and its interaction with the free surface, or a solid surface. The report describes the solutions for axisymmetric problems. The approach is shown in good agreement with available experimental data, and other analytical approaches.

The author gratefully acknowledges the advice, patience and expertise of Dr. A. Prosperetti of the Department of Mechanics, the Johns Hopkins University who provided the technical foundation for this work. The author also gratefully acknowledges the efforts of Mr. K. Kiddy who provided the PISCES analysis included in this work.

REFERENCES

1. Guerri, L., Lucca, G., and Prosperetti, A., "A Numerical Method for the Dynamics of Non-Spherical Cavitation Bubbles," JPL, Vol. 82-7 1982. pp. 175-181
2. Prosperetti, A., "Bubble Dynamics: A Review and Some Recent Results," Applied Scientific Research, Vol. 38 1982. pp. 145-164
3. Prosperetti, A., and Jones, A. U., "pressure Forces in Dispersed Two-Phase Flow," J. Multiphase Flow, Vol. 10 NO. 4, 1984. pp. 425-444
4. Prosperetti, A., "A Generalization of the Rayleigh Plesset Equation of Bubble Dynamics," Phys. Fluids, Vol. 25 No 3 Mar 1982. pp. 409-410
5. Prosperetti, A., "Bubble Phenomena in Sound Fields, Part Two," Ultrasonics, May 1984. pp. 115-125
6. Prosperetti, A., "Physics of Acoustic Cavitation," Frontiers in Physical Acoustics, 1986. pp. 145-188
7. Prosperetti, A., Lezzi A., "Bubble Dynamics in a Compressible Liquid, Part 1. First Order Theory," J. Fluid Mechanics, Vol. 168 1986. pp. 457-478
8. Lezzi, A., Prosperetti, A., "Bubble Dynamics in a Compressible Liquid, Part 2. Second Order Theory," J. Fluid Mechanics, Vol. 185 1987. pp 289-321

9. Prosperetti, A., Crum, L. A., Commander, K. W., "Nonlinear Bubble Dynamics," J. Acoust. Soc. Am 83 (2), Feb 1983.
10. Prosperetti, A., "The Equation of Bubble Dynamics in a Compressible Liquid," Phy Fluids, Vol. 30 No.11, 1987.
pp. 3626-3628
11. Chahine, G. L., Sivian, C. R., "Collapse of a simulated Multibubble System," ASME, Cavitation and Multiphase Flow Form, Albuquerque, New Mexico, 1985.
12. Chahine, C. L., Genoux, Ph.F., and Liu, H. L., "Flow Visulation and Numerical Simulation of Cavitating Self Oscillating Jets," 7th International Symposium on Jet Cutting Technology, 26-28 Jun 1984.
Paper A2,
pp. 13-32
13. Genoux, Ph.F., Chahine, C. L., "Collapse of a Toroidal Bubble Near a Solid Wall," ASME Cavitation and Multiphase Flow Form, New Orleans, Louisiana, 1984. pp. 69-72
14. Chahine, G. L., Bovis A. G., "Pressure Field Gererated by Non-Spherical Bubble Collapse," Journal of Fluid Engineering 105 No. 3, Sep 1983. pp. 356-364
15. Chahine, G. L., Genoux, Ph.F., "Collapse of a Cavitating Vortex Ring," Journal of Fluids Engineering, Vol. 105, Dec 1983. pp.400-405
16. Chahine, G. L., "Experimental and Asymptotic Study of Non Spherical Bubble Collapse," Applied Scientific Research Vol. 38 1982. pp. 187-197
17. Chahine G. L. "Interaction Between an Oscillating Bubble and a Free Surface," ASME Publication 77-FE-6 pp. 2-11
18. Johnson et al. V. E. Jr., "Cavitation and Structured Jets for Mechanical Bits to increase Drilling Rates," ASME Publication 82-Pet-13.
19. Taib, B. B., "Boundary Integral Method Applied to Cavitation Bubble Dynamics," Ph.D. Thesis, University of Wollongong, Australia., 1985.
20. Blake, J. R. and Gibson, D. C. "Growth and Collapse of a Vapor Cavity Near a Free Surface," J. Fluid Mechechanics, Vol 111 1981. pp. 123-140
21. Blake, J. R., Taib, B. B. and Doherty, G. "Transient Cavities Near Boundaries. Part 1. Rigid Boundary," J. Fluid Mechechanics, Vol 170 1986. pp. 479-497
22. Chapman, R. B. and Plesset, M. S., "Non-Linear Effects in the Collapse of a Nearly Spherical Cavity in a Liquid," Transactions of the ASME Mar 1972. pp. 142-146

23. Chapman, R. B. and Plesset, M. S., "Thermal Effects in the Free Oscillations of Gas Bubbles," Office of Naval Research, Report No. 85-50 Jun 1970.
24. Cole, R. H., Underwater Explosions, Princeton University Press, New Jersey, 1948.
25. Landau, L. D., and Lifshitz, E. M., Fluid Mechanics, Pergamon Press, Addison-Wesely Publishing Company, Inc., 1959.
26. Wilkerson S. A. A Method for the Calculation of Abscissas and Weight Factors Using Gaussian Integration for Integrands with a Logarithmic Singularity, NSWC TR 87-372, 20 Nov 1987
27. Swift, Jr., E. and Decius, J. C., "Measurement of Bubble Pulse Phenomena, III Radius and Period Studies," The Gas Globe, Underwater Explosions Research, Vol II , ONR, 1950.

DYNAMIC ANALYSIS

MODELING OF VIBRATION TRANSMISSION IN A DAMPED BEAM STRUCTURE USING STATISTICAL ENERGY ANALYSIS

S. S. Sattinger
Westinghouse Research and Development Center
Mechanics Department
Pittsburgh, PA 15235

Statistical energy analysis (SEA) methods provide means for predicting vibration transmission in systems where there are too many modes to examine individually over the frequency range of interest. In this paper, calculations are compared with L-beam tests that were performed to verify SEA vibration transmission modeling approaches for heavily damped, rib-stiffened machinery support structures. The results demonstrate a general need for high levels of SEA modeling detail for damped structures, especially those having ribs or other impedance discontinuities. The implementation of this detail and the resulting improvement in predictions for the damped L-beam assembly are described.

INTRODUCTION

Statistical energy analysis (SEA) methods have been successfully used to predict vibration transmission in a variety of complex structures. In SEA modeling, the structure is divided into a number of regions or components, each having vibration modes that are further categorized into subsystems, or groups of similar vibration modes. The transmission of vibration is expressed in terms of the vibrational power flows among subsystems. The kinds of statistical parameters required to perform SEA modeling, together with analytical expressions for evaluating them, are identified in [1].

The end results of SEA calculations on a given structure are predicted distributions of mean vibration response levels in bands of frequencies. SEA methods are used to greatest advantage when size and construction give rise to too many natural vibration modes to examine individually over the frequency range of interest, whereas a high density of modes limits the usefulness of finite-element and other discrete modeling methods. The statistical aspect of SEA is the underlying assumption that the responses are randomly distributed in frequency and space. This assumption is generally more accurate for higher-order modes than for lower-order modes, and therefore SEA tends to be best suited to high-frequency applications.

SEA methods have been used to analyze high-frequency vibration transmission in a variety of marine machinery components [2]. SEA calculations on representative structures have been compared to tests and other methods of analysis [3], [4]. These SEA applications have also included certain kinds of heavily damped, rib-stiffened support structures for machinery. The L-beam tests described in this paper were conducted for reduced-scale benchmark comparisons to verify the SEA modeling approaches used on these structures. In that the specimen configurations were extremely regular in geometry and limited the flow of vibrational power to a

single direction, they were atypical of the actual support structures and represented a severe test of SEA methods.

This paper compares measurements and SEA calculations of vibration transmission in the L-beam assembly. The quantities compared consist of power-averaged transfer functions relating far-field acceleration responses to force excitations applied at several different locations. These results are compared for both an undamped and a constrained-layer-damped configuration of the test assembly. A general need for high levels of SEA modeling detail for damped structures is demonstrated, and the implementation of this detail and resulting improvement in predictions for the damped L-beam assembly are described. The SEAM computer program [5] has been used for all of the SEA calculations.

DESCRIPTION OF L-BEAM TESTS

The design details for the L-beam test assembly are shown in Figure 1. The legs of the structure consisted of wide-flange steel beams of small cross-section, stiffened at intervals by welded steel plate ribs.

An initial test assembly mass of 68.5 kg (151 lb.) was increased to 79.8 kg (176 lb.) by the installation of constrained-layer damping treatment segments on the flanges and web of both beam legs of the assembly. The shear layer of each segment was a 0.051 mm (0.002 in.) thick film of 3M ISD 112 viscoelastic damping polymer. The cover layers were cold-rolled steel. All bays of the assembly received damping treatment except for the bay at the intersection of the beam legs.

Dwg. 4284060

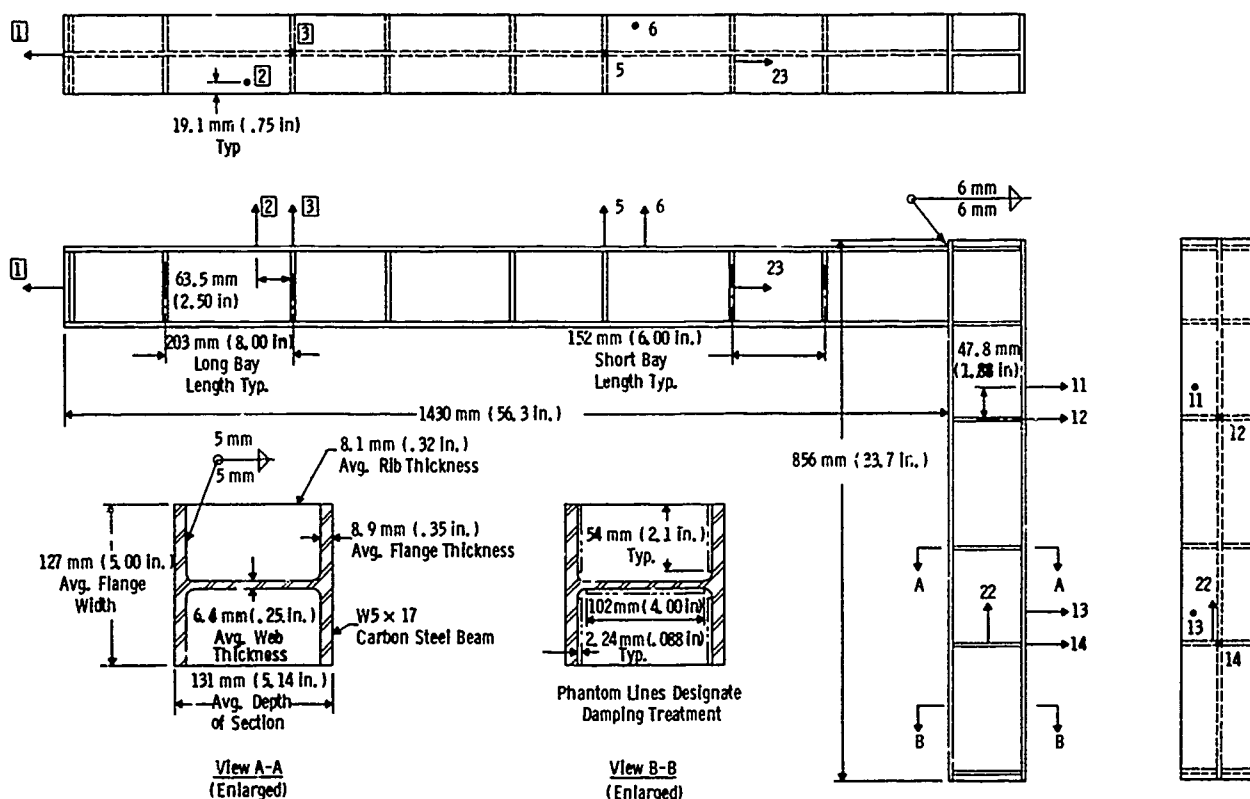


Fig. 1 Construction details of steel L-beam vibration test assembly showing excitation and response measurement locations. Numbers in squares show locations at which excitation was applied.

Vibration tests were conducted with the assembly suspended on shock cords in an undamped configuration, followed by a repeat series with the damping treatment installed. These tests included a number of different structural frequency response measurements plus damping measurements on a number of lower-frequency modes. The frequency responses consisted of transfer accelerance (acceleration/force) functions relating far-field acceleration responses to force excitations applied at three different locations. Most of the response locations were chosen with the intent of sensing specific groups of modes, e.g., local plate bending modes, so that SEA-calculated responses for specific subsystems could be compared with the measurements.

The transfer functions were first measured in narrowband form using a fast Fourier transform (FFT) analyzer in "zoom" analysis bands that were just wide enough to envelop standard 1/3-octave frequency bands. The structure was shaker-excited using random noise with filter-shaped spectra to concentrate the input power in these bands. The narrowband transfer functions were then condensed to single values for each frequency band to enable clearer comparisons between measured and SEA-calculated results. The condensed results were in the form of power-averaged transfer function magnitudes generated by the formula

$$\bar{H}, \text{ dB} = 10 \log_{10} \langle |H(f)|^2 \rangle_{\Delta f}$$

where $|H(f)|$ denotes the magnitude of a measured narrowband transfer function and $\langle \rangle_{\Delta f}$ denotes average value over a 1/3-octave frequency band Δf . This quantity is independent of the shape of the excitation frequency spectrum. It can be shown that the ratio of mean squares of response and excitation is equivalent to this power average but only if the excitation spectrum is uniform over the frequency band. Typical relationships between power-averaged transfer functions and the narrowband functions from which they were obtained are shown in Figure 2.

The damping measurements were obtained by FFT analyzer-generated curve fits to resonant peaks of driving-point accelerance functions. Using very narrow "zoom" frequency bands lengthened the sampling times and helped minimize the effects of Fourier transform leakage due to long reverberation times in the undamped configuration.

DAMPING VALUES

Estimated dissipation loss factor values for the various groups of vibration modes were generated for use as inputs to the SEA analyses. Modal surveys identified modes which were nearly pure plate bending, beam bending, or extensional modes with little coupling among these types. Thus there were no significant coupling losses among the different types of mode groups during damping measurements on these particular modes. To the extent that the vibration levels decreased with distance from the driving point in these damping measurements, there were axial flows of power that represented coupling losses among similar subsystems. Therefore the measured damping values may have somewhat overestimated the true dissipation loss factors and are to be regarded as estimates. Henceforth the terms "damping" and "dissipation" will be used interchangeably in this paper.

The damping levels for the undamped configuration were very light, i.e., the magnification "Q" factors ranged from approximately 200 to 4,000 over the range of frequencies and types of modes considered. This was the result of a total lack of bolted joints, lubricating oil films, or other damping agents normally present.

Measured damping values for individual modes in the damped configuration are shown as the data points in Figure 3. Each value is expressed as a damping loss

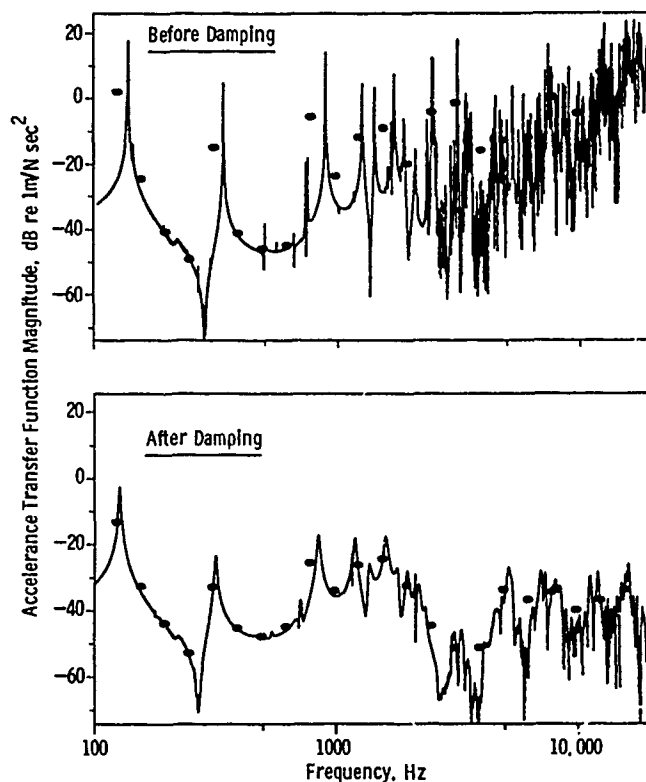


Fig. 2 Sample comparisons of power-averaged transfer function magnitude (data points) versus the narrowband functions from which they were obtained (curves): A_{14}/F_3 measured before and after damping. Narrowband curves are composites of one-third-octave "zoom" measurements.

factor, which is equivalent to two times the percent critical damping divided by 100, and which equals the inverse of the "Q" factor. The data points tend to be clustered at the lower frequencies, because coupling among the various types of modes began to occur just above the onset of the plate bending modes, precluding individual mode measurements at higher frequencies. The damping values for the damped configuration were estimated from these limited data as supplemented by calculations. The calculation methods included a constrained-layer damping treatment performance solution for panels with continuous damping treatments undergoing plate bending vibrations [6]. Also used were formulas for members under quasi-static oscillating extensional and bending stress, damped with segmented constrained-layer treatments [7],[8]. These calculations used dynamic shear property values measured on the lot of viscoelastic damping polymer used in the test assembly [8].

Figure 3 shows the measured and calculated damping values and the curve fits used as SEA modeling inputs for the damped configuration. The discrepancies between measured and calculated plate mode damping values are noteworthy. The measurements pertain to the lowest-order plate modes of the beam flange panels, in which motion restraints were imposed on three sides by the web and ribs. In all likelihood, these restraints caused the mode shapes and strain energy distributions to differ substantially from the sinusoidal wave shape assumed in the calculation method. The discrepancies in damping values are attributed to these deviations. It was assumed that with increasing frequencies and shortening of wavelengths, the support conditions became less important and the actual damping values for the plate modes approached the calculated values in the manner shown.

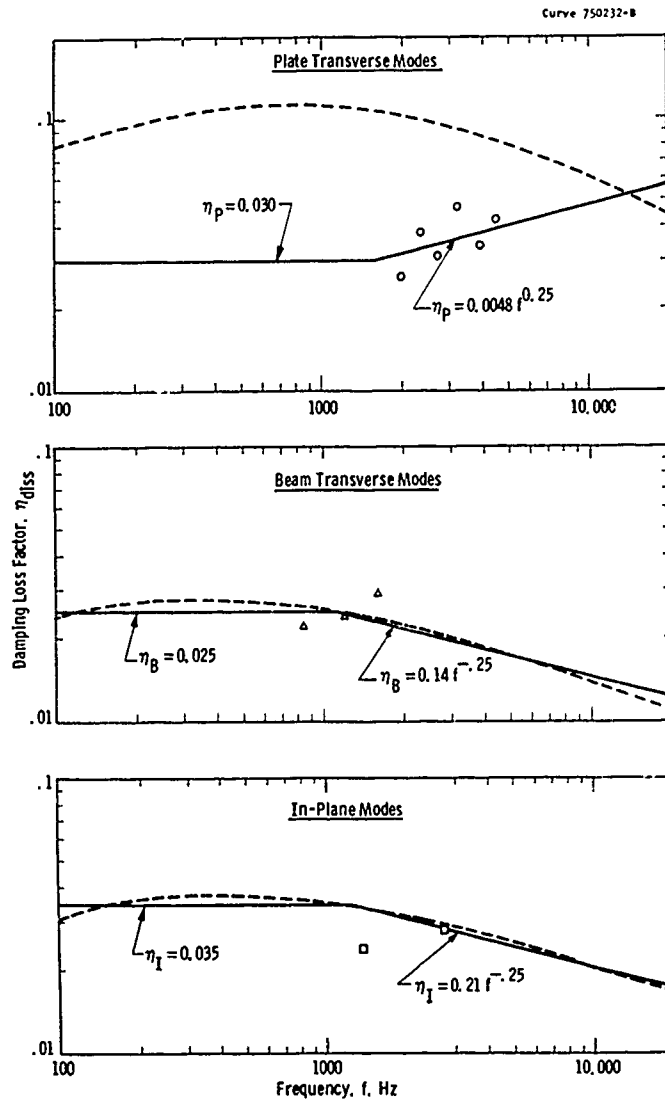


Fig. 3 Dissipation loss factor values for L-beam vibration modes after constrained-layer damping treatment installation. Dashed lines represent calculated damping values; data points are measured values. Solid lines are curve fits used as SEA modeling inputs.

COARSE SEA MODEL

The SEAM computer program, developed by Cambridge Collaborative, Inc., Cambridge, MA, was used for all SEA calculations on the L-beam assembly. The SEAM program generates and solves the sets of equations that predict system-wide responses in structures, fluids, and combined fluid/structural systems. The program generates these solutions after evaluating the SEA parameters for each subsystem that the analyst creates to model the physical system.

Figure 4 shows the coarse subsystem modeling initially used to calculate vibration transmission in the L-beam assembly. A single set of plate mode, in-plane mode, and beam mode subsystems modeled each leg. Subsystems 1 PLT and 2 PLT represented transverse plate bending and shear modes in the flanges, web, and ribs collectively. Subsystems 1 BEAM and 2 BEAM represented transverse beam bending and shear modes of the beam legs; these global modes were expected to dominate the low-frequency responses. All of the foregoing subsystems were PLATE subsystem

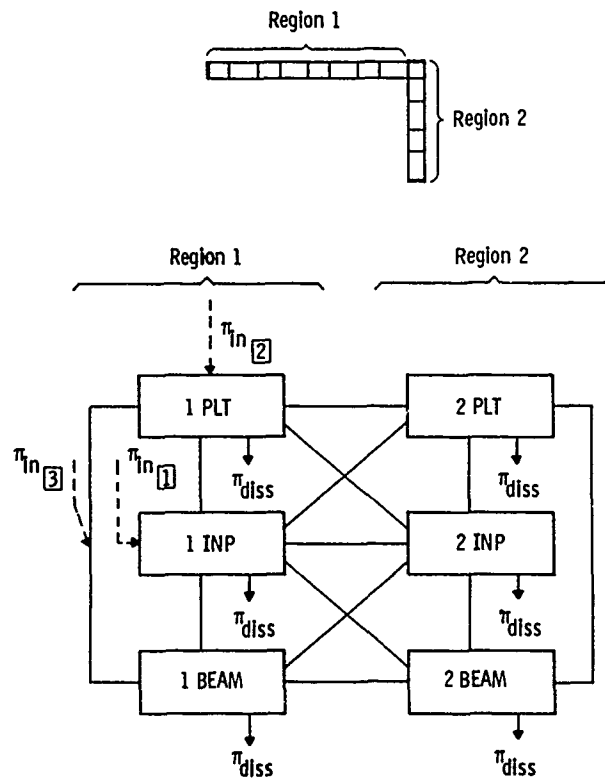


Fig. 4 Coarse SEA subsystem modeling of the L-beam test assembly. The π quantities are vibrational power flows.

types in the SEAM program.¹ Subsystems 1 INP and 2 INP represented in-plane shear and extensional modes of the beam legs and were INPLANE subsystem types.

Vibrational power inputs corresponding to assumed force fluctuations at each of three excitation locations were calculated by the program. SEA-predicted transfer function magnitudes were obtained by specifying unit rms force levels at each excitation location in turn. Because the values of transfer functions, as distinct from driving-point frequency responses, were the desired quantities, they could be taken as the farfield responses for the various subsystems. Driving point response predictions, on the other hand, require the addition of a nearfield response that may be the predominant portion of the total response.

It was our expectation that the lengthwise decays of response in the damped test configuration would render this coarse SEA model inadequate for reasonably accurate predictions. The amplitudes of vibration waves at a given frequency, traveling in the positive x-direction in damped members, decay as follows [9]:

- bending wave amplitudes decay in proportion to $e^{-\eta kx/4}$;
- longitudinal and shear wave amplitudes decay in proportion to $e^{-\eta kx/2}$,

where

$$\eta = \text{damping loss factor}$$

$$k = 2\pi/\lambda = \omega/c = \text{wavenumber}$$

¹ The beam modes were modeled as the modes of solid plates chosen for dynamic equivalence to the actual members.

λ = wavelength
c = wave speed.

Accordingly, the vibrational energies (amplitudes squared) of waves at 16 KHz in the damped L-beam assembly were estimated to decay by a factor of two over the following axial lengths:

- plate bending waves - 280 mm (11 in.)
- in-plane shear waves - 990 mm (39 in.)
- beam bending waves - 2920 mm (115 in.).

Two out of these three decay lengths are substantially shorter than the long leg of the assembly.

Nonetheless it was of interest to compare transfer functions in both the damped and the undamped configurations using the coarse SEA model. The transition from undamped to damped configuration modeling was accomplished by making appropriate changes to the material models, which specify the densities, wavespeeds, and damping values for the various subsystems.

MEASUREMENTS VS COARSE MODEL CALCULATIONS

Figures 5 and 6 compare 1/3-octave average transfer function magnitudes calculated with the coarse SEA model versus measured results. Figure 5 pertains to excitations and responses at locations on the beam flanges that were well-removed from the ribs and web. Plate bending modes of the flange were directly excited at a relatively mobile driving point in these measurements. Figure 6 pertains to excitations and responses at the web/rib intersections. Primarily beam bending modes were excited at a higher-impedance driving point in these measurements.

The large undulations in the measured magnitudes at low frequencies were due to the wide spacing of resonant peaks seen in the narrowband transfer functions, Figure 2. Because individual resonances are not calculated by SEA, the calculated averages were within large standard deviations of the measurements in this range.² An onset of high densities of modes occurred near the middle of the logarithmic scale of frequencies, however, bringing about considerable smoothing of the power-averaged measurements.

The agreement between measurements and calculations was good in the undamped configuration at the midrange of frequencies. In the damped configuration, major differences were observed at midrange and above, as expected. An unexpected result, however, was that the discrepancies for the damped configuration in the lower plots of Figure 5 were smaller than those in the lower plots of Figure 6. If the Figure 5 transfer functions involved transmission primarily by the more heavily damped plate modes, the coarse model would be expected to generate less accurate results for these transfer functions, based on the reasoning of the previous section. In any case, the need for refined modeling for the damped configuration was confirmed.

² A necessary condition for close matches of measurements with SEA predictions is that at least several vibration modes of a given type occur in each frequency band.

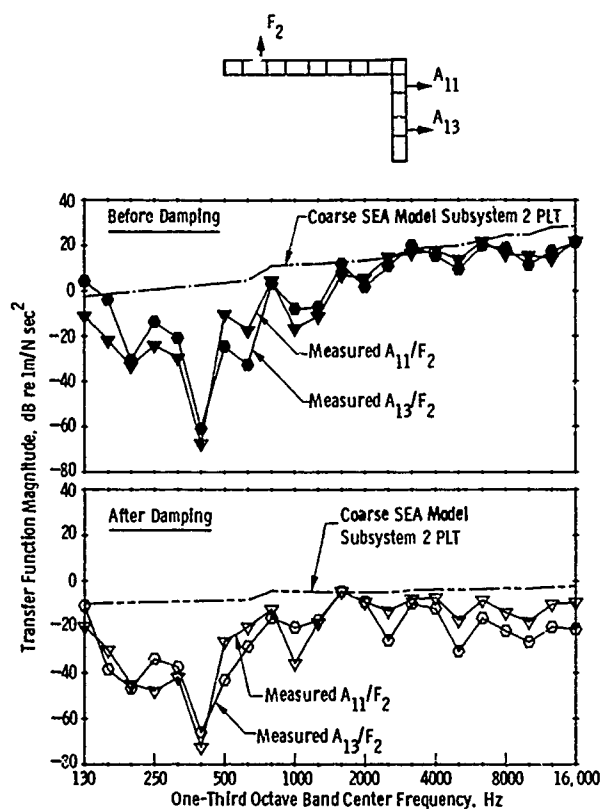


Fig. 5 Coarse SEA model calculations vs. measurements of acceleration functions before and after damping: plate mode responses in short leg, transverse excitation at flange.

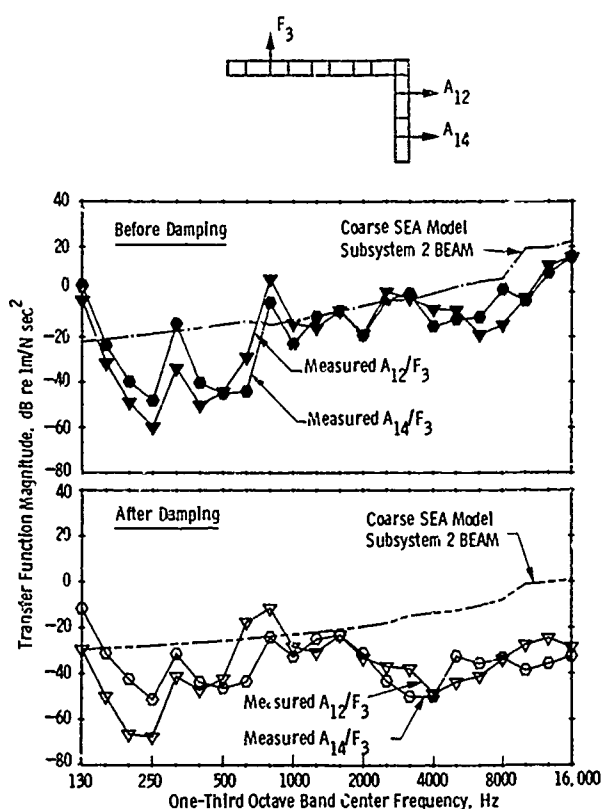


Fig. 6 Coarse SEA model calculations vs. measurements of acceleration functions before and after damping: beam mode responses in short leg, transverse excitation at web/rib intersection.

REFINED SEA MODEL

Separate SEA calculations helped to clarify the issue of model refinement. Shown in Figure 7 are two different models of plate vibration modes in one of the damped flanges of the long beam leg. The coupling among these modes and other groups of modes in the assembly was temporarily ignored. For the same level of input power and for the identical damping values, the two-subsystem model generated a mid-length power value that was inflated by nearly 8 dB compared to the six-subsystem model. Consequently the right-side response amplitudes in the two-subsystem model were similarly inflated. This occurred because the two-subsystem model simulated uniform distributions of response over large regions. The six-subsystem model injected the input power more locally and generated a distribution of responses that more nearly resembled an exponential decay.

Another calculation dealt with the representation of the ribs, which were uncamped but did interact with the flanges and web. In Figure 8, power flows are compared for models with and without explicit modeling of a rib. Reductions of .p to 3 dB in power transmitted at a single junction were obtained by adding the rib modeling. These reductions were attributed to the reflection of vibration waves back toward their source due to impedance discontinuities imposed by the ribs. The inclusion of rib in-plane mode subsystems was found to be unnecessary if junctions were appropriately specified.

A refined SEA model of the entire assembly which implemented these features is shown in Figure 9. The subdivision of plate vibration mode subsystems is not as

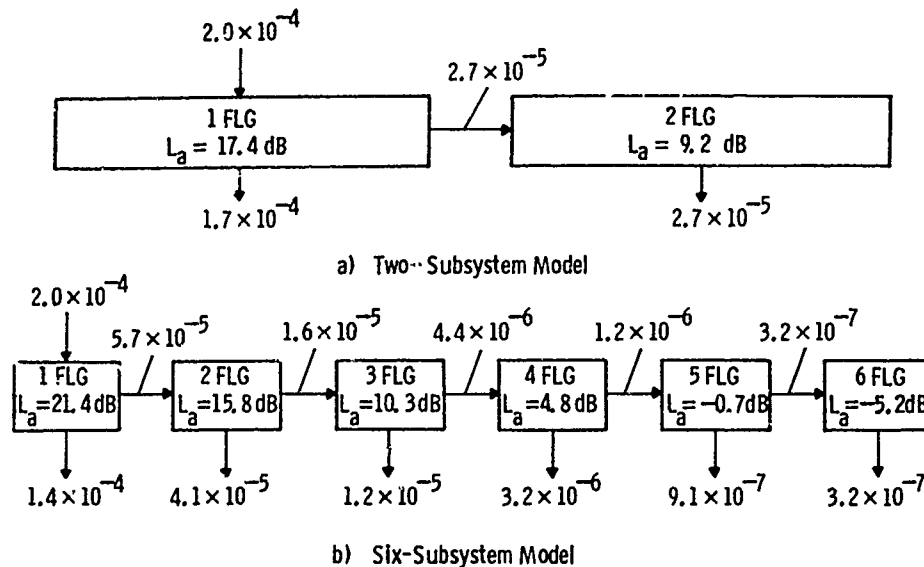


Fig. 7 Effect of refining modeling of plate transverse vibration modes of one long flange of the damped L-beam assembly. Arrows indicate vibrational power flows in watts for a 1N rms force excitation in the 16 KHz band. The symbol L_a denotes acceleration level in dB re 1 m/sec² rms.

fine as in Figure 7b (four regions along the length of the long leg vs. six regions). This lesser extent of detail was judged to be adequate because of the flanking paths through the BEAM and the INP subsystems that shared in the transmission of power. These mode groups, being less strongly damped than the PLT modes, would have the effect of reducing the lengthwise gradients of response in the case of excitation at the flange. On the other hand, the coupling among beam and plate modes represented in this model would enable the heavily damped plate modes to absorb energy from the beam modes when the web/rib intersections were excited. This coupling was expected to help reduce the discrepancies seen in Figure 6.

One other change implemented in the refined model was the addition of the in-plane subsystem AUXINP at the junction where power input simulated excitation at the web/rib intersection. In the highest four 1/3-octave bands, the previously calculated drive point impedance decreased markedly below measured impedance values because of a predicted burst of modes in the equivalent solid plate that modeled each BEAM subsystem. The AUXINP subsystem provided the additional components of junction impedance needed to represent the local high impedance of the drive point. This feature ensured that the calculated vibrational power inputs would truly represent the intended unit force excitations.

MEASUREMENTS VS REFINED MODEL CALCULATIONS OF DAMPED RESPONSES

The refined modeling results that are discussed here pertain only to the damped configuration. Figures 10-12 show comparisons for transfer functions involving each of the three excitation locations. The refinement of the SEA model has brought about marked improvements over the damped assembly comparisons in Figures 5 and 6. In both plots of Figure 11 and the upper plot of Figure 10, the revised calculations match the measurements at and above the mid-range of frequencies to within 10 dB or less on the average. These transfer functions were dominated by plate and in-plane modes of vibration. The reductions in the

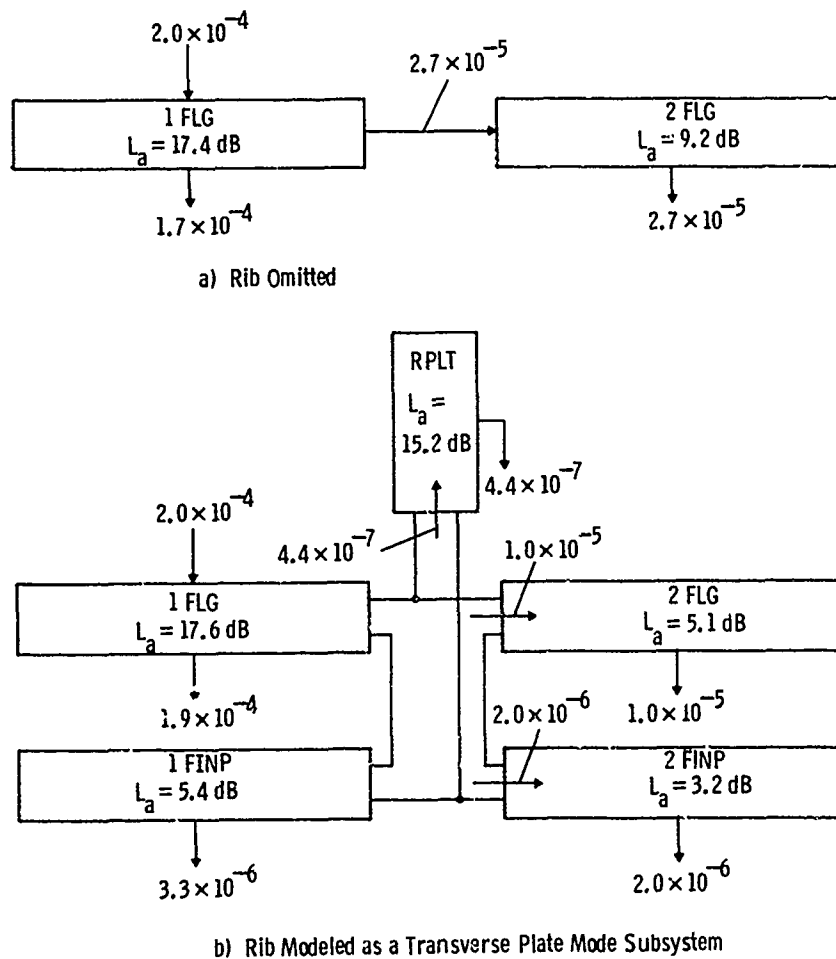


Fig. 8 Effect of adding explicit modeling of a rib to the damped flange. Flange in-plane mode subsystems have been included to account for flange mode coupling produced by rib.

calculated response levels that make the Figure 11 comparison much more favorable than Figure 5 are the result of better representing the dissipation of plate mode vibrational energy as it flowed from the long to the short leg of the beam assembly.

The measurements of transfer functions that were dominated by beam modes, e.g. Figure 12, dipped well below the calculated levels in the neighborhood of 4000 Hz. Special measurements at these frequencies revealed a burst of modes in which flange bending vibrations were strongly coupled to the global beam bending modes of the entire structure. The action of the flanges on the beam modes is believed to have been similar to that of sets of nearly identical auxiliary mass dampers. This kind of action is not forecast by SEA methods, which are derived on the assumption of randomness and irregularities in the structure. Stated in other terms, if the flanges had varied in width and in symmetry about the web intersection line, the measured transfer function dips would have been much weaker, and the agreement with SEA results much closer.

At frequencies above these dips, the agreement with measured responses has been improved in that previous overpredictions as large as 30 dB on average (Figure 6) have been reduced to about 10 dB (Figure 12). Further scrutiny has

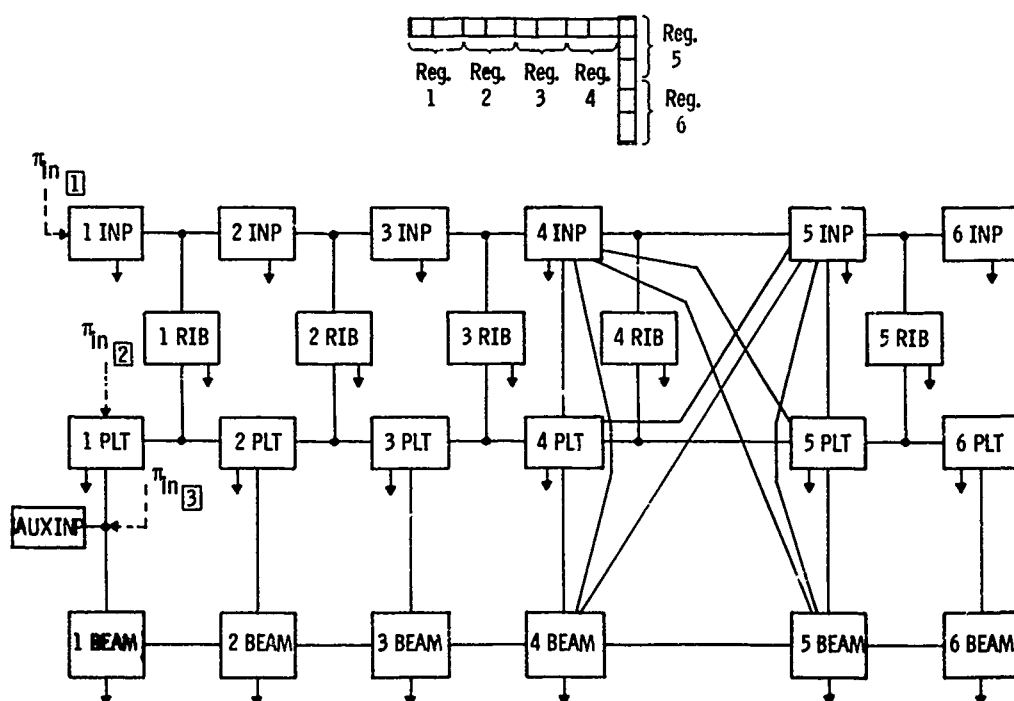


Fig. 9 Refined SEA subsystem modeling of the L-beam test assembly. Subsystems 1 RIB, 2 RIB, etc. represent transverse plate vibration modes of the ribs.

shown that most of this remaining difference is the result of having modeled the beam modes as PLATE mode subsystems of equivalent solid plates having the full width of the flanges. There are many possible choices of equivalent solid plates that would give the proper mass and wavespeed values, and it has been determined that a much narrower equivalent plate would impart more realistic modal densities. Examples of the improvement of results obtained by this change are shown by the curves labelled "narrow-width equivalent plate subsystems" in Figure 12.

CONCLUSIONS

Reasonably good matches of measured transfer functions were obtained with a coarse SEA model of the undamped L-beam test configuration. As expected, predictions obtained with a damped version of this coarse model differed substantially from measurements on the damped configuration despite the use of damping values based partly on experimental data. A refined model, which better represented the dissipation and confinement of vibrational power along the length of the structure, yielded much closer agreement with measured transfer functions for the damped configuration. These results demonstrate the need for substantial SEA modeling detail in predicting vibration transmission in damped structures, especially those having ribs or other impedance discontinuities. This need was underscored in the case of the L-beam assembly, in which response gradients were heightened by the entire flow of vibrational power having been in a single direction.

Differences remained between predictions and measurements of those transfer functions that involved power transmission by global beam vibration modes. Large dips in the measurements in the vicinity of 4000 Hz, which were not forecast by SEA modeling, are attributed to the flanges having acted as sets of auxiliary mass

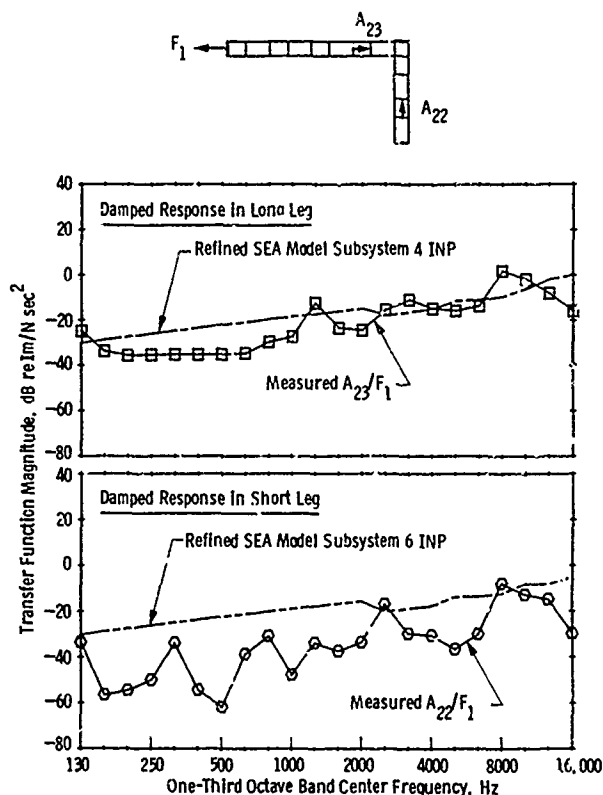


Fig. 10 Refined SEA model calculations vs. measurements of accelerance functions after damping: extensional responses, axial excitation at web.

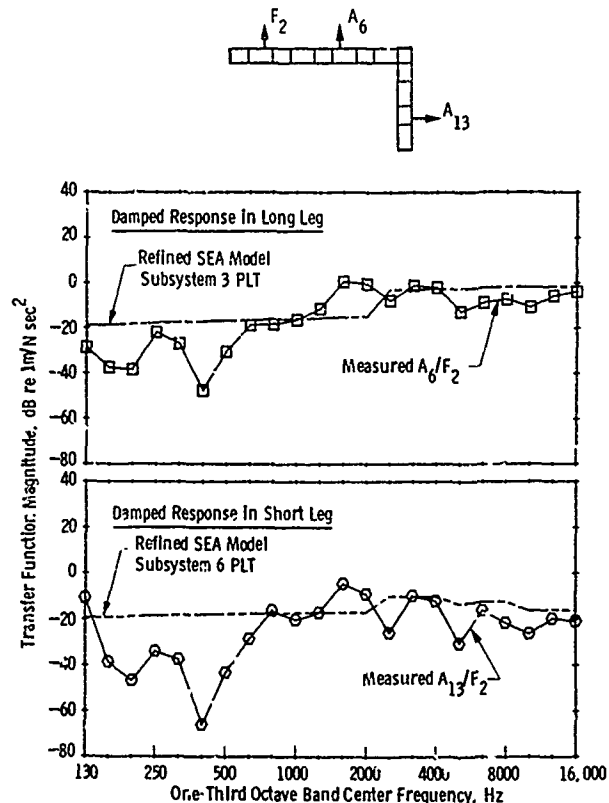


Fig. 11 Refined SEA model calculations vs. measurements of accelerance functions after damping: plate mode responses, transverse excitation at flange.

dampers for the beam modes. This action was a consequence of the uniformity of the structure.

Many of the uncertainties that arise in SEA modeling may be resolved by examining simple example cases such as those shown in Figures 7 and 8. SEA is an effective and useful tool for the noise and vibration design of structures and fluid/structural systems and in many cases is the only means available for evaluations at high frequencies. The prediction of responses for the L-beam assembly represented a severe test of SEA methods, which are more readily adapted to systems that have variations in geometry and offer multiple paths for power flow.

ACKNOWLEDGMENTS

The encouragement and support of L. K. H. Lu, W. B. Rockwood, and P. C. Garner of the Westinghouse Marine Division, Sunnyvale, California, sponsors of this investigation, are appreciated. Helpful discussions were held with R. G. DeJong of Cambridge Collaborative, Inc. (now at Calvin College, Grand Rapids, Michigan) and D. V. Wright of the Westinghouse R&D Center. Technicians J. P. Condle, K. B. Wilner, and R. J. Wheeler provided testing and data handling support.

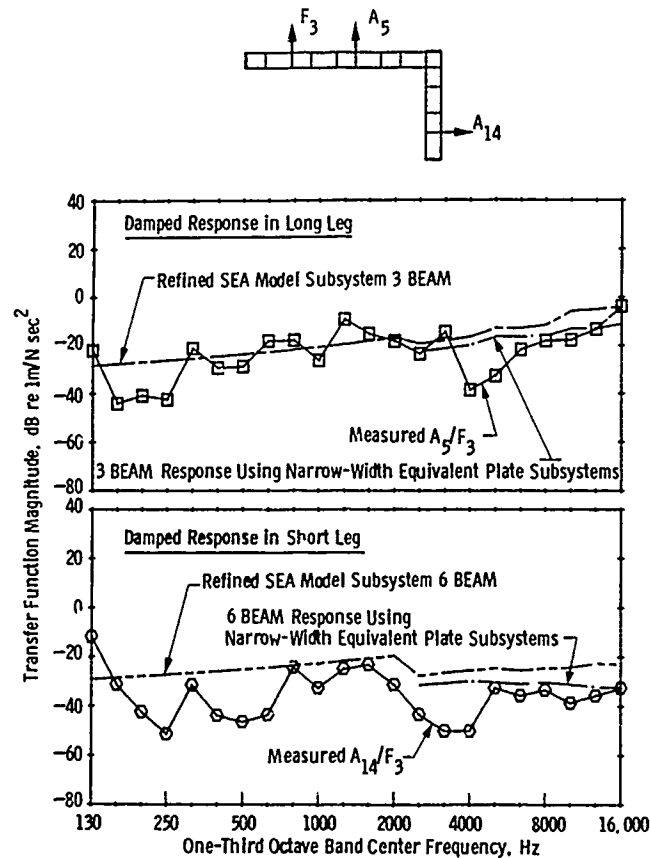


Fig. 12 Refined SEA model calculations vs. measurements of accelerance functions after damping: beam mode responses, excitation at web/rib intersection.

REFERENCES

1. Lyon, R. H., Statistical Energy Analysis of Dynamic Systems: Theory and Applications, The MIT Press, Cambridge, MA, 1975.
2. Lu, L. K. H., Rockwood, W. B., Warner, P. C. and DeJong, R. G., "An Integrated Gear System Dynamics Analysis Over a Broad Frequency Range," Shock and Vibration Bulletin, No. 55, Part 3, June 1985, pp. 1-11.
3. Lu, L. K. H., Hawkins, W. J., Downard, D. F., and DeJong, R. G., "Comparison of Statistical Energy Analysis and Finite Element Analysis Vibration Prediction with Experimental Results," Shock and Vibration Bulletin, No. 53, Part 4, May 1983, pp. 145-154.
4. Lu, L. K. H. and Warner, P. C., "Vibration Analysis of a Large Naval Gear," ASME Paper No. 81-DET-142, Design Engineering Technical Conference, Hartford, CT, September 1981.
5. SEAM User's Manual, Revision 1.8, Cambridge Collaborative, Inc., Cambridge, MA, March 1985.
6. Beranek, L. L., Noise and Vibration Control, McGraw-Hill Book Co., New York, 1971, pp. 462-468.

7. Torvik, P. J., "The Analysis and Design of Constrained Layer Damping Treatments," Damping Applications for Vibration Control, AMD-Vol. 38, ASME, 1980, pp. 85-112.
8. Sattinger, S. S., "A Study of Extensional Damping Performance Discrepancies in Certain Constrained-Layer Treatments," The Role of Damping in Vibration and Noise Control, DE-Vol. 5, ASME Publication H00405, 1987, pp. 33-40.
9. Cremer, L., Heckl, M., and Ungar, E. E., Structure-Borne Sound, Springer-Verlag, Berlin, 1973, p. 174.

SOLAR ARRAY DEPLOYMENT NONLINEAR DYNAMICS ANALYSIS¹

**Raymond A. Mills
GE Astro-Space Division
B100, M4018
Philadelphia, PA 19101**

The deployment dynamics of NASA's Upper Atmosphere Research Satellite (UARS) solar array are modeled using a unique combination of computer analysis methods. The purpose of the analysis is to determine the loads in the solar array synchronization cables induced by the on-orbit firing of four pyrotechnic retention bolts. The solar array deployment simulation models panel and joint flexibilities, damping effects, friction effects, and bolt impact dynamics while considering nonlinearities in synchronization cable and power hinge mechanisms. The analysis is performed using MSC/NASTRAN and Automatic Dynamics Analysis of Mechanical Systems (ADAMS) software combined with a user-written FORTRAN subroutine which interacts with ADAMS in real time. The analysis provides greatly increased insight into the deployment dynamics while allowing a 67 percent reduction in the synchronization cables' design load and increased design confidence compared to a more conventional momentum/energy conservation hand analysis.

INTRODUCTION

Analyses performed in support of spacecraft design are often linear or statistical in nature. Such analyses as coupled launch vehicle/payload transient loads determination or vibroacoustic environment prediction typically do not consider nonlinear or large displacement effects while still producing acceptable results. Highly nonlinear problems, such as pyrotechnic retention bolts impacting a solar array prior to deployment, have typically been analyzed using conservative simplifying assumptions corroborated by testing. The effort required to formulate and solve multiple degree of freedom (DOF) equations of motion which consider many types of nonlinearities and large displacements can be prohibitive and may not yield results with a high degree of confidence. However, simplifying assumptions usually produce design parameters which are over-conservative.

The advent of large dynamics analysis computer programs which model nonlinearities and large displacements, such as the Automatic Dynamics Analysis of Mechanical Systems (ADAMS) software, enable sophisticated analyses to be performed with more ease and confidence. Theoretical work behind programs such as ADAMS was performed

(1) The work reported in this paper was performed under NASA-GSFC contract number NAS5-28666.

in the 1970s [1],[2]. ADAMS uses stiff integration techniques [3],[4] and sparse matrix theory [5] in numerically integrating the equations of motion formulated in terms of the system Jacobian. The capability exists to model limited types of flexible members undergoing large nonlinear displacements [6],[7]. Although some effort is spent in familiarization with the syntax and idiosyncrasies of a large dynamics analysis computer program, once this is done a wide variety sophisticated, multi-DOF problems can be systematically and accurately modeled and studied. This paper considers the application of ADAMS with MSC/NASTRAN and a user-written subroutine to the deployment dynamics of NASA's Upper Atmosphere Research Satellite (UARS) to obtain a significant reduction in the synchronization cable design load.

SOLAR ARRAY AND SOLAR ARRAY DEPLOYMENT DESCRIPTIONS

The UARS solar array consists of six 128 in by 60 in by 1.25 in aluminum facesheet/honeycomb core panels (see Figure 1). The nominal facesheet thickness is 0.008 in and the panels are 1.0 in apart.

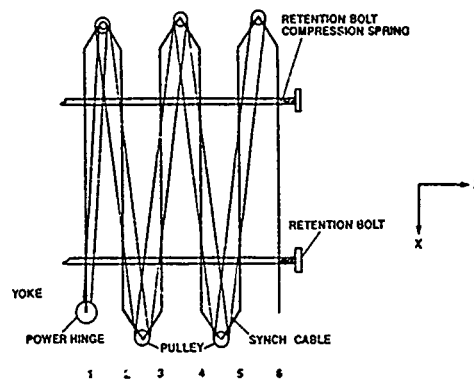


Figure 1a. Solar Array Showing Synchronization Cables and Retention Bolts

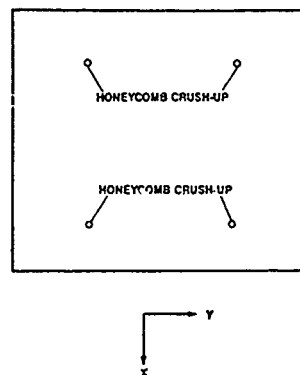


Figure 1b. Solar Array Panel 6 Showing Retention Bolt Impact Points

The mass of panel 1 (the inboard or +Y panel) is 73.0 lb_m, the mass of panels 2 through 5 is 62.5 lb_m, and the mass of 6 is 68.6 lb_m. The panels are connected by hinges which allow the panels to be stacked during launch (see Figure 1). The hinges are 1.58 inches in Z from the panel endpoints and are spring loaded to deploy the array on orbit. The rotational springs in the hinges are governed by the equation

$$M = 64 \text{ in-lb} + [(32/\pi) \text{ in-lb/rad}]\theta \quad (1)$$

The hinge kinetic Coulomb friction torque is approximately 15 in-lb. This value was obtained from a Landsat-D solar array hinge test with a similar, four panel solar array and hinges.

The solar array is attached to the spacecraft through a yoke with a power hinge at the yoke/panel 1 interface. The power hinge controls the deployment rate, provides a backup deployment mechanism, and enables the array to be refolded on-orbit. When passive, the power hinge acts as a 2.1 E4 in-lb/rad torsional spring until the load on it reaches 450 in-lb, at which point no additional restraining torque is provided. The power hinge acts through a series of pulleys and preloaded cables whose purpose is also to synchronize the deployment. The pulley at a given hinge is locked to one panel and free to rotate relative to the other panel. Successive pulleys are free to rotate relative to the panel between them. For example, in Figure 1a the pulley at hinge 4-5 is fixed to panel 4 and free to rotate relative to panel 5. Similarly, the pulley at hinge 5-6 is fixed to panel 6 and free to rotate relative to panel 5. The synchronization cable which wraps around any two pulleys is pinned to both pulleys, effectively acting as a pair of cables creating a torsional spring which tends to keep alternate panels parallel during deployment. This effect also allows the power hinge to control and even reverse the deployment, even though it is directly connected to only the first two panels. The possibility exists of one or both synchronization cables in a given pair going slack if the preload is released due to flexible motion.

Prestressed bolts support the solar array and prevent the hinge springs from opening it during launch. On orbit, pyrotechnic charges separate the bolts from the spacecraft two (diagonally opposite) at a time. The retention system is designed such that the second pair of bolts supports the array and prevents appreciable deformation when the first pair fires. The bolt prestress together with a compression spring between the bolt head and the outboard side of panel 6 causes the 1.82 lb_m bolt to fly towards panel 6. Properties of the retention bolts, retention bolt compression springs, and synchronization cables are shown in Table 1. To prevent space debris, the bolts must be retained by the satellite and are therefore designed with a flange on the inboard end which strike an energy absorbing honeycomb crush-up embedded in panel 6 with a velocity of 370 in/sec. The honeycomb crush-ups are designed to provide 750 psi of resistance. The crush-ups are slightly pre-crushed to prevent transmitting to the solar array the higher loads necessary to achieve buckling than to sustain it. Since each of the four crush-ups has a surface area of 0.885 in², each bolt should impact panel 6 with a force not exceeding 664 lb. While the honeycomb crush-ups help, the bolt impacts still induce significant shock loads in the synchronization cables.

Table 1. Solar Array Deployment System Parameters

Synchronization Cables

Young's modulus = $28.E6 \text{ lb/in}^2$

Diameter = $3/32 \text{ in}$

Preload = $30. \text{ lb}$

Cable pair between yoke and panel 2:

Length = 61.57 in (free)

Pulley diameter = 2.12 in

All other cables:

Length = 63.19 in (free)

Pulley diameter = 3.09 in

Retention Bolts

Young's modulus = $28.E6 \text{ lb/in}^2$

Length $\approx 16. \text{ in}$

Diameter = 0.5 in

Flying mass = 1.82 lb_m

Preload = $11500. \text{ lb}$

Initial velocity (before compression spring extends) = $286. \text{ in/sec}$

Retention Bolt Compression Springs

Spring constant = 0.877 lb/in

Free length = 23.00 in

Length before firing = 3.35 in

Length after firing (with honeycomb crushing) = 15.35 in

COMPUTER SIMULATION DESCRIPTION

The retention bolt impact and initial solar array deployment is modeled using ADAMS. However, ADAMS does not have the capability of modeling flexible plates, yet the panel flexibility is important to include in the analysis. Since ADAMS does have flexible beam elements and the effect of out-of-plane dynamics on the synchronization cable loads is considered second order, a two-dimensional simulation is used (no motion or dimension in Y) with flexible beam elements to represent the panels. The beams are given the actual mass per unit length in X (see Figure 1) of the panels, lumped at element endpoints, while their stiffnesses are obtained by matching the fundamental bending mode about Y, axial mode in X, and bending mode about X (beam torsion) of panel 6 constrained at its hinge. The panel 6 modes are obtained using the MSC/NASTRAN normal modes solution with the panel restrained in six DOFs at the -Y end of the hinge, DOFs 2,3,5, and 6 at the hinge midpoint, and DOFs 2 through 6 at the +Y end. The NASTRAN finite element model contains 750 static DOFs and 39 dynamic DOFs. The matching is done using fundamental bending, axial, and torsional frequency results from Reference 9, solving for stiffness parameters using the actual projected Y-Z plane area. In the ADAMS simulation, panel 5 is represented by four beam elements, with a node at the midpoint and nodes at each of the two X stations at which bolt impact occurs. For the remaining panels, four equal length beam elements are used for each panel to avoid numerical difficulties encountered in attempting to use one element per panel. A conservative structural damping factor of 0.002 is used for the panel beam elements.

The panel hinge springs are modeled with rotational spring elements defined with the ADAMS SFORCE [8] statement. The kinetic Coulomb hinge friction is modeled using the ADAMS SFORCE statement with the IF function to make the constant magnitude frictional torque between adjacent panels dependent only on the sign of the relative rotational velocity at the hinge. The power hinge is also modeled with a rotational spring, but with an IF statement which does not allow the torque to exceed the maximum 450 in-lb.

Each pair of synchronization cables is modeled equivalently as a rotational spring and a translational spring between the center points of the two pulleys the cables connect. However, the cable preloads and the scenarios in which one or both cables in a given pair go slack due to panel deformation are contained in the spring definitions. For example, the ADAMS SFORCE statement for the equivalent rotational spring between the panel 4 pulley (denoted by MARKER [8] 1401, aligned with -Y) and the panel 6 pulley (denoted by MARKER 0201, aligned with -Y) is:

```
SFOR/214, I=0201, J=1401, ROT, FUNC=IF(ABS(AZ(0201,1401)) -  
  ABS((DM(0201,1401)-63.19025193)/1.545): IF(DM(0201,1401) -  
  63.19025193: 0., 0., -14597.*AZ(0201,1401)), IF(DM(0201,1401) -  
  63.19025193: 0., 0., -14597.*AZ(0201,1401)), IF(AZ(0201,1401) -  
  ABS((DM(0201,1401)-63.19025193)/1.545): 7298.*(-AZ(0201,1401) +  
  (DM(0201,1401)-63.19025193/1.545), -7298.*(AZ(0201,1401) +  
  (DM(0201,1401)-63.19025193/1.545), -7298.*(AZ(0201,1401) +  
  (DM(0201,1401)-63.19025193/1.545)))
```

Definition of the ADAMS command syntax can be found in Reference 8. The statement for the corresponding translational spring is:

```
SFOR/2141, I=0201, J=1401, TRANS, FUNC=IF(ABS(AZ(0201,1401)) -  
  ABS((DM(0201,1401)-63.19025193)/1.545): IF(DM(0201,1401) -  
  63.19025193: 0., 0., -6115.*(DM(0201,1401))-63.19025193)),  
  IF(DM(0201,1401)-63.19025193: 0., 0., -6115.*(DM(0201,1401) -  
  63.19025193)), IF(AZ(0201,1401) -  
  ABS((DM(0201,1401)-63.19025193)/1.545): -3057.*(-1.545*AZ(0201,1401) +  
  (DM(0201,1401)-63.19025193/1.545), -3057.*(1.545*AZ(0201,1401) +  
  (DM(0201,1401)-63.19025193/1.545), -3057.*(1.545*AZ(0201,1401) +  
  (DM(0201,1401)-63.19025193)))
```

The translational retention bolt compression springs are also modeled using the SFORCE statement. The retention bolts are modeled as rigid masses and their impact of the honeycomb crush-ups is modeled using the ADAMS IMPACT function. The IMPACT function characterizes impacts by a viscous damping parameter and a stiffness parameter [8]. These parameters are chosen using the knowledge that the bolt strikes the crush-up with a velocity of 370 in/sec. This velocity is found by equating the potential energy of the compression spring and bolt preload before firing to the compression spring potential energy and bolt kinetic energy at impact, combined with the fact that the crush-up is designed to transmit a force of 664 lb. The damping parameter is chosen such that the impact force at a slight (0.1 in) initial penetration is 664 lb, when the force due to the stiffness parameter is near zero since there is almost no crush-up deflection. The IMPACT statement uses a cubic function to evaluate the damping force up to the initial penetration distance, at which point the damping parameter is used as a linear viscous damping constant, with the damping force proportional to the relative closing velocity of the impacting surfaces. The stiffness parameter is chosen such that the force between the bolt and the crush-up is 664 lb when the bolt reaches the full crush-up distance of 0.84 in (assuming a 70 percent crush-up efficiency). At this point, the damping force is zero, assuming the bolt has come to rest.

The simulation is started by giving the retention bolts an initial velocity of 286 in/sec found by equating initial bolt kinetic energy to the potential energy of bolt preload. It was assumed that the first pair of bolts had already fired and were attached to panel 6. An ADAMS graphics plot of the 80 DOF model at time $t=0$ (bolt firing) is shown in Figure 2. The graphics' purpose is to show the position of the system and not to indicate the modeling complexity (e.g., the synchronization cables are not plotted but they are included in the simulation).

A user-written FORTRAN subroutine is used to obtain the synchronization cable loads. While ADAMS provides time histories of translational or rotational forces, accelerations, velocities, or displacements between any two MARKERS in the model using the REQUEST statement, the load in a synchronization cable is a nonlinear function of the relative translation and rotation of the two pulleys it connects. Requesting the time history of the force between these two points would not yield the synchronization cable load. For example, panel 5 might be bent and panels 4 and 6 parallel such that both cables of the synchronization cable pair between

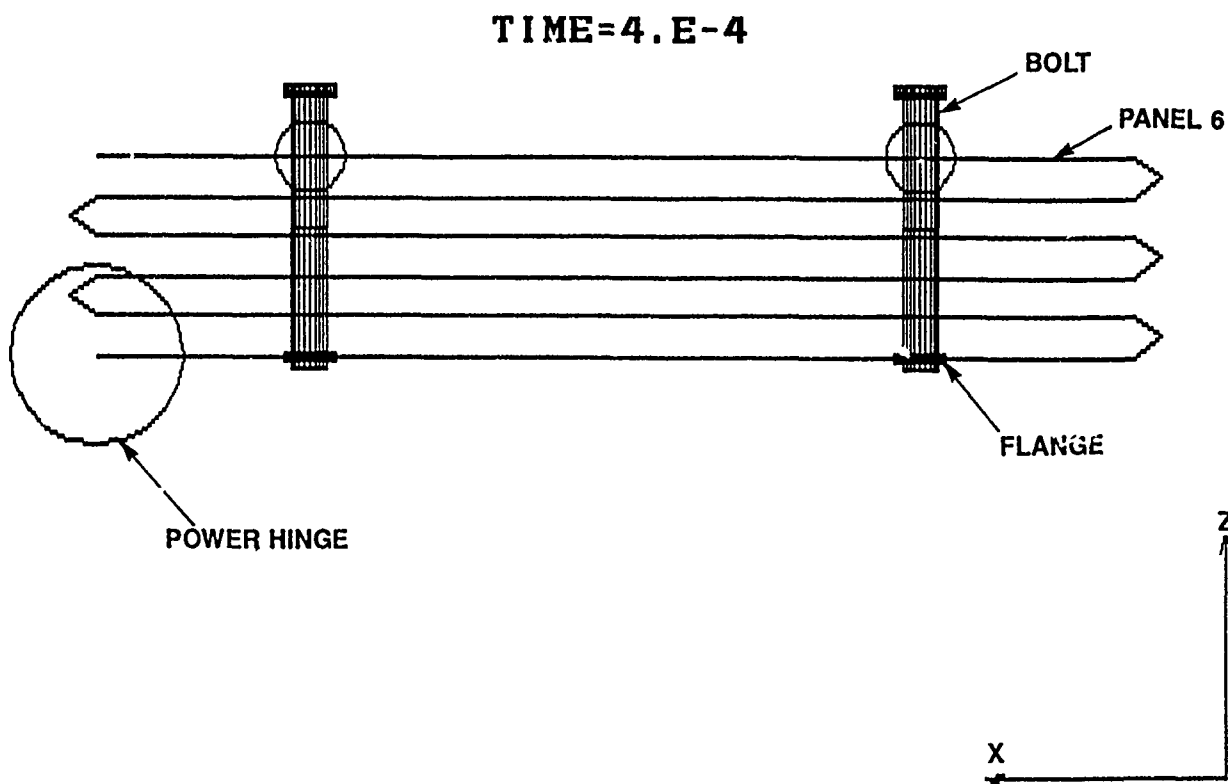


Figure 2. ADAMS Model

panels 4 and 6 are slack. In this case, the synchronization cable load would be zero but the force between the pulleys would be nonzero for compatibility with the deformation of panel 5. The compiled FORTRAN subroutine linked to the ADAMS object file receives translational and rotational displacement data from ADAMS and returns the maximum of the two cable loads in each of the five synchronization cable pairs to ADAMS. These loads can then be post-processed tabularly or graphically by ADAMS using the REQUEST statement with the FUNCTION=USER option.

COMPUTER SIMULATIC., RESULTS

Natural frequencies and mode shape descriptions from MSC/NASTRAN for panel 6 (constrained at its hinge) used for ADAMS beam element tuning are shown in Table 2. The resulting tuned beam element properties are shown in Table 3. These properties are meant to match only the fundamental vibration mode frequencies and not necessarily higher modes. Calculated properties which govern motion in Y, about X, or about Z are not presented since the ADAMS simulation is two-dimensional and allows no motion in Y.

An ADAMS-generated graphical representation of the system at time $t = 0.034$ sec, just after bolt impact at $t = 0.033$ sec, is shown in Figure 3. Figure 4 shows the array at $t = 0.045$ sec, where the bolts are rebounding from the surface of panel 6 (to be drawn back by the bolt compression springs). Figure 5, at $t = 0.49$ sec, shows the array beginning to open. Note that the synchronization cables are tending to hold alternate panels parallel. The impact force between the +X bolt

Table 2. Panel 6 Natural Frequencies and Mode Shape Descriptions

Mode	Frequency (HZ)	Description
1	3.17	First bending about Y
2	8.90	First bending about X
19	149.	First axial in X

Table 3. Tuned Beam Element Properties

Young's modulus	= 2.37 E4 psi
Shear modulus	= 84.4 psi
Area	= 160. in ²
IYY	= 52.0 in ⁴

and the panel 6 honeycomb crush-up is shown in Figure 6. Note that the maximum force does not exceed about 670 lb.

The maximum load at a given time in the synchronization cable pair connecting panels 4 and 6 (cable pair 5) is plotted versus time in Figure 7. Figure 8 shows the maximum load in cable pair 2 versus time, where the highest load in any cable pair of 131 lb occurs in the 2 sec simulation.

HAND ANALYSIS DESCRIPTION AND RESULTS

The hand analysis performed to calculate the synchronization cable design load considers panel 6 only. The panel is assumed to be rigid and the only motion allowed it is rotation about its hinge. The synchronization cable pair connecting panel 6 to panel 4 is considered to be connected to ground instead creating a torsional spring between panel 6 at its hinge and ground (see Figure 9). Thus, this analysis assumes that only panel 6 moves when the bolts strike and that synchronization cable pair 5 is the only energy absorbing medium other than the honeycomb crush-up.

The analysis assumes that the bolt impact is perfectly plastic. This is a simplifying but nonconservative assumption, since a perfectly plastic impact dissipates the maximum energy possible. However, it is not an unreasonable one given the nature of the honeycomb crush-up and the presence of the retention bolt compression springs. Assuming plastic impact, the equation conserving angular momentum of the two-bolt/one-panel system across impact is

$$mv(r_1 + r_2) = [m(r_1^2 + r_2^2) + I] \dot{\theta}_0 \quad (2)$$

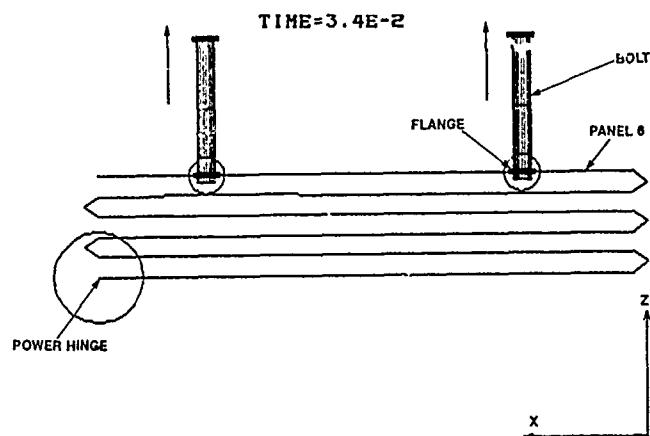


Figure 3. Retention Bolt Impact

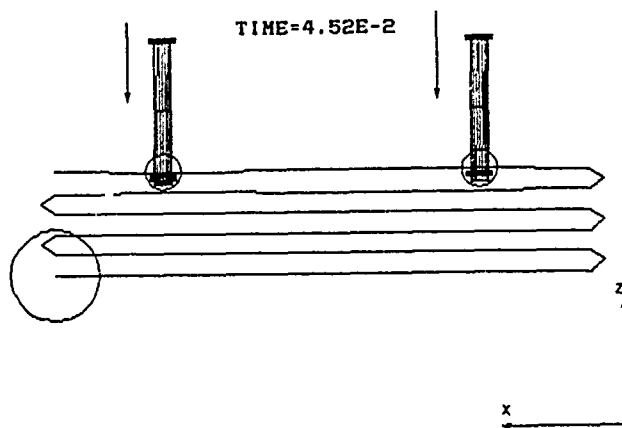


Figure 4. Retention Bolt Rebound

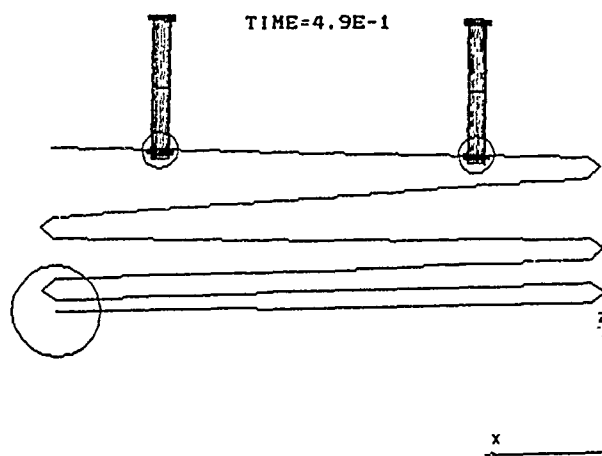


Figure 5. Solar Array Opening

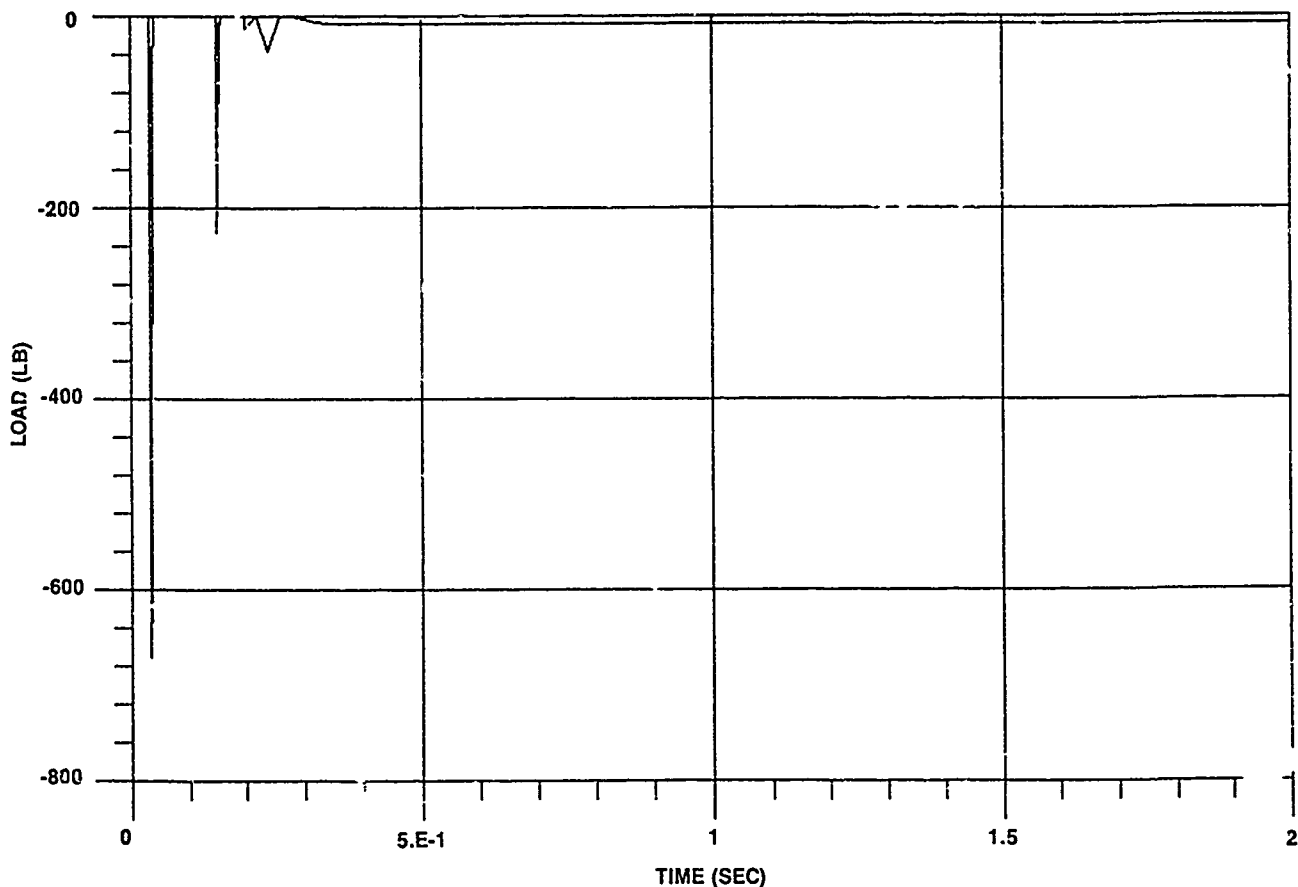


Figure 6. Impact Force

where

m = mass of one bolt

I = mass moment of inertia of panel 6 about hinge (pulley center)

v = velocity of bolts at impact

$\dot{\Theta}_0$ = angular displacement of panel 6 from vertical

A subscript Θ denotes the time of impact and r_1 and r_2 are the distances from the pulley center to each of the impact points as shown in Figure 9.

The angular velocity $\dot{\Theta}_0$ can be determined from (2) and used to find the kinetic energy of the system just after impact:

$$T_0 = 1/2 \dot{\Theta}_0^2 [m(r_1^2 + r_2^2) + I] \quad (3)$$

This post-impact kinetic energy is conservatively assumed to be equal to the potential strain energy in the synchronization cables when the system momentarily comes to rest at Θ_{\max} and the kinetic energy is zero. To obtain the kinetic energy in the cables, the two-cable mechanism is modeled equivalently as a rotational spring as in the computer simulation. This equivalent rotational spring has two spring constants. The first constant (denoted by a subscript 1)

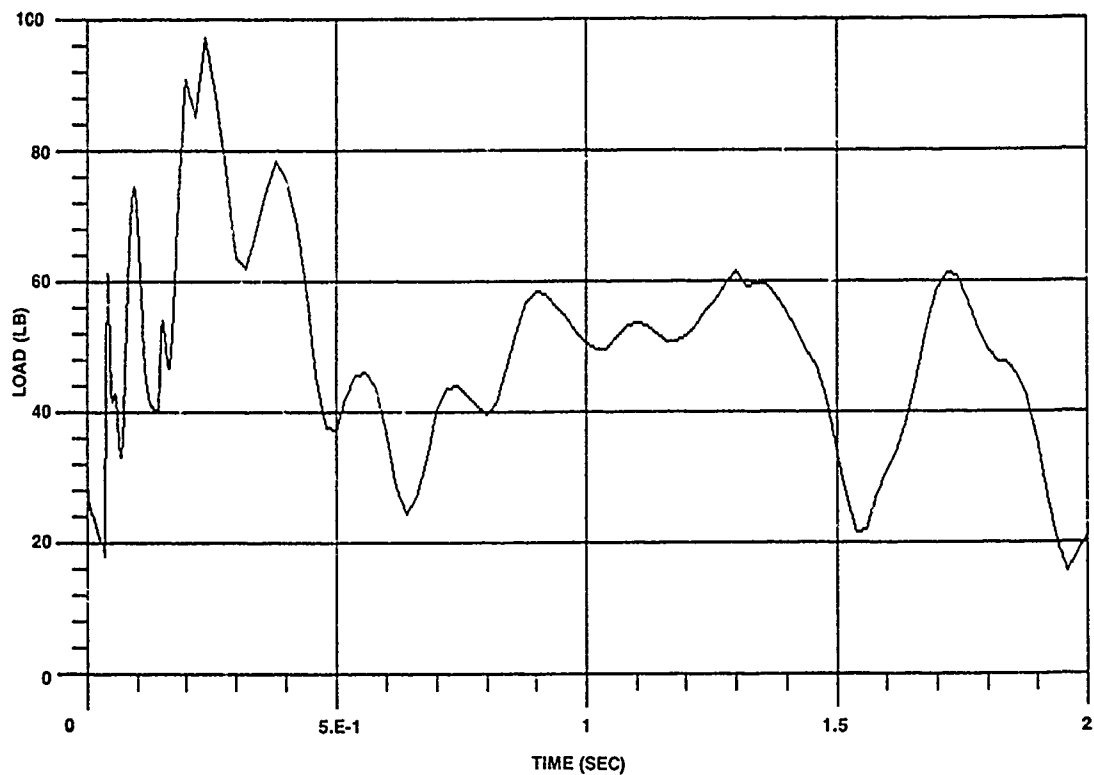


Figure 7. Maximum Load in Cable Pair 5 vs. Time

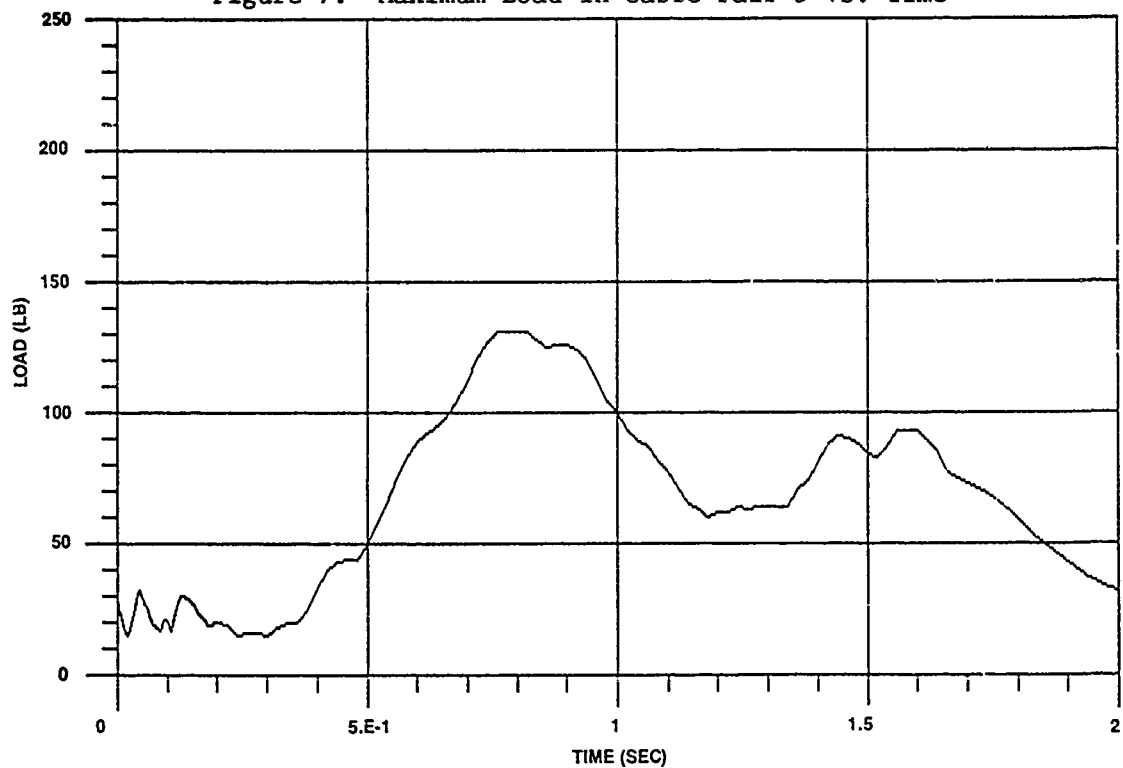


Figure 8. Maximum Load in Cable Pair 2 vs. Time

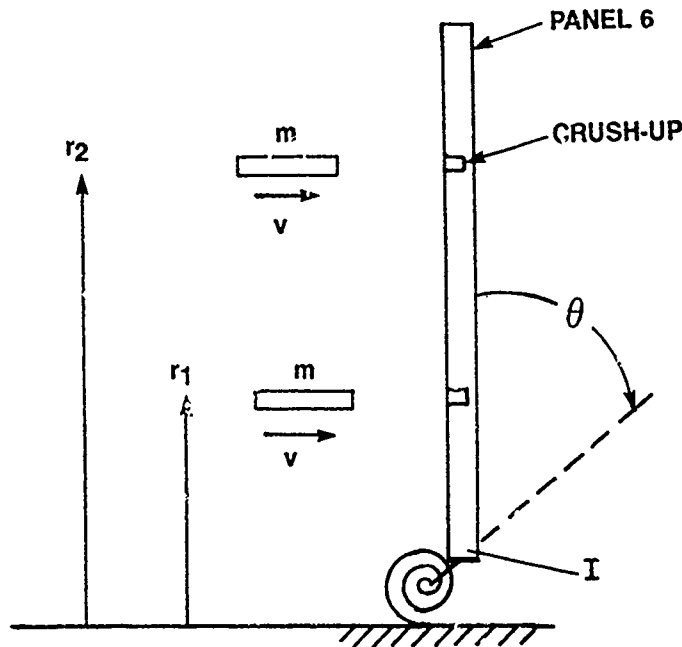


Figure 9. Hand Analysis Representation

applies when both cables are taut (due to the preload). The second constant applies when one cable is taut and the other has gone slack. The potential energy expression is then

$$V_{\max} = 1/2 k_1 \theta_1^2 + k_2 (1/2 \theta_{\max}^2 + \theta_1 \theta_{\max} - 3/2 \theta_1^2) \quad (4)$$

where

$$k_1 = 2EA/L r^2 \quad (5)$$

$$k_2 = EA/L r^2 \quad (6)$$

and

E = Young's modulus of cable
A = area of cable
L = cable length (free)
r = pulley radius

as given in Table 1. The angle θ_{\max} is found by equating V_{\max} to T_0 . Once this is done, the maximum cable load is determined from

$$P_{\max} = EA/L r \theta_{\max} + P_0 \quad (7)$$

where P_0 is the cable preload. Substituting the UARS values, the resulting maximum cable load from the momentum/energy conservation analysis is 394 lb. Therefore, the computer simulation allows the synchronization cable design load to be reduced by 67 percent to 131 lb.

CONCLUSIONS

The computer simulation performed using MSC/NASTRAN and ADAMS with user-written FORTRAN allows the solar array synchronization cable design load to be reduced by 67 percent compared to the value resulting from a more conventional momentum/energy conservation hand analysis. This reduction comes about because the computer simulation is much more sophisticated. The consideration of various nonlinearities and the use of many more degrees of freedom by the computer simulation allows for a significant reduction in conservatism from the hand analysis. The computer simulation also provides much more insight into the solar array deployment dynamics and automatically provides data in convenient tabular and graphical forms. The results achieved with ADAMS might also be obtained through a hand or symbolic manipulation program formulation of equations of motion with the solution programmed on a computer, but at the expense of considerably more time and effort and most likely less organization and reliability. Such a formulation and solution would most likely be problem dependent or restricted to one class of analyses. In contrast, the time and effort spent learning to use a large dynamics analysis code such as ADAMS can be applied to an extremely broad range of problems.

REFERENCES

1. Orlande, N., "Development and Application of Node-Analogous Sparsity-Oriented Methods for Simulation of Mechanical Dynamic Systems," Ph.D. thesis, University of Michigan, 1973.
2. Orlande, N., Chace, M. A., and Calahan, D. A., "A Sparsity-Oriented Approach to Dynamic Analysis and Design of Mechanical Systems - Parts I and II," Papers 76-DET-19 and 76-DET-20, ASME Mechanisms Conference, Montreal, Quebec, Canada, October 1976.
3. Gear, C. W., "Simultaneous Numerical Solution of Differential-Algebraic Equations," IEEE Transactions on Circuit Theory, Vol. CT-18, No. 1, January 1971.
4. Gear, C. W., "The Numerical Solution of Problems which may have High Frequency Components," Proceedings of the NATO ASI on Computer Aided Analysis and Optimization of Mechanical System Dynamics, August 1983.
5. Chua, L. O. and Lin, Pen-Min, Computer Aided Analysis of Electronic Circuits: Algorithms and Computational Techniques, Prentice-Hall, Englewood Cliffs, New Jersey, 1975.
6. Wielenga, T. J., "Simplifications in the Simulation of Mechanisms Containing Flexible Members," Ph.D. thesis, University of Michigan, 1984.
7. Benson, D. J., "The Simulation of Deformable Mechanical Systems using Vector Processors," Ph.D. thesis, University of Michigan, 1983.
8. ADAMS User's Manual, Mechanical Dynamics, Inc., Ann Arbor, Michigan, October 1987.
9. Timoshenko, S., Young, D. H., and Weaver, W. Jr., Vibration Problems in Engineering, John Wiley and Sons, New York, 1974.

EXPERIMENTAL OBSERVATIONS OF LOW AND ZERO GRAVITY NONLINEAR FLUID-SPACECRAFT DYNAMICS¹

Lee D. Peterson
Sandia National Laboratories
Applied Mechanics Division 1524
P.O. Box 5800
Albuquerque, NM 87185

ABSTRACT

Low and zero gravity simulation experiments of the motion of a spacecraft coupled to the nonlinear slosh of a contained fluid are presented and discussed. A generic study model, in which a linear, spring-mass-damper spacecraft mode was coupled to the slosh of a fluid within an attached cylinder, has been studied experimentally using a unique, scale model apparatus. Low gravity was simulated in a 1 g laboratory using capillary (Bond number) scaled models, and zero gravity was simulated during experiments on the NASA KC-135 Reduced Gravity Test Facility. The mass fraction of fluid, the tuning ratio of the fluid and spacecraft vibrations, the spacecraft damping ratio, and the nondimensional gravity level were systematically varied. The nonlinear free decay response of the experimental systems exhibited system natural frequencies which varied in proportion to the square of the amplitude of the motion. The nonlinear resonance responses displayed harmonic, nonharmonic, planar, nonplanar, and spatially chaotic motions. These experimental responses can only be modeled by a nonlinear analytical model of the fluid coupled to the spacecraft model, and cannot be predicted by the simple linear slosh models currently in use.

INTRODUCTION

Under the proper dynamic conditions, the vibration of a spacecraft can couple to the slosh of a fluid contained within it, forming a coupled fluid-spacecraft dynamic system. In the limit

¹This paper reports research sponsored by the Boeing Aerospace Company and by NASA Headquarters Grant NAGW-21 at the Massachusetts Institute of Technology, and by Department of Energy Contract Number DE-AC04-76DP00789 at Sandia National Laboratories.

of vanishingly small motion of the fluid, the spacecraft dynamic response resembles a simple, linear coupled oscillator. For such a system, it is convenient to consider the fluid and spacecraft components of the fluid-spacecraft system separately: uncoupled, linear models of the fluid and the spacecraft motion can be formed independently, and then superposed or connected in series to describe the coupled system response. Such a linear dynamic model of the fluid-spacecraft motion, however, may apply only over a very small range of motion amplitudes. This is because the dynamics of the fluid slosh motion are controlled and driven by highly nonlinear boundary effects at the free surface. As a result, the spacecraft motion can take on the nonlinear character of the fluid slosh motion, and respond much differently from the prediction of a linear model. Furthermore, because superposition does not apply to a nonlinear system, the nonlinear response of the fluid in the coupled fluid-spacecraft system may vary significantly from the nonlinear motion of the fluid alone. It is important to understand and analytically describe these differences before designing any fluid-spacecraft system.

The experiments presented in this paper were part of a combined analytical-experimental research program which focused on describing the nonlinear response of a generic fluid-spacecraft system. In the study model investigated in this research (Figure 1), a right circular cylinder, partially filled with fluid, is allowed to move in a horizontal plane perpendicular to its axis. The spacecraft motion is idealized as a spring-mass-damper system, characterized in the study model by the dry mass of the tank and the two restraining springs and dampers which act against the motion of the tank. Although the analysis examined this general case, the experiment considered only the special case in which the motion of the tank in the y direction was constrained to be zero. This study model is simple enough to yield an analytical (as opposed to numerical) model of the nonlinear fluid motion, but is complex enough to exhibit the dynamic effects expected to be important. These effects include:

1. The coupled system motion will be dominated by the resonant interaction of the first fluid mode with the spring-mass mode of the spacecraft.
2. The motion will depend on the amplitude of the system excitation in an undetermined and possibly nonlinear manner.
3. The system natural frequencies will change with amplitude of the motion.
4. At sufficiently large amplitudes, and for steady, harmonic excitation near the system resonances, the fluid motion will have a component in the transverse or *nonplanar* (y) direction. This nonplanar fluid motion can be harmonic, multiply-harmonic, or nonharmonic with the system excitation.
5. Two principal parameters are expected to jointly determine the degree of nonlinearity observed in the fluid: the fluid mass fraction and the linear slosh frequency tuning ratio.
6. The nonlinearity of the coupled system motion will change as the steady-state gravity level (g) is lowered.

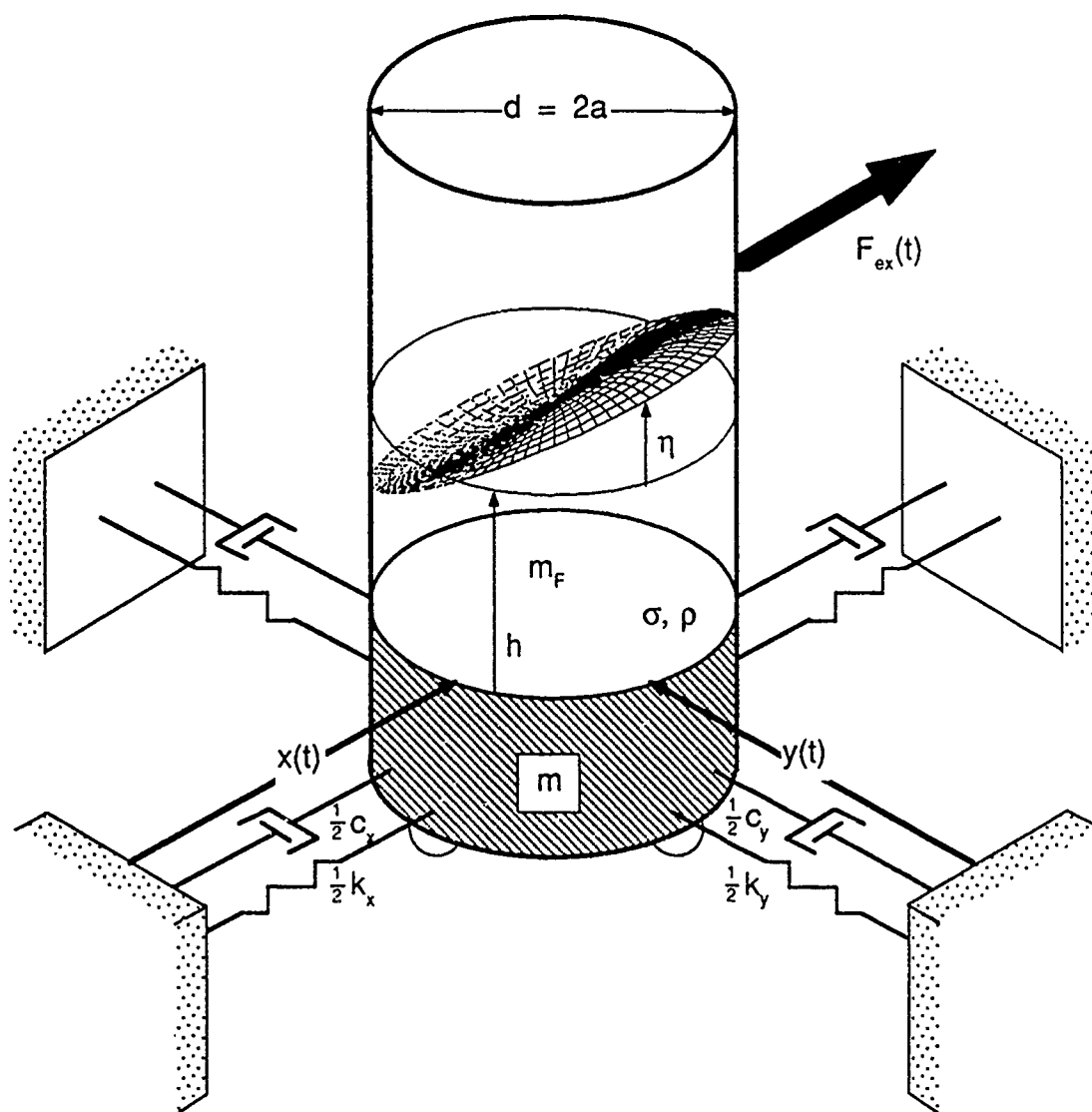


Figure 1. Fluid-spacecraft study model investigated in this research. Although the analysis examined this general case, the experiment was restricted to the special case in which the motion of the tank in the y direction was constrained to be zero. This is equivalent to assuming that the stiffness, k_y , is much greater than k_x .

This experimental program was integral to the companion analytical research effort.^{[1],[2],[3]} Beyond simply confirming the analysis, the experimental results actually compelled the development of more complicated analytical models. Although the original analytical models were sufficiently general to describe any type of coupled system response, it was not possible to determine, based only upon analytical considerations, the minimum content of the analytical model which was sufficient to describe the dynamics. The original intuition, based largely on *linear* expectations, was modified to recognize obviously neglected effects in the dynamics. These experimental results therefore provide an independent description of the nonlinear coupled system motion apart from the analysis.

The approaches, methods, and results of this experimental research program are presented in the sections below. First, the experimental approach and apparatus are presented and discussed. Then, typical experimental results are presented to illustrate the main conclusions.

EXPERIMENTAL APPROACH AND APPARATUS

Nondimensional Parameters

A new experimental apparatus and procedure were developed to study the dynamics of the fluid-spacecraft study model of Figure 1. The experiment was a scale model of an actual, full-scale system, whose size and parameters were determined to match the important nondimensional parameters for the fluid-spacecraft system. Four nondimensional parameters govern the dynamics of this system. The nondimensional inertia scaling parameter is the mass ratio μ , the ratio of total fluid mass, m_F , to total dry mass m :

$$\mu = \frac{m_F}{m} \quad (1)$$

The nondimensional frequency scaling parameter is the frequency ratio, ν , the ratio of the first slosh mode natural frequency in the linear limit, ω_s , to the tank undamped natural frequency, ω_o :

$$\nu = \frac{\omega_s}{\omega_o} = \frac{\omega_s}{\sqrt{\frac{k}{m}}} \quad (2)$$

in which k is taken to be the spring rate in the x direction.² A closely coupled system is one in which $\nu \approx 1$. As will be seen in the experimental results, the more nonlinear response is observed in systems with small mass ratios, μ .

Because any nonlinear response of the fluid-spacecraft system will depend on the amplitude of the tank motion, it will depend on the magnitude of the applied force, F_{ex} , relative to the

²Note that the experiment considered only the case of $y = 0$.

spring stiffness. The applied force F_{ex} should therefore be normalized by the spring rate, k , and the tank diameter, d , to give the following nondimensional force:

$$\Xi_{ex} = \frac{F_{ex}}{kd} \quad (3)$$

The fluid gravity force to capillary force ratio will determine the relative significance of the capillary forces. The usual normalization of the capillarity of the fluid free surface gives the Bond number,^[4]

$$B_o = \frac{\rho g a^2}{\sigma} \quad (4)$$

in which ρ is the fluid density and σ is the surface tension. B_o determines the equilibrium fluid free surface shape^[5] and the linear slosh frequency, ω_s .^{[4],[6]} Because B_o affects the equilibrium geometry of the fluid, it will affect the linear and nonlinear slosh modal masses and stiffnesses as well. The damping ratios of the spacecraft mode, ζ , and the fluid slosh modes, ζ_{q_i} , are assumed to be light (< 0.10). The ζ_{q_i} will depend on the fluid viscosity and B_o , and must, in general, be determined experimentally. The spacecraft modal damping, ζ , is chosen *a priori* to be near the damping level observed in the fundamental slosh mode, ζ_{q_1} .

Low and Zero Gravity Simulation Procedures

The most important dynamic parameter for low gravity fluid dynamics is the Bond number, because a 'low gravity' condition actually refers to a 'low Bond number' condition. Referring to equation (4), low B_o can be achieved by lowering g or a .³ In this experiment, low Bond numbers were simulated using small containers in 1 g^[7] and similar scale models in 0 g on the NASA KC-135 Reduced Gravity Test Facility, as shown in Table 1. Bond numbers of 33 and 58 were obtained in 1 g using water as a modeling fluid in 3.1 and 4.1 cm diameter pyrex glass tanks. Because previous investigations^{[7],[4]} have noted difficulty predicting the natural frequency of water in glass due to a particularly high contact line hysteresis level (Γ),⁴ a series of test results were obtained in 1 g using a 2% photoflo-water solution in a 3.1 cm diameter pyrex glass. Photoflo is a surfactant which reduces σ by a factor of two, giving a Bond number of 66. In addition, photoflo reduces the fluid-container contact angle, α , to zero, and reduces the contact angle hysteresis constant, Γ , to zero.

Bond numbers less than 20 to 30 cannot be modeled in 1 g because the slosh damping ratio, ζ_{q_1} , becomes unacceptably high.^[7] For this reason, a Bond number of zero was obtained in tests in 0 g on the NASA KC-135 Parabolic Flight Test Facility (Figure 2). This aircraft flies a series of 15,000 ft tall parabolic arcs to produce a free-fall environment for the experiments carried inside (Figure 3). Typical RMS gravity levels of 0.01 g for periods of 20-25 seconds are maintained during these maneuvers, as shown in Figures 4 and 5. Although the KC-135 test

³The ratio ρ/σ is usually fixed by the choice of modeling fluid.

⁴ Γ is defined to be the ratio of the dynamic contact line slope to the free surface motion amplitude at the container wall.

Table 1. Simulated Bond numbers studied in this research with identified linear limit slosh frequencies, damping ratios, and hysteresis constants.

Fluid Dynamic Test Condition				Identified Planar Slosh Mode Parameters		
$d(\text{cm})$	g	Fluid	B_o	$\omega_s/2\pi$ (hz)	ζ_{q_1}	Γ
3.1	1.0	photoflo	66	5.43	3.48%	0
4.1	1.0	water	58	5.28	4.20%	-5.0
3.1	1.0	water	33	6.65	4.64%	-7.8
4.1	0.01	water	~ 0	2.05	22.8%	-9.8

environment requires unusual and carefully planned test procedures, it can serve as an appropriate bridge between 1 g simulated low gravity and extended period shuttle flight experiments (as are currently planned for this experimental program).

Coupled Fluid-Spacecraft Motion Simulation

The use of small scale fluid model tanks in 1 g and in 0 g required the development of a unique experimental apparatus to generate a coupled fluid-spacecraft system. This apparatus, called a *compliant actuator*, is discussed in detail in Reference [1], and is briefly described here (Figure 6 and Figure 7). The model fluid tank was supported by a sensitive deterministic force reaction balance which measured 3 support forces eccentric to the center of mass at 120 degree intervals in the horizontal plane. The force and moment components in the horizontal plane (F_x , F_y , M_z) were resolved by an analog electronic matrix transformation of the transducer force signals. The dry mass inertia force contributions were removed electronically by addition of a signal equal to the measured acceleration of the tank support times the known system dry mass. After removing the dry mass inertia force from the measurement, only the reaction slosh forces, F_{xs} and F_{ys} , remained. The reaction slosh force measurement in the planar direction, F_{xs} , served as the input to an analog computer which solved the differential equation for the spacecraft motion:

$$m\ddot{x} + c\dot{x} + kx = F_{ex} + F_{xs} \quad (5)$$

The excitation force, F_{ex} , was provided by an electronic waveform generator. The output of the analog computer, a voltage proportional to the spacecraft motion, x , drove the motion of the tank through a servo-shaker system. Using this system to simulate and drive the model tank lateral motion, the fluid slosh was coupled to the motion of the tank. By adjusting the feedback gains in the analog computer, the simulated spacecraft modal mass, damping, and frequency could be adjusted independently. This method greatly increased the experimental fluid mass fractions which were possible, and enabled precise adjustment of the spacecraft modal dynamics.

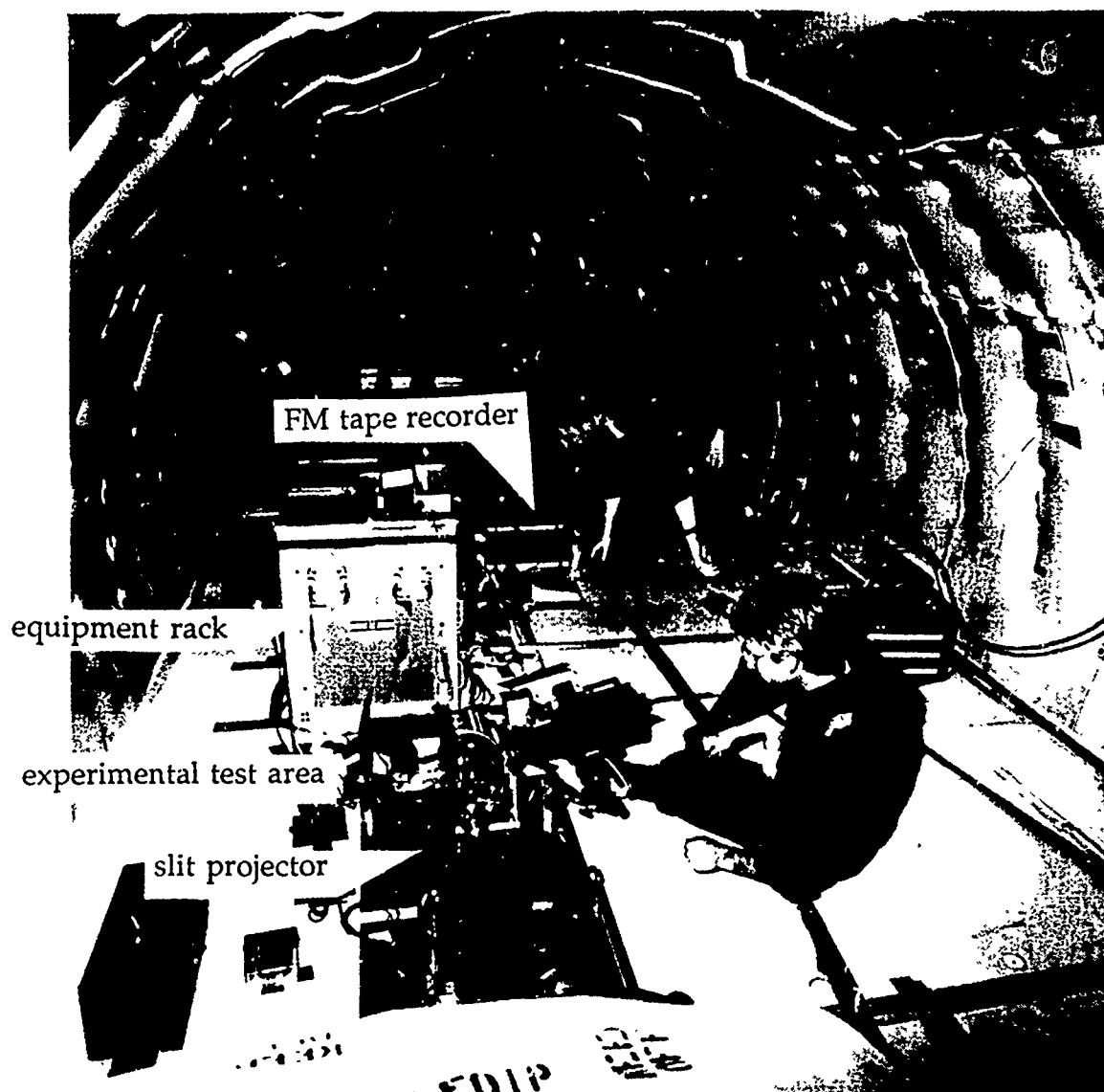


Figure 2. The NASA KC-135 Reduced Gravity Test Facility environment during a typical parabola

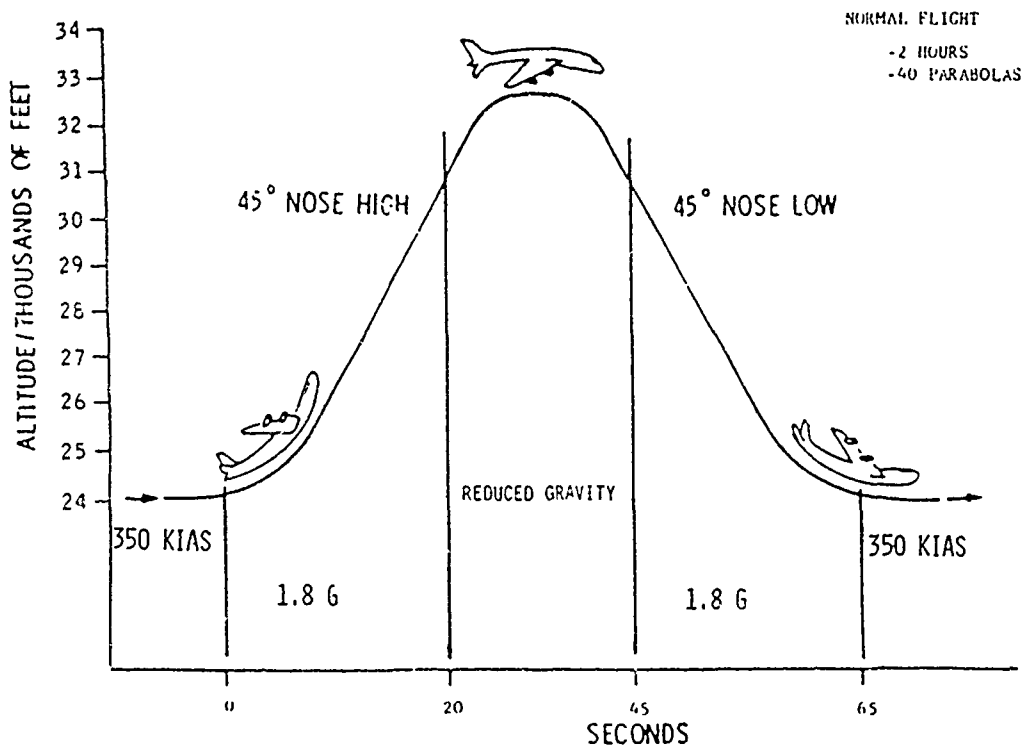


Figure 3. NASA KC-135 Parabolic Flight Test Maneuver

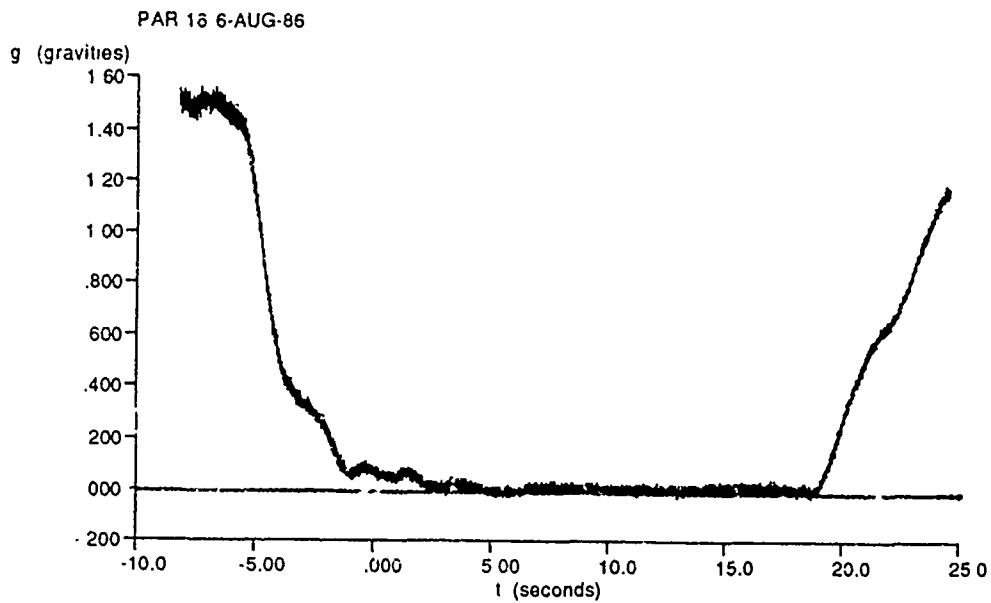


Figure 4. Gravity level profile during a typically 'good' parabola aboard the NASA KC-135.

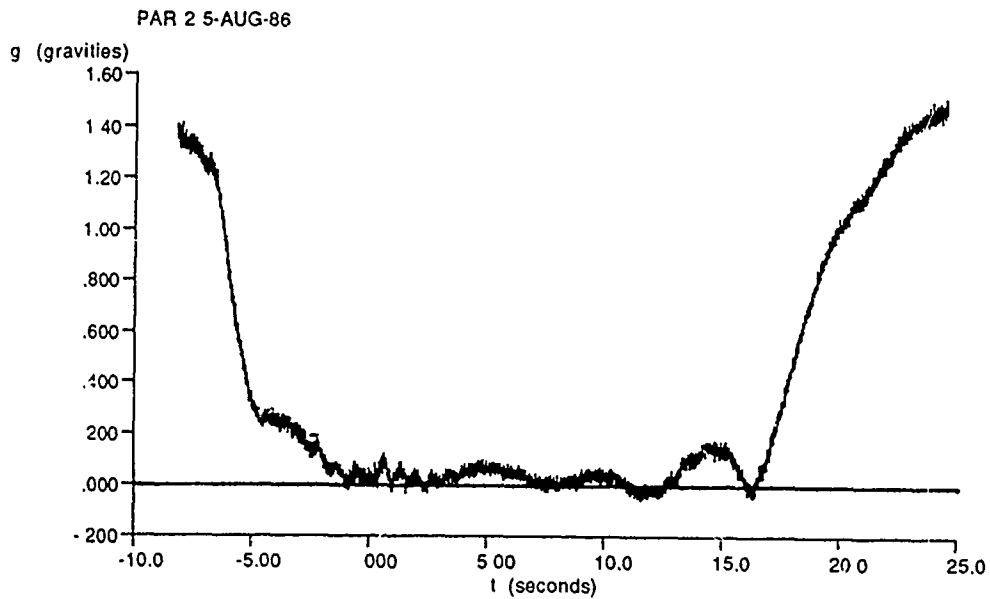


Figure 5. Gravity level profile during a typically 'bad' parabola aboard the NASA KC-135. The measured gravity transients were unacceptably high.

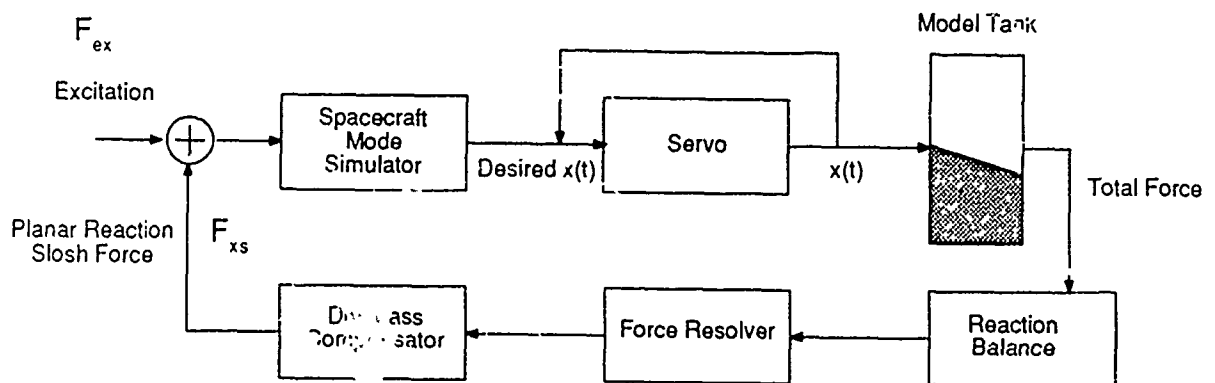


Figure 6. Component Block Diagram of the Compliant Actuator Spacecraft Mode Simulator

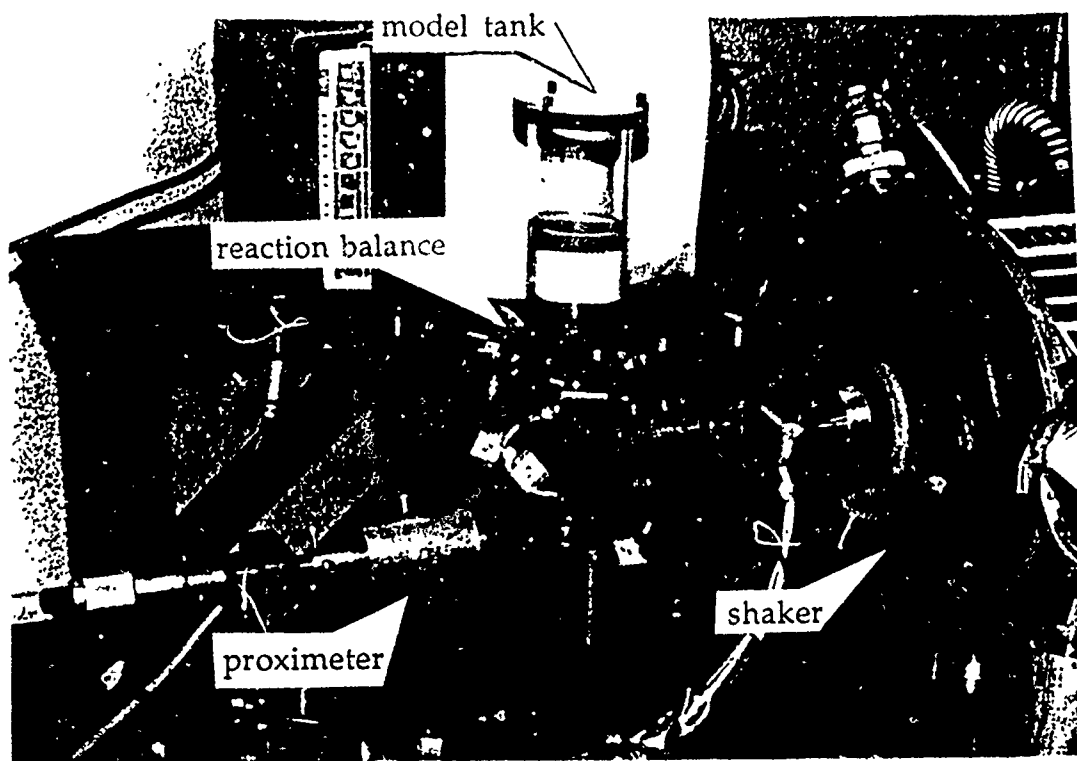


Figure 7. Close-up photograph of the experimental test section

Experimentally Observed Quantities

Five main quantities were monitored and recorded during all the 1 g and 0 g tests.

- F_{ex} : Input excitation force applied at the input port of the compliant actuator.
- F_{xs} : Reaction slosh force in the direction of the excitation and the tank motion ('planar' or 'lateral' force).
- F_{ys} : Reaction slosh force in the direction perpendicular to the excitation and the tank motion ('nonplanar' or 'transverse' force).
- x : Spacecraft (tank) motion in the direction of the excitation ('transverse').
- g : Gravity level in the 'vertical' direction normal to the direction of tank motion

In the 0 g tests, the lateral and transverse gravity levels were also monitored and recorded.

EXPERIMENTAL RESULTS

For each of the four Bond numbers simulated in this research (Table 1), a total of 11 different scaled coupled systems were studied, each characterized by a particular combination of μ , ν , and ζ . Mass ratios between 0.12 and 0.41 were studied at frequency ratios near 0.80, 1.0, and 1.2 times the frequency ratio predicted to produce the closest tuning in the eigenfrequencies for the

particular mass ratio. The nonlinear system response was studied for two types of force input: impulsive free decay and harmonic resonance. For each of the 44 different systems, impulsive free decays were studied at three values of excitation Ξ_{ex} . Resonance response sweeps at five different amplitudes of Ξ_{ex} were generated for the coupled systems with $\mu = 0.16$ and $\mu = 0.41$ at each of the four B_o levels.

The results of these experiments are presented and discussed in the following sections. The nonlinear response to impulse and harmonic resonance are presented separately.

Nonlinear Impulse Response

For impulsive free decays, impulses of equal bandwidth but varying amplitude were applied to the spacecraft degree of freedom:

$$\Xi_{ex} = \delta(t)\epsilon^2 \quad (6)$$

Figure 8 overplots the response of the same coupled system to three different amplitudes of impulse ($\epsilon^2 = 0.013, 0.043$, and 0.060). The response, x , has been normalized by the amplitude of the initial impulse to remove the *linear* part of the response and produce the normalized measurement:

$$\frac{x}{\Xi_{ex}d} \quad (7)$$

If the response of the coupled fluid-spacecraft system were entirely linear, then this normalized measurement would be independent of the amplitude of the applied impulse. The fact that it is not is entirely due to nonlinearity in the dynamics caused by the fluid slosh dynamics. From the plot, it appears that the oscillation frequency changes with the amplitude of the motion, with those responses from higher impulse amplitudes lagging behind those from lower impulse amplitudes.

To isolate and quantify this nonlinear frequency shift, the frequencies of the free decay motion were identified using the Eigensystem Realization Algorithm.^[8] ERA finds a signal reconstruction of the form:

$$x(t) = \sum_{n=1}^{N_{modes}} x_n e^{-i\zeta_n t} \cos(\omega_n t - \theta_n) \quad (8)$$

It was expected that the eigenfrequencies of the response (ω_1 and ω_2) would change not only with amplitude of the applied impulse, but also during the decay period. Thus, ERA was used to identify frequencies as a function of *time* during the decay, and the 'frequency vs time' plots of the response to different amplitudes were compared. The identification of the frequency content of the measurement signal required a finite width sampling window. As shown in Figure 9 for the larger amplitude response of Figure 8, ERA produces a reasonable estimate of the response only over the width of the data window. To obtain a qualitative (as opposed to quantitative) measure of how the frequencies changed with time, the identifications were repeated for successive data windows shifted uniformly in time during the decay period. The time increment between windows was much less than the window period. The identified eigenfrequencies for a particular data window were plotted at the time corresponding to the beginning of the data window.

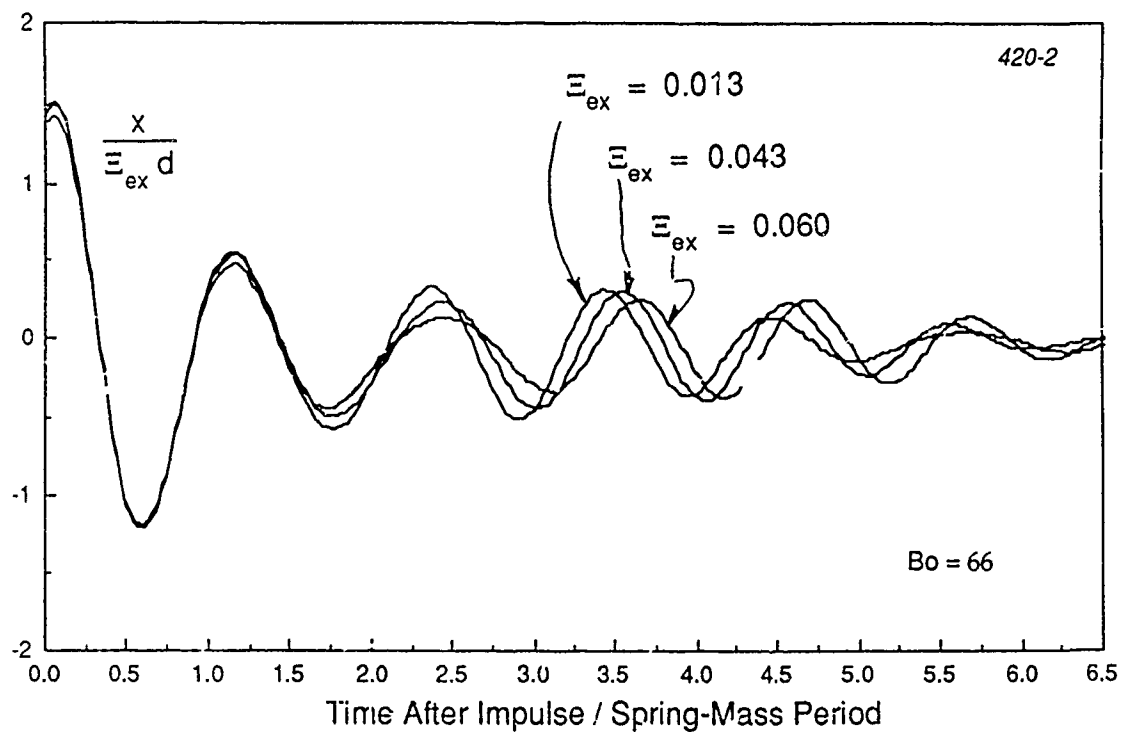


Figure 3. Normalized Free Decay Response in the Spacecraft DOF x for the Coupled System [$B_o = 66$, $\mu = 0.16$, $\nu = 1.07$, $\zeta = 5\%$, photoflo] at Three Values of Initial Impulse Amplitude, Ξ_{ex}

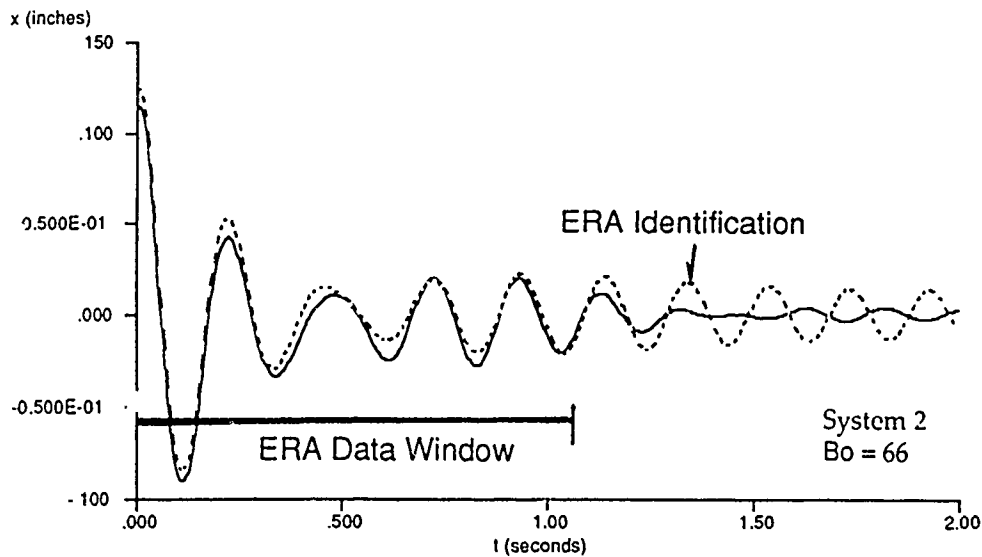


Figure 9. Measured Response and ERA Identified Response for the Large Amplitude Free Decay of Figure 8.

Figure 10 plots the frequency vs time curve for the response to all three impulse amplitudes previously presented in Figure 8. The identified eigenfrequencies have been normalized by the spring-mass frequency:

$$\nu_1 = \frac{\omega_1}{\sqrt{\frac{k}{m}}} \quad , \quad \nu_2 = \frac{\omega_2}{\sqrt{\frac{k}{m}}} \quad (9)$$

The eigenfrequencies expected from a linear analysis of the system dynamics are also indicated. It is seen that:

1. The eigenfrequencies of the nonlinear coupled system tend towards the linear predictions as the amplitude of the motion decays.
2. The amount of the nonlinear frequency shift decreases as the amplitude of the initial condition decreases.

This nonlinear impulsive free decay technique is used in the next two subsections to illustrate how the nonlinearity depends on the coupled fluid-spacecraft system mass and frequency ratios (μ and ν), and on the Bond number (B_o).

Strength of the Nonlinearity vs μ and ν By comparing the amount of frequency shift from the linear eigenfrequencies at $t = 0$ for various systems, the effect of changing fluid mass fraction μ

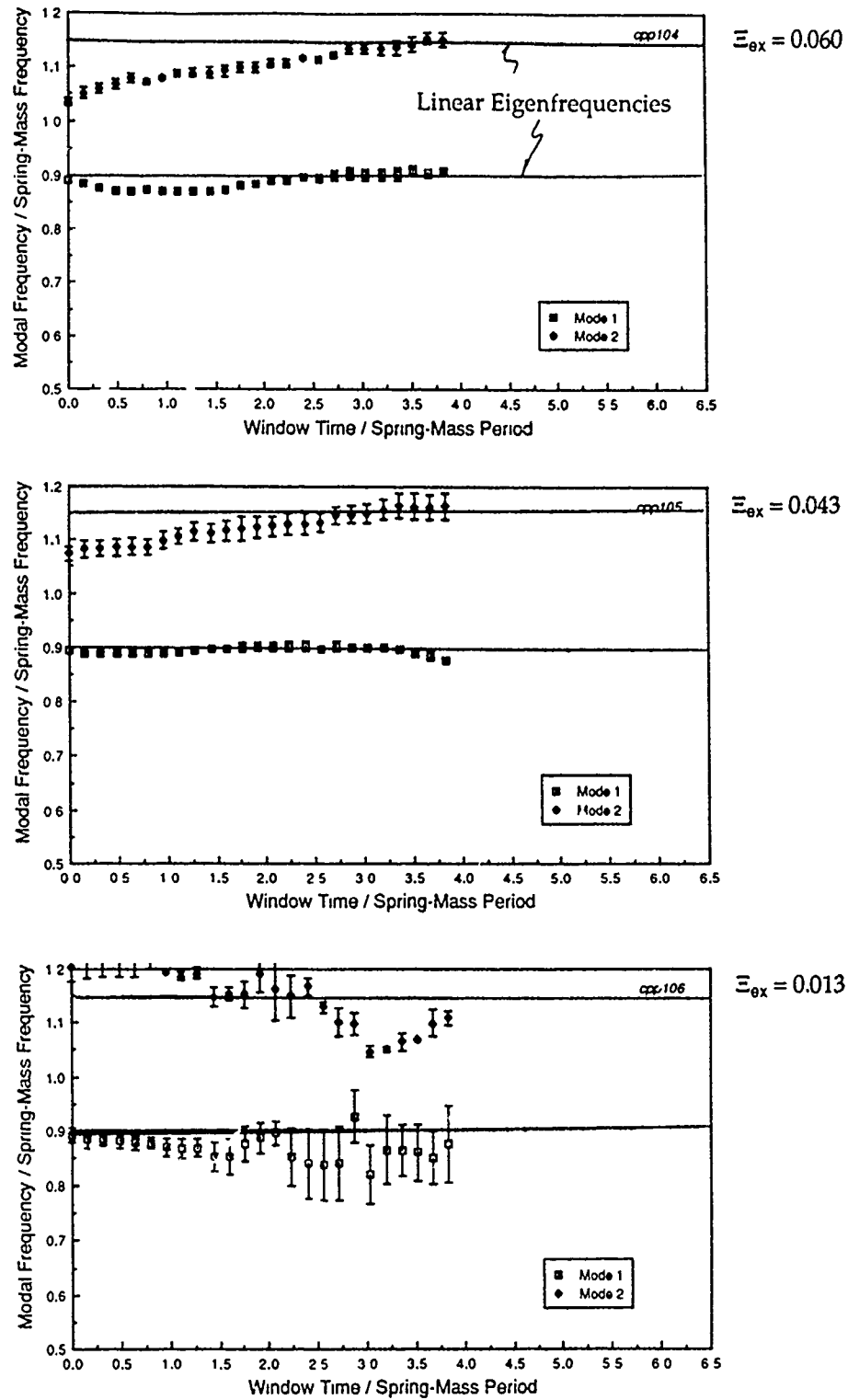


Figure 10. Windowed ERA Identifications for the Free Decays of Figure 8.

and tuning ratio ν can be illustrated. The *strength of the nonlinearity* is defined to be:

$$\frac{\delta\nu_i}{\epsilon^2} = \frac{\nu_{ERA_i}(t=0) - \nu_{linear}}{\epsilon^2} \quad (10)$$

in which $\nu_{ERA_i}(t=0)$ is the eigenfrequency identified by ERA at $t=0$ and ϵ^2 is the amplitude of the applied impulse. For a fixed Bond number of 66, this number is plotted in Figure 11 as a function of fluid slosh frequency ratio ν for two different values of fluid slosh mass fraction $\mu = 0.40$ and $\mu = 0.16$. Two conclusions are deduced from this plot:

1. The nonlinearity is stronger for systems with lighter fluid mass fractions.
2. The nonlinearity is stronger for systems with frequency ratios near 1.

These two main results are confirmations of an analytical prediction, and were observed consistently throughout the impulse free decay data that was collected.^[1] The nonlinearity is stronger for systems with less fluid mass because the coupled system eigenfrequencies are more closely tuned for these systems. The analysis predicts that the nonlinearity is stronger when the coupled system eigenfrequencies are more closely resonant.^[2]

Strength of the Nonlinearity vs Bond Number The experimental results generally indicate that the nonlinear eigenfrequency shifts observed during a free decay will increase as the Bond number is decreased. This is shown in Figure 12, which plots the identified eigenfrequencies vs time for the same coupled system [$B_o = 66$, $\mu = 0.16$, $\nu = 1.07$, $\zeta = 9.5\%$, photoflo] at each of the four Bond numbers studied. The prediction of the nonlinear analytical model is also plotted in each case.

This trend is expected by the analytical model.^{[1],[2]} It is due to two effects:

1. As the Bond number decreases, the capillary forces at the free surface contribute additional nonlinear spring stiffnesses to the equations of motion.
2. As the Bond number decreases, certain 'singular' conditions of the analysis which predicate highly nonlinear responses occur for many more coupled systems in the range of frequency ratios $0.5 < \nu < 1.5$.

Nonlinear Resonance Response

For the harmonic resonance experiments, a harmonic excitation at fixed frequency was applied:

$$\Xi_{ex} = \epsilon^3 \cos 2\pi ft \quad (11)$$

The excitation amplitudes ϵ^3 were varied logarithmically over a factor of 10 from a lowest magnitude in which the response is essentially linear to a largest magnitude in which the response

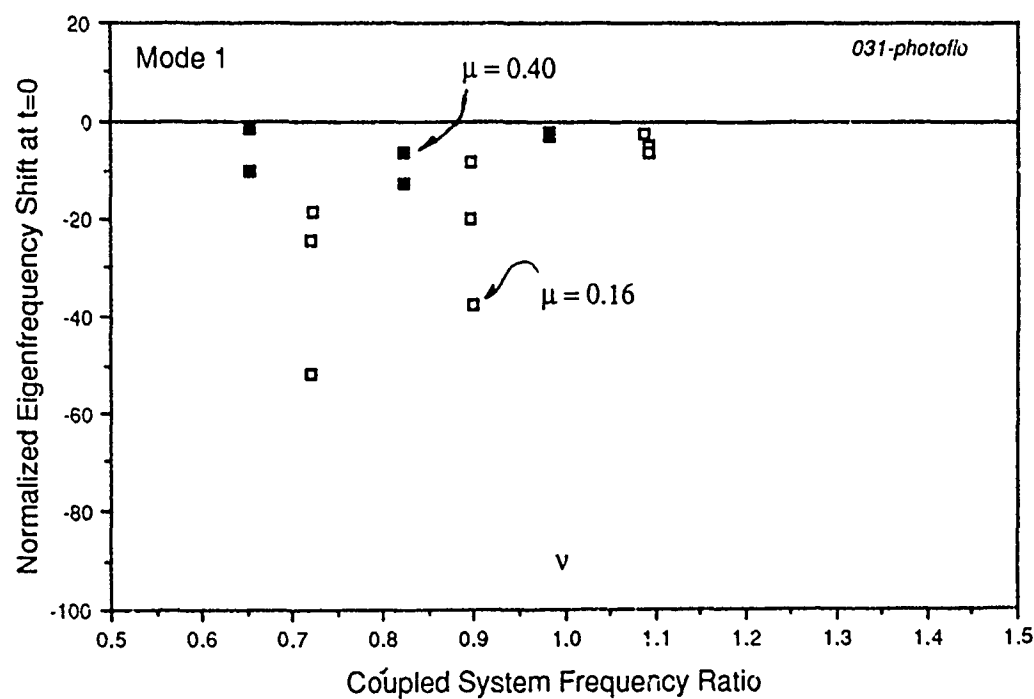
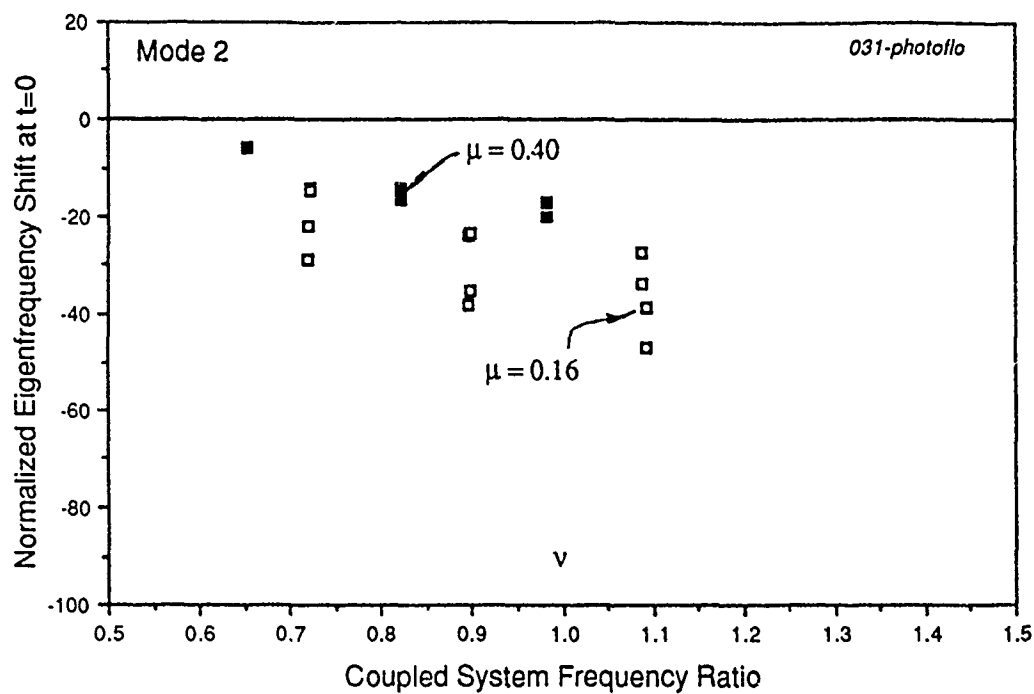


Figure 11. Normalized Identified Eigenfrequency Shifts at $t = 0$ for 9 Different Coupled Fluid-Spacecraft Systems at a Fixed Bond number of 66.

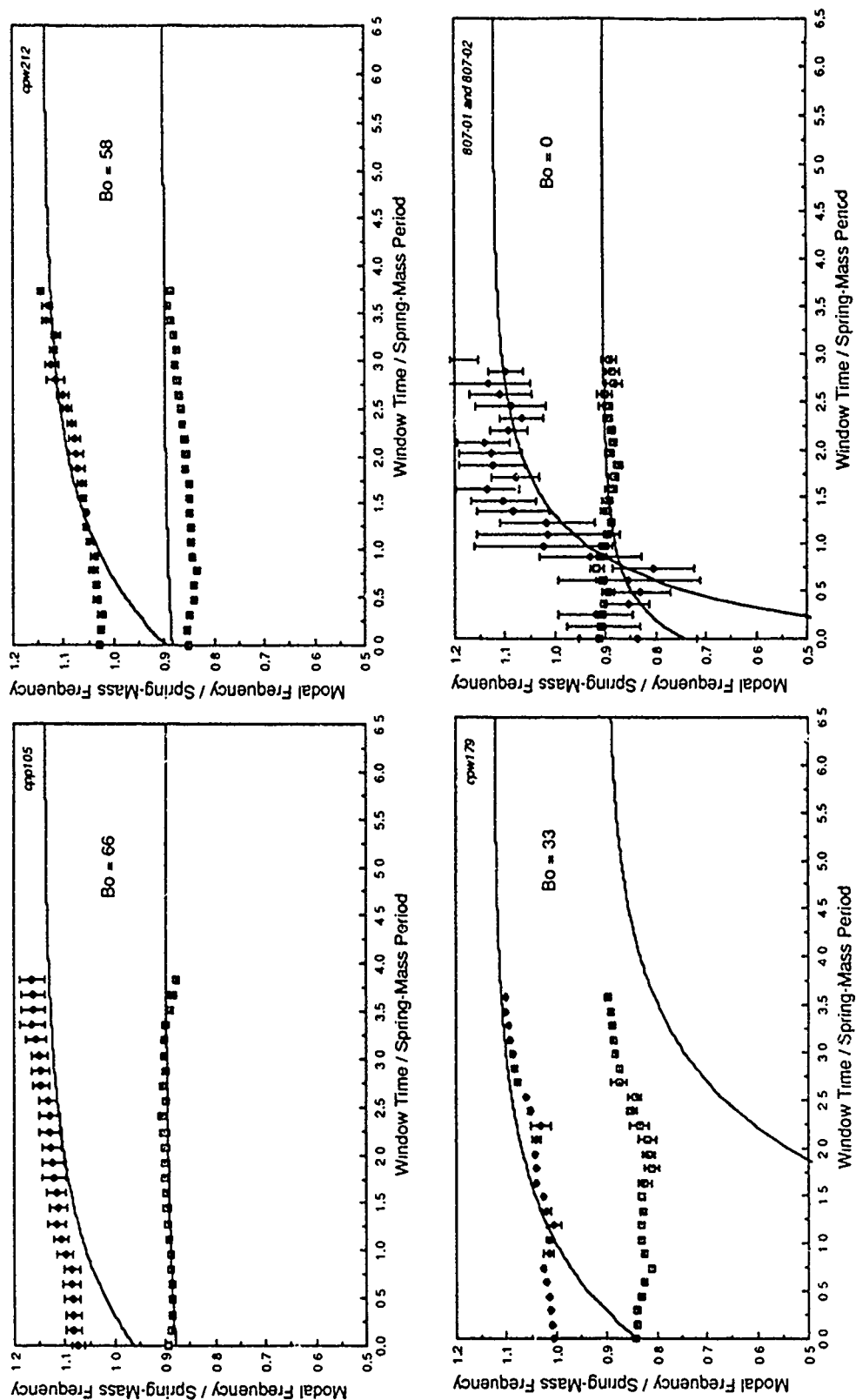


Figure 12. Identified Eigenfrequencies for the Coupled System [$B_o = 66$, $\mu = 0.16$, $\nu = 1.07$, $\zeta = 9.5\%$, photofo] at all Four Bond Numbers Studied in this Research. The prediction of the nonlinear analytical model is also plotted in each case. Note that the $B_o = 0$ case is KC-135 data.

is grossly nonlinear. At each amplitude, the excitation frequency f was incremented through the coupled system resonances first from below and then from above. At each frequency, the harmonic component of the response variables, x , F_{xs} , F_{ye} , and their phases were measured with a spectrum analyzer. The presence of additional harmonics was also noted.

Figure 13 shows a typical resonance plot of x generated in this manner. As the excitation amplitude is increased, the frequencies of maximum response are shifted to progressively lower frequencies. This is consistent with the observation from the impulsive response measurements that the eigenfrequencies decrease (for this system) with amplitude of the motion. The peaks closely correspond to the locations predicted by the nonlinear analytical model. In addition, the amplitude of the peak response is not proportional to the amplitude of the excitation, an indication of amplitude-dependent damping effects. While such effects are not predicted by the perturbation analysis of Reference [1], they are allowed by the nonlinear equations of motion.

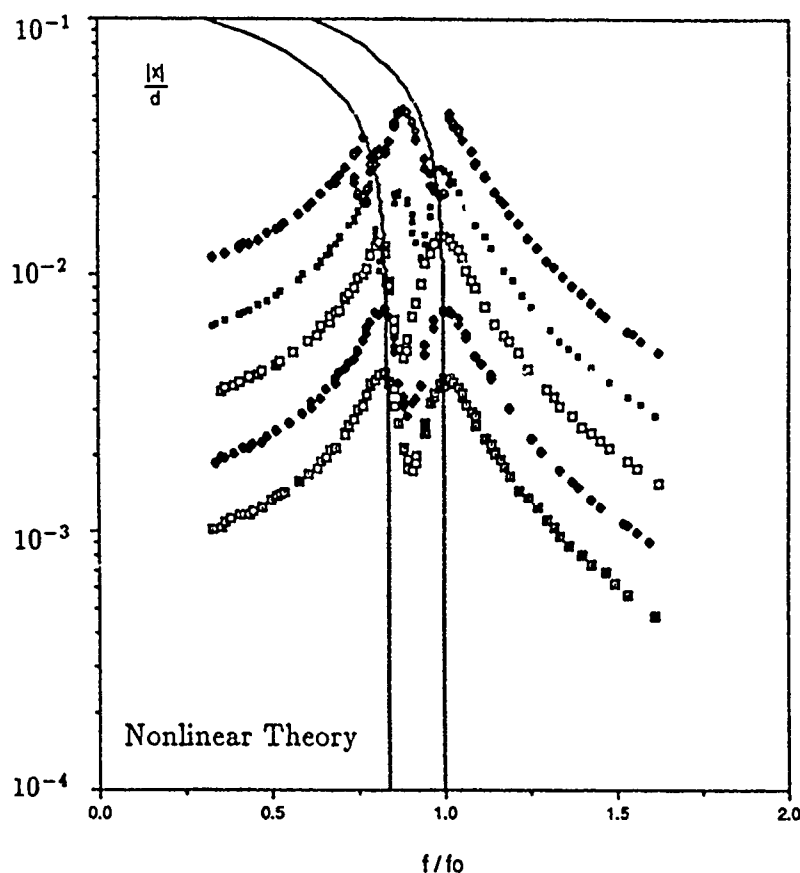


Figure 13. Resonance of the Spacecraft Degree of Freedom x for the system [$B_o = 66$, $\mu = 0.16$, $\nu = 0.90$, photoflo] at $|E_{ex}| = 0.0010, 0.0018, 0.0032, 0.0056$, and 0.0100 . The theoretical position of the resonance peaks for planar motion are also plotted.

As the excitation amplitude increases, the system begins to resonate in more than one type

of motion. Each type of motion can be distinguished by the motion of the free surface and by a sudden shift in amplitude or phase as the excitation frequency is incremented. Figure 14 shows the resonance plot at the largest excitation amplitude of the previous figure ($\epsilon^3 = 9.55 \times 10^{-3}$). Distinct regions of the resonance plot are observed, most separated by sudden 'bifurcations' or jumps in the resonance curves. While this system exhibits only four types of large amplitude motions, at least six different and distinct resonance motions have been observed (Figure 15). Three of these types of motion are not observed in the nonlinear fluid resonance when uncoupled from the spacecraft motion. This leads to an important conclusion: a nonlinear system embedded in a larger and otherwise linear system does not necessarily respond as simply as the nonlinear system in isolation. The types of resonance motion are described in detail below:

Planar I Planar I motion is the same motion observed when the coupled system response is essentially linear. The lateral slosh force F_{xs} and spacecraft motion differ in phase from the excitation as predicted by a linear model. The transverse slosh force F_{ys} is zero.

Planar II Planar II motion resembles the Planar I motion only in the fact that the transverse slosh force F_{ys} is zero. It is unique to the coupled fluid-spacecraft system. The transition to Planar II motion is marked by a sudden jump in slosh force amplitude, F_{xs} , as well as hysteresis in the resonance plot. The slosh wave amplitude is approximately a radius in height during this motion. The transition to Planar II is also indicated by the sudden generation of higher harmonics in the coupled system response.

Skew Nonplanar This type of motion is not observed in the nonlinear uncoupled response of the fluid, and is unique to the coupled fluid-spacecraft system. It is characterized by the existence of a slosh force component in the transverse direction, F_{ys} , which is in phase with the lateral slosh force component, F_{xs} . The motion of the fluid free surface appears to be skewed because the node line of the motion is no longer perpendicular to the tank motion, but remains stationary. Higher harmonics are observed in this motion.

Periodically Modulated Nonplanar Resonance (PMNR) PMNR is a type of motion also observed in the nonlinear response of the fluid slosh uncoupled from the spacecraft motion. The lateral (F_{xs}) and transverse (F_{ys}) slosh force components respond not only at the harmonic frequency of the excitation, but also at multiples of this harmonic. The resulting superposition creates a free surface motion in which the node line appears to oscillate in a multiply-periodic manner. The spacecraft degree of freedom, x , also responds in a similar multiply periodic motion.

Harmonic Nonplanar Resonance (HNR) HNR, also observed in the nonlinear uncoupled response of the fluid, is a degeneration of the PMNR motion. The multiple harmonics in PMNR are significantly suppressed, and the response of the fluid and the spacecraft are primarily at the harmonic frequency of the excitation. The transverse slosh force F_{ys} is separated in phase from the lateral slosh force F_{xs} by $\pi/2$, so that the free surface node line appears to rotate at the frequency of the excitation. This type of motion is also known in the literature as 'rotary slosh.'

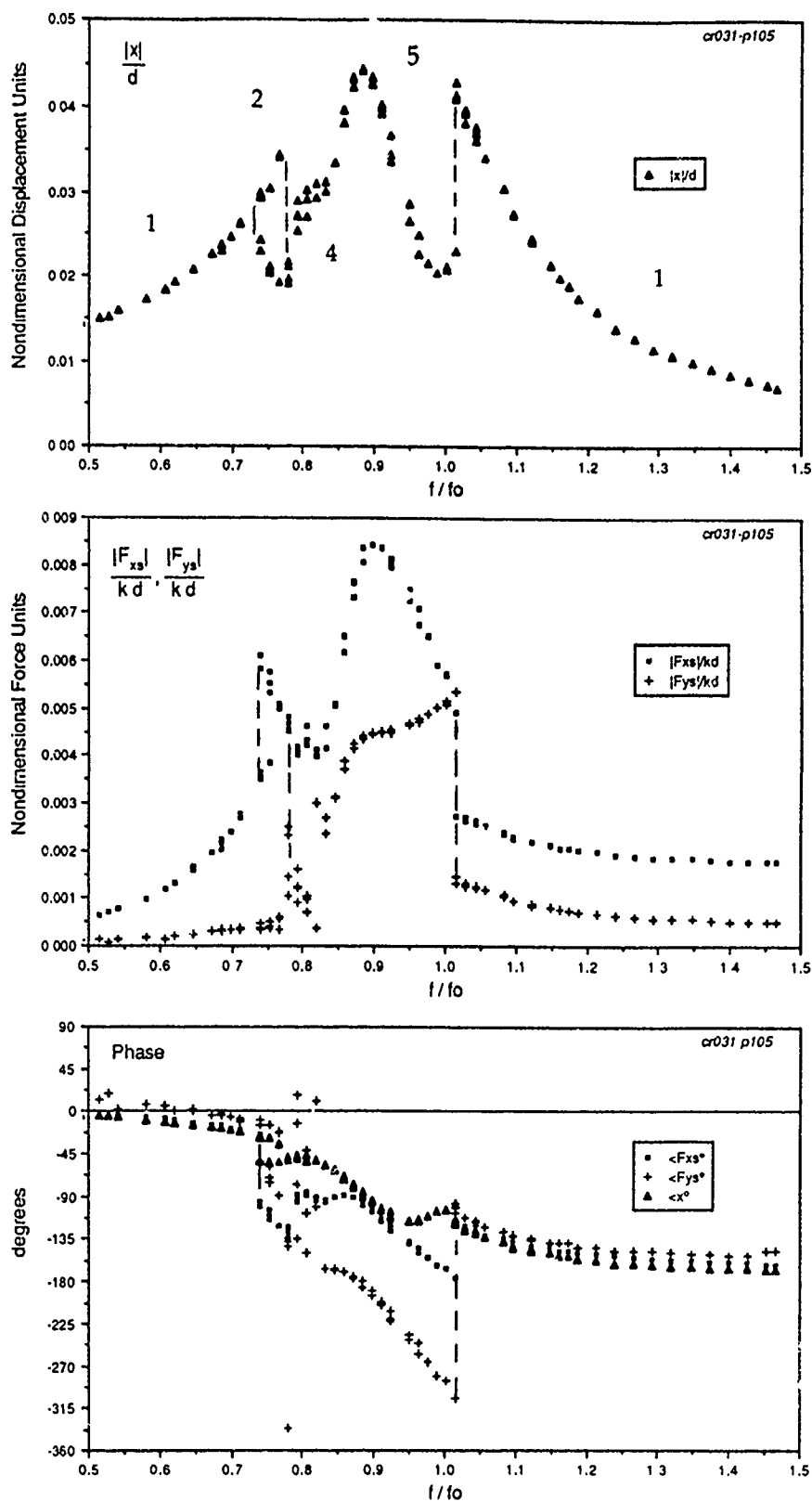


Figure 14. Expanded Resonance Plot at the Largest Excitation Amplitude of the Previous Figure.

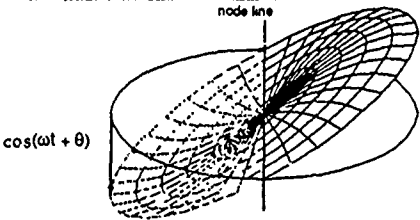
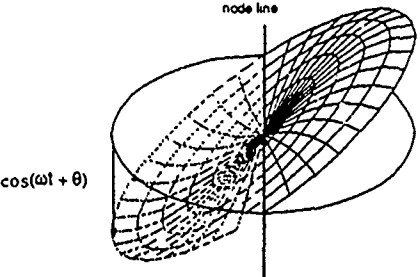
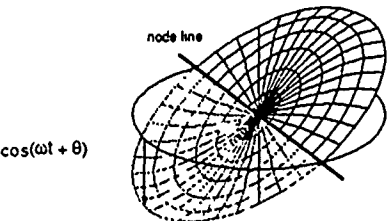
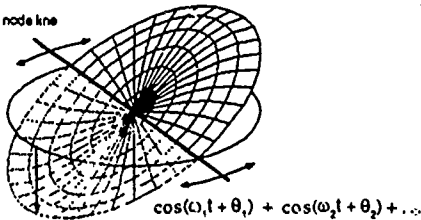
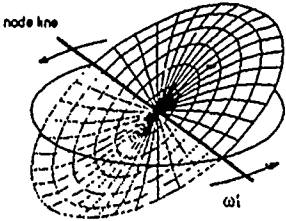
Free Surface Motion Sketch	Type of Motion and Description
	<p>1. Planar I</p> <p>Node line stationary and perpendicular to direction of tank motion</p>
	<p>2. Planar II</p> <p>Node line stationary and perpendicular to direction of tank motion.</p> <p>Motion amplitude much larger than for Planar 1 motion.</p>
	<p>3. Skew Nonplanar</p> <p>Node line stationary but skewed at a constant angle from the direction of tank motion. Response is harmonic.</p>
	<p>4. Periodically Modulated, Nonplanar Resonance (PMNR)</p> <p>Node line rotates at multiple harmonics of the excitation.</p> <p>Tank motion also modulated</p>
	<p>5. Harmonic Nonplanar Resonance (HNR)</p> <p>Node line rotates at excitation frequency</p>
	<p>6. Asymmetric PMNR (APMNR)</p> <p>Has no simple analogy in motion of the free surface. This motion is a very complex modulated nonlinear response.</p>

Figure 15. Types of Nonlinear Fluid Motion Observed in the Large Amplitude Resonance of the Coupled Systems

Asymmetric PMNR/Spatial Chaos APMNR is not observed in the nonlinear uncoupled response of the fluid, and is another type of motion unique to the coupled fluid-spacecraft system. It occurs slightly above the higher of the two system resonances, and is marked by a sudden transition from HNR motion. APMNR is characterized by the existence of many harmonics in the system response, and is distinguished by the unusual shape of the free surface during the motion. The regular, modal patterns exhibited in the other types of motion are not observed. Instead, the free surface oscillation is no longer symmetric about a node line, and does not appear to decompose into a superposition of the familiar eigenmodes of the fluid. This appears to be an experimental example of spatially chaotic motion.

CONCLUSIONS

The experimental results reported above confirm the analytical predictions that the motion of a coupled fluid-spacecraft dynamic system is fundamentally nonlinear. The free decay and harmonic resonance results confirm that the natural frequency of the coupled system motion decreases with increasing amplitude of the motion. In the nonlinear harmonic resonances, some of the types of motions excited in the fluid were different from those observed when the fluid is uncoupled from the spacecraft motion. Periodically modulated harmonic and nonharmonic fluid-spacecraft motions are possible, but spatially chaotic motions and other types of modulated motions are only observed for coupled systems. This underscores the fact that approximate analytical slosh models, including linear spring-mass models and even nonlinear pendulum models, although possible accurate representations of the uncoupled slosh dynamics, are inadequate descriptions of the slosh dynamics for modeling coupled fluid-spacecraft nonlinear dynamics.

The results of this research have important implications for the modeling of more complicated systems. It should not be assumed that a linear model of the fluid or even a nonlinear uncoupled model of the fluid will lead to an accurate analytical model if the fluid slosh and spacecraft motions are closely coupled. Higher fluid modes are central to the nonlinear coupled fluid-spacecraft motion, and must always be retained in any analysis. Furthermore, capillarity should be included for Bond numbers as high as 60 to 100 because of its effect on the natural frequency of the higher fluid modes. The natural frequency and the type of resonance response of the coupled nonlinear motion will depend on the amplitude of the coupled motion in a way that can only be predicted by a nonlinear coupled model.

REFERENCES

- [1] Peterson, L. D. (1987) *The Nonlinear Coupled Dynamics of Fluids and Spacecraft in Low Gravity*. PhD Dissertation, Department of Aeronautics and Astronautics, Massachusetts Institute of Technology. MIT SSL Report No. 22-87.

- [2] Peterson, L. D. "Nonlinear Analysis of the Coupled Motion of Fluid-Spacecraft Systems" (under preparation)
- [3] Peterson, L. D., Crawley, E. F., and Hansman, R. J. (1988) "The Nonlinear Dynamics of a Spacecraft Coupled to the Vibration of a Confined Fluid" Proceedings of the AIAA/ASME/ASCE/AHS 29th Structures, Structural Dynamics and Materials Conference, April 1988. Submitted to the *AIAA Journal*.
- [4] Satterlee, H. M. and Reynolds, W. C. (1964) *The Dynamics of the Free Liquid Surface in Cylindrical Containers Under Strong Capillary and Weak Gravity Conditions* Stanford University Report TR-LG-2.
- [5] Hastings, Leon J. and Rutherford III, Reginald. (1968) "Low Gravity Liquid-Vapor Interface shapes in Axisymmetric Containers and a Computer Simulation" NASA TM X-53790
- [6] Abramson, H. N. (1966) *The Dynamic Behavior of Liquids in Moving Containers* NASA-SP-106
- [7] Dodge, F. T. and Ferreira, L.R. (1967) "Experimental and Theoretical Studies of Liquid Sloshing at Simulated Low Gravity" *J. Applied Mech.* vol 34 series E no 3. pp 555-562.
- [8] Juang, J. and Pappa, R.S. (1985) "An Eigensystem Realization Algorithm for Parameter Identification and Model Reduction" *J. Guidance* 8:5,620-627.

VIBRATORY SYSTEM DYNAMIC ANALYSIS USING A GRAPHICS BASED SELF-FORMULATING PROGRAM

James Alanoly and Seshadri Sankar
CONCAVE (Concordia Computer Aided Vehicle Engineering)
Research Centre
Concordia University
Montréal, Québec
Canada

A very wide range of vibratory mechanical systems can be modelled as lumped parameter multibody systems. We present a new, interactive graphics based self-formulating program for the modelling and analysis of these systems whereby models of varying complexity can be built in a modular fashion. The user does this by graphically assembling its schematic from a menu of components. The formalism allows for customary modelling techniques in which each body may have an arbitrary number of degrees of freedom. The system equations are generated symbolically and can be solved for a wide variety of analysis options. We illustrate the use of the program by applying it to some typical problems.

INTRODUCTION

Simulation plays a major role in almost all fields of science and engineering. Simulation can be defined as "experimentation with models" [1]. In computer simulation, the emphasis can be either on experimentation or models. Traditionally, the emphasis has been on experimentation whereby one generates trajectories of certain descriptive variables. This is especially true in engineering sciences where models of some physical systems have survived many generations of computers. There is, perhaps, some inherent robustness in the structure of these models which is responsible for this; but we suspect that the more important reason is that modelling is often too costly and error prone.

In a typical application of computer simulation in engineering, the engineer often starts by forming a conceptual model of the system and making a schematic diagram to represent it. He then derives the system equations, decides on a solution procedure, programs it in computer language, debugs it and obtains graphical results. Despite the tremendous advances in computer hardware and software technology, this is the procedure that has been followed by most researchers. But in a truly intelligent computer aided engineering environment, most of these individual tasks could be relegated to the computer.

This is the aim of so-called *self-formulating* programs. For dynamic analysis of mechanical systems, there are several such programs available, as listed in ref. [2]. They include IMP, DADS, ADAMS, DRAM etc.. One important drawback of many of these is that the problem formulation can be very tedious and that the user is required to know specialized theory and syntax. The analytical methods used in these programs for modelling constrained mechanical systems give rise to a very large number of differential equations, leading

to numerical difficulties in solving them.

A model should be "no more complicated than absolutely necessary to provide the necessary information with the desired accuracy and timeliness, while minimizing the use of resources" [3]. The self-formulating programs should be flexible enough to allow the user to build models of varying complexity in a modular fashion. Furthermore, to be useful at a conceptual design stage, it should not require low level descriptions of system components, which are not yet available. On the other hand, models of existing systems may also be made from "black-box" components whose output/input characteristics have been experimentally determined.

Based on these considerations, We present a new interactive graphics based general purpose modelling and analysis program, called CAMSYD, for lumped parameter multibody systems. The user builds his model by graphically assembling its schematic from a menu of components. The formalism allows for customary modelling techniques in which each body may have an arbitrary number of degrees of freedom. The equations of motion are generated symbolically in state-space form, and can be solved for a wide variety of analysis options. We illustrate the use of the program by applying it to some typical problems.

MODELS OF VIBRATORY SYSTEMS

A special class of lumped parameter mechanical systems we address in this paper is characterized by rigid bodies interconnected by springs, dampers and revolute joints. The bodies may undergo small angular motions; the forces generated in springs and dampers can be passive or active, linear or nonlinear. The majority of system models in vehicle dynamics, machinery vibration, rotor dynamics, etc. can be represented by models of this sort.

Illustrations of this class of models are shown in Figures 1 through 5, and 8. These figures are taken from published literature, and we would like to point out some distinguishing features of these models. Figure 1 shows the modelling steps involved in studying the dynamics of cam mechanism [4]. The modeller's knowledge of the behaviour of such a system leads to an abstract representation of the model as shown in Figure 1(c). The flexibilities and inertias of various links are lumped at discrete points. Each of the masses has a single degree of freedom. The model shown in Figure 1(c) can also be used to represent a wide range of other systems such as disk-shaft systems. Figure 2(a) shows some models used in gear dynamics [5]. In some models the gears have a single rotational degree of freedom. The shafts have rotational stiffnesses and the gear meshing is represented by the linear stiffness of the contacting teeth. In some other models, some of the gears have a single rotational degree of freedom, while others possess an additional linear degree of freedom. Figure 2(b) shows the roll plane model of a railroad flatcar [6]. Once again we observe that different bodies are modelled with different number of degrees of freedom.

Figure 3 shows the model of an aircraft taxiing on a runway [7]. The aircraft is represented by a three degrees-of-freedom rigid body with translational and rotational inertias. The wheel axles are modelled as point masses with one degree of freedom. The landing gear with oleo-pneumatic shock struts are represented by its nonlinear force generation model. Similar situations exist for models of automobiles, Figure 4 [8], and tractor semi-trailers, Figure 7 [9].

When we manually derive the differential equations of motion for these systems, we do not explicitly write six equations for six of the possible degrees of freedom and then write additional constraint equations to represent

the gearing, bearings etc.. These constraints are automatically taken care of when the actual degrees of freedom are identified in the modelling stage and equations are written only for those degrees of freedom. We embody this customary modelling and equation derivation strategy in an interactive graphics based software package called CAMSYD.

SPECIFICATIONS OF CAMSYD

The mechanical systems we consider can be represented by free-multibody systems or mutibody systems in tree configuration. Each rigid body may have any number of degrees of freedom between one and six. (At present CAMSYD is limited to planar systems.) The implicit constraints are automatically taken care of in the formulation so that a minimal set of differential equations is generated.

The program CAMSYD is fully interactive, taking advantage of the interactive graphics facilities of modern engineering workstations. It communicates to the user via on-screen menus and queries, and the user responds with inputs from a mouse or the keyboard. The user need not know any specialized theory of problem formulation or syntax of model description. He simply draws the schematic diagram of the mechanical system essentially as those shown in the figures referred to earlier. This is done by assembling the schematic on the graphics screen by selecting components from a menu. The menu contains rigid bodies with various degrees of freedom, linear and nonlinear springs and dampers, revolute joints, and user-definable force generators, etc.. The user may make up his model by assembling these components in whatever manner he chooses. Model generation is carried out using the CAMSYD pre-processor.

Once the model creation is complete, the equations of motion are generated after checking for proper topology. Closed kinematic loops are not allowed. The equations are generated symbolically as FORTRAN subroutines. The system parameters are represented symbolically in the equations and their values are supplied at the solution stage. This facilitates easy parameter variations and optimization studies. The equations are written in standard state-space form and the user may use it with his own special analysis programs to carry out analysis options which are not provided in CAMSYD. This feature provides tremendous flexibility to the use of CAMSYD.

After the model is created, the user specifies the analysis he wishes to perform. A wide range of analysis options are available, such as time simulation for transient inputs, eigenanalysis (frequencies and mode shapes), transfer functions, stochastic analysis etc.. Nonlinear models may be automatically linearized about an operating point before it is used in frequency domain analysis. The program has several special features for vehicle system dynamic analysis. For example, various wave forms are available to be used as transient wheel inputs. For vehicles travelling with constant velocity over a given profile, the program automatically computes delayed inputs at each wheels. Similarly, for stochastic analysis with single variate input process, the input spectral density matrix is also computed from the spectral density of the single input.

The results are examined using the graphics post-processor. It can select output data and display X-Y plots, mode shapes, write data to files etc..

APPLICATION

We illustrate the application of CAMSYD to the modelling and analysis of vibratory mechanical systems. Examples are taken from published literature to show the versatility of CAMSYD as a general purpose modelling and analysis tool. The models are built from the components in the CAMSYD menu and the analysis and the graphical display of results are also carried out.

The first example of an automobile vertical vibration problem is taken from ref. [8]. Figure 4(a) shows a two degree-of-freedom quarter car model. This model is very widely used to evaluate the ride and road holding abilities of passive and active vehicle suspensions. The parameter values are selected as $m_1 = 200$ kg, $m_2 = 80$ kg, $k_1 = 30000$ N/m, $k_2 = 320000$ N/m, $d_1 = 4800$ Ns/m and $d_2 = 0$. We want to evaluate the eigenvalues and eigenvectors of the dynamical system, and study its transient response for a set of initial conditions.

Using the CAMSYD pre-processor we build the model and specify the analyses that are to be performed. The differential equations are automatically generated in state-space form in terms of the state-vector $[y_1, y_2, \dot{y}_1, \dot{y}_2]^T$. The eigenvalues are : $\lambda_{1,2} = -30.253 \pm 57.003i$, and $\lambda_{3,4} = -1.747 \pm 4.578i$. Transient response of the system for an initial condition with $y_1(0) = 1.0$ is shown in Figure 5.

One proposal to reduce vehicle vibrations employs vibration absorbers at the wheel axles. The absorber is a relatively small mass (20 kg) elastically attached to the axle. Figure 4(b) shows the model of the total system, which now has three degrees of freedom. In CAMSYD this model is easily made by attaching the mass and spring-damper to the previous model. The parameter k_3 is set as 60000 N/m. We wish to evaluate the frequency response of the car body vertical acceleration for different values of the absorber damping, d_3 .

At the analysis stage, the time domain state-space equations are transformed into frequency domain and the transfer matrix relating the output, \ddot{y}_1 , to the input y_e is determined. This is numerically evaluated at discrete frequencies to get a plot of the body acceleration frequency response function. Efficient numerical techniques are implemented in CAMSYD which avoid repeated matrix inversions for this operation. The response of the system is shown in Figure 6. Total absorption takes place for zero damping. At other frequencies the amplitude is larger. With increasing damping one actually loses the effect of total absorption, but this is compensated for by improved performance at other frequencies.

As an example of a more complex system, we select a six degree of freedom articulated vehicle model proposed in ref [9]. Figure 7 shows the model of a tractor-semitrailer used for ride comfort studies. The tractor and the semitrailer are connected through the fifth-wheel, which is modelled as a revolute joint. The system has a total of six degrees of freedom: tractor pitch and bounce, trailer pitch relative to the tractor, and bounce of each of the three wheels. In ref. [9] the damping in the three main suspension units are optimized considering a stochastic input. We take the parameters of the optimized vehicle and study the effect of varying the location of the fifth-wheel coupling between the tractor and the trailer. This is a very practical design variation and it is expected to have a large influence on the ride performance. To evaluate this we look at the transfer function relating the tractor CG bounce and pitch accelerations to the road input.

Magnitudes of the bounce and pitch acceleration transfer functions are shown in Figure 8. Two variations of the fifth wheel location are studied,

0.5m behind the nominal position (+0.5m), and 0.5 m ahead of it (-0.5m). From Fig. 8(a) we see that the -0.5m position leads to higher amplitudes at lower frequencies and lower amplitudes at higher frequencies. In the case of +0.5m position, the situation is reversed. But the pitch acceleration response shows a very different picture. The +0.5 position gives consistently lower amplitudes for the frequency range considered. Similarly, the -0.5 position leads to higher acceleration amplitudes throughout the frequency range.

CONCLUSION

We have presented a general purpose program, called CAMSYD, for the modelling and analysis of vibratory systems. The system models are described to the program by assembling its graphical schematic on the computer screen. The program is self-formulating in that it can automatically generate the equations of motion from this graphical input. The analysis options implemented in the program covers a range of vibration analysis techniques. We have illustrated the use of CAMSYD by applying it to a number of vibration problems.

REFERENCES

1. A. Korn, and J.V. Wait, *Digital Continuous System Simulation*, Prentice Hall, Englewood Cliffs, New Jersey, 1978.
2. Haug, E.J., "Elements and Methods of Computational Dynamics", in *Computer Aided Analysis and Optimization of Mechanical System Dynamics*, Haug, E.J., ed., pp. 3-38, NATO ASI Series, Springer-Verlag, Heidelberg, 1984.
3. A.W. Wymore, *System Engineering Methodology for Inter Disciplinary Teams*, John Wiley & Sons, New York, 1976.
4. Young, S.-S.D., and Shoup, T.E., "The Sensitivity Analysis of Cam Mechanism Dynamics", *ASME Paper No. 80-DET-93*, Design Engineering Technical Conference, Beverly Hills, California, Sept. 28-Oct. 1, 1980.
5. Özgüven, H.N., and Houser, D.R., "Mathematical Models Used in Gear Dynamics- A Review", *Journal of Sound and Vibration*, 121(3), pp. 383-411, 1988.
6. White, R.C., "Car Rocking Simulations of Two 140-Ton Railroad Flatcars", in *Symposium on Simulation and Control of Ground Vehicles and Transportation Systems*, L. Segel, et al, Eds., AMD-Vol. 80, pp. 399-410, American Society of Mechanical Engineers, New York, 1986.
7. Ottens, H.H., "Predicted and Measured Landing Gear Loads for the NF-5 Aircraft Taxiing over a Bumpy Runway", *Nato AGARD Congerence Proceedings No. 326*, pp. 13.1-13.14, 1980.
8. Müller P.C., and Schiehlen, W.O., *Linear Vibrations*, Martinus Nijhoff Publishers, Dordrecht, The Netherlands, 1985.
9. ElMadany, M.M., "A Procedure for Optimization of Truck Suspensions", *Vehicle System Dynamics*, 16, pp. 297-312, 1987.

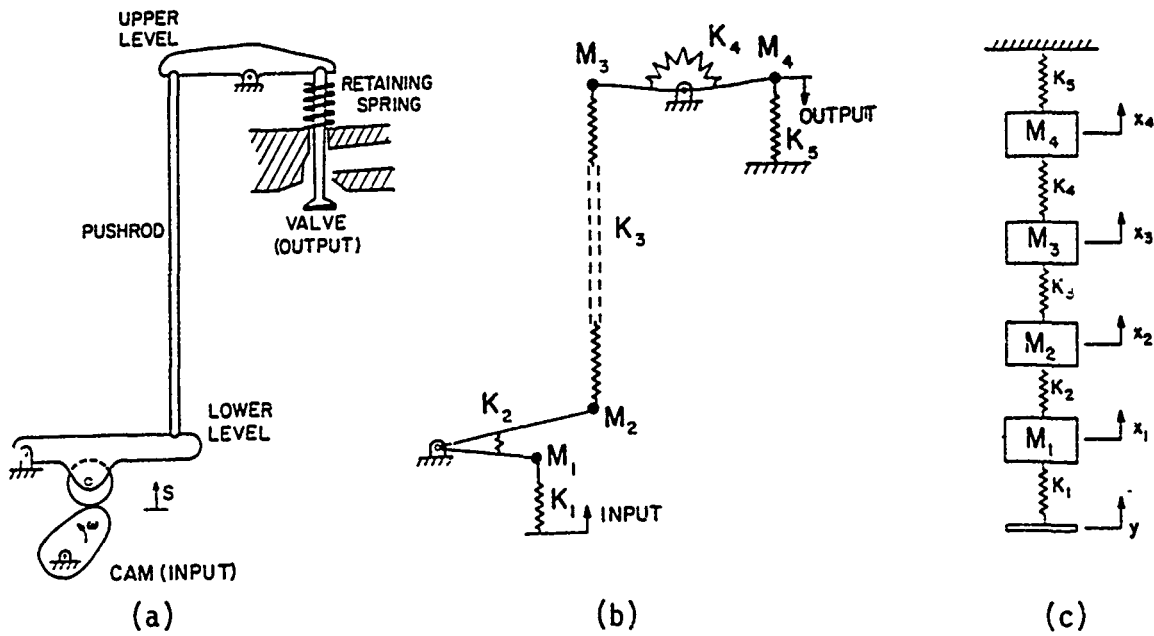


Fig. 1: (a) Double lever cam follower system;
(b) Initial model; (c) Final model.

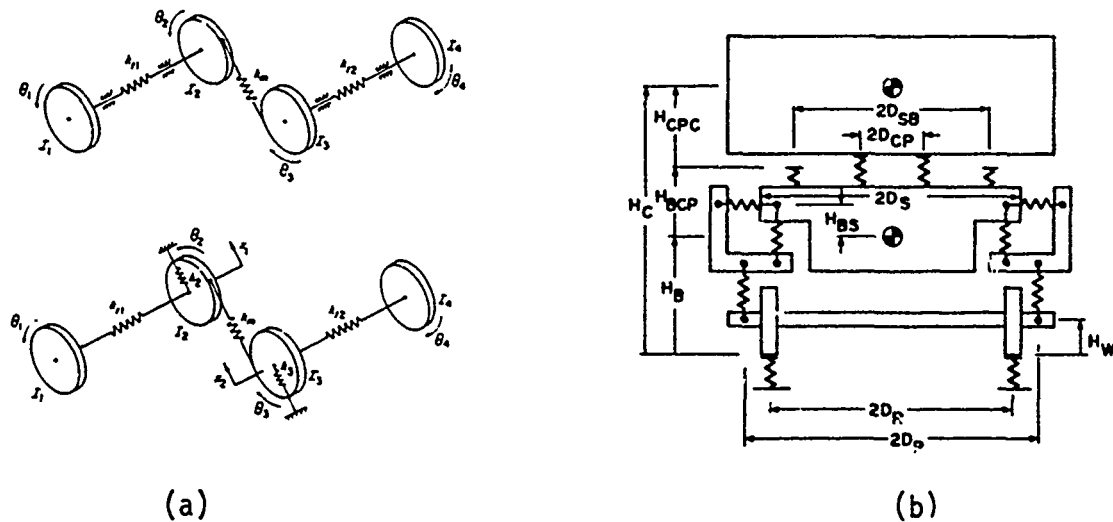
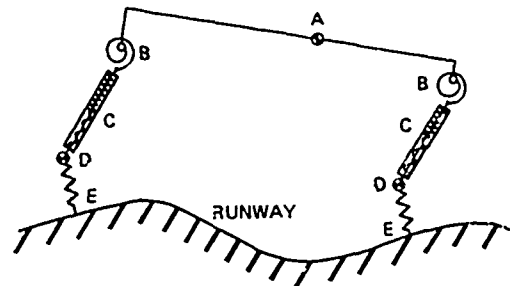
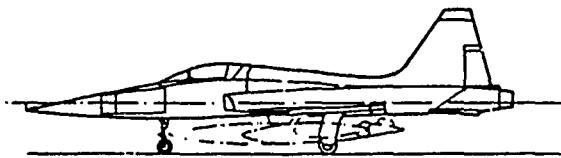


Fig. 2: (a) Typical models for gear dynamics;
(b) Roll plane model of a railroad flatcar.



- A NF-5A AIRCRAFT** e.g. position and mass and inertia properties vary with payload and fuel configuration
- B TORSIONAL SPRINGS** representing drag strut flexibilities
- C SLIDING MEMBERS** with stiffness and damping properties derived from design drawings

- D WHEEL AXLES** lumped mass representing axles, wheels, tyres and brakes
- E SPRINGS** representing tyre flexibility

Fig. 3: Model of a NF-5A aircraft taxiing on a runway

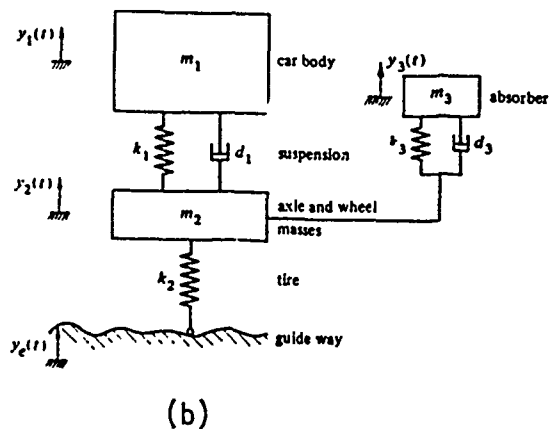
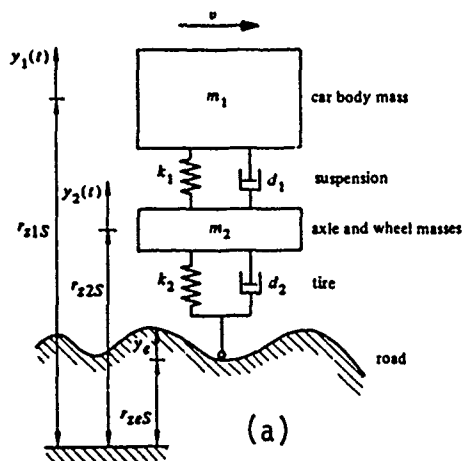


Fig. 4: (a) Model of the vertical vibration of an automobile;
(b) Automobile suspension with vibration absorber.

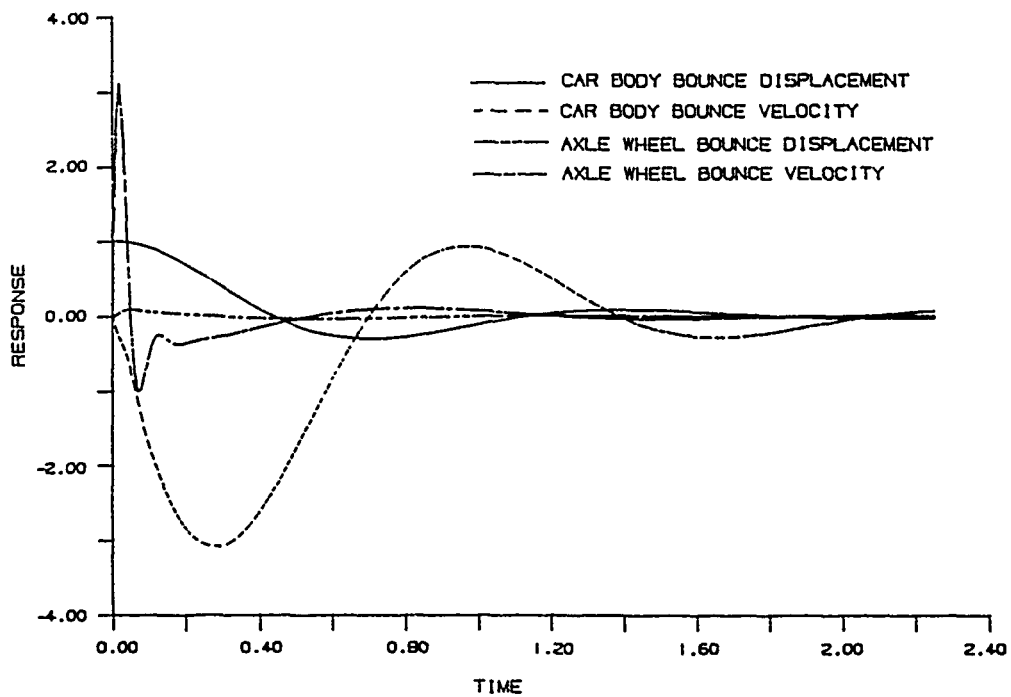


Fig. 5: Transient response of the system in Fig. 3(a).

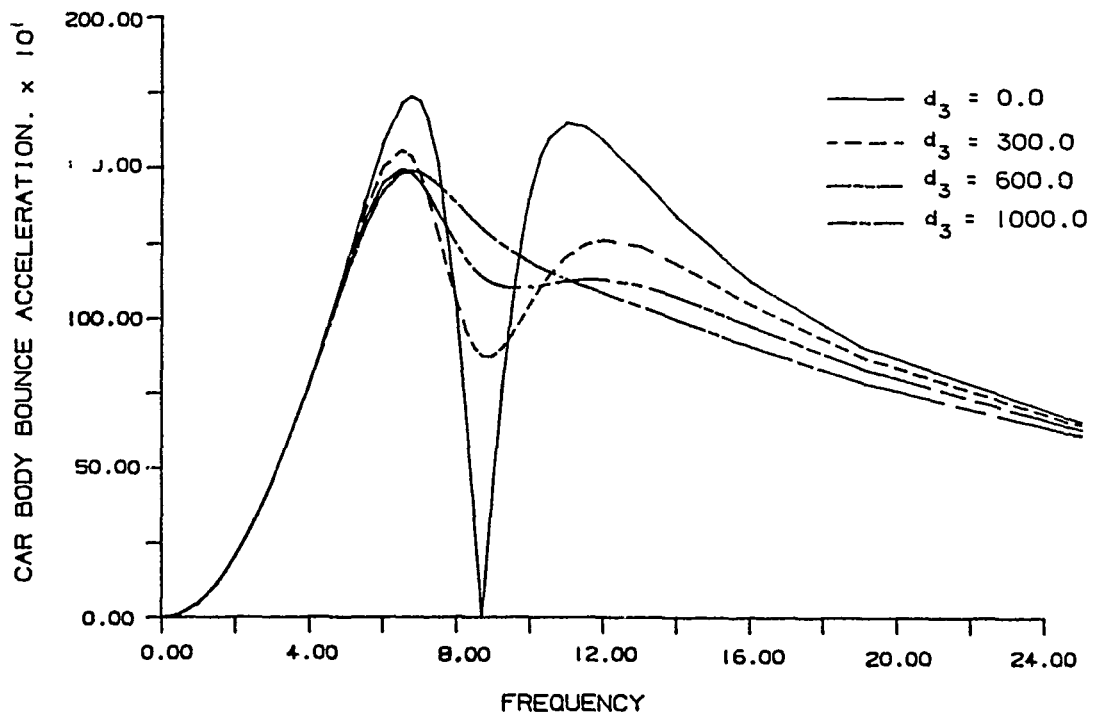


Fig. 6: Vehicle body acceleration frequency response for automobile with vibration absorber

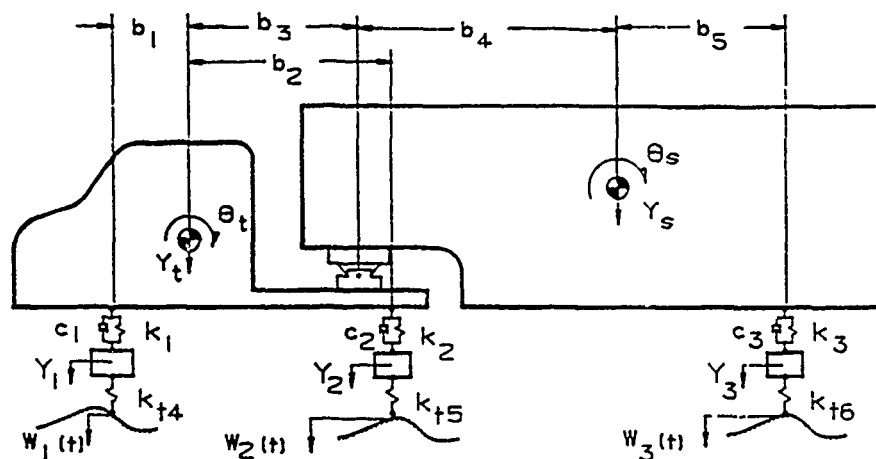


Fig. 7: Tractor semi-trailer model used in ride comfort studies.

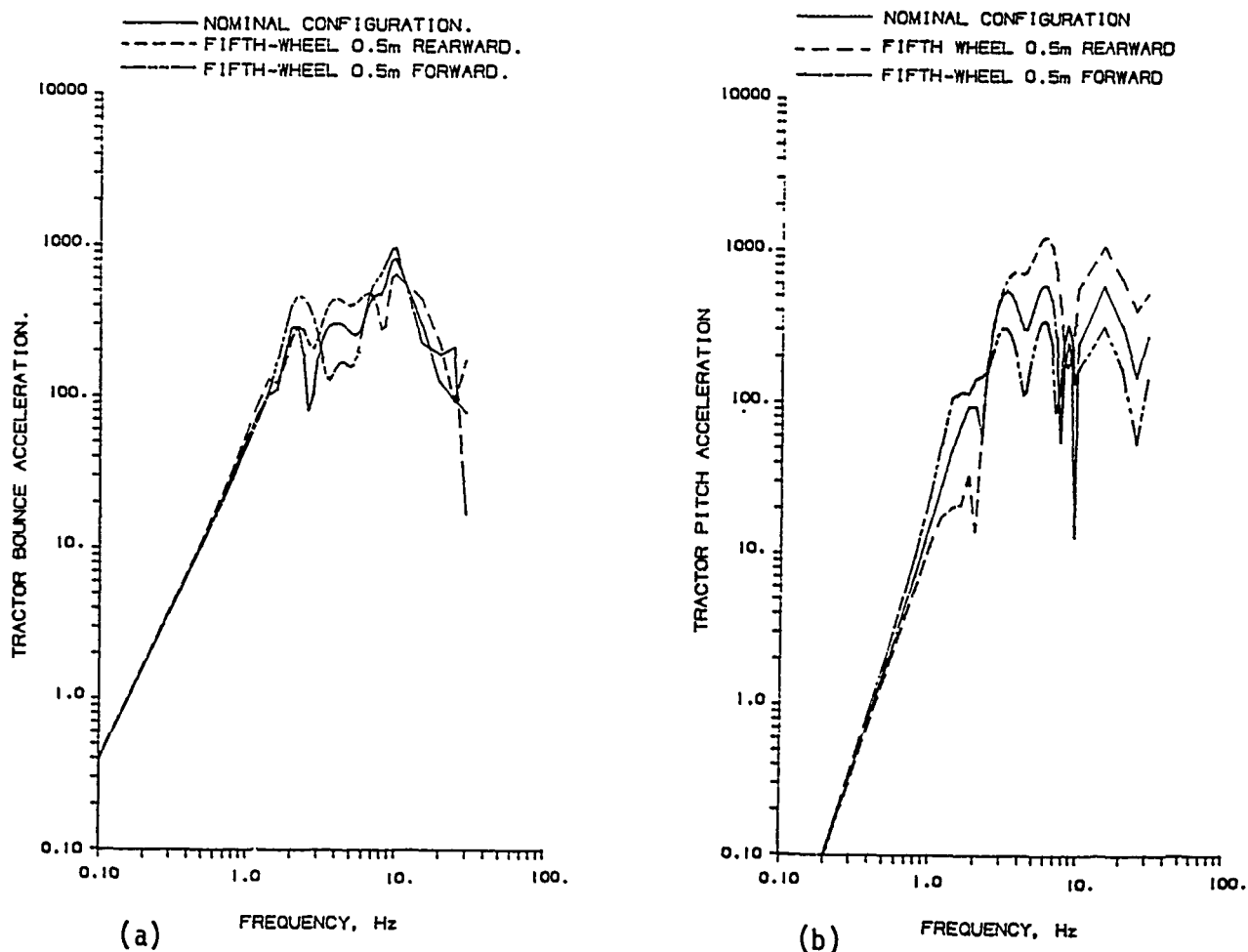


Fig. 8: Acceleration frequency response of tractor CG:
(a) vertical motion; (b) pitch motion.

DESIGN OF UPPER ATMOSPHERE RESEARCH SATELLITE (UARS) USING TRANSIENT LOADS ANALYSIS¹

S. Mittal, M. Garnek, and C. Stahle
General Electric Astro Space Division
P.O. Box 8555
Philadelphia, PA 19101

This paper presents an improvement over the normal procedure of using the quasi-static load factors for spacecraft design and analysis. The transient loads analysis method was used successfully on the UARS program to minimize design changes and reduce weight when original design parameters and the STS forcing functions changed.

INTRODUCTION

The Upper Atmosphere Research Satellite (UARS) uses a large truss structure to position an array of 12 instruments and to support them during its launch from the space shuttle. The UARS orbital configuration is shown in Figure 1. There has been an increasing concern about the sensitivity of the Earth's atmosphere to external influences associated with natural phenomena and to changes arising from byproducts of various human activities. Long standing curiosity about atmospheric evolution and the influence of factors affecting climate and weather has been sharpened and refocused by the discovery of technological threats that introduce the possibility of atmospheric modification. The UARS mission is aimed at improving our knowledge of the atmosphere above the troposphere including those regions that are known to be susceptible to substantial changes by external agents. To accomplish this mission, an array of approximately 12 scientific instruments is used to make simultaneous complimentary measurements of various related phenomena. Because of the field of view requirements, the instruments are separated from each other by a relatively large distance and joined together by a stiff, stable graphite epoxy truss. In order to meet pointing requirements, the large instruments are mounted to the thermally stable truss structure on kinematic mounts. The other instruments are mounted to honeycomb panel structures. Some of the instruments are mounted to a movable Solar Stellar Pointing Platform (SSPP). The spacecraft is approximately 32 feet long and weighs about 15000 pounds.

The usual procedure for designing a complex spacecraft structure is to develop a set of preliminary quasi-static design load factors with enough conservatism to prevent extensive design changes later in the program. A coupled payload/launch vehicle loads analysis is then performed to verify the preliminary sizing. A

(1) The work reported in this paper was performed under NASA-GSFC contract number NAS5-28666.

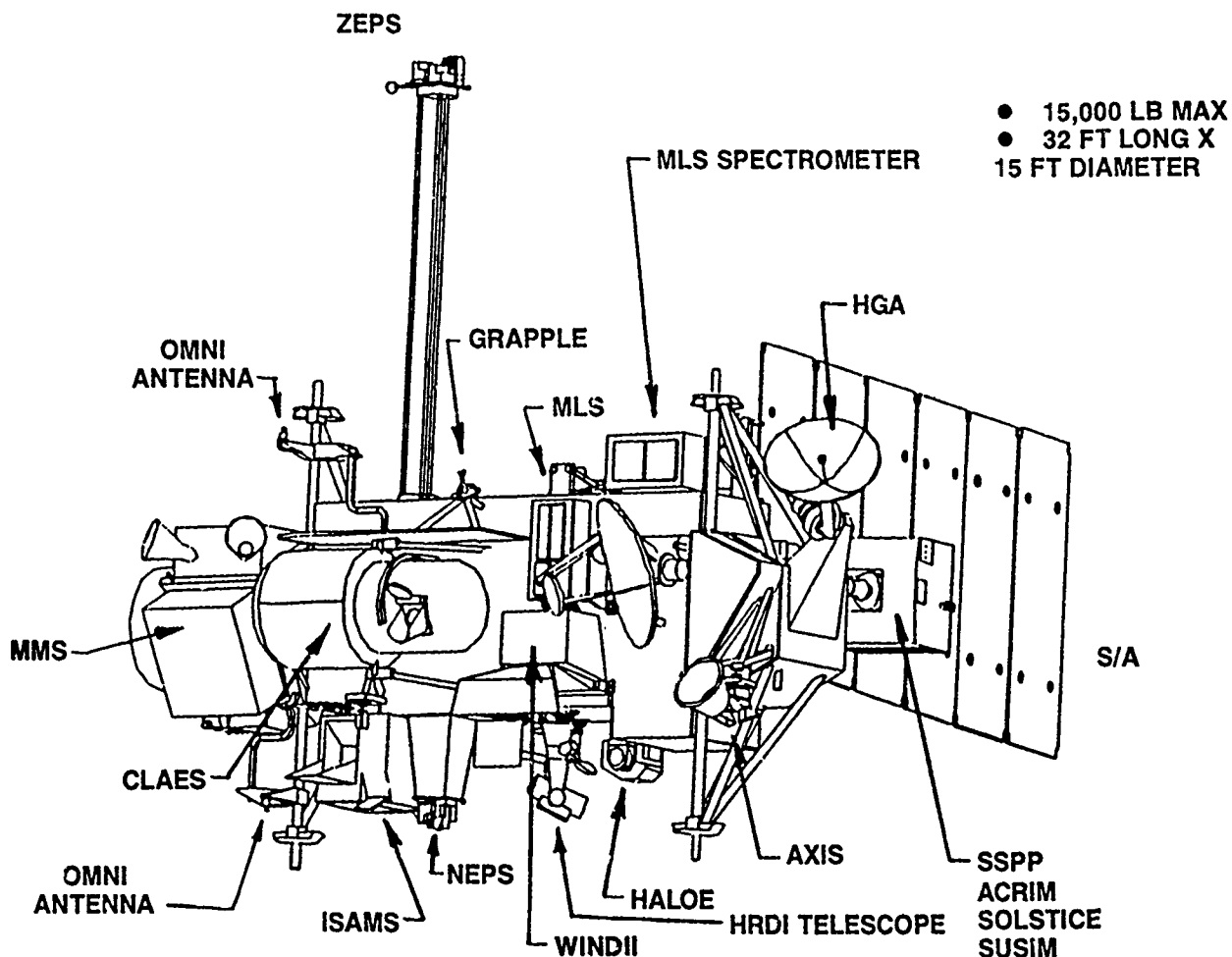


Figure 1. UARS Orbital Configuration

relatively small set of elemental loads are retrieved by a Loads Transformation Matrix (LTM) to verify the adequacy of the quasi-static load factors. The preliminary load factors are revised, if necessary, and the new set of load factors is used in the Design Load Cycle (DLC) phase to reconfirm the structural element sizing.

For the UARS, due to be launched from the Space Shuttle Bay, Figure 2, in early 1990's, this method of analysis would have resulted in an extensive redesign of the structure due to several unforeseen factors. More stringent shuttle safety requirements, after the accident of the flight 51L, resulted in changing the major cryogen from liquid hydrogen to solid CO₂/Neon. This increased the payload weight by about 1500 pounds. In addition, the shuttle (STS) forcing functions were updated by NASA JSC to obtain a better correlation between the test data and analysis. As a result of these and other changes, the payload weight grew from a preliminary design goal of 10000 pounds to nearly 15000 pounds. It was decided to use the transient elemental loads, wherever possible, to preserve the existing design. This resulted in an iterative analysis approach but it was performed

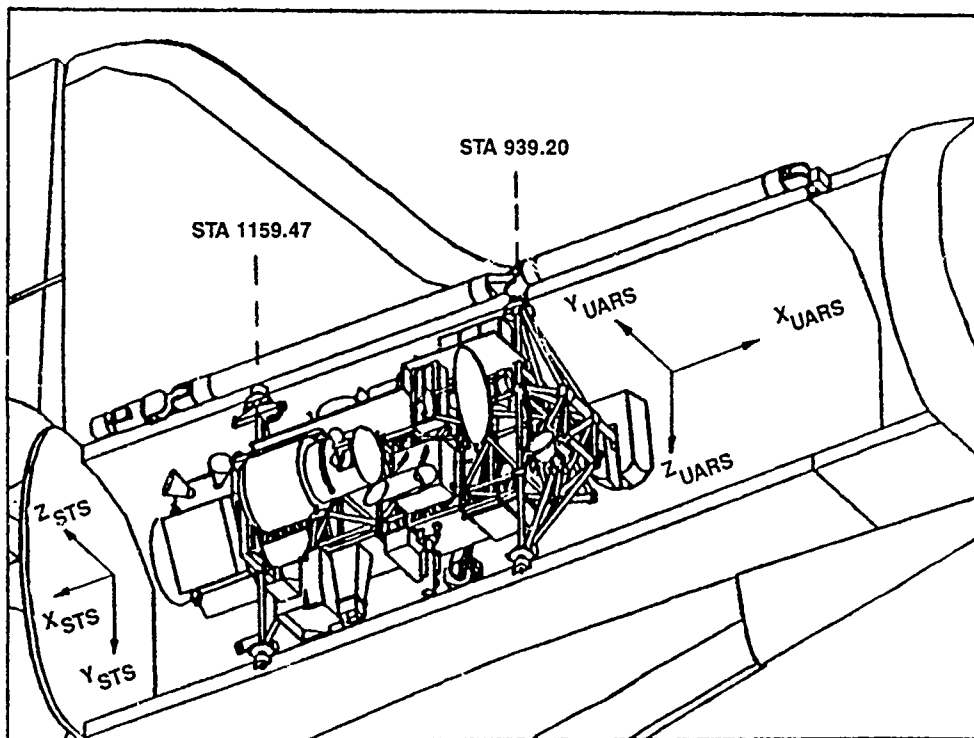


Figure 2. UARS in STS Bay (Stowed Configuration)

rapidly (on an IBM mainframe) making this approach feasible and highly effective. This approach reduced the design changes to a minimum, avoiding increased cost to design and drafting, while significantly shortening the schedule. Tube sizes for the primary structure were preserved and the impact on the schedule was minimized.

The paper describes the mathematical model, the analytical techniques used, the design approach, the results of dynamics analysis performed, and documents the benefits of this unusual approach to spacecraft design and analysis. An overall flow chart of the analysis approach is shown in Figure 3.

Spacecraft Math Model

The mathematical model for the dynamics analysis consisted of a modal synthesized model for the coupled STS/UARS configuration. The UARS spacecraft model itself, comprising of 12 substructures, was assembled by the modal synthesis technique. The main spacecraft carrying truss-like structure, called the Instrument Module (IM), was represented by an MSC/NASTRAN finite element model (FEM) developed by the GE Astro Space Division. Three of the substructure models were also developed in-house, whereas 8 substructure models were supplied by the GSFC. One of these was a math model consisting of generalized mass and stiffness matrices, and the others were MSC/NASTRAN compatible FEM's. Each of the models was reduced to a Craig-Bampton (Reference 1) model represented by its own fixed boundary modes and reduced boundary stiffness and mass matrices. The substructure break-down is shown in Table 1. The coupled UARS model consisted of a total of 2842 dynamic

Table 1. UARS Substructure Models & Weights

Substructure Qualifier	Component Name	Dynamic DOF'S	Boundary DOF'S	Weight Pounds
01	IM0077	557	8	6664.1
02	ISAMS	290	9	419.2
03	HALOE	78	6	197.0
04	MLS	120	9	381.0
05	CLAES	396	31	2890.0
06	HRDI - INTERFEROMETER	162	9	172.8
07	HIGH GAIN ANTENNA (HGA)	130	6	129.3
08	WINDII	96	9	308.0
09	SSPP/SUSIM	295	12	791.1
10	SOLAR ARRAY	316	26	476.2
11	HRDI - TELESCOPE	189	9	121.0
12	MMS	213	18	2450.3
TOTAL		2842	152	15000.0

configurations. A modal synthesis technique was used that included residual stiffness terms at the S/S/payload interface to reduce errors due to modal truncation effects. For the liftoff model, 395 system modes up to 35 Hz were kept for the transient response analyses. The modal damping ratios used were 1% of critical below 10 Hz and 2% of the critical above 10 Hz. For the landing model, a total of 226 system modes up to 35 Hz were used along with a modal damping ratio of 1% for all modes.

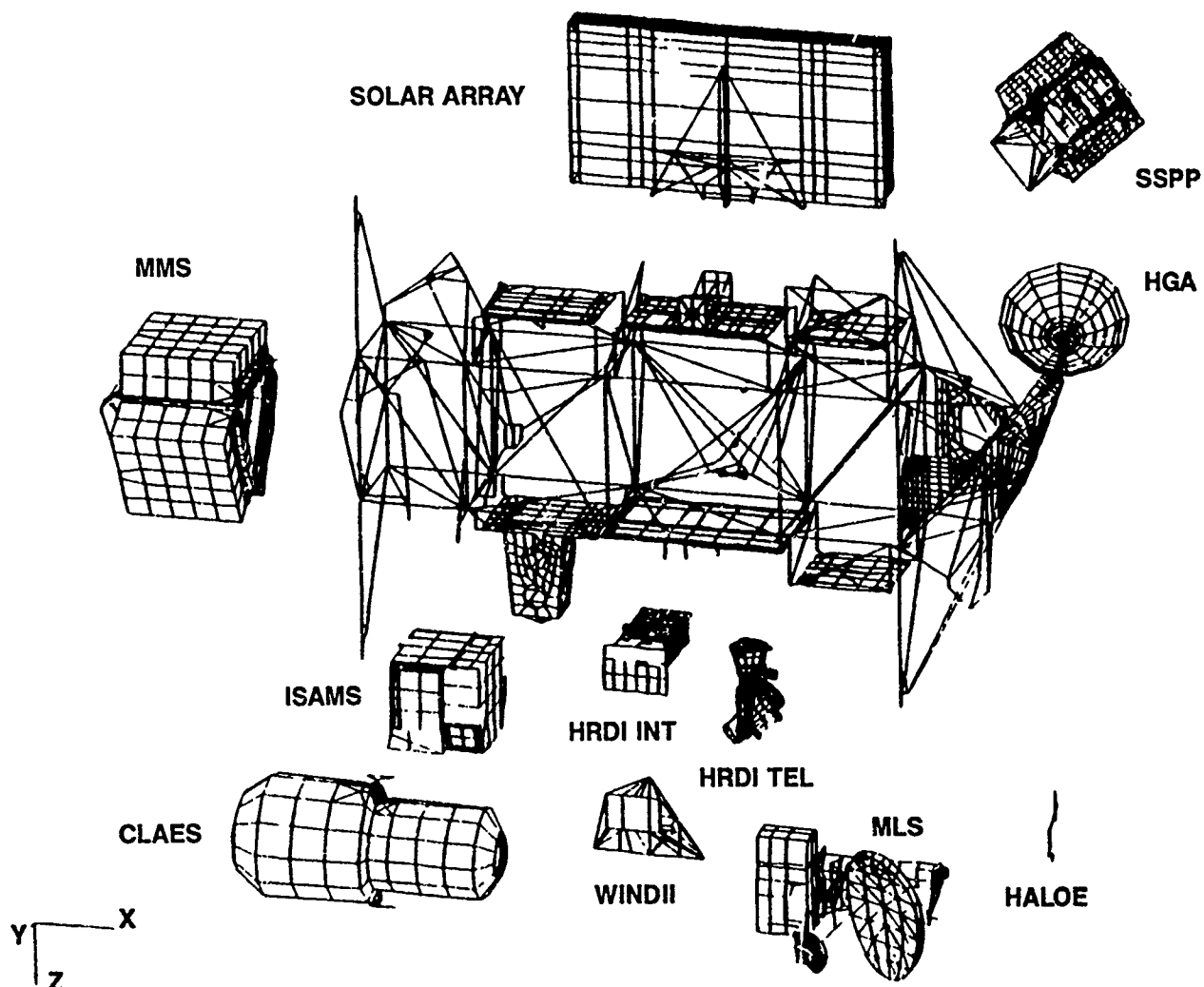


Figure 4. UARS Finite Element Model (Exploded View)

Loads Analysis Technique and Data Recovery

The modal responses due to STS transient forcing functions were calculated using a FORTRAN routine called MERTA from the in-house library 'DYNAMO' for dynamic solutions. A Loads Transformation Matrix (LTM) was then developed to solve for elemental forces, elemental stresses, or displacements as described in the following equation:

$$\{L\} = [T] \begin{Bmatrix} \ddot{x}_B \\ \ddot{q} \end{Bmatrix} + [V] \{x_B\} \quad (1)$$

Table 2. UARS IM DLC Finite Element Model Summary

Total Number of Grid Points:	2958
Total Number of Structural Finite Elements:	4963
Number of BEAM Elements:	2744
Number of BAR Elements:	30
Number of QUAD4 Elements:	1935
Number of TRIA3 Elements:	253
Number of ELAS2 Elements:	1
Total Number of Rigid (RBE2) Elements:	23
Total Number of Concentrated Mass Elements:	224
Number of CONM1 Elements:	134
Number of CONM2 Elements:	90
Total Number of DOF's in the Model:	17748
Number of DOF's in MPC set:	1046
Number of DOF's in SPC set:	1057
Number of Boundary DOF's:	8
Number of DOF's in OMIT set:	15080
Total Number of DOF's in the Dynamics ASET:	557

where $\begin{Bmatrix} L \end{Bmatrix}$ = physical quantity (Load, Stress, Displacement) vector
 $\begin{Bmatrix} \ddot{X}_B \end{Bmatrix}$ = payload interface boundary acceleration response
 $\begin{Bmatrix} \ddot{q} \end{Bmatrix}$ = payload modal acceleration response vector
 $\begin{Bmatrix} X_B \end{Bmatrix}$ = payload interface boundary displacement vector
and $[T]$, $[V]$ = LTM matrices.

The T and V matrices are themselves generated using special DMAP alters in NASTRAN by first formulating matrices TD and VD defined as follows:

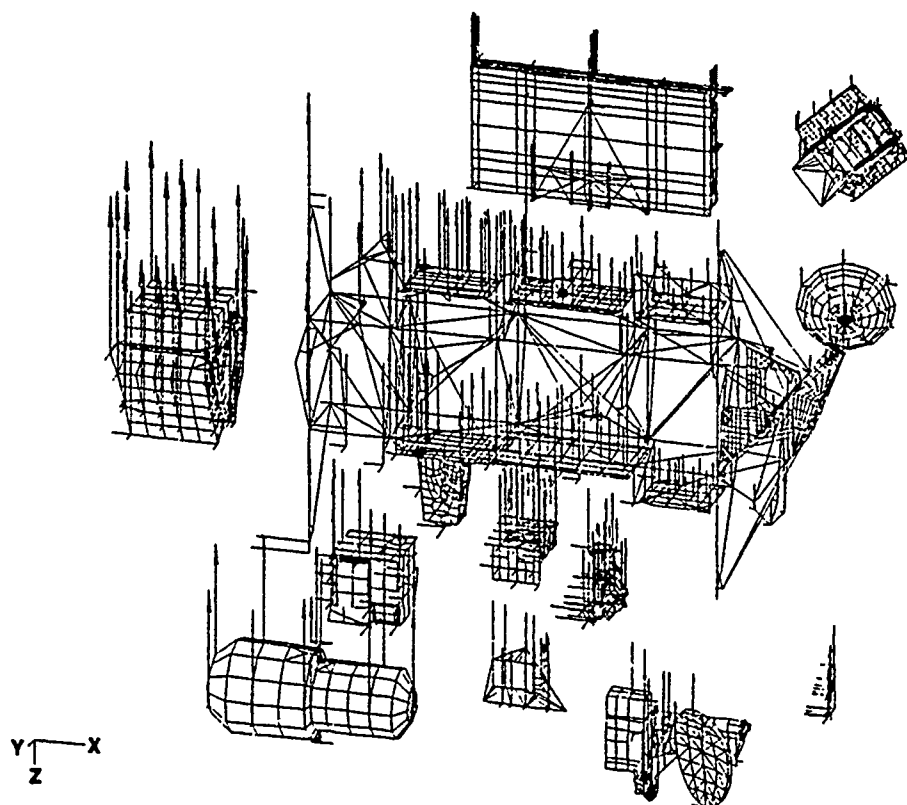


Figure 5. First Bending Mode (Freq = 6.3 Hz)

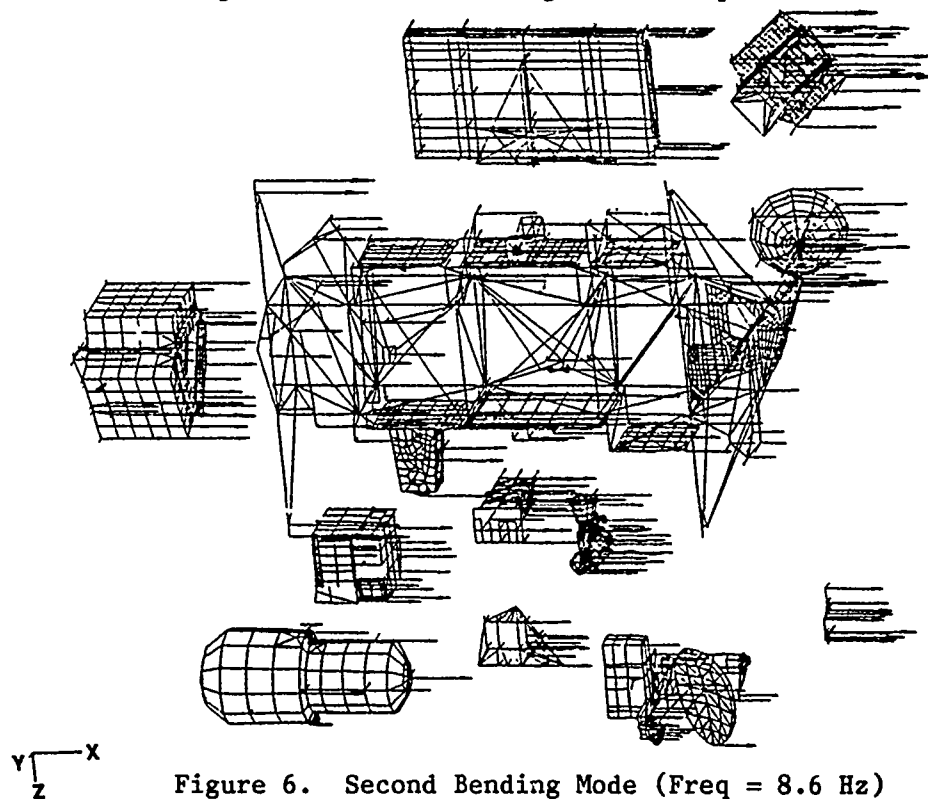


Figure 6. Second Bending Mode (Freq = 8.6 Hz)

$$[TD] = \begin{bmatrix} 0 & 0 \\ -1 & -1 \\ -K_{II} (M_{IB} + M_{II} T_B) & -K_{II} M_{II} \phi \end{bmatrix} \quad (2)$$

$$[VD] = \begin{bmatrix} I \\ T_B \end{bmatrix} \quad (3)$$

where

- K_{II} = UARS internal stiffness matrix
- M_{II} = UARS internal mass matrix
- M_{IB} = UARS internal-boundary coupling mass matrix
- T_B = UARS constraint modes
- ϕ = UARS eigenvectors

The TD and VD matrices are passed through NASTRAN modules SDR1, SDR2, and DRMS1. Module SDR1 expands A-set deflections to G-set size, SDR2 recovers physical displacements as controlled by the case control deck and the module DRMS1 converts the table format data to matrix form. The output matrices from the DRMS1 module are the T and V LTM matrices.

The modal responses are now multiplied by LTM's to compute the time-histories or frequency responses. For the liftoff condition, a base shake random analysis was also performed to calculate the response due to random vibration transmitted through the STS trunnions. Also, for components with large surface areas like the equipment benches, the solar arrays, the SSPP, the antennae dishes, an acoustic analysis was performed using the NASTRAN Solution 30. The loads computed from the transient, the random, and the acoustic response analyses were then combined with the appropriate factors applied to account for model uncertainty. Transient loads were computed for the Orbiter landing cases in a similar manner.

For any design verification, three separate environments needed to be considered. First, the combined lift-off conditions including the effects of transient, mechanically transmitted random, and flight acoustic environments, second, the landing conditions, and third, the qualification level acoustic environment. Overall worst-case loads were then examined for margins of the recommended design loads and member sizes. In the situations where the overall maximum values did not indicate positive margins, all the force components from the same environment were used to verify design parameters and member sizes. In many situations the individual time-slice data was also used before a redesign of the members was contemplated. All the elemental force components at specific time instances resulting in the highest peak values were combined with the random and acoustic response results and the individual member designs were reassessed.

In order to keep the design changes to a minimum extensive use was made of dynamic analysis results. In local regions, where the dynamic analysis based on selected information from the LTM's showed close margins, more extensive LTM's were recovered and more and more use was made of the transient and combined dynamic response results. The original size of the LTM was 1539 rows of elemental loads data for the preliminary load cycle analysis. This grew to a size of more than 6565 rows in addition to acceleration, displacement, and dynamic clearance loss data for the final design load cycle analysis. At no stage, however, was the design compromised and whenever the dynamics results indicated, a local design change or member resizing was enforced. The LTM procedure was setup so that the additional LTM generation was accomplished with minimal computer time and human resources being spent. Most LTM regeneration was accomplished by simple NASTRAN restarts with a minimum post processing requiring day time submittal of NASTRAN solution 3 runs with DMAP alters. Such an approach was responsible for the quick turn-around and thus avoiding the more expensive redesign efforts based on revised quasi-static design load factors.

Comparison of Quasi-static and Transient Loads

The preliminary spacecraft design was sized using quasi-static load factors, with a selective set of elements checked by transient loads. When the design parameters changed (e.g. a new payload model with higher Shuttle loads), instead of using the old design load factors and thus paying a weight penalty, actual transient and combined dynamic elemental loads were used to compute margins. The load factors were updated based on the results of the transient analyses. The original and revised sets of load factors for both liftoff and landing are shown in Table 3.

Table 3. UARS Design Load Factors

	Load Factors (G's)		
	X	Y	Z
LIFTOFF:			
Original Set	5.6	3.2	4.8
Revised Set	4.6	2.0	3.6
LANDING (Abort):			
Original Set	3.0	2.3	6.3
Revised Set	2.0	1.6	4.6

Note: Directions shown are in the STS coordinate system.

The new approach was to use the reduced load factors based on the transients being enveloped by the new quasi-static loads, as much as possible, and then strengthen the individual members as required. Figure 7 shows the distribution of elements being enveloped by quasi-static load factors for both cases. The percent of exceedance for the two methods is shown against the number of elements enveloped. It can be seen that the original set of load factors overdesigned 88% of the members and under-designed 12% of the members whereas the revised set of load factors reduced the percentage of overdesigned elements to 73%. Transient load results were used to design the remaining 27% of the members.

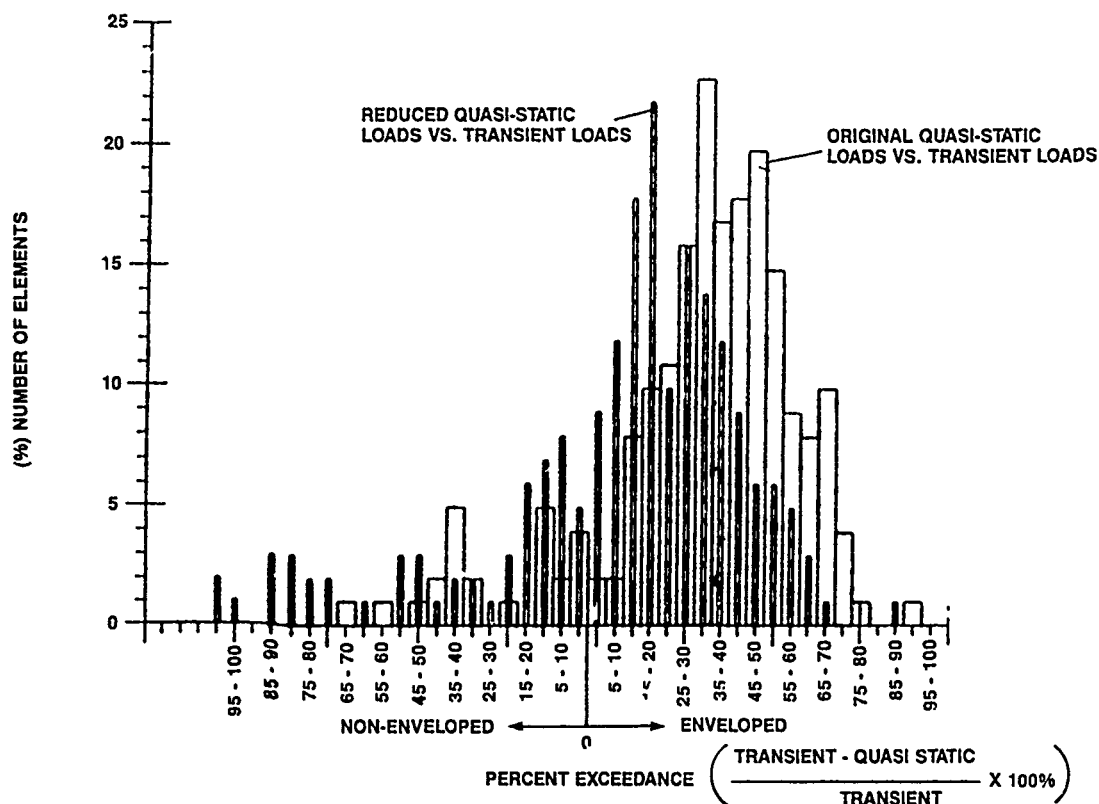


Figure 7. Quasi-Static Loads Vs Transient Loads

Large costs were averted through the extensive use of transient loads which provided ease of fabrication, minimum redesign and reduced structural weight. A key factor was the potential growth of the graphite epoxy longeron maximum tube size. Mandrel development and fabrication methods were the long lead items and were under development for a 3 1/2 inch diameter tube. Tube diameter changes impacted all the existing drawings because of fitting and tube length changes. Significant increases to the structural weight would also result from tube change and, to a larger degree, growth in the tube fittings. Through the use of the transient loads, the tube sizes were maintained averting major effects on the design. It is estimated that between one third and one half of the members were ultimately designed to the transient loads.

The loads analysis was also used to implement design changes which would assure instrument compatibility and to address critical design features. Early specification of instrument structural design loads were essential to the timely development of the space system. During the course of the program, it became necessary to provide added stiffness to parts of the structure to maintain instrument design compatibility. In addition, specific instrument mounting loads and member loads on the SSPP gimbals and retention system were evaluated. The iterative loads analysis was performed rapidly and in increasing depth to define detailed design requirements and optimize the structural design to satisfy instrument interface requirements.

Concluding Remarks

The UARS design development demonstrates the effective use of coupled spacecraft/launch vehicle transient loads analysis which is not possible with standard load cycle analysis methods. The methodology enabled accurate iterative loads prediction and eliminated errors caused with other techniques such as base excitation. Through the use of graduated uncertainty factors that allowed for design variations, an orderly design development was accomplished. With the increased computational capabilities now available at most aerospace facilities, this approach is compatible with most spacecraft development contractor capabilities. In this instance, the extensive use of transient loads had large rewards in averting large cost increases and longer development times.

As the spacecraft community prepares to make more extensive use of Expendable Launch Vehicles, it appears beneficial to make this approach available to spacecraft contractors. This requires the launch vehicle contractor to use a similar approach to that currently being used on the space shuttle, i.e., the development of a limited number of critical loading conditions which envelope the maximum expected dynamic loading. With the forcing functions and launch vehicle models being made available to the spacecraft contractor, timely analyses can be performed to support the effective development of the spacecraft. Reduced weight, lower cost and shortened schedules are the benefits that can be achieved with this loads analysis approach.

Reference

1. W. A. Benfield and R. F. Hruda, "Vibration Analysis of Structures by Component Mode Substitution", AIAA Journal, Vol. 9, NO. 7, pp. 1255-1261, July 1971.

ANALYTICAL APPROACHES FOR DETERMINING EFFECTIVE WEIGHTS USED IN THE METHOD OF WEIGHTED ACCELERATIONS FOR FORCE MEASUREMENTS

Timothy J. Kreitinger, Graduate Student
Ming Wang, Prof. of Civil Engineering
H. L. Schreyer, Prof. of Mechanical Engineering
University of New Mexico
Albuquerque, NM 87131

Force identification is the process of determining input excitation for a system. Since direct measurements of forces are almost impossible for most cases, an experimental procedure called the method of weighted accelerations has been developed. Previous work used experimental data to determine the weighting coefficients by least squares formulations. This paper provides analytical procedures for determining the weighting coefficients based on either mode shapes or finite elements.

INTRODUCTION

Force identification is the process of determining input excitation using measured response from a system. Since direct measurements of forces are almost impossible for most cases, an experimental procedure that can provide an indirect method for determining the forces is valuable. As force identification is perfected, its needs for structural problems will increase. An example is the design of penetrators for either water or earth media where the interaction forces between the structure and the target are required for the structural design process. Also, there are applications in controlling the movement of tall buildings due to wind loads, vehicles moving through space and large space antennas and platforms.

The response measurements in structure identification include strain, acceleration, velocity, and displacement. Doyle [1,2] used strain response from beams to determine input forces. Hillary and Ewins [3] investigated sinusoidal loadings on cantilever beams using both strain and acceleration measurements.

A model proposed by Gregory, Coleman, Priddy, and Smallwood [4,5,6] used the sum of weighted accelerations from a structure to predict input forces. This model readily predicted random input forces as verified by other authors [7,8]. The model formulation showed that for linear systems the weighting coefficients or effective weights can be determined analytically with knowledge of the mode shapes of the structure rather than experimentally determining the weights.

This paper further expands on this idea by presenting alternative formulations for the determination of the effective weights in the method of weighted accelerations. These approaches allow estimation of effective weights without experimental data which is valuable for large complex structures where known forces

can not be easily applied. These mathematical formulations provide advantages for determining the effective weights analytically rather than through the use of the known forces on the actual or prototypical structure. Results indicate the procedures have a wide range of applicability which is of considerable importance for large multidegree-of-freedom structures.

THE METHOD OF WEIGHTED ACCELERATION

Consider a linear elastic body free in space and subjected to a force with known spatial distribution over the body but unknown variation in time described by the function $F(t)$. Suppose acceleration traces $a_i(t)$ are available from n points on the body. The method of weighted accelerations is the statement that if weighting coefficients w_i are chosen appropriately, then

$$F = \sum_{i=1}^n w_i a_i \quad (1)$$

In other words, the acceleration records can be used to obtain the unknown applied forcing function which caused the motion of the body in the first place.

The first methods used to obtain w_i were experimental in that known forces were applied to specific structures and the w_i were obtained by minimizing the difference (in some norm) between the predicted and known forcing functions. Then Eq. (1) could be used for the actual situation in which the forcing function is not known.

For the structure in Fig. 1 frequency and time domain approaches were used to determine the effective weights. In this case 4 acceleration measurements were used. A known force applied to the structure was correlated with the response

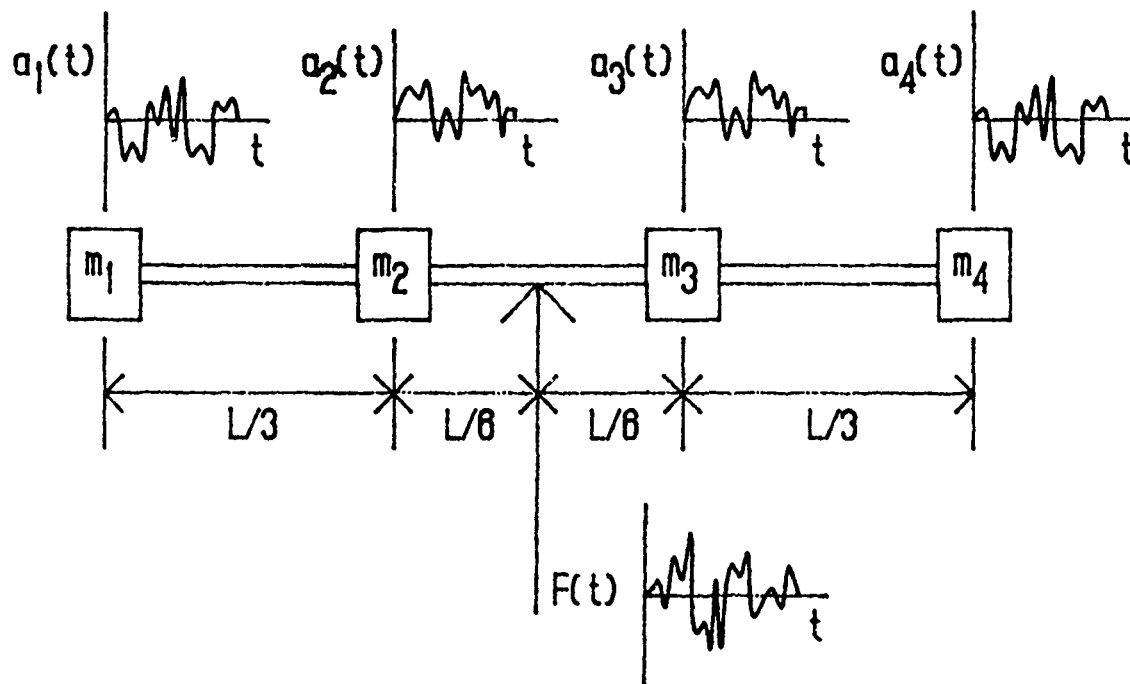


Figure 1. Lumped Mass System.

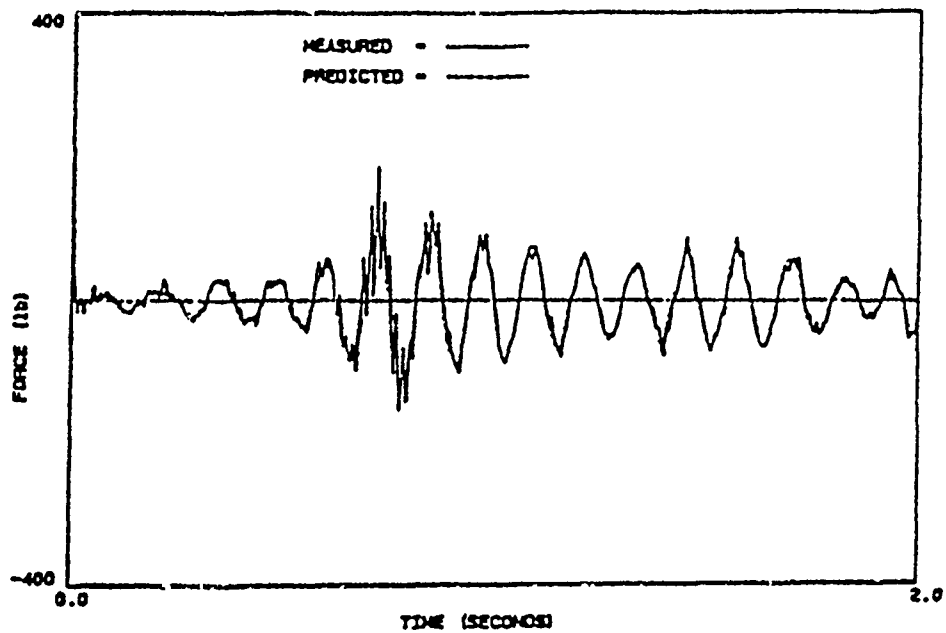


Figure 2. Predicted Force and Measured Force using Time Domain Determine Effective Weights.

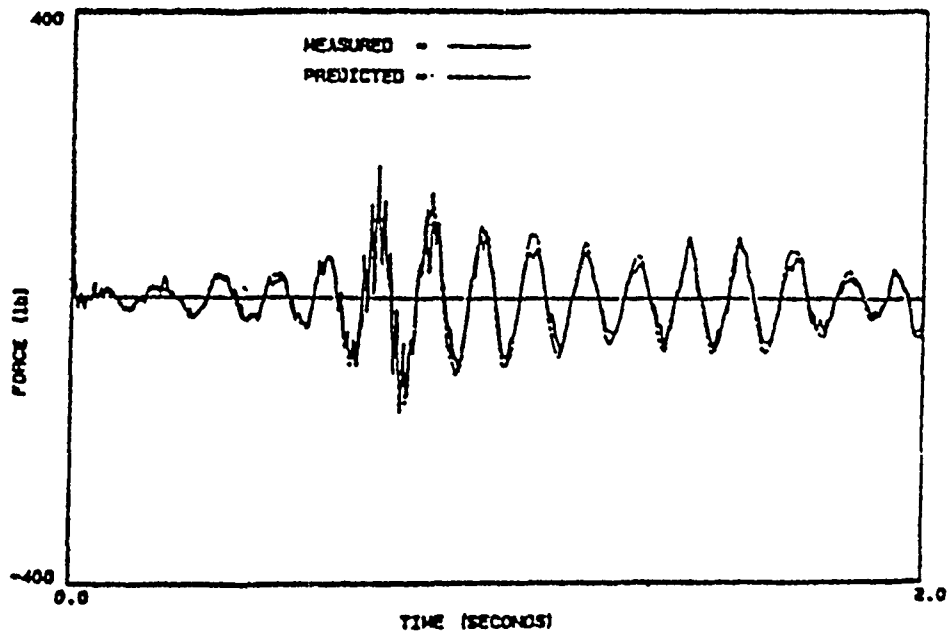


Figure 3. Predicted Force and Measured Force using Frequency Domain Determined Effective Weights.

measurements and other independent tests were used to compared predicted and measured forces. Results for the time and domain approaches are shown in Figs. 2 and 3 respectively.

Observations from this earlier study [6,8] are extremely encouraging with regard to the potential usefulness of the method. It was noted that

1. The prediction model is bandlimited.
2. The equations are highly correlated to the mode shapes of the structure.
3. The effective weights may be negative.

Since many structures are too complicated to perform the tests necessary to experimentally determine the weighting coefficients, alternative analytical approaches could prove to be valuable for engineering applications. The next sections provide derivations and preliminary evaluations of schemes which appear to be useful.

AN ANALYTICAL METHOD BASED ON MODE SHAPES

A method described by Priddy et al. [6] uses mode shapes in analytical expressions for determining the effective weights. Since the finite element procedure can be used to obtain mode shapes, this procedure can be considered quite general. Therefore, for the sake of completeness, a derivation is given which is different from that given in reference 6 and which may provide additional insight into the method.

Suppose an elastic body is subjected to a surface traction t^* and a body force b of the following type:

$$t^* = F(t) \chi^*(r^s) \quad (2a)$$

$$b = F(t) \chi(r) \quad (2b)$$

in which $\chi(r)$ and $\chi^*(r^s)$ are known functions, defined over the volume and surface, respectively. In other words, the forcing function is assumed to be separable with the spatial distribution known and one unknown time dependent coefficient described by the vector F . The position vector r assumes the value r^s on the surface. Since the method of weighted accelerations is applicable only if there are no displacement prescribed boundary conditions, χ^* is defined (perhaps zero) over the complete surface.

If ρ denotes the mass density, u the displacement vector and $\underline{\sigma}$ the symmetric Cauchy stress tensor, then the equation of motion is

$$\rho \underline{u}' = \nabla \cdot \underline{\sigma} + b \quad (3)$$

in which $\nabla \cdot ()$ denotes the divergence operator and a prime denotes a derivative with respect to the time. For a linearly elastic body, the constitutive equation is

$$\underline{\sigma} = \underline{\underline{E}} : \underline{e} \quad (4)$$

in which $\underline{\underline{E}}$ is the elasticity tensor and \underline{e} the strain tensor. For small deformations

the strain is the symmetric part of the displacement gradient:

$$\underline{e} = (\nabla \underline{u})_{\text{symm}} \quad (5)$$

A modal solution to Eq. (3) is given by

$$\underline{u} = \sum_{i=1}^{\infty} \eta_i(t) \varphi_i(\underline{r}) \quad (6)$$

in which φ_i denote the eigenfunctions. The first two eigenfunctions represent rigid body translation

$$\varphi_1 = \underline{c} \quad \underline{c} \cdot \underline{c} = 1 \quad (7)$$

in which \underline{c} is independent of \underline{r} , and rigid body rotation

$$\varphi_2 = \underline{R} \cdot (\underline{r} - \underline{r}_c) \quad (8)$$

The position vector to the center of mass is denoted by \underline{r}_c and \underline{R} is a rotation tensor, also independent of \underline{r} , and orthogonal:

$$\underline{R}^T \cdot \underline{R} = \underline{I} \quad (9)$$

in which the superscript T denotes the transpose and \underline{I} the identity tensor. The functions φ_i with $i \geq 3$ represent deformation modes of vibration associated with natural frequencies ω_i .

The first step in the procedure of reference 6 is to note that the total mass of the body is given by

$$M = \int_D \rho \, dv \quad (10)$$

in which D denotes the domain of volume integration and dv a volume element. It is also known that the modes are orthogonal to each other. In particular consider the orthogonality of the second mode to the first one, i.e.,

$$\int_D \underline{c} \cdot \varphi_2 \, dv = 0 \quad (11)$$

Since \underline{c} and \underline{R} are independent of \underline{r} , and because the resulting expression must hold for arbitrary values of \underline{c} and \underline{R} , the result of substituting Eq. (8) in Eq. (11) is that

$$\int_D (\mathbf{r} - \mathbf{r}_c) dv = 0 \quad (12)$$

which is, of course, another identity.

The orthogonality of \mathbf{c} with the other modes yields

$$\int_D \mathbf{c} \cdot \boldsymbol{\varphi}_i dv = 0 \quad i = 3, 4, \dots \quad (13)$$

but since \mathbf{c} is constant and arbitrary it follows that

$$\int_D \boldsymbol{\varphi}_i dv = 0 \quad i = 3, 4, \dots \quad (14)$$

Equations (10), (12) and (14) prove to be the key ones for obtaining the weighting coefficients.

If these integrals are computed using numerical quadrature, then a typical integral of a function $G(\mathbf{r})$ is approximated as follows:

$$\int_D G(\mathbf{r}) dv = \sum_{i=1}^n w_i G(\mathbf{r}_i) \quad (15)$$

in which \mathbf{r}_i is the position vector of the integration point and w_i is the weight. The number of integration points is denoted by n . Numerous schemes exist (e.g., Gaussian quadrature) for which specific values are assigned to w_i and rules are given for choosing \mathbf{r}_i . However, here the w_i 's are left unassigned for the moment, and the points \mathbf{r}_i are defined to be those points where accelerometers are placed. Then the result of utilizing Eq. (15) in Eqs. (10), (12) and (14) is the following:

$$\begin{aligned} \sum_{j=1}^n \rho w_j &= M \\ \sum_{j=1}^n (\mathbf{r}_j - \mathbf{r}_c) w_j &= 0 \\ \sum_{j=1}^n \boldsymbol{\varphi}_{ij} w_j &= 0 \quad i = 3, 4, \dots \end{aligned} \quad (16)$$

in which

$$\boldsymbol{\varphi}_{ij} = \boldsymbol{\varphi}_i(\mathbf{r}_j) \quad (17)$$

Now Eq. (16) is used as the governing set of equations for obtaining the weighting coefficients w_j . In three dimensions, only $n - 6$ deformable modes can be accommodated with the scheme.

To derive the equation that is actually used to obtain the resultant force $F(t)$, integrate each term in Eq. (3) over the domain:

$$\int_D \rho \mathbf{u}'' \, dv = \int_D \nabla \cdot \underline{\sigma} \, dv + \int_D \mathbf{b} \, dv \quad (18)$$

The Gauss-Green theorem yields

$$\int_D \nabla \cdot \underline{\sigma} \, dv = \int_{\partial D} \boldsymbol{\eta} \cdot \underline{\sigma} \, ds = \int_{\partial D} \mathbf{t} \, ds \quad (19)$$

in which ∂D denotes the surface and ds an area element. Then the use of Eqs. (2a) and (2b) results in

$$\int_D \rho \mathbf{u}'' \, dv = F(t) \, \psi \quad (20)$$

in which

$$\psi = \int_D \chi \, dv + \int_{\partial D} \chi^s \, ds \quad (21)$$

is a constant vector which is presumably known. Suppose the scale factor is absorbed in F so that

$$\psi = 1 \quad (22)$$

If numerical quadrature is used, then Eq. (20) becomes

$$\sum_{i=1}^n \rho \mathbf{u}_i'' \, w_i = F(t) \quad (23)$$

which is the general form of the method of weighted accelerations.

As reported by Priddy et al. [6] very good results have been obtained using this approach to obtain the weighting coefficients. However, it seems that other orthogonality relations may serve equally well, and there may even be a possibility that alternative schemes may be viable in which it is not necessary to obtain the mode shapes at all. The next section indicates how the finite element approach might be applied directly.

WEIGHTED RESIDUALS AND THE FINITE ELEMENT METHOD

The finite element method can be considered as a systematic procedure for developing compact nodal basis functions for use in a weak formulation such as the method of weighted residuals. To illustrate that various analytical approaches can

be used to obtain suitable factors for use in the procedure involving the sum of weighted accelerations, the more general approach involving weak formulations is given in this section. Then the specialization to finite elements is made.

To illustrate the concepts in as simple a manner as possible, consider the one-dimensional model problem of motion in a bar of length L . Since the method of weighted accelerations applies only to unsupported bodies, the boundaries defined by $x=0$ and $x=L$ are free. Acceleration time histories $a_i(t)$ are presumed to be available from accelerometers placed at the n points x_i , $i=1 \dots n$. Consider a forcing function that is separable in space and time

$$f(x,t) = F(t) \chi(x) \quad \int_0^L \chi(x) dx = 1 \quad (24)$$

in which the spatial distribution, $\chi(x)$, is assumed known but the temporal part, $F(t)$, is unknown. The normalization on χ is done for future convenience. The procedure states that with a suitable choice of scalar weight variables, w_i , the force is given by the formula

$$F(t) = \sum_{i=1}^n w_i a_i(t) \quad (25)$$

Normally the weight variables are obtained by performing an experiment in which the forcing function is known and then adjusting the variables by the method of least squares so that the function $F(t)$ is as close as possible to the measured function. Then the weight variables are used in the actual problem in which the forcing function is desired but unknown.

The governing differential equation for an elastic bar with unit cross-sectional area is

$$(ku_x)_x + F(t)\chi(x) = \rho u'' \quad 0 < x < L \quad (26)$$

in which k is the elastic stiffness.

Label the points at which the accelerometers are placed, x_j , as nodes. Introduce nodal basis functions $N_i(x)$ which are defined to have the value one at associated nodes and zero at all other nodes. Lagrange polynomials are examples of such basis functions which are complete polynomials and, hence, will automatically represent rigid body modes in the following representation for u :

$$u = \sum_{i=1}^n u_i(t) N_i(x) \quad (27)$$

Let $q(x)$ denote a weight function with continuity of at least C^0 . A weak form of the equation of motion is obtained by multiplying each term in Eq. (26) by q and integrating over the domain. With the use of Eq. (27), an integration by parts, and the use of the free end boundary conditions the result is:

$$\sum_{i=1}^n \int_0^L \rho q(x) N_i(x) dx u_i'' + \sum_{i=1}^n \int_0^L k q_{,x} N_{i,x} dx u_i = F(t) \int_0^L q(x) \chi(x) dx \quad (28)$$

If a representation similar to Eq. (27) is used for q :

$$q = \sum_{i=1}^n q_i N_i(x) \quad (29)$$

then with q_i considered to be arbitrary, Eq. (28) becomes

$$[M] \{u''\} + [K] \{u\} = F(t) \{f\} \quad (30)$$

in which standard matrix notation has been used. The column vector $\{u\}$ consists of the time dependent components $u_i(t)$ while components of the remaining matrices are:

$$K_{ij} = \int_0^L k N_{i,x} N_{j,x} dx \quad M_{ij} = \int_0^L \rho N_i N_j dx \quad f_i = \int_0^L \chi N_i dx \quad (31)$$

Let $\{R\}$ denote the rigid body mode. Since the associated stiffness eigenvalue is zero, it follows that

$$\langle R \rangle [K] = \langle 0 \rangle \quad \langle R \rangle = \langle 1, 1, \dots, 1 \rangle \quad (32)$$

in which $\langle R \rangle$ is the transpose of $\{R\}$. Also, because the basis functions must represent complete polynomials up to the first order for convergence to be assured, these basis functions will automatically satisfy the relation

$$\sum_{i=1}^n N_i(x) = 1 \quad (33)$$

With the use of Eq. (33) and the normalizing result of Eq. (24), it follows that

$$\langle R \rangle \{f\} = 1 \quad (34)$$

Thus the inner product of $\langle R \rangle$ with each term in Eq. (30) yields

$$\langle W \rangle \{u''\} = F(t) \quad (35)$$

where

$$\langle W \rangle = \langle R \rangle [M] \quad (36)$$

and Eq. (35) is identical in form to Eq. (25) which is the method of weighted accelerations.

Under rigid body motion

$$\{u''\} = u_c'' \{R\} \quad (37)$$

in which u_c'' denotes the rigid body acceleration which is also the acceleration of the center of mass. Because of the use of nodal basis functions, it can be shown that

$$\langle R \rangle [h] \{R\} = M \quad (38)$$

where M is the total mass of the body. Then for rigid body motion Eq. (35) reduces to

$$P(t) = M u_c'' \quad (39)$$

as it should.

The result of the formulation is that once nodal basis functions are chosen, the mass matrix can be constructed from Eq. (31) and the weighting parameters from Eq. (36). In particular, for the first node, the result is

$$w_1 = \int_0^L \rho N_1 [N_1 + N_2 + \dots] dx \quad (40)$$

The use of Eq. (33) yields

$$w_1 = \int_0^L \rho N_1 dx \quad (41)$$

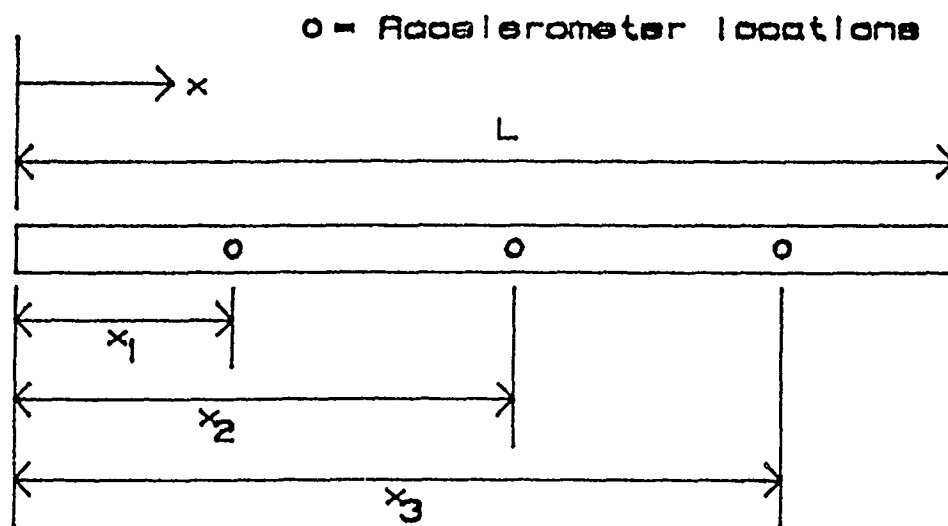
with a similar expression for each of the other weighting parameters.

With reference to Fig. 4a which represents a bar on which three accelerometers are placed, Lagrange polynomials (See Fig. 4b) represent one possible choice for nodal basis functions:

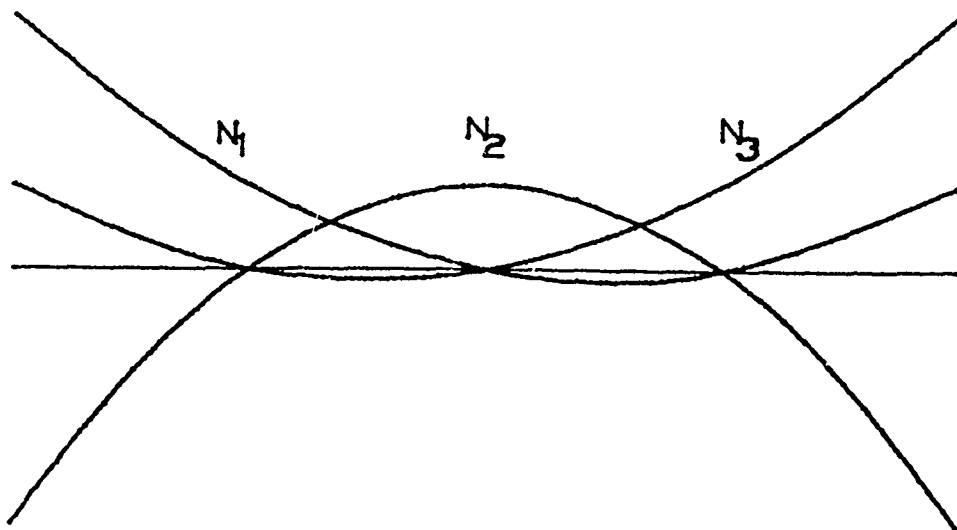
$$\begin{aligned} N_1 &= \frac{(x - x_2)(x - x_3)}{(x_1 - x_2)(x_1 - x_3)} & N_2 &= \frac{(x - x_1)(x - x_3)}{(x_2 - x_1)(x_2 - x_3)} \\ N_3 &= \frac{(x - x_1)(x - x_2)}{(x_3 - x_1)(x_3 - x_2)} \end{aligned} \quad (42)$$

from which weight factors can be determined.

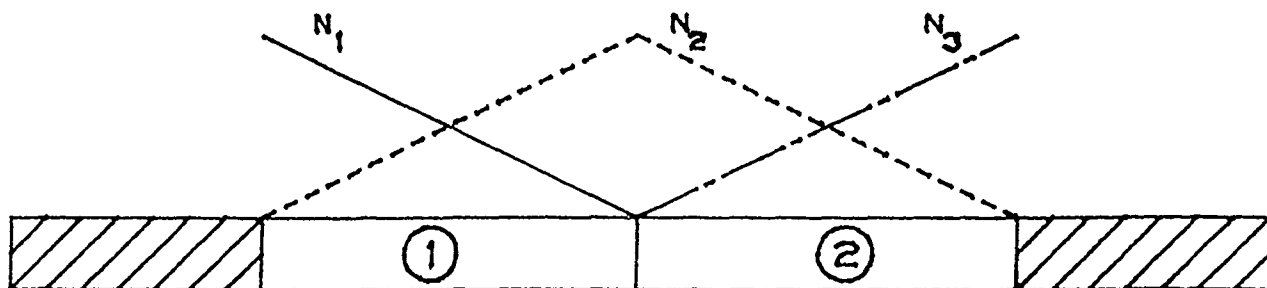
Alternatively, the points x_1 , x_2 , and x_3 can be used to define the two elements shown in Fig. 4c. Finite elements also define nodal basis functions, which are shown in Fig. 4c, for elements that provide C^0 continuity. The effect of using basis functions based on finite elements is that one-half of the mass of each element is assigned to each of the two nodes used to define the element. The net



(a) Bar with Three Accelerometers



(b) Sketch of Lagrange Polynomials as Nodal Basis Functions



○ = Element Number

(c) Nodal Basis Functions for C^0 Elements.

Figure 4. Nodal Basis Functions for a Bar.

result is a very intuitive procedure for assigning weights to each node. The problem is that the hash marked areas at the ends are not included within the elements. A possible approach is to lump the mass represented by the hashed marked area with the adjacent node.

An engineering rule of thumb in finite element analysis is that $2m$ nodes are required to accurately represent m mode shapes. It is to be expected that lumping masses based directly on finite elements rather than on mode shapes can only provide accurate predictions for a limited number of frequency components in the result for the forcing function. Examples given in a later section tend to support this hypothesis.

APPLICATION OF THE FINITE ELEMENT METHOD TO BEAMS

For elementary Euler-Bernoulli beam theory, an element can be defined in which two degrees of freedom are associated with each node. If the first degree of freedom corresponds to translation and the second to rotation, then the consistent element mass matrix is

$$[M] = \frac{M^e}{420} \begin{bmatrix} 156 & 22h & 54 & -13h \\ 22h & 4h^2 & 13h & -3h^2 \\ 54 & 13h & 156 & -22h \\ -13h & -3h^2 & -22h & 4h^2 \end{bmatrix} \quad (43)$$

in which M^e denotes the element, and h the length. Now both rigid body translation and rotation are possible. However, normally transverse forces are of primary interest rather than applied moments, so the appropriate rigid body mode to use in the matrix equation of motion is that of rigid body translation in which results similar to those of the previous section continue to hold. In particular, the vector defining rigid body translation for an element is

$$\langle R \rangle = \langle 1, 0, 1, 0 \rangle \quad (44)$$

and the element weight factors become

$$\langle R \rangle [M] = \frac{M^e}{420} \langle 210, 35h, 210, -35h \rangle \quad (45)$$

The translational terms are the first and third components in this vector which indicates that the result is a simple assignment of one-half the mass of an element to each translational degree of freedom. Again, any excess mass at the ends of the beam not defined within an element would have to be lumped at the appropriate nodes. Similar results can be derived for elements used to model other structural members. Sample results for beams and plates are given in the next section.

EXPERIMENTAL RESULTS

Effective weights, determined by the mode shape and finite element approaches discussed in the previous sections, for a free-free beam of two different acceleration configurations were used to predict input forces. These forces of random and impact loadings were compared by plots with the measured forces. A

Table 1 Effective Weights for Each Case

Case Number	Effective weights determined from mode shapes.	Effective weights determined from finite elements.
Case 1	$w_1 = w_5 = 1.91 \text{ lb}$	$w_1 = w_5 = 1.99 \text{ lb}$
Free-Free Beam	$w_2 = w_4 = 2.50 \text{ lb}$	$w_2 = w_4 = 2.43 \text{ lb}$
(See Fig. 5)	$w_3 = 2.54 \text{ lb}$	$w_3 = 2.53 \text{ lb}$
Case 2	$w_1 = w_5 = 4.34 \text{ lb}$	$w_1 = w_5 = 2.83 \text{ lb}$
Free-Free Beam	$w_2 = w_4 = -1.46 \text{ lb}$	$w_2 = w_4 = 1.93 \text{ lb}$
(See Fig. 10)	$w_3 = 5.60 \text{ lb}$	$w_3 = 1.84 \text{ lb}$
Case 3		$w_1 = w_2 = w_3 = w_4 =$
Plate		$w_5 = w_6 = 1.84 \text{ lb}$
(See Fig. 14)		

third case used a free-free plate which the effective weights were determined by the finite element approach.

The first case is that of a free-free steel beam with the five accelerometers placed at the nodes of the fourth vibrational mode (See Fig. 5). This is considered to be a strategic placement of the gauges [6]. From Eqs. (16) two of the five equations for this setup come from rigid body translation and rotation. The other three equations involve the first three vibrational modes. This forms the set of equations

$$\begin{bmatrix} 1.0 & 1.0 & 1.0 & 1.0 & 1.0 \\ 34.48 & 18.01 & 0.0 & 18.01 & -34.48 \\ 1.323 & -0.392 & -1.216 & 0.392 & 1.323 \\ 0.861 & -1.282 & 0.0 & 1.282 & -0.861 \\ 0.423 & -1.043 & 1.422 & 1.043 & 0.423 \end{bmatrix} \begin{Bmatrix} w_1 \\ w_2 \\ w_3 \\ w_4 \\ w_5 \end{Bmatrix} = \begin{Bmatrix} 11.36 \\ 0.0 \\ 0.0 \\ 0.0 \\ 0.0 \end{Bmatrix} \quad (46)$$

where 11.36 lb_m is the mass of the beam. The effective weights from Eqs. (46) are tabulated in Table 1 as effective weights determined from the mode shapes.

A second set of effective weights for this beam setup were determined from the finite element approach (See Table 1). For this beam, case 1, the two different set of effective weights were very close. The difference of random and impact loadings determined from both set of effective weights to the measured forces was small (See Figs. 6, 7, 8, and 9).

The second case is for the same beam and number of accelerometers with the gauges moved to a reasonable location, but where the modal shape approach yielded a

All Dimensions in Inches.

Mass = 11.38 lb.

O - Location of an accelerometer.

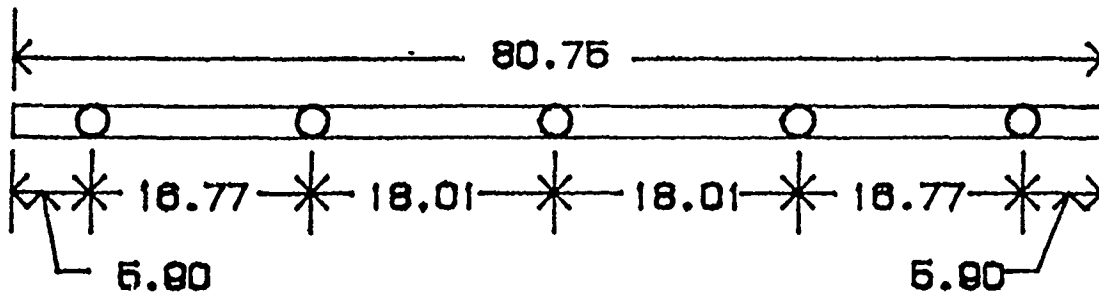


Figure 5. Case 1 - Free-Free Beam Configuration of Accelerometers
(A Strategic Location).

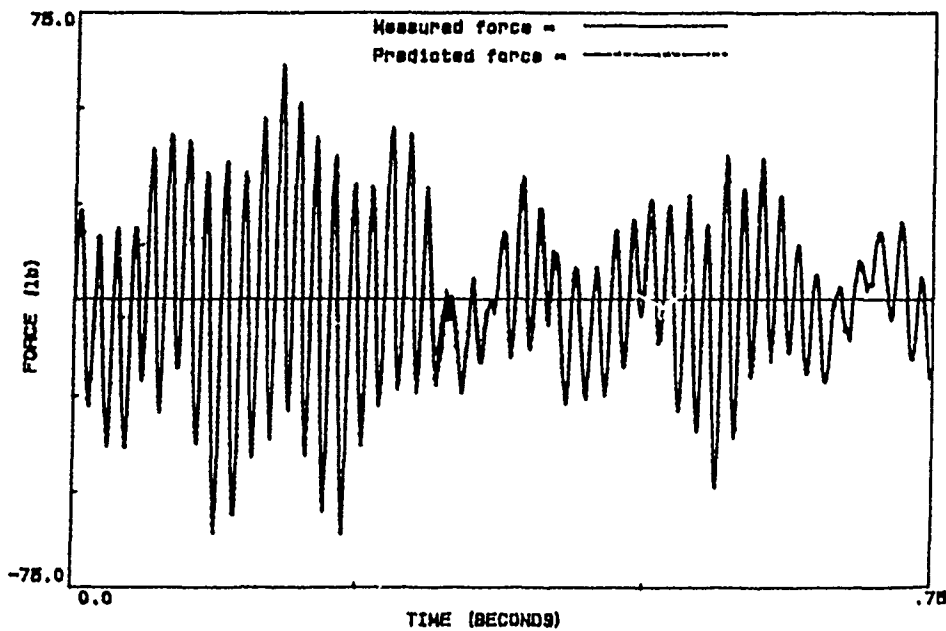


Figure 6. Case 1 - Free-Free Beam. Predicted Force Calculated from the
Effective Weights Determined from the Mode Shape Approach.

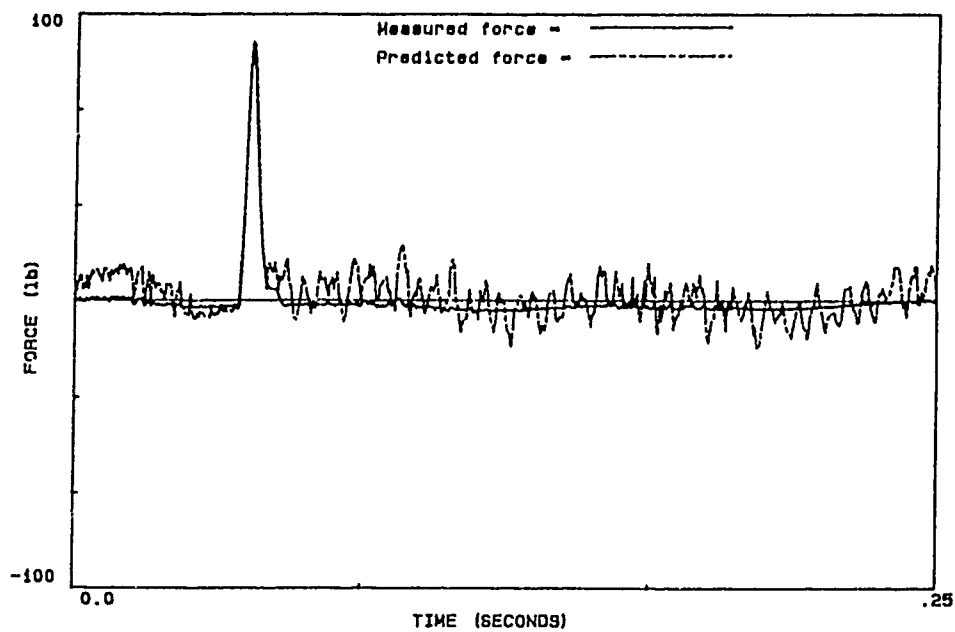


Figure 7. Case 1 - Free-Free Beam. Predicted Force Calculated from the Effective Weights Determined from the Mode Shape Approach

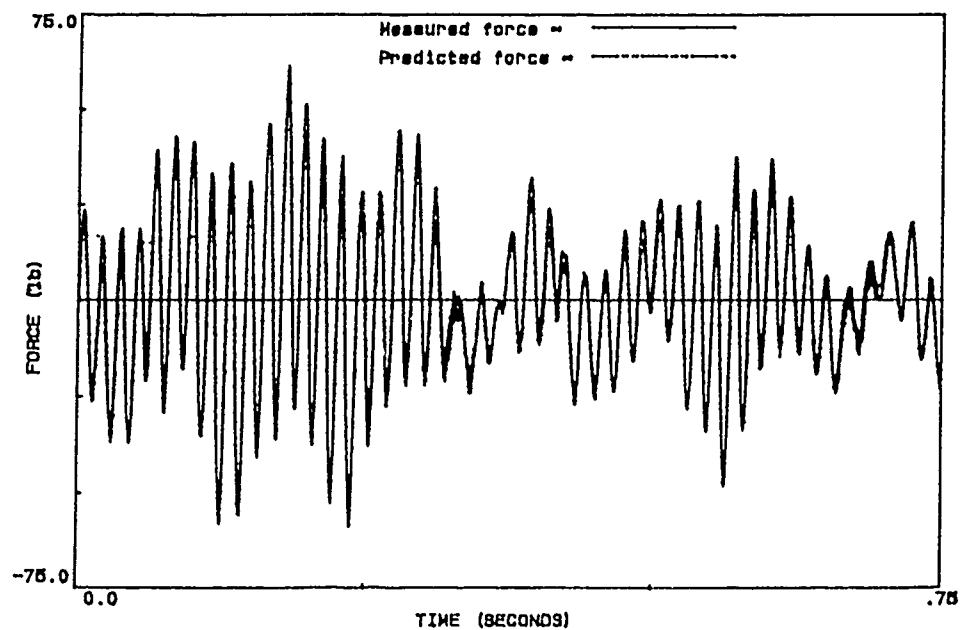


Figure 8. Case 1 - Free-Free Beam. Predicted Force Calculated from the Effective Weights Determined from the Finite Element Approach.

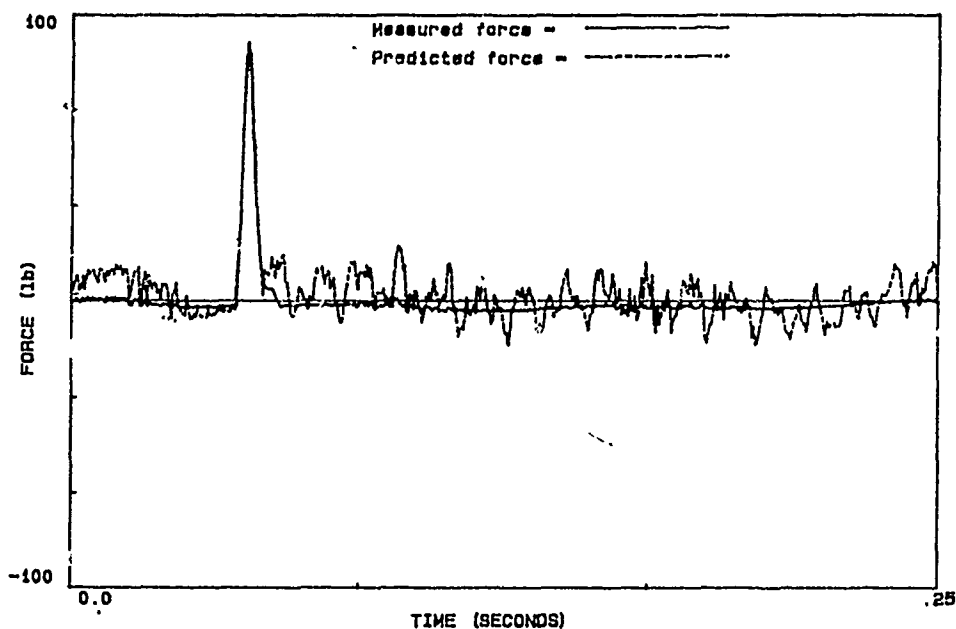


Figure 9. Case 1 - Free-Free Beam. Predicted Force Calculated from the Effective Weights Determined from the Finite Element Approach.

negative effective weight (See Fig. 10). The results of using Eq (16) in this case is

$$\begin{bmatrix} 1.0 & 1.0 & 1.0 & 1.0 & 1.0 \\ 27.37 & 13.08 & 0.0 & -13.08 & -27.37 \\ 0.527 & -0.766 & -1.216 & -0.766 & 0.527 \\ -0.371 & -1.287 & 0.0 & 1.287 & 0.371 \\ -1.008 & -0.270 & 1.422 & -0.270 & -0.008 \end{bmatrix} \begin{Bmatrix} w_1 \\ w_2 \\ w_3 \\ w_4 \\ w_5 \end{Bmatrix} = \begin{Bmatrix} 11.36 \\ 0.0 \\ 0.0 \\ 0.0 \\ 0.0 \end{Bmatrix} \quad (47)$$

The effective weights determine by the mode and finite element approach are much different (See Table 1). This was expected because for the finite element approach the effective weights are always positive. The results comparing the random input to this beam show small difference between the predicted and the measured force (See Figs. 11 and 13). The impact loading showed high amplitude oscillation after the removal of the load for both set of predicted forces (See Figs. 12,14). The impact loading has a higher bandwidth of frequencies.

The third case is that of an aluminum plate (See Fig. 15). Only the finite element approach was used to determine the effective weights. These weights and the response accelerations were used to predict an impact loading which is compared with the measured loading in Fig. 16.

All Dimensions in Inches.

Mass = 11.38 lb.

O = Location of an accelerometer.

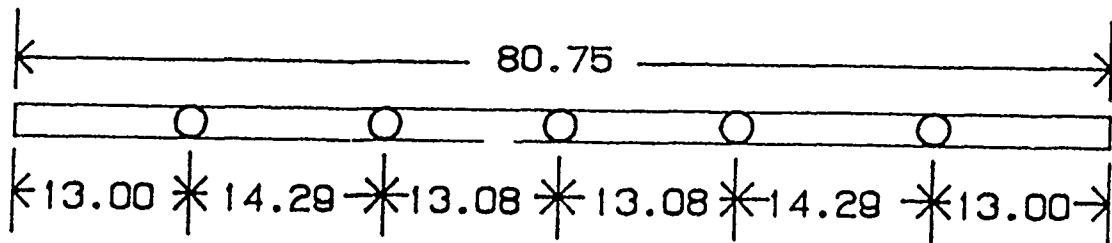


Figure 10. Case 2 - Free-Free Beam Configuration of Accelerometers (An routine Location).

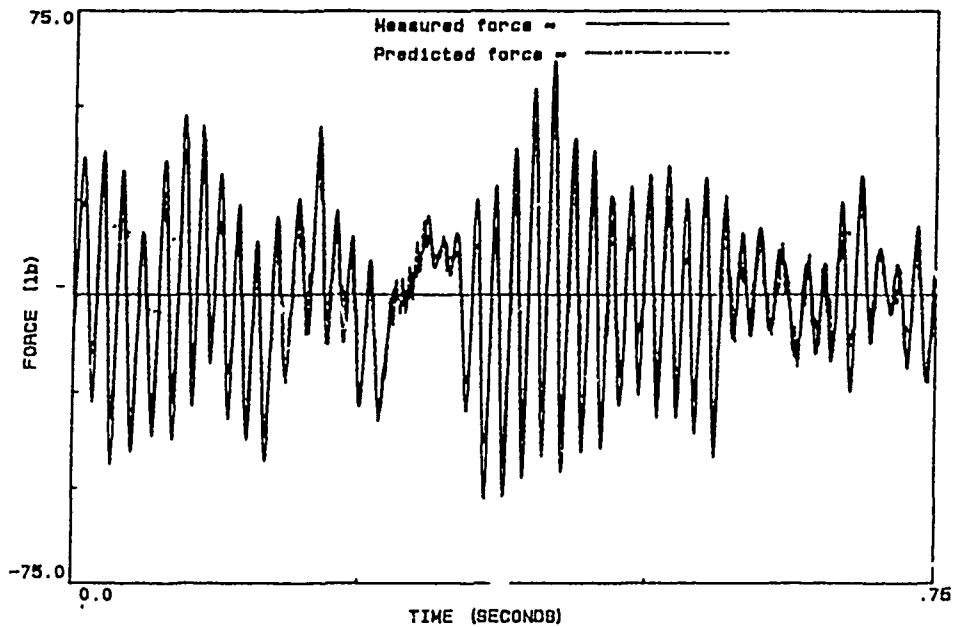


Figure 11. Case 2 - Free-Free Beam. Predicted Force Calculated from the Effective Weights Determined from the Mode Shape Approach.

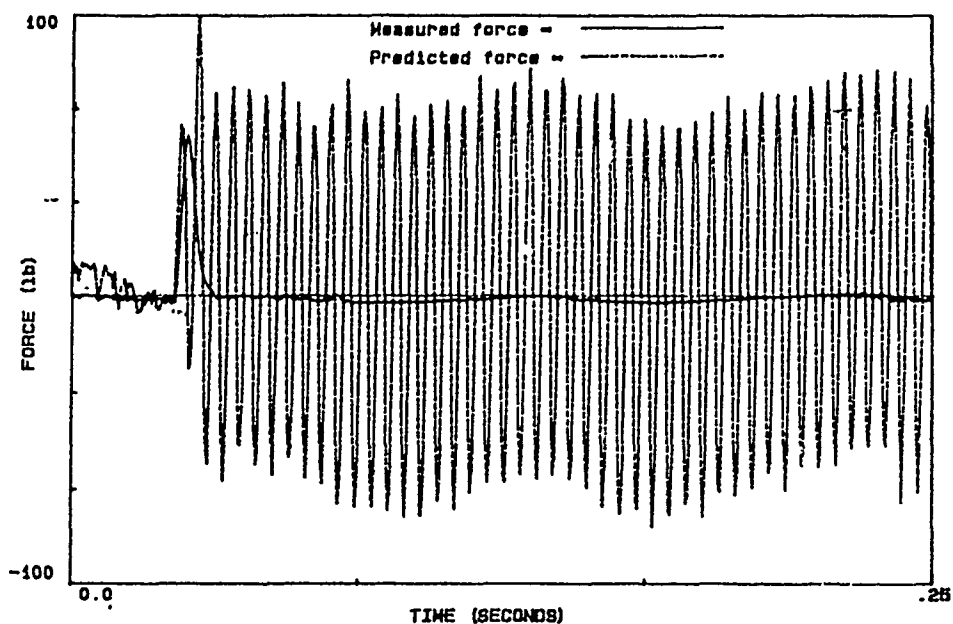


Figure 12. Case 2 - Free-Free Beam. Predicted Force Calculated from the Effective Weights Determined from the Mode Shape Approach.

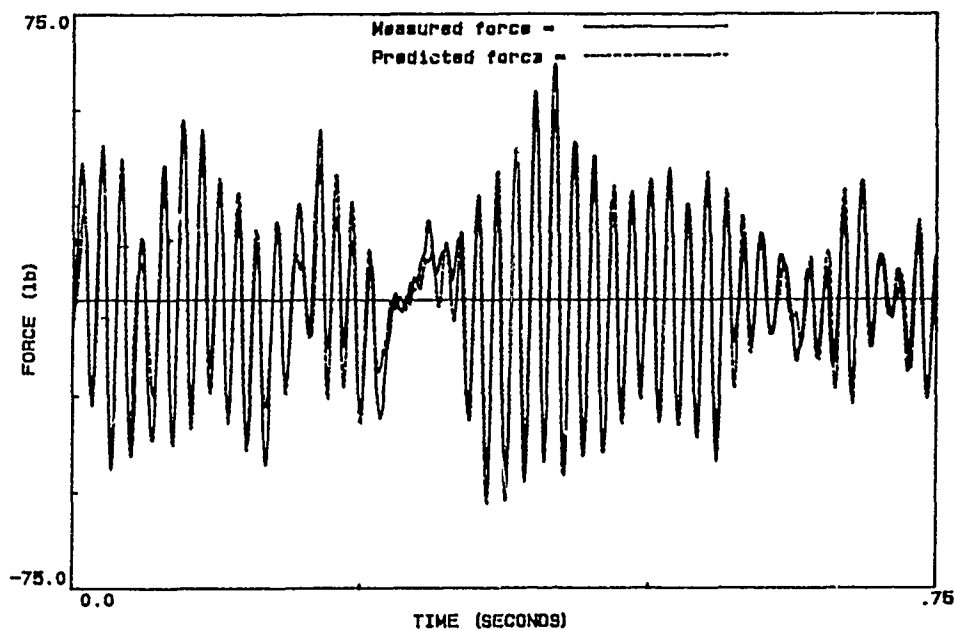


Figure 13. Case 2 - Free-Free Beam. Predicted Force Calculated from the Effective Weights Determined from the Finite Element Approach.

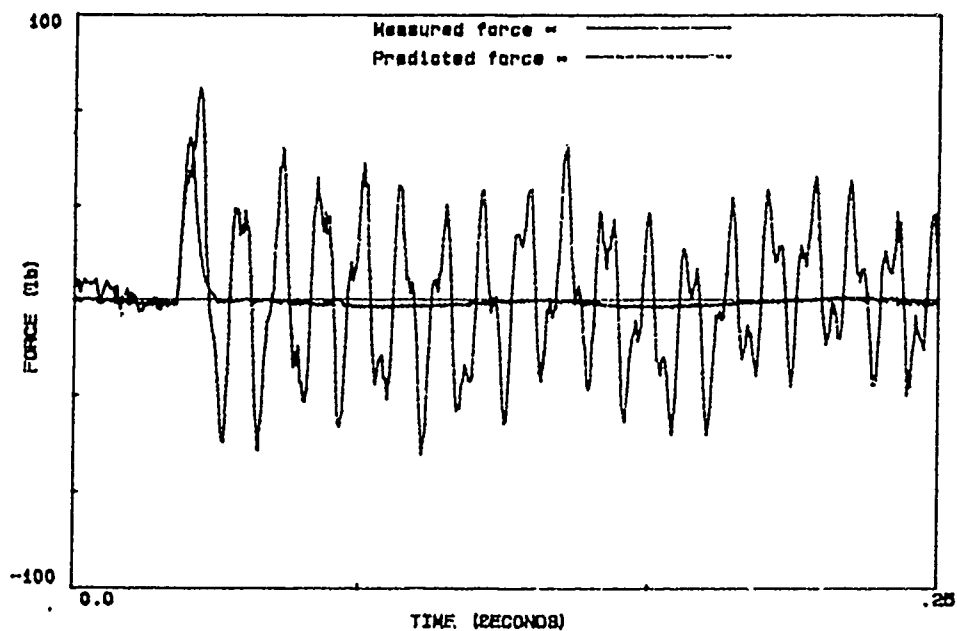


Figure 14. Case 2 - Free-Free Beam. Predicted Force Calculated from the Effective Weights Determined from the Finite Element Approach.

All Dimensions in Inches.

Mass = 11.06 lb.

o = Location of an Accelerometer.

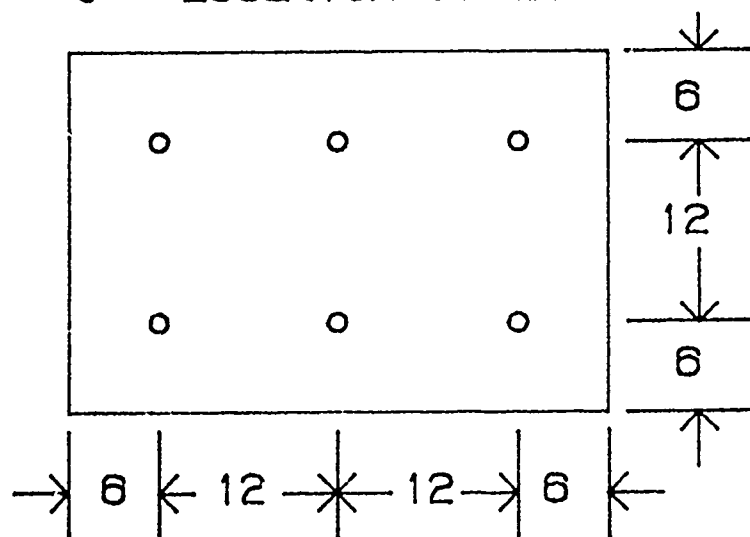


Figure 15. Case 3 - Plate Configuration.

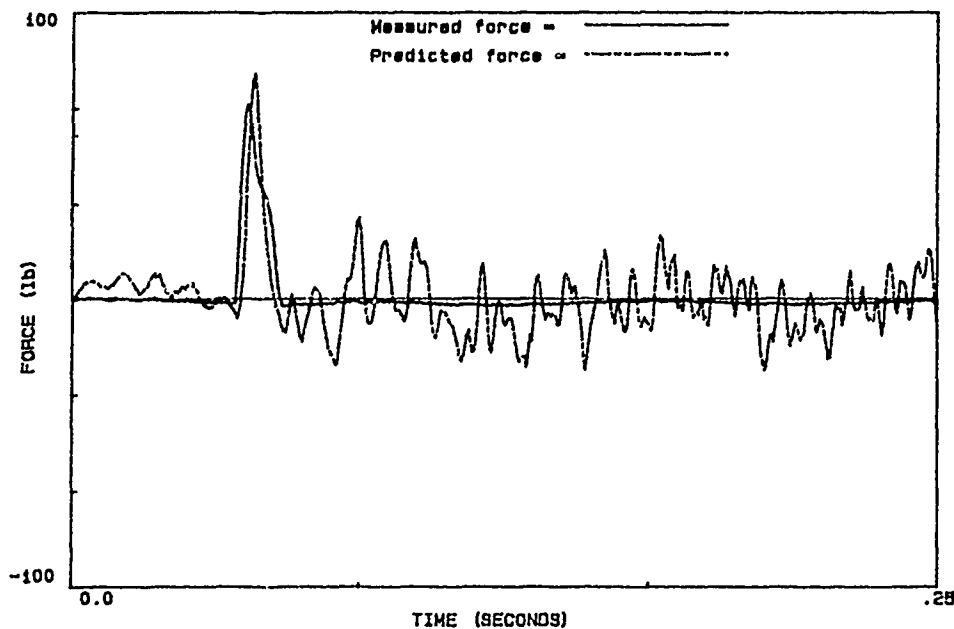


Figure 16. Case 3 - Predicted and Measured Forces for the Plate.

CONCLUSION

The sum of weighted acceleration method determines the resulting force for a multi degree of freedom system. The use of finite element approach opens the avenue for more practical applications. If the mode shape approach is used, the mode shapes may be determine from a number of different methods such as finite elements or finite differences. A more direct finite element approach provide estimations of the effective weights. For the second case which had a negative effective weight, the finite element approach effective weights predicted the random input, but it was shown by the impact loading the method of weighted accelerations is bandlimited, that is the weights are for a specific range of frequencies. To eliminate this discrepancy further study is needed.

ACKNOWLEDGEMENT

This work has been supported by a research contract from Sandia National Laboratory. The author wishes to express appreciation for this support and the valuable discussions with Tom Priddy of Sandia National Laboratory.

REFERENCES

1. Doyle, J. F., "An Experimental Method for Determining the Dynamic Contract Law, "Experimental Mechanics", March 1984.

2. Doyle, J. F., "Further Developments in Determining the Dynamic Contact Law," Experimental Mechanics, December 1984.
3. Hillary, B., and D. J. Ewins, "The use of Strain Gauges in Force Determination and Frequency Response Function Measurements," Proceedings of the 2th IMAC, Orlando Florida, 1984.
4. Gregory, Dan, Ron Coleman, and Tom Priddy, "Measurement of Dynamic Forces Acting on Non-Rigid Bodies," Vibration Test Division 7542, Sandia National Laboratories, Albuquerque, NM.
5. Gregory, D. L., T. G. Priddy, and D. O. Smallwood, "Experimental Determination of the Dynamic Forces Acting on Non-Rigid Bodies," SAE Technical Paper 861791, Aerospace Technology Conference, Long Beach, CA.
6. Priddy, Tom G., Dan L. Gregory, and Ron G. Coleman, "Strategic Placement of Accelerometers to Measure Forces by the Sum of Weighted Accelerations," Proceedings of the 6th IMAC, Kissimmee, Florida.
7. Wang, M. L., T. J. Kreitinger, and H. L. Luo, "Force Identification from Structural Responses, " Proceedings of the 1987 SEM Spring Conference on Experimental Mechanics, Houston Texas.
8. Kreitinger, Timothy J., and Ming L. Wang, "Force Identification from Nonlinear Structure Response," Proceedings of the 6th IMAC, Kissimmee Florida.

SHOCK RESPONSE OF A MINE HUNTER DUE TO SEA GROUND MINE EXPLOSIONS - NUMERICAL SIMULATIONS

Wilhelm E. Pfrang and Horst Lütje
Industrieanlagen Betriebsgesellschaft mbH
Einsteinstraße 20
8012 Ottobrunn, West Germany

Jürgen Freercks
Fed. Bureau for Military Technology & Procurement
5400 Koblenz, West Germany

The numerical simulation of underwater explosions against vessels by the code DYSMAS/ELC is a powerful method to predict the shock response behaviour in an early state of the development. This is demonstrated discussing the results of the investigation of the shock response behaviour of a new German mine hunter

INTRODUCTION

The Federal German Navy has started to replace its fleet of Mine Countermeasure Vessels (MCMV) by a new generation. The first generation vessels still in service are wood constructions, no glass fibre reinforced plastics (GFRP) was used at that time. At the beginning of the preconcept phase naval architects had to select a suitable hull material. Due to the positive experience gained from the construction and the long term operation of the submarine Class 206 the German industry could offer non-magnetic steel (NM-steel) as a third competitor for the construction of MCMV-hulls.

Meanwhile, in the wake of extensive research work and investigation, the German Ministry of Defense has adopted NM-steel for the construction of the hull and superstructure of the first project, e. g. the Fast Mine Warfare Vessel Class 343 and the Minehunter Class 332 (fig. 1). The main dimensions of the vessels are:

Length (between perpendiculars)	51.0 m
Breadth (moulded)	9.2 m
Draft (at full load displacement)	2.5 m
Design displacement approx.	590 t

The design and the cost of a modern MCMV are determined by its capability regarding the passive ship protection, meaning that these vessels must possess

- a low magnetic and acoustic signature and
- a high resistance against the impact of underwater explosions.

Primarily these capabilities provide the standard according to which the hull material is to be selected. The most simple technical and the best economic approach would be the use of standard shipbuilding steel. Studies have shown, however, that hulls made of ferritic steel, even in the case of an optimized magnetic self-protection system, would ex-

ceed the permissible safe depth for MCMVs considerably. The selection of the material was preceded by comprehensive experimental investigations and competitive studies during the concept phase. Thereby the non-magnetic steel proved to be superior to wood and GFRP in nearly all important respects. NM-steel achieved the highest results with respect to the important criteria:

- shock resistance
- acoustic impacts
- electromagnetic compatibility
- magnetic impacts

The fully welded NM-steel construction of the vessel is characterized by a thin-walled sheet metal structure having a plate thickness of 4 to 6 mm and narrowly spaced struts as frames and girders.

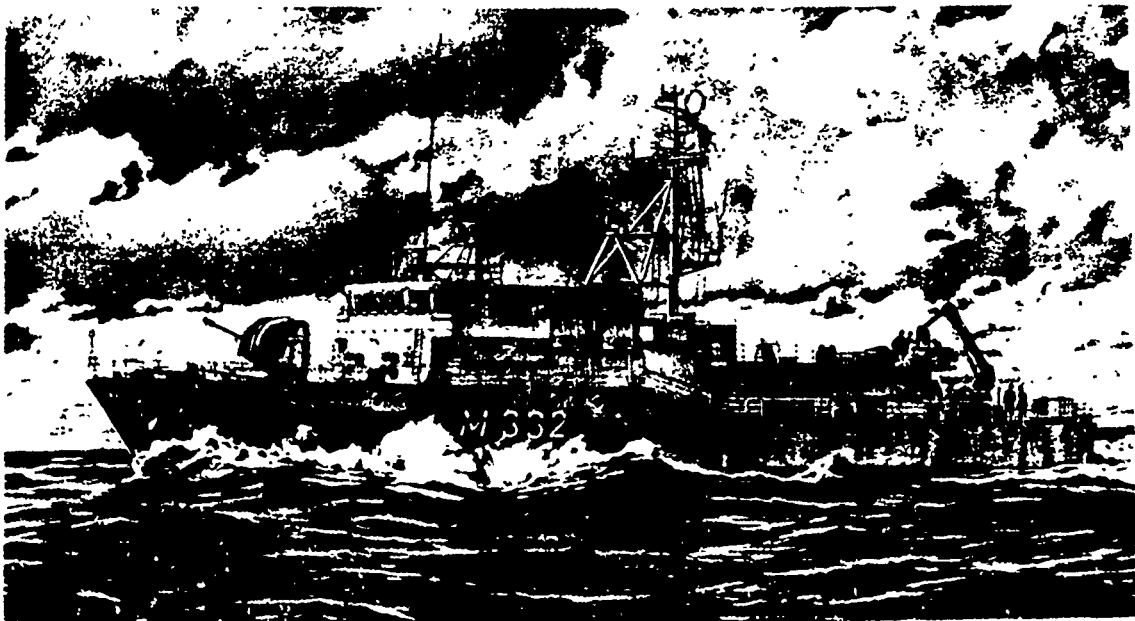


Fig. 1 Sketch of the Minehunter MJ332

The general design is distinguished by a high degree of standardization of the two types of vessels and different sets of role equipment for mine warfare operations to which the variants will be tailored :

- minelaying / minesweeping
- minehunting / minelaying
- solenoid sweep control / minelaying

In addition to these prime mission variants, there are requirements for antithreat defense:

- passive protection
- ABC protection for crew's quarters and ship control stations
- defense capability against air and surface targets

Already during the concept phase of the SM343 numerical simulations were carried out in order to predict the global shock response of the

ship in the case of a typical sea ground mine explosion in shallow water. On the basis of these predictions and in connection with experimental experience the shock design values were fixed according to the design goal. Some time later in the course of the definition phase of the MJ332-boat again numerical simulations were done in order to verify the former results for the latest updated version of the vessel and to get further information by the meanwhile refined modelling techniques on one hand and different explosion load cases on the other hand.

NUMERICAL METHOD

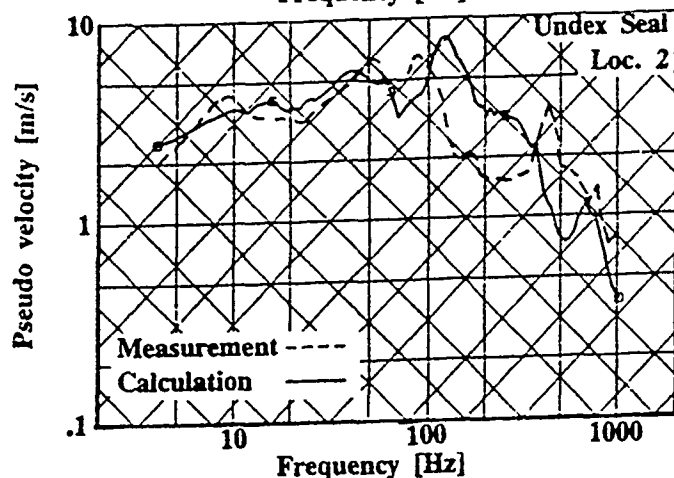
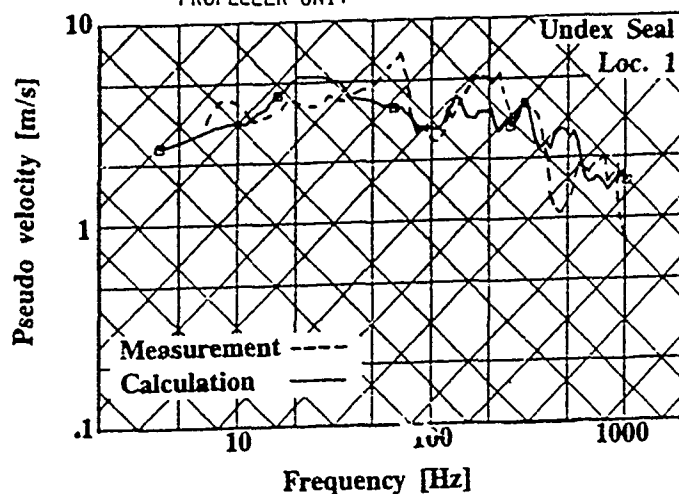
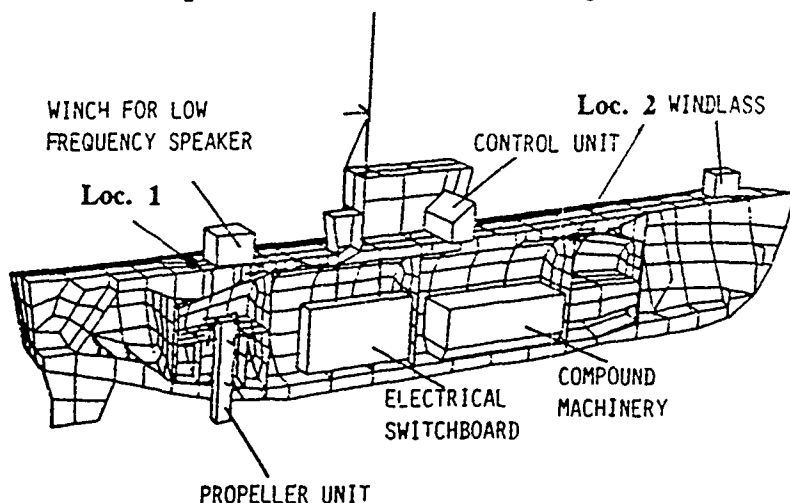
The numerical simulation was done using the coupled three-dimensional FE/FD-code DYSMAS/ELC [1]. The code consists of two stand-alone parts DYSMAS/L, a FE-Lagrangian code, and DYSMAS/E, a FD-Eulerian code and additionally the DYSMAS/ELC package in which both are coupled together in two and three dimensions. It has been developed to simulate highly dynamic processes arising in short time physics. In the present case, as in most naval applications, fluid dynamics, structural dynamics and fluid-structure interaction phenomena have to be accounted for. This is advantageously managed by an explicit finite formulation, which is suited to handle the various nonlinearities effectively.

The structure code DYSMAS/L uses a FE-description within a material-fixed reference frame for the spatial discretisation and an explicit time integration scheme, i. e. the central difference operator in connection with the lumped mass model, in the time domain. For the most applications in the short time range, e. g. crash, impact and penetration, this has proved to be a powerful tool [2,3]. The formulation of the basic equations permits the treatment of large displacements and distortions. Extensive material models are available in the L-modul to handle large plastic flow including effects of work hardening and strain rate dependency [2,3]. Material failure is judged by different instantaneous or cumulative criteria. Post-failure behaviour is modelled by stress tensor modification with the option of a residual shear strength or by procedures like crack-opening or erosion which can be denoted as dynamic rezoning techniques [3]. A 3D-multibody contact processor completes the capacity of DYSMAS/L to simulate impact, penetration and crash processes.

The fluid code DYSMAS/E is based on a FD-formulation within a space and time fixed reference frame. The classical integral balance equations for mass, momentum and energy are integrated by the FLIC-integration scheme [1,4], a second order scheme with exception of the convective phase where a donor cell upwind differencing method is used. A large number of material models and equations of state for different materials such as water, explosives, soil and air is included. Explosion is modelled by different complex procedures for initiation and burn of the explosive.

Fluid-structure interaction phenomena are distinguished by nonlinearities present both in structure and in fluid. The low compressibility of water in compression and its cavitation properties under tension have great influence for instance on the transient loading of vessels subjected to underwater explosions. Therefore coupling is done explicitly in each time step of the simulation within a loop over all elements of the structural interface. This interface is treated as a time varying geometric boundary condition for the fluid while it describes a transient load condition for the structure. Additionally energy and momen-

tum exchange at the interface are considered. DYSMAS/ELC uses an extensive interface description, especially suited to naval applications which are characterized by thin walled, stiffened structures modelled by beam and plate elements undergoing severe deformations and displacements. The algorithm allows interfaces consisting of one or more simply closed surfaces of any shape which are allowed to be deformed and moved arbitrarily as far as basic assumptions are fulfilled.



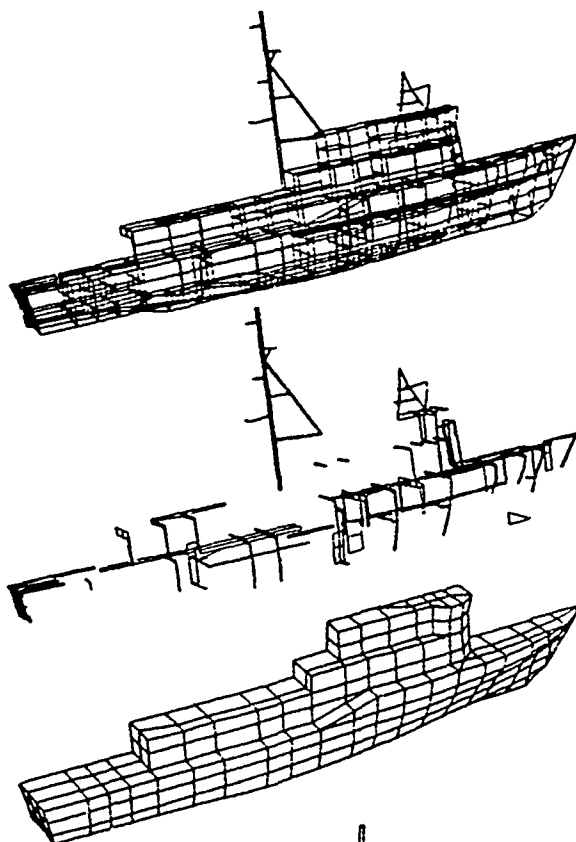
The coupled code had been applied primarily to naval problems in the past with an emphasis on weapon effectiveness studies [5]. In the recent years the code has been extended by an option of dynamic soil-structure interaction including the transfer of deviatoric stresses and a procedure to treat separation of soil from the structure [6]. Code verification is mostly done in connection with certain projects. For the actual problem of simulating the shock response of a surface vessel due to an undex, a calculation of the full scale test of the remote controlled minesweeping boat SEEHUND (seal) executed by the German navy was performed [7]. The comparison of the results of numerical simulation and measurement shows excellent agreement for all measured data records which are counted to be consistent and reliable. Fig. 2 shows one half of the FE-model of the SEEHUND together with two shock response spectra (SRS) from experiment and calculation respectively. Especially at the foundation of the low frequency speaker (loc. 1) it is evident that

Fig. 2 Under Seal - FE-model and comparison of SRS at Loc. 1 and 2

over the whole frequency range the calculated SRS is very well within the scattering of the measured SRS. At top of the pressure hull bulkhead (loc. 2) there is a nearly perfect coincidence to be observed below 100 Hz, while beyond that value local properties of the structure cause little differences. It could be proved by this fully three-dimensional simulation of the shallow water explosion from an athwartships position that even in the case of a very complex structure consisting of different structural members and different materials reliable predictions could be made by using DYSMAS/ELC.

MODEL DESCRIPTION

The Structure of the MJ332 is modelled as shown in Fig. 3 by means of



240 beam elements, 580 orthotropic plate elements, 7 rigid-body systems and 40 spring elements yielding 1105 nodes for the half symmetric FE-model. Heavy stiffeners such as frames and girders are mapped exclusively by beam elements, building up a framework for the whole ship (see Fig. 3). Bending and membrane stiffnesses of the small and narrowly spaced struts are combined with the isotropic properties of the plating into the orthotropic plate properties. This is an adequate method of modelling a global shock model. It keeps the total number of elements and the simulation time step of the structural model within efficient limits.

Fig. 3 FE-model of the structure in a complete glass-body representation, framework of beam elements and hull and superstructure plating.

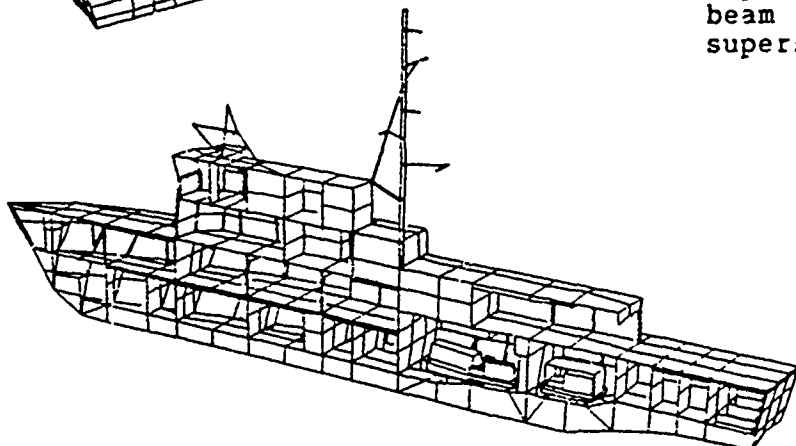
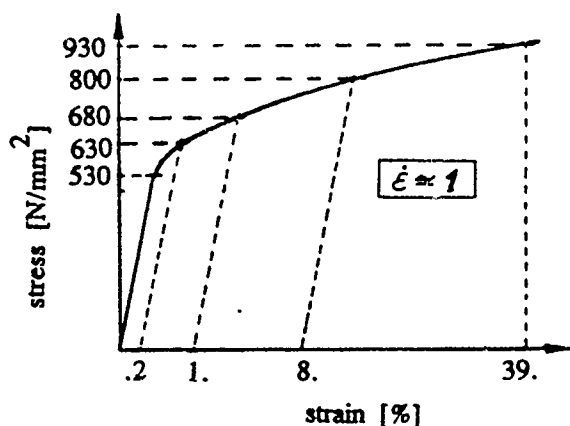


Fig. 4 Hidden line representation of the fully assembled FE-model containing the rigid-body systems.

The heavy components of the machinery are considered by rigid-body systems with double elastic mountings via intermediate foundations (see Fig. 4). The rigid-body elements are connected among each others and with the foundation respectively by spring elements which are formulated as structural members with properties defined by characteristic curves and an initial condition including the prestressing. Two encapsulated Diesel-generators are arranged in compartment III and an uncapsulated one is mounted between the two propulsion engines in compartment IV. The propulsion engines consist of a gear-box fixed at the intermediate foundation, a deck mounted slow motion link and a muffler mounted to the ceiling and connected with the engine by a compensator.



The stress-strain relationship of the NM-steel used as input for the simulation is shown in Fig. 5. This relationship is taken from a family of curves prescribing the strain rate dependency of the strength of the material for an average strain rate of 1. This value has been proved by a lot of calculations to be characteristic for underwater explosions against vessels in a load range below structural damage occurs. The material behaviour is characterized by a very high ultimate strain and remarkable work hardening. The Young's modulus is 195000 N/mm² and the density is 7.91 g/cm³.

Fig. 5 Stress-strain relationship of the NM-steel

The coupling interface is described by the hull and superstructure plating elements forming a simply closed surface around the whole ship. It consists of 248 interface elements in the halfsymmetric case (see Fig. 3).

A number of consistency checks concerning the overall properties of the structure has to be performed before the simulations could start. The location of the waterline and the depth of immersion are determined by a special preprocessor in order to prove the consistency of the hull shape with the mass distribution in the ship where the small equipment and the payload are considered by nodal masses. Furthermore the floating stability is checked by the distance between weight and buoyancy vectors as a function of virtual rotations. The mass distribution in the model has to be optimized until a realistic stable floating condition was reached and the global properties of the model are in coincidence with the real ship.

LOAD CASES INVESTIGATED

In this paper only two load cases are discussed although meanwhile a third load case was simulated to predict the full scale test which will be performed by the German Navy. To keep this paper open to public charge weights must not be mentioned. The different explosion geometries are defined in a sketch in Fig. 6. Both cases are half symmetric and consequently the charges are positioned below keel. In case 1 charge is longitudinally centered at a rather large depth on the sea

bed. Case 2 is a really shallow water explosion with the charge straight behind stern. Load case 1 can be denoted as a very severe explosion geometry for a certain shock factor because the whole ship is affected by a rather plane shock wave nearly at the same time. Load case 2 is quite different due to the fact, that the shock wave at first strikes the stern of the ship and then moves forward under steady loss of energy and will be disturbed by the reaction of the ship itself.

The coupled problem grids for both simulations are shown in Fig. 7. The structure is represented there by the interface only. The division of the Euler-grid is drawn in the border planes of the plotted windows of the 3D-representations. The size of the E-grid is 39600 cells in case 1 and 37440 cells in case 2. Bottom reflection properties are taken into

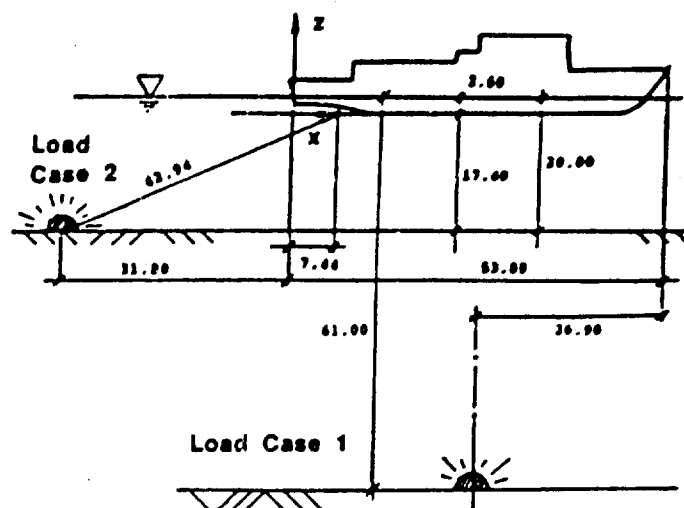


Fig. 6 Explosion geometries

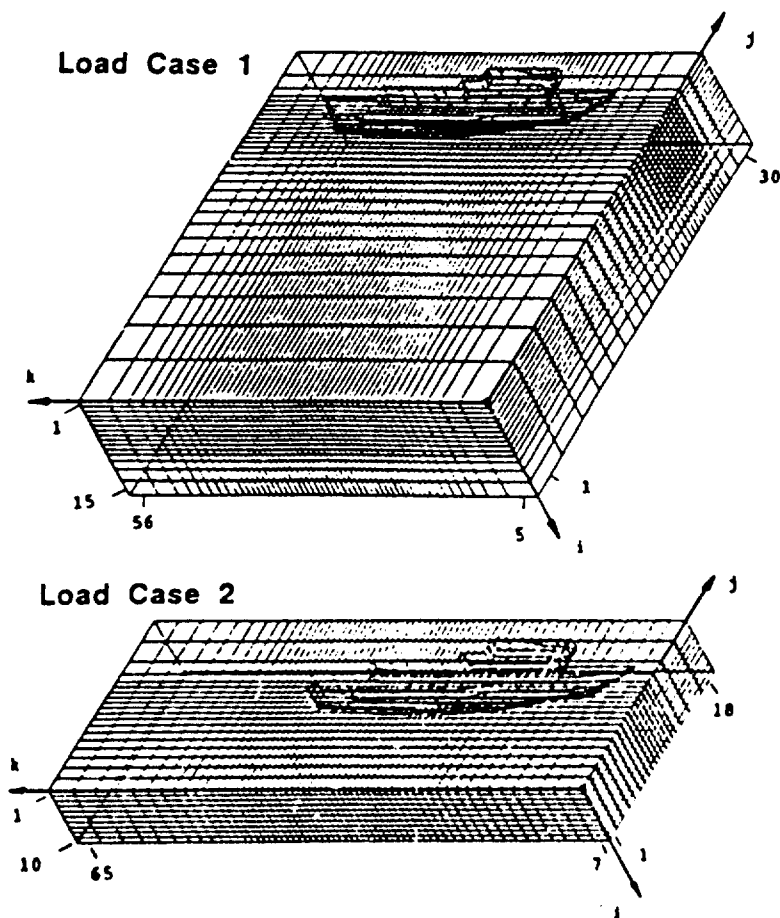


Fig. 7 Coupled problem grids (without remote regions)

account by a reflection coefficient at the buffer of the Euler-grid. The grid division rate in all directions is kept rather constant remote areas as the charge location need not to be divided very fine because the explosion of the charge and the propagation of the shock wave through the water towards the ship hull is done in pre-calculations using very fine grid divisions. Just before the arrival of the shock wave at the hull from these axis-symmetric pre-runs a rezoning step is performed into the final 3D-grid. So the coupled simulation starts at a problem time of $t = 37.23$ ms in the first and at $t = 22.1$ ms in the second load case respectively. In the case of farfield explosions this rezoning technique guarantees the lowest possible numerical affection of the shock wave on its way towards the ship.

NUMERICAL RESULTS

A transient coupled simulation provides a lot of information after complete evaluation of the results. Within the frame of this paper only a choice of transients and shock-response spectra (SRS) can be discussed with the aim of illustrating the physical phenomena arising during the simulated process. Both simulations were performed up to a real time of 100 ms after arrival of the shock wave at the structure allowing the generation of SRS from about 6 Hz upwards.

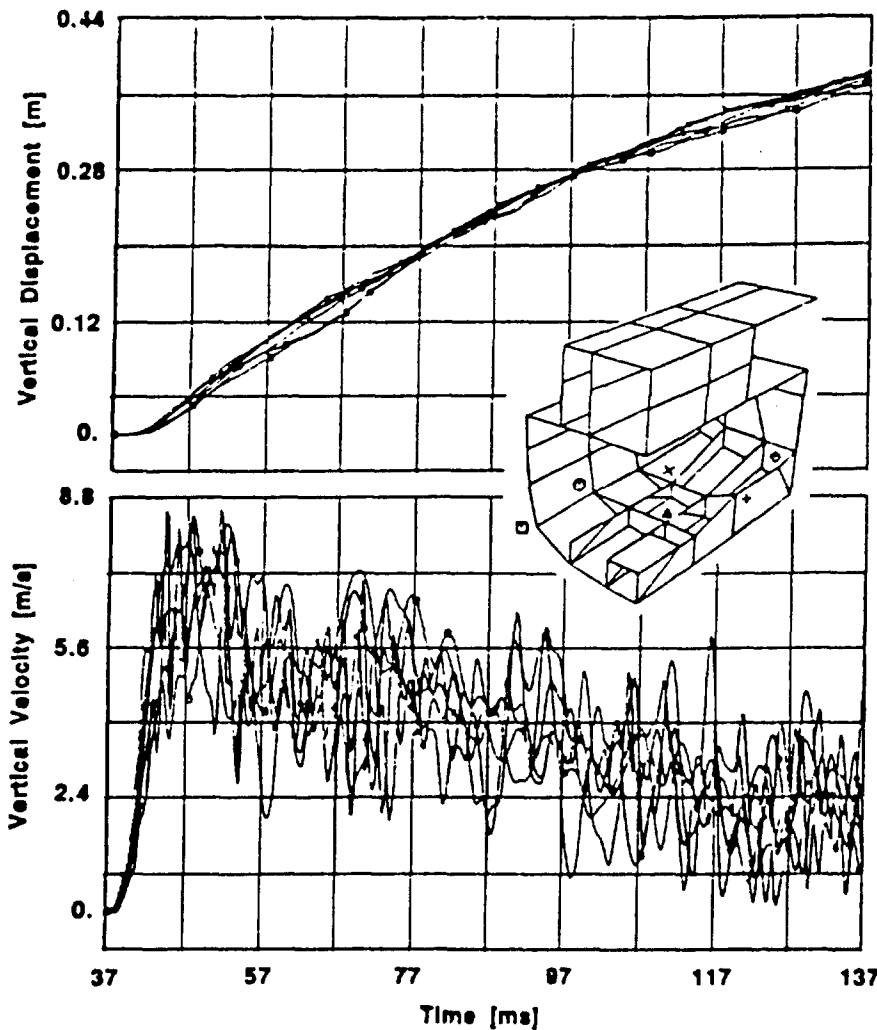


Fig. 8 Vertical velocities and displacements of nodes of the engine compartment (case 1)

In load case 1 the velocity transients from nodal points of the engine room (Fig. 8) show an initial steep increase due to the impact of the shock wave. In the further course of time a nearly linear decrease is to be observed which is superimposed by high frequency and low frequency oscillations. The decreasing of the mean velocities can be attributed to the long term action of the cavitation pressure below the ship together with gravity forces. The time of zero-velocity and maximum displacement can be estimated eliminating the oscillations to be about 180 ms after explosion. The corresponding displacement transients of these nodal points are dominated by a smooth rigid-body movement showing an additional oscillation of 10 to 15 Hz with an amplitude of about 2 cm within the engine compartment. The maximum displacements can be extrapolated as about 40 cm.

A very high shock level over the whole frequency range is visible in the SRS of these nodes (Fig. 9). The smoothness of the curves below 100 Hz may result from the elastic coupling of the heavy components with these nodal points. The larger bandwidth of the SRS beyond 100 Hz is caused by the local structural properties and the uncoupling of the large elastically mounted masses in this frequency range. For low frequencies the SRS are coinciding at relative displacements of more than 100 mm. The observed peak values of response acceleration at high

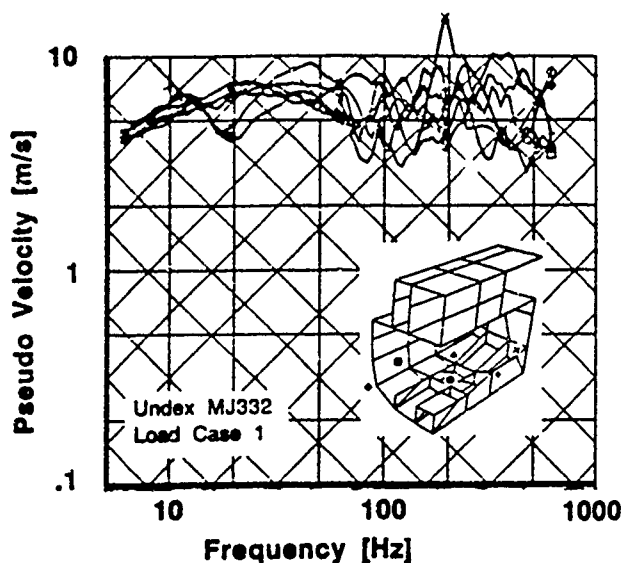


Fig. 9 SRS of nodes of the engine compartment (case 1)

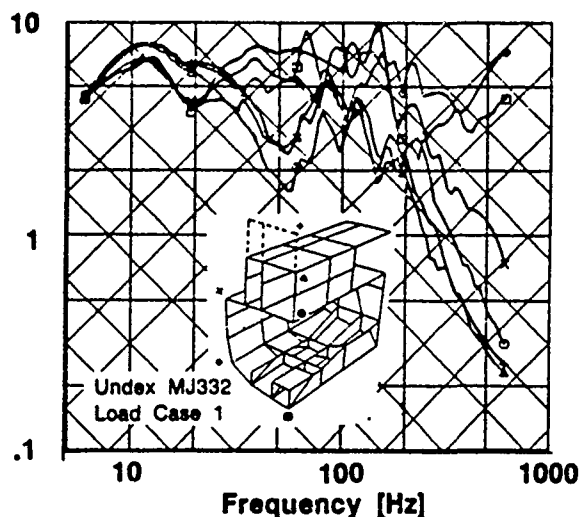


Fig. 10 SRS at front bulkhead of engine compartment (case 1)

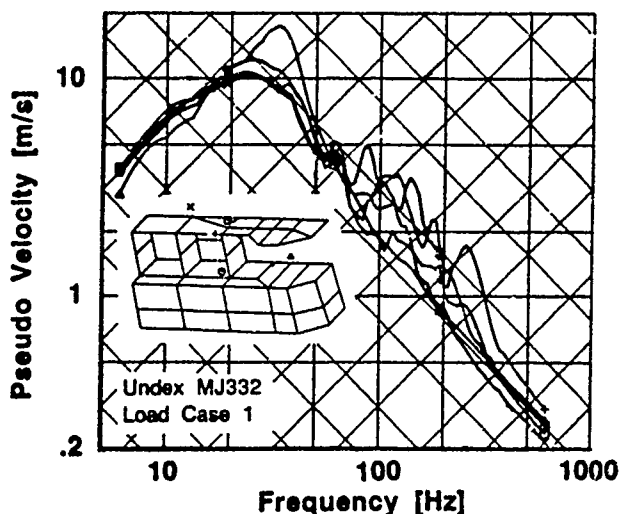


Fig. 11 SRS of nodes of the superstructure (case 1)

do velocities are arising in the range of 20 to 30 Hz, while the maximum relative displacements are slightly lower than those at the bottom of the ship. The superstructure itself is acting like a low pass filter which can be traced back to the low stiffness of this structural member.

Although load case 2 is of the same nominal shock hardness measured in terms of the shock factor, it shows a completely different sequence of physical events and response levels to will be emphasised in the following discussion.

The vessel is struck first at stern by the water shock wave. The further longitudinal propagation is running with sound speed both in

frequencies decrease clearly at the neighboured bulkhead which has lower stiffness combined with a higher mass density than the bottom region (see Fig. 10). Especially around 50 Hz and above 200 Hz the response in the upper regions of the bulkhead is distinctly lower than at the bottom nodes. Like in Fig. 9 the SRS of the bulkhead are also converging for low frequencies at relative displacements of more than 100 mm.

The high frequency shock response is calmed down during its way through the ship in vertical direction. This is clearly evident from the compilation of SRS in Fig. 11 covering nodal points of the superstructure. In this part of the structure high pseu-

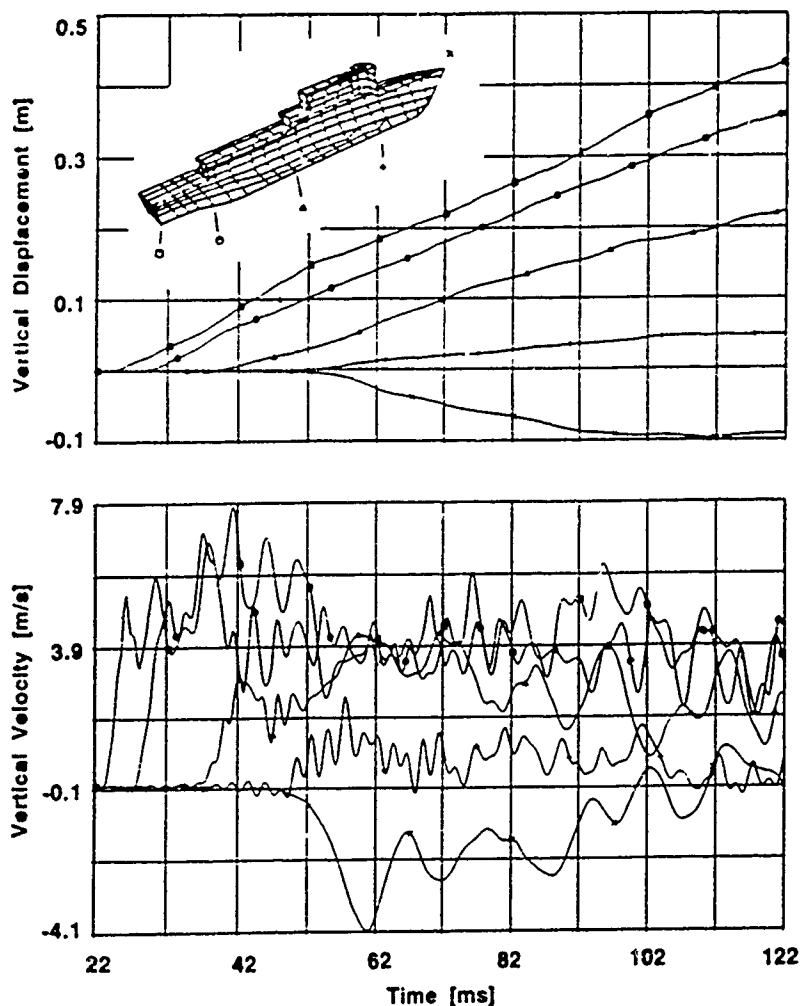


Fig. 12 Vertical velocities and displacements of nodes along the keel (load case 1)

end of the simulation backwards. The maximum vertical displacements are varying strongly over the length of the ship from nearly 50 cm at stern to -10 cm at bow. That means, that the bow of the ship is immersing into the water even in the early time range. In the engine compartment maximum displacements are clearly below those of load case 1.

The shock response of load case 2 along the keel is dominated by these phenomena, too (Fig. 13). The response levels over the whole frequency range are decreasing steadily with the longitudinal position of the observed nodal points. Additionally the characteristics of the SRS are changing over the length of the ship. At stern high levels for all frequencies can be registered whereby the maximum relative displacements are lower although the absolute displacements (Fig. 12) at stern are higher than in load case 1. The decrease of the relative displacements in the SRS along the keel comprises a whole magnitude between both ends of the vessel. So in the engine room for instance the response level is already much lower than in load case 1.

structure and in water which differs by a factor of three. This causes a delay in the excitation of bow nodes of more than 10 ms for the structural shock and up to 35 ms for the water shock respectively. So the nodal points along the keel shown in Fig. 12 start to move with an individual time delay. For instance at the midship nodes there are two phases of excitation to be observed in the velocity transient (Fig. 12), the first by structural shock and the second by the additional water shock which is less efficient because the structure is already moving upwards at its arrival.

This strong dependancy of the loading from time and location causes a global heaving and a global pitching of the vessel superimposed by bending deformations around the lateral axis. The center of rotation is incidentally near the bow of the vessel and is moving towards the

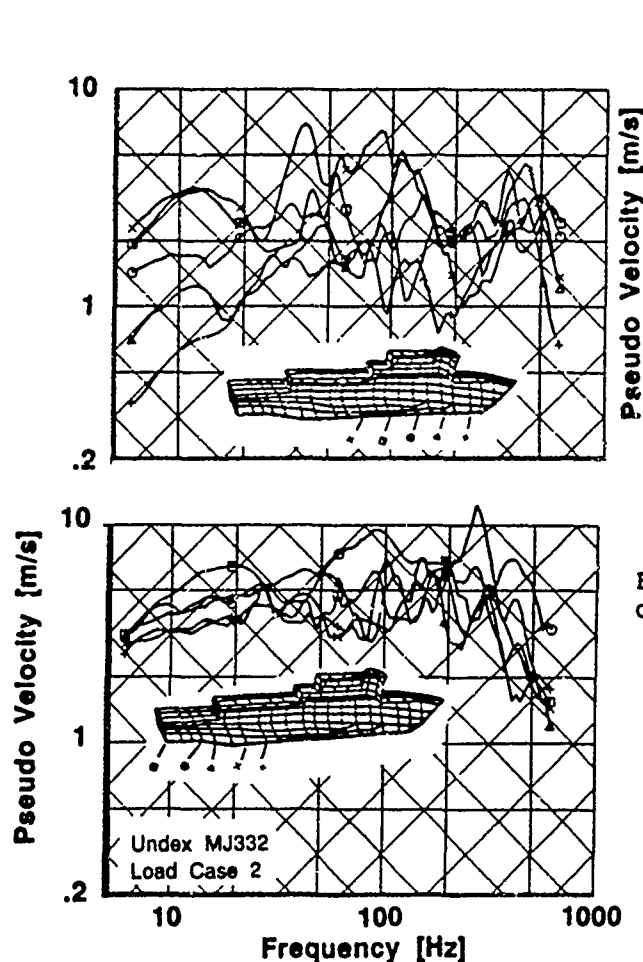


Fig. 13 SRS of nodes along the keel (load case 2)

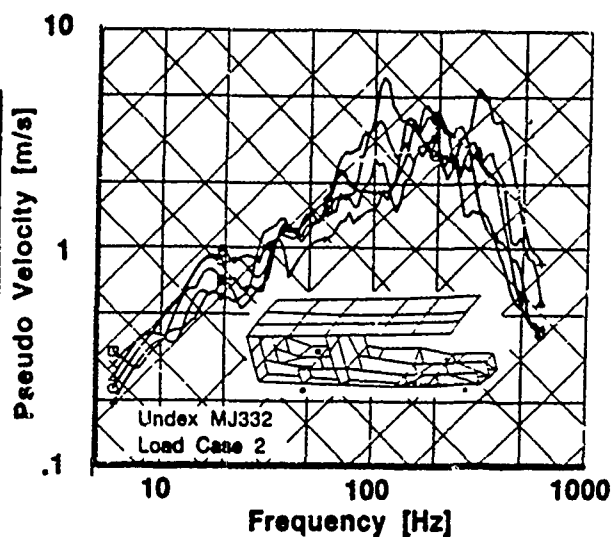


Fig. 14 SRS of nodes of the engine compartment (case 2) -longitudinal

In case 1 the longitudinal shock is predominantly excited by the bending oscillation of the ship around the lateral axis, while in load case 2 longitudinal shock is excited directly by the shock wave acting from the stern of the ship up to compartment III. As Fig. 14 shows, this mainly high frequency shock is moving along the very stiff bottom construction causing high acceleration levels above 100 Hz and nearly constant relative displacements below 10 mm in the range of frequencies up to 100 Hz.

GLOBAL VALUATION OF THE LOAD CASES

For the valuation of the overall response of the vessel global physical variables and compilations of all generated SRS shall be cited.

The total kinetic energy transients for both simulations shown in Fig. 15 give an impression of the transmission of the shock loading of the MJ332 into its structural motion. In load case 1 a practically plane shock wave strikes the whole ship within short time and causes a steep increase of the total kinetic energy. The second increase of the kinetic energy with a maximum at about 70 ms seems to be caused by the global bending of the ship, which is vanishing rather rapidly. After that maximum the kinetic energy is continuously descending due to the decay of the vibration on one hand and the reversal of the global rigid-body movement on the other hand. As already mentioned before the maximum of the total kinetic energy of load case 2 is by more than a factor of 2 below the maximum of case 1 although both have the same shock factor. This can be related to the long duration of loading of

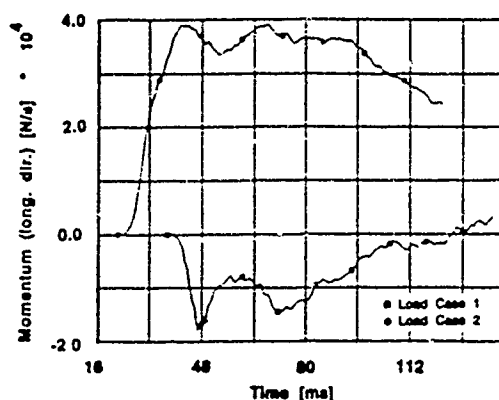


Fig. 15 Total kinetic energy

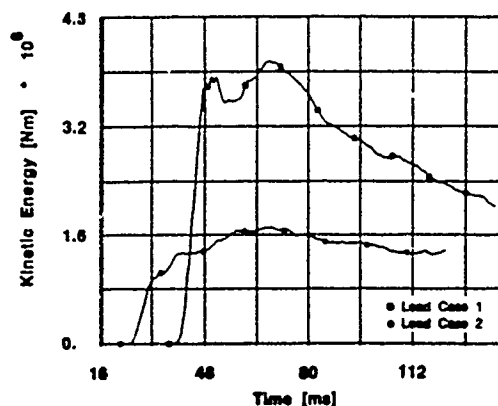


Fig. 17 Total longit. momentum

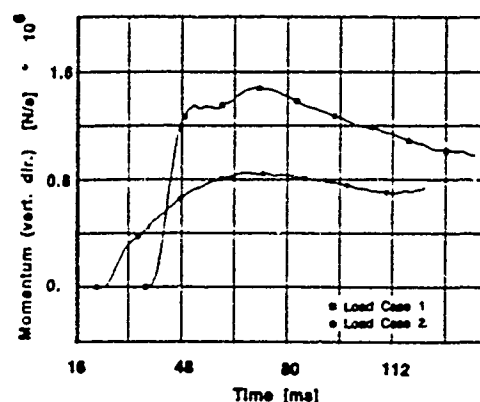


Fig. 16 Total vertical momentum

about 40 ms and the strong decay of load amplitudes in this period in load case 2. Only in the initial phase the gradient of the total kinetic energy is comparable to that of load case 1.

This will be confirmed by the observation of the transients of the total vertical momentum (Fig. 16) which are less steep but qualitatively similar to the total kinetic energies. The absolute difference between the curves of both load cases varies between kinetic energy and momentum due to the quadratic and linear influence of the velocity respectively.

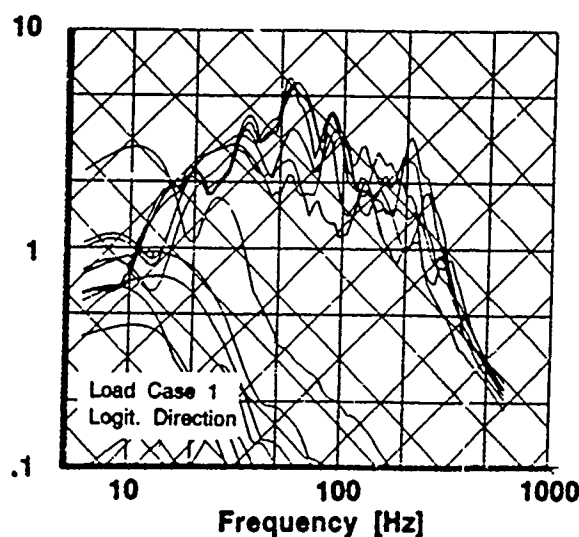
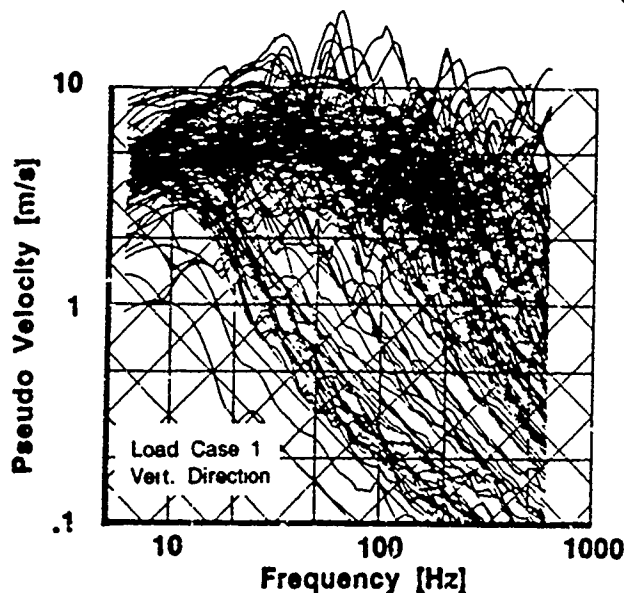


Fig. 18 Assembly of SRS from load case 1 (vertical and longit.)

The total longitudinal momentum shown in Fig. 17 is for both load cases in good correspondence with the vertical total momentum and the total kinetic energy as well. In case 1 the steep incident increase of the total longitudinal momentum caused by the shock wave impact is followed by a distinct oscillation due to global bending. The absolute values of the transient of case 2 are, as expected beforehand, by a factor of two higher than those of case 1. The path of the curve however gives evidence that also in case 2 a global bending oscillation of lower amplitude is superimposed.

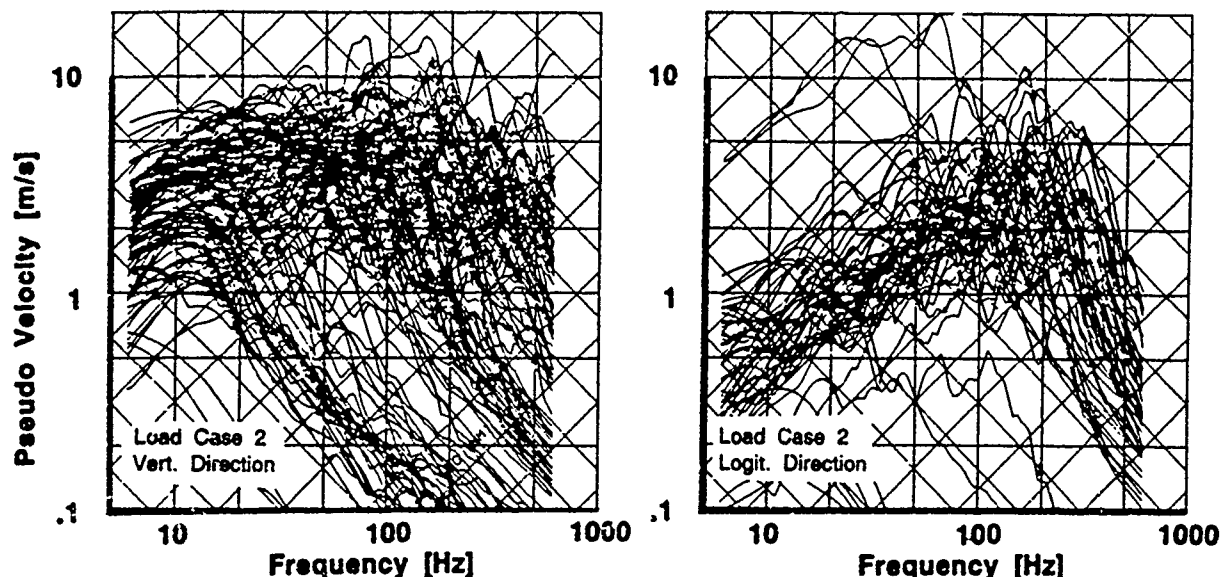


Fig. 19 Assembly of SRS for load case 2 (vertical and longit.)

From all this global information it can be derived, that in both load cases at least after about 50 ms after the first impact of the shock wave on the ship hull the main loading process is finished and the vibrations are decaying.

Maximum displacements of about 40 cm are occurring in load case 1 all over the vessel and are dominated by the rigid-body contribution. In case 2 at stern about 50 cm maximum displacement can be extrapolated. Due to the heavy rotation only 25 cm are reached in the midship area, so that for the largest part of the ship the maximum global velocities and displacements are rather low and not dangerous.

Finally the differences of shock response shall be valued by assemblies of SRS shown in Fig. 18 and 19. In these assemblies for both load cases the vertical SRS contain two types of curves. One type shows the typical low pass behaviour and is mostly generated from acceleration transients from nodal points situated on elastically mounted equipment and in the center of decks respectively. The second type is characterized by high shock levels over the whole frequency range and results mostly from nodes on the bottom of the vessel or from bulkheads. The vertical shock niveau of load case 1 is higher than that of load case 2 and a lower scattering of the upper family of curves can be recognized. The relative displacements at low frequencies of load case 1 with a mean value of 100 mm over the whole vessel are also clearly above those of load case 2. The strong variation of the SRS of load case 2 in

terms of relative displacements as well as pseudo velocities results from the loading condition already discussed.

The longitudinal SRS of both cases are quite different, too. Apart from some low pass type SRS the longitudinal shock response peak levels are reached at different frequencies, in case 1 at 50 Hz and in case 2 at 250 Hz. This can be traced back to the type of stressing of the structure, namely by bending in load case 1 and by normal forces excited directly by the shock wave in the very stiff girders and bottom region in load case 2. Consequently higher maximum acceleration values but lower maximum relative displacements are evident in load case 2 in comparison with load case 1.

CONCLUSIONS

The design of structure and equipment of the investigated vessel is strong enough to endure the simulated load cases without severe damage. This is a result of the applied procedure of simulating the response behaviour of a vessel in an early state of the development like the concept phase and checking the differences by investigating the final construction again.

Generally the shock design values for equipment for instance can be determined by this method under consideration of individual properties of the vessel such as stiffness, mass distribution and hull shape and can be optimized for the design goal. Furthermore a more accurate differentiation concerning type of equipment and location in the ship can be worked out even under consideration of a certain critical explosion geometry.

The presented method is fast and cheap in comparison to experimental programs and allows the variation of interesting parameters. The results of such numerical simulations can be used like measured data for further investigations of substructures or equipment for instance by the program FEDMAS [8] as realistic excitation functions. These single simulations can easily be performed over a large time range in order to investigate the long term behaviour of low frequency tuned systems.

REFERENCES

1. J. Massmann, et al., "The Program Family DYSMAS", IABG-Report B-TF-V197/2, Dec. 1986
2. W. Pavel, et al., "Experimental and Numerical Investigations of the Failure Behaviour of Glass Targets Under Impact Loading by Rigid Projectiles", Proc. of 10th Int. Symp. on Ballistics, San Diego CA., Oct. 1987
3. W. Jarzab, et al., "Numerical Simulation and Experimental Validation in Crashworthiness Applications", Structural Design and Crashworthiness of Automobiles, ed. by T.K.S. Murthy and C.A. Brebbia, Springer Verlag, Berlin-Heidelberg-New York, 1987
4. W. Renn, et al., "Numerical Simulation of Fuel Spillage Following an Aircraft Impact onto a Nuclear Power Plant", Proc. of 8th Int. Conf. on Struct. Mech. in Reactor Techn., Brussels, Aug. 1985
5. W. Bergerhoff, et al., "The Program DYSMAS/ELC and its Application on Underwater Shock Loading of Vessels", Proc. of 1st Int. Symp. on Maritime Simulation, Munich, June 1985, ed. by M.R. Heller, Springer-Verlag, Berlin-Heidelberg-New York, 1985

6. W. Pfrang, et al., "Die Numerische Simulation einer verdämmten Bodendetonation", Proc. 3rd Int. Symp. on Interaction of Non-Nuclear Munitions With Structures, Mannheim, West Germany, Mar. 1987
7. W. Pfrang, "Shock Loading of a Vessel by an Underwater Explosion - a Numerical Simulation Compared With a Full Scale Test", Presentation (Present only -mode), 57th Shock & Vibration Symposium, New Orleans, Oct. 1986
8. W. Mohr, "FEDMAS Users Manual (Version 3.0)", IABG, Munich, 1988

AN ANALYSIS OF NEWMARK BETA INTEGRATION FOR STRUCTURAL DYNAMICS

R. L. Bort

Naval Research Laboratory, Washington, D.C. 20375-5000

An elementary analysis of the formulas for numerical integration proposed by Newmark shows that the formulas calculate exact samples from the responses of oscillators that have frequencies and dampings different from the intended values. The formulas can provide absolute stability by reducing all frequencies to fall below the Nyquist limit, but they also decrease damping. Responses of high-frequency heavily-damped structures can be greatly overestimated by the Newmark-Beta formulas.

MATHEMATICAL PRELIMINARIES

The difference equation

$$e^{\rho\omega h} x(t+h) - 2 \cos(\omega\sqrt{1-\rho^2} h) x(t) + e^{-\rho\omega h} x(t-h) = 0 \quad (1)$$

is satisfied by the function

$$x = e^{\rho\omega t} [A \cos(\omega\sqrt{1-\rho^2} t) + B \sin(\omega\sqrt{1-\rho^2} t)] \quad (2)$$

that represents the motion of an oscillator with angular frequency ω and damping ρ relative to critical. Direct substitution shows that Equation 2 is the solution to Equation 1 for all times t and for any values of A , B and the time step h .

Equation 2 is also the solution to the differential equation

$$\ddot{x} + 2\rho\omega \dot{x} + \omega^2 x = 0 \quad (3)$$

for the oscillator. (Again this can be verified by direct substitution.) If Equation 1 is written in the form

$$x(t+h) = 2C x(t) - D x(t-h), \quad (4)$$

with

$$C = e^{\rho\omega h} \cos(\omega\sqrt{1-\rho^2} h) \quad (5)$$

and

$$D = e^{-2\rho\omega h} \quad (6)$$

Equation 4 can be used as a step-ahead equation to generate successive samples from the motion of the oscillator.

BACKGROUND

Equation 4, in different notations and with different derivations, appears frequently as a recommended method for numerical integration of second-order linear differential equations. Reports by O'Hara¹ (1962) and Lane² (1964) are early examples. The use of difference equations that correspond exactly to differential equations, however, goes back to the treatise written by George Boole³ in 1872.

There are two great advantages to the use of Equation 4 for generating numerical solutions to the differential equation for the damped oscillator. First, the equation runs very rapidly on a digital computer. The constants $2C$ and D can be calculated once at the beginning, and each step ahead thereafter requires only two multiplications and one subtraction. Second, the samples as calculated are exact within roundoff error *for any value of the time step h* .

If a proposed method of integration can be placed in the form of Equation 4, the method can be evaluated immediately by comparing its coefficients with those of the exact step-ahead formula.

NEWMARK BETA METHOD

A method of integration proposed by Newmark⁴ is given by the equations

$$\dot{x}(t+h) = \dot{x}(t) + (1 - \gamma) \ddot{x}(t) h + \gamma \ddot{x}(t+h) h \quad (7)$$

for stepping the velocity ahead, and by

$$x(t+h) = x(t) + \dot{x}(t) h + \left(\frac{1}{2} - \beta\right) \ddot{x}(t) h^2 + \beta \ddot{x}(t+h) h^2 \quad (8)$$

for the displacement. The β and the γ are parameters by which the characteristics of the method can be varied. The method is a popular one that is included as an option in many computer programs for dynamic structural analysis.

¹G. J. O'Hara, "A Numerical Procedure for Shock and Fourier Analysis," Washington, DC. Naval Research Laboratory NRL Report 5772 (June 5, 1962).

²D. W. Lane, "Digital Shock Spectrum Analysis by Recursive Filtering," Shock, Vibration and Associated Environments, Bulletin 33 Part II (February 1964) pages 173 to 181.

³G. Boole, "A Treatise on the Calculus of Finite Differences," New York. Dover Publications Inc., Reprint of the Second Edition (1960).

⁴Nathan M. Newmark, "A Method of Computation for Structural Dynamics," Transactions of the American Society of Civil Engineers Volume 127 Part I (1962) pages 1406 to 1435.

ANALYSIS

The Newmark Beta method can be applied to the differential equation for the damped oscillator and reduced to the form

$$x(t+h) = 2Ex(t) - Fx(t-h), \quad (9)$$

with

$$E = \frac{1 - \frac{1}{2} \left(\frac{1}{2} + \gamma - 2\beta \right) \omega^2 h^2 - (1 - 2\gamma) \rho \omega h}{1 + \beta \omega^2 h^2 + 2\gamma \rho \omega h} \quad (10)$$

and

$$F = \frac{1 + \left(\frac{1}{2} - \gamma + \beta \right) \omega^2 h^2 - 2(1 - \gamma) \rho \omega h}{1 + \beta \omega^2 h^2 + 2\gamma \rho \omega h}. \quad (11)$$

The algebra for this reduction is outlined in Appendix A.

A comparison with Equation 4 allows the integration method to be evaluated by setting

$$e^{\rho' \omega' h} \cos(\omega' \sqrt{1 - \rho'^2} h) = E \quad (12)$$

and

$$e^{2\rho' \omega' h} = F, \quad (13)$$

where the ω' and the ρ' represent the frequency and damping of the oscillator whose response is actually being calculated, according to Equation 4, when the integration method is applied to an oscillator with frequency ω and damping ρ .

Equations 12 and 13 can be combined to show that the Newmark Beta integration generates samples from the motion of an oscillator whose damping is given by

$$\rho' \omega' h = -\frac{1}{2} \log(F) \quad (14)$$

in natural units of decay per time step, and whose damped frequency is

$$\omega' \sqrt{1 - \rho'^2} h = \arccos\left(\frac{E}{\sqrt{F}}\right) \quad (15)$$

in radians or degrees per step.

ACCURACY AND STABILITY FOR THE UNDAMPED OSCILLATOR

The case of an undamped oscillator is of special interest. There the integration method calculates the response of an oscillator whose decay rate is

$$\rho' \omega' h = -\frac{1}{2} \log \left(\frac{1 + (\frac{1}{2} - \gamma + \beta) \omega^2 h^2}{1 + \beta \omega^2 h^2} \right) \quad (16)$$

and whose damped frequency is given by

$$\omega' \sqrt{1 - \rho'^2} h = \arccos \left(\frac{1 - \frac{1}{2} (\frac{1}{2} + \gamma - 2\beta) \omega^2 h^2}{\sqrt{1 + \beta \omega^2 h^2} \sqrt{1 + (\frac{1}{2} - \gamma + \beta) \omega^2 h^2}} \right). \quad (17)$$

Equation 16 shows that the calculation will represent an undamped oscillator only if γ is set equal to one-half. Then Equation 17 reduces to

$$\omega' h = \arccos \left(\frac{1 - (\frac{1}{2} - \beta) \omega^2 h^2}{1 + \beta \omega^2 h^2} \right). \quad (18)$$

A chart of Equation 18 is shown in Figure 1.

Figure 1 shows that the frequency calculated for the undamped oscillator approaches the true frequency when the frequency is low. At higher frequencies the calculation can diverge for some values of β when Equation 18 produces a cosine with a value less than -1; this can be seen in Figure 1 as the curves for $\beta = 0, 0.1$, and 0.2 run off the top of the graph at a frequency of 180 degrees per time step. With larger values of β all possible frequencies of the oscillator from zero to infinity are mapped into the range from zero to $\arccos(1 - \frac{1}{2\beta})$. A value of $\beta = \frac{1}{4}$ produces absolute stability for an undamped oscillator by converting its frequencies into the reduced range from zero to 180 degrees per time step.

EFFECT OF DAMPING ON FREQUENCY

When damping is included, the calculation remains stable but the calculated damped frequencies of the oscillator increase with increase in the damping, as shown in Figure 2.

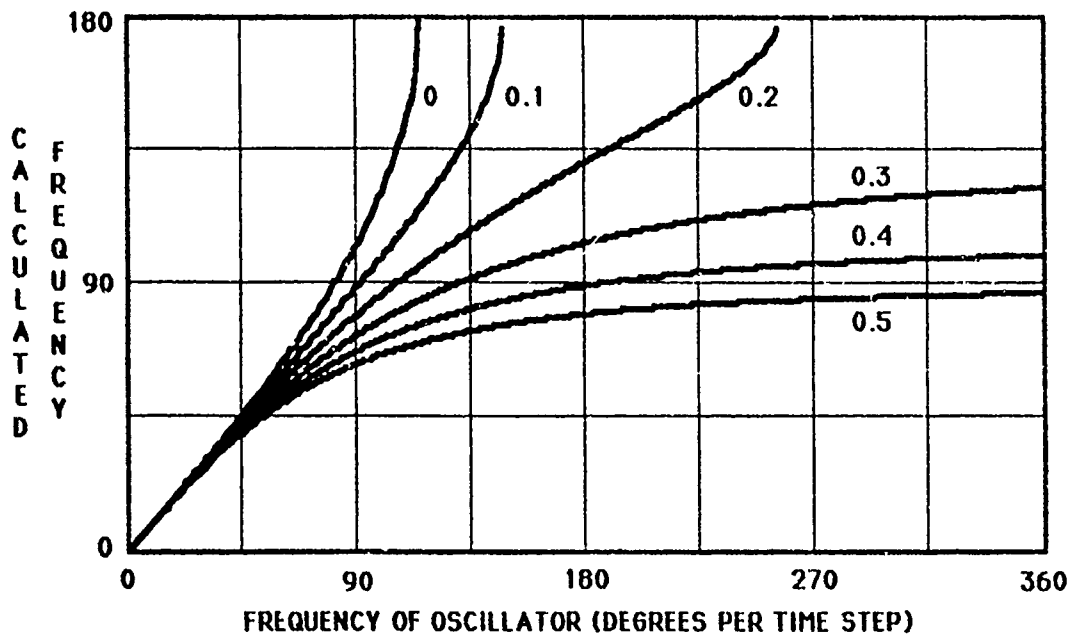


Figure 1. Effect of beta on frequency. Curves are labeled with values of beta. The parameter gamma is set to one-half and damping is zero.

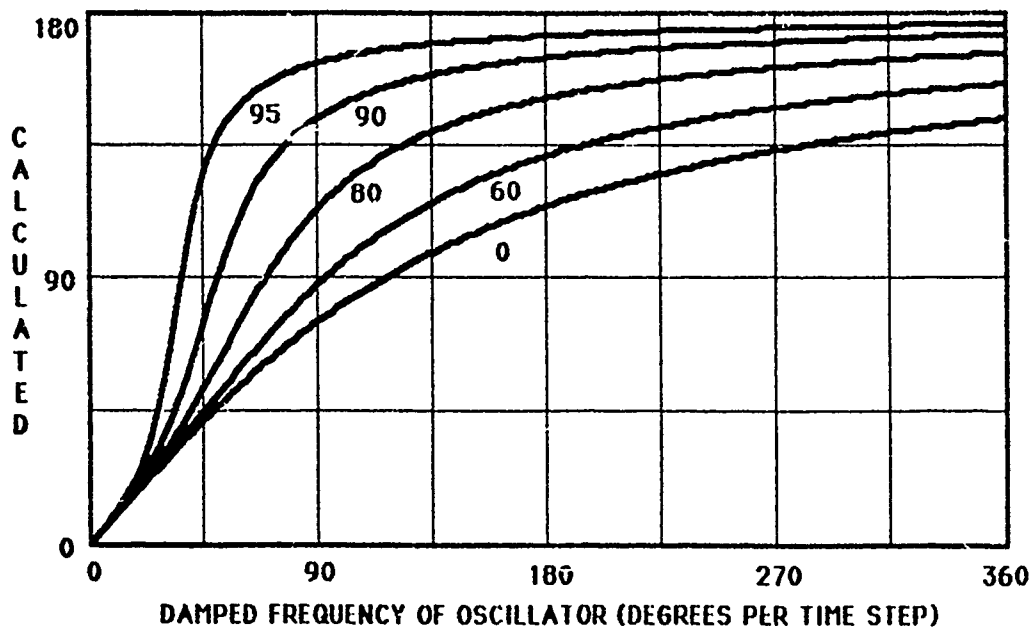


Figure 2. Effect of damping on frequency. Curves are labeled with values of damping in percent of critical. Gamma is one-half and beta is one-quarter.

Choosing $\beta = \frac{1}{3}$ instead of $\frac{1}{4}$ causes greater compression of frequencies (to the range from zero to 120 degrees per time step) and decreases the effect of damping on the calculated damped frequency, as shown in Figure 3.

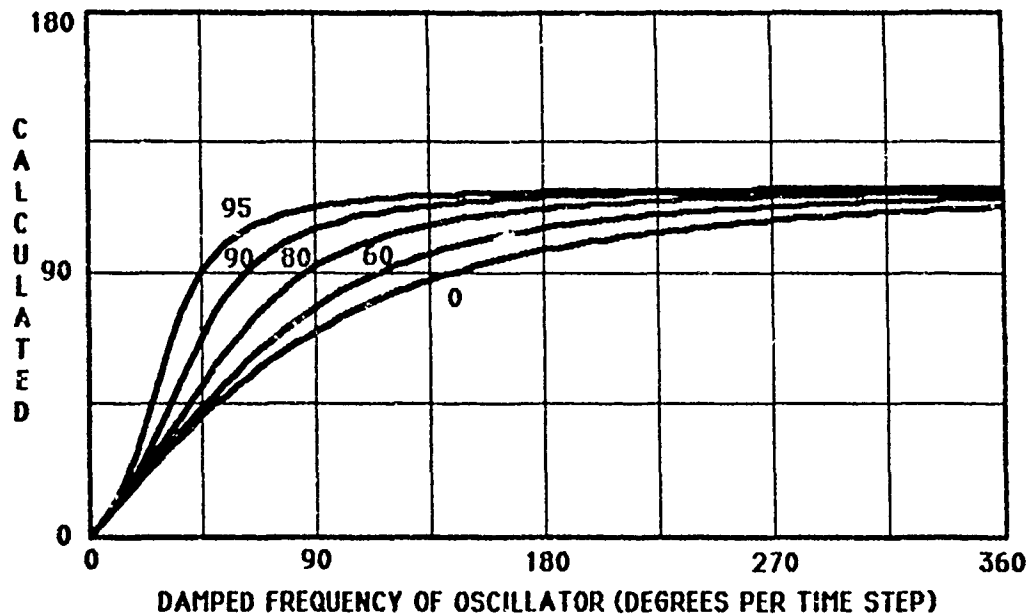


Figure 3. Reduced effect of damping on frequency when beta is one-third. Curves are labeled with values of damping in percent of critical. Gamma is one-half.

EFFECT ON DAMPING

In addition to changing the frequencies, the Newmark-Beta formulas also change the decay rates. Figure 4 shows that at low frequencies the decay rate may be either decreased or increased, while at higher frequencies there is a great decrease in the rate of decay.

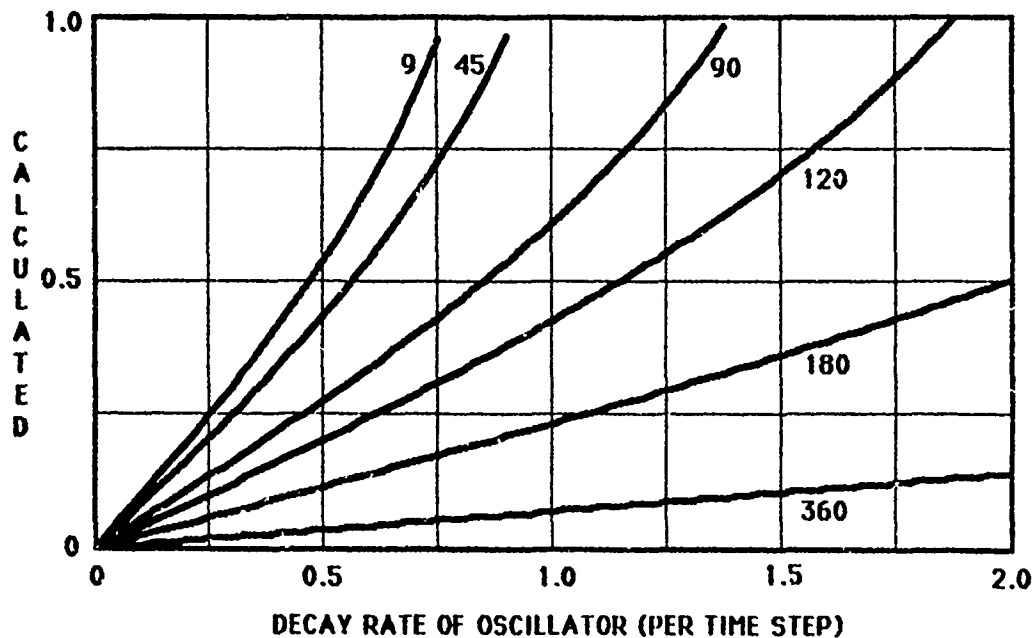


Figure 4. Effect of frequency on decay rate. Curves are labeled by frequency in degrees per time step. Gamma is one-half and beta is one-third.

Newmark-Beta integration decreases damping relative to critical, as shown in Figure 5.

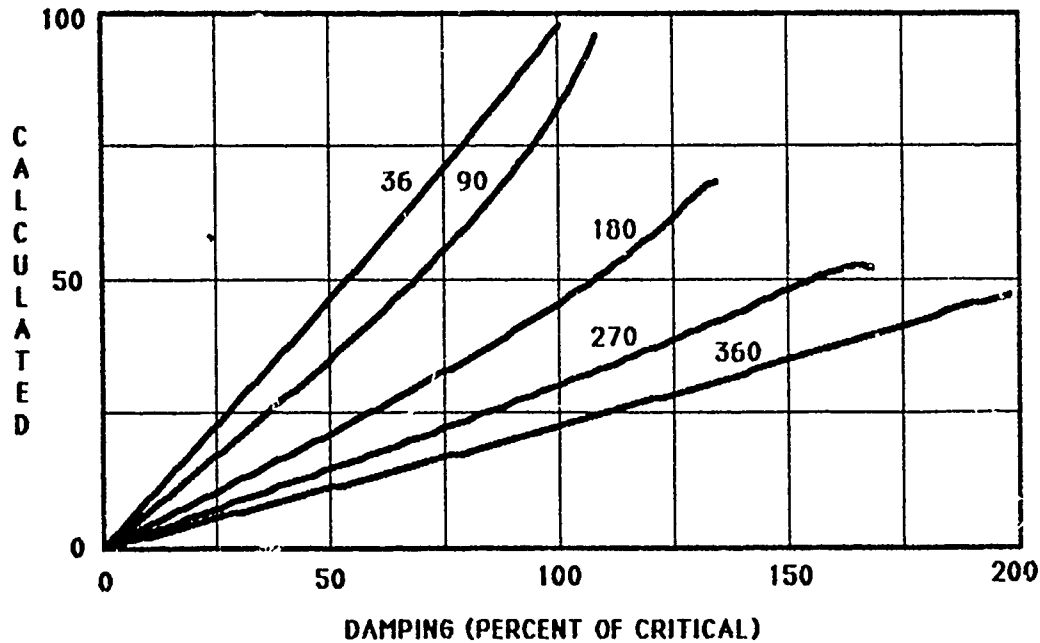


Figure 5. Effect of frequency on damping. Curves are labeled with frequency in degrees per time step. Gamma is one-half and beta is one-third.

EXAMPLE

The displacement calculated for a critically-damped oscillator using Newmark Beta with a time step of 1 millisecond is shown in Figure 6.

The Newmark-Beta formulas lower the frequency of the 1000-Hertz oscillator to 331 Hertz (119 degrees per time step) and decrease its 100-percent damping to 23 percent of critical. The smooth curve drawn through the samples in Figure 6 is the response for 331 Hertz with 23 percent damping. As shown by the graph, the calculated response is stable but produces a fictitious peak displacement more than three times the correct value.

APPENDIX A - DERIVATION OF THE STEP-AHEAD FORMULA

Write the Newmark-Beta formulas to show changes over the time intervals from $t-h$ to t and from t to $t+h$:

$$\dot{x}(t+h) - \dot{x}(t) = \gamma h \ddot{x}(t+h) + (1 - \gamma) h \ddot{x}(t), \quad (A-1)$$

$$\dot{x}(t) - \dot{x}(t-h) = \gamma h \ddot{x}(t) + (1 - \gamma) h \ddot{x}(t-h), \quad (A-2)$$

$$x(t+h) - x(t) = h \dot{x}(t) + \beta h^2 \ddot{x}(t+h) + \left(\frac{1}{2} - \beta\right) h^2 \ddot{x}(t), \quad (A-3)$$

$$x(t) - x(t-h) = h \dot{x}(t-h) + \beta h^2 \ddot{x}(t) + \left(\frac{1}{2} - \beta\right) h^2 \ddot{x}(t-h). \quad (A-4)$$

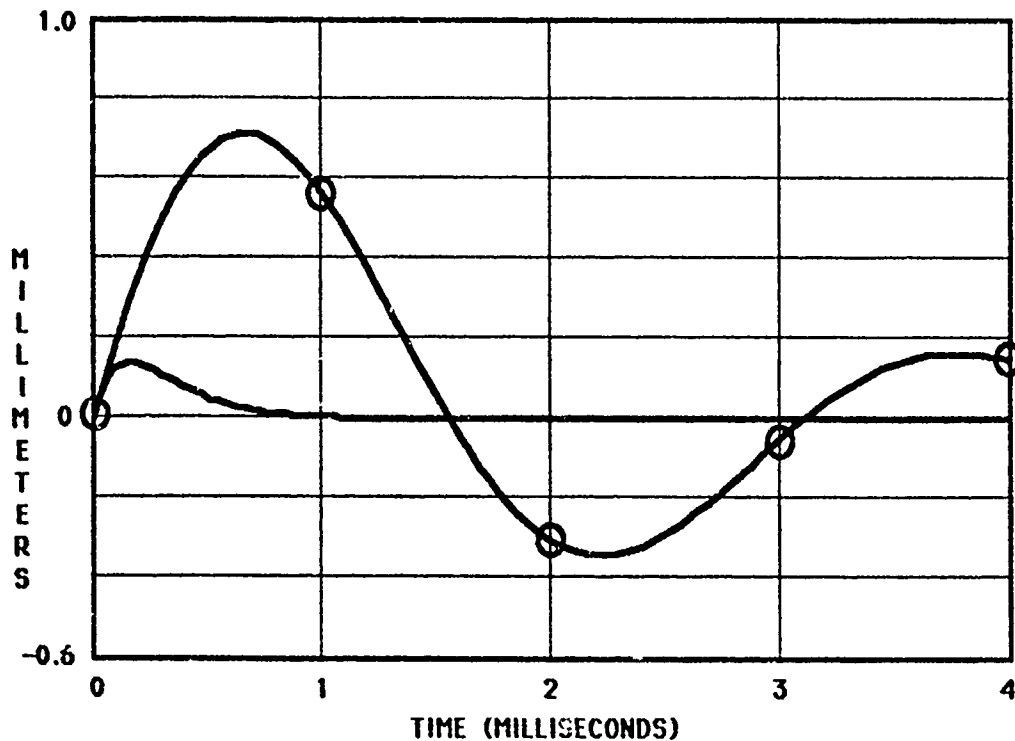


Figure 6. Calculated response of a high-frequency, heavily-damped oscillator. The circles show samples calculated using gamma one-half and beta one-third for an oscillator with frequency 1000 Hertz and damping 100 percent of critical, starting from an initial velocity of 4 meters per second. The smaller curve is actual response of the oscillator.

Subtract Equation A-4 from Equation A-3 and substitute for the change in velocity from Equation A-2 to obtain

$$x(t+h) - 2x(t) + x(t-h) = \beta h^2 \ddot{x}(t+h) + \left(\frac{1}{2} + \gamma - 2\beta\right) h^2 \ddot{x}(t) + \left(\frac{1}{2} - \gamma + \beta\right) h^2 \ddot{x}(t-h). \quad (A-5)$$

Add γ times Equation A-3 to $1-\gamma$ times Equation A-4 and substitute for the accelerations from Equations A-1 and A-2 to obtain

$$\gamma x(t+h) + (1-2\gamma)x(t) - (1-\gamma)x(t-h) = \beta h \dot{x}(t+h) + \left(\frac{1}{2} + \gamma - 2\beta\right) h \dot{x}(t) + \left(\frac{1}{2} - \gamma + \beta\right) h \dot{x}(t-h). \quad (A-6)$$

Fit the formulas to the differential equation for a damped oscillator,

$$\ddot{x} + 2p\omega \dot{x} + \omega^2 x = 0, \quad (A-7)$$

by using the coefficients on the right side of Equation A-5 to combine the equations for the oscillator evaluated at times $t+h$, t , and $t-h$. The accelerations can then be eliminated by Equation A-5 and the velocities by Equation A-6, leaving

$$\begin{aligned} & \left[(1 + \beta\omega^2 h^2 + 2\gamma p\omega h) x(t+h) + \left[-2 + \left(\frac{1}{2} + \gamma - 2\beta\right)\omega^2 h^2 + 2(1-2\gamma)p\omega h \right] x(t) \right. \\ & \left. + \left[1 + \left(\frac{1}{2} - \gamma + \beta\right)\omega^2 h^2 - 2(1-\gamma)p\omega h \right] x(t-h) \right] = 0. \end{aligned} \quad (A-8)$$

Divide by the coefficient of $x(t+h)$ to obtain the step-ahead formula shown in Equation 9.

RESPONSE OF NONLINEAR CONTINUOUS SYSTEMS SUBJECTED TO TRANSIENT LOADS: AN ANALYTICAL APPROACH

S. C. Sinha
Department of Mechanical Engineering
Auburn University
Auburn, AL 36849

The general problem of nonlinear continuous systems subjected to transient loads is formulated. Upon application of normal mode method or finite-element technique, the problem is reduced to a set of second order ordinary nonlinear differential equations subjected to pulse excitations. These system equations are solved through an application of a modified version of the well-known Krylov-Bogoliubov method. The approach is illustrated through an example of a beam subjected to transient loading conditions.

INTRODUCTION

In numerous situations, structures are subjected to transient loads. These loadings may result from a variety of sources, such as, a conventional or a nuclear blast, sudden change of pressure due to a wind gust, transient movements of supports or other unexpected excitations of aperiodic nature. Inherently all structures are nonlinear and can be modeled as continuous structural elements, e.g., cables, beams, plates, shells, etc., or as a combination of these elements. There are several books and thousands of papers which deal with the linear and nonlinear dynamic analysis of such systems. A recent review of nonlinear analysis of beams has been presented by Sathyamoorthy [1] while reviews of linear and nonlinear plate vibrations have been provided by Leissa [2,3] and Sathyamoorthy [4]. In most studies the nonlinear problems have been restricted to the situation where the forcing function is sinusoidal in nature.

In general, a continuous problem can be reduced to a set of ordinary differential equations through an application of normal mode method, finite-element technique, Galerkin's approach or other similar procedures. For transient problems, most investigators have applied a finite-difference scheme of one form or the other to these nonlinear equations in order to obtain a numerical solution. Such solutions are certainly important, however, they do not provide an understanding of the general behavior of the system as a function of its various parameters. On the other hand an analytical solution, whether approximate or exact, renders valuable information about the general behavior pattern of such systems. Except for some very special cases, exact solutions are not available and one has to resort to approximate analysis of these systems. Bapat and Srinivasan [5-7], Sinha and Srinivasan [8], Anderson [9], Reed [10] and Sinha and Chou [11] have presented approximate analyses of nonlinear vibrational systems subjected to step excitations.

The response due to an arbitrary pulse excitation has been studied by Ariaratnam [12], Bauer [13] and Olberding and Sinha [14], among others. These analyses have been limited to problems of single degree of freedom only. Such problems with multiple degrees of freedom have been discussed by Bauer [15], Rangacharyulu et al. [16] and Sinha and Jagannathan [17]. All of these studies utilize either a perturbation method or the well-known method of Krylov-Bogoliubov and Mitropolsky.

In this study it is shown that the general problem of nonlinear continuous systems subjected to transient loading can be reduced to a set of nonlinear differential equations and an approximate analytical solution can be obtained through a modified version of Krylov-Bogoliubov technique.

EQUATION OF MOTION AND GENERAL ANALYSIS

The equation of motion for a continuous system subjected to a transient load may be written as

$$m(\underline{x}) \frac{\partial^2 r}{\partial t^2} + L_{\underline{x}}(r) + N_{\underline{x}}(r, \partial r / \partial t) = F(\underline{x}, t) \quad (1)$$

where $r(\underline{x}, t)$ is the transverse deflection of the structural element, $m(\underline{x})$ is the mass per unit volume, $L_{\underline{x}}$ is a linear spatial differential operator, $N_{\underline{x}}$ is a nonlinear operator and $F(\underline{x}, t)$ is the transient load on the system.

If 'normal mode' method is used for the analysis, then the deflection $r(\underline{x}, t)$ is expressed in the form [18]

$$r(\underline{x}, t) = \sum_{j=1}^N \phi_j(\underline{x}) T_j(t) \quad , \quad (2)$$

where $\phi_j(\underline{x})$ are the normal modes of the linear homogeneous system

$$m(\underline{x}) \frac{\partial^2 r}{\partial t^2} + L_{\underline{x}}(r) = 0 \quad , \quad (3)$$

subject to some appropriate boundary conditions.

Substituting equation (2) in equation (1) one obtains

$$\sum_{j=1}^N m(\underline{x}) \phi_j T_j'' + L_{\underline{x}}(\phi_j) T_j + N_{\underline{x}}(\phi_j T_j, \phi_j T_j') = F(\underline{x}, t) \quad , \quad (4)$$

where the prime denotes $d(\)/dt$.

Multiplying equation (4) by ϕ_i and integrating over the domain V yields

$$\int_V \left\{ \sum_{j=1}^N m(\underline{x}) \phi_i \phi_j T_j'' + \phi_i L_{\underline{x}}(\phi_j) T_j + \phi_i N_{\underline{x}}(\phi_j T_j, \phi_j T_j') \right\} d\underline{x} \\ = \int_V \phi_i F(\underline{x}, t) d\underline{x} \quad , \quad i = 1, 2, \dots, N. \quad (5)$$

Utilizing the orthogonality property of ϕ_i , equation (5) can be expressed as

$$m_i T_i'' + k_i T_i + \epsilon f_i(T_j, T_j') = U_i(t) \quad , \quad i, j = 1, 2, \dots, N. \quad (6)$$

where

$$m_i = \int_V m(\underline{x}) \phi_i^2 d\underline{x} \quad , \quad k_i = \int_V \phi_i L(\phi_i) d\underline{x} \quad , \quad (7)$$

$$f_i(T_j, T_j') = \int_V \phi_i N_{\underline{x}}(\phi_j T_j, \phi_j T_j') d\underline{x} \quad , \quad (8)$$

$$U_i(t) = \int_V \phi_i F(\underline{x}, t) d\underline{x} \quad , \quad (9)$$

and ϵ is a suitably defined small nonlinearity parameter.

It is observed that the linear terms in equation (6) are decoupled because ϕ_i and ϕ_j are orthogonal. However, if a finite-element discretization in the space dimension is used then it can be shown that equation (1) reduces to the form [19]

$$m_{ij} T_j'' + k_{ij} T_j + \epsilon f_i(T_j, T_j') = U_i(t) \quad , \quad i, j = 1, 2, \dots, N. \quad (10)$$

The repeated index imply sum and it is noticed that the linear terms in equation (10) are no longer decoupled. Similar sets of equations are obtained if one uses Galerkin's method where the 'trial functions' are not orthogonal.

Therefore, in general, the solution of the original problem can be reduced to the solution of equation (10). It is to be noted that although the nonlinearities $f_i(\cdot)$ have been assumed small and expressed in terms of a small parameter ϵ , the forcing terms $U_i(t)$ are not, and they are transient in nature. Therefore a direct application of any of the techniques of nonlinear analysis (such as perturbation, averaging or other) is not possible. To alleviate this problem, the following transformation of the dependent variable is employed.

$$T_j(t) = y_j(t) + p_j(t) \quad . \quad (11)$$

Thus equation (10) transforms to

$$m_{ij}(y_i'' + p_j'') + k_{ij}(y_j + p_j) + \epsilon f_i(y_i + p_j, y_j' + p_j') = U_i(t) . \quad (12)$$

Choosing $p_j(t)$ such that

$$m_{ij}p_j'' + k_{ij}p_j = U_i(t) , \quad (13)$$

yields

$$m_{ij}y_j'' + k_{ij}y_j + \epsilon f_i(y_i + p_j, y_j' + p_j') = 0 . \quad (14)$$

Therefore equation (10) can be solved by finding solutions of the linear problem given by equation (13) and the nonlinear problem represented by equation (14). $p_j(t)$ can be obtained from equation (13) through an application of the superposition integral (or any other convenient method such as Laplace transform) technique and substituted into equation (14) to yield

$$m_{ij}y_j'' + K_{ij}y_j + \epsilon f_i(y_j, y_j', t) = 0 . \quad (15)$$

Without any loss of generality, initial conditions are assumed as

$$r = \frac{\partial r}{\partial t} = 0 \quad \text{at } t = 0 , \quad (16)$$

which, in view of equations (2) and (11), implies

$$y_j(t) = -p_j(t) , \quad y_j'(t) = -p_j'(t) \quad \text{at } t = 0 . \quad (17)$$

In the following, an approximate analytical solution of equation (15) is obtained through an application of the Krylov-Bogoliubov method. The analysis follows the developments suggested by Butenin [20] and Sinha and Jagannathan [17].

Application of the Krylov-Bogoliubov Method

First, consider the unperturbed equations by setting $\epsilon = 0$ in equation (15), i.e.,

$$m_{ij}y_j'' + k_{ij}y_j = 0 ; \quad i, j = 1, 2, \dots, N. \quad (18)$$

This has a solution of the form

$$y_j = \sum_{k=1}^N \alpha_{jk} a_k \cos \psi_k \quad \text{and} \quad \frac{dy_j}{dt} = - \sum_{k=1}^N \alpha_{jk} \omega_k a_k \sin \psi_k \quad i, j = 1, 2, \dots, N \quad (19a, b)$$

where

$$\psi_k = \omega_k t + \theta_k \quad (20)$$

The a_k , α_{jk} and θ_k are the amplitudes, amplitude ratios and phase respectively. The natural frequencies ω_k are obtained from the frequency equation

$$\det[k_{ij} - m_{ij}\omega^2] = 0 \quad , \quad i, j = 1, 2, \dots, N \quad (21)$$

and the amplitude ratios α_{jk} are determined for every eigenvalue ω_k from

$$[k_{ij} - m_{ij}\omega_k^2] \alpha_{jk} = 0 \quad . \quad i, j = 1, 2, \dots, N \quad (22)$$

Since α_{jk} represent the amplitude ratios, α_{11} , α_{12} , α_{1N} can be set to unity without any loss of generality. In order to include the effect of the nonlinearities, a solution of equation (15) can be assumed in the same form as equation (19a), however a_k and θ_k are assumed to be functions of time. Then by differentiating equation (19a), one obtains

$$\frac{dy_j}{dt} = \sum_{k=1}^N (\alpha_{jk} \cos \psi_k) \frac{da_k}{dt} - \sum_{k=1}^N (\alpha_{jk} a_k \sin \psi_k) \left(\omega_k + \frac{d\theta_k}{dt} \right). \quad (23)$$

By requiring the derivatives of y_j to be of the same form as equation (19b), the following condition is obtained

$$\sum_{k=1}^N (\alpha_{jk} \cos \psi_k) \frac{da_k}{dt} - \sum_{k=1}^N (\alpha_{jk} a_k \sin \psi_k) \frac{d\theta_k}{dt} = 0. \quad (24)$$

Substituting for dy_j/dt in equation (15) and utilizing the results of equations (23) and (24) yields

$$- \sum_{k=1}^N (m_{ij} \alpha_{jk} \omega_k \sin \psi_k) \frac{da_k}{dt} - \sum_{k=1}^N (m_{ij} \alpha_{jk} \omega_k \cos \psi_k) \frac{d\theta_k}{dt} = - \varepsilon f_i(y_j, y_j', t) \quad (25)$$

Equations (24) and (25) represent a set of $2N$ simultaneous equations in da_k/dt and $d\theta_k/dt$ and may be rearranged in matrix form

$$\begin{bmatrix} P_1 & P_2 \\ \vdots & \vdots \\ P_3 & P_4 \end{bmatrix} \begin{Bmatrix} \frac{da}{dt} \\ \frac{d\theta}{dt} \end{Bmatrix} = \begin{Bmatrix} 0 \\ \vdots \\ Q \end{Bmatrix} \quad (26)$$

where

$$\begin{aligned}
\frac{da}{dt} &= \begin{Bmatrix} \frac{da_1}{dt} \\ \vdots \\ \frac{da_N}{dt} \end{Bmatrix} \quad \text{and} \quad \frac{d\theta}{dt} = \begin{Bmatrix} \frac{d\theta_1}{dt} \\ \vdots \\ \frac{d\theta_N}{dt} \end{Bmatrix} \\
P_1 &= \begin{bmatrix} \alpha_{11} \cos \psi_1 & \dots & \alpha_{1N} \cos \psi_N \\ \vdots & & \vdots \\ \alpha_{N1} \cos \psi_1 & \dots & \alpha_{NN} \cos \psi_N \end{bmatrix} \\
P_2 &= \begin{bmatrix} \alpha_{11} a_1 \sin \psi_1 & \dots & \alpha_{1N} a_N \sin \psi_N \\ \vdots & & \vdots \\ \alpha_{N1} a_1 \sin \psi_1 & \dots & \alpha_{NN} a_N \sin \psi_N \end{bmatrix} \\
P_3 &= \begin{bmatrix} -\sum_{j=1}^N m_{1j} \alpha_{j1} \omega_1 \sin \psi_1 & \dots & -\sum_{j=1}^N m_{1j} \alpha_{jN} \omega_N \sin \psi_N \\ \vdots & & \vdots \\ -\sum_{j=1}^N m_{Nj} \alpha_{j1} \omega_1 \sin \psi_1 & \dots & -\sum_{j=1}^N m_{Nj} \alpha_{jN} \omega_N \sin \psi_N \end{bmatrix} \\
P_4 &= \begin{bmatrix} -\sum_{j=1}^N m_{1j} \alpha_{j1} a_1 \omega_1 \cos \psi_1 & \dots & -\sum_{j=1}^N m_{1j} \alpha_{jN} a_N \omega_N \cos \psi_N \\ \vdots & & \vdots \\ -\sum_{j=1}^N m_{Nj} \alpha_{j1} a_1 \omega_1 \cos \psi_1 & \dots & -\sum_{j=1}^N m_{Nj} \alpha_{jN} a_N \omega_N \cos \psi_N \end{bmatrix} \\
Q &= \begin{Bmatrix} -\varepsilon f_1(y_1, \dots, y_N, y'_1, \dots, y'_N, t) \\ \vdots \\ -\varepsilon f_N(y_1, \dots, y_N, y'_1, \dots, y'_N, t) \end{Bmatrix}
\end{aligned}$$

Equation (26) yields $2N$ quantities, da_k/dt and $d\theta_k/dt$ representing rates of change in amplitude and phase respectively. For a system of multiple degrees of freedom, it can be quite cumbersome to obtain expressions for the amplitude and phase variations. However, they can be expressed in functional forms as

$$\frac{da_k}{dt} = F_k(a_1, a_2, \dots, a_N, \psi_1, \psi_2, \dots, \psi_N, t) \quad (27a)$$

$$\frac{d\theta_k}{dt} = G_k(a_1, a_2, \dots, a_N, \psi_1, \psi_2, \dots, \psi_N, t) \quad (27b)$$

From these, the approximate expressions can be determined by averaging the right hand side over a period $2\pi t$ yield

$$\frac{da_k}{dt} = \varepsilon F_k^*(a_1, a_2, \dots, a_N, t), \quad k = 1, 2, \dots, N \quad (28a)$$

$$\frac{d\theta_k}{dt} = \varepsilon G_k^*(a_1, a_2, \dots, a_N, t), \quad k = 1, 2, \dots, N \quad (28b)$$

where

$$F_k^* = \frac{1}{(2\pi)^N} \int_0^{2\pi} \int_0^{2\pi} \dots \int_0^{2\pi} F_k(\) d\psi_1 d\psi_2 \dots d\psi_N \quad (29a)$$

$$G_k^* = \frac{1}{(2\pi)^N} \int_0^{2\pi} \int_0^{2\pi} \dots \int_0^{2\pi} G_k(\) d\psi_1 d\psi_2 \dots d\psi_N \quad (29b)$$

Equation (28a) represents a set of N first order nonlinear differential equations in a_k and generally a closed form solution is not possible. Under certain circumstances, depending on the type of nonlinearity, simplification may occur. By use of a simple integration scheme, the amplitudes may be solved for and substituted into the phase equations, and the θ_k can then be determined from a single quadrature. By knowing the α_{jk} from equation (22) the total solution T_j is then found from equation (11).

One Term Approximation:

The analysis presented above can become complicated if the number of terms in approximation becomes large. In the 'normal mode' approach, one or two term approximation may be sufficient for the purpose of design.

For $i=j=1$, equation (13) and (14) take the forms

$$m_{11}p_1'' + k_{11}p_1 = U_1(t), \quad (30)$$

and

$$m_{11}y_1'' + k_{11}y_1 + \varepsilon f_1(y_1 + p_1(t), y_1' + p_1'(t)) = 0, \quad (31)$$

respectively. The solution of equation (30) is given as [18]

$$p_1(t) = \frac{1}{(k_{11}m_{11})^{1/2}} \int_0^t U_1(\tau) \sin \omega_1(t-\tau) d\tau, \quad (32)$$

where

$$\omega_1 = (k_{11}/m_{11})^{1/2}. \quad (33)$$

Following equation (19), the solution of equation (31) is assumed as

$$y_1 = a_1(t) \cos \psi_1(t), \quad \psi_1 = \omega_1 t + \theta_1 \quad (34)$$

Then from equation (28)

$$\frac{da_1}{dt} = \frac{\varepsilon F_1^*}{m_{11} \omega_1}, \quad \frac{d\theta_1}{dt} = \frac{\varepsilon G_1^*}{m_{11} a_1 \omega_1} \quad (35a, b)$$

where

$$F_1^* = \frac{1}{2\pi} \int_0^{2\pi} f_1(a_1, \psi_1, t) \sin \psi_1 d\psi_1, \quad (36a)$$

$$G_1^* = \frac{1}{2\pi} \int_0^{2\pi} f_1(a_1, \psi_1, t) \cos \psi_1 d\psi_1 \quad (36b)$$

Integration of equation (35a) yields the amplitude $a_1(t)$ and then from (35b) one has

$$\theta_1(t) = \frac{\varepsilon}{m_{11} \omega_1} \int_0^t \frac{G_1^*}{a_1(\tau)} d\tau + \theta_1(0). \quad (37)$$

$a_1(0)$ and $\theta_1(0)$ are determined from the initial conditions. From equation (17) one finds

$$a_1(0) \cos \psi_1(0) = -p_1(0); \quad -\omega_1 a_1(0) \sin \psi_1(0) = -p_1'(0). \quad (38a, b)$$

Solving simultaneously

$$a_1(0) = -\frac{p_1(0)}{\cos \psi_1(0)}; \quad \psi_1 = \arctan \left[-\frac{p_1'(0)}{\omega_1 p_1(0)} \right]. \quad (39)$$

Thus the one term approximate solution is given by equations (2), (11), (32), (37) and (39).

Two Term Approximation:

If a two term approximation is used in equation (2), then equation (10) can be explicitly written for $i=j=1,2$ as

$$m_{11}T_1'' + k_{11}T_1 + \epsilon f_1(T_1, T_2, T_1', T_2') = U_1(t) \quad (40)$$

$$m_{22}T_2'' + k_{22}T_2 + \epsilon f_2(T_1, T_2, T_1', T_2') = U_2(t) \quad (41)$$

Note that k_{12} , k_{21} , m_{12} , m_{21} are identically zero due to the orthogonal properties of ϕ_i and ϕ_j . Following the general analysis, equation (13) implies

$$m_{11}p_1'' + k_{11}p_1 = U_1(t) , \quad (42)$$

and

$$m_{22}p_2'' + k_{22}p_2 = U_2(t) . \quad (43)$$

The solutions are

$$p_1(t) = \frac{1}{(k_{11}m_{11})^{1/2}} \int_0^t U_1(\tau) \sin \omega_1(t-\tau) d\tau ; \quad \omega_1 = \left(\frac{k_{11}}{m_{11}} \right)^{1/2} , \quad (44)$$

$$p_2(t) = \frac{1}{(k_{22}m_{22})^{1/2}} \int_0^t U_2(\tau) \sin \omega_2(t-\tau) d\tau ; \quad \omega_2 = \left(\frac{k_{22}}{m_{22}} \right)^{1/2} . \quad (45)$$

From equation (15) one obtains

$$m_{11}y_1'' + k_{11}y_1 + \epsilon f_1(y_1, y_1', y_2, y_2', t) = 0 , \quad (46)$$

$$m_{22}y_2'' + k_{22}y_2 + \epsilon f_2(y_1, y_1', y_2, y_2', t) = 0 , \quad (47)$$

Since the equations are decoupled for $\epsilon = 0$, the solution is assumed as

$$y_1(t) = a_1(t) \cos \psi_1(t) , \quad y_2(t) = a_2(t) \cos \psi_2(t) , \quad (48a,b)$$

where

$$\dot{\psi}_1(t) = \omega_1 + \theta_1'(t) \text{ and } \dot{\psi}_2(t) = \omega_2 + \theta_2'(t) . \quad (49a,b)$$

The amplitude and the phase equations can be written from equation (28) as

$$\frac{da_1}{dt} = \frac{\epsilon F_1^*}{\omega_1 m_{11}} , \quad \frac{da_2}{dt} = \frac{\epsilon F_2^*}{\omega_2 m_{22}} , \quad (50a,b)$$

$$\frac{d\theta_1}{dt} = \frac{\epsilon G_1^*}{a_1 \omega_1 m_{11}}, \quad \frac{d\theta_2}{dt} = \frac{\epsilon G_2^*}{a_2 \omega_2 m_{22}}, \quad (51a, b)$$

where

$$F_j^* = \frac{1}{4\pi^2} \int_0^{2\pi} \int_0^{2\pi} f_j(a_1, a_2, \psi_1, \psi_2, t) \sin \psi_j d\psi_1 d\psi_2,$$

$$G_j^* = \frac{1}{4\pi^2} \int_0^{2\pi} \int_0^{2\pi} f_j(a_1, a_2, \psi_1, \psi_2, t) \cos \psi_j d\psi_1 d\psi_2, \quad j=1, 2. \quad (52a, b)$$

In general equations (50 a and b) represent two simultaneous first order nonlinear equations in a_1 and a_2 . For simple cases the solutions may be obtained in the closed form otherwise a numerical quadrature may be used. Once a_1 and a_2 are determined, equations (51a,b) can be integrated to obtain the expressions for the phase angles. The constants of integrations $a_1(0)$, $a_2(0)$, $\psi_1(0)$ and $\psi_2(0)$ are once again determined from equation (7) to yield

$$a_1(0) = -p_1(0)/\cos \psi_1(0) \quad ; \quad a_2(0) = -p_2(0)/\cos \psi_2(0) \quad (53)$$

$$\psi_1(0) = \arctan [-p_1'(0)/\omega_1 p_1(0)] \quad ; \quad \psi_2(0) = \arctan [-p_2'(0)/\omega_2 p_2(0)]. \quad (54)$$

Therefore the solutions for $T_1(t)$ and $T_2(t)$ are given by equations (11) and (44) through (54).

ILLUSTRATIVE EXAMPLE

As an illustrative example the transverse response of a hinged-hinged beam subjected to a transient load is considered. If the stretch of the neutral axis is included, the nonlinear differential equation for the beam can be shown to be given by

$$\rho A \frac{\partial^2 r}{\partial t^2} + EI \frac{\partial^4 r}{\partial x^4} - \left[\frac{EA}{2l} \int_0^l \left(\frac{\partial r}{\partial z} \right)^2 dz \right] \frac{\partial^2 r}{\partial x^2} + 2c \frac{\partial r}{\partial t} = g(x)u(t) \quad (55)$$

where

E = elastic modulus
 I = cross sectional moment of inertia of the beam
 ρ = mass per unit length of the beam
 A = area of the cross section
 l = length of the beam
 r = transverse deflection
 $g(x)u(t) = f(x, t)$ = transverse transient load
 c = damping constant

It is observed that equation (55) is of the form of equation (1) where the linear damping term is treated as a part of the nonlinear operator $N_{\underline{x}}$. For simplicity the transverse load is considered to be a separable function of time and space.

Introducing the nondimensional quantities

$$x = lx^* \quad , \quad r = \frac{\gamma^2}{l} r^* \quad , \quad t = \frac{l^2}{\gamma} \left(\frac{P}{E}\right)^{1/2} t^*$$

$$c = \frac{2A\gamma^3}{l^4} (\rho E)^{1/2} c^* \quad \text{and} \quad \varepsilon = \frac{\gamma^2}{l^2} \quad ,$$

equation (55) is reduced to the nondimensional form

$$\frac{\partial^2 r}{\partial t^2} + \frac{\partial^4 r}{\partial x^4} = - \varepsilon \left[\frac{1}{2} \int_0^1 \left(\frac{\partial r}{\partial z} \right)^2 dz \right] \frac{\partial^2 r}{\partial x^2} + 2\varepsilon c \frac{\partial r}{\partial t} = \Delta g(x)u(t) \quad (56)$$

where $\Delta = EA\gamma^4/l^5$.

Note that the asterisks have been dropped for brevity.

It is well known that for a hinged-hinged beam $\phi_j = \sin j\pi x$ and equation (2) takes the form

$$r(x,t) = \sum_{j=1}^N T_j(t) \sin j\pi x \quad . \quad (57)$$

Substituting equations (57) and (55) in (5) and integrating from 0 to 1 yields

$$T_j'' + \omega_j^2 T_j + \varepsilon [2cT_j' + f_j(T_1, T_2, \dots, T_N)] = U_j(t) \quad , \quad j=1, 2, \dots, N, \quad (58)$$

where

$$\omega_j = j^2 \pi^2 \quad , \quad U_j(t) = (2\Delta \int_0^1 g(x) \sin j\pi x dx) u(t) \quad , \quad (59)$$

$$\text{and} \quad f_j(T_1, T_2, \dots, T_N) = \frac{j^2 \pi^4}{4} T_j \sum_{k=1}^N k^2 T_k^2 \quad . \quad (60)$$

For $j=1$, the one term approximation can be obtained from equation (58) as

$$T'' + \pi^4 T + \varepsilon [2cT' + \frac{\pi}{4} T^3] = U(t) \quad . \quad (61)$$

The subscript 1 has been dropped for convenience. Consider the case where $u(t)$ takes the form of a blast loading which may be represented as

$$U(t) = \Gamma (e^{-bt} - e^{-dt}) ; b, d > 0 , b \leq d , \quad (62)$$

where Γ is a constant.

As outlined earlier the solution is expressed as

$$T(t) = a(t)\cos\psi(t) + p(t) \quad (63)$$

where $p(t)$ is obtained from (32) as

$$p(t) = \Gamma \left[\frac{e^{-bt}}{(b^2 + \pi^4)} - \frac{e^{-dt}}{(d^2 + \pi^4)} \right] . \quad (64)$$

The amplitude and phase equations (35a,b) yield

$$\frac{da}{dt} = -\varepsilon ca ; \quad \frac{d\psi}{dt} = \pi^2 + \frac{3\varepsilon\pi^2 a^2}{32} + \frac{3\varepsilon\pi^2 p^2(t)}{8} . \quad (65)$$

One can integrate these to obtain

$$a(t) = a(0)\exp(-\varepsilon ct) , \quad (66)$$

and

$$\psi(t) = \pi^2 t - \frac{3\pi^2}{64c} a^2(t) + \frac{3\varepsilon\pi^2}{8} P(t) + \psi_0 \quad (67)$$

where

$$P(t) = \Gamma^2 \left[\frac{-e^{-2bt}}{2b(b^2 + \pi^4)^2} - \frac{-e^{-2dt}}{2d(d^2 + \pi^4)^2} + \frac{2e^{-(b+d)t}}{(b+d)(b^2 + \pi^4)(d^2 + \pi^4)} \right] . \quad (68)$$

$a(0)$ and ψ_0 may be evaluated easily from equation (39). The expressions are omitted.

Therefore $T(t)$ is completely known in an analytical form and a one term solution is readily obtained from equation (5). Figure 1 shows the response for some typical values of the parameters.

Similarly a two term approximation may be obtained from equation (58). It is observed from equation (59) that $U_j(t)$ are identically zero for $j = 2, 4, 6, \dots$ and therefore such an approximation is obtained with $j = 1$ & 3 as

$$T_1'' + \omega_1^2 T_1 + \varepsilon [2cT_1' + \frac{\pi^4}{4} T_1(T_1^2 + 9T_3^2)] = U_1(t) , \quad (69)$$

$$T_3'' + \omega_3^2 T_3 + \varepsilon [2cT_3' + \frac{9\pi^4}{4} T_3(T_1^2 + 9T_3^2)] = U_3(t) , \quad (70)$$

Where $\omega_j = j^2 \pi^2$, $j=1,3$.

As before, the solutions are assumed in the form

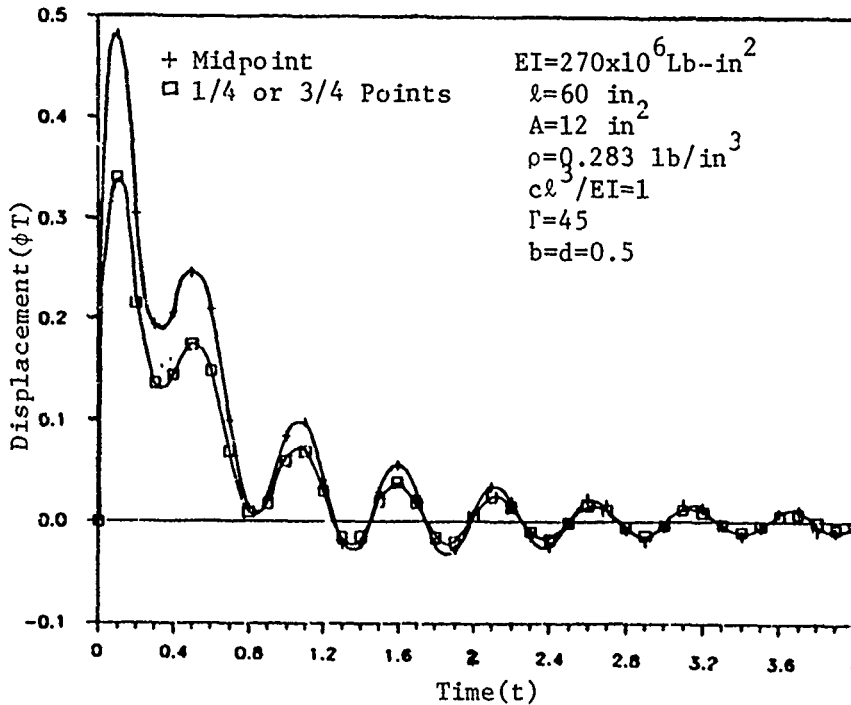
$$T_1(t) = a_1(t)\cos\psi_1(t) + p_1(t) ; T_3(t) = a_3(t)\cos\psi_3(t) + p_3(t) . \quad (71)$$

$U_1(t)$ and $U_3(t)$ can be assumed in the form of equation (62) as

$$U_1(t) = \Gamma_1(e^{-bt} - e^{-dt}) ; U_3(t) = \Gamma_3(e^{-bt} - e^{-dt}) , \quad (72)$$

where the constants Γ_1 and Γ_3 can be obtained from equation (59).

Fig.1. Pulse Response of a Simply-Supported Beam
(one term approximation)



Then equations (44) and (45) yield

$$p_1(t) = \Gamma_1 \left[\frac{e^{-bt}}{b^2 + \omega_1^2} - \frac{e^{-dt}}{d^2 + \omega_1^2} \right] \text{ and } p_3(t) = \Gamma_3 \left[\frac{e^{-bt}}{b^2 + \omega_3^2} - \frac{e^{-dt}}{d^2 + \omega_3^2} \right] . \quad (73)$$

Equations (50a,b) provide the amplitude variations

$$a_1(t) = a_1(0)\exp(-\epsilon t) ; a_3(t) = a_3(0)\exp(-\epsilon t) , \quad (74)$$

while the phase equations (51a,b) take the form

$$\frac{d\theta_1}{dt} = \omega_1 + \frac{\varepsilon\pi^4}{4\omega_1} \left[\frac{3}{8} a_1^2(t) + \frac{3}{2} p_1^2(t) + \frac{9}{4} a_3^2(t) + \frac{9}{2} p_3^2(t) \right], \quad (75)$$

and

$$\frac{d\theta_3}{dt} = \omega_3 + \frac{9\varepsilon\pi^4}{4\omega_3} \left[\frac{27}{8} a_3^2(t) + \frac{27}{2} p_3^2(t) + \frac{1}{4} a_1^2(t) + \frac{1}{2} p_1^2(t) \right]. \quad (76)$$

Since $a_1(t)$, $a_3(t)$, $p_1(t)$ and $p_3(t)$ are known from equations (74) and (73), respectively, $\theta_1(t)$ and $\theta_3(t)$ can also be obtained in closed forms. Therefore the two term solution from equation (57) is given as

$$r(x,t) = T_1(t)\sin\pi x + T_3(t)\sin 3\pi x,$$

where $T_1(t)$ and $T_3(t)$ are known from equation (71).

DISCUSSION AND CONCLUSION

It is shown that the general problem of nonlinear continuous systems subjected to arbitrary transient loads can be reduced to a set of ordinary differential equations and approximate analytical solutions can be obtained through an application of the well-known Krylov-Bogoliubov method. The approach presented here is restricted to the case of first-order approximation, although construction of higher order approximation is certainly possible. It has been shown by Olberding and Sinha [14] that higher-order approximations for nonstationary discrete systems do not necessarily improve the accuracy. Usually a one or two term first-order approximation may be adequate in many situations. Of course, more accurate numerical solutions can always be obtained by utilizing an integrating scheme such as the Newmark method or the Runge-Kutta technique.

In conclusion, an approximate analytical technique has been presented to study the nonlinear response of continuous systems subjected to transient loads. The approach is simple and can be applied to a general class of problems including beams, plates, shells, etc.

REFERENCES

1. M. Sathyamoorthy, "Recent Research in Nonlinear Analysis of Beams," Shock & Vibration Digest, Vol. 15, No. 9, pp. 19-27, Sept. 1985.
2. A.W. Leissa, "Recent Studies in Plate Vibrations: 1981-1985 Part I. Classical Theory", Shock & Vibration Digest, Vol. 19, No. 2, pp. 11-17, Feb. 1987.
3. A.W. Leissa, "Recent Studies in Plate Vibrations: 1981-85 Part II. Complicating Effects", Shock & Vibration Digest, Vol. 19, No. 3, pp. 10-24, March 1987.
4. M. Sathyamoorthy, "Recent Advances in Nonlinear Plate Vibrations", Shock & Vibration Digest, Vol. 20, No. 5, pp. 14-20, May 1988.

5. V.A. Bapat and P. Srinivasan, "Response of Undamped Nonlinear Spring Mass System Subjected to Constant Force Excitation", Jr. Sound & Vibration, Vol. 9, pp. 53-58, 1969.
6. V.A. Bapat and P. Srinivasan, "Response of Undamped Nonlinear Spring Mass System Subjected to Constant Force Excitation", Jr. Sound & Vibration, Vol. 9, pp. 438-446, 1969.
7. V.A. Bapat and P. Srinivasan, "Approximate Methods for Step Function Response of Undamped Nonlinear Spring Mass System with Arbitrary Hardening Type Spring Characteristics", Jr. Sound & Vibration, Vol. 10, pp. 430-443, 1969.
8. S.C. Sinha and P. Srinivasan, "An Approximate Analysis of Non-linear Non-conservative Systems Subjected to Step Function Excitation", Jr. Sound & Vibration, Vol. 23, pp. 211-219, 1972.
9. G.L. Anderson, "Application of Ultraspherical Polynomials to Non-linear Non-Conservative Systems Subjected to Step Excitation", Jr. Sound & Vibration, Vol. 52, pp. 101-108, 1974.
10. R.R. Reed, "Analysis of Structural Response with Various Forms of Damping", NASA TND-3861, 1967.
11. S.C. Sinha and C.C. Chou, "On Non-linear Oscillation with Slowly Varying System Parameters", Jr. Sound & Vibration, Vol. 61, pp. 293-301, 1978.
12. S.T. Ariaratnam, "Response of Nonlinear System to Pulse Excitation", Jr. Mech. Engg. Sci., Vol. 6, pp. 26-31, 1964.
13. H.F. Bauer, "The Response of a Nonlinear System to Pulse Excitation", Int. Jr. Nonl. Mech., Vol. 1, pp. 267-282, 1966.
14. D.J. Olberding and S.C. Sinha, "Response of Non-linear Non-Stationary Systems Subjected to Pulse Excitation", Jr. Sound & Vibration, Vol. 112, pp. 227-235, 1987.
15. H.F. Bauer, "The Response of a Non-linear n Degrees of Freedom System to Pulse Excitation", Int. Jr. Nonl. Mech., Vol. 3, pp. 157-171, 1968.
16. M.A.V. Rangacharyulu et al., "Approximate Analysis of Coupled Non-linear Non-Conservative Systems Subjected to Step Function Excitation", Jr. Sound & Vibration, Vol. 37, pp. 359-366, 1974.
17. S.C. Sinha and M. Jagannathan, "Pulse Response of Non-linear Non-Stationary Vibrational Systems with N Degrees of Freedom", Jr. Sound & Vibration, Vol. 112, pp. 237-248, 1987.
18. L. Meirovitch, Analytical Methods in Vibrations, The Macmillan Co., New York, 1967.
19. O.C. Zienkiewicz, The Finite Element Method, pp. 527-568, McGraw-Hill, New York, 1977.
20. N.V. Butenin, Elements of the Theory of Nonlinear Oscillations, Blaisdell Publishing Co., New York, 1965 (Translated from Russian).

INFLUENCE OF ELASTIC COATING ON THE PLASTIC DEFORMATION OF A BEAM IN WATER SUBJECTED TO A SHOCK WAVE

A. L. Stiehl

**Department of Mechanical Engineering
Pennsylvania State University
McKeesport, PA 15135**

R. C. Haberman

**BBN Laboratories Incorporated
Union Station
New London, CT 06320**

A computer-simulation parametric study is undertaken to determine the effect of an elastic sublayer attached to a beam in water on the beam's peak plastic deflection when subjected to a shock wave. The study is performed by employing a one dimensional two degree of freedom model of the fundamental mode of the beam. This model was verified by a more rigorous dynamic elastic-plastic finite element model. Although the results show that the sublayer is effective in most cases, there are situations where an elastic coating can actually cause an increase in the deflection.

INTRODUCTION

As a means of reducing the peak plastic deflection of a beam in water subjected to a shock wave, an elastic sublayer attached to the beam is considered. This appears to be a reasonable method for mitigating shock since the trivial case of vanishing stiffness produces vanishing forces in the beam. Furthermore, the elastic coating provides a means for absorbing energy.

In a computer-simulation parametric study, elastic sublayers of various stiffnesses are considered along with beams of various lengths and end conditions. The mass of the coating along with wave effects are not included in this investigation. The loading is from a shock wave and is mathematically expressed as $p = p_0 e^{-t/\theta}$ where p_0 is the blocked pressure and θ is the time decay constant.

Two analytical models are used in this investigation. They are (1) a dynamic elastic-plastic finite element model, and (2) a one dimensional model of the beam's fundamental mode. The models are used to calculate the beam's deflection and system energies to the applied shock load. Both models are developed with the ANSYS [Reference 1] finite element code.

Results show that for the more flexible beams, a reduction of peak plastic deflection occurs over the entire range of sublayer stiffnesses of the study. An increase in deflection occurs in more rigid beams with the use of a relatively stiff sublayer. A relatively soft sublayer is required to achieve a reduction of deformation in the stiffer beams.

DESCRIPTION OF ANALYTICAL MODELS

Figure 1 shows the dynamic elastic-plastic finite element model for a simple support condition. Fixed end supports are also considered. The model consists of eight equal length beam elements attached to seven springs. A damper is attached to the end of each spring and mass is attached to the end of each damper. The springs are used to model the elastic sublayer, and the dampers and masses are used to model fluid-structure interaction effects as represented by the doubly asymptotic approximation, DAA [Reference 2]. Cavitation effects are not included in the model, and wave effects are not included in the elastic coating.

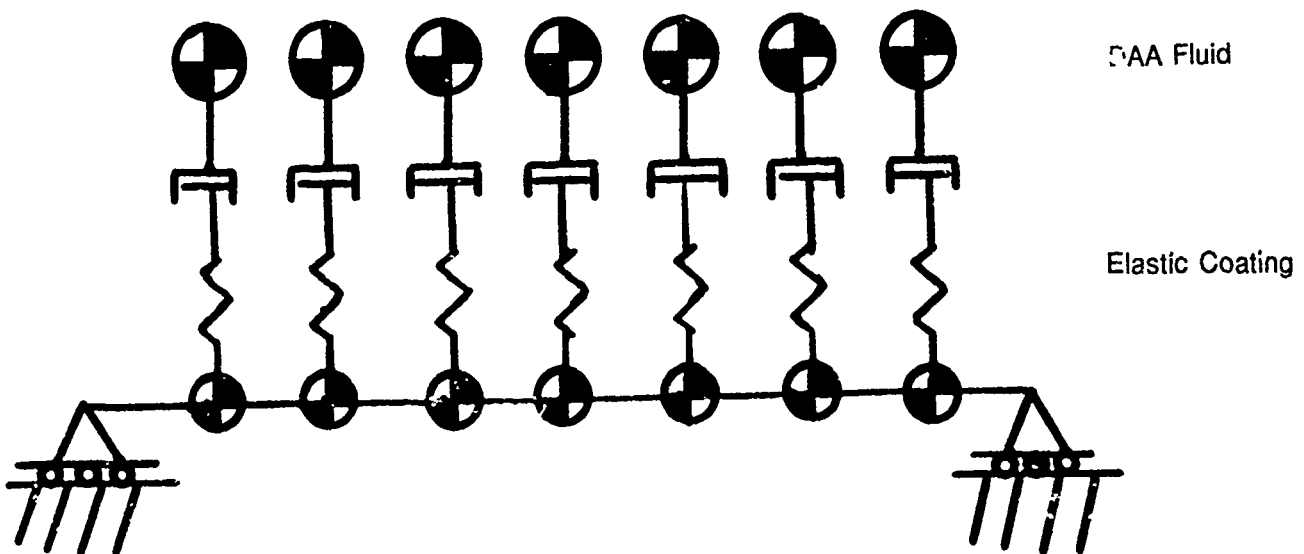


Figure 1. Finite Element Model with Elastic Coating

The simplified one-dimensional model representing the beam's fundamental mode is shown in Figure 2. The beam's non-linear spring characteristic is obtained with the use of the elastic-plastic response of a static model [Reference 3]. The model includes elastic unloading along a line parallel to the initial linear segment of the force-deflection curve for the beam. Characteristics of the fluid mass and damping, elastic sublayer stiffness, beam mass and stiffness, and the generalized applied force from the shock wave are obtained by applying Lagrange's equation of motion to the fundamental mode of the beam. The 1D model gives very good comparisons for beam center deflection with the ANSYS finite element model. Consequently, the 1D is used to generate the results of this study.

Static Elastic-Plastic Force Deflection Character of Beam

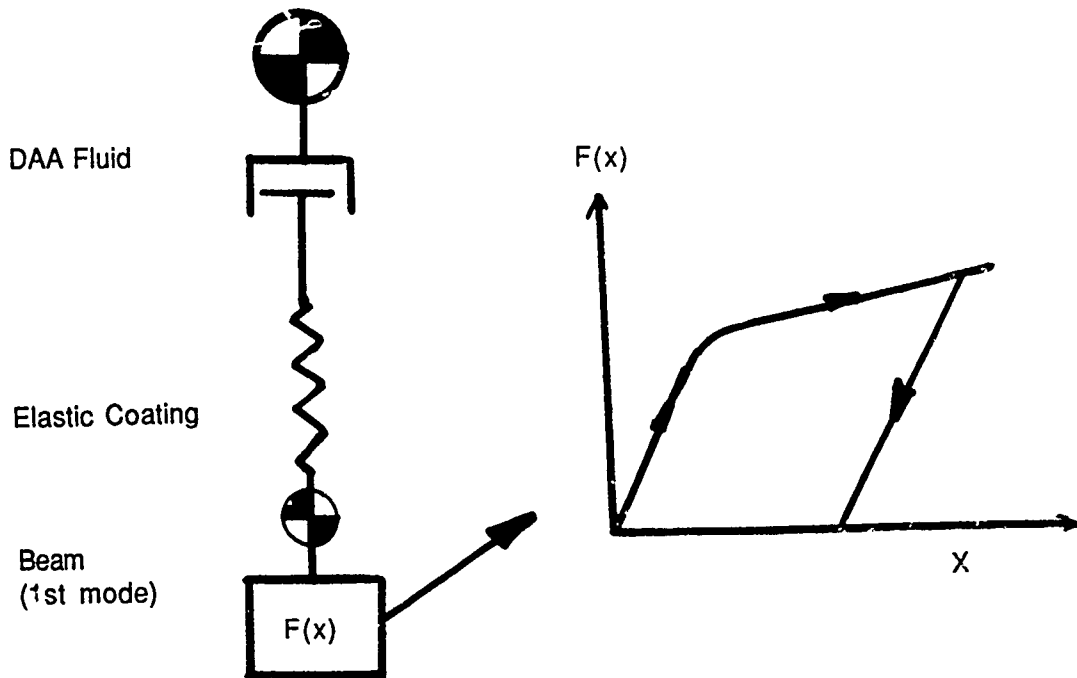


Figure 2. Two Degree of Freedom Model with Elastic Coating

PARAMETERS OF STUDY

The study includes beams of 50, 75, and 100 inches long. The width and thicknesses are 6 inches and 2 inches respectively. Both simple support (ss) and clamped support (cs) conditions are assumed. The material is steel with a yield stress of 80000 psi and very little work-hardening. The only shock loading of the study is expressed as $p = p_0 e^{-t/\theta}$ where p_0 is the blocked pressure and θ is the decay constant. A pressure value of 2500 psi is used for the purpose of producing significant plastic deflections. The decay constant is .001 seconds.

The stiffness of the elastic sublayer springs is expressed as a fraction of the beam stiffness, i.e. $k = \epsilon_{ps} k_{beam}$ where ϵ_{ps} is the fractional value and k_{beam} is the elastic stiffness of the beam based upon a uniform pressure loading and center deflection. Fractional values used in this study are 0.1, 0.3, 0.5, 0.7, and 1012. The latter value corresponds to the limit situation where no sublayer exists.

ANALYTICAL MODEL COMPARISONS

Figure 3 compares the elastic response of the two models for the 75 inch simple support (ss) beam. Referring to this figure it may be seen that the comparison is very good. This comparison is made to verify the 1D model. Figures 4.a and b compare the early-time elastic-plastic response of the two models for two sublayer spring stiffness for the 75 inch ss beam (i.e. $\epsilon_{ps} = .7$ and .3). As

seen, there is a good comparison of the peak plastic deflection between the two models. Comparison of the elastic-plastic response between the two models is shown in Figure 5 for the 100 inch cs beam with no sublayer. Again, the agreement between the early time responses of the two models is very good. The latter time response agreement is however not as good. The difference in plastic behavior between the two models would account for the lack of better agreement. Also, the fundamental mode shape changes once plastic behavior of the beam occurs. This is not accounted for in the 1D model.

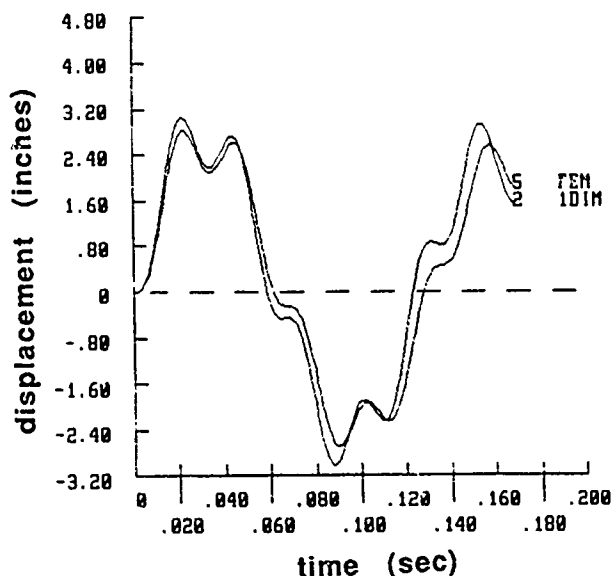


Figure 3. Comparison of Elastic Response for 75 Inch S.S. Beam

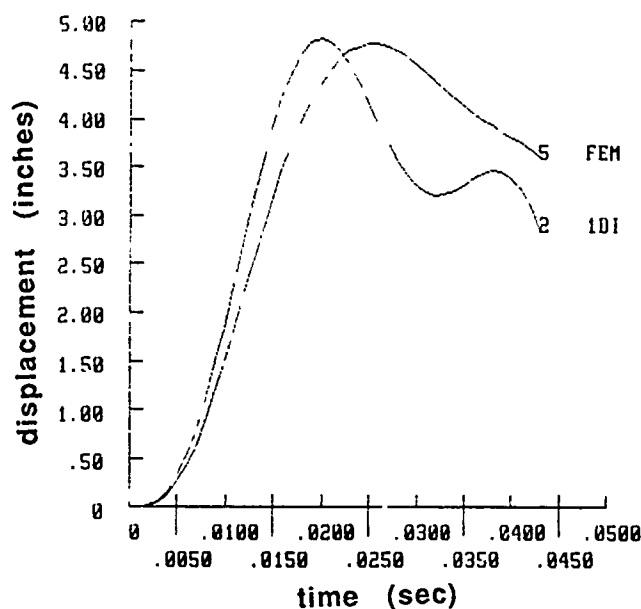


Figure 4A. Comparison of Elastic-Plastic Response for 75 Inch S.S. Beam with EPS = .7

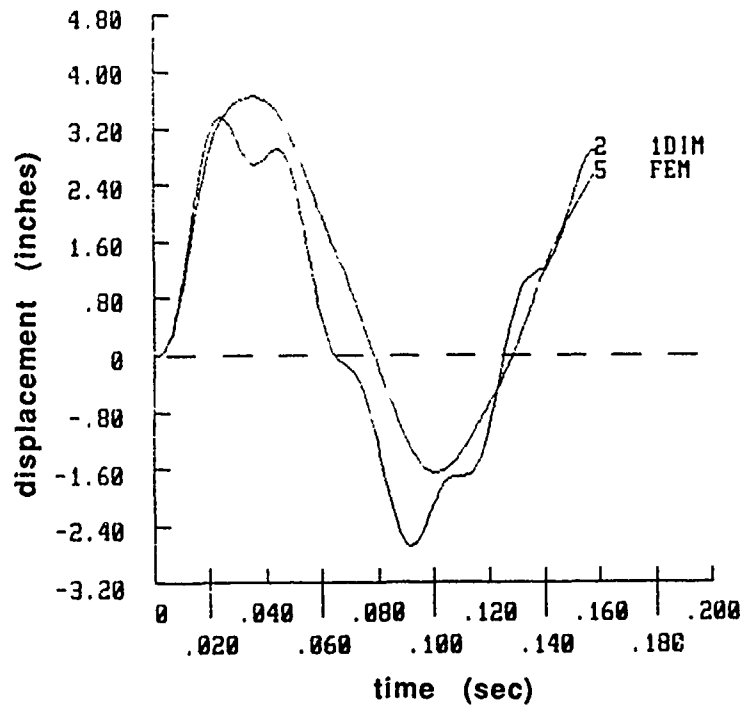


Figure 4B. Comparison of Elastic-Plastic Response for 75 Inch S.S. Beam with EPS = .3

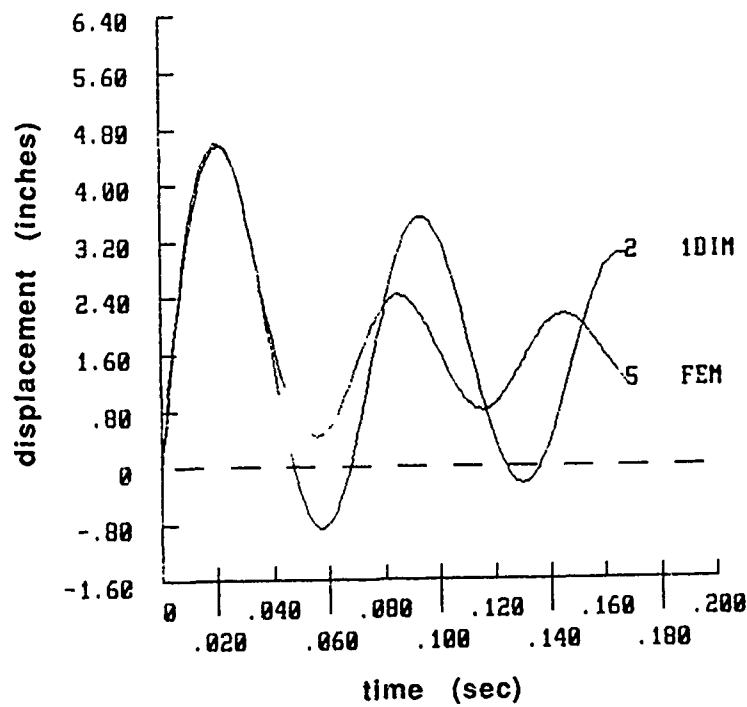


Figure 5. Comparison of Elastic-Plastic Response for 100 Inch C.S. Beam with No Coating

Because of the excellent agreement of the two models for the early time response, the 1D model is used to calculate the peak plastic beam deflection in this study. The 1D model could also be used to give estimates of the permanent deflection as indicated by the latter time response comparison in Figure 5. How good the estimates would be would depend upon the particular application of the model.

RESULTS

Table 1 presents results of the normalized peak plastic deflection of the beam center for all cases of beam length and boundary conditions and sublayer spring stiffnesses considered. The deflections are normalized to the case of no sublayer. For the more flexible beam cases, the sublayer reduced the beam's deflection regardless of the sublayer's stiffness. However, for the stiffer beam cases (shorter and clamped cases) the normalized deflection is greater than unity with the use of the stiffer sublayers. A relatively soft sublayer stiffness is required to get a reduced beam deflection as indicated in Table 1.

Table 1 Effectiveness of Sublayer on the Reduction of Beam Deflection

SUBLAYER FRACTIONAL STIFFNESS VALUES	.1	.3	.5	.7	1012
BEAM LENGTH & BOUNDARY COND.	NORMALIZED BEAM DEFLECTION				
100" SS	.28	.46	.64	.83	1.00
100" CS	.35	.55	.68	.79	1.00
75" SS	.28	.62	.82	.93	1.00
75" CS	.35	.61	.86	.98	1.00
50" SS	.30	1.04	1.21	1.23	1.00
50" CS	.39	1.01	1.15	1.18	1.00

The sublayer absorbs much of the applied energy from the shock wave. The softer the spring the greater these effects. This is illustrated in Figures 6a, b, and c, which show the system energies for the different sublayer spring stiffnesses corresponding to the 50 inch c.s. beam. Note that the beam's peak kinetic energy decreases with the softer spring. The peak kinetic energy of the water however actually increases with the softness of the sublayer spring. Reference 3 showed that the deflection of the beam was driven primarily by the kinetic energy of the water when no sublayer was used. The kinetic energy of the water is absorbed by the spring itself and a portion is absorbed by the beam. The additional kinetic energy in the water with the use of the sublayer results from greater energy input into the system which is also shown in the figures.

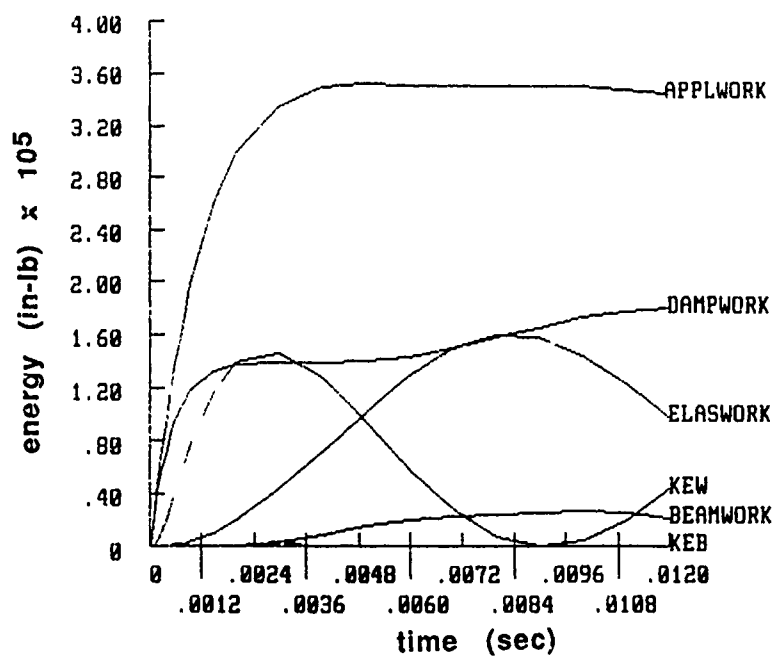


Figure 6A. Comparison of Energies for 50 Inch C.S. Beam with EPS = .1

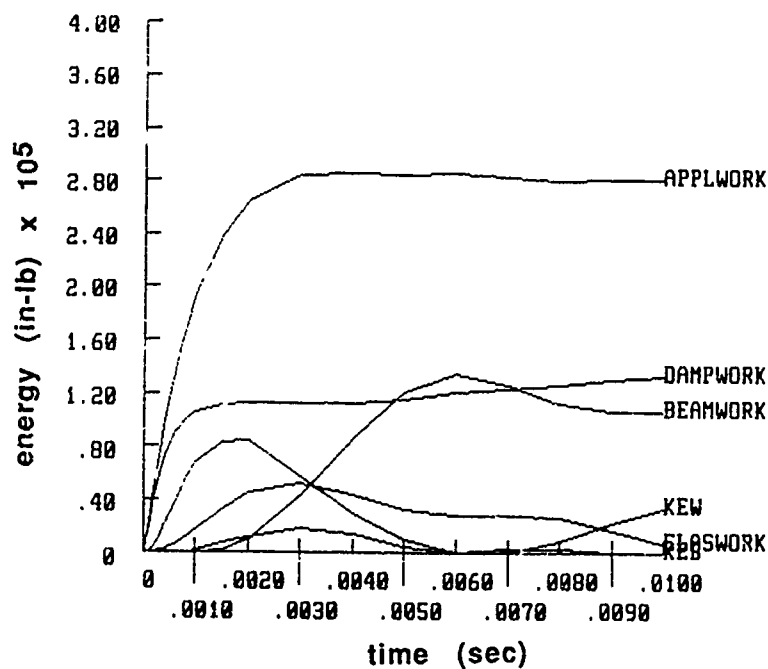


Figure 6B. Comparison of Energies for 50 Inch C.S. Beam with EPS = .5

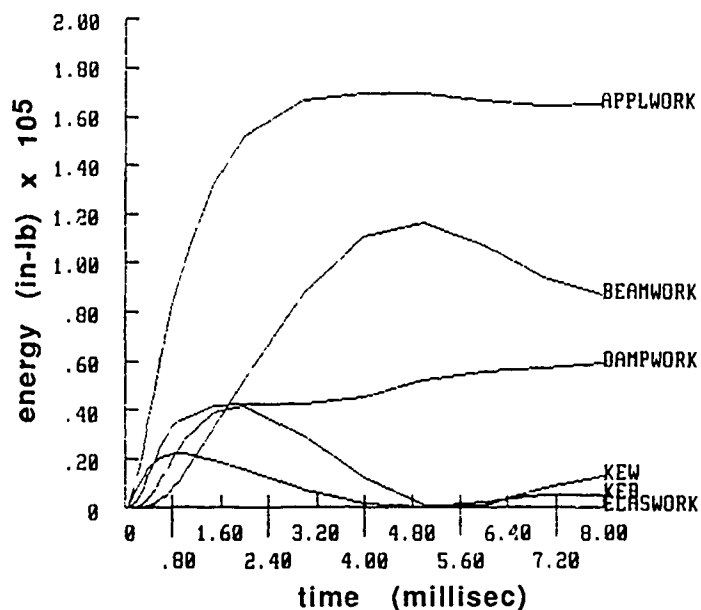


Figure 6C. Comparison of Energies for 50 Inch C.S. Beam with No Coating

The amplification effect shown in Table 1 for the 50 inch c.s. beam with $\epsilon_{ps} = .3, .5$ and $.7$ is also demonstrated in more detail for the completely elastic response. This is shown in Figure 7 which contains curves of normalized displacement versus ϵ_{ps} for the 50 inch c.s. beam. The curves were obtained analytically by a Fourier transform solution to the differential equations for the 2dof system. Inversion of the transform was accomplished by summing the residues in the complex plane. Three curves are shown in Figure 7 corresponding to time decays $\theta = .3, 1$ and 3 milliseconds. As the figure clearly illustrates, a soft coating ($\epsilon_{ps} \ll 1$) reduces the peak deflection, however a stiff coating (ϵ_{ps} on the order of the beam stiffness) can result in amplification.

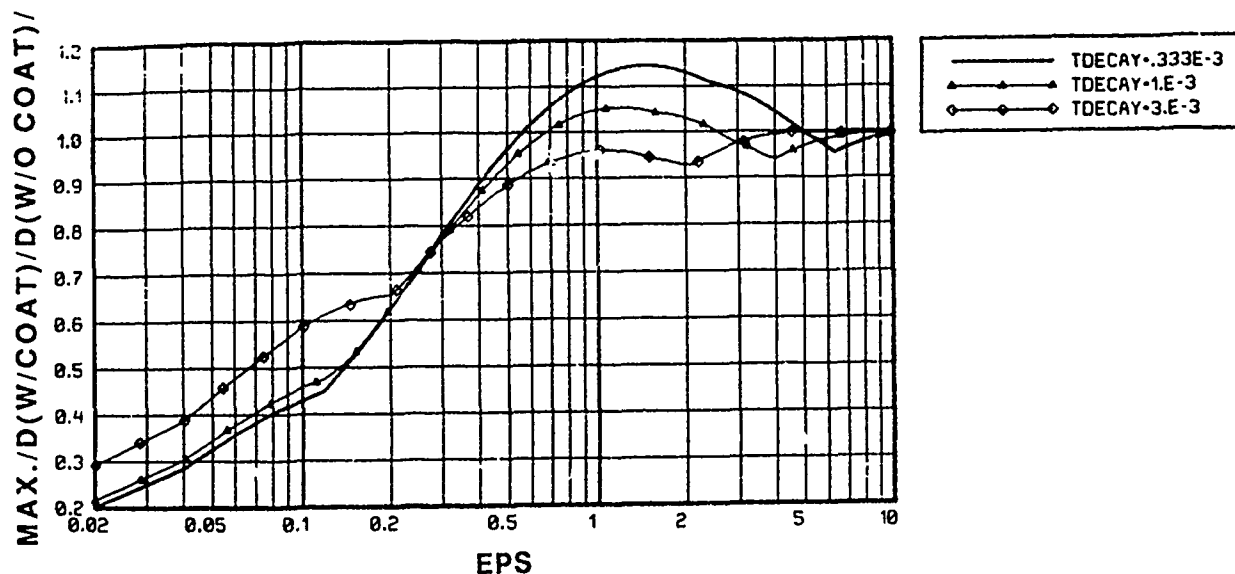


Figure 7. Comparison of Maximum Normalized Elastic Displacement for 50 Inch C.S. Beam

CONCLUSIONS AND RECOMMENDATIONS

Computer simulations reveal that an elastic coating can reduce the dynamic response of a beam subjected to a shock wave in water. The stiffness of the coating however must be considerably less than the stiffness of the beam in order to realize a reduction in the response. If the stiffness is comparable to the beam stiffness, some amplification may occur. Physically it appears that the coating increases the work applied to the system by the shock wave and the kinetic energy in the water. The compensating effect of the coating is to absorb most of the kinetic energy before it is absorbed by the beam. Based upon the encouraging results of this preliminary investigation, it is recommended that further studies be performed with actual coatings. The models could also be refined to include the mass and wave bearing effects in the coating, and cavitation of the fluid, which is very likely to occur for soft coatings.

REFERENCES

1. "ANSYS FINITE ELEMENT CODE, REVISION 3.2", Swanson Analysis Systems Inc., Houston, PA
2. T.L.Geers, "Doubly Asymptotic Approximations for Transient Motions of Submerged Structures", Journal of the Acoustical Society of America, Vol. 64, No. 5, pp 1500-1508, Nov. 1978
3. A.L. Stiehl, R.C. Haberman and J.H. Cowles, "Approximate Method for Predicting the Permanent Set of a Beam in Vacuo and in Water Subject to a Shock Wave", 58th Shock and Vibration Symposium, NASA Conference Publication 2488, Vol. II, pp 197-205, Oct. 1987

APPROXIMATE METHOD FOR PREDICTING THE PERMANENT SET IN A CIRCULAR PLATE IN WATER SUBJECTED TO A SHOCK WAVE

A. L. Stiehl
Department of Mechanical Engineering
Pennsylvania State University
McKeesport, PA 15135

R. C. Haberman
BBN Laboratories Incorporated
Union Station
New London, CT 06320

An approximate method to compute the maximum deflection and permanent set of a circular plate subjected to a shock wave loading in water was investigated. The method equates the maximum kinetic energy of the plate and water to the elastic plastic work done by a static uniform load applied to the plate. The simplified approach can result in significant savings in computer time or it can expediently be used as a check for a more rigorous approach i.e., a finite element solution. The accuracy of the method is demonstrated by various examples of plates with simple support and clamped support boundary conditions.

INTRODUCTION

Computer codes exist today to calculate the elastic-plastic deformation of structures subjected to shock wave loading, such as the finite element codes ANSYS reference [1], and STAGS reference [2]. Although these and other codes offer the analyst a large variety of elements and several plasticity theories, the computational effort to calculate the dynamic plastic deformation of a large structure may be substantial. To reduce the computational effort an approximate method based upon energy considerations was investigated for a circular plate. Calculated quantities of interest are maximum deformation and permanent set. The method equates maximum kinetic energy to the elastic-plastic work done by a static uniform load applied to the structure. The kinetic energy is calculated from a relatively simple time dependent elastic analysis of the structure and the work is calculated from another relatively simple elastic-plastic static analysis. Essential savings in computer time and effort on the part of the analyst can be realized by the simplified method. The method is similar to approximate methods developed over a decade ago for structures in air subjected to impulsive loadings, references [3], [4] and [5]. It is exactly the same method as that applied to a beam in vacuo and water subjected to a shock wave, reference [6].

The method is applied to several examples consisting of plates of various radii and boundary conditions subject to shock wave loadings at normal incidence in water. The shock loading is from an exponentially decaying shock wave, with decay time much smaller than the period of vibration.

Under these conditions, the loading tends to apply an impulse to (at least) the fundamental mode of the structure, with the maximum kinetic energy occurring primarily in the fundamental mode at a very early time and after the shock wave pressure has diminished to nearly zero. These are very important considerations in the energy balance method because the method does not account for the additional external work performed by the shock wave pressure after the peak kinetic energy occurs in the structure. Furthermore, the uniform pressure used in the elastic-plastic static analysis exactly simulates the applied load distribution and approximates the inertia load distribution corresponding to the fundamental mode of the plate. Fluid structure interaction forces on the plate are mathematically represented by the doubly asymptotic approximation, DAA reference [7]. This approximation is easily introduced into the dynamic elastic-plastic finite element model.

DESCRIPTION OF ANALYTICAL MODELS

Four analytical models were used in this investigation. Models (1) and (2) were ANSYS dynamic elastic plastic finite element models used to calculate the plate's deflection and kinetic energy (and the water's kinetic energy) due to the shock wave. One model used axi-symmetric solid elements and the other used axi-symmetric plate elements. The results of both models agreed very well and therefore only the results of the plate element model are presented. Model (3) was an ANSYS static elastic-plastic finite element model (axi-symmetric plate elements) to calculate the plate's deflection and external work performed by a uniform pressure. The last model was a simplified two degree of freedom (2dof) model to calculate the elastic-plastic response of the plate's fundamental mode to the shock wave. This model was developed with the ANSYS code also.

Figure 1 shows the dynamic finite element model for the simple support condition. The model consisted of five axi-symmetric plate elements. The surface areas of the inner two elements were of equal magnitude, as were the surface areas of the three outer elements. The outer elements had an area twice that of the inner elements. As mentioned, the displacements of this model closely agreed to those of a model consisting of twenty-two triangular shaped axi-symmetric solid elements.

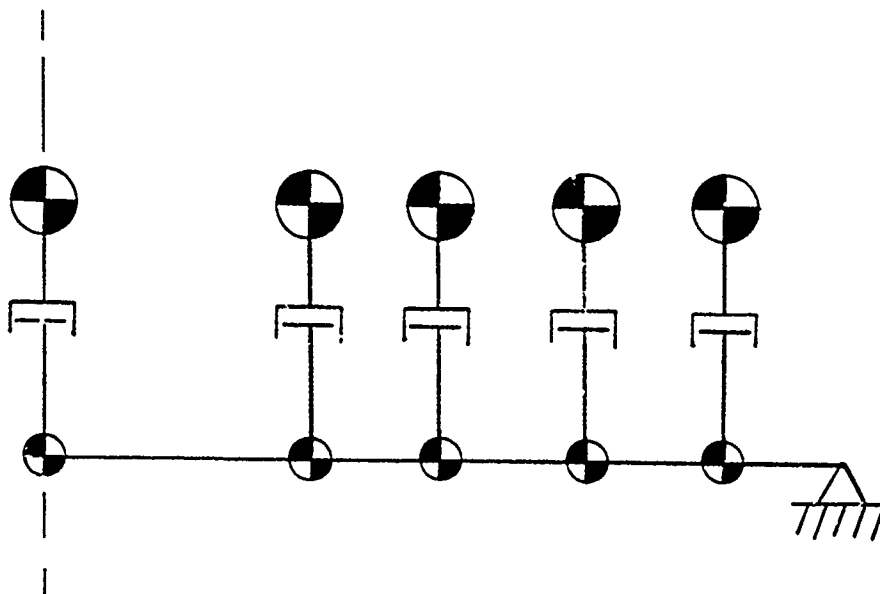


Figure 1. Finite Element Model

The elastic-plastic static finite element model consisted of five plate elements also. This model was subjected to a statically applied pressure loading. The external work by the pressure load was calculated from this model by simply integrating the pressure-displacement response.

The simplified 2dof model is shown in Figure 2. The spring characteristic is obtained from the elastic-plastic pressure-deflection response of the static model, and the mass, damping and applied force terms are obtained by applying Lagrange's equation of motion to the fundamental mode of the plate. This model can be used to estimate the maximum deflection and permanent set of the plate. It will be shown to give very good comparisons with the finite element model of Figure 1, thereby demonstrating the dominant contribution of the fundamental mode to the elastic-plastic response. Reference [6] showed the same response for beams.

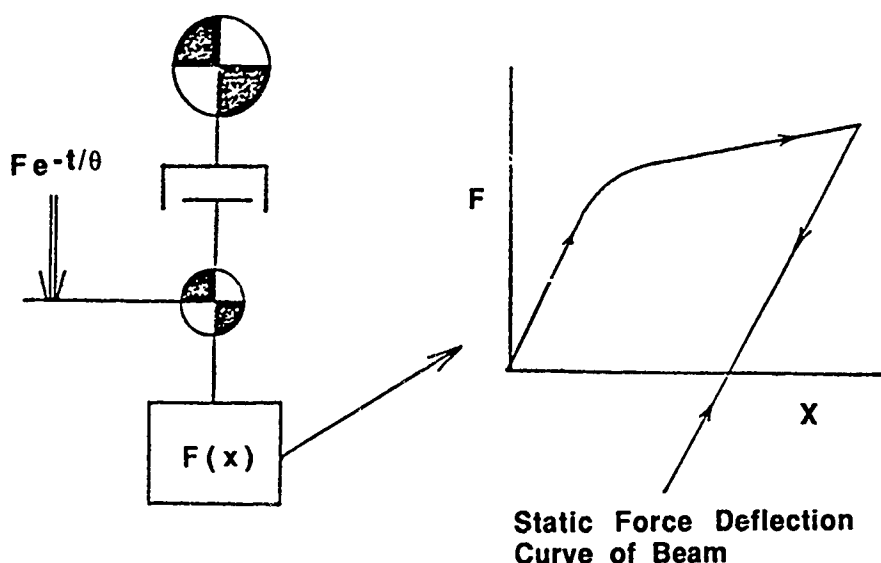


Figure 2. Simplified 2dof Model

RESULTS

The energy-balance method was applied to several examples of circular plates. Radii of 60, 90 and 120 inches were considered along with simple and fixed support conditions. The thickness was 2 inches and the material was steel with a yield stress of 80000 psi with very little work-hardening. The applied shock loading was expressed as $p = p_0 e^{-t/\theta}$ where p_0 is the blocked pressure. A decay constant of $\theta = .001$ second was used which for most of the examples was small compared to the fundamental period of vibration. A blocked pressure of 3000 psi was used to give significant plastic deformation. Cavitation of the water was not included in the analysis.

Figure 3 shows the non-linear pressure-displacement response for the simply supported 120 inches diameter plate and Figure 4 shows the static work functions for the three simple support plates. Similar curves were also obtained for the fixed support condition. The plate's dynamic

maximum deflection predicted by the energy balance method is obtained by entering into Figure 4 the peak kinetic energy of the plate and water induced by the dynamic load. The peak kinetic energy occurred during early time while the response was still elastic. The permanent deflection is obtained by subtracting from the maximum deflection a recoverable deflection the plate would experience under removal of a static uniform pressure.

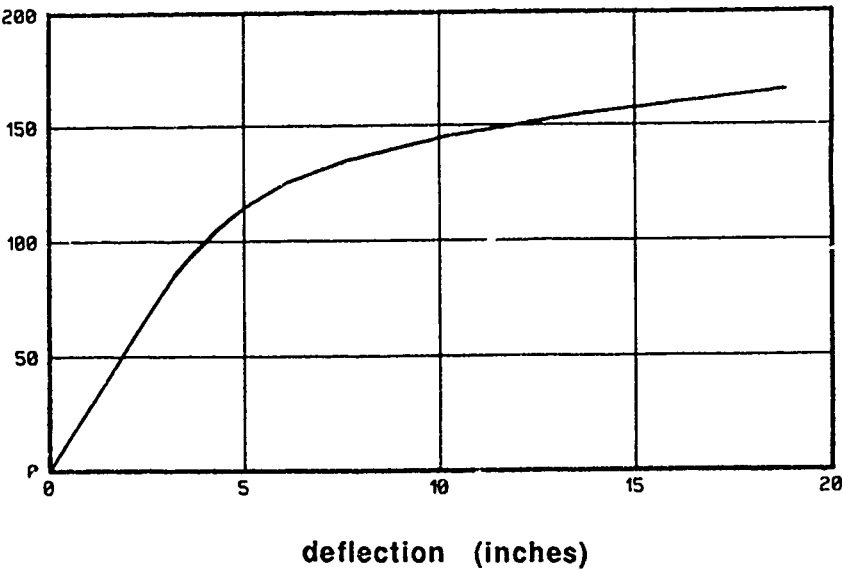


Figure 3. Pressure-Deflection for 120 Inch Diameter S.S. Plate

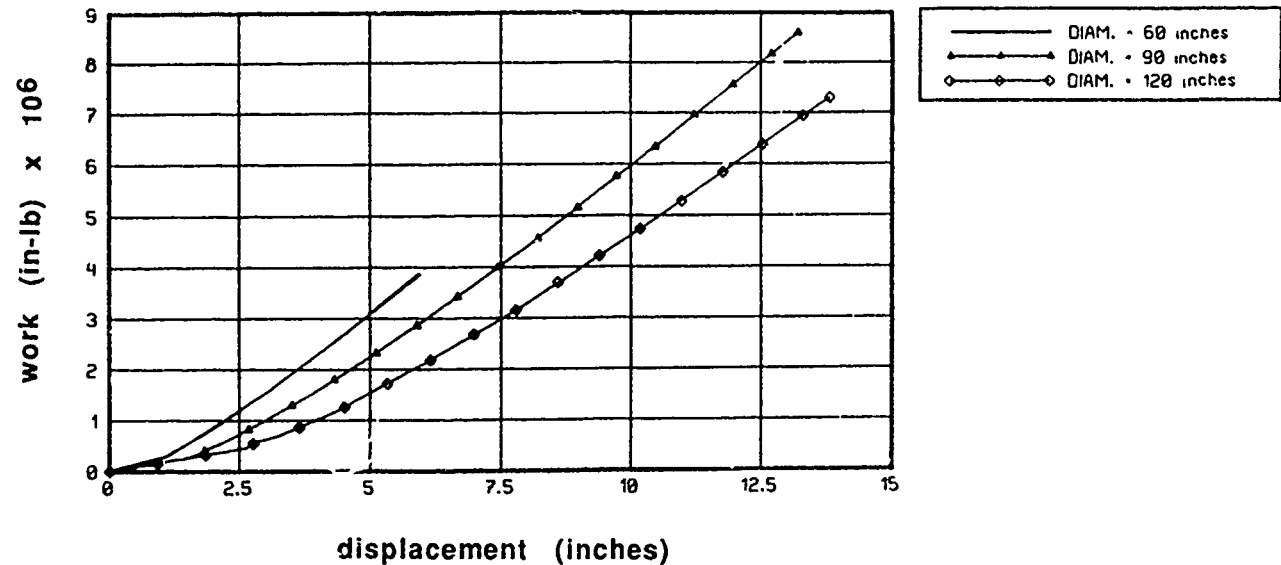


Figure 4. Work Function for S.S. Plates

Figure 5 illustrates the actual time dependent response of the center of the plate for the simple support condition. The permanent set was obtained by drawing a mean line through the later time decayed response. Figure 6 shows the kinetic energy occurring at a very early time for the 120 inch s.s. plate. This figure also shows that most of the kinetic energy resides in the water as was also the case for the beam in reference [6].

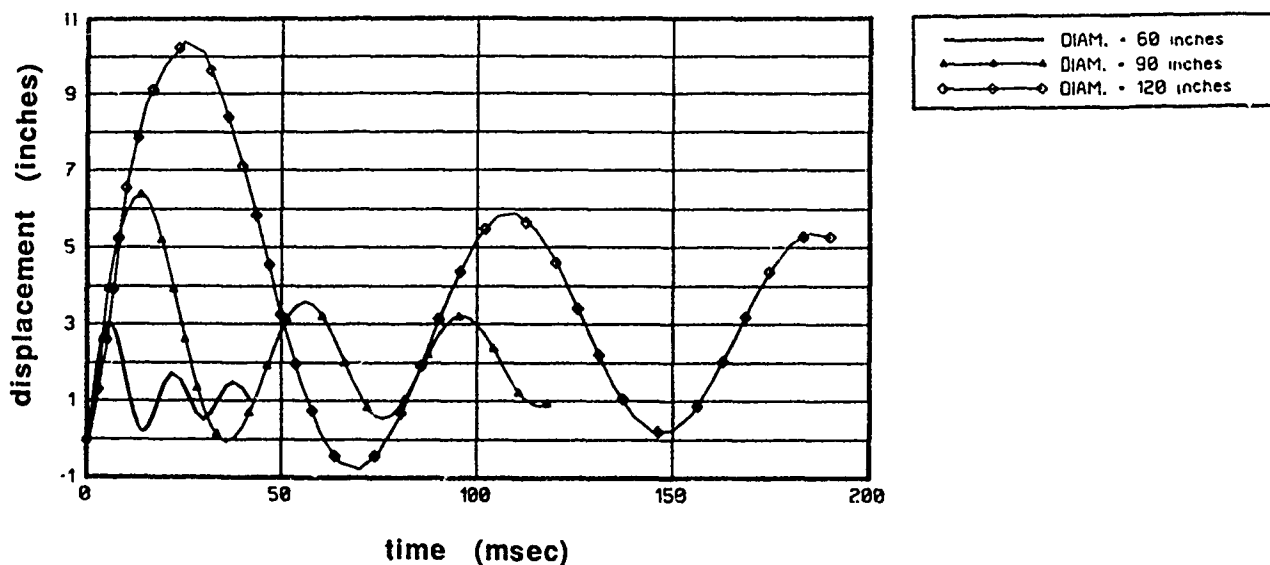


Figure 5. Displacement of S.S. Plates

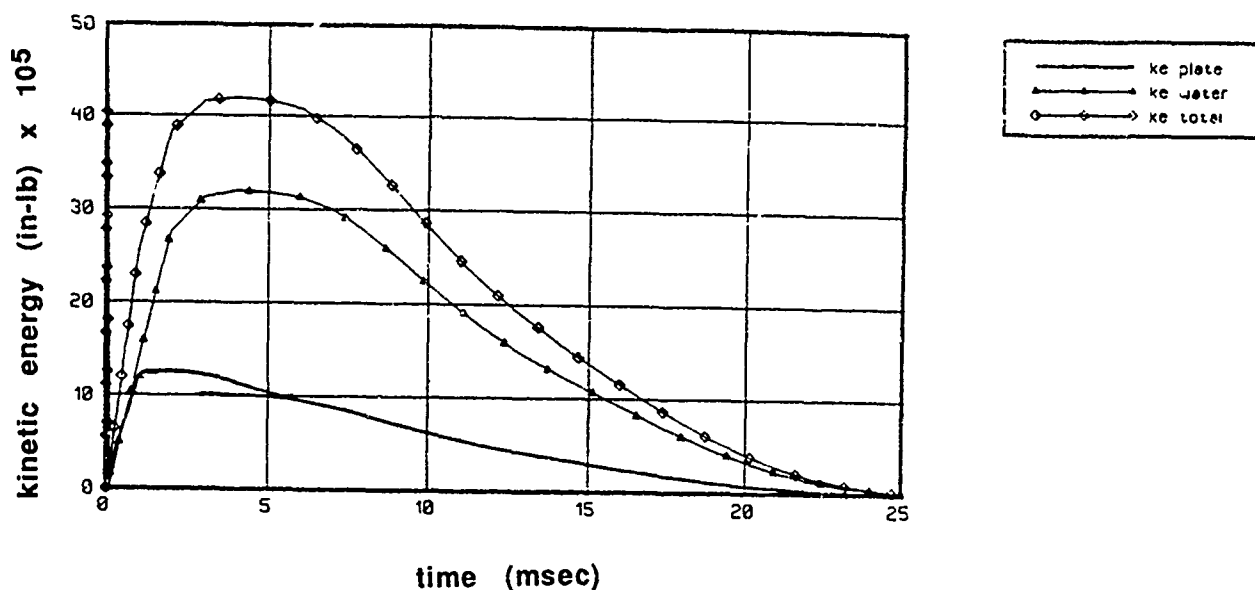


Figure 6. Kinetic Energy of 120 Inch Diameter S.S. Plate

Table 1 compares the peak deflections and permanent deflections obtained from the ANSYS dynamic model and the energy balance method, and Table 2 lists the fundamental period of vibration for the six plates in this study. As can be seen the comparisons are better for the larger plates because of their longer period of vibration. The same observation was made in reference [6] for the longer beams. This is illustrated in Figure 7 which shows the period of vibration dependence of the % difference between the energy balance and finite element results for the peak deflection of the plates (Table 1 results) and for the beams of reference [6]. Note that the difference increases as the period of vibration decreases and that the difference is very large for periods near the decay constant of 1 millisec. As the period approaches that of the decay time of the shock load, the kinetic energy of the beam reaches a maximum before the shock wave diminishes to zero. Thus there is additional dynamic work performed by the shock wave which is not accounted for in the energy balance method. Another consideration is the influence of higher frequency modes. If they are excited to any appreciable extent, the static work function would therefore not be a good approximation of the strain energy in the dynamically deformed plate. The static work function is only valid for plates responding primarily in their fundamental mode since the work function is based on a uniform pressure.

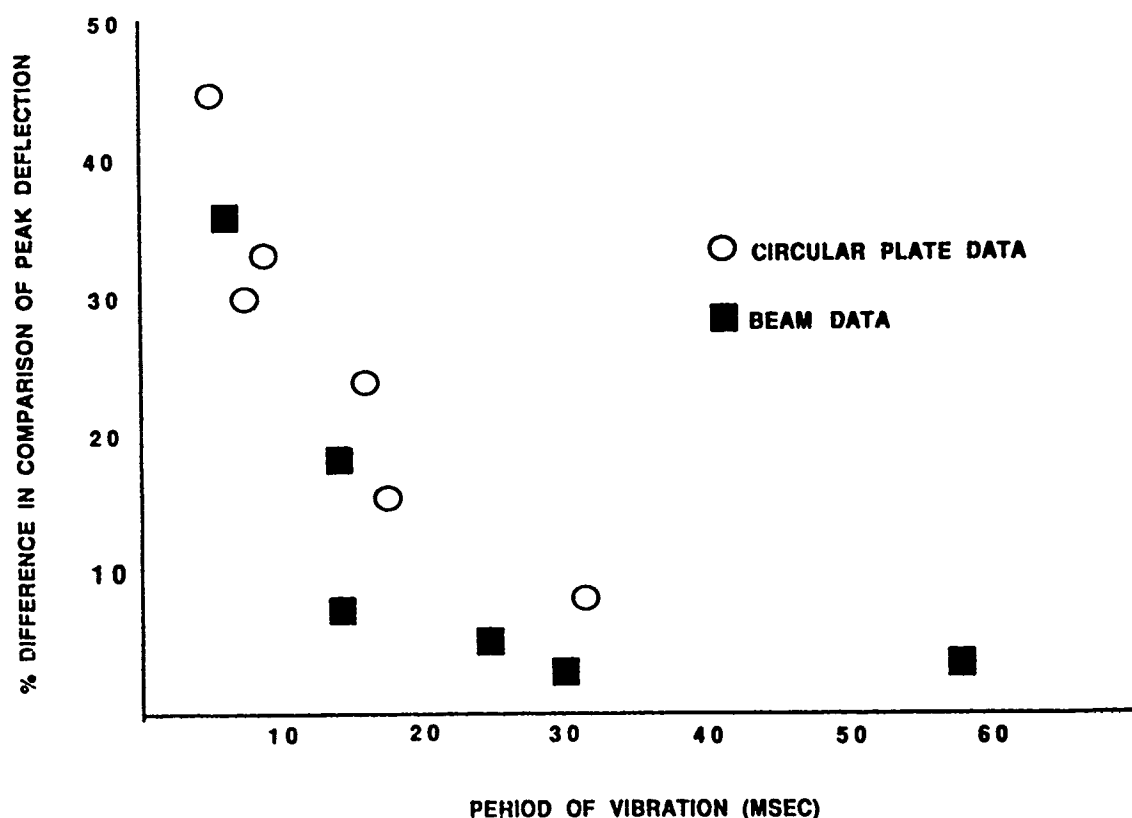


Figure 7. Effect of Period of Vibration on Comparisons Between Finite Element Method and Energy Balance Method

Table 1 Comparison of ANSYS and Energy Balance for Circular Plate

BOUNDARY CONDITIONS AND DIAMETER	PEAK DEFLECTION		PERMANENT DEFLECTION	
	ANSYS	ENERGY BALANCE (INCHES)	ANSYS	ENERGY BALANCE (INCHES)
Simple Support				
120" dia.	10.40	9.60	2.77	2.90
90" dia.	6.37	5.35	1.89	2.50
60" dia.	3.02	2.10	1.00	0.60
Fixed Support				
120" dia.	5.10	4.00	1.53	1.50
90" dia.	2.89	1.96	0.91	0.50
60" dia.	1.09	0.60	0.32	0.05

Table 2 Fundamental Periods of Vibration

Boundary Condition	Diameter (inches)	Period (seconds)
Simple Support	120	.031
	90	.018
	60	.008
Fixed Support	120	.016
	90	.009
	60	.004

Figures 8 and 9 compare results of the spring-mass-damper 2dof model with the ANSYS finite element model for the 60 inch diameter c.s. plate. As shown, the comparisons are reasonably good especially in the elastic case Figure 8. The elastic-plastic case (Figure 9) comparison isn't as good

as the elastic case. This could be due to differences in plastic behavior of the two models and also to a change of mode shape after the plate behaves plastically (i.e., the 2dof model assumes an elastic mode shape). Since the 2dof model is based on the fundamental mode of the plate and considering the agreement of the two models (Figures 8 and 9), it may be concluded that higher order modes do not contribute significantly to the plate's deflection.

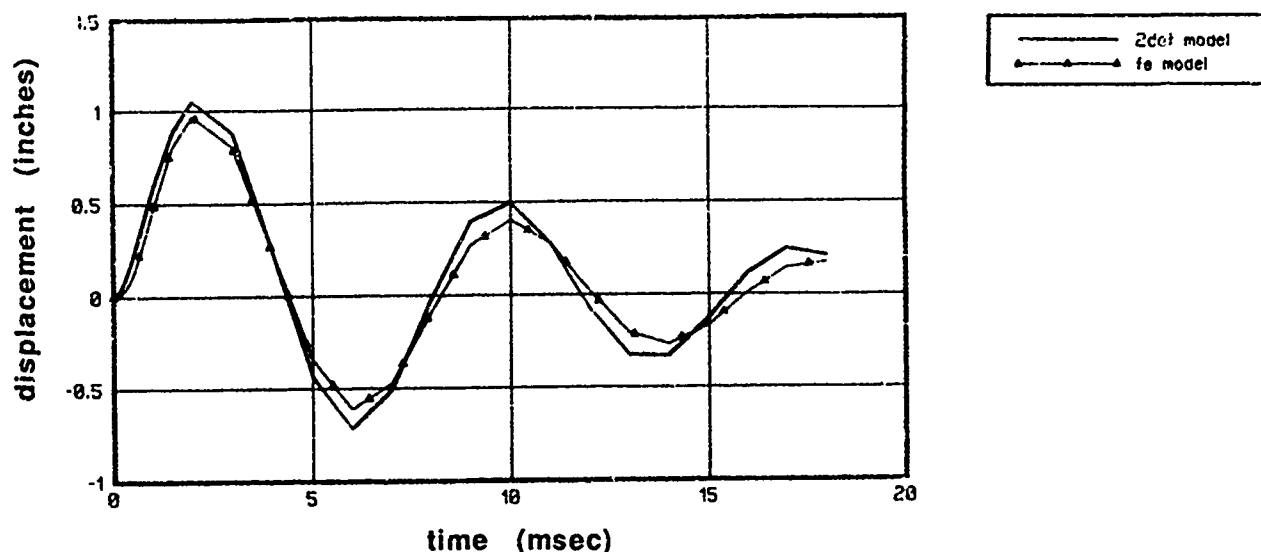


Figure 8. Comparison for 60 Inch Diameter Plate, C.S., Elastic Response

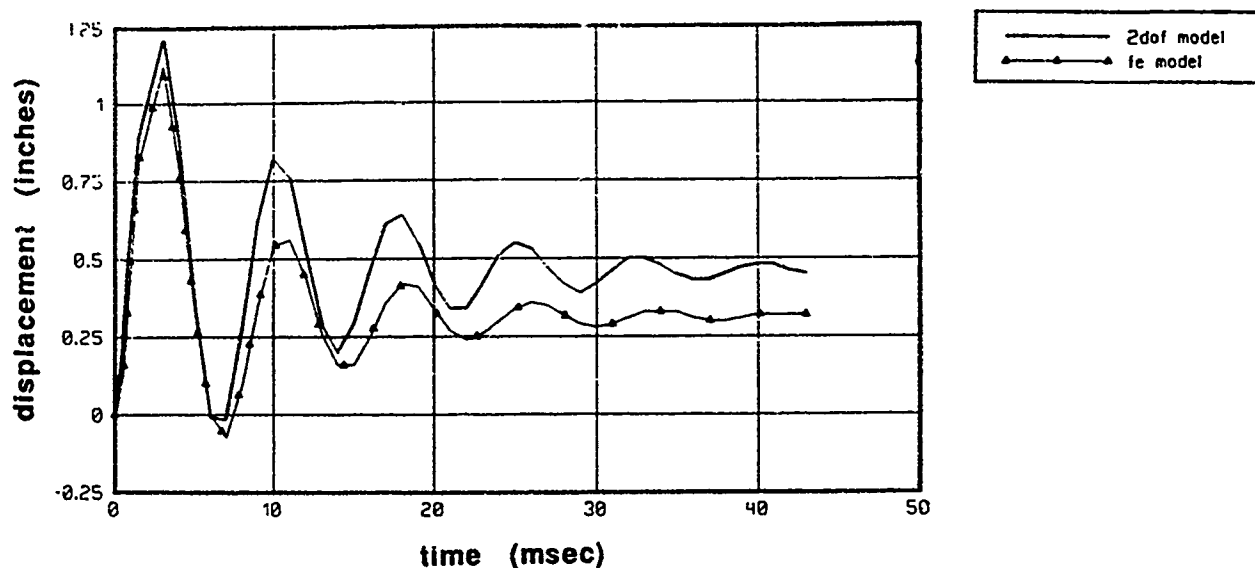


Figure 9. Comparison for 60 Inch Diameter Plate, C.S., Elastic-Plastic Response

Using the 2dof model, Figures 10 and 11 compare the kinetic energies with the external work of the applied shock wave, the lost work due to acoustic radiation, and the strain energy of the deformation for the 120 inch s.s. and 60 inch c.s. plates. For the energy balance method to be accurate the peak kinetic energy should occur after most of the external work has been completed and before there is appreciable strain energy in the plate. These criteria are best obtained in structures with the larger period of vibration as is the case with the 120 inch s.s. plate.

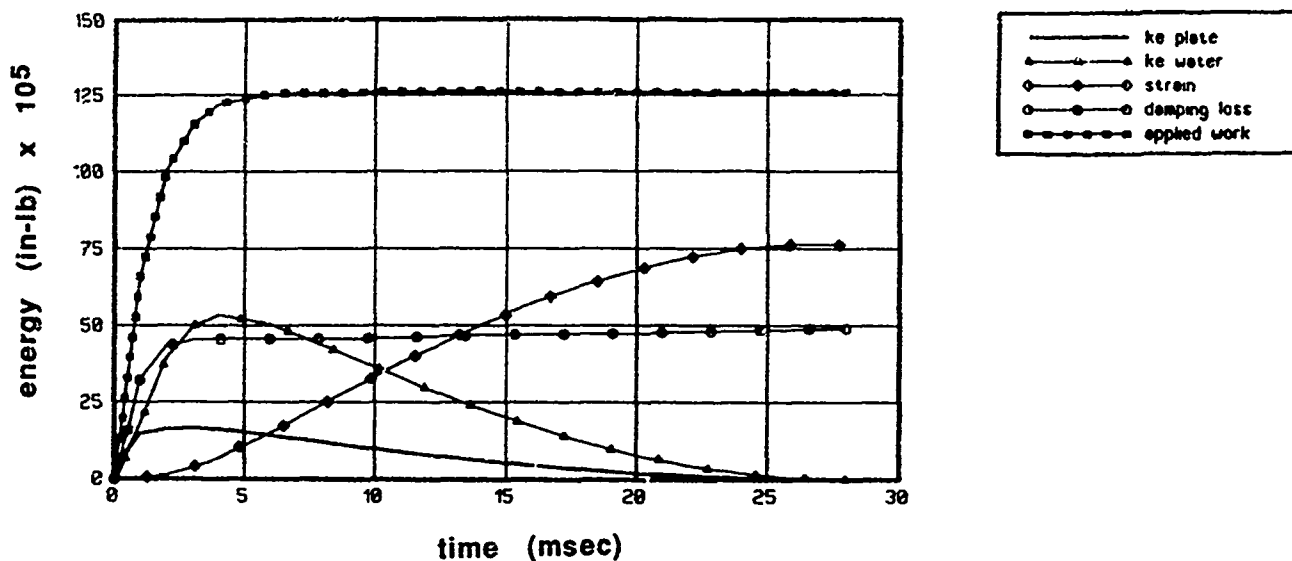


Figure 10. System Energies for 2dof Model, 120 Inch Diameter, S.S. Plate

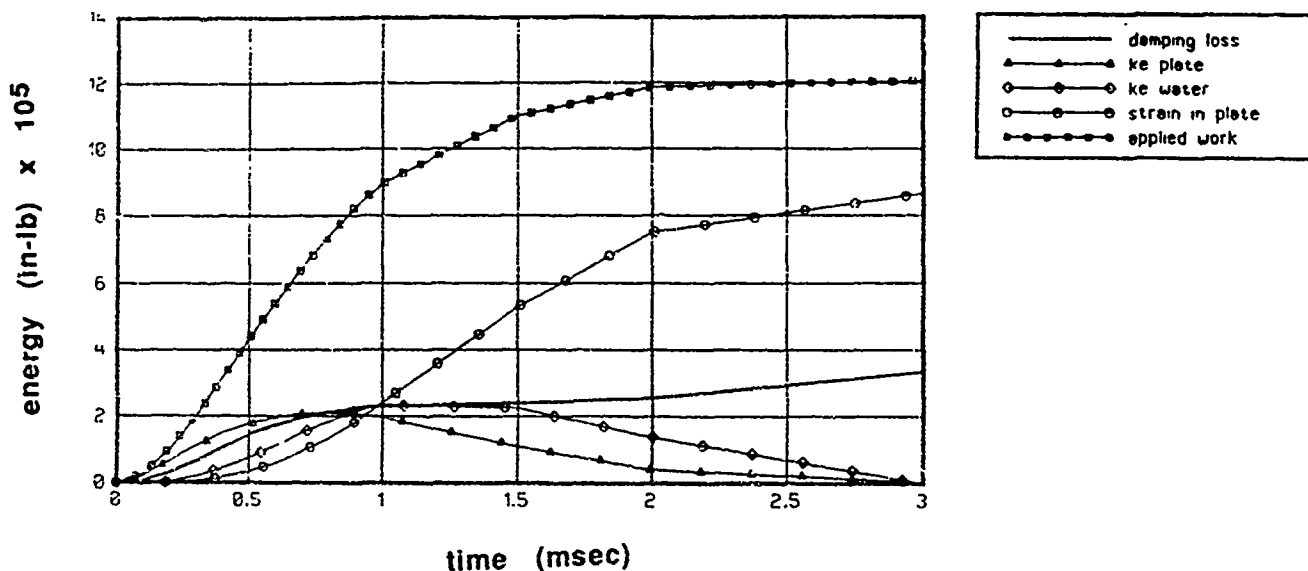


Figure 11. System Energies for 2dof Model, 60 Inch Diameter, C.S. Plate

CONCLUSIONS AND RECOMMENDATIONS

The energy balance method has been shown to give reasonably accurate results for the prediction of the peak deflection and permanent set in a circular plate in water subjected to a shock wave whose decay time is small compared to the fundamental period of vibration. The results indicate that the deformation is primarily controlled by the kinetic energy of the water. Improvements in the method could be realized by (1) accounting for the actual mode shape in the static work function, and (2) utilizing the improved second order doubly asymptotic approximation, reference [7]. Further validation of the model could be carried out by using fluid finite elements to model the fluid. This model could also investigate the importance of fluid cavitation.

REFERENCES

1. "ANSYS FINITE ELEMENT CODE, REVISION 3.2", Swanson Analysis Systems Inc., Houston, PA
2. B.L. Almroth, F.A. Brogan and G.M. Stanky, Structural Analysis of General Shells Volume II LMSCD633873, Lockheed Palo Alto Research Laboratory, January 1983
3. W.E. Baker, "Approximate Techniques for Plastic Deformation of Structures under Impulsive Loading", Shock Vibration Dig. Vol. 7, No. 7, pp 107-117, 1975
4. W.E. Baker, "Approximate Technique for Plastic Deformation of Structures under Impulsive Loading II", Shock Vibration Dig. Vol. II, No. 7, pp 19-24, 1979
5. W.E. Baker, P.A. Cox, P.S. Westine, J.J. Kulesz, and R.A. Strehlow, Explosion Hazards and Evaluation, pp 300-330. Elsevier Scientific Publishing Co., Amsterdam, 1982
6. A.L. Stiehl, R.C. Haberman, and J.H. Cowles, "Approximate Method for Predicting the Permanent Set in a Beam in Vacuo and in Water subjected to a Shock Wave", NASA Conference Publication 2488, Vol. II, pp 197-205, 1987
7. T.L. Geers, "Doubly Asymptotic Approximations for Transient Motions of Submerged Structures", Journal of the Acoustical Society of America, Vol. 64, No. 5, pp 1500-1508, Nov. 1978

COMPUTER CODE SPIDS; SHOCK PROPAGATION IN DUCTING SYSTEMS

**R. H. Fashbaugh, Ph.D.
Mechanical Engineering Department
University of Nevada-Reno
Reno, NV 89557**

**T. C. Knight
U.S. Army Corps. of Engineers
Omaha District, Omaha, NE 68102**

The computer code SPIDS which was developed under U.S. Army Corps of Engineers, Omaha District, contract numbers DACA4587PO153 and DACA4582M2881 is described. This computer code is used for calculation of shock wave propagation in a system of air ducts. The source of the shock waves can be either a surface or air nuclear burst or a conventional high explosive detonation which occur outside the entrance of the ducting system. Each duct in the system can have ten branches up to a total of 1000 branch ducts for the entire system. The equation of state for real air is used which is accurate up to 24000 K. Duct inlet losses and wall friction losses are included through empirical relations.

Included with the SPIDS code is a pre-processing microcomputer program which is used to generate an input file for this code. The wave shape parameters for a nuclear wave and junction loss factors for various types of duct junctions are included in this pre-processing program.

Also included with the SPIDS Code is a post-processing microcomputer program which allows plotting of all the output parameters of SPIDS on the computer screen or on an external plotter. Seventeen plots in all are available included in which are pressure, temperature, and dynamic pressure as a function of location in a given duct, or these parameters as a function of time at a given location in a duct.

INTRODUCTION

This paper describes the structure and use of the computer code SPIDS which has been developed for predicting shock wave propagation in a system of air ducts [1]. The source creating the shock wave that propagates over the entrance to the ducting system can be a surface or air nuclear burst or a conventional high explosive detonation; a multiple shock front of known waveform shape can also be specified at the system entrance. The ducting system configuration is shown in Fig. 1 and can be a main air duct with up to ten ducts branching from it. Each of these branch ducts can have up to ten ducts branching from them; and further, up to ten branch ducts from each of these branches is possible. Each of the ducts in the system can have one change in cross section area. The computer program is a one-dimensional variable area hydrodynamic solution which includes friction effects at the duct wall. A centered finite-difference scheme is utilized in a Lagrangian formulation which includes pseudo-viscosity to remove shock front discontinuities [2]. Equations of state for real air up to a temperature of 24000 K, the temperature corresponding to a shock wave overpressure of approximately 30,000 psi, are included. The types of branch duct junctions available are illustrated in Fig. 2. The shock wave losses at these junctions are included empirically.

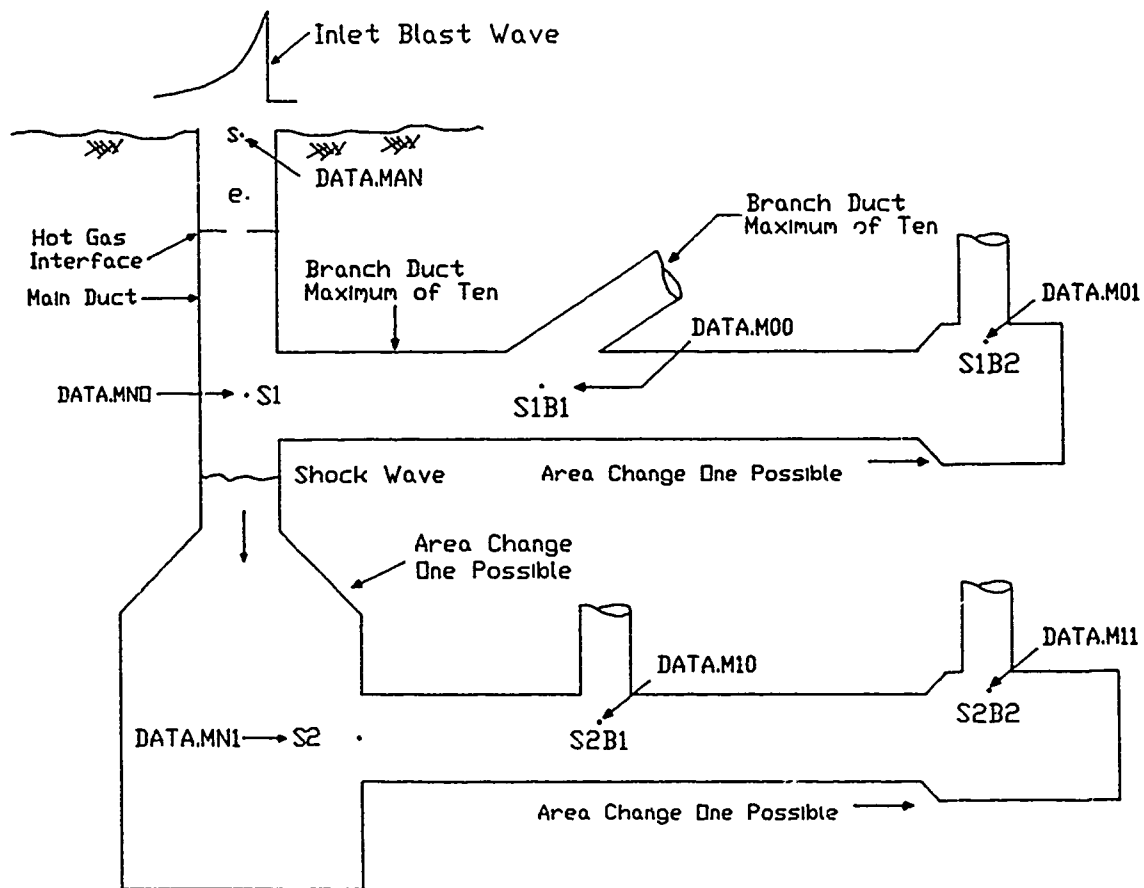


Figure 1. Sketch of an example ducting system.

The SPIDS Code was developed from the CEL Blast Wave Propagation Code for Air Ducts [3.] The CEL Code is a modification of the WUNDY Code for one-dimensional nuclear-explosion calculations [4,5,6,7], and the WUNDY Code evolved from the KO-Code of the University of California Radiation Laboratory.

A pre-processor microcomputer program is available which greatly simplifies the writing of an input file for SPIDS. A post-processing microcomputer program is also available which provides either spatial or temporal plotting of the SPIDS output variables such as pressure and temperature. The output can be plotted either on the microcomputer CRT or an external plotter. Both of these programs are written in Turbo Pascal language for an IBM-AT computer utilizing menu style programming.

COMPUTER PROGRAM SPIDS DESCRIPTION AND USE

The basic structure of the SPIDS computer code and the input and output variables are described below. Also presented are explanations of the various code options. The detail input and output variables and formats is given in Reference 1. The computer code is written in F77 Fortran and consists of a main control program with sixteen auxiliary subroutines. Table 1 is presented to outline the Code structure and provide the basic function of each subrouting.

TABLE 1. SPIDS Subroutine Structure.

<u>Subroutine Name</u>	<u>Function</u>
MAIN	Controls main logical flow and reads input data
BDY2	Specifies a rigid closed end at a duct exit
DATEXP	Specifies duct inlet losses using experimental data
EQST	Controls equation of state subroutine acquisition
EQS1	Equation of state for an ideal gas; $T < 1,000^{\circ}\text{K}$
EQS3	Equation of state for real air; $T < 24,000^{\circ}\text{K}$
GENR	Initializes problem; establishes zones in a duct and initial pressure, density, and velocity
GEOM	Calculates cross-sectional area and zone volume
HEBDY	Specifies motion of interface at duct inlet for a high explosive wave input
HTEMP	Calculates compressibility factor Z for real air
HYDR	Computes hydrodynamic motions for all zones in the duct
LINT	Interpolation subroutine; used when reading files as inputs to branch ducts
NUBDY	Specifies motion of interface at duct inlet for a nuclear wave input
OUT1	Prints overpressure, velocity, etc., in each zone in a duct at specific times; simplified printout or complete printout
OUT3	Prints time history of overpressure, velocity, etc., at up to ten locations in a duct; simplified printout or complete printout
REZEN1	Adjusts zones at duct entrance for mass inflow or outflow.
TIMEST	Calculates time step

The following Code characteristics are illustrated through Table 1: a duct inlet boundary condition can be the specification of either a nuclear shock wave or a high explosive shock wave; a duct exit boundary condition is always a rigid closed end; duct inlet losses are accounted for empirically, using experimental data [8,9] with junction types as shown in Fig. 2; equations of state for air can be for an ideal gas or for real air at temperatures to 24000 K; mass inflow or outflow is calculated at a duct entrance; flow variables such as pressure, temperature, and dynamic pressure are outputted for each finite difference zone at desired calculation cycles; and a time history of pressure, temperature, and dynamic pressure can be outputted at up to ten desired locations in a duct. The time history of pressure, temperature, and dynamic pressure can be written to a file at points in a duct where branch ducts are located; these files are then used to describe the input wave for the branch duct calculation.

The calculation of the propagation of a shock wave in a system of ducts is done sequentially. For example, considering a main air duct with one branch duct, the shock propagation in the main duct is calculated and the time history of pressure, temperature, and dynamic pressure is saved on a computer file at the location of this branch duct. This file then serves to specify the pressure, temperature and dynamic pressure at the inlet of the branch duct and the shock propagation in this branch duct can be calculated. This procedure can be used for any number of branches but only ten branches can be specified for any specific duct. This procedure poses some limitations in the SPIDS Code. For instance, reflected shock waves that propagate from a branch duct entrance back into a main duct cannot be accounted for; when using the code, one should therefore record the pressure time history at a branch duct entrance so that any significant reflected shock waves can be detected. In the case of blast shock waves in branch ducts, it is the author's experience that a reflection from a duct closed end is attenuated substantially by rarefaction and wall friction effects when the wave reaches the duct inlet; i.e., the reflected wave has usually a much lower overpressure than the initial shock wave. Another limitation also is that the losses of a shock wave as it passes by a branch duct is not accounted for which, of course, yields a conservative shock wave prediction; Reference 1 shows an approximate method for accounting for shock wave losses due to passing a branch junction for exponential waves.

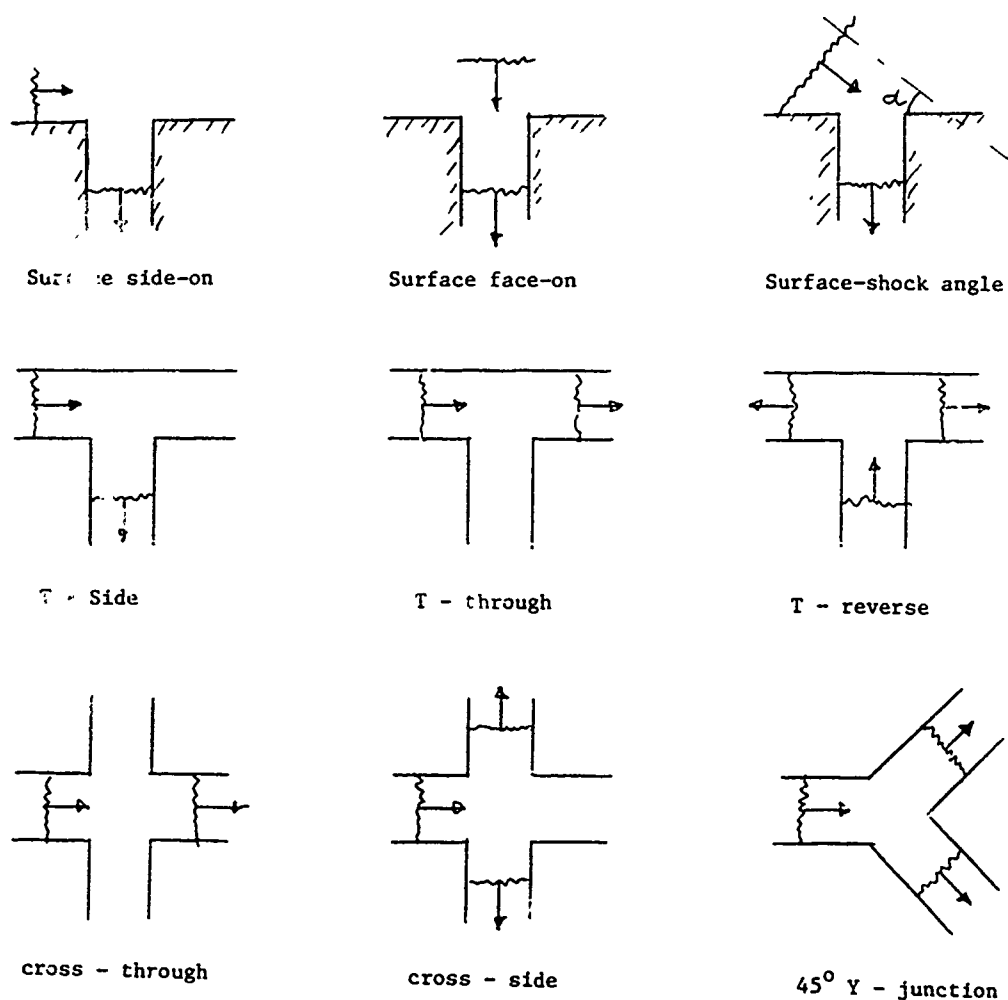


Figure 2. Duct Junction Types Included in SPIDS

A high explosive input wave is approximated by a step overpressure at the wave front followed by an exponential decay which can be with or without a negative phase. Inputting a series of five pressure waves is possible. The relationship that is used for the pressure wave is:

$$P_s = P_a + P_{so} e^{-B_1 \tau} (1 - A_1 \tau) \quad (1)$$

where

$$\tau = \frac{t}{D_p}$$

t = time

P_a = ambient pressure

D_p = duration of positive pressure phase

P_{so} = shock peak overpressure

A_1, B_1 = wave constants.

If the constant A_1 , is zero the wave will have no negative pressure phase, B_1 is taken as one, and D_p becomes the initial slope time intercept of the wave, t_i .

A series of five high explosive waves at a duct inlet are simulated as exponential waves described above with each separate shock wave starting at a specific but different time. The wave parameters P_{so} , D_p , and t_i , and the time the peak overpressure occurs at the duct inlet need to be known for each separate wave in the series of waves.

A classical nuclear blast wave at the inlet to a main duct can be specified in the form of Reference 10. Either a surface burst or an air burst at a given slant range can be specified [11]. The relationships for pressure, temperature, and dynamic pressure are given below.

$$P_s = P_a + P_{so} \left[A_1 e^{-B_1 \tau} + A_2 e^{-B_2 \tau} + A_3 e^{-B_3 \tau} \right] (1 - \tau) \quad (2)$$

where

$$\begin{aligned} \tau &= (t - t_s)/D_p \\ t &= \text{time from detonation} \\ t_s &= \text{shock arrival time} \\ D_p &= \text{duration of positive pressure phase} \\ P_{so} &= \text{shock peak overpressure at } t = t_s \end{aligned}$$

The quantities A_1 , A_2 , A_3 , B_1 , B_2 , and B_3 are constants for which values are given in References 10 and 11 for a one-megaton surface burst. In addition to a relationship for the surface pressure (P_s), relationships for the dynamic pressure (Q_s) and the temperature (T_s), are required.

$$Q_s = Q_{so} \left[A_4 e^{-B_4 \omega} + A_5 e^{-B_5 \omega} \right] (1 - \omega)^2 \quad (3)$$

$$T_s = T_{so} \left(\frac{t}{t_s} \right)^{B_6} \quad (4)$$

where

$$\begin{aligned} \omega &= (t - t_s)/D_u \\ D_u &= \text{duration of positive velocity phase} \\ Q_{so} &= \text{peak dynamic pressure at } t = t_s \\ T_{so} &= \text{shock temperature at } t = t_s \end{aligned}$$

The quantities A_4 , A_5 , B_4 , B_5 , and B_6 are constants for which values are obtained from References 10 and 11. For defining the temperature-time history using Equation (4), the parameters T_{so} and B_6 have different values for the time interval between t_s and the time when peak temperature is reached and the time interval after peak temperature. Equations 2, 3, and 4 completely define the dynamic and thermodynamic state of the air outside a duct inlet.

When using the computer code to predict wave propagation in a duct when a given time variant flow state is known at the inlet boundary to this duct, the time histories are provided in the code in the form of polynomials. Specifically, the pressure, the temperature, and the dynamic pressure are in the form

$$P_s = a_0 + a_1 t + a_2 t^2 + \dots + a_7 t^7 \quad (5)$$

$$T_s = b_0 + b_1 t + b_2 t^2 + \dots + b_7 t^7$$

$$Q_s = c_0 + c_1 t + c_2 t^2 + \dots + c_7 t^7$$

For this case, Equations 5 replace Equations 2, 3 and 4. The parameters a_0 through a_7 , b_0 through b_7 , and c_0 through c_7 are known constants.

Simulation of a duct entrance, such as the side-on type entrance shown in Figure 1, is achieved by evaluating the flow losses from point s to point e through the use of experimental data reported in Reference 8 and Reference 9. This flow loss is measured by the entropy increase from point s to point e . Assuming that the compressibility factor Z , gas constant R , and ratio of specific heats γ do not change significantly from point s to point e , this entropy can be expressed in terms of static variables as

$$S_e - S_s = ZR \ln \left[\left(\frac{T_e}{T_s} \right)^{\frac{\gamma}{\gamma-1}} \left(\frac{P_s}{P_e} \right) \right] \quad (6)$$

and this entropy change in terms of stagnation variables is

$$S_e - S_s = ZR \ln \left[\left(\frac{T_{te}}{T_{ts}} \right)^{\frac{\gamma}{\gamma-1}} \left(\frac{P_{ts}}{P_{te}} \right) \right] \quad (7)$$

In the above equation, P_s , P_e , T_s , and T_e are static temperatures and pressures at points s and e , respectively, and T_{ts} , P_{ts} , T_{te} , and P_{te} are stagnation temperatures and pressures. Equating relationships (Equations 6 and 7) yields a desired relation for the duct entrance static pressure, P_e , in the form

$$P_e = P_s \left(\frac{P_{te}}{P_{ts}} \right) \left[\left(\frac{T_e}{T_{te}} \right) \left(\frac{T_{ts}}{T_s} \right) \right]^{\frac{\gamma}{\gamma-1}} \quad (8)$$

In this relationship, γ is evaluated at point s . The stagnation pressure ratio can be expressed by the relation

$$\frac{P_{te}}{P_{ts}} = A(2) \exp (-2.3026 A(1) M_s) \quad (9)$$

where M_s is the flow Mach number at point s , and $A(1)$ and $A(2)$ are empirical constants determined from the experimental data of References 8 and Reference 9. A plot of this experimental data for the side-on entrance is shown in Figure 3, which shows the linear relationship between $\log (P_{te}/P_{ts})$ and M_s . The ratio T_{ts}/T_s in relation 8 is determined directly from M_s , which is known from the given flow state at point s . In order to determine the ratio T_e/T_{te} , the flow Mach number at point e , M_e , must be determined. The value of M_e is evaluated as a function of M_s , also from the data of References 8 and 9; therefore, T_e/T_{te} is also determined from the known value of M_s . The relationship between M_e and M_s is shown in Figure 4.

The value of the empirical constants $A(1)$ and $A(2)$ in Equation 9 depends upon the geometrical configuration at the duct entrance; e.g., a side-on entrance, a T-junction, or a Y-junction, etc.. Table 2 presents the values of $A(1)$ and $A(2)$ for the possible junctions as determined from data of References 8 and 9.

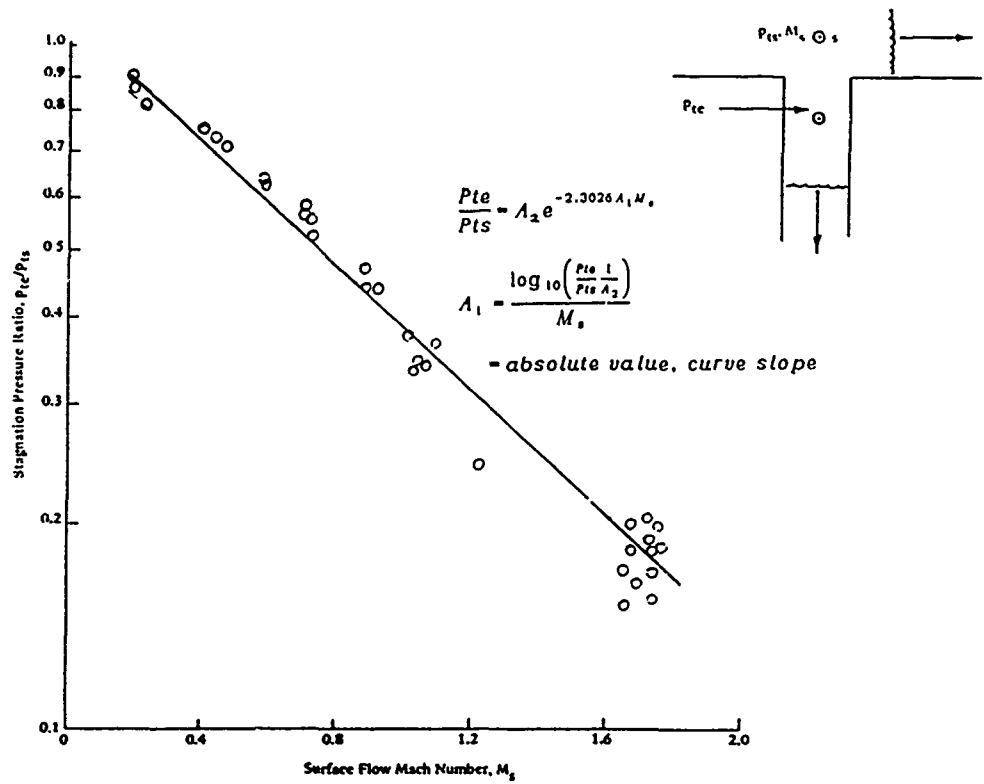


Figure 3. Stagnation pressure loss versus surface Mach number for side-on entrance.

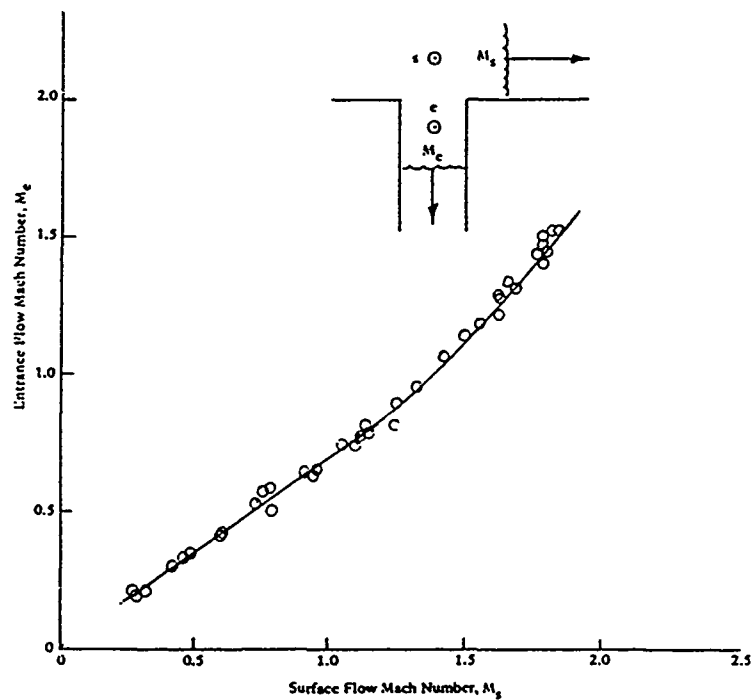


Figure 4. Surface flow Mach number versus entrance flow Mach number for side-on entrance.

Table 2. Duct Inlet Type and Parameters

Type of Inlet	Value of loss coefficient	
	A(1)	A(2)
No inlet loss	0.00	1.00
Surface side-on	0.495	1.24
Surface face-on	-0.0608	1.30
T-junction, side transmission	0.534	1.14
T-junction, through transmission	0.148	0.99
T-junction, reverse transmission	0.2475	1.07
45 Degree Y-junction	0.265	1.00
Cross-junction, side transmission	0.521	1.02
Cross-junction, through transmission	0.1129	0.93
Surface side-on, 50 deg. air burst	0.265	1.52
Surface side-on, 60 deg. air burst	0.221	1.61
Surface side-on, 70 deg. air burst	0.1477	1.61
Surface side-on, 80 deg. air burst	0.0521	1.56
Surface side-on, 90 deg. air burst (same as surface face-on)	-0.0608	1.30

Shock wave attenuation due to viscous friction at the walls of a duct is calculated by the SPIDS program. A friction factor for a smooth wall used in the calculations is determined by the flow state in each finite difference zone. The Reynolds number and Mach number is calculated in each zone and the friction factor for the zone is determined from the relations,

$$\begin{aligned} f &= C_1 (Re)^{N_1} \\ \text{for } M \leq 0.30, \text{ and} \\ f &= C_2 (Re M)^{N_2} \end{aligned} \quad (10)$$

for $M > 0.30$. The Reynolds number is defined as $Re = \rho Du / \mu$, where ρ is the air density, u is the flow particle velocity, μ is the absolute viscosity, and D is the duct diameter. The Mach number is defined as $M = u/c$, where c is the local acoustic velocity. The values of the coefficients C_1 and C_2 and the exponents N_1 and N_2 were determined by comparing the computer code pressure attenuation predictions to the experimental shock tube data reported in Reference 12 for smooth wall ducts. A comparison of the SPIDS code prediction of peaked shock wave attenuation with the experimental data is given in Figure 5. The calculated predictions show a small decrease in shock attenuation with increase in duct diameter when plotted nondimensionally. The experimental data shows a trend similar to this but the trend is not conclusive since enough data does not exist at the large values of the duct length. The values of C_1 , C_2 , N_1 , and N_2 that were determined as explained above are: for a shock overpressure less than 100 psi, $C_1 = C_2 = 0.2845$, $N_1 = -0.30$, and $N_2 = -0.2334$; for a shock overpressure greater than 100 psi and less than 300 psi, $C_1 = C_2 = 0.2845$, $N_1 = -0.25$, and $N_2 = -0.1946$; and for a shock overpressure greater than 300 psi, $C_1 = C_2 = 0.3414$, $N_1 = -0.25$, and $N_2 = -0.1946$.

A constant value of friction is used in the program for ducts with rough walls. The friction factor depends upon the roughness of the wall and is a function of the wall roughness ratio which is the ratio of average wall protrusion height to duct diameter, ϵ/D . There is considerable variation in the data for friction factors for rough wall ducts as can be seen in Figure 6. In References 6 and 7 it is shown that for a smooth wall duct a friction factor of $f = 0.016$ predicts shock attenuation for short ducts, so a value of $f = 0.016$ is taken on Figure 6 for $\epsilon/D = 0$. A linear curve then is assumed through this point and through the mean values of the data. The equation of this curve in terms of $\sqrt{\epsilon/D}$, which is the variable commonly used is

$$f_a = 0.016 + 0.00491 \sqrt{\epsilon/D} + 0.258 (\sqrt{\epsilon/D})^2 \quad (11)$$

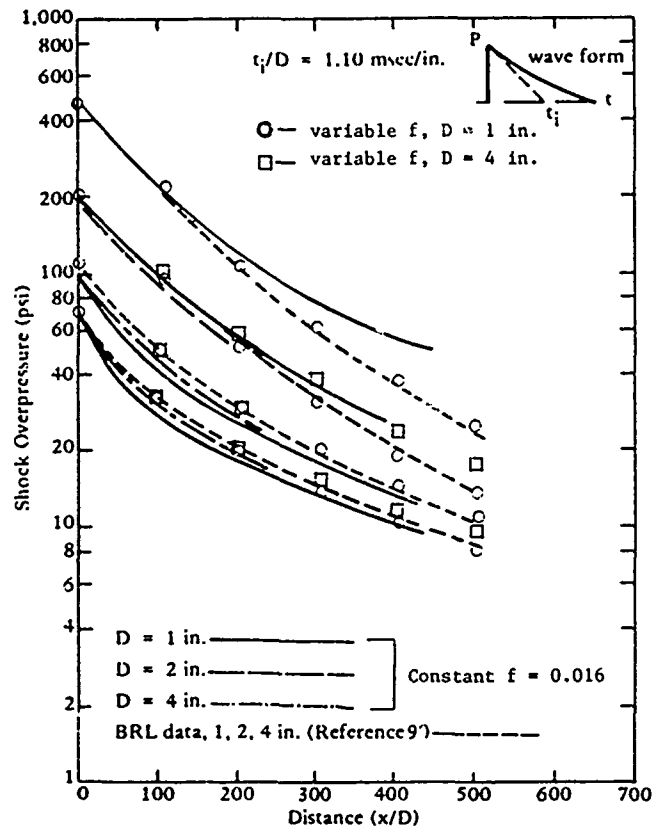


Figure 5. Shock wave attenuation, computed results compared with data; smooth wall.

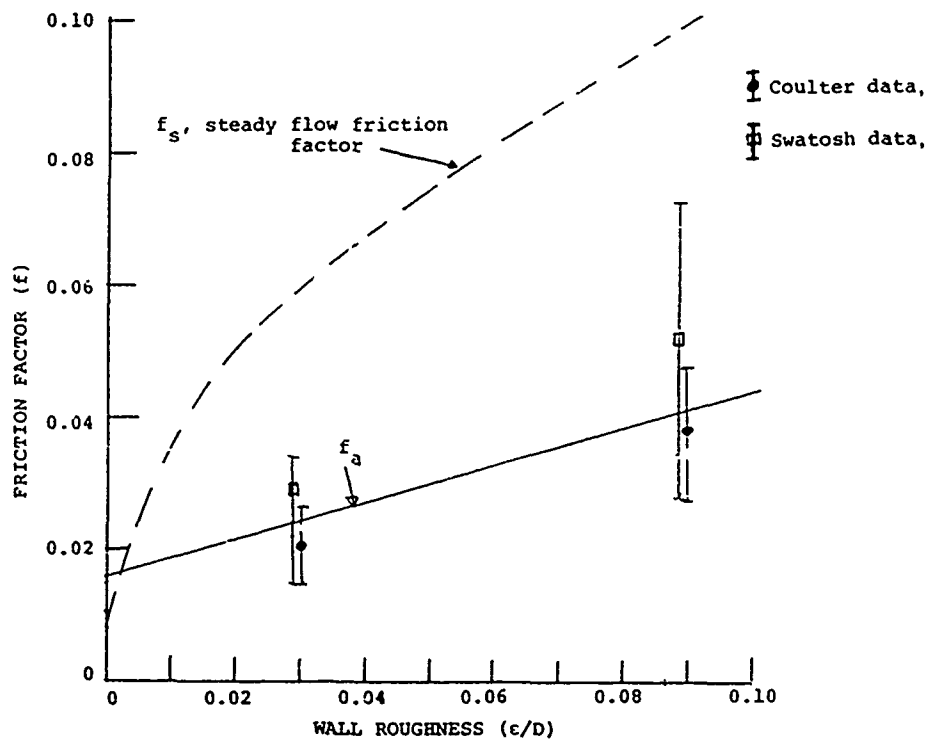


Figure 6. Friction factor f_a for shock wave attenuation; rough wall.

The SPIDS code will predict shock wave pressure change due to the change in the cross section area of a duct. A comparison of this prediction with experimental data for an area increase is presented in Fig. 7. The predictions are compared with shock tube data [15] and the full scale data of the DIAL PACK experiment where the wave source is a 500 ton TNT explosion [16]. This comparison shows that the code adequately predicts shock attenuation due to an area increase in a duct.

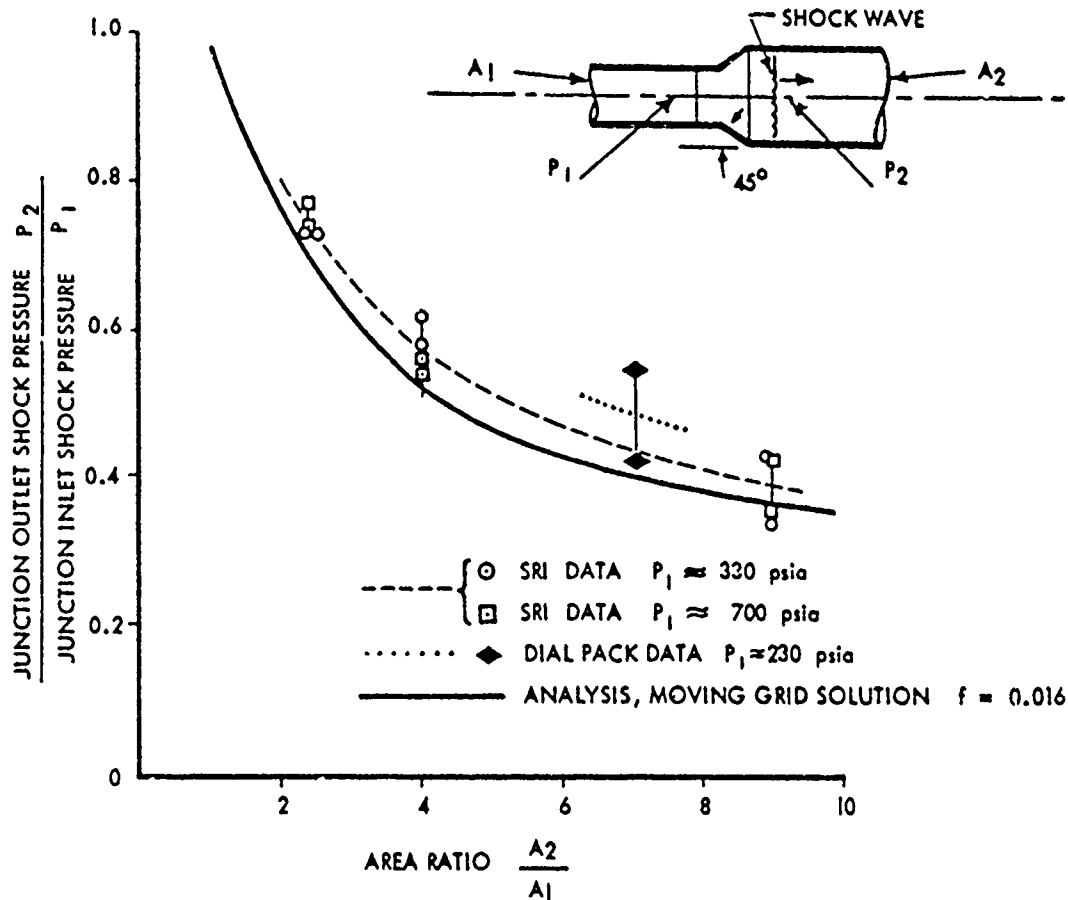


Figure 7. Effect of area change on shock pressure.

DESCRIPTION OF CALCULATION PROCEDURE

A description of the equations used in the SPIDS Code and of the calculation procedure is given in the following. The momentum equation is

$$\frac{\partial u}{\partial t} = -V \frac{\partial PQ}{\partial x} - \frac{f}{2D} u |u| \quad (12)$$

and the energy equation is

$$\frac{\partial e}{\partial t} = -PQ \frac{\partial V}{\partial t} + \frac{f}{2D} u^2 |u| \quad (13)$$

Where

P = pressure
Q = pseudo-viscosity
PQ = P + Q
u = particle velocity
e = internal energy per unit mass
V = specific volume
f = wall friction factor
D = duct diameter

The equation for conservation of mass is

$$\frac{\partial V}{\partial t} = V \frac{\partial u}{\partial x} + \frac{uV}{A} \left(\frac{\partial A}{\partial x} \right) \quad (14)$$

where A is the duct cross section area.

The system of equations is completed by the equation of state that, for the analysis presented here, takes the form

$$e = \frac{P}{\gamma - 1} V \quad (15)$$

where, in the above, γ is the adiabatic exponent for real air. For purposes of computation, Equations 12, 13, and 14 with the equation of state 15 are written in finite difference form utilizing the pseudo-viscosity method of shock wave treatment of Reference 2. The reader is referred to references 6 and 7 for these finite difference relations.

The pseudo-viscosity Q is introduced to remove the shock front discontinuity [2] and is defined as

$$Q = \frac{l_1^2}{V} \left(\frac{\partial V}{\partial t} \right)^2 + \frac{l_2 c}{V} \left(\frac{\partial V}{\partial t} \right) \quad (16)$$

where l_1 and l_2 are constants which affect the stability of the numerical calculation, and c is the local acoustic velocity. This pseudo-viscosity smears a shock wave front over about five finite difference zones without affecting the pressure rise across the shock wave. Q only has a value at a shock wave front and is a maximum value where the wave front is actually located; in the SPIDS post-processing program Q is called the shock location index and is plotted when shock front locations are desired.

MICROCOMPUTER BASED PRE-PROCESSOR AND POST-PROCESSOR PROGRAMS

Two microcomputer programs have been written to simplify and reduce the work required to utilize the SPIDS computer code when analyzing a problem concerned with shock wave propagation in ducts. A pre-processing program that generates the SPIDS input files and a post-processing program that creates plots from the a SPIDS output file are described in this section. Both of these programs are written in Turbo Pascal language and are compatible with an IBM-AT microcomputer. The pre-processing program is named SPIDS1 and the post-processing program is named SPIDS2. Both programs are written in an interactive menu style.

The SPIDS1 program generates an input file for computer code SPIDS. The program is divided into three primary operations: 1) problem editing, 2) microcomputer data file control, and 3) terminating or quitting the input data file program and return to the computer operating system. A 'pull down' menu is activated when one of the above selections is made. This program greatly simplifies the use of the SPIDS Code. All nuclear parameters of References 10 and 11 are 'built into' the program as well as the junction loss parameters. For illustration of SPIDS1 the wave selection screen is presented in Fig. 8 and the duct geometry selection screen is presented in Fig. 9.

Wave selection and edit					
Current wave type : High Explosive					
Wave	Arrival Time (msec)	Overpressure (psi)	Positive phase duration (msec) Initial Slope Time Intercept (msec)	Negative phase	Pressure shape
1	0.0	300.000	1.200	No	decaying
2	3.0	200.000	1.700	No	decaying
3	not used	0.000	0.000	No	decaying
4	not used	0.000	0.000	No	decaying
5	not used	0.000	0.000	No	decaying

Active Function Keys	
1:Abort 3:Exit 5:Help	9:Back 10:Forward

Shock Propagation in Ducting Systems - Input Program

Figure 8. Wave selection computer screen in SPIDS1.

The SPIDS2 program processes the output file of the computer code SPIDS. The program is divided into four primary operations: 1) Name file to process, 2) Plot on the computer screen, 3) plot on an external plotter, and 4) Quit and return to the operating system. A "pull down" menu is activated when one of the above selections is made. Overpressure, temperature, dynamic pressure, and impulse can be plotted versus location in a duct at given times, or versus time at given locations. The maximum value of these variables can be plotted versus location; also, the time these maximums occur can be plotted versus location. Seventeen plots in all are available.

Two curves or a single curve can be plotted on the computer screen. The curve options that are available are as follows: overpressure, temperature, dynamic pressure, and a shock location index versus time at given locations or versus location in the duct at given calculation cycles (or times); the impulse growth versus time at the given locations, which is on the same graph as overpressure when using a plotter; maximum values of overpressure, temperature, and dynamic pressure versus location in the duct for the time of the computation; the time the maximum values of overpressure, temperature, and dynamic pressure occur versus location (for shock arrival time); and the value of maximum impulse versus location and the inlet pressure versus time. Any of these curves can be plotted by an external plotter.

```

Duct selection - Total ducts: 1

Current branch : Main
Entrance       : Surface side-on           Altitude :      0.00
Length        : 100.00   Diameter :      2.00
Roughness     : 0.0000   Zones    :      100   Cycles   :      300
Taper Start   : 0.00     End      :      0.00   End Dia. :      2.00
Zone data stored every 30 cycles, format : simplified
Time data stored every 10 cycles, format : simplified
Branch point  Location      Type      Plot time history data
1             10.00         T - Side      Yes
2             20.00         No Junction    Yes
3             30.00         No Junction    Yes
4             40.00         No Junction    Yes
5             50.00         No Junction    Yes
6             60.00         No Junction    Yes
7             70.00         No Junction    Yes
8             80.00         No Junction    Yes
9             90.00         No Junction    Yes
10            95.00         No Junction    Yes

```

```

Active Function Keys
1:Abort 3:Exit 5:Help 6:Edit
Alt FN; Goto N

```

Shock Propagation in Ducting Systems - Input Program

Figure 9. Duct selection computer screen in SPIDS1.

CODE OUTPUT EXAMPLES

The capability of the SPIDS code is illustrated through two examples. One example is propagation of a shock wave in a typical air entrainment system; the shock wave is from a 1 - MT nuclear burst 1500 foot range from the inlet. The second example is the shock wave from a conventional high explosive propagating in a typical command center air intake shaft.

In Figure 10 is shown a typical air entrainment system of a hardened facility which displays the shock wave location 0.0063 seconds after arrival of a nuclear burst shock wave. The nuclear burst was a one megaton surface burst located 1500 feet from the system entrance. The shock wave locations and pressure rise are shown in the main duct and also in a branch duct. Also shown are the contact surfaces or cold-hot gas interfaces which show the penetration of hot gases into the system.

The second example is the prediction of shock wave propagation of a high explosive wave in a typical command center air intake shaft shown in Figure 11. The shock wave overpressure inside the system side-on entrance is 1650 psi and the wave initial slope time intercept is 0.287 milliseconds. Selected SPIDS output curves plotted using the SPIDS2 post-processing program are given in Figures 12, 13, 14 and 15. Figure 12 shows the pressure time history in the main duct at the location of the branch duct. The figure shows the initial shock wave and the shock wave reflection from the end of the main shaft. Figures 13 and 14 illustrate the pressure variation versus distance in the branch duct. Figure 13 is the pressure variation at a time of 23.5 msec. after shock arrival at the system inlet; the curve shows the initial shock wave and the main duct reflected wave. In Figure 14 is the pressure variation 12.6 msec. later which shows the reflected wave merging with the initial shock wave thus increasing the shock front overpressure. In Figure 15 is shown the pressure time history five feet from the end of the branch duct. This curve shows the initial shock wave pressure and the pressure of the wave reflected from the end of the branch duct; the initial shock overpressure is 34 psi and the reflected shock overpressure 97 psi.

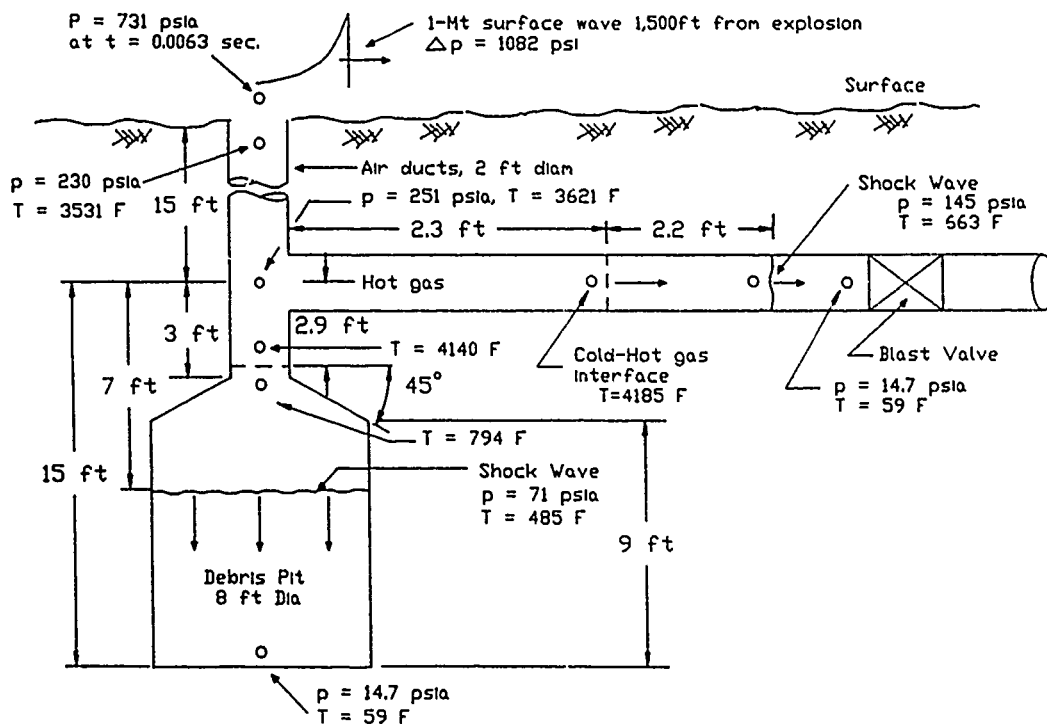


Figure 10. Computed results at 0.0063 seconds after nuclear shock wave arrival at air entrainment system entrance.

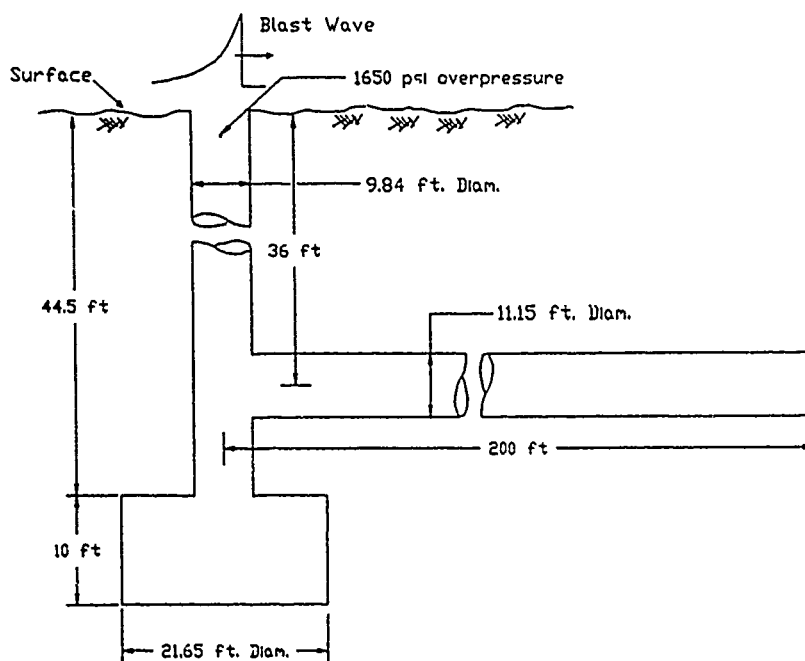


Figure 11. Typical command center air intake shaft.

TYPICAL COMMAND CENTER AIR INTAKE SHAFT. 1650 PSI INLET PRESSURE.
SHOCK ATTENUATION DOWN SHAFT & BRANCH TUNNEL.

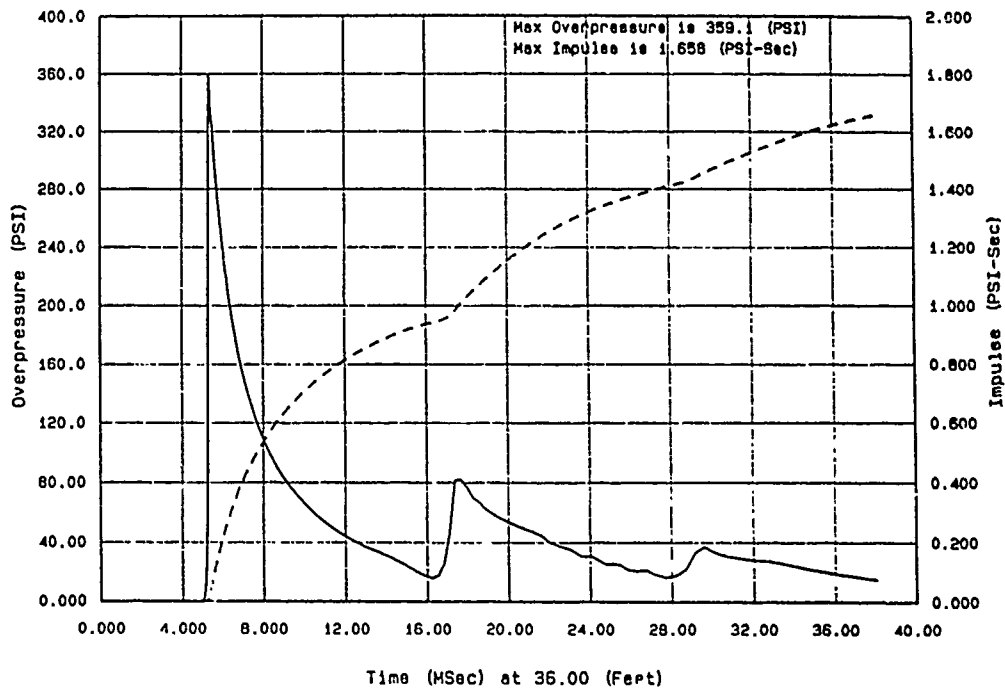


Figure 12. Pressure time history in main duct of air intake system at branch duct location.

TYPICAL COMMAND CENTER AIR INTAKE SHAFT. 1650 PSI INLET PRESSURE.
SHOCK ATTENUATION DOWN SHAFT & BRANCH TUNNEL.

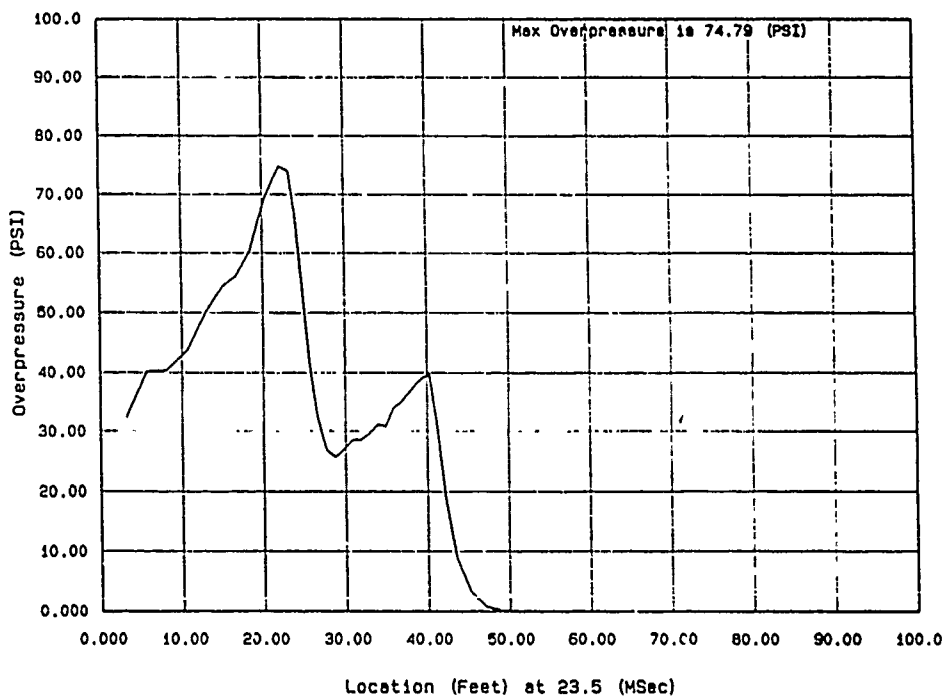


Figure 13. Pressure verses location in the branch duct of an air intake system 23.5 msec. after shock wave arrival.

TYPICAL COMMAND CENTER AIR INTAKE SHAFT. 1650 PSI INLET PRESSURE.
SHOCK ATTENUATION DOWN SHAFT & BRANCH TUNNEL.

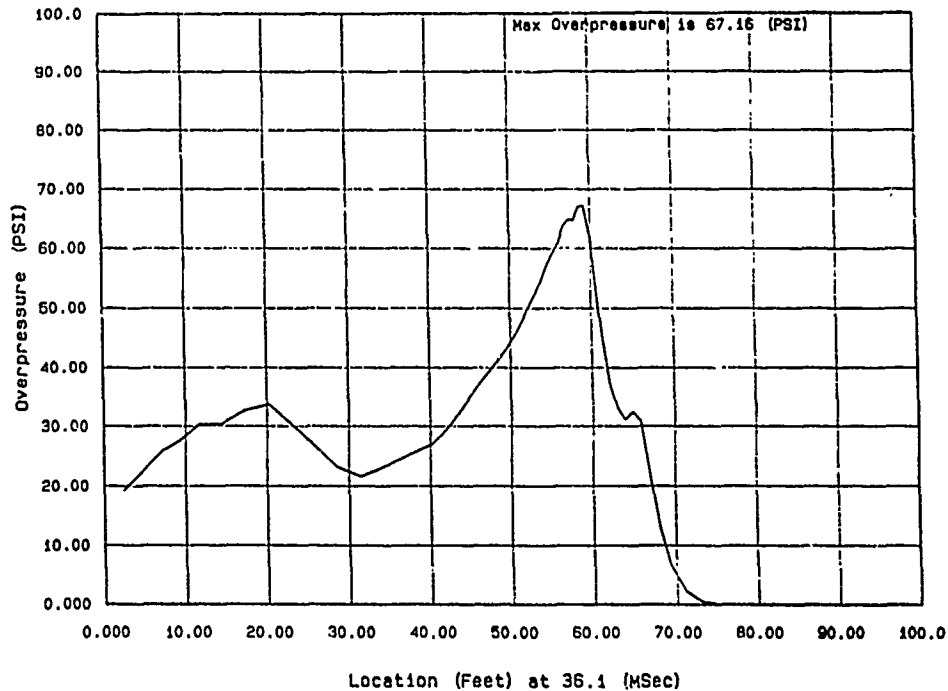


Figure 14. Pressure verses location in the branch duct of an air intake shaft; 36.1 msec. after shock wave arrival.

TYPICAL COMMAND CENTER AIR INTAKE SHAFT. 1650 PSI INLET PRESSURE.
SHOCK ATTENUATION DOWN SHAFT & BRANCH TUNNEL.

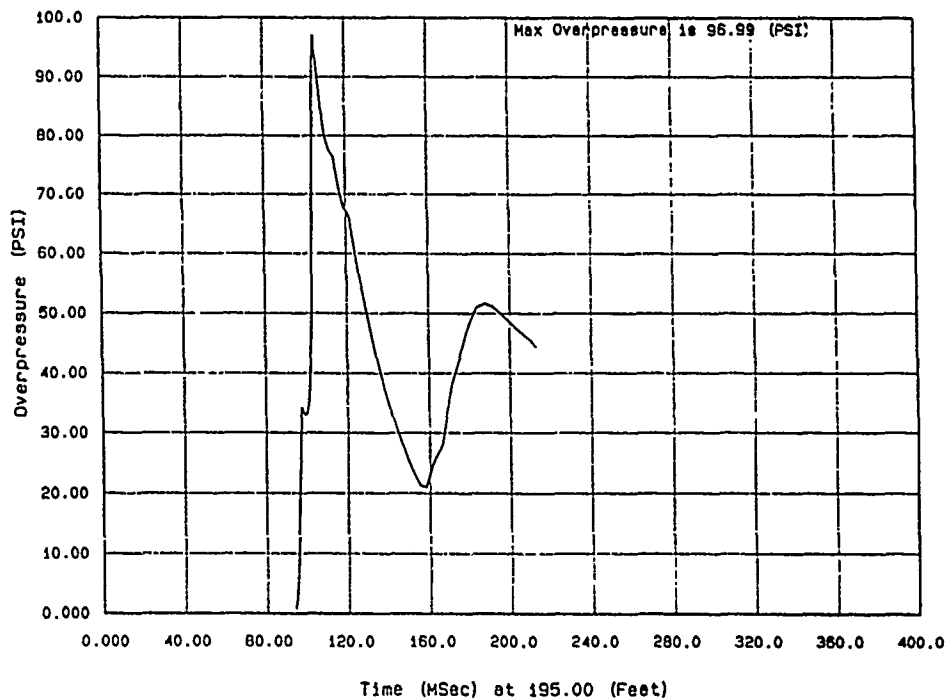


Figure 15. Pressure time history at the end of the branch duct of an air intake shaft.

CONCLUSIONS

The SPIDS computer code can be used to calculate the propagation of blast waves in systems of air ducts of constant or variable cross section. Branched ducts may be analyzed by sequential application to each branch. Peak overpressures of reflected waves which follow the primary wave in a branch are somewhat higher than the real case because some energy losses of the reflected wave at the branch inlet junction are neglected. However, all losses in the primary wave are included at a branch inlet. Blast wave attenuation due to friction is included through a variable wall friction factor with the friction factor relation determined through experimental data.

The computer code gives the air intake shaft or air entrainment system designer a means for estimating blast wave propagation in any duct system for blast waves generated either by nuclear or high explosive weapons or by explosion-driven blast waves from any cause where the incident waveforms can be described by up to three 7th-order polynomial equations for the pressure, the dynamic pressure, and the temperature. Use of the code has an advantage over empirical relations available because of the ability to calculate the propagation of shock wave reflections which can overtake and strengthen a primary shock front in a branch duct.

ACKNOWLEDGMENT

The development of computer code SPIDS was sponsored by the U.S. Army Corps of Engineers, Omaha District under contract numbers DACA4587PO153 and DACA4582M2881.

REFERENCES

1. R.H. Fashbaugh and J.W. Muran, "Shock Propagation in Ducting Systems," U.S. Army Corps of Engineers, Omaha District, contract report DACA4587PO153, Nov. 1987.
2. R.D. Richtmyer and K.W. Morton, Difference Methods for Initial-Value Problems, pp. 288-388, Interscience Publishers, 1957.
3. R.H. Fashbaugh and R.S. Chapler, "CEL Blast Wave Propagation Code For Air Ducts," CEL TN N-1543, Jan. 1979.
4. D. Lehto and M. Lutsky, "One Dimensional Hydrodynamic Code For Nuclear Explosion Calculations," NOL TR 62-168, Mar. 1965.
5. R.H. Fashbaugh and A. Widawsky, "Shock Wave Propagation Through Air Entrainment Systems-Phase I," NCEL TN-1205, Feb. 1972.
6. R.H. Fashbaugh and A. Widawsky, "On Difference Methods for Shock Wave Propagation in Variable Area Ducts Including Wall Friction," J. of Fluid Engineering, Transactions of ASME, pp. 327-332, June 1973.
7. R.H. Fashbaugh and A. Widawsky, "Nuclear Shock Wave Propagation Through Air Entrainment Systems of Hardened Facilities," CEL Technical Report R-820, April 1975.
8. Ballistic Research Laboratory Shock Tube Staff, "Information Summary of Blast Patterns in Tunnels and Chambers," BRL Memorandum Report No. 1390, Mar. 1962.
9. A.R. Kriebel et al., "Air Blast in Tunnels and Chambers," DASA 1200-II Supplement 1, Oct. 1972.
10. H.L. Brode, "A Review of Nuclear Explosion Phenomena Pertinent to Protective Construction," Rand Corp. Report No. R-425-PR, May 1964.
11. R.E. Crawford et al., "The Air Force Manual for Design and Analysis of Hardened Structures," AFWL-TR-74-102, Oct. 1974.

12. G.A. Coulter, "Attenuation of Peaked Air Shock Waves in Smooth Tunnels," BRL Memorandum Report No. 1809, Nov. 1966.
13. G.A. Coulter, "Attenuation of Shock Waves in Roughened Tunnels," BRL Memorandum Report No. 1903, Jan. 1968.
14. F.R. Gilmore, "Equilibrium Composition and Thermodynamic Properties of Air to 24,000 K," Rand Corp. Research Memorandum RM-1543, Aug. 1955.
15. H.R. Bredfeldt et al., "Measurement of Shock Wave Attenuation in Various Duct Components - Phase II and III," Stanford Research Institute Report No. C-0096, July 1968.
16. D.E. Williams and R.H. Fashbaugh, "High Explosive Field Test of a Hardened Air Entrainment System," NCEL Technical Note N-1181, Oct. 1971.

☆ U.S. GOVERNMENT PRINTING OFFICE: 1968-573-049/81005